TU Clausthal
Clausthal University of Technology

Thermo-Mechanical Behavior of a Zinc Die Casting Alloy Considering Natural Aging

Doctoral Thesis
(Dissertation)

to be awarded the degree of
Doctor of Engineering (Dr.-Ing.)

submitted by

Dipl.-Ing. Maria de los Angeles Martinez Page

from Murcia, Spain

approved by the Faculty of
Mathematics/Computer Science and Mechanical Engineering,
Clausthal University of Technology

Date of oral examination
14.10.2019

Dean
Prof. Dr.-Ing. Volker Wesling

Chairperson of the Board of Examiners
Prof. Dr.-Ing. Armin Lohrengel

Supervising tutor
Prof. Dr.-Ing. Stefan Hartmann

Reviewer
Prof. Dr.-Ing. Stefan Diebels

Vorwort und Danksagung

Die vorliegende Arbeit entstand während meiner Zeit als wissenschaftliche Mitarbeiterin am Institut für Technische Mechanik der TU Clausthal aus einer Kooperation mit der Firma Huf Hülsbeck & Fürst GmbH & Co. KG und wurde mit einem Projekt der Deutschen Forschungsgemeinschaft (DFG) fortgesetzt.

Da eine Arbeit dieses Umfangs nicht ohne die Hilfe von Anderen bewerkstelligt werden kann, möchte ich an dieser Stelle all diesen Personen danken, die maßgeblich zum Gelingen dieser Arbeit beigetragen haben.

Mein größter Dank gilt meinem Doktorvater Prof. Dr.-Ing. Stefan Hartmann für die Möglichkeit, meine Promotion in seiner Arbeitsgruppe durchführen zu können. Sein Verdienst liegt nicht nur in der sehr guten Betreuung meiner Arbeit, sondern vor allem bei meiner persönlichen Entwicklung und Lernerfahrung. Seine pragmatische Weise und seine hohen Ansprüche prägen nicht nur das Institut allgemein sondern mittlerweile auch mich selbst und ich bin sicher, dass ich bei meinen zukünftigen Tätigkeiten stets davon profitieren werde. Zudem gilt mein Dank auch Herrn Prof. Dr.-Ing. Stefan Diebels von der Universität des Saarlandes für die Übernahme des Zweitgutachtens meiner Arbeit. Für den Prüfungsvorstitzes von Prof. Dr.-Ing. Armin Lohrengel bedanke ich mich ebenfalls.

Für die vielfältige Kooperation bei verschiedenen Messungen möchte ich mich bei Herrn Dr.-Ing. Bernd Weidenfeller bedanken. Für weitere Messungen danke ich auch der Arbeitsgruppe von Prof. Dr.-Ing. Alexander Lion von der Universität der Bundeswehr in München.

Ein ganz besonderer Dank geht an meinen Freund Stephan Krämer für die moralische Unterstützung, die guten Ratschläge und die fachlichen Diskussionen.

Ein weiterer großer Dank gilt meinem Bürokollegen und guten Freund Rose Rogin Gilbert für die schöne Zeit während der Promotion, den fachlichen Austausch und die Diskussionen über Gott und die Welt. Außerdem möchte ich mich ganz herzlich bei Matthias Grafenhorst bedanken für die nicht selbsverständliche sehr gute Beratung in Bezug auf die Numerik und die ständige Unterstüzung am Institut, insbesondere in Bezug auf TASAFEM.

Ich möchte außerdem der Abteilung Festkörpermechanik einen sehr großen Dank aussprechen. Die äußerst freundliche und kooperative Atmosphäre hat den Abschluß dieser Arbeit überhaupt erst möglich gemacht. Daher geht ein großer zusätzlicher Dank an Chris Leistner, Jithin Mohan, Ali Kheirimarghzar, Pranav Kumar Dileep, Raad Al-Kinani, Steffen Rothe und Carmen Sguazzo.

Für die außergewöhnliche Hingabe und Aufmunterung möchte ich mich auch bei Frau Heidi Andresen bedanken, ihre freundliche und offene Art hat das Institut zu einem zweiten Zuhause für mich gemacht.

Darüber hinaus geht ein großer Dank an Laura Mignanelli, Sara Rayado Perez, Matthias Ruf, Jan Schlecht und Thorben Ziemer für die schöne gemeinsame Zeit in Clausthal, die ich nicht vergessen werde.

Zuletzt möchte ich mich bei meiner Mutter bedanken, da sie mir stets ein großes Vorbild war und mir immer wieder als Inspiration dient.

Esslingen am Neckar, Oktober 2019

Maria Angeles Martinez Page

Abstract

Nowadays, a main task in the production sector is the optimization of components and production processes in order to reduce costs and improve the quality of products. Numerical simulations have become a fundamental tool, as they allow the optimization even before the actual production starts. For the simulation of the mechanical behavior of component parts, an appropriate constitutive material model is necessary. Since material behavior is usually very complex, models are developed for a specific application area.

The zinc die casting alloy *Zamak 5* is widely used in the automotive industry because of its excellent castability and its good mechanical properties. However, it exhibits a complex thermo-mechanical behavior, which additionally changes gradually over the course of time. This effect is known as aging and is caused by microstructural changes such as diffusion, phase transformation and precipitation in the material. These processes are temperature activated.

This thesis proposes a material model of thermo-viscoplasticity with the goal of reproducing the thermo-mechanical behavior of the alloy Zamak 5 considering the influence of natural aging in finite element computations. This is performed on the basis of an extensive experimental campaign, in which the thermo-mechanical behavior is characterized with tension, compression and torsion tests at different loading conditions and for different aging times. The material shows a strong rate and temperature dependence and a moderate dependence on natural aging. Additionally, several thermo-physical properties which are necessary in the heat equation are also measured. Moreover, the microstructure of the alloy is investigated with a scanning electron microscope and X-ray diffractometry for different aging times in order to describe the microstructural processes which take place during aging.

At first, the material model is developed for the small deformation case since, in this case, the torsion tests can be considered as one-dimensional and purely deviatoric, which is advantageous during the identification process. Moreover, several temperature and aging dependent material functions are developed during the identification process. The model is extended later on to the finite strain case in order to be able to compute processes in which the strains are larger than 5%. The models are based on the additive decomposition of the strain tensor (for the small strain model) or multiplicative decomposition of the deformation gradient (for the finite strain model). In both cases, there is a component representing each of the different effects contained in the model: aging, temperature and rate-dependence. Furthermore, the total stress is decomposed into an equilibrium and an overstress part in order to identify them in a partitioned manner.

The model is implemented in the finite element code Abaqus. The behavior of the model is demonstrated using several simulation examples. Finally, simulations of a real component part (steering-wheel lock of a car), and a cylinder with a hole are compared with complex experiments in which inhomogeneous stress and strain states are reached for different loading conditions. With this information, the developed material model is validated.

Contents

1 Introduction

In the engineering world, numerical simulations are an extremely useful tool. They allow to design, analyze, and optimize all kind of components or processes – and the possibility to analyze the behavior of such processes is improved as well. As a consequence, there is an increase in the accuracy of the production process, and the production cost of the obtained products can be reduced enormously. In this work, a model of finite deformations of the zinc die casting alloy Zamak 5 is provided, which is supposed to be used in simulations of component parts made of this alloy. The model is based on an extensive experimental campaign, which enlarges the currently available knowledge of the thermo-mechanical behavior with the effect of natural aging of this alloy.[1]

1.1 Motivation

Around 13 million tons of zinc are produced annually worldwide, according to the International Zinc Association (IZA, 2018). From this amount, approximately $15\,\%$ is used for the production of zinc-based alloys, mainly in order to supply the die casting industry. Zinc die casting alloys can usually be found in components of mechanisms in cars and machines. On average, a car contains roughly $10\,\mathrm{kg}$ of zinc, and half of this amount is present in the form of zinc die casting components. Zinc die casting is also used in the electronic, construction and appliance industries, see (IZA, 2018; Leis and Kallien, 2011). The name Zamak denotes a family of zinc alloys with a constant amount of aluminum of 4% and, moreover, copper and magnesium as further alloying elements. A very small amount of other impurities is allowed as well. Zamak is produced with the so-called *hot-chamber die casting process*, in which the molten metal is injected into a reusable steel mold at high pressure. There are several aspects which make Zamak attractive to the industry in the scope of the production of component parts. The low melting point of the alloy and its extraordinary castability allow to produce a large number of components in one batch, with low production costs. Moreover, the material has very good mechanical properties compared to alternative materials in its application area, such as die casting aluminum or magnesium alloys, as well as injection molding polymers. The high density of the alloy can be compensated by producing thin compo-

---

[1] The first part of this project is connected to the interest of the industry – specifically the Huf Hülsbeck & Fürst GmbH & Co. KG – to obtain an accurate thermo-mechanical model of the alloy Zamak 5. It was partly financed by the Huf-group. The extension of the project to include the aging dependence was funded by the German Research Foundation DFG, with the project number DFG HA2024-18/1.

nent parts. A disadvantage is to be seen in the low melting point, which implies a strong viscoplastic behavior. The mechanical behavior is also affected by temperature changes. Creep occurs at loads higher than $50\,\mathrm{MPa}$. Moreover, the change of its microstructure over the course of time, which is known as *aging*, and the porosity – which affects die casting materials in general – are problems to be considered in the design process of components made of Zamak.

Since Zamak alloys are, from the point of view of Continuum Mechanics, hardly investigated, the goal of this work is to extend this field of knowledge by experimentally characterizing and modeling the thermo-mechanical behavior of the alloy Zamak 5, including the effect of aging. The effect of porosity is not included, since the project setup did not allow to obtain or produce specimens with a variety of controllable porosity levels. The experimental campaign itself involves a challenge due to its scale. Moreover, the modeling process is a challenging task as well. Experiments, modeling, and identification form an iterative process, see Fig. 1.1. The model is developed considering the behavior observed in the experiments. With this model, an identification of the material parameters is performed. Usually, the results of an identification process are not satisfactory or complete at first, so that the model has to be modified accordingly – and it can be necessary to conduct additional steps of identification for certain aspects of the model. In other cases, additional information might be needed for the development of the model or for the identification, which implies the necessity to perform additional experiments.

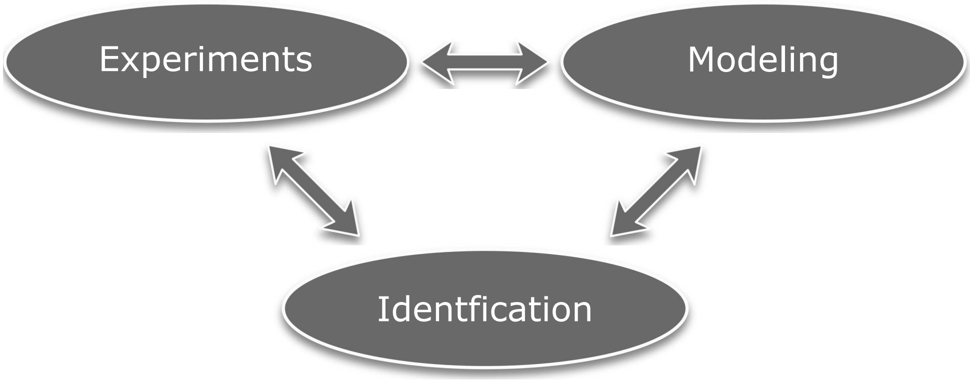

Figure 1.1: Representation of the modeling process

1.2 Literature Overview

Although zinc die casting alloys are known for their good castability, they are not yet as thoroughly investigated as other materials such as wrought aluminum alloys or steel. This is reflected in, for example, the annual world production of aluminum, which was five times higher than for zinc in 2016. In the literature, one can find several investigations from the point of view of Material Science, in which the microstructure is characterized for different zinc die casting alloys under different thermal conditions. From the point of view of Continuum Mechanics, there are currently almost no publications specifically related to Zamak alloys, apart from the publications of the author of this thesis.

The development of the properties and mechanical response of a material over the course of time due to microstructural changes is known as aging. In metals, these changes are due to precipitation of alloying elements or phases with low solubility, phase decomposition, and changes in the crystallographic structure. The diffusion processes in the microstructure are influenced by the temperature, which determines the rate of the aging process, see (Callister and Rethwisch, 2016). As mentioned in (Lion and Johlitz, 2012), in the field of polymers, aging is associated to physical or chemical changes. The aging of a component part can imply an overestimation (or underestimation) of its mechanical response, which can lead to failures. From the point of view of Material Science, the microstructural changes of zinc-aluminum alloys became subject of investigations in the last century. Gebhard (1940, 1941, 1942) investigated the micro-structure, phase transformations, and volume changes of the zinc-aluminum and zinc-aluminum-copper alloys over time. In (Johnen, 1981), general technical information about zinc die casting alloys is given. Additionally, the reduction of dimensions (shrinkage) in zinc die casting alloys over the course of time is described. The equilibrium phase diagram of zinc-aluminum alloys was investigated by Murray (1983), and their different crystal structures are described as well. In (Hänsel, 1988), one can find an analysis of the influence of the alloying elements on the mechanical properties – as well as studies focusing on other aspects such as the creep behavior, aging, the consequent volume changes, as well as inter-crystalline corrosion. Since the nineties, zinc die casting alloys became less popular, due of steel and aluminum alloys. In the past years, new investigations in this field started to appear again. At the beginning of the 21st century, phase transformations and precipitation of several Zn-Al alloys were extensively characterized in Zhu (2001, 2004), and Zhu et al. (2002, 2003a,b). Moreover, an exothermic reaction of Zn-Al alloys at early stages of aging is investigated in Zhu et al. (1999). The work of (Kallien and Busse, 2009; Leis and Kallien, 2011) covers a characterization of the influence of temperature, natural and artificial aging, the thickness-dependence of the specimen, and die casting conditions on several mechanical parameters such as the Young's modulus, yield strength, or tensile strength. Jareño et al. (2010) investigated the effects on the micro-structure of Zn–4Al–(3–5.6)Cu alloys both due to the amount of Cu as well as the cooling rate after casting. The phase decomposition of a supersaturated ZA27 alloy after a heat treatment and its effect on the mechanical properties is studied in Liu et al. (2013). More recently, the influence of the alloy components on the micro-structure and mechanical properties of several Zn–15Al alloys was investigated in (Savaskan and Pasa Hekimoglu, 2014). The effect of diluted Mg addition in the micro-structure and mechanical properties of the ZnAl4Cu1 alloy is characterized in (Wu et al., 2016). The aging behavior of the Zn15Al1Cu alloy was experimentally investigated in Pola et al. (2015) with the help of tensile tests and a micro-structural analysis.

With Zamak, it is possible to produce geometries with thicknesses between $0.3\,\mathrm{mm}$ and $6\,\mathrm{mm}$, see (ZD, 2019). Another characteristic of Zamak is the so-called size dependence, meaning that the mechanical response of the material is different for different thicknesses. The size-dependent mechanical behavior of zinc die casting alloys is investigated in (Gelfi et al., 2004; Leis and Kallien, 2011). Here, it is found that the specimen's thickness has an influence on mechanical parameters such as the overall elasticity modulus, the tensile strength, or the hardness. One possible cause of this effect could lie in the skin layer that is formed during the die casting process. It is about $100\,\mathrm{\mu m}$ thin and has a fine grain microstructure, see (Gelfi et al., 2004). This microstructure differs from the one in the bulk showing a coarse grain, which could be responsible for a different mechanical response. Another possible reason is the porosity of the specimens. Porosity is the most common defect of die casting materials, and it can have significant influence on different aspects of the mechanical behavior, see (Buffiere et al., 2001; Gutman et al., 1998) for aluminum and magnesium casting alloys. In (Martinez Page et al., 2018), a proposal for the thickness-dependent elastic behavior for Zamak is given. This model is based on the ideas proposed in (Steeb and Diebels, 2004), and also presented in (Diebels et al., 2005, 2007; Dippel et al., 2014; Johlitz et al., 2008a,b; Johlitz and Diebels, 2011b), for the case of polymers or (Diebels and Steeb, 2002) for the case of metal foams. In these works, the size effects are modeled with the help of an additional field variable. Since it was not possible to obtain specimens with different porosity levels in order to model and identify the effect of the thickness, this aspect could not be investigated further. Finally, in relation to Zamak, the recently published work (Korzeniowski and Weinberg, 2018) has to be mentioned, in which a Markov chain approach to damage evolution is presented.

Regarding the modeling of the aging effect in Continuum Mechanics, Krempl (1979) defines aging as a modification of the micro-structure, in such a way that the same loading process – performed in the same environment at different times (or ages of the material) – will lead to different mechanical responses. Based on this concept, Marquis and Lemaitre (1988) proposed a model coupling elasto-plasticity, damage and aging for small deformations. Additionally, a model for plasticity and aging is suggested in Marquis and Costa Mattos (1991). In these models, the effect of aging is included with a new internal variable. Non-metallic construction materials such as concrete represent another area of interest of aging effects. The viscoelasticity model proposed in Carol and Bazant (1993) accounts for aging of concrete in terms of an integral involving the relaxation function of the non-aging constituent and variable volume fraction of the solidified constituent. The three-dimensional multisurface viscoplasticity model proposed by (Meschke, 1996) is able to represent the time-dependent behavior of shotcrete. Here, the aging effects are modeled by an additional component of the strain tensor. Moreover, an integral form for aging viscoelasticity without internal variables is suggested in Bazant and Huet (1999) – and the problem of aging is treated for the case of polymers. Maghous and Creus (2003) proposed a homogenized thermoviscoelasticity model including aging effects. In (Diebels and Geringer, 2012), chemical aging is included in a model for adhesive bonds in a polymer using an additional field variable to describe the diffusive processes. Moreover, in (Johlitz, 2012), a model for small deformations with aging as an internal variable is developed. In (Johlitz and Lion, 2013; Johlitz and Diercks, 2014; Lion and Johlitz, 2012), a chemo-thermomechanical and a chemical aging model for elastomers for small deformations is suggested, and Dippel et al. (2014) offers a solution for polymer bonds at large deformations. In general, volume changes due to aging are not considered in the aforementioned models, and the tendency is to model the effect of aging with an internal variable. However, in the case of polymers, the use of a field variable in diffusion processes connected to aging is also a common option.

The thermo-mechanical coupled problem has been treated in a high amount of works and thermodynamical consistent modeling proposals for thermo-viscoplastic material behavior can be found in, for example (Lubliner, 1990; Lubarda, 2001; Haupt, 2002; Lemaitre and Chaboche, 1990). Regarding material modeling in thermo-mechanics, Chaboche (2008) offers an extensive overview of small-strain viscoplasticity models considering the thermo-mechanical coupling. In respect of the multiplicative decomposition of the deformation gradient in the finite strain case, in (Lion, 2000a), constitutive equations for finite thermo-viscoplasticity are deduced from rheological models. In this work, an additional multiplicative split of the deformation gradient is proposed in order to consider each physical effect included in the model. The equivalence between the two possible decompositions of the deformation gradient is shown in (Hartmann, 2012). On the other side, a framework for the description of elasto-plastic materials is given in (Bertram, 2003), which is based on the notion of isomorphic thermoelastic ranges instead of the multiplicative decomposition of the deformation gradient. In the field of thermo-viscoplasticity of metals, one can find many different proposals for aluminum alloys and steel, but – to the author's best knowledge – there are no proposals for the quasi-static behavior of Zamak, see the literature review offered in (Martinez Page and Hartmann, 2018b). Investigations in the field of thermo-elasticity and thermo-viscoelasticity can be found in (Miehe, 1988; Lion, 2000b; Reese, 2001). An extensive literature review for the coupled thermo-viscoelastic problem for polymers is offered in (Hamkar, 2013) and for the case of thermo-viscoplasticity for steel see also (Quint, 2012).

Since the experimental data currently available in the literature is insufficient for a full characterization of Zamak 5, one of the goals of this thesis is to provide an experimental characterization. Moreover, a new model of thermo-viscoplacity is developed, which is able to reproduce the observed experimental behavior. The results of several publications are used for the development of this thesis, see (Martinez Page and Hartmann, 2018b,a; Martinez Page et al., 2018, 2019).

1.3 Scope of the Thesis

The objective of this work is the development of a constitutive model for the alloy Zamak 5, in which the rate dependence, temperature dependence, and the effect of natural aging are included. To this end, all aspects that are to be modeled need to be characterized experimentally. Since the number of investigations on zinc die casting alloys during the last century is quite small, compared to aluminum alloys or steel, there is little accurate information regarding the thermo-mechanical behavior of this material available at the moment. The mechanical characterization requires tests in which the volumetric and deviatoric behavior are considered. This characterization is performed with tension, compression, and torsion tests at different strain-rates with a thin-walled cylindrical tube. The temperature-dependent mechanical response is included by performing the experiments at different temperatures. Analogously, for the aging dependence, the tests are also performed for each temperature at different natural aging times. This extensive experimental campaign, which includes around 450 single tests, characterizes a broad spectrum of the mechanical behavior of the alloy Zamak 5, which has not been done so far. Furthermore, several physical properties such as the thermal expansion, the shrinkage caused by aging, the thermal conductivity, and the specific heat capacity are measured. The thermal expansion and shrinkage are necessary in order to model the mechanical response. Additionally, the shrinkage experiments are used as a basis for the description of the aging development over time. With them, an aging variable is motivated, which is later on included in the model as an internal variable to describe the influence of aging. The experimental campaign is finished with experiments in more complex geometries in which the stress and strain state are not homogeneous. These tests are used to validate the constitutive model.

Based on the information obtained from the experiments, a thermodynamical consistent finite strain model is developed. The modeling process is closely connected to the identification, forming an iterative process in which an assumption is developed for the modeling, and the suitability of this assumption is verified in the identification process. If the assumption turns out to be inadequate, the model is changed and the process is repeated until an appropriate response is obtained.

After that, the material model is implemented in the commercial finite element software Abaqus. Since the documentation of Abaqus does not provide an in-depth description of the equations of its code, the general numerical solution of the resulting thermo-mechanical coupled problem with the Finite Element Method is exposed in detail. The behavior of the model is shown for three numerical examples. In the last one, the behavior of the model is validated with the previously performed experiments.

1.4 Structure of the Thesis

This thesis is divided into eight chapters. Chapter 2 provides the theoretical fundamentals of Continuum Mechanics, which are necessary to understand the derivations performed in the following chapters. First, the kinematics are discussed, including basic definitions of material body, configuration, and motion – and strain and strain-rate tensors, stress tensors, and heat flux are introduced. Moreover, the thermo-mechanical balance equations are derived. In the last section, general considerations for material modeling are given.

All aspects related to the experimental campaign are covered in Chapter 3. To begin with, a brief introduction to the die casting process is given, followed by further information regarding the specimens used for the material characterization, such as composition and dimensions. Important aspects concerning the experimental setup of the thermo-mechanical experiments and data evaluation of the experimental results are discussed. This is followed by a description and the results of the different experiments. For the thermo-mechanical experiments, the results are given in the order of consideration for the modeling. First, the basic rate-dependent mechanical behavior is characterized with experiments at room temperature. The characterization of the equilibrium state is exposed, with the main difficulty that the relaxation needs several days to reach a saturation value. Moreover, the temperature-dependent and aging-dependent results are given, while the results of the thermo-physical properties are discussed in the next section. Since the thermal diffusivity shows a dependence of the aging state, the microstructure is investigated in order to get a better understanding of the effects of aging. The chapter ends with the validation experiments with two different geometries. The first one is a completely aged complex geometry with a real application in the steering-wheel of a car. Here, the temperature and rate dependence are investigated. The aging dependence is tested in a cylinder with a hole.

Chapter 4 discusses the constitutive model. First, an overview of the modeling possibilities is given, motivated by the experimental observations of Chapter 2. The modeling is first performed for the small deformations case. Since this case is simpler than finite deformations, it is easier to derive the equations for the different effects. Also, the connection with the identification is more simple in this case, since the problem of torsion of a thin-walled cylinder is one-dimensional. The possibility of one-dimensional purely deviatoric considerations is advantageous for a first approach of the model. After that, a generalization for the finite deformations case is carried out. In both cases, the derivations of the constitutive equations are based on the thermodynamical consistency of the model, which is provided as well. The model of finite deformations is motivated by the multiplicative decomposition of the deformation gradient in four components, which cover the different effects of the model. At the end of the chapter, the heat conduction equation is treated. This leads to the evaluation of the thermo-physical properties, which have to be modeled as well.

The parameter identification is treated in Chapter 5. Here, basic definitions and concepts of the identification problem are introduced. Due to the complexity of the identification, an overview of the identification process is provided, in which the results of the roughly 450 experiments[2] plus the measurements of the thermal properties are used to identify 31 material parameters, which describe seven different effects in the model: rate, temperature and aging dependence, thermal expansion, shrinkage, specific heat capacity, and aging-dependent thermal conductivity. The details of the identification are provided first for the small deformations model and then for the model of finite deformations. For the last one, the bulk modulus is extrapolated from the small deformations case.

Chapter 6 has two main sections. The first one covers the entire aspect of the initial boundary value coupled thermo-mechanical problem, which is first expressed in its local form and then converted into its variational form. The second part covers the treatment of the numerical solution of the variational formulation of the problem with the Finite Element Method. The solution is given for the h-version of finite elements and a monolithic approach. Due to the fact that in Abaqus the Backward Euler method is used for the time integration, this method is presented. The resulting system of non-linear equations is solved with the Newton-Rhapson method for the small deformations case, since the value of all internal variables at the current time step can be computed directly with the information from the last time step, without the necessity of a local Newton-Raphson method. This is not the case for the model of finite deformations, so the Multilevel Newton Algorithm has to be applied. The stress algorithm is provided for the local level, as well as necessary information for the computation of the consistent tangent.

The behavior of the model is demonstrated in Chapter 7, with three different examples. In the first one, the stiffness of the system of differential equations composed by the evolution equations of the internal variables is investigated, since the rate at which the aging variable develops is generally much slower than the mechanical effects. The second example covers the behavior of the aging in a process at different time scales for the mechanical processes and temperature changes. The last example aims to validate the developed model by comparing simulations with the experimentally measured response of more complex geometries.

Finally, in Chapter 8, a summary and conclusions about the presented investigations are discussed, followed by an outlook regarding possible future work in this area.

---

[2] For the experiments with several repetitions, the average value is determined and used in the identification.

2 Fundamentals of Continuum Mechanics

The aim of this chapter is to introduce general concepts of Continuum Mechanics, which are needed to develop the constitutive model in Chapter 4, and the balance equations which will compose the initial boundary value problem in Chapter 6. The theory illustrated in this chapter is based mainly on the works of Haupt (2002), Truesdell and Noll (2004), Altenbach (2015), Becker and Bürger (1975), Holzapfel (2000), Lubarda (2001), and Malvern (1969).

The foundations of Continuum Mechanics lie in the assumption that matter is distributed continuously in space. In order to describe the motion and deformation of a material body under the influence of external loads, there are three main statements that have to be considered, see Haupt (2002). On the one hand, there are the kinematics and balance equations – which are known as general statements, since they are considered as universal laws of nature which are valid to all material systems. On the other hand, individual statements which refer to particular material properties are necessary.

Kinematics describes the geometry of motion and deformation of a material body without considering the cause of such motion. The concept of balance equations is founded on the free body principle, according to which, in mechanics, the effect of the surroundings of a body can be represented by means of volume and surface forces – or by heat flux in thermo-mechanical problems. For each particular material behavior, material equations provide a connection between the kinematic quantities and the quantities appearing in the balance equations.

In this chapter, the kinematics are treated first, including an introduction to the fundamental concepts of the motion and deformation of a material body, such as configuration, deformation gradient, or strain measures. After that, the concept of stress and heat flux is developed. The subsequent section addresses the balance equations of mass, linear and angular momentum, as well as the laws of thermodynamics. Finally, in order to connect the effect of stresses to the deformation of the material body, a material model is needed. It will be provided in Chapter 4. The last section of this chapter serves to introduce several common principles that are generally accepted in material modeling.

2.1 Kinematics

In this section, the concepts of material body, configuration, and motion are explained. Moreover, the deformation gradient is introduced and, with it, the definition of various strain tensors. In the last part of this section, strain-rate tensors are treated.

2.1.1 Material Body, Configuration and Motion

The goal of Continuum Mechanics is to describe the deformation of material bodies. The first question that has to be clarified is the concept of a material body itself. A material body in the sense of Continuum Mechanics represents a region of the space in which matter is distributed continuously. It consists of a set of material points $\mathcal{B} = \{\mathcal{P}\}$, with the following properties:

1. There is a set $\mathcal{K} = \{\mathcal{P}\}$ of one-to-one mappings
$$\chi : \begin{cases} \mathcal{B} \to \chi[\mathcal{B}] \subset \mathbb{R}^3 \\ \mathcal{P} \to \chi(x_1, x_2, x_3) \Leftrightarrow \mathcal{P} = \chi^{-1}(x_1, x_2, x_3) \end{cases} \tag{2.1}$$
where every mapping $\chi \in \mathcal{K}$ is called *configuration*.

2. If χ_1 and χ_2 are two configurations, then their composition
$$\chi_2 \circ \chi_1^{-1} : \begin{cases} \chi_1[\mathcal{B}] & \to \chi_2[\mathcal{B}] \\ (x_1, x_2, x_3) & \to (y_1, y_2, y_3) = \chi_2(\chi^{-1}(x_1, x_2, x_3)) \end{cases} \tag{2.2}$$
is continuously differentiable.

The first condition guarantees that each material point occupies only one point of space that is not shared by any other material point. The second one ensures that two neighboring material points remain neighbors. In order to obtain a time-independent reference for the motion of the material body, a *reference configuration* $\mathcal{R}(\mathcal{P})$ is chosen. With this configuration, the material points $\mathcal{P} \in \mathcal{B}$ are uniquely assigned to a spatial point

$$(X_1, X_2, X_3) = \mathcal{R}(\mathcal{P}) \Leftrightarrow \mathcal{P} = \mathcal{R}^{-1}(X_1, X_2, X_3), \tag{2.3}$$

which commonly represents the initial position of a material point, with the number triplet (X_1, X_2, X_3) as its initial coordinates, see Fig. 2.1. The motion of a material point is defined by the continuous sequence of current configurations $\chi_t(\mathcal{P})$, which for each time t corresponds to the position vector $\vec{x} \in \mathbb{V}^3$,

$$\vec{x} = \vec{\chi}_t(\mathcal{P}) \Leftrightarrow \mathcal{R} = \vec{\chi}_t^{\,-1}(\vec{x}). \tag{2.4}$$

The time-dependent configuration $\vec{\chi}_t$ is called *current configuration*, which can be identified with the number triplet (x_1, x_2, x_3). A representation of the motion of the material

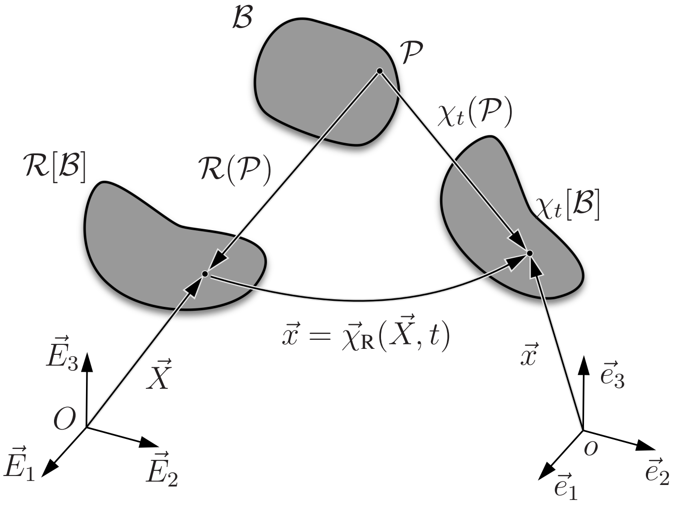

Figure 2.1: Representation of the reference and current configurations

point in dependence of the position vector of the reference configuration $\vec{X}$ and the time t as parameters can be obtained through the mapping

$$\vec{x} = \vec{\chi}_t(\mathcal{R}^{-1}(\vec{X})) = \vec{\chi}_{\mathrm{R}}(\vec{X}, t). \tag{2.5}$$

The number triplets (X_1, X_2, X_3) and (x_1, x_2, x_3) can be interpreted as coordinates of the material point $\mathcal{P}$ in the three-dimensional euclidean space $\mathbb{E}^3$, referring to the coordinate systems with the origins O in the reference and o in the current configuration, respectively, and a frame of reference of vectors $\vec{E}_i$ and $\vec{e}_i$, $i = 1, 2, 3$. For the sake of simplicity, the same coordinate system is used for both configurations in the following, which means that $\vec{e}_i = \vec{E}_i$. The motion of a material body involves two aspects: the displacement of the points and its deformation. The displacement of a material point $\vec{u}$ is defined as the difference between its position vectors in the current configuration $\vec{x}$ and the reference configuration $\vec{X}$, see Fig. 2.2,

$$\vec{u}(\vec{X}, t) = \vec{x} - \vec{X} = \vec{\chi}_{\mathrm{R}}(\vec{X}, t) - \vec{X}. \tag{2.6}$$

In order to describe the deformation of the material body, the deformation gradient is introduced

$$\mathbf{F}(\vec{X}, t) = \operatorname{Grad} \vec{\chi}_{\mathrm{R}}(\vec{X}, t) = \frac{\partial \vec{\chi}_{\mathrm{R}}(\vec{X}, t)}{\partial \vec{X}}. \tag{2.7}$$

The deformation gradient is an asymmetric second-order tensor, which serves to locally characterize the motion of the material body. In general, it is assumed that $\det \mathbf{F} > 0$. The deformation gradient $\mathbf{F}$ and the displacement $\vec{u}$ are related to each other through the expression

$$\mathbf{F} = \mathbf{I} + \mathbf{H}, \tag{2.8}$$

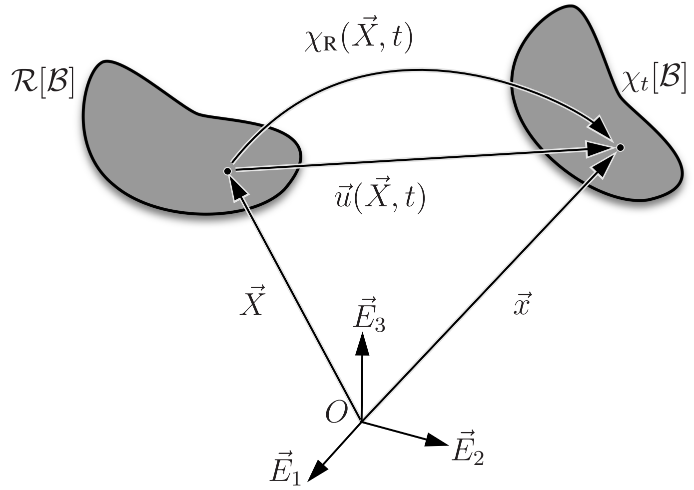

Figure 2.2: Displacement vector

where $\mathbf{H}(\vec{X},t) = \mathrm{Grad}\,\vec{u}(\vec{X},t)$ represents the displacement gradient and **I** is the second-order unity tensor. The concept of the deformation gradient can be understood considering a smooth curve composed of a set of points of the material body, parametrized by α

$$\alpha \to \vec{C}(\alpha), \quad \text{with} \quad \vec{C}(\alpha_0) = \vec{X}, \tag{2.9}$$

also called material lines, see Fig. 2.3. The material line in the current configuration is obtained with the help of the mapping $\vec{\chi}_{\mathrm{R}}$

$$\alpha \to \vec{x} = \vec{c}(\alpha) = \vec{\chi}_{\mathrm{R}}(\vec{C}(\alpha),t), \quad \text{with} \quad \vec{c}(\alpha_0) = \vec{x}. \tag{2.10}$$

Computing the Fréchet derivatives of expressions Eq. (2.9) and (2.10) and considering the chain rule, one obtains

$$\mathrm{d}\vec{X} = \frac{\mathrm{d}}{\mathrm{d}\alpha}\vec{C}(\alpha)\mathrm{d}\alpha|_{\alpha=\alpha_0} = C'(\alpha_0)\mathrm{d}\alpha, \tag{2.11}$$

$$\mathrm{d}\vec{x} = \mathrm{Grad}\,\chi_{\mathrm{R}}(\vec{X},t)|_{\vec{X}=\vec{C}(\alpha_0)}\vec{C}'(\alpha_0)\mathrm{d}\alpha = \vec{c}\,'(\alpha_0)\mathrm{d}\alpha. \tag{2.12}$$

The derivatives $\mathrm{d}\vec{X}$ and $\mathrm{d}\vec{x}$ represent tangent vectors to the material lines at α_0 in the reference and current configuration, respectively, and are called *material line element* in the reference and current configuration. Since they are equal to

$$\mathrm{d}\vec{X} = \vec{C}'(\alpha_0)\mathrm{d}\alpha \quad \text{and} \quad \mathrm{d}\vec{x} = \mathbf{F}\,\vec{C}\,'(\alpha_0)\mathrm{d}\alpha, \tag{2.13}$$

the deformation gradient can be interpreted as the mapping from the material line elements in the reference configuration to the current configuration, see Fig. 2.3,

$$\mathrm{d}\vec{x} = \mathbf{F}\mathrm{d}\vec{X}. \tag{2.14}$$

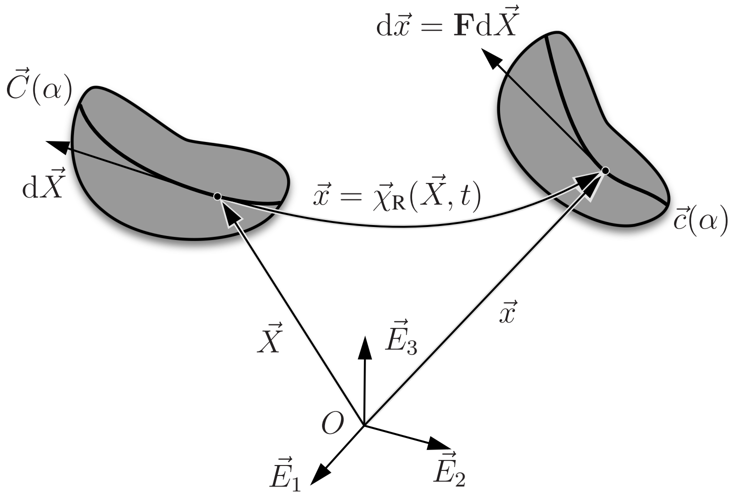

Figure 2.3: Transformation of material line elements by the deformation gradient

The concept described in relation (2.14) for the material line element can be extended to the case of a material surface element defined through two material line elements $(\mathrm{d}\vec{X}_1, \mathrm{d}\vec{X}_2)$ in the reference and $(\mathrm{d}\vec{x}_1, \mathrm{d}\vec{x}_2)$ in the current configuration

$$\mathrm{d}\vec{a} = (\det \mathbf{F})\mathbf{F}^{-\mathrm{T}}\mathrm{d}\vec{A}, \tag{2.15}$$

with $\mathrm{d}\vec{A} = \mathrm{d}\vec{X}_1 \times \mathrm{d}\vec{X}_2$ and $\mathrm{d}\vec{a} = \mathrm{d}\vec{x}_1 \times \mathrm{d}\vec{x}_2$, and a material volume element

$$\mathrm{d}v = (\det \mathbf{F})\mathrm{d}V, \tag{2.16}$$

with $\mathrm{d}V = (\mathrm{d}\vec{X}_1 \times \mathrm{d}\vec{X}_2) \cdot \mathrm{d}\vec{X}_3$ in the reference and $\mathrm{d}v = (\mathrm{d}\vec{x}_1 \times \mathrm{d}\vec{x}_2) \cdot \mathrm{d}\vec{x}_3$ the current configuration.

The deformation gradient has the disadvantage that it does not vanish for rigid body motions, which is why it is not suitable to describe the deformation of a body directly. However, it can be multiplicatively decomposed into an orthogonal tensor $\mathbf{R}$ and a symmetric positive definite tensor $\mathbf{U}$ or $\mathbf{V}$, also known as right and left stretch tensors

$$\mathbf{F} = \mathbf{R}\mathbf{U} = \mathbf{V}\mathbf{R}. \tag{2.17}$$

This is called polar decomposition and can be interpreted as a decomposition of the local deformation into a pure rotation $\mathbf{R}$ and a pure stretch $\mathbf{U}$ or $\mathbf{V}$. Moreover, the following relations hold

$$\mathbf{U}^2 = \mathbf{C} = \mathbf{F}^{\mathrm{T}}\mathbf{F}, \tag{2.18}$$

$$\mathbf{V}^2 = \mathbf{B} = \mathbf{F}\mathbf{F}^{\mathrm{T}}. \tag{2.19}$$

The tensors $\mathbf{C}$ and $\mathbf{B}$ are known as *right and left Cauchy-Green tensors*. They are symmetric positive definite[1] tensors, and they will be used to describe the strain measures in the following section.

---

[1] A symmetric tensor $\mathbf{A}$ is positive definite if the condition $\vec{v} \cdot \mathbf{A}\vec{v} > 0$ is valid for any vector $\vec{v} \neq \vec{0}$.

2.1.2 Strain Tensors

A strain measure has the goal of quantifying the deviation of the deformation of a deformable body from a rigid one, see (Altenbach, 2015). This quantity has to be zero in the case of a pure rigid body motion. Moreover, it has to be a monotonous, continuous, and continuously differentiable function of the displacement gradient $\mathbf{H}$, and it has to be equal to the linearized strain tensor $\mathbf{E}_\mathrm{L}$ in the case of small deformations, introduced in Section 2.4.3. Considering these requirements, it is possible to define any desired strain measure. In the following, only the strain measures used in this work are mentioned. The Green strain tensor $\mathbf{E}$ is defined in dependence of the right Cauchy-Green tensor $\mathbf{C}$ by

$$\mathbf{E} = \frac{1}{2}(\mathbf{C} - \mathbf{I}) = \frac{1}{2}(\mathbf{F}^\mathrm{T}\mathbf{F} - \mathbf{I}). \tag{2.20}$$

It can be motivated from the difference of the squares of material line elements in the current and reference configuration

$$|\mathrm{d}\vec{x}|^2 - |\mathrm{d}\vec{X}|^2 = \mathrm{d}\vec{X} \cdot (\mathbf{F}^\mathrm{T}\mathbf{F} - \mathbf{I})\mathrm{d}\vec{X} = \mathrm{d}\vec{X} \cdot 2\mathbf{E}\mathrm{d}\vec{X}. \tag{2.21}$$

The Green strain tensor operates in the tangent space of the reference configuration. Another commonly used strain measure operating in the current configuration is the Almansi strain tensor $\mathbf{A}$

$$\mathbf{A} = \frac{1}{2}(\mathbf{I} - \mathbf{B}^{-1}). \tag{2.22}$$

Analogously to the Green strain tensor, $\mathbf{A}$ can be introduced by Eq. (2.21), but this time expressed in dependence of the line elements of the current configuration

$$|\mathrm{d}\vec{x}|^2 - |\mathrm{d}\vec{X}|^2 = \mathrm{d}\vec{x} \cdot (\mathbf{I} - \mathbf{B}^{-1})\mathrm{d}\vec{x} = \mathrm{d}\vec{x} \cdot 2\mathbf{A}\mathrm{d}\vec{x}. \tag{2.23}$$

In this way, the relation between the Almansi and Green strain tensor is given by

$$\mathbf{A} = \mathbf{F}^{-\mathrm{T}}\mathbf{E}\mathbf{F}^{-1} \quad \text{and} \quad \mathbf{E} = \mathbf{F}^\mathrm{T}\mathbf{A}\mathbf{F}. \tag{2.24}$$

Moreover, the logarithmic (or true) strain $\mathbf{E}_\mathrm{ln}$, which is used in the measurements with the DIC-system in Section 3.8 and in the simulations with Abaqus in Chapter 7, is defined by

$$\mathbf{E}_\mathrm{ln} = \ln \mathbf{V} = \sum_{i=1}^{3} (\ln \lambda_i)\, \vec{n}_i \otimes \vec{n}_i \tag{2.25}$$

with λ_i being the eigenvalues of $\mathbf{V}$ and $\vec{n}_i$ their corresponding eigenvectors.

2.1.3 Strain-Rate Tensors

Since the relations for the material line, surface elements, and volume elements are functions of time, it is necessary to determine the time derivative of these quantities. For the material line element, this leads to

$$\mathrm{d}\dot{\vec{x}} = \dot{\mathbf{F}}\mathrm{d}\vec{X} = \dot{\mathbf{F}}\mathbf{F}^{-1}\mathrm{d}\vec{x}. \tag{2.26}$$

The time derivative is denoted by a dot. Here, the term $\dot{\mathbf{F}}\mathbf{F}^{-1}$ represents the spatial velocity gradient $\mathbf{L}$

$$\mathbf{L} = \dot{\mathbf{F}}\mathbf{F}^{-1} = \operatorname{grad} \bar{\vec{v}}(\vec{x}, t), \tag{2.27}$$

where $\bar{\vec{v}}(\vec{x}, t)$ represents the velocity field in spatial representation. The time derivative of the deformation gradient $\dot{\mathbf{F}} = \operatorname{Grad} \hat{\vec{v}}(\vec{X}, t)$ is the material velocity gradient. Considering the spatial velocity gradient, the time derivative of the material line element, surface element, and volume element can be expressed as

$$\mathrm{d}\dot{\vec{x}} = \mathbf{L}\,\mathrm{d}\vec{x}, \tag{2.28}$$

$$\mathrm{d}\dot{\vec{a}} = \left[(\operatorname{tr}\mathbf{L})\,\mathbf{I} - \mathbf{L}^{\mathrm{T}}\right]\mathrm{d}\vec{a}, \tag{2.29}$$

$$\mathrm{d}\dot{v} = (\operatorname{tr}\mathbf{L})\,\mathrm{d}v = (\operatorname{div}\vec{v})\,\mathrm{d}v. \tag{2.30}$$

Here, the trace operator is represented by 'tr'. The operator 'div' denotes the divergence with respect to the spatial coordinates $\vec{x}$. The divergence with respect to the material coordinates $\vec{X}$ is written as 'Div'.

The spatial velocity gradient can be decomposed into a symmetric $\mathbf{D} = \mathbf{D}^{\mathrm{T}}$ and an anti-symmetric part $\mathbf{W} = -\mathbf{W}^{\mathrm{T}}$

$$\mathbf{L} = \mathbf{D} + \mathbf{W} = \frac{1}{2}\left(\mathbf{L} + \mathbf{L}^{\mathrm{T}}\right) + \frac{1}{2}\left(\mathbf{L} - \mathbf{L}^{\mathrm{T}}\right). \tag{2.31}$$

The symmetric part $\mathbf{D}$ is known as the *strain-rate tensor*. It describes the rate at which the material line elements changes its length and relative angle. The tensor $\mathbf{W}$ is called *spin* or *vorticity tensor*, see (Haupt, 2002). The relation between the time derivative of the Green strain tensor and the strain-rate tensor is given by

$$\dot{\mathbf{E}} = \mathbf{F}^{\mathrm{T}}\mathbf{D}\mathbf{F} \quad \text{and} \quad \mathbf{D} = \mathbf{F}^{-\mathrm{T}}\dot{\mathbf{E}}\mathbf{F}^{-1}. \tag{2.32}$$

Moreover, with Eq. (2.24), the following relation between the Almansi strain tensor $\mathbf{A}$ and the strain-rate tensor $\mathbf{D}$ is valid

$$\mathbf{D} = \mathbf{F}^{-\mathrm{T}}\dot{\mathbf{E}}\mathbf{F}^{-1} = \mathbf{F}^{-\mathrm{T}}\frac{\mathrm{d}}{\mathrm{d}t}\left(\mathbf{F}^{\mathrm{T}}\mathbf{A}\mathbf{F}\right)\mathbf{F}^{-1} = \dot{\mathbf{A}} + \mathbf{L}^{\mathrm{T}}\mathbf{A} + \mathbf{A}\mathbf{L} = \overset{\triangle}{\mathbf{A}}, \tag{2.33}$$

where $\overset{\triangle}{\mathbf{A}}$ represents the covariant Oldroyd derivative. This derivative will be introduced in Section 2.4.2.

2.2 Stress Tensor and Heat Flux

As a result of mechanical, thermal, or other types of loads (such as electromagnetic, chemical...), an internal stress state originates in the material body. In order to describe it, a plane cut of a body is considered as shown in Fig. 2.4. An infinitesimal force $\mathrm{d}\vec{f}$ acting on the area of the cut in the current configuration $\mathrm{d}\vec{a} = \vec{n}\,\mathrm{d}a$ can be defined with the help of the Cauchy stress vector $\vec{t}$

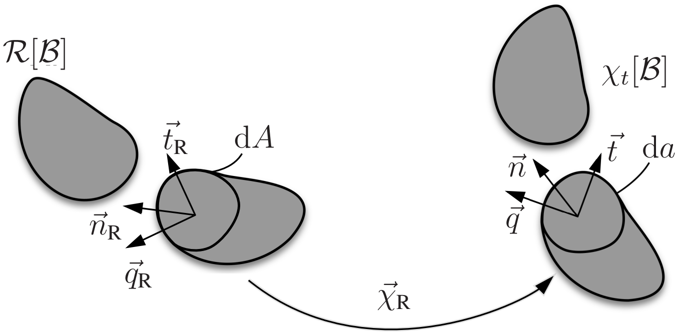

Figure 2.4: Stress and heat flux vectors

$$\mathrm{d}\vec{f} = \vec{t}\,\mathrm{d}a. \tag{2.34}$$

The Cauchy's stress theorem provides a connection between the Cauchy stress vector and the Cauchy stress tensor $\mathbf{T}$

$$\vec{t}(\vec{x}, t, \vec{n}) = \mathbf{T}(\vec{x}, t)\vec{n}, \tag{2.35}$$

with $\vec{n}$ being the unity vector normal to the surface of the cut. The Cauchy stress tensor is related to the material point $\vec{X}$ occupying the position $\vec{x} \in \partial\chi_t(\mathcal{B})$. This tensor is also known as *true stress tensor*, since it acts on the surface element of the current configuration $\mathrm{d}\vec{a}$. In the case that the surface element is referred to the reference configuration $\mathrm{d}\vec{A} = \vec{n}_\mathrm{R}\mathrm{d}A$, the infinitesimal force vector can be expressed by

$$\mathrm{d}\vec{f} = \vec{t}_\mathrm{R}\mathrm{d}A = \mathbf{T}_\mathrm{R}\mathrm{d}\vec{A}, \quad \text{with} \quad \vec{t}_\mathrm{R} = \mathbf{T}_\mathrm{R}\vec{n}_\mathrm{R}, \tag{2.36}$$

where $\vec{t}_\mathrm{R}$ is called *Piola-Kirchhoff stress vector* and $\vec{n}_\mathrm{R}$ represents the unity vector normal to the surface $\mathrm{d}A$ of the reference configuration. The stress tensor $\mathbf{T}_\mathrm{R}$ is called *first Piola-Kirchhoff tensor*. From Eqns. (2.15) and (2.34), a relation between the Cauchy stress and the first Piola-Kirchhoff tensor can be provided

$$\mathbf{T}_\mathrm{R} = (\det \mathbf{F})\,\mathbf{T}\mathbf{F}^{-\mathrm{T}}. \tag{2.37}$$

Another commonly used stress quantity related to the reference configuration is the *second Piola-Kirchhoff tensor* $\tilde{\mathbf{T}}$. It is introduced by multiplying the first Piola-Kirchhoff tensor with $\mathbf{F}^{-1}$. It is related to the aforementioned stress tensors through the relations

$$\tilde{\mathbf{T}} = \mathbf{F}^{-1}\mathbf{T}_{\mathrm{R}} = (\det \mathbf{F})\, \mathbf{F}^{-1}\mathbf{T}\mathbf{F}^{-\mathrm{T}}. \tag{2.38}$$

Moreover, another stress tensor operating in the current configuration is the Kirchhoff stress tensor $\mathbf{S}$, which is related to the Cauchy stress by

$$\mathbf{S} = (\det \mathbf{F})\mathbf{T}. \tag{2.39}$$

Based on Eqns. (2.38) and (2.39), the Kirchhoff stress tensor and the second Piola-Kirchhoff tensor are then related to each other by

$$\mathbf{S} = \mathbf{F}\tilde{\mathbf{T}}\mathbf{F}^{\mathrm{T}}. \tag{2.40}$$

The meaning of the tensors $\tilde{\mathbf{T}}$ and $\mathbf{S}$ becomes clear when considering the formulation of the stress power in the reference and current configuration, as well as the formulation of material properties, see also (Haupt, 2002). The transformations between the different stress tensors are shown in Tab. 2.1.

Table 2.1: Transformation of the different stress tensors

	$\mathbf{T}_{\mathrm{R}}$	$\tilde{\mathbf{T}}$	$\mathbf{S}$	$\mathbf{T}$
$\mathbf{T}_{\mathrm{R}}$		$\mathbf{F}\tilde{\mathbf{T}}$	$\mathbf{S}\mathbf{F}^{-\mathrm{T}}$	$(\det \mathbf{F})\mathbf{T}\mathbf{F}^{-\mathrm{T}}$
$\tilde{\mathbf{T}}$	$\mathbf{F}^{-1}\mathbf{T}_{\mathrm{R}}$		$\mathbf{F}^{-1}\mathbf{S}\mathbf{F}^{-\mathrm{T}}$	$(\det \mathbf{F})\mathbf{F}^{-1}\mathbf{T}\mathbf{F}^{-\mathrm{T}}$
$\mathbf{S}$	$\mathbf{T}_{\mathrm{R}}\mathbf{F}^{\mathrm{T}}$	$\mathbf{F}\tilde{\mathbf{T}}\mathbf{F}^{\mathrm{T}}$		$(\det \mathbf{F})\mathbf{T}$
$\mathbf{T}$	$(\det \mathbf{F})^{-1}\mathbf{T}_{\mathrm{R}}\mathbf{F}^{\mathrm{T}}$	$(\det \mathbf{F})^{-1}\mathbf{F}\tilde{\mathbf{T}}\mathbf{F}^{\mathrm{T}}$	$(\det \mathbf{F})^{-1}\mathbf{S}$	

Analogously to the stresses, a quantity related to the thermal loading is introduced. The heat flux in the current configuration can be defined by

$$q(\vec{x}, t, \vec{n}) = -\vec{q}(\vec{x}, t) \cdot \vec{n}. \tag{2.41}$$

The vector field $\vec{q}$ is known as *Cauchy heat flux* or *true heat flux*, and it has the property $-\vec{q} \cdot \mathrm{d}\vec{a} = -\vec{q} \cdot \vec{n}\, \mathrm{d}a$, with the minus sign indicating that the heat flux is defined positive when the body absorbs energy, see Fig. 2.4. The heat flux can be expressed in terms of the reference configuration by

$$q_{\mathrm{R}}(\vec{X}, t, \vec{n}_{\mathrm{R}}) = -\vec{q}_{\mathrm{R}}(\vec{X}, t) \cdot \vec{n}_{\mathrm{R}}. \tag{2.42}$$

The vector $\vec{q}_{\mathrm{R}}$ is known as *Piola-Kirchhoff heat flux*. A connection between $\vec{q}$ and $\vec{q}_{\mathrm{R}}$ can be found considering the equivalence $-\vec{q}\cdot\vec{n}\mathrm{d}a = -\vec{q}_{\mathrm{R}}\cdot\vec{n}_{\mathrm{R}}\mathrm{d}A$ and condition (2.15) for the surface elements $\mathrm{d}A$ and $\mathrm{d}a$. Thus, the relation between the Cauchy and the Kirchhoff heat flux is given by

$$\vec{q}_{\mathrm{R}} = (\det \mathbf{F})\, \mathbf{F}^{-1}\vec{q}. \tag{2.43}$$

2.3 Thermo-Mechanical Balance Equations

In order to obtain a connection between the effects of the surroundings of a material body and the body itself, a group of general principles known as balance equations is introduced. The foundation of these balance equations lies in the free-body principle, where the body of study is isolated from its environment and the effect of its environment is described with the help of physical quantities such as external forces or heat supply.

To begin with, there are three purely mechanical principles that have to be considered: the balance of mass, the balance of linear momentum, and the balance of rotational momentum. Two additional principles for thermodynamical processes have to be introduced as well.

Thermodynamics allow a description of the energy transformations connected to the mechanical processes with the help of the first law of thermodynamics, which postulates the equivalence of mechanical and non-mechanical work, see (Haupt, 2002). Moreover, the second law of thermodynamics offers a criterion to determine which processes of transforming thermal energy into mechanical work are physically possible.

2.3.1 Balance of Mass

In Continuum Mechanics, mass is a positive scalar magnitude $m(\mathcal{B},t) > 0$ related to a material body, which is a measure of the effect of the force of gravity (gravitational mass) and the resistance of the body to change its velocity (inertial mass), see (Haupt, 2002). It is defined as the integral of the mass density in the reference configuration ρ_{R} or current configuration ρ over the volume of the body

$$m(\mathcal{B},t) = \int_V \rho_{\mathrm{R}}(\vec{X},t)\mathrm{d}V = \int_v \rho(\vec{x},t)\mathrm{d}v. \tag{2.44}$$

The balance of mass stipulates that the mass of a material body remains constant over time

$$\frac{\mathrm{d}}{\mathrm{d}t} m(\mathcal{B},t) = 0. \tag{2.45}$$

The local formulation of the balance of mass in the reference configuration states that the mass density ρ_{R} remains constant over time

$$\rho_{\mathrm{R}} = \rho_{\mathrm{R}}(\vec{X}). \tag{2.46}$$

The spatial representation of Eq. (2.45) with definition (2.44) results in a time-dependent expression equal to

$$\frac{\mathrm{d}\rho}{\mathrm{d}t} + \rho \operatorname{div} \vec{v} = 0 \Leftrightarrow \frac{\partial \rho}{\partial t} + \operatorname{div}(\rho \vec{v}) = 0, \tag{2.47}$$

since the temporal variation of the integration area has to be considered. The mass densities in the current and reference configuration are related by

$$\rho_{\mathrm{R}} = (\det \mathbf{F})\rho. \tag{2.48}$$

This expression is obtained considering Eq. (2.16).

2.3.2 Balance of Linear Momentum

The linear momentum $\vec{I}$ is a fundamental quantity in Continuum Mechanics. It characterizes the effect of the velocity field combined with the mass distribution of a material body, and it is defined by

$$\vec{I}(\mathcal{B}, t) = \int_V \rho_{\mathrm{R}}(\vec{X})\vec{v}(\vec{X}, t)\mathrm{d}V = \int_v \rho(\vec{x}, t)\vec{v}(\vec{x}, t)\mathrm{d}v. \tag{2.49}$$

The balance of linear momentum states that the temporal change of the linear momentum originates in the effect of external forces acting on the material body

$$\dot{\vec{I}}(\mathcal{B}, t) = \vec{F}(\mathcal{B}, t). \tag{2.50}$$

The external forces $\vec{F}$ can be decomposed into surface forces and volume forces. The global form of the balance of linear momentum in the spatial formulation is

$$\frac{\mathrm{d}}{\mathrm{d}t}\int_v \rho(\vec{x}, t)\vec{v}(\vec{x}, t)\mathrm{d}v = \int_a \mathbf{T}(\vec{x}, t)\vec{n}\mathrm{d}a + \int_v \rho(\vec{x}, t)\vec{k}(\vec{x}, t)\mathrm{d}v, \tag{2.51}$$

where $\vec{k}$ is the volume force density. The local form of Eq. (2.51) can be obtained with the help of the Gauss's theorem and the Cauchy's divergence theorem[2], see (Haupt, 2002), leading to

$$\rho\dot{\vec{v}} = \operatorname{div}\mathbf{T} + \rho\vec{k}. \tag{2.52}$$

---

[2] The Gauss' integral theorem stipulates the equivalence of the expressions

$$\int\limits_V (\operatorname{Div}\vec{v})\,\mathrm{d}V = \int\limits_A \vec{v}\cdot\vec{n}\,\mathrm{d}A, \quad \text{and} \quad \int\limits_V (\operatorname{Div}\mathbf{T})\,\mathrm{d}V = \int\limits_A \mathbf{T}\vec{n}\,\mathrm{d}A,$$

with $\vec{v}$ a vector and $\mathbf{T}$ a tensor variable, V the volume of a region and A its outer surface. The Cauchy's divergence theorem provides the product rules

$$\operatorname{Div}(\Psi\vec{v}) = \operatorname{Grad}\Psi\cdot\vec{v} + \Psi\cdot\operatorname{Grad}\vec{v}, \quad \text{and} \quad \operatorname{Div}(\Psi\mathbf{T}) = \mathbf{T}\operatorname{Grad}\Psi + \Psi\operatorname{Div}\mathbf{T}.$$

Both theorems are exposed in Chapter 6, page 168.

The material representation of Eq. (2.51) can be obtained with the help of relations (2.15) and (2.16)

$$\frac{\mathrm{d}}{\mathrm{d}t}\int_V \rho_\mathrm{R}(\vec{X})\vec{v}(\vec{X},t)\mathrm{d}V = \int_A \mathbf{T}_\mathrm{R}(\vec{X},t)\vec{n}_\mathrm{R}\mathrm{d}A + \int_V \rho_\mathrm{R}(\vec{X})\vec{k}(\vec{X},t)\mathrm{d}V, \tag{2.53}$$

and its local formulation is

$$\rho_\mathrm{R}\dot{\vec{v}} = \mathrm{Div}\,\mathbf{T}_\mathrm{R} + \rho_\mathrm{R}\vec{k}. \tag{2.54}$$

2.3.3 Balance of Angular Momentum

Another quantity that characterizes the kinetic state of a material body is the rotational momentum $\vec{D}_{\vec{c}}$, which has to be defined with respect to a fixed arbitrary point $\vec{c}$ in the space

$$\vec{D}_{\vec{c}} = \int_V (\vec{\chi}_\mathrm{R}(\vec{X}) - \vec{c}) \times \vec{v}(\vec{X},t)\rho_\mathrm{R}(\vec{X})\mathrm{d}V = \int_v (\vec{x} - \vec{c}) \times \vec{v}(\vec{x},t)\rho(\vec{x},t)\mathrm{d}v. \tag{2.55}$$

The balance of rotational momentum states that the temporal change of the rotational momentum $\vec{D}_c$ is caused by the resulting torque relative to the point $\vec{c}$ of the volume and the surface forces acting on the material body

$$\dot{\vec{D}}_{\vec{c}}(\mathcal{B},t) = \vec{M}_{\vec{c}}(\mathcal{B},t). \tag{2.56}$$

This can be expressed in the spatial representation, decomposing the resultant torque $\vec{M}_{\vec{c}}$ into a surface and a volume component by

$$\frac{\mathrm{d}}{\mathrm{d}t}\int_v (\vec{x} - \vec{c}) \times \vec{v}(\vec{x},t)\rho(\vec{x},t)\mathrm{d}v = \int_a (\vec{x} - \vec{c}) \times \mathbf{T}\vec{n}\mathrm{d}a + \int_v (\vec{x} - \vec{c}) \times \rho\vec{k}\mathrm{d}v. \tag{2.57}$$

By applying the Gauss’s theorem, the surface integral can be transformed into a volume integral. Moreover, with the help of the divergence theorem, Eq. (2.57) can be rewritten as

$$\int_v (\vec{x} - \vec{c}) \times (\rho\dot{\vec{v}} - \mathrm{div}\,\mathbf{T} - \rho\vec{k})\mathrm{d}v = \int_v T^{ij}\vec{g}_i \times \vec{g}_j\mathrm{d}v. \tag{2.58}$$

Here, the Cauchy stress $\mathbf{T} = T^{ij}\vec{g}_i \otimes \vec{g}_j$ is expressed in contravariant representation, see (Haupt, 2002). Considering the balance of linear momentum, expression (2.58) is equal to zero, which leads to

$$T^{ij}\vec{g}_i \times \vec{g}_j = 0. \tag{2.59}$$

Eq. (2.59) states the symmetry of the Cauchy stress

$$\mathbf{T} = \mathbf{T}^\mathrm{T}. \tag{2.60}$$

From Eqns. (2.39) and (2.40), one obtains as a consequence that the Kirchhoff and the second Piola-Kirchhoff tensors are also symmetric, $\mathbf{S} = \mathbf{S}^{\mathrm{T}}$ and $\tilde{\mathbf{T}} = \tilde{\mathbf{T}}^{\mathrm{T}}$. From Eq. (2.38) and the symmetry of $\tilde{\mathbf{T}}$, one obtains for the first Piola-Kirchhoff tensor

$$\mathbf{T}_{\mathrm{R}} = \mathbf{F}\mathbf{T}_{\mathrm{R}}^{\mathrm{T}}\mathbf{F}^{-\mathrm{T}}, \tag{2.61}$$

which implies that the first Piola-Kirchhoff tensor is generally asymmetric. Under the premise that the tensor $\mathbf{T}$, $\mathbf{S}$, and $\tilde{\mathbf{T}}$ are symmetric – and considering Eq. (2.61) – the balance of rotational momentum is fulfilled.

2.3.4 Balance of Energy

The first law of thermodynamics, also known as balance of energy, provides a relation between the mechanical work of a system with the thermal energy. At first, it is necessary to introduce several physical quantities. The kinetic energy K is defined by the volume integral

$$K = \frac{1}{2}\int_v \vec{v}(\vec{x},t)\cdot\vec{v}(\vec{x},t)\rho(\vec{x},t)\mathrm{d}v. \tag{2.62}$$

The internal energy E is defined as the volume integral of the energy density e

$$E = \int_v \rho(\vec{x},t)e(\vec{x},t)\mathrm{d}v. \tag{2.63}$$

The mechanical power of external forces L_{e} can be divided into a component from the surface forces and a component of the volume forces

$$L_{\mathrm{e}} = \int_a \vec{t}\cdot\vec{v}\mathrm{d}a + \int_v \vec{k}\cdot\rho\vec{v}\mathrm{d}v. \tag{2.64}$$

The thermal energy consists of one component acting through the surface of the body and of a component distributed over its volume

$$Q = \int_a q(\vec{x},t)\mathrm{d}a + \int_v \rho(\vec{x},t)r(\vec{x},t)\mathrm{d}v, \tag{2.65}$$

where $q(\vec{x},t)$ denotes the heat flux defined in Eq. (2.41). The scalar r is the specific thermal energy production, which can be caused by radiation or internal processes. The balance of mechanical energy stipulates that the change over time of the sum of kinetic K and internal energy E is a consequence of the energy supply Q and the power of the external forces L_{e} acting on the material body

$$\frac{\mathrm{d}}{\mathrm{d}t}\left(K(\mathcal{B},t) + E(\mathcal{B},t)\right) = L_{\mathrm{e}}(\mathcal{B},t) + Q(\mathcal{B},t). \tag{2.66}$$

By inserting the definitions (2.62)-(2.65) into Eq. (2.66) and considering Eqns. (2.35) and (2.41), we obtain

$$\frac{\mathrm{d}}{\mathrm{d}t}\int_v \rho\left(\frac{1}{2}\vec{v}\cdot\vec{v}+e\right)\mathrm{d}v = \int_a (\mathbf{T}^{\mathrm{T}}\vec{v}-\vec{q})\cdot\vec{n}\mathrm{d}a + \int_v \rho(\vec{k}\cdot\vec{v}+r)\mathrm{d}v. \tag{2.67}$$

Considering the divergence theorem and the balance of linear and angular momentum, Eq. (2.67) can be expressed in the local formulation in the spatial representation by

$$\dot{e}(\vec{x},t) = -\frac{1}{\rho}\mathrm{div}\,\vec{q} + \frac{1}{\rho}\mathbf{T}\cdot\mathbf{D} + r. \tag{2.68}$$

The material representation of Eq. (2.68) is

$$\dot{e}(\vec{X},t) = -\frac{1}{\rho_{\mathrm{R}}}\mathrm{Div}\,\vec{q}_{\mathrm{R}} + \frac{1}{\rho_{\mathrm{R}}}\tilde{\mathbf{T}}\cdot\dot{\mathbf{E}} + r. \tag{2.69}$$

2.3.5 Balance of Entropy

The second law of thermodynamics is also known as the principle of irreversibility. It provides a criterion to determine in which direction the energy transformations occur. The basis of this second principle is the concept of entropy. Entropy is a physical quantity which represents the degree of molecular disorder of a system. It is used to describe the irreversibility of a process. Moreover, it can be interpreted as the amount of energy of a physical process that is dissipated into heat and, thus, does not contribute to other processes, e.g. mechanical work, see (Altenbach, 2015). Entropy can be expressed as the volume integral of the specific entropy s

$$S(\mathcal{B},t) = \int_v s(\vec{x},t)\rho(\vec{x},t)\mathrm{d}v. \tag{2.70}$$

Now, the entropy supply H to a system from its surroundings is introduced. It can be expressed as the sum of a surface component and a volume part

$$H = \int_a \Sigma\mathrm{d}a + \int_v \sigma\rho\mathrm{d}v = -\int_a \frac{\vec{q}}{\Theta}\cdot\vec{n}\mathrm{d}a + \int_v \frac{r}{\Theta}\rho\mathrm{d}v, \tag{2.71}$$

where the surface component of the entropy supply $\Sigma = -\vec{q}/\Theta\cdot\vec{n}$ is defined analogously to the heat flux and $\sigma = r/\Theta$. Moreover, a system possesses an entropy production

$$\Gamma = \int_v \gamma\rho\mathrm{d}v. \tag{2.72}$$

The entropy balance states that the change in entropy over time is caused by the entropy supply and the internal entropy production

$$\dot{S} = H + \Gamma. \tag{2.73}$$

The second law of thermodynamics states that the entropy production of a system Γ cannot be negative

$$\Gamma = \dot{S} - H \geq 0. \tag{2.74}$$

Now, by inserting Eqns. (4.89)-(2.72) into Eq. (2.74), we obtain

$$\int_v \gamma \rho \mathrm{d}v = \frac{\mathrm{d}}{\mathrm{d}t} \int_v s \rho \mathrm{d}v + \int_a \frac{1}{\Theta} \vec{q} \cdot \vec{n} \mathrm{d}a - \int_v \frac{1}{\Theta} r \rho \mathrm{d}v \geq 0. \tag{2.75}$$

Considering the energy balance from Eq. (2.68), Eq. (2.75) can be rewritten in the local formulation as

$$\Theta \gamma = -\dot{e} + \Theta \dot{s} + \frac{1}{\rho} \mathbf{T} \cdot \mathbf{D} - \frac{1}{\rho \Theta} \vec{q} \cdot \operatorname{grad} \Theta \geq 0. \tag{2.76}$$

In constitutive modeling, it is common to use the Helmholz free energy

$$\psi = e - \Theta s, \tag{2.77}$$

whose time derivative is $\dot{\psi} = \dot{e} - s\dot{\Theta} - \Theta \dot{s}$, which leads to the time derivative of the internal energy

$$\dot{e} = \dot{\psi} + s\dot{\Theta} + \Theta \dot{s}. \tag{2.78}$$

Inserting Eq. (2.78) into Eq. (2.76) leads to the Clausius-Duhem inequality in the spatial representation

$$-\dot{\psi} - s\dot{\Theta} + \frac{1}{\rho} \mathbf{T} \cdot \mathbf{D} - \frac{1}{\rho \Theta} \operatorname{grad} \Theta \cdot \vec{q} \geq 0. \tag{2.79}$$

In the material representation, Eq. (2.79) is equal to

$$-\dot{\psi} - s\dot{\Theta} + \frac{1}{\rho_\mathrm{R}} \tilde{\mathbf{T}} \cdot \dot{\mathbf{E}} - \frac{1}{\rho_\mathrm{R} \Theta} \operatorname{Grad} \Theta \cdot \vec{q}_\mathrm{R} \geq 0. \tag{2.80}$$

The Clausius-Duhem inequality plays an important role in the development of material models. It provides a criterion to fulfill the principle of irreversibility, and thus, to obtain thermodynamical consistent material models.

2.4 General Considerations in Material Modeling

In this section, several general concepts for the development of material models are illustrated. A group of main principles for a proper definition of a material model is presented first. Moreover, the concept of dual variables and intermediate configuration is explained. These considerations are important from the perspective of modeling inelastic material behavior. The last point considers the case of small deformations providing the kinematics and the balance equations after a geometric linearization.

2.4.1 Material Behavior

The goal of material theory in Continuum Mechanics is to provide a systematic way to develop suitable mathematical models to describe the behavior of particular materials, normally for a specific application, since, at the moment, it is not possible to offer a general material model which is universally valid in every case. According to Haupt (2002), there are three levels, in which modeling is realized: material symmetry properties, conditions of kinematic constraints and constitutive equations.

Material Symmetry

The consideration of material symmetry leads to simplifications in formulation of constitutive models, since concrete stress-strain relations can be dependent of the material direction. Hence, it is possible to distinguish between fluids and solids because of its symmetry behavior. Moreover, in a solid, the direction-independence (isotropy) or direction-dependence (anisotropy) of the material behavior has to be considered in the constitutive equations.

Kinematic Constraints

A kinematic constraint represents a restriction of the material body's motion, which can a priori be defined as a material property. An example is the assumption of incompressibility, where a material can only perform volume preserving motions. Another common used constraint is the assumption that volume changes are purely elastic, see (Altenbach, 2015).

Constitutive Equations

Contrary to the kinematic and balance equations, which are generally valid, constitutive equations represent the particular answer of a material body under a given loading process. In order to obtain a systematic development of constitutive equations, the following axioms can be followed, see for example (Haupt, 2002; Altenbach, 2015):

- First, the *causality principle* states that the choice of the dependent and independent variables of the model has to be determined from its relation of cause and effect. Normally, the displacement and temperature are chosen as independent variables and depending on them, stress, heat flux, free energy and entropy are deduced.

- According to the *principle of determinism*, the current state of stress in one material point is uniquely determined by the past history of a body's motion.

- The *principle of equipresence* states that the set of independent variables has to be the same for all material equations.

- Moreover, the *principle of local action* stipulates that the state of stress in a material point is only influenced by the motion history of the point's environment and not by the motion of all body particles. A common way to express this principle is the use of the deformation gradient for the strain definition.

- Additionally, the *principle of frame-indifference* states that the representation of material properties has to be independent of the frame of reference. A variable can be called objective when for an scalar φ, a vector $\vec{v}$ and a tensor $\mathbf{A}$, the relations

  $$\varphi^* = \varphi, \quad \vec{v}^* = \mathbf{Q}\vec{v}, \quad \mathbf{A}^* = \mathbf{Q}\mathbf{A}\mathbf{Q}^{\mathrm{T}}, \tag{2.81}$$

  are valid, where $\mathbf{Q}(t)$ is an orthogonal tensor representing a rotation of the system of reference. An example of an objective variable is the Cauchy stress $\mathbf{T}$ or the stress power $\mathbf{T} \cdot \mathbf{D}/\rho$ or $\tilde{\mathbf{T}} \cdot \dot{\mathbf{E}}/\rho_{\mathrm{R}}$. In general, even if a variable is objective, its rate could be not objective. This happens in the case of stress and strain tensors. In order to express the constitutive equations with an objective time rate, two different rates, which are used in this work, are introduced. The covariant Oldroyd-rate is defined by

  $$\overset{\triangle}{\mathbf{A}} = \dot{\mathbf{A}} + \mathbf{L}^{\mathrm{T}}\mathbf{A} + \mathbf{A}\mathbf{L}, \tag{2.82}$$

  and the contravariant Oldroyd-rate is given by

  $$\overset{\triangledown}{\mathbf{A}} = \dot{\mathbf{A}} - \mathbf{L}\mathbf{A} - \mathbf{A}\mathbf{L}^{\mathrm{T}}. \tag{2.83}$$

  In both cases $\mathbf{L}$ represents the spatial velocity gradient, see Eq. (2.27).

- The last requirement is the *compatibility with the balance equations*, especially the Clausius-Duhem inequality, see Eqns. (2.79) or (2.80). It is common to arrange the constitutive equations during modeling a priori in a way that guarantees the principle of irreversibility.

2.4.2 Dual Variables

In material modeling, it is common to make use of tensor-valued stress and strain variables which operate in a configuration different to the initial or the current configuration, which is called *intermediate configuration*. The concept of dual variables proposed by Haupt and Tsakmakis (1989), see also (Haupt and Tsakmakis, 1996; Haupt, 2002), is connected to the concept of intermediate configuration in the sense that it allows the development of equations for elastic and inelastic material response separately, due to the fact that they are formulated in different configurations. It is based on the so-called dual variables of stresses and strains, and its rates. With them, it is possible to formulate the stress power, complementary stress power, incremental stress power and accumulated work, which remain independent of the chosen configuration. An intermediate configuration is a tensor field $\mathbf{\Psi}$ with the property

$$(\vec{X}, t) \to \mathbf{\Psi}(\vec{X}, t), \qquad \det \mathbf{\Psi} \neq 0. \tag{2.84}$$

The tensor field $\mathbf{\Psi}$ transforms material lines from the reference configuration $\vec{X}$ into the intermediate configuration $\mathrm{d}\vec{\xi}$

$$\mathrm{d}\vec{\xi} = \mathbf{\Psi}\mathrm{d}\vec{X}. \tag{2.85}$$

This implies a multiplicative decomposition of the deformation gradient

$$\mathbf{F}(\vec{X}, t) = (\mathbf{F}\mathbf{\Psi}^{-1})\mathbf{\Psi} = \mathbf{\Phi}\mathbf{\Psi}, \tag{2.86}$$

accompanied by an additive decomposition of the strain tensor $\mathbf{\Pi}$ in the intermediate configuration equal to

$$\mathbf{\Pi} = \frac{1}{2}(\mathbf{\Phi}^{\mathrm{T}}\mathbf{\Phi} - \mathbf{\Psi}^{-\mathrm{T}}\mathbf{\Psi}^{-1}) = \mathbf{\Pi}_{\Phi} + \mathbf{\Pi}_{\Psi}. \tag{2.87}$$

The stress tensor of the intermediate configuration is denoted by $\mathbf{\Sigma}$. The family of strain and stress tensors operating in the intermediate configuration ($\mathbf{\Pi}$, $\mathbf{\Sigma}$) and their rates are called dual strain and stress tensors, when the following transformations between the reference and the intermediate configuration are valid

$$\mathbf{\Pi} = \mathbf{\Psi}^{-\mathrm{T}}\mathbf{E}\mathbf{\Psi}^{-1}, \tag{2.88}$$

$$\overset{\triangle}{\mathbf{\Pi}} = \mathbf{\Psi}^{-\mathrm{T}}\dot{\mathbf{E}}\mathbf{\Psi}^{-1} = \dot{\mathbf{\Pi}} + \mathbf{\Lambda}^{\mathrm{T}}\mathbf{\Pi} + \mathbf{\Pi}\mathbf{\Lambda}, \tag{2.89}$$

$$\mathbf{\Sigma} = \mathbf{\Psi}\tilde{\mathbf{T}}\mathbf{\Psi}^{\mathrm{T}}, \tag{2.90}$$

$$\overset{\triangledown}{\mathbf{\Sigma}} = \mathbf{\Psi}\dot{\tilde{\mathbf{T}}}\mathbf{\Psi}^{\mathrm{T}} = \dot{\mathbf{\Sigma}} - \mathbf{\Lambda}\mathbf{\Sigma} - \mathbf{\Sigma}\mathbf{\Lambda}^{\mathrm{T}}, \tag{2.91}$$

with $\mathbf{\Lambda} = \dot{\mathbf{\Psi}}\mathbf{\Psi}^{-1}$ the relative rate of change of the intermediate configuration. With Eqns. (2.88)-(2.91), the following relations between the dual variables in the intermediate configuration and the stress and strain in the reference configuration and its derivatives are equivalent

$$\tilde{\mathbf{T}} \cdot \mathbf{E} = \mathbf{\Sigma} \cdot \mathbf{\Pi} \quad \text{accumulated work} \tag{2.92}$$

$$\tilde{\mathbf{T}} \cdot \dot{\mathbf{E}} = \mathbf{\Sigma} \cdot \overset{\triangle}{\mathbf{\Pi}} \quad \text{stress power} \tag{2.93}$$

$$\dot{\tilde{\mathbf{T}}} \cdot \mathbf{E} = \overset{\triangledown}{\mathbf{\Sigma}} \cdot \mathbf{\Pi} \quad \text{complementary stress power} \tag{2.94}$$

$$\dot{\tilde{\mathbf{T}}} \cdot \dot{\mathbf{E}} = \overset{\triangledown}{\mathbf{\Sigma}} \cdot \overset{\triangle}{\mathbf{\Pi}} \quad \text{incremental stress power} \tag{2.95}$$

In relation to the reference configuration, the dual stress variable of the Green strain $\mathbf{E}$ is the second Piola-Kirchhoff tensor $\tilde{\mathbf{T}}$. Moreover, the Almansi strain $\mathbf{A}$ and the Kirchhoff stress tensor $\mathbf{S}$ are dual variables related to the current configuration. There are other pairs of dual variables such as the Piola strain tensor and the Kirchhoff stress, or the Finger tensor and the convective stress tensor, which are not treated in this work. For more information see (Haupt, 2002).

2.4.3 The Case of Small Deformations

In several application areas, the deformations which the material body experiences are very small. In these cases, the kinematic relations from Section 2.1 can be simplified through the so-called geometric linearization. A geometric linearization represents the process in which the kinematic quantities are express by means of the displacement gradient $\mathbf{H}(\vec{X},t) = \mathrm{Grad}\,\vec{u}(\vec{X},t)$. In this process, all relations of higher order than one are neglected for scalar, vector and tensor variables. To this end, the displacement gradient is considered as reference to define the magnitude of the deformation. One can talk about small deformations, when

$$||\mathbf{H}|| \ll 1. \tag{2.96}$$

Here, $||\mathbf{H}|| = \sqrt{\mathbf{H}\cdot\mathbf{H}}$ represents the Frobenius norm. Considering Eq. (2.8), it means that the deformation gradient differs only slightly from the identity tensor

$$||\mathbf{F}-\mathbf{I}|| \ll 1. \tag{2.97}$$

Neglecting all the terms of higher order, the following relations are valid

$$\det\mathbf{F} \approx 1 + \mathrm{tr}\,\mathbf{H}, \tag{2.98}$$

$$\mathbf{F}^{-1} \approx \mathbf{I} - \mathbf{H}, \tag{2.99}$$

$$\mathbf{C} \approx \mathbf{B} \approx \mathbf{I} + \mathbf{H} + \mathbf{H}^{\mathrm{T}}, \tag{2.100}$$

$$\mathbf{E} \approx \frac{1}{2}(\mathbf{H} + \mathbf{H}^{\mathrm{T}}) \approx \mathbf{A}. \tag{2.101}$$

Eq. (2.101) implies that the current configuration is very close to the reference configuration, and thus, there will be no distinction between configurations in the case of small deformations. This holds for the stress vectors and tensor

$$\vec{t} \approx \vec{t}_{\mathrm{R}}, \tag{2.102}$$

$$\tilde{\mathbf{T}} \approx \mathbf{T}_{\mathrm{R}} \approx \mathbf{S} \approx \mathbf{T}, \tag{2.103}$$

as well as for the heat flux

$$\vec{q} \approx \vec{q}_{\mathrm{R}}. \tag{2.104}$$

Thus, in the case of small deformations, only one representation for density ρ, the linearized strain $\mathbf{E}$, the stress $\mathbf{T}$ and the heat flux $\vec{q}$ is necessary. With the previous considerations, the balance equations from Section 2.3 in the small deformations case can be written as

$$\rho = \text{const.}, \tag{2.105}$$

$$\operatorname{div} \mathbf{T} + \rho \vec{k} = \rho \dot{\vec{v}}, \tag{2.106}$$

$$\mathbf{T} = \mathbf{T}^{\mathrm{T}}, \tag{2.107}$$

$$\dot{e} = -\frac{1}{\rho} \operatorname{div} \vec{q} + \frac{1}{\rho} \mathbf{T} \cdot \dot{\mathbf{E}} + r, \tag{2.108}$$

$$-\dot{\psi} - s\dot{\Theta} + \frac{1}{\rho} \mathbf{T} \cdot \dot{\mathbf{E}} - \frac{1}{\rho\Theta} \operatorname{grad} \Theta \cdot \vec{q} \geq 0. \tag{2.109}$$

3 Experimental Characterization

Experiments are a fundamental part of science. They are necessary to obtain information regarding the investigated area of interest for modeling purposes and to test the validity of the developed mathematical models. In Continuum Mechanics, one main field of investigation is the determination of material behavior. Here, the test specimen can be seen as an operator, see (Haupt, 2002). Experiments are necessary to model the relations between input quantities (strain, temperature) and output quantities (stress, heat flux), and after that, they are used to calibrate the material model through a parameter identification procedure.

During the modeling process, it is necessary to carry out an idealization of the mechanical behavior owing to the high complexity of the materials in reality. Regarding this point, the generation of homogeneous strain and stress states is essential. In order to decide which experiments have to be included into the experimental campaign, the first question to clarify is "which aspects of the material response are essential to be included in the model". The next step consists of designing a suitable set of experiments that allows to isolate these effects from the other influence factors. However, this is not always possible. For a quasistatic mechanical characterization, one can obtain the basic response of the shear behavior of a material with torsion or shear experiments, while the volumetric information can be obtained from tensile and compression tests. Moreover, there are a lot of other possible tests that can be performed for identification purposes, such as bending, indentation, or biaxial tests. However, if it is not possible to generate a homogeneous strain or stress state, they are less appropriate for material modeling.

In this work, the focus of interest lies in describing the thermo-mechanical behavior of the alloy Zamak 5, including the influence of the aging, from a macroscopic point of view. In this chapter, an extensive experimental campaign for the characterization of the thermo-mechanical behavior of this material is presented. First, general information about the die casting process, the material, and the geometry of the specimens is provided. Moreover, the experimental setup is described and the considerations of data evaluation are exposed. The mechanical behavior of the material is characterized by means of tension, compression, and torsion experiments at different strain-rates, temperatures, and aging times. Both the thermal expansion as well as the shrinkage caused by aging are characterized with dilatometer experiments. Additionally, several physical properties such as the thermal conductivity, thermal diffusivity, and specific heat capacity are measured in order to perform thermo-mechanical simulations later on. Finally, validation experiments are carried out to obtain an indicator of the accuracy of the predictions of the proposed model in Chapter 4.

3.1 Die Casting Process

In this section, basic concepts of the die casting process are explained with an emphasis on zinc die casting. The section is based mainly on information from (Nogowizin, 2011) and (Johnen, 1981), as well as (IZA, 2018; ILZG, 2019; IZ, 2019; ZD, 2019) and the literature cited therein.

The die casting process is a highly productive manufacturing process that is suitable for mass production, in which molten metal is injected into a reusable steel mold cavity under high pressure. There are two main possibilities for die casting: cold chamber die casting and hot chamber die casting , see Fig. 3.1. The main difference between them is that, in cold chamber die casting, the molten metal is injected to the shot chamber from an external source, whereas in the hot chamber process, the source of molten material is attached to the machine, which is why several machine components are always in contact with molten metal. As a consequence, materials with high melting points tend to cause problems with regard to the machinery. In cold chamber die casting, the material must be brought in for every shot or cycle of production, which slows down the production rate. Moreover, it requires higher pressures. Hot chamber die casting, on the other hand, is suitable to produce castings without interruptions. With regard to productivity, hot chamber die casting is the method of choice, provided that the melting point of the material is low enough and that the component parts are small enough.

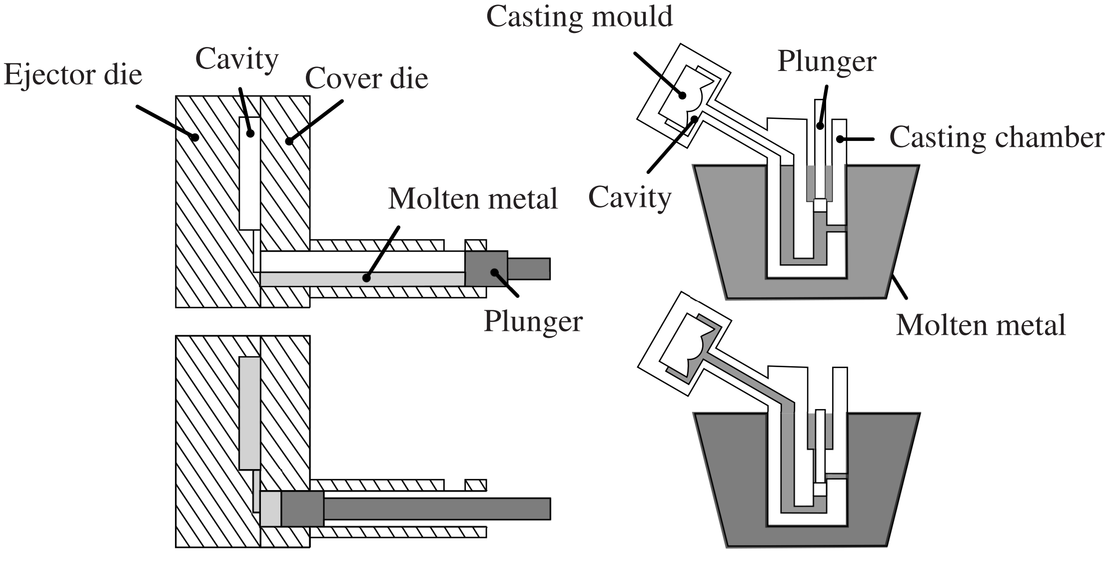

(a) Cold chamber die casting process (b) Hot chamber die casting process

Figure 3.1: Representation of die casting process, from Nogowizin (2011)

Mainly, the question whether a material is suitable for die casting is subject to its chemical composition and microstructure. It has to exhibit good castability properties, such as corrosion and wear resistance, and, moreover, a melting point that is not too high.

The most important alloys that are used for this process are aluminum, magnesium, zinc-based alloys – and, though less common, copper alloys, see Nogowizin (2011), being aluminum and zinc alloys predominant. Aluminum, magnesium and copper alloys are commonly used in the cold chamber die casting process, whereas zinc alloys are more suitable for hot chamber die casting because of their low melting point of around $380\,^{\circ}\mathrm{C}$[1]. It is possible to use magnesium-alloys in hot chamber die casting – but rather unusual.

Although aluminum die casting alloys are cheaper and have a lower density than zinc alloys, the mechanical properties of zinc die casting alloys are better than aluminum with regard to, for example, tensile strength, Young's modulus, hardness, and elongation at fracture. Moreover, the high density of zinc alloys of around $6.7\,\mathrm{g/cm^3}$ can be compensated by the possibility of constructing thinner components. Disadvantages of zinc die casting components are the creep at room temperature and the degradation of its mechanical properties over the course of time, also known as aging. These effects are connected to the low melting point of the alloy.

In comparison to sand and permanent mold casting, the die casting process allows to produce parts with highly complex geometries and very small thicknesses. With other manufacturing processes, this complexity level could only be achieved by producing several compound parts that need to be assembled. The die casting process is highly productive, since it is possible to produce a high amount of components in a short time from one mold. Moreover, die casting components show a high dimensional accuracy and an enhanced surface quality, without the necessity of further processing. Normally, die casting alloys are recyclable.

The quality of a die casting part is determined by several factors which influence its final microstructure, such as the design of the mold, pressure and pressing velocity during a casting cycle, and the alloy and mold temperature, which drives the solidification process. Porosity represents the main problem of die casting parts. It cannot be circumvented completely, and attempts to reduce it can lead to an exponential increase in production costs, see (Nogowizin, 2011; Gelfi et al., 2004; Buffiere et al., 2001; Gutman et al., 1998).

Overall, zinc alloys are considered to be the best castable of all the commonly used alloys because of lower costs related to the production process – lower temperatures and pressures during die casting, and less material use due to the commonly thin-walled parts – as well as the fast production rates and the excellent finishing capabilities. Most importantly, casting components are used in cars, machinery, electronics, computers, mobile phones, construction appliances, and in toys.

---

[1] The melting point of aluminum and magnesium die casting alloys is around $550 - 600\,^{\circ}\mathrm{C}$.

3.2 Material

The investigated material is the zinc die casting alloy Zamak 5 (ZnAl4Cu1). The specimens, provided by the company Wagenaar GmbH & Co. KG (Germany), were produced in the same batch of die casting. They were approximately one month old after die casting when the sample preparation started. The composition of the specimens is defined by the German standard DIN EN 1774 (1997), as shown in Tab. 3.1. If we take a look at the microstructure of the material in Fig. 3.2, we find zinc-rich globular-dendritic grains (bright phase), fine dark precipitates in the zinc-rich grains, and a eutectic phase (gray phase). The grains have an average diameter of $8.5\,\mu\mathrm{m}$. The grain size is determined by the standard intercept method described by the ASTM E112-12. The material also shows porosity, which will not be considered in this work. In this investigation, we restrict ourselves to a phenomenological description of the thermo-mechanical behavior of the alloy and therefore assume an isotropic material behavior.

Table 3.1: Chemical composition of the specimens

Element	Al	Cu	Mg	Pb	other impurities	Zn
Amount in wt $\%$	$4.0\,\%$	$0.86\,\%$	$0.045\,\%$	$0.002\,\%$	$0.0028\,\%$	Balance

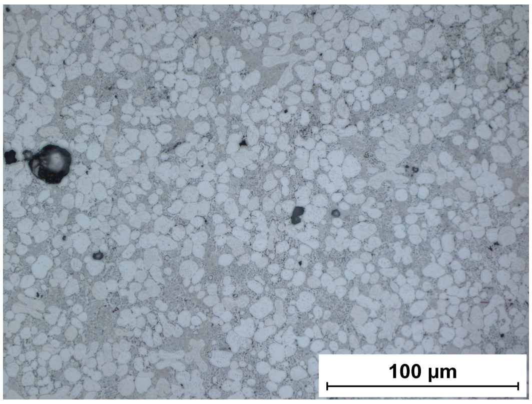

Figure 3.2: Micrograph of the specimen

In order to perform the experiments, hollow cylindrical specimens with an inner radius of $R_i = 13\,\mathrm{mm}$, a wall-thickness of $d = 2\,\mathrm{mm}$, and a length of $L = 90\,\mathrm{mm}$ were produced, see Fig. 3.3. The provided specimens were stored at a constant temperature

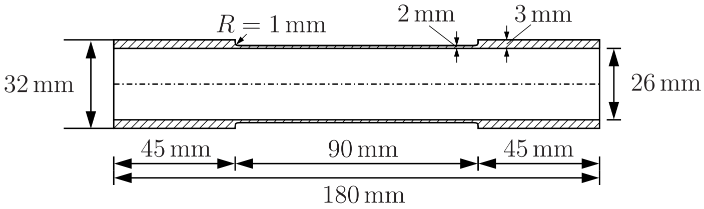

(a) Geometry of the specimens

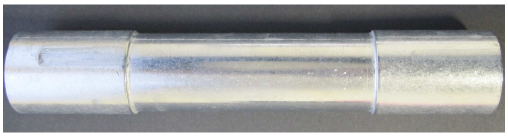

(b) Specimen

Figure 3.3: Specimen's geometry

of $-24\,^{\circ}\mathrm{C}$ in order to prevent further aging. This state is considered the initial unaged state of the material. As specified in (Kallien and Busse, 2009), at this temperature, the material would need more than 100 years to reach the final aged state. In order to obtain specimens at different aging stages, some specimens were stored at a constant temperature of $19\,^{\circ}\mathrm{C}$ for 3, 6, and 12 months, respectively.

3.3 Experimental Setup

The performed experiments and measurements are classified in four areas. The experiments for the determination of the thermo-mechanical behavior are the main goal of this investigation. Moreover, dilatometric experiments are performed in order to measure the thermal expansion and the shrinkage. The measurement of thermo-physical properties such as the specific heat capacity and thermal diffusivity are carried out as well. The last set of experiments are validation experiments with the goal of comparing the developed material model in Chapter 4 with the real behavior for a complex stress state. In this section, information about the experimental setup for the thermo-mechanical experiments is provided. For the remaining experiments, the according information is given in the respective section.

The main experimental campaign was carried out at the Institute of Applied Mechanics of the Clausthal University of Technology. The thermo-mechanical experiments were performed with a servo-hydraulic multiaxial Zwick material testing machine Z100, which operates in a range up to $100\,\mathrm{kN}$ in tension/compression and $1000\,\mathrm{N\,m}$ in torsion, see Fig. 3.4(a). The force sensor and a torque sensor of the testing machine were used to measure the applied force and torque. The rotational angle of the cross-head was used for the measurement in the torsion experiments. Furthermore, for the measurements of the axial strains, a fine strain extensometer was used, see Fig. 3.4(b). All mechanical ex-

(a) Testing machine (b) Specimen with extensometer

Figure 3.4: Testing machine and measurement of the deformation

periments are strain-controlled. The testing machine was also equipped with a thermal chamber that was used to control the temperature, allowing to perform experiments in the temperature range between $-60\,^{\circ}\mathrm{C}$ and $250\,^{\circ}\mathrm{C}$. In addition, validation experiments

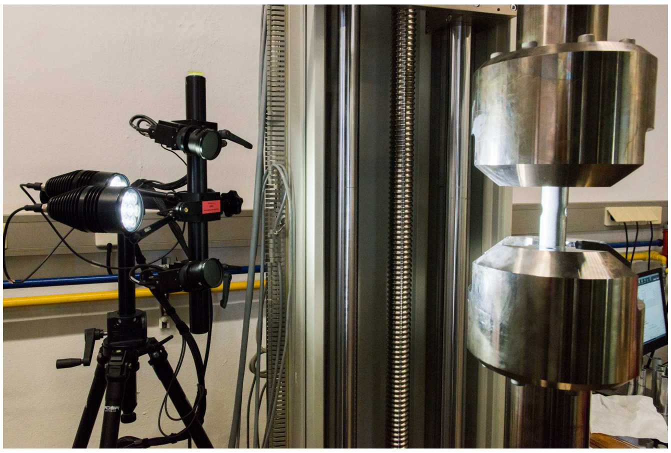

Figure 3.5: GOM-system

were carried out with the help of the digital image correlation system Aramis of the company GOM, see (GOM, 2011). This system is able to measure the displacements and deformations on the surface of the specimen with the help of a pattern generated by a white background color covered with black dots.

3.4 Considerations for Data Evaluation

In order to evaluate the experimental data, there are several aspects that have to be considered. First, the rotational angle in the torsion tests is measured with the traverse of the testing machine. Since the machine deforms elastically during the tests, the measurement is influenced by the deformation of the machine. Thus, these measurements have to be calibrated. Moreover, the treatment of the experimental data is exposed for small and large deformations. In the last part of this section, a study of the dispersion of the specimens is shown.

3.4.1 Calibration of Torsion Experiments

In the case of tension and compression, the change in the length of the specimen is measured with the help of an extensometer placed in the center of the specimen. However, in the torsion tests, the rotational angle is measured with the traverse of the testing machine. The latter measurement is influenced by the elastic deformation of the machine during the experiment. The deformation of the machine has to be determined in order to calibrate the data. The measured angle of the testing machine $\varphi_{\text{measured}}$ is equal to the rotated angle of the specimen $\varphi_{\text{specimen}}$ plus the rotation of the machine φ_{machine},

$$\varphi_{\text{measured}} = \varphi_{\text{specimen}} + \varphi_{\text{machine}}. \tag{3.1}$$

The real rotational angle of the specimen can be calculated by

$$\varphi_{\text{specimen}} = \varphi_{\text{measured}} - \varphi_{\text{machine}}. \tag{3.2}$$

In order to find the rotation of the testing machine due to elastic deformation in dependence of the torque $\varphi_{\text{machine}}(M_T)$, a reference specimen with a high stiffness is used, so that the deformation of the specimen during the calibration is very small and stays in the linear elastic range. In this case, a full cylindrical steel specimen with the length $L = 150\,\mathrm{mm}$ and a radius $R = 30\,\mathrm{mm}$ is tested up to a torque of $600\,\mathrm{N\,m}$. The measurements are fitted with a linear equation, $\varphi_{\text{measured}} = m_{\text{cal}} M_T$, with the parameter $m_{\text{cal}} = 2.5 \times 10^{-3}\,{}^\circ(\mathrm{N\,m})^{-1}$, see Fig. 3.6. The cylindrical steel specimen deforms elastically in the range of the applied torque with the chosen dimensions. The shear stress at the outer surface in a cylindrical specimen can be calculated by

$$\tau = \frac{M_T}{I_T} R, \tag{3.3}$$

see (Hartmann, 2015). For linear elasticity, the relation between the shear stress τ and the rotation angle φ is obtained by

$$\tau = G\gamma = G\frac{R}{L}\varphi. \tag{3.4}$$

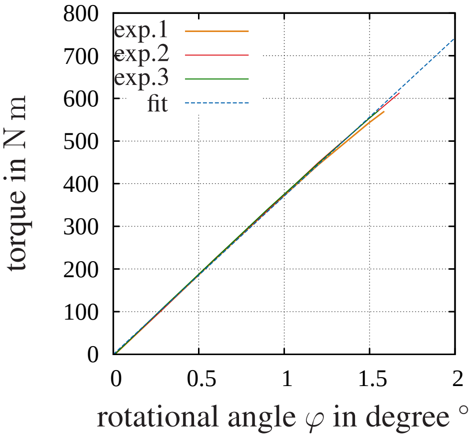

Figure 3.6: Calibration of the testing machine up to $600\,\mathrm{N\,m}$

The dependence between the rotation angle of the steel specimen and torque is obtained by inserting Eq. (3.3) into Eq. (3.4)

$$\varphi_{\text{steel}} = \frac{L}{GI_T} M_T. \tag{3.5}$$

The calibration curve of the machine is then calculated by the measured angle minus the rotation angle of the steel

$$\varphi_{\text{machine}} = m_{\text{cal}} M_T - \frac{L}{GI_T} M_T = m_{\text{machine}} M_T, \tag{3.6}$$

with $m_{\text{machine}} = 2.413 \times 10^{-3}\,{}^{\circ}(\mathrm{N\,m})^{-1}$. In this way, the real rotational angle of the specimen during the torsion tests can be determined with

$$\varphi_{\text{specimen}} = \varphi_{\text{measured}} - m_{\text{machine}} M_T. \tag{3.7}$$

3.4.2 Data Evaluation of Mechanical Experiments

The generation of a homogeneous strain or stress state is a useful procedure for material modeling in Continuum Mechanics, see (Lion, 1994; Haupt and Lion, 1995; Haupt, 2002), and (Becker and Bürger, 1975). With this approach, one can consider the one-dimensional material behavior for preliminary modeling concepts – and afterwards, the model is generalized to the three-dimensional case. The chosen specimen's geometry is assumed to be a thin-walled cylinder. This allows the assumption of a homogeneous stress state in the case of torsion for small deformations, as well as for tension/compression tests. Torsion tests in a thin-walled cylinder for small deformations are of particular interest for the parameter identification process, since the material response can be assumed to be purely deviatoric. In Chapter 4, a model for small deformations will be developed. This model will be extended to the large deformations case later on. The question which model is more appropriate for further computations has to be answered with regard to the specific application case. In this section, the connection between the measured quantities (forces/torques and displacements/rotations) with the quantities of the model (stresses and strains) is given first for the small deformation case and, after that, for large deformations.

Small Deformations

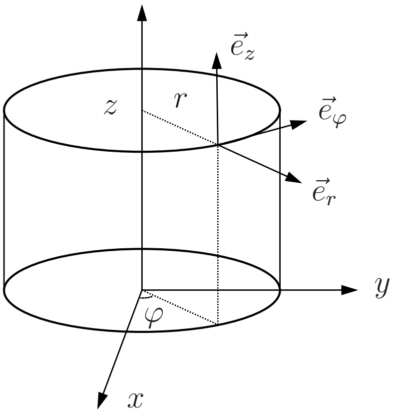

Figure 3.7: Cylindrical coordinates

For the following derivations, the cylindrical coordinate system from Fig. 3.7 is considered, see also (Lion, 1994). The equilibrium conditions neglecting the body forces $\operatorname{div}\mathbf{T} = \vec{0}$ in cylinder coordinates are given by

$$\begin{aligned}
\frac{\partial \sigma_{rr}}{\partial r} + \frac{1}{r}\frac{\partial \tau_{r\varphi}}{\partial \varphi} + \frac{\partial \tau_{rz}}{\partial z} + \frac{\sigma_{rr} - \sigma_{\varphi\varphi}}{r} &= 0, \\
\frac{\partial \tau_{r\varphi}}{\partial r} + \frac{1}{r}\frac{\sigma_{\varphi\varphi}}{\varphi} + \frac{\partial \tau_{\varphi z}}{\partial z} + 2\frac{\tau_{r\varphi}}{r} &= 0, \\
\frac{\partial \tau_{rz}}{\partial r} + \frac{1}{r}\frac{\tau_{\varphi z}}{\partial \varphi} + \frac{\partial \sigma_{zz}}{\partial z} + \frac{\tau_{rz}}{r} &= 0.
\end{aligned} \tag{3.8}$$

Due to axisymmetry, and because of the homogeneous stress state in the thin-walled specimen, the stresses are assumed to be independent of the φ- and z-coordinate, i.e. all derivatives with respect to φ and z vanish. Accordingly, Eq. (3.8) can be simplified to

$$\frac{\partial \sigma_{rr}}{\partial r} + \frac{\sigma_{rr} - \sigma_{\varphi\varphi}}{r} = 0, \tag{3.9a}$$

$$\frac{\partial \tau_{r\varphi}}{\partial r} + 2\frac{\tau_{r\varphi}}{r} = 0, \tag{3.9b}$$

$$\frac{\partial \tau_{rz}}{\partial r} + \frac{\tau_{rz}}{r} = 0. \tag{3.9c}$$

The solution of the ordinary differential equations (3.9b) and (3.9c) leads to the shear components $\tau_{r\varphi}(r) = C_1/r^2$ and $\tau_{rz}(r) = C_2/r$. Since it is also assumed that these components are zero at the surface of the specimen, the constants are determined as $C_1 = 0$ and $C_2 = 0$, i.e. $\tau_{r\varphi} = \tau_{rz} = 0$. Finally, under consideration of the thinness, one can neglect the dependence of σ_{rr}, $\sigma_{\varphi\varphi}$, σ_{zz} and $\tau_{\varphi z}$ on the coordinate r. From Eq. (3.9a), we obtain $\sigma_{rr} = \sigma_{\varphi\varphi}$. Due to the fact that $\sigma_{rr} = 0$ at the surface of the specimen, it can be concluded that $\sigma_{rr} = \sigma_{\varphi\varphi} = 0$. The stress component in z-direction is spatially constant $\sigma_{zz}(r) = \sigma = \text{const}$, as well as $\tau_{\varphi z}(r) = \tau$. Thus, the stress tensor for the case of tension/compression, where $\tau = 0$, and torsion for small deformations, with $\sigma = 0$, can be written as

$$\mathbf{T}_{\text{tension}} = \begin{bmatrix} 0 & 0 & 0 \\ 0 & 0 & 0 \\ 0 & 0 & \sigma \end{bmatrix} \vec{e}_i \otimes \vec{e}_j, \qquad \mathbf{T}_{\text{torsion}} = \begin{bmatrix} 0 & 0 & 0 \\ 0 & 0 & \tau \\ 0 & \tau & 0 \end{bmatrix} \vec{e}_i \otimes \vec{e}_j, \tag{3.10}$$

with $i, j = r, \varphi, z$. A further consideration treats the kinematics, see also Chapter 2. In the case of small deformations, the Green strain tensor $\mathbf{E}$ can be linearized by

$$\mathbf{E} = \frac{1}{2}(\mathbf{H} + \mathbf{H}^{\mathrm{T}}) \qquad \text{with} \qquad \mathbf{H} = \operatorname{Grad} \vec{u}(\vec{x}, t). \tag{3.11}$$

In the case of tension, compression, and torsion for a thin-walled cylinder, the displacement vector in cylindrical coordinates $\vec{u}$ is independent of the coordinate φ due to rotational symmetry. Moreover, since the measurement area is far away enough from the clamping area, so that the deformation in the measurement area is not affected by the clamping, the radial displacement u_r can be assumed to be independent of the z-coordinate, as well as the displacement u_z is assumed to be independent of the radial coordinate r. Thus, the displacement vector $\vec{u}$ can be formulated as

$$\vec{u} = u_r(r)\vec{e}_r + u_\varphi(r, z)\vec{e}_\varphi + u_z(z)\vec{e}_z. \tag{3.12}$$

The strain tensor in cylindrical coordinates can be written as

$$\mathbf{E} = \begin{bmatrix} \dfrac{\partial u_r}{\partial r} & \dfrac{1}{2}\left(\dfrac{\partial u_\varphi}{\partial r} - \dfrac{u_\varphi}{r}\right) & 0 \\ \dfrac{1}{2}\left(\dfrac{\partial u_\varphi}{\partial r} - \dfrac{u_\varphi}{r}\right) & \dfrac{u_r}{r} & \dfrac{1}{2}\dfrac{\partial u_\varphi}{\partial z} \\ 0 & \dfrac{1}{2}\dfrac{\partial u_\varphi}{\partial z} & \dfrac{\partial u_z}{\partial z} \end{bmatrix} \vec{e}_i \otimes \vec{e}_j, \tag{3.13}$$

with $i, j = r, \varphi, z$. In the case of a homogeneous strain state, the strain will be constant in the middle plane of the specimen, meaning that it is independent of the z-coordinate in this range. The components of the strain tensor can be derived from Eq. (3.13). Since the axial strain is independent of the radius, it has the constant value of

$$\frac{\partial u_z}{\partial z} = \varepsilon = \text{const.} \tag{3.14}$$

Under the assumption of thinness, the lateral strain ε_Q has a constant value across the thickness

$$\frac{\partial u_r}{\partial r} = \frac{u_r}{r} = \varepsilon_Q = \text{const.} \tag{3.15}$$

The shear strain is also independent of the z-coordinate

$$\frac{\partial u_\varphi}{\partial z} = \hat{f}(r), \tag{3.16}$$

with $\hat{f}(r)$ a function. Integrating Eq. (3.16) over z, we obtain

$$u_\varphi(r, z) = z\hat{f}(r) + C(r). \tag{3.17}$$

The integration constant $C(r) = 0$ can be calculated with the boundary condition $u_\varphi(r, 0) = 0$. The function $\hat{f}(r)$ can now be obtained considering the case of torsion in Fig. 3.8. For a rotational angle $\varphi = \varphi_L$ applied at the length $z = L$, the displacement in φ-direction is equal to $u_\varphi(r, L) = r\varphi_L = \hat{f}(r)L$, which leads to $\hat{f}(r) = r\,\varphi_L/L$. The displacement component u_φ is then equal to

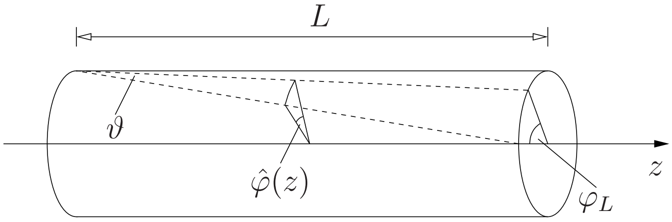

Figure 3.8: Cylinder under torsion

$$u_\varphi(r, z) = r\frac{\varphi_L}{L}z. \tag{3.18}$$

Moreover, under the assumption of thinness, the radius can be substituted by the middle radius $r \approx R_m = (R_i + R_o)/2$. Here, R_i is the inner radius of the thin-walled cylinder, and R_o is the outer radius. With expression (3.18), one obtains from Eq. (3.13)

$$\frac{1}{2}\left(\frac{\partial u_\varphi}{\partial r} - \frac{u_\varphi}{r}\right) = 0. \tag{3.19}$$

In the case of tension and compression, the rotational angle is equal to $\varphi_L = 0$, which implies that $u_\varphi = 0$. In pure torsion, there is no displacement in z- and r- direction, which leads to $\varepsilon = \varepsilon_Q = 0$. Thus, the strain tensor has the following form in the case of tension/compression and torsion for a thin-walled cylinder

$$\mathbf{E}_{\text{tension}} = \begin{bmatrix} \varepsilon_Q & 0 & 0 \\ 0 & \varepsilon_Q & 0 \\ 0 & 0 & \varepsilon \end{bmatrix} \vec{e}_i \otimes \vec{e}_j, \qquad \mathbf{E}_{\text{torsion}} = \begin{bmatrix} 0 & 0 & 0 \\ 0 & 0 & \gamma/2 \\ 0 & \gamma/2 & 0 \end{bmatrix} \vec{e}_i \otimes \vec{e}_j, \tag{3.20}$$

with $i, j = r, \varphi, z$. From the data obtained by the experiments, the axial stress and strain in tension and compression can be calculated by

$$\sigma = \frac{F}{A_0}, \qquad \varepsilon = \frac{L_e - L_0}{L_0}, \tag{3.21}$$

where $A_0 = \pi(R_o^2 - R_i^2)$ is the initial cross-section of the specimen, with $R_o = R_i + d$. $d = 2\,\mathrm{mm}$ is the thickness of the cylinder, see Fig. 3.9. F is the measured force, $L_0 = 20\,\mathrm{mm}$ the initial length of the extensometer, which is placed at the middle of the specimen, and L_e is the current length of the extensometer. In the case of torsion, the shear stress can be calculated from the first Bredt's equation, see for example (Hartmann, 2015), and the shear strain can be approximated in the case of small deformations to $\gamma \approx \tan\vartheta$, see Fig. 3.8. The shear stress τ and shear strain γ are equal to

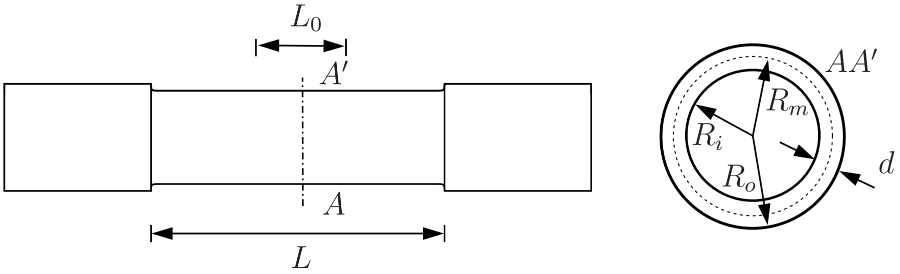

Figure 3.9: Cylinder geometry

$$\tau = \frac{M_T}{2A_m d}, \qquad \gamma = \frac{R_m}{L}\varphi_L. \tag{3.22}$$

In these expressions, $R_m = d + R_i/2 = 14\,\mathrm{mm}$ and $L = 90\,\mathrm{mm}$ are the middle radius and the length of the specimen, respectively, while φ_L is the rotation angle, M_T is the measured torque, and A_m is the surface of the circle with the radius R_m, see Fig. 3.9.

Data evaluation error The assumption of a thin-walled cylinder is not completely fulfilled, which leads to an error in the evaluation of the torsion experiments. This error can only be quantified for the case of linear elasticity, since finite element computations are necessary for plasticity. Comparing the ratio of the exact shear stress at the outer surface and the shear stress in the center area, we obtain for the estimation for linear elasticity

$$f_{\text{err}} = \frac{\tau(R_o)}{\tau_m} = \frac{1+\zeta}{1+\zeta^2} = 1.066, \tag{3.23}$$

see (Hartmann, 2015). In this specific case, the ratio between the inner R_i and outer R_o radius is $\zeta = R_i/R_o = 13/15 = 0.86667$ and results in an error of 6.6%. This corresponds to the *maximal* error generated because of the assumption of a thin-walled cylinder. This value is lower for plastic material behavior, since the slope of the stress-strain diagram decreases – and because of that, the sensitivity of the stresses with respect to the strain reduces as well.

Finite Deformations

In the case of torsion for finite deformations, we can observe an axial force and a buckling of the outer surface, which is why the problem can not be reduced to the one-dimensional case. Because of that, only the tensile and compression tests are considered for the identification later on, see also Krämer et al. (2015). In the case of isothermal tension and compression, the deformation gradient in Cartesian coordinates is equal to

$$\mathbf{F} = \begin{bmatrix} \lambda_Q & & \\ & \lambda_Q & \\ & & \lambda \end{bmatrix} \vec{e}_i \otimes \vec{e}_j, \quad \text{with} \quad i,j = x,y,z, \tag{3.24}$$

where the axial stretch λ is equal to the current length L divided by the initial length L_0

$$\lambda = \frac{L}{L_0}. \tag{3.25}$$

Moreover, in an analogous way as for small deformations, from the equilibrium conditions, the Cauchy stress has components in axial (z-)direction

$$\mathbf{T} = \begin{bmatrix} 0 & & \\ & 0 & \\ & & \sigma \end{bmatrix} \vec{e}_i \otimes \vec{e}_j, \quad \text{with} \quad i,j = x,y,z. \tag{3.26}$$

The stress $\sigma = F/A$ is the so-called true stress , since it is referred to the current area A. Since the current area was not measured, the magnitude obtained from the experiments is the engineering stress $\sigma_{zz}^{1PK} = F/A_0$, which is related to the area in the reference configuration A_0. In case of large deformations, it corresponds to the component of the first Piola-Kirchhoff tensor, see Chapter 2.

3.4.3 Dispersion Considerations

The dispersion of the specimens is considered by investigating the reproducibility at room temperature in tension, compression, and torsion – see also Section 3.5. All the experiments for the material without aging were repeated five times at room temperature. As an example, the stress-strain curves at different rates in tension are presented in Fig. 3.10. Tab. 3.2 provides the maximum standard deviation of the stress for each velocity in tension, compression, and torsion. The standard deviation s_d of a quantity d is calculated by

$$s_d = \sqrt{\frac{1}{n-1}\sum_{i=1}^{n}\left(d_i - \bar{d}\right)^2}, \tag{3.27}$$

where n is the number of measurements of d and its mean value is $\bar{d}$. The obtained reproducibility of the experiments is acceptable, see Fig. 3.10(b). The compression experiments show a higher standard deviation, since the maximal reached strains are larger than in tension, see Tab. 3.2. The deviation in the results originates from several sources. First, there are small deviations in the specimen's geometry. Secondly, environmental influences (such as environmental temperature changes that affect the testing machine) were present during the long period of the experimental campaign, which took place over the course of about three years. Finally, there are inevitable small differences in the microstructure of the specimens, since the porosity varies from specimen to specimen. The porosity is a general characteristic of die casting materials, and it is difficult to control, see Section 3.2. Since the experimental program is quite extensive, only specific experiments are performed several times. The experiments at different temperatures and aging times are repeated three times, while the multi-step and the long-term relaxation tests are only performed once for the specimens with aging, considering that one experiment alone can take up to approximately 2 days. The results shown in Section 3.5, as well as the curves used for the identification, correspond to the mean value of the repetitions of the same experiment.

Table 3.2: Standard deviation in % of the maximum reached stress for the four different strain-rates in tension, compression, and torsion

	$s_{\dot{\varepsilon}_1}$	$s_{\dot{\varepsilon}_2}$	$s_{\dot{\varepsilon}_3}$	$s_{\dot{\varepsilon}_4}$
Tension	0.58	2.33	1.04	1.36
Compression	4.21	2.56	1.64	1.82
	$s_{\dot{\gamma}_1}$	$s_{\dot{\gamma}_2}$	$s_{\dot{\gamma}_3}$	$s_{\dot{\gamma}_4}$
Torsion	2.85	0.98	1.34	0.73

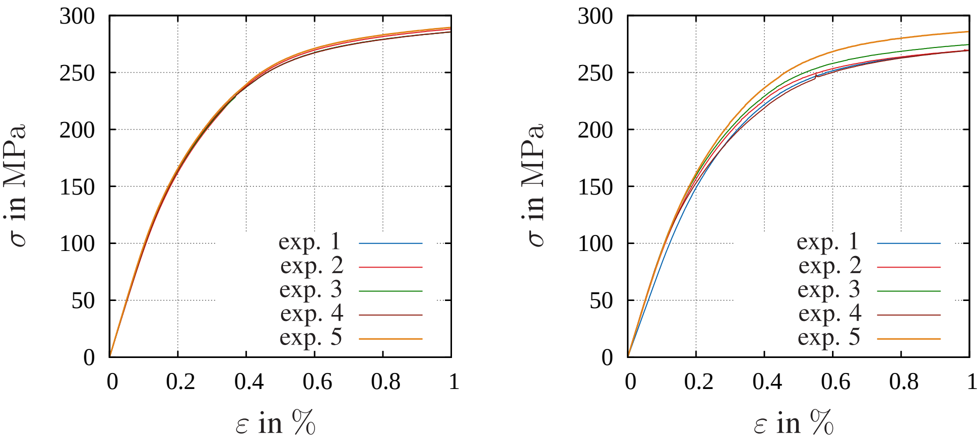

(a) Strain-rate $\dot{\varepsilon}_1 = 3.3 \times 10^{-4}\,\mathrm{s}^{-1}$ (b) Strain-rate $\dot{\varepsilon}_2 = 3.3 \times 10^{-5}\,\mathrm{s}^{-1}$

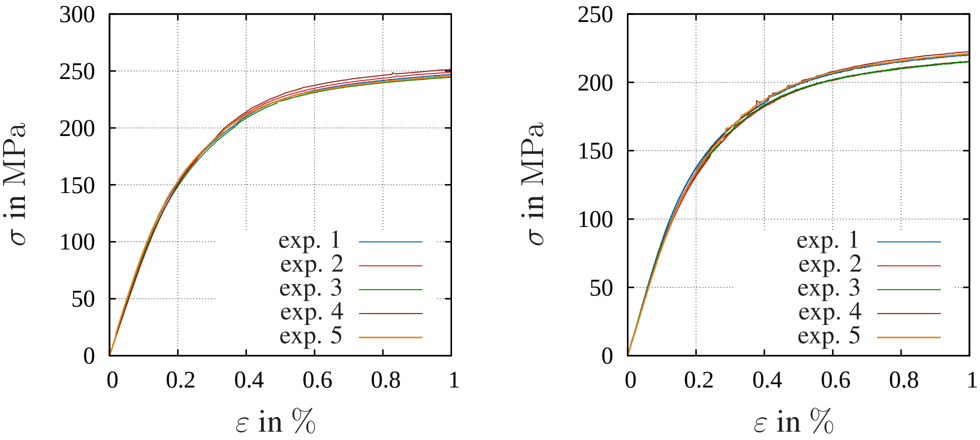

(c) Strain-rate $\dot{\varepsilon}_3 = 3.3 \times 10^{-6}\,\mathrm{s}^{-1}$ (d) Strain-rate $\dot{\varepsilon}_4 = 3.3 \times 10^{-7}\,\mathrm{s}^{-1}$

Figure 3.10: Dispersion of the specimens in tension

3.5 Thermo-Mechanical Experiments

The focus of this section lies in the experimental characterization of the mechanical behavior of the material considering the influence of temperature and aging. This information is necessary for the development of the material model and for the material parameter identification. The following investigations are based on the assumptions resulting from torsion of a thin-walled cylinder made in Section 3.4.2. The main behavior of the alloy is first characterized at room temperature with different loading paths. After that, the temperature and aging dependence are included by performing experiments at four different temperatures and four aging times. In order to obtain information about the volumetric and shear behavior for the identification in Chapter 5, tension, compression, and torsion tests are performed.

The first challenge of the experimental campaign is to determine the material class to which the material belongs. According to Haupt (2002), the material behavior can be classified experimentally into rate-dependent or rate-independent response, and into material behavior with or without an equilibrium hysteresis (that means, a history-dependent or independent response of the equilibrium state). This classification matches the four theories of material behavior: elasticity, plasticity, viscoelasticity, and viscoplasticity. In order to assess whether the material is rate-dependent, experiments at four different strain-rates at room temperature are performed. These strain-rates differ in one order of magnitude. Fig. 3.11(a) shows a representation of the prescribed strain paths for experiments at different strain-rates.

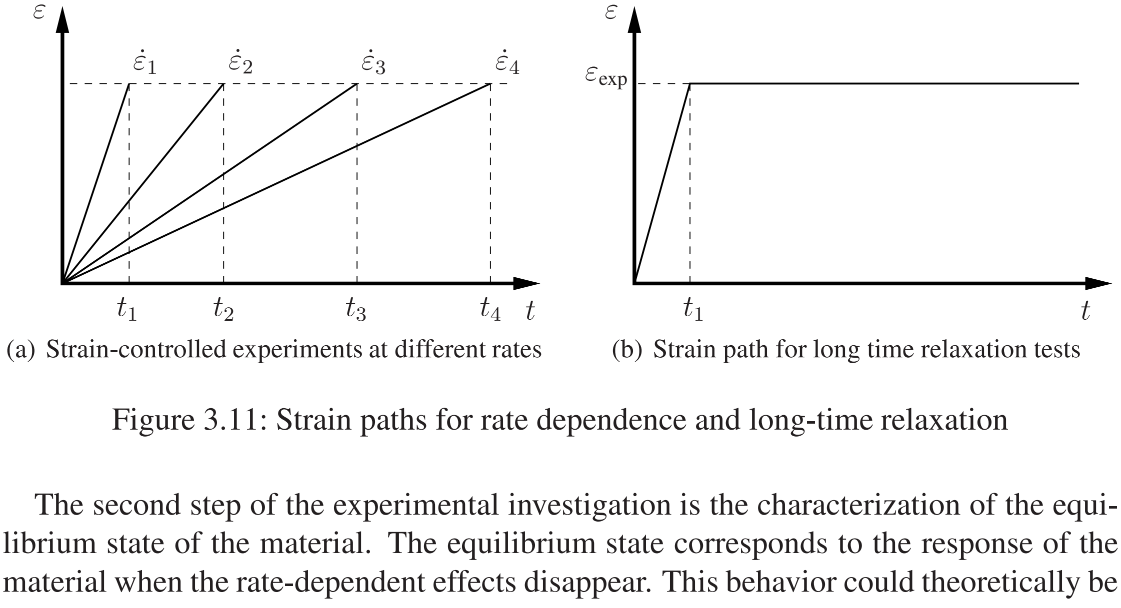

(a) Strain-controlled experiments at different rates (b) Strain path for long time relaxation tests

Figure 3.11: Strain paths for rate dependence and long-time relaxation

The second step of the experimental investigation is the characterization of the equilibrium state of the material. The equilibrium state corresponds to the response of the material when the rate-dependent effects disappear. This behavior could theoretically be obtained with an infinitely slow loading process. The equilibrium state of viscoelastic material is a single curve, and that of a viscoplastic one is represented by a hysteresis. The equilibrium hysteresis represents permanent deformations. The equilibrium state of

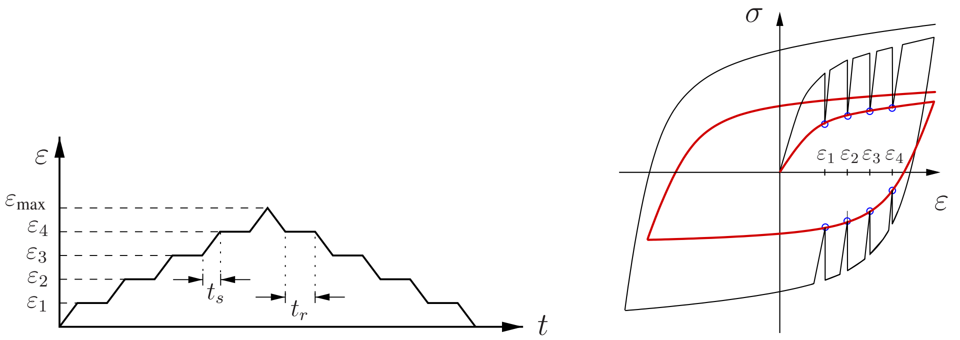

(a) Strain-path of the multi-step relaxation test

(b) Determining the termination points of the equilibrium hysteresis

Figure 3.12: Experiments for the estimation of equilibrium state

the material can also be reached in a relaxation process, in which, during the relaxation, the rate-dependent effects reduce over time until they vanish. Since it is not possible to carry out an infinitely slow experiment, a long-time relaxation test is performed to determine the relaxation time of the material – which is the time until the equilibrium state is reached in a relaxation process, starting from a certain stress state. Fig. 3.11(b) shows the loading path of the long-term relaxation test. In this test, the specimen is loaded up to a certain strain ε_{exp}. Then, the strain is kept constant over time. With this information, a multi-step relaxation experiment is performed to approximate the equilibrium stress state at different relaxation points. In a multi-step relaxation test, the specimen is loaded step-wise at certain strains ε_i, $i = 1, 2, 3, 4$, and afterwards the strain is kept constant during the time t_r, see Fig. 3.12(a). During this time, the stress relaxes and approaches the equilibrium stress state, see Fig. 3.12(b).

In the third step of the characterization, temperature dependence is considered. The previous experiments are repeated at four different temperatures. For all experiments presented in this section, the temperature was controlled with the help of a thermal chamber.

The last phenomenon to be investigated is *natural aging*, meaning changes in the alloy's microstructure due to precipitation, *without* the material being exposed to a heating process. Otherwise, such an aging process would have to be described as *artificial aging*. To this end, the described experiments are carried out with specimens at different aging times. Since we consider natural aging, the specimens were stored at the temperature of $19\,^\circ\mathrm{C}$ for 3, 6, and 12 months. Moreover, reference specimens without aging were store after die casting at $-24\,^\circ\mathrm{C}$[2].

Tab. 3.3 shows an overview of the performed experiments for the material without aging. These experiments have the goal to characterize the thermo-mechanical behavior

---

[2] According to (Kallien and Busse, 2009, page 62), the material needs more than 100 years at this temperature to reach the aged state.

in tension, compression, and torsion. The experiments at room temperature $\Theta_1 = 20\,^\circ\mathrm{C}$ were performed 5 times in order to investigate the reproducibility of the experiments, see also Section 3.4.3. After observing a sufficient reproducibility, the experiments at other temperatures were performed 3 times each. During this phase, 216 experiments were performed in total. Part of the results from this section were published in (Martinez Page and Hartmann, 2018b). After the investigations with the unaged material, the tension/compression asymmetry is neglected, see also Section 3.5.1. The next phase of the experimental campaign investigates the material with three different aging times, see Tab. 3.4. Tension and torsion experiments are performed at the different strain-rates. In order to reduce the extension of the experimental campaign, only the multi-step relaxation test in torsion is performed in order to determine the equilibrium behavior. Here, 252 experiments were performed for the material with natural aging.

Table 3.3: Number of times an experiment is performed for the specimens without aging; total number of 216 experiments for the unaged material

loading path in tension,compression/torsion	Θ_1	Θ_2	Θ_3	Θ_4
$\dot{\varepsilon}_1/\dot{\gamma}_1$	5 tests	3 tests		
$\dot{\varepsilon}_2/\dot{\gamma}_2$				
$\dot{\varepsilon}_3/\dot{\gamma}_3$				
$\dot{\varepsilon}_4/\dot{\gamma}_4$				
long time test	5 tests	1 test		
multi-step test				

Table 3.4: Number of times an experiment is performed for the specimens with three different aging times; total number of 252 experiments with the aged material

loading path in tension/torsion	Θ_1	Θ_2	Θ_3	Θ_4
$\dot{\varepsilon}_1/\dot{\gamma}_1$	3 tests			
$\dot{\varepsilon}_2/\dot{\gamma}_2$				
$\dot{\varepsilon}_3/\dot{\gamma}_3$				
$\dot{\varepsilon}_4/\dot{\gamma}_4$	1 test			
multi-step test	1 test, only torsion			

3.5.1 Rate Dependence

The monotonic tension and compression tests are performed at the four different strain-rates of $\dot{\varepsilon}_k = 3.3 \times 10^{-k}\mathrm{s}^{-1}$, $k = 4, 5, 6, 7$. The shear rates are given by $\dot{\gamma}_k = 3.2 \times 10^{-k}\mathrm{s}^{-1}$, $k = 4, 5, 6, 7$. The rate dependence at room temperature for the unaged material is shown in Fig. 3.13(a) for the torsion tests, and in Fig. 3.13(b) for the tension and compression tests.

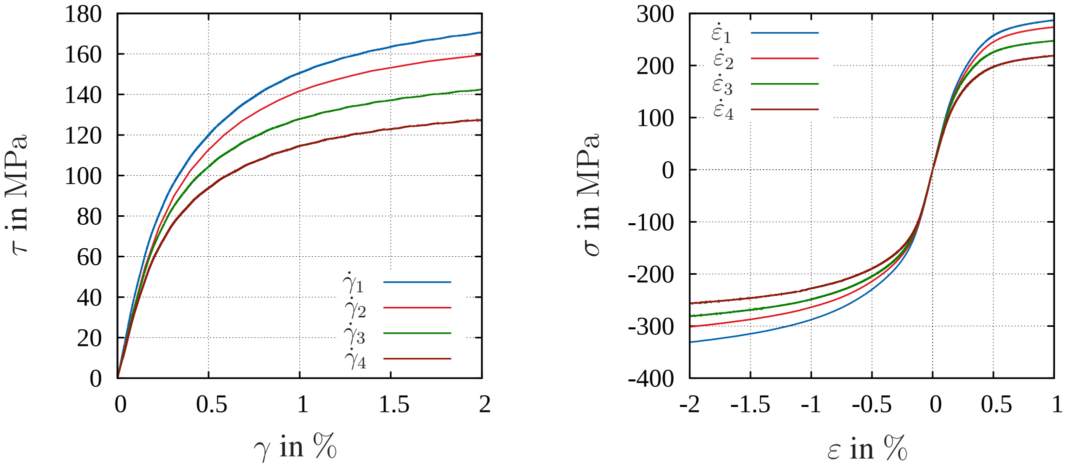

(a) Results in torsion

(b) Results in tension (positive area) and compression (negative area)

Figure 3.13: Rate dependence at $20\,^\circ\mathrm{C}$, see also (Martinez Page and Hartmann, 2018b)

The compression and torsion tests were carried out up to a strain of $2\,\%$. For the tension tests, however, it was only possible to reliably obtain a maximal strain of $\varepsilon_{\max} = 1\,\%$ because of the sensitivity of the material due to its porosity, see (Kallien and Busse, 2009). If the experiments are performed beyond 1% strain, the specimens tend to break uncontrollably at different strains. The behavior displayed in Fig. 3.13 is clearly rate-dependent. This is reflected in the level of the stresses as well as in the different initial slopes of the stress-strain curves for the experiments with different strain-rates. The response at lower strain-rates is “weaker”. The material shows a light tension-compression asymmetry, which will not be considered in the model. Moreover, no clear yield stress is visible. The transition between the initial steeper part of the stress-strain curve to the more plain zone at higher strains occurs monotonously through a continuous curvature.

3.5.2 Determination of the Equilibrium State

For the characterization of the equilibrium state, long-term and multi-step relaxation tests were carried out. The strain-rates $\dot{\varepsilon}_3 = 3.3 \times 10^{-6}\,\mathrm{s}^{-1}$ in tension and compression, and $\dot{\gamma}_3 = 3.2 \times 10^{-6}\,\mathrm{s}^{-1}$ in torsion, were chosen for the loading and unloading during the tests. These strain-rates are fast enough to ensure a moderate loading time, and slow enough to start the relaxation close to the equilibrium hysteresis. The long-time relaxation behavior for the torsion case at room temperature is displayed in Fig. 3.14.

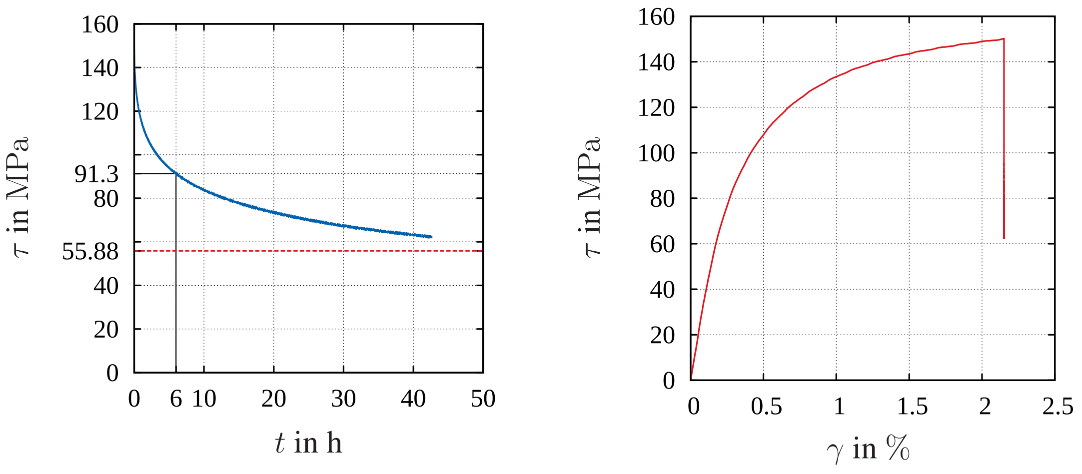

(a) Shear stress over the time

(b) Shear stress over shear strain in a relaxation process

Figure 3.14: Example of the relaxation behavior in torsion at $20\,^\circ\mathrm{C}$, see also (Martinez Page and Hartmann, 2018b)

Here, the material is not completely relaxed after more than 40h. Moreover, the relaxation is very pronounced at this point, since it corresponds to more than $50\,\%$ of the initial value of the shear stress. The same behavior was observed in tension and compression tests. Due to the magnitude of the relaxation time and the large amount of experiments, the long-time relaxation tests were only performed for approximately $40\,\mathrm{h}$. The saturation value of the relaxation τ_∞ in torsion and σ_∞ in tension/compression is estimated with the help of a function that consists of three exponential parts, see Fig. 3.14(a). The hold-time of the multi-step relaxation process is set equal to $t_r = 6\,\mathrm{h}$, owing to the magnitude of the relaxation time. Due to this relaxation time, one multi-step relaxation test takes approximately 2 days. Accordingly, points of the relaxation are estimated with a linear relationship between the relaxation time and the relaxation percentage. Fig. 3.15 shows an example of the estimated relaxation points in the cases of tension/compression and torsion at room temperature for the unaged material. It is clear that the viscous effects are very strong in the material at room temperature. This strong viscous behavior is connected to the low melting point of the alloy, which lies at $380\,^\circ\mathrm{C}$. According to (Lemaitre and Chaboche, 1990), metals show a viscoplastic behavior at temperatures higher than one third of the *absolute* melting temperature. In this case, this temperature is equal to $217.15\,\mathrm{K}/-55\,^\circ\mathrm{C}$ – implying that the material behaves in a viscoplastic manner within the chosen temperature range. Another effect that was observed in the multi-step relaxation tests is a different initial slope for the loading m_{load} and the unloading m_{unload}, see for example Fig. 3.15(a). The initial slope for the unloading is smaller than for the loading. This effect will be included in the modeling part in Chapter 4.

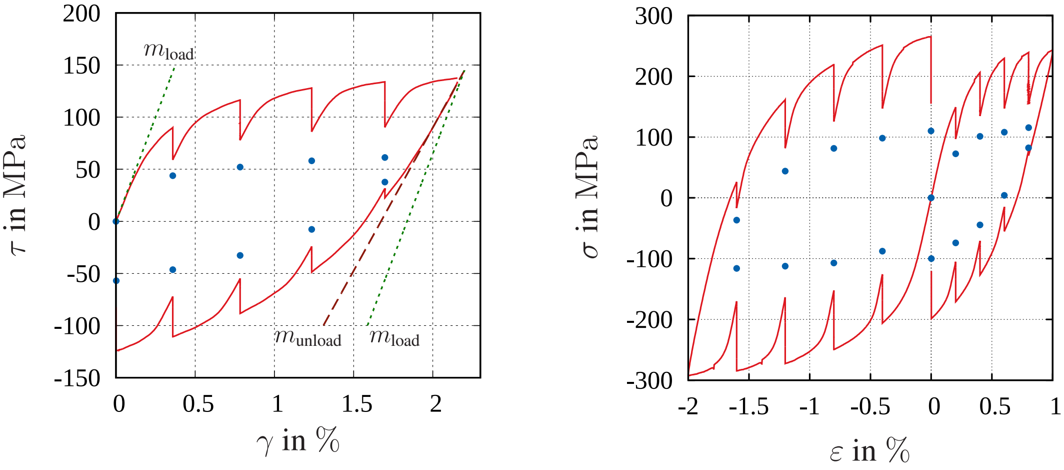

(a) Multi-step relaxation test (red line) and estimated equilibrium hysteresis (blue points) torsion

(b) Multi-step relaxation test (red line) and estimated equilibrium hysteresis (blue points) tension/compression

Figure 3.15: Example of termination points of the relaxation at room temperature, see also (Martinez Page and Hartmann, 2018b)

3.5.3 Temperature Dependence

Due to the fact that the application temperature range of the alloy in the automotive industry[3] goes from $-40\,^\circ\mathrm{C}$ up to $85\,^\circ\mathrm{C}$, the previous experiments are repeated at the four different temperatures of $-40\,^\circ\mathrm{C}$, $20\,^\circ\mathrm{C}$, $60\,^\circ\mathrm{C}$, and $85\,^\circ\mathrm{C}$ in order to obtain the temperature dependence of the material. The temperature is kept constant with the help of a thermal chamber. An extensometer is positioned in the middle of the specimen

---

[3] The investigations had the goal to offer a model for this application area.

after the desired temperature of the experiment is reached, so that the thermal expansion of the specimen can be neglected. The influence of the temperature on the mechanical response is shown in Figs. 3.16 for torsion and in 3.17 for tension and compression. Since the material is very brittle at $-40\,°\mathrm{C}$, it was not possible to perform all the tensile tests up to a strain of 1% at this temperature. The specimens tend to break unpredictably at smaller strains. These results are for specimens without aging.

As can be seen in Figs. 3.16-3.17, the temperature clearly affects the level of the stresses, which increases for lower temperatures for the same strain. The reached stress range in torsion, for example, starts at around $40\,\mathrm{MPa}$ for the slowest strain-rate at $\Theta = 85\,°\mathrm{C}$ and increases up to $180\,\mathrm{MPa}$ at $\Theta = -40\,°\mathrm{C}$ for the fastest strain-rate. The initial slope is influenced by temperature as well, which decreases strongly with an increase of the temperature. Moreover, one can observe an influence of the temperature on the viscous effects, which increase with the temperature too. The stress maximum of the equilibrium hysteresis also becomes smaller for growing temperatures. The influence of the temperature on the viscosity can clearly be seen in Fig. 3.18, where the results in torsion for the fastest and the slowest strain-rate of the four temperatures are shown. For lower temperatures, the material response tends towards rate-independent plasticity, while the viscous effects become predominant with growing temperatures. A similar behavior was observed in the tension and compression tests. In Fig. 3.18, one can clearly see the increase in the viscous effects with the temperature. For high temperatures and low strain-rates, see Fig. 3.18(b), one can observe that the material can be deformed under a constant small load (over $40\,\mathrm{MPa}$) if the load is applied long enough.

3.5.4 Influence of Aging

In order to characterize the influence of aging, the previously exposed experiments at different strain-rates and temperatures are repeated for specimens with the three additional aging times of 3, 6, and 12 months at $19\,°\mathrm{C}$ (natural aging). Since the tension/compression asymmetry is neglected in the model, only tension and torsion experiments are carried out for these three aging times. The results of the torsion tests for the four temperatures and aging times are shown in Fig. 3.19, and for the case of tension in Fig. 3.20. Apparently, the main influence of aging occurs at room temperature, see Figs. 3.19(b) and 3.20(b). Here, a reduction of 15% in the stresses over the aging time is observed. This reduction seems to affect all strain-rates equally. One can see that the difference between the initial state and 3 months of aging is larger than the difference between 3 and 6 months of aging. The reason for this effect lies in the aging kinetics. Since the material is far away from a micro-structural equilibrium, the diffusion processes are more pronounced in the beginning and decrease over time. Moreover, there is also a reduction in the initial slope with increasing aging. For higher temperatures and lower strain-rates, the influence of aging seems to decline, meaning that the viscous effects are affected by aging, see Figs. 3.19(c)-3.19(d) and Figs. 3.20(c)-3.20(d). The aging dependence reduces for lower strain-rates until it almost vanishes at $85\,°\mathrm{C}$ at the

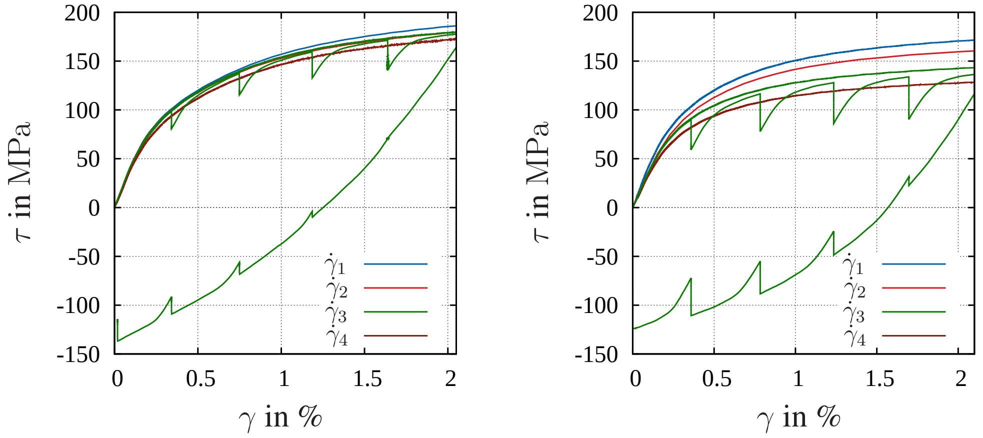

(a) $\Theta = -40\,°\mathrm{C}$

(b) $\Theta = 20\,°\mathrm{C}$

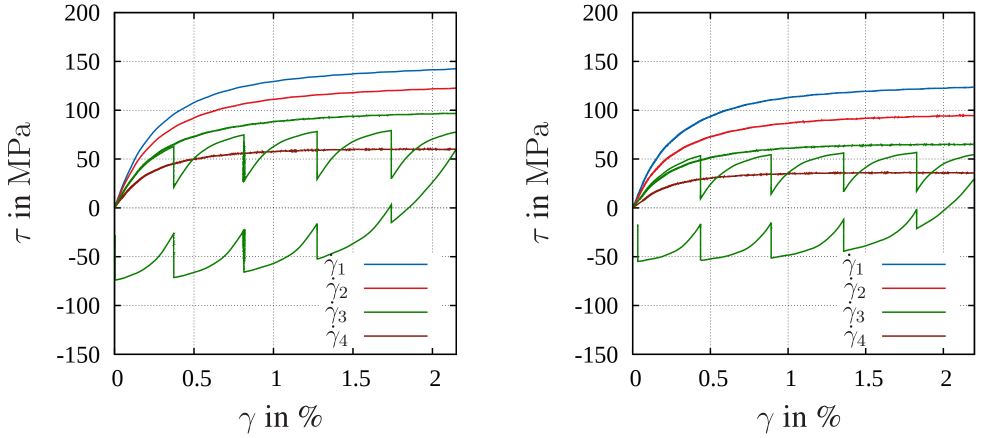

(c) $\Theta = 60\,°\mathrm{C}$

(d) $\Theta = 85\,°\mathrm{C}$

Figure 3.16: Temperature and rate dependence under torsion. Experiments at different strain-rates and multi-step relaxation test. Different strain-rates are represented by different colors

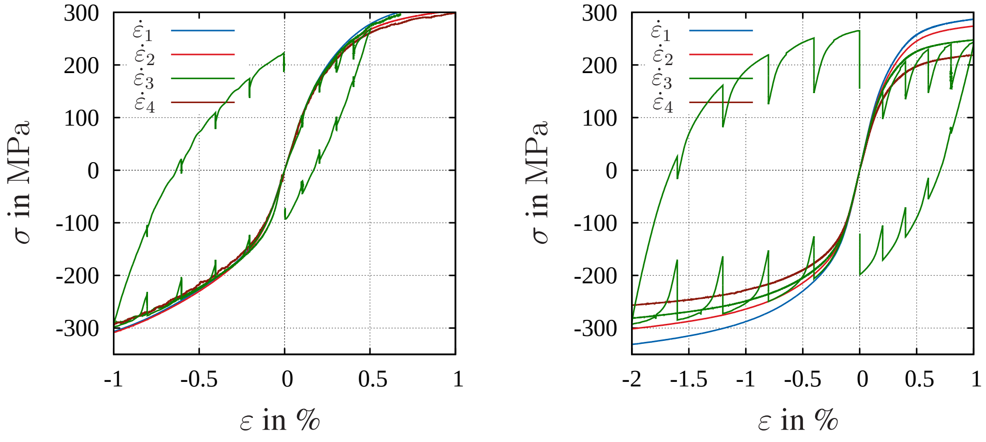

(a) $\Theta = -40\,^{\circ}\mathrm{C}$ (b) $\Theta = 20\,^{\circ}\mathrm{C}$

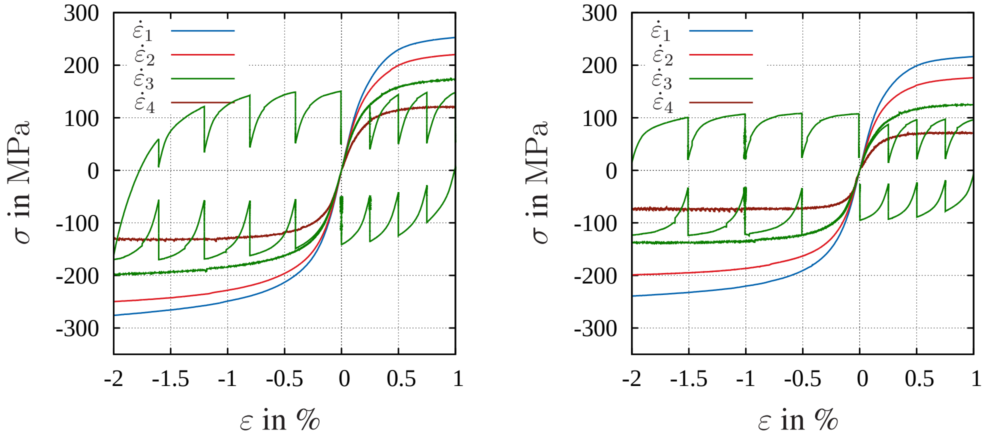

(c) $\Theta = 60\,^{\circ}\mathrm{C}$ (d) $\Theta = 85\,^{\circ}\mathrm{C}$

Figure 3.17: Temperature and rate dependence in tension/compression. Experiments at different strain-rates and multi-step relaxation test. Different strain-rates are represented by different colors

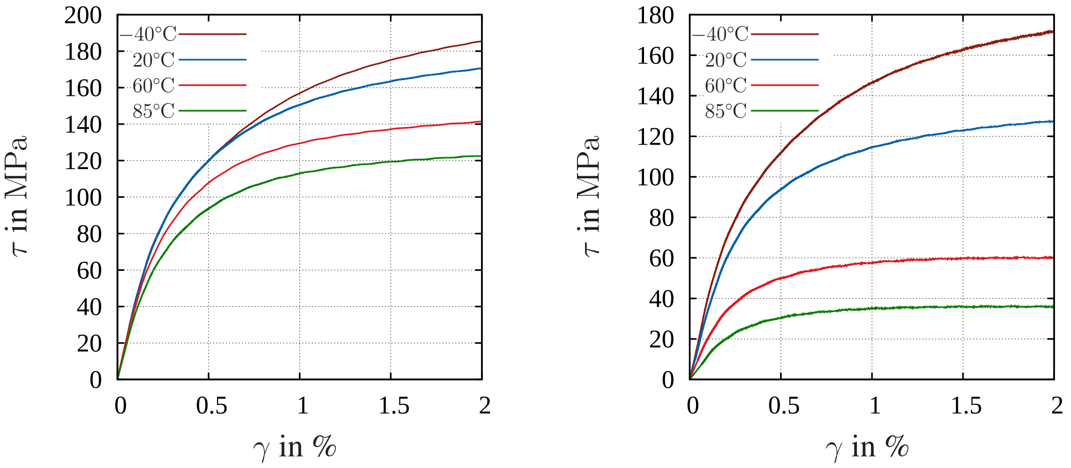

(a) Torsion experiments at four different temperatures at the fast strain-rate $\dot{\gamma}_1 = 3.2 \times 10^{-4}\mathrm{s}^{-1}$

(b) Torsion experiments at four different temperatures at the slow strain-rate $\dot{\gamma}_4 = 3.2 \times 10^{-7}\mathrm{s}^{-1}$

Figure 3.18: Influence of the temperature on the viscous behavior, see also (Martinez Page and Hartmann, 2018b)

slowest strain-rate. The results at $-40\,^\circ\mathrm{C}$ show a small dependence on the aging, which is represented more clearly in Fig. 3.21 for only two strain-rates $\dot{\gamma}_1$ and $\dot{\gamma}_4$ in torsion and tension. Fig. 3.22 shows the equilibrium hysteresis for the different aging times at the four temperatures. Here, one can observe a slight dependence of the equilibrium state with the aging at room temperature. This dependence decreases with increasing temperatures, until it becomes hardly perceptible at $85\,^\circ\mathrm{C}$. At higher temperatures, the viscous effects are predominant and the equilibrium state is very small.

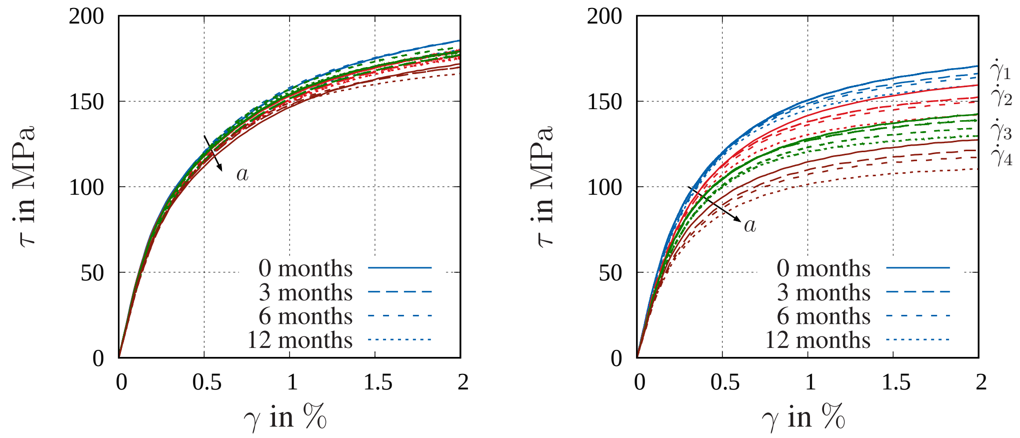

(a) Results for $\Theta = -40\,^\circ\mathrm{C}$

(b) Results for $\Theta = 20\,^\circ\mathrm{C}$

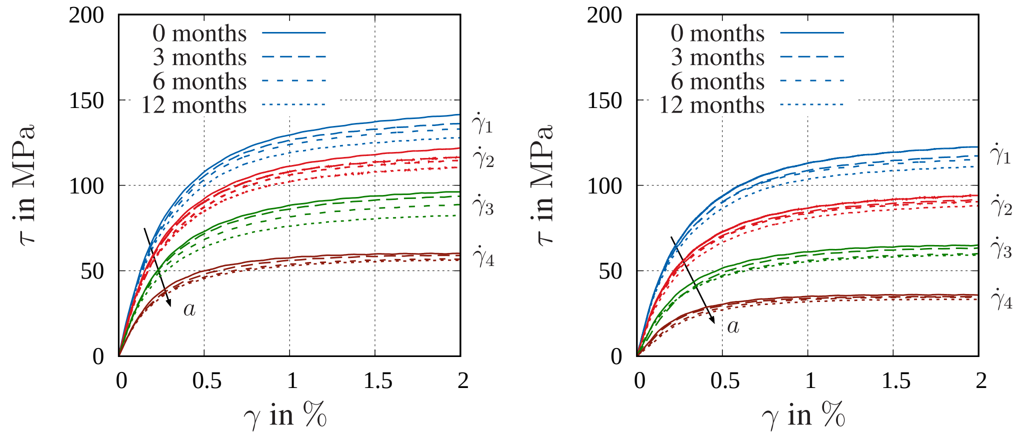

(c) Results for $\Theta = 60\,^\circ\mathrm{C}$

(d) Results for $\Theta = 85\,^\circ\mathrm{C}$

Figure 3.19: Aging effects in torsion for different temperatures and strain-rates. Different strain-rates represented by different colors according to Fig. 3.16. Different aging times represented by different line styles. The arrow points in the direction of increasing aging time a

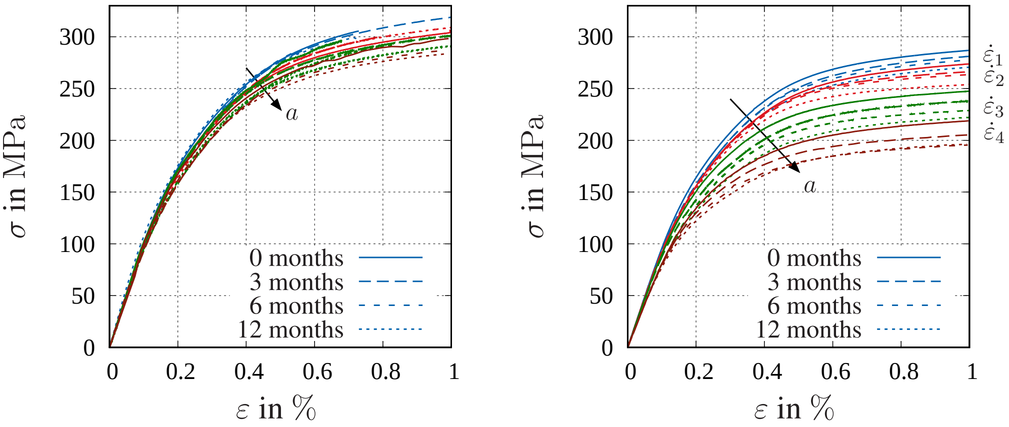

(a) Results for $\Theta = -40\,°\mathrm{C}$

(b) Results for $\Theta = 20\,°\mathrm{C}$

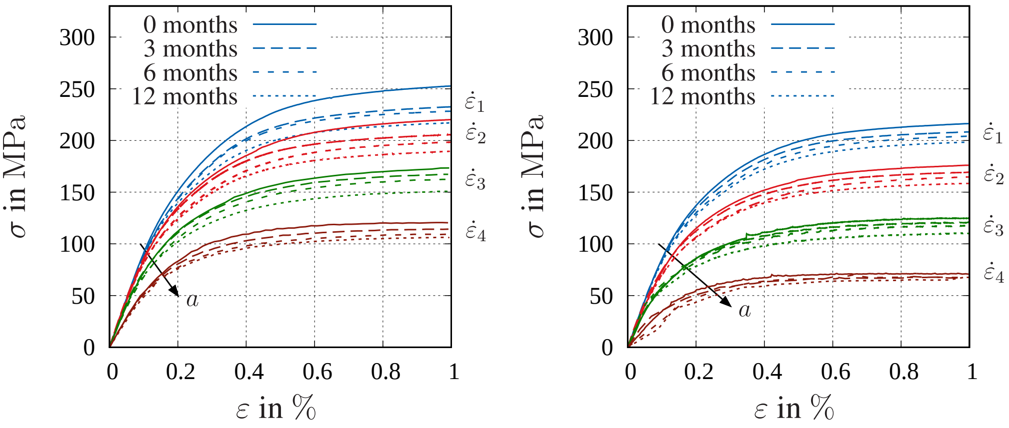

(c) Results for $\Theta = 60\,°\mathrm{C}$

(d) Results for $\Theta = 85\,°\mathrm{C}$

Figure 3.20: Aging effects in tension for different temperatures and strain-rates. Different strain-rates represented by different colors according to Fig. 3.17. Different aging times represented by different line styles. The arrow points in the direction of increasing aging time a

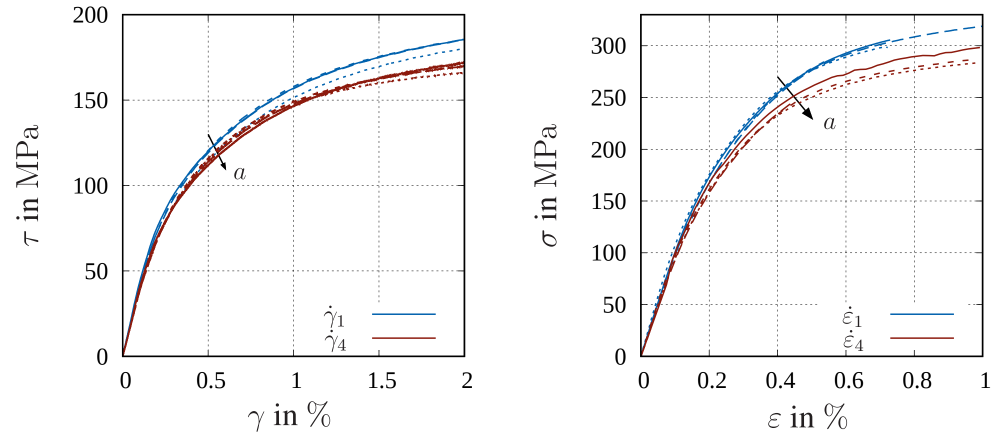

(a) Aging-dependence in torsion at two different strain-rates

(b) Aging-dependence in tension at two different strain-rates. At this temperature, specimens break frequently before $\varepsilon = 1\,\%$ is reached

Figure 3.21: Influence of aging on rate-dependence at $-40\,°\mathrm{C}$. Different strain-rates represented by different colors. Different aging times represented by different line styles. The arrow points in the direction of increasing aging time a

In summary, aging has the greatest influence in the behavior at room temperature and is less pronounced at low and high temperatures. Moreover, it affects the viscous behavior of the material more than the equilibrium state. One can observe that the influence of natural aging is moderate compared to the effect of the temperature or the strain-rate. Nonetheless, these changes due to aging have to be considered for certain application areas. It has to be pointed out that the 12 months of natural aging do not represent the final state of aging in the sense that the micro-structure reaches an equilibrium state. This aging time was chosen at the beginning of the investigations following the indications made in (Kallien and Busse, 2009, page 62). However, as observed in Section 3.7.2, the period of time to reach the final state at room temperature is approximately 5 years. This is also in agreement with the observations shown in (Johnen, 1981). Therefore, a further reduction in the initial slope and the maximum stresses would be expected for longer aging times than 12 months. Moreover, aging also has strong influence on other mechanical properties that are not treated in this work, for instance elongation at fracture, see (Leis and Kallien, 2011).

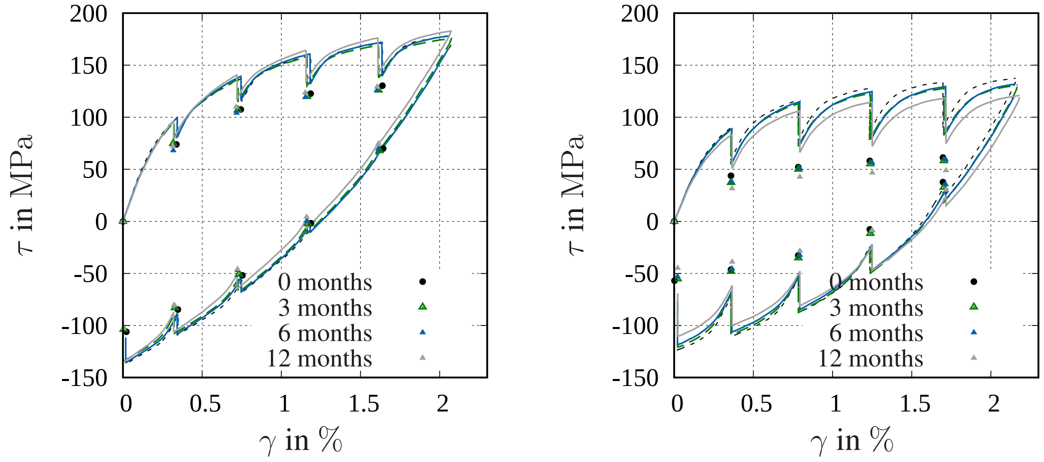

(a) Results for $\Theta = -40\,^{\circ}\mathrm{C}$

(b) Results for $\Theta = 20\,^{\circ}\mathrm{C}$

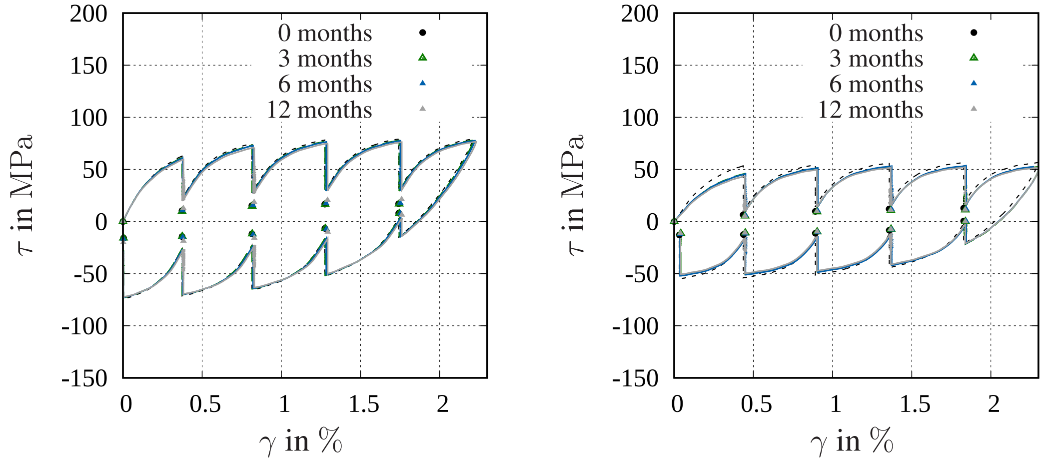

(c) Results for $\Theta = 60\,^{\circ}\mathrm{C}$

(d) Results for $\Theta = 85\,^{\circ}\mathrm{C}$

Figure 3.22: Influence of aging and temperature on the equilibrium state in torsion. Multi-step relaxation tests represented by lines and termination points of the relaxation by points

3.6 Dilatometer Experiments

Two main effects are characterized with dilatometer experiments: the thermal expansion and the shrinkage caused by aging. The measurement of both quantities was performed with a small piece of the center of the specimen shown in Fig. 3.3(b). The specimens for the dilatometer experiments have a length of approximately $2\,\mathrm{mm}$ and a transversal section smaller than $4 \times 4\,\mathrm{mm}^2$.

3.6.1 Thermal Expansion

The thermal expansion coefficient α_Θ is required to compute the deformations in the material routine in a non-isothermal process. It was measured with a dilatometer (TMA 600). The applied heating rate is chosen to be high enough so that aging effects can be neglected during the measurement. Thus, the heating rate is equal to $5\,\mathrm{K/min}$. Moreover, we can consider a homogeneous distribution of the temperature in the specimen during the measurement, due to the good thermal conductivity of the material and the small dimensions of the specimen. Under the assumption of homogeneity, the thermal strain can be calculated by

$$\varepsilon_\Theta = \frac{L(\Theta) - L(\Theta_0)}{L(\Theta_0)}. \tag{3.28}$$

The results of the measurement are shown in Fig. 3.23. The abscissa shows the temperature increment $\Delta\Theta = \Theta - \Theta_0$, with the reference temperature $\Theta_0 = 20\,°\mathrm{C}/293.15\,\mathrm{K}$, and the ordinate represents the thermal expansion ε_Θ calculated from Eq. (3.28). One can see that the thermal expansion is linear for the tested temperature range. The thermal

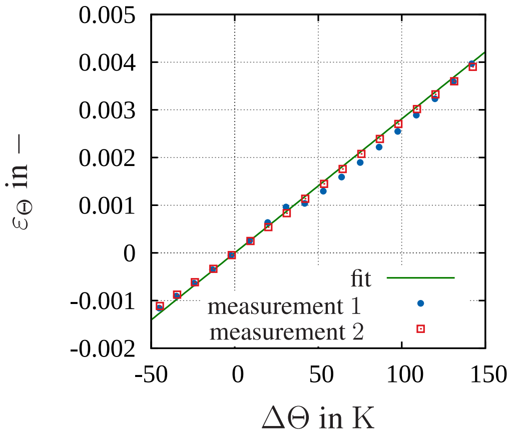

Figure 3.23: Thermal expansion

expansion coefficient is identified as the slope of the line from Fig. 3.23 with a value of $\alpha_\Theta = 2.8109 \times 10^{-5}\,\mathrm{K}^{-1}$.

3.6.2 Shrinkage

The results of the experiments in Fig. 3.19 and Fig. 3.20 show a change in the mechanical response of the alloy in dependence of the aging time. The influence of the aging is included in the model in Chapter 4 with an internal variable, which is motivated by microstructural changes over the course of time. Judging from the aforementioned results, it is not possible to make a direct connection[4] between the aging development and the measured quantities. This makes these experiments unsuitable for identifying an aging variable, since the relation between experiment and modeled phenomenon is not direct. Because of that, there is no unique solution for the modeling and identification of an aging variable. In (Kallien and Busse, 2009) and (Johnen, 1981), however, it is mentioned that there is an additional reduction of the dimensions in zinc die casting alloys over the course of time. This shrinkage is associated to a change in the crystallization system from fcc (face-centered cubic) to hcp (hexagonal close-packed), and it is also connected to changes in the lattice parameter of some phases of the alloy. The deformation in this case is a purely volumetric deformation associated to aging. According to the measurements at room temperature made by (Johnen, 1981), it reaches a maximum value of about $-0.1\,\%$. Since this volume change is only connected to the microstructural changes which occur during the aging process, measurements of the shrinkage are an appropriate option to identify an internal process variable for aging in a unique manner, even if the volume change due to aging is very small. Measuring the shrinkage provides a connection between the microstructural changes – the causes of aging – and a quantity that can be measured – the specimen's length. Since the microstructural changes during the aging process are related to diffusion and precipitation of some alloying elements, the process is temperature-activated. The shrinkage develops faster for higher temperatures. At room temperature, it takes more than one year to reach the completely aged stage. For this reason, the measurements of the shrinkage have to be performed at higher temperatures, so that the measurement takes place in a reasonable period of time.

In order to measure the shrinkage, the specimen is first heated up to the temperature of the measurement Θ_{exp}, with a heating rate equal to $10\,\mathrm{K/min}$. The heating rate is chosen to be fast enough so that shrinkage caused by the aging can be neglected during the heating phase. After that, the temperature is kept constant over the time. The specimen with the initial length L_1 shrinks over time until the length reaches a saturation value L_∞, as shown in Fig. 3.24. The current longitudinal deformation $\varepsilon_{\text{exp}} = (L - L_1)/L_1$ (the shrinkage) can be used as a measure of the aging development.

---

[4] There is no direct connection between the aging development and the mechanical experiments, since a connection between them would require some modeling assumption. The goal is to obtain information regarding the aging development purely from an experiment.

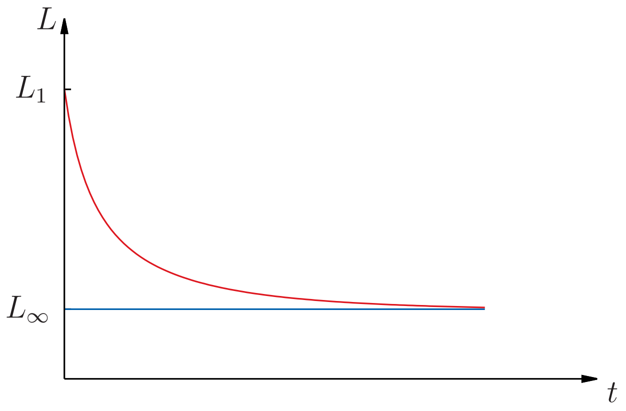

Figure 3.24: Representation of a shrinkage measurement

The measurements of the shrinkage were performed with a Mettler Toledo (TMA 841^e) at the Institute of Mechanics of the Bundeswehr University Munich. They were carried out at a temperatures of $85\,^\circ\mathrm{C}$, $105\,^\circ\mathrm{C}$ and $125\,^\circ\mathrm{C}$. Fig. 3.25 shows the results of the measurements. In Fig. 3.25(b), the time is plotted in logarithmic representation in order to compare these measurements with the shrinkage measurement at $20\,^\circ\mathrm{C}$ for the same alloy shown in (Johnen, 1981). Here, we observe a faster development of the measurement at the higher temperatures. While the measurement at $125\,^\circ\mathrm{C}$ almost reaches a saturation value in the time of the experiment of $18\,\mathrm{h}$, and can thus be interpreted as having reached its final state, the measurement at $105\,^\circ\mathrm{C}$ is still far away from the final state after $24\,\mathrm{h}$. In (Johnen, 1981), it is shown that the material reaches the final stage after approximately 5 years at $20\,^\circ\mathrm{C}$, see Fig. 3.25(b). The saturation value of the strain in the measurement from (Johnen, 1981) is lower in absolute value than the one observed in the measurement at $125\,^\circ\mathrm{C}$, by approximately $-0.14\,\%$. The results from Fig. 3.25 do not coincide with the results for Zamak 5 shown in (Kallien and Busse, 2009), where the alloy reaches the final stage at $120\,^\circ\mathrm{C}$ after 0.4 days. Moreover, the measurement from (Johnen, 1981) at $20\,^\circ\mathrm{C}$ contradicts the results from (Kallien and Busse, 2009), where the specimen reaches the completely aged state after only one year of natural aging. In order to determine whether the specimens with 12 months of natural aging represent the completely aged state, further specimens were artificially aged at temperatures of $80\,^\circ\mathrm{C}$ for $24\,\mathrm{h}$, $100\,^\circ\mathrm{C}$ for $24\,\mathrm{h}$, and $120\,^\circ\mathrm{C}$ for $44\,\mathrm{h}$. This last specimen reaches a completely aged state, see Fig. 3.25(a). A torsion test at room temperature and the fastest strain-rate $\dot{\gamma}_1$ was performed, see Fig. 3.26. The response of the specimens with natural aging at 0, 6, and 12 months is compared to the artificially aged specimens. The results are shown in Fig. 3.26. Here, one can see that the material with one year of natural aging still does not correspond to the final aged state.

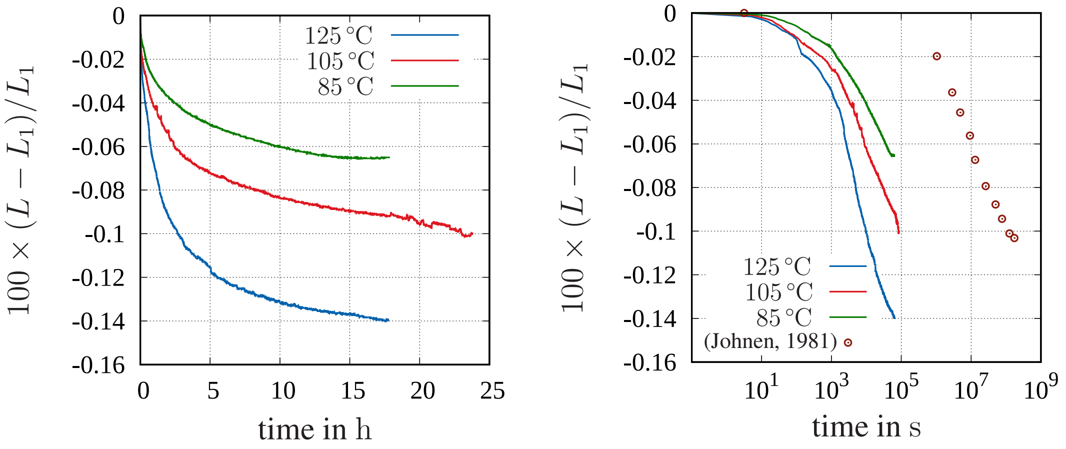

(a) Shrinkage at the temperatures of 85 °C, 105 °C and 125 °C over time

(b) Shrinkage at the temperatures of 85 °C, 105 °C and 125 °C over time in logarithmic scale and measurement from (Johnen, 1981) at 20 °C

Figure 3.25: Results of the shrinkage measurements

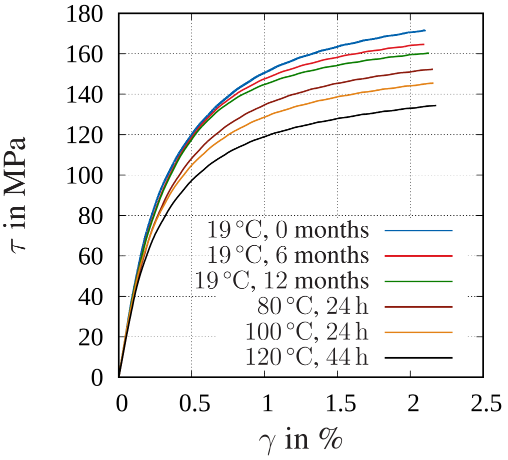

Figure 3.26: Comparison of torsion tests at 20 °C of specimens with natural aging and specimens with artificial aging near to the completely aged stage

This deviation in the results from (Kallien and Busse, 2009) could indicate further dependencies of the development of aging in dependence not only on the composition of the alloy, but also on other parameters of the die casting process. Moreover, it is also possible that the final microstructural state reached after a long heating process does not correspond completely to the same microstructural equilibrium state at lower temperatures. Since a more detailed investigation of this effect is out of the scope of this work, such dependencies are not further investigated. Nevertheless, it is taken into account that 12 months of natural aging does *not* correspond to the completely aged state.

3.7 Thermo-Physical Properties and Microstructure

For the computation of temperature-dependent processes, the material parameters of the heat conduction equation are required – specifically the density ρ, the specific heat capacity c_p, and the thermal conductivity κ_Θ. The measurements of these parameters were performed at the Institute of Electrochemistry of the Clausthal University of Technology. Moreover, an investigation of the microstructure at different aging times with the scanning electron microscope (SEM) and X-ray diffraction (XRD) was performed in order to observe what happens in the microstructure during aging.

The density and the thermal diffusivity were measured in cylinders with a diameter of $10\,\mathrm{mm}$ and a height of $2\,\mathrm{mm}$, which were cut from the middle area of the specimens, all of them approximately at the same position. For the measurements of the specific heat capacity, a piece of the middle area of the specimen was used. Moreover, an additional specimen was artificially aged during a measurement at $120\,^\circ\mathrm{C}$ over 7 days, in order to obtain a completely aged specimen. Part of the results shown in this section are published in (Martinez Page et al., 2019).

3.7.1 Density

The density ρ is determined as the mass m of the specimen divided by its volume V. The weight was measured with a Mettler Toledo Newclassic MF, MS105 Du. The dimensions of the specimen were determined with a caliper with an accuracy of $0.01\,\mathrm{mm}$. The porosity of the specimen produces an inhomogeneous density distribution through the thickness, which varies slightly between the specimens. The porosity originates from the die casting process and is higher in the middle of the specimen, see (Martinez Page et al., 2018). The mass dispersion originating in the porosity is smaller than 3%, which is below the accuracy of the measurement devices.

The dependence of the density on the temperature can be determined considering the thermal expansion. The thermal expansion coefficient α_Θ is constant in the temperature range between $-50\,^\circ\mathrm{C}$ and $150\,^\circ\mathrm{C}$, see Fig. 3.23. The thermal expansion can be expressed as $\varepsilon_\Theta = \alpha_\Theta(\Theta - \Theta_0)$, with $\Theta_0 = 20\,°\mathrm{C}/293.15\,\mathrm{K}$ the reference temperature and the thermal expansion coefficient $\alpha_\Theta = 2.8109 \times 10^{-5}\,\mathrm{K}^{-1}$, see Section 3.6.1. The density ρ_0 of the specimen at the reference temperature and the density ρ_Θ at the current temperature are

$$\rho_0 = \frac{m}{\pi r_0^2 h_0}, \qquad \text{and} \qquad \rho_\Theta = \frac{m}{\pi r_\Theta^2 h_\Theta}. \tag{3.29}$$

The radius r_Θ and height h_Θ of the specimens at the current temperature can be obtained from the values at the reference temperature r_0 and h_0 by

$$r_\Theta = r_0(1 + \varepsilon_\Theta), \qquad \text{and} \qquad h_\Theta = h_0(1 + \varepsilon_\Theta). \tag{3.30}$$

Expressions Eq. (3.29) and Eq. (3.30) lead to a relation between the current density and reference density equal to

$$\frac{\rho_0}{\rho_\Theta} = (1 + \varepsilon_\Theta)^3 = 1 + 3\varepsilon_\Theta + 3\varepsilon_\Theta^2 + \varepsilon_\Theta^3. \tag{3.31}$$

This expression is approximately equal to one for values of ε_Θ of the order of 10^{-3}. This condition is fulfilled for the given expansion coefficient. Thus, the density is assumed to be temperature independent for the determination of the thermal conductivity in the temperature-range from $-60\,°\mathrm{C}$ to $120\,°\mathrm{C}$. The determined density is in this case equal to $\rho = 6.152 \times 10^3\,\mathrm{kg/m}^3$, see Tab. 3.5.

Table 3.5: Measurement of the mass and determination of the density. See also (Martinez Page et al., 2019)

aging time	0 months	3 months	6 months	12 months	artificial aging
mass in g	1.002	0.973	1.011	0.985	1.027
density in $\mathrm{g/cm}^3$	5.709	6.307	5.730	6.462	6.554

3.7.2 Thermal Diffusivity

The thermal conductivity κ_Θ of a material describes its ability to transport heat. It can be determined with help of the thermal diffusivity $\hat{\lambda}$ and the specific heat capacity c_p by

$$\kappa_\Theta = \rho(\Theta)\hat{\lambda}(\Theta)c_\mathrm{p}(\Theta), \tag{3.32}$$

where the density $\rho(\Theta) = \rho_0$ is assumed to be constant in the considered temperature range, see Section 3.7.1. The thermal diffusivity was measured with a laser flash apparatus (LFA 427, Netzsch-Gerätebau GmbH, Germany) from $-60\,°\mathrm{C}$ to $120\,°\mathrm{C}$ under helium atmosphere. For the measurement, the samples were covered with a thin graphite layer to ensure a sufficient absorption of the laser light. The curves of the detector signals after the laser pulse showed the best fit with the applied Cowan model, see (Cowan, 1963). The accuracy of this measurement method is better than 3%. The measurements were performed with specimens with the different natural aging times of 0, 3, 6, and 12 months over the temperature range from $-60\,°\mathrm{C}$ up to $100\,°\mathrm{C}$. In order to obtain the final state of the material, a measurement of an unaged specimen at the constant temperature of $120\,°\mathrm{C}$ over the time was carried out until the value of the thermal diffusivity stabilized, see Fig. 3.27(a). A measurement over the temperature was carried out with this artificially aged specimen to obtain the thermal diffusivity for the completely aged state. Fig. 3.27(b) shows the measurements of the thermal diffusivity over the temperature for the five specimens. An increase in the thermal diffusivity with the

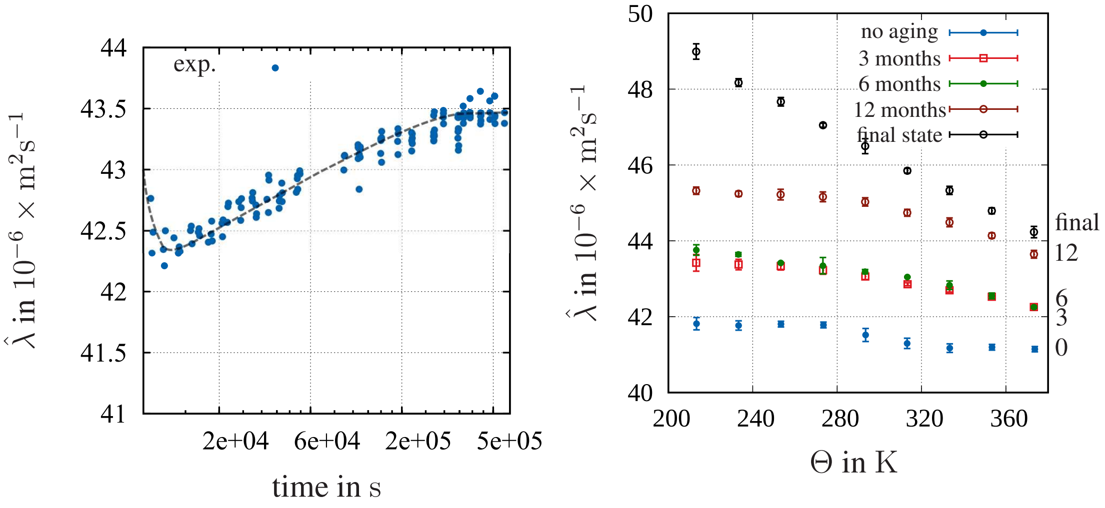

(a) Thermal diffusivity over time at $120\,°\mathrm{C}$ for an unaged specimen

(b) Thermal diffusivity over temperature for different aging times

Figure 3.27: Influence of temperature and aging on the thermal diffusivity, see also (Martinez Page et al., 2019)

age of the material is observed, which can be explained by the Al-rich precipitations in the zinc grains observed in Figs. 3.32 and 3.33. The formation of a more homogeneous phase with precipitates from an inhomogeneous phase leads to a growth in diffusivity, see Section 3.7.5. One can observe a decrease of $\hat{\lambda}$ with the temperature for a given age. This decrease is stronger for the specimens with 12 month of aging and artificial aging. The development of the thermal diffusivity is a result of two different effects. An increase in temperature accelerates the aging development of the alloy, which in turn increases the thermal diffusivity. Moreover, the thermal diffusivity decreases for the same aging state with the temperature. Thus, one can observe an approximately constant development of the thermal diffusivity for the unaged specimen. For specimens of age 3, 6, and 12 months, there is a reduction of $\hat{\lambda}$ with increasing temperature, which causes a change in the slope of the thermal diffusivity. The completely aged material (final state) shows a continuous linear decrease of the thermal diffusivity over the temperature. With the points obtained in Fig. 3.27(b) at room temperature, it is possible to estimate the necessary time to reach the final state at room temperature. To this end, the values of the thermal diffusivity at 20 °C for the aging times of 0, 3, 6, and 12 months aging are fitted in logarithmic time scale with a linear function $\hat{\lambda}(t) = \hat{\lambda}_0 + n\ln(t)$, see Fig. 3.28. Here, it is taken into account that the initial state of the specimens has already aged one month, i.e. the time scale is adapted in Fig. 3.28. The fit is performed with a linear least-squares method. We obtain a value for $R^2 = 0.902$. The fitted values are $n = 1.246 \times 10^{-6}\,\mathrm{m^2s^{-1}}$ and $\hat{\lambda}_0 = 2.294 \times 10^{-5}\,\mathrm{m^2s^{-1}}$. With this information, the final state at 20 °C would be reached after a time of $1.625 \times 10^{8}\,\mathrm{s}$. This estimated time corresponds to approximately 5 years of natural aging, which coincides with the estimated time to reach the final state in (Johnen, 1981) for the same alloy, see also Section 3.6.2.

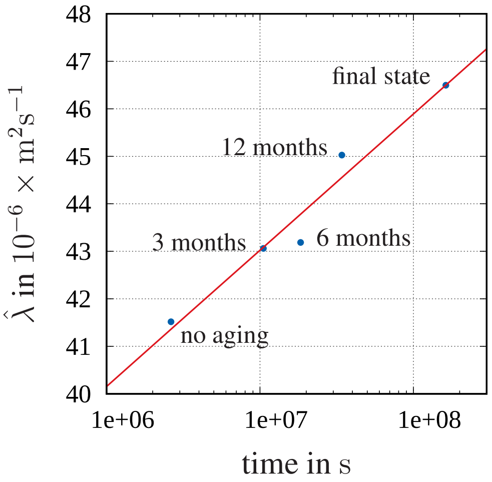

Figure 3.28: Thermal diffusivity over time at room temperature. The time to reach the final state is determined by fitting the points from Fig. 3.27 at 20 °C over time, see also (Martinez Page et al., 2019)

3.7.3 Specific Heat Capacity

The specific heat capacity was measured with a differential scanning calorimeter Netzsch DSC F204 Phoenix (Netzsch Germany). Measurements were carried out in the temperature range from −40 °C up to 120 °C with a heating rate of $10\,\mathrm{K/min}$. The DSC was calibrated in the temperature region using a sapphire sample as standard with a well-known specific heat capacity, leading to an accuracy of less than 2% for the present data. Fig. 3.29 shows the results of the measurements of the specific heat capacity at the different aging times of 0, 3, 6, and 12 months (natural aging) and 7 days of artificial aging at $120\,^{\circ}\mathrm{C}$ over the temperature. These measurements show an approximately linear

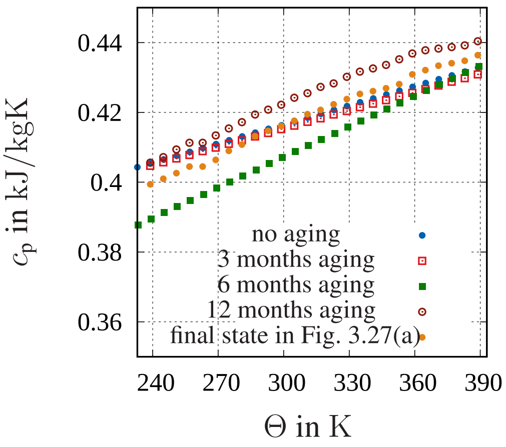

Figure 3.29: Specific heat capacity in dependence on temperature for different aging times. See also (Martinez Page et al., 2019)

dependence of the specific heat capacity on the temperature. Nevertheless, a dependence on the aging time is not observed.

3.7.4 Thermal Conductivity

With the help of Eq. (3.32) and the measurements provided in Section 3.7.1 - 3.7.3, the thermal conductivity κ_Θ is determined and presented in Fig. 3.30. Here, one can observe that, analogously to the thermal diffusivity, the thermal conductivity increases with the aging time. There is an almost linear development of κ_Θ over the temperature, where the slope of the linear function is reduced for higher aging times. This is a result of the different sign of the slope for the specific heat capacity and the thermal diffusivity over the temperature. The positive change in the slope of c_p in Fig. 3.29 is compensated by the negative change of $\hat{\lambda}$, see Fig. 3.27(b). This effect is especially visible for the final aging state. Here, the slope is slightly negative in contrast to the positive value for the other aging times.

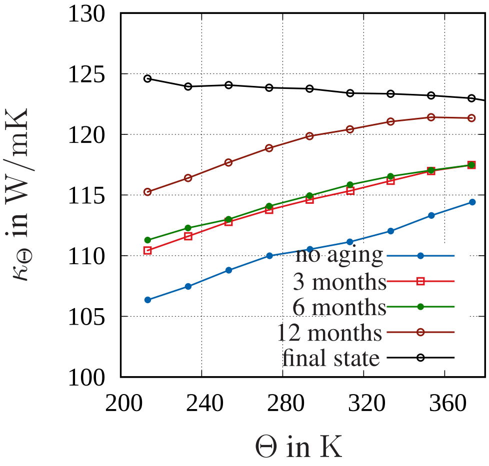

Figure 3.30: Thermal conductivity in dependence of aging and temperature. See also (Martinez Page et al., 2019)

3.7.5 Microstruture

In the last century, several authors have investigated microstructural changes in zinc die casting alloys. Gebhard (1940, 1941, 1942) investigated the microstructure, phase transformations, and volume changes over time in Zn-Al and Zn-Al-Cu alloys. Moreover, the equilibrium phase diagram of Zn-Al alloys is described in (Murray, 1983). After a period of time in which these alloys got less attention, which was due to an increased interest in steel and aluminum alloys, the next intensive investigations on this topic were performed by Zhu (2001); Zhu et al. (2002, 2003a,b); Zhu (2004). Here, phase transformations and precipitation of several Zn-Al alloys are extensively investigated and characterized. In (Pola et al., 2015), one can find investigations of the aging behavior of a Zn-Al-Cu alloy with tensile tests and microstructural analysis. Nevertheless, the complete aging process is still not completely understood. In this section, the microstructure of the material is investigated for the different aging times in order to better understand the changes during aging.

The microstructure of the specimens with five different aging times was investigated with a JSM-7610F Scanning Electron Microscope (Jeol, Japan). Atomic number contrasting imaging (COMPO) is used in all micrographs. The investigations were complemented by determining the phases of the material at every aging stage by means of X-ray diffraction. The record of X-ray diffraction patterns was performed at room temperature with a PANalytical Empyrean diffractometer with Cu K_α radiation. The results of the XRD are shown in Fig. 3.31. It is known that the microstructure of Zn-Al-Cu alloys after die casting consists of a hexagonal close-packed zinc-rich phase (η-phase), a face-centered cubic aluminum-rich α-phase, moreover, a face-centered cubic zinc-rich β-phase, a hexagonal close-packed phase of zinc and copper ε, and finally, a ternary body-centered cubic phase T'. During the aging, several metastable phases derived from the mentioned phases are built (see, for example, (Zhu et al., 2003b)). In the XRD pattern, the main peaks are at $2\theta = 36.55°$, $2\theta = 38.95°$, $2\theta = 43.30°$. Two small peaks are at $2\theta = 42.1°$ and $2\theta = 44.47°$. Moreover, the peak at $2\theta = 38.95°$ shows a small shoulder at $2\theta = 38.60°$ on its left-hand side. According to (Zhu et al., 2003b,a), these peaks correspond to the phases $\eta'_s(0002)$ at $2\theta = 36.55°$, $\alpha(111)$ at $2\theta = 38.60°$, $\eta(10\bar{1}0)/\beta' s(111)$ at $2\theta = 38.95°$, $\varepsilon(0002)$ at $2\theta = 42.1°$, $\eta(10\bar{1}\bar{1})$ at $2\theta = 43.30°$, and $\alpha(200)$ at $2\theta = 44.75°$. As can be seen in Fig. 3.31, the initial state of the alloy shows the phases $\eta'_s(0002)$, $\alpha(111)$, $\eta(10\bar{1}0)$, $\beta'_s(111)$, $\eta(10\bar{1}1)$, and $\alpha(200)$. An increase in aging influences the intensity of the phase $\alpha(111)$, which becomes more pronounced. The phase $\eta'(0002)$ transforms into $\eta(0002)$, which can first be observed with a small displacement of the peak at $2\theta = 36.55°$. This is related to an increase in the d-spacing of the crystal plane η'_s as mentioned in (Zhu et al., 2003a). The found amount of the phase $\varepsilon(0002)$ is generally quite low and increases slightly after the artificial aging. The ternary phase T' could not be found in the XRD-measurements.

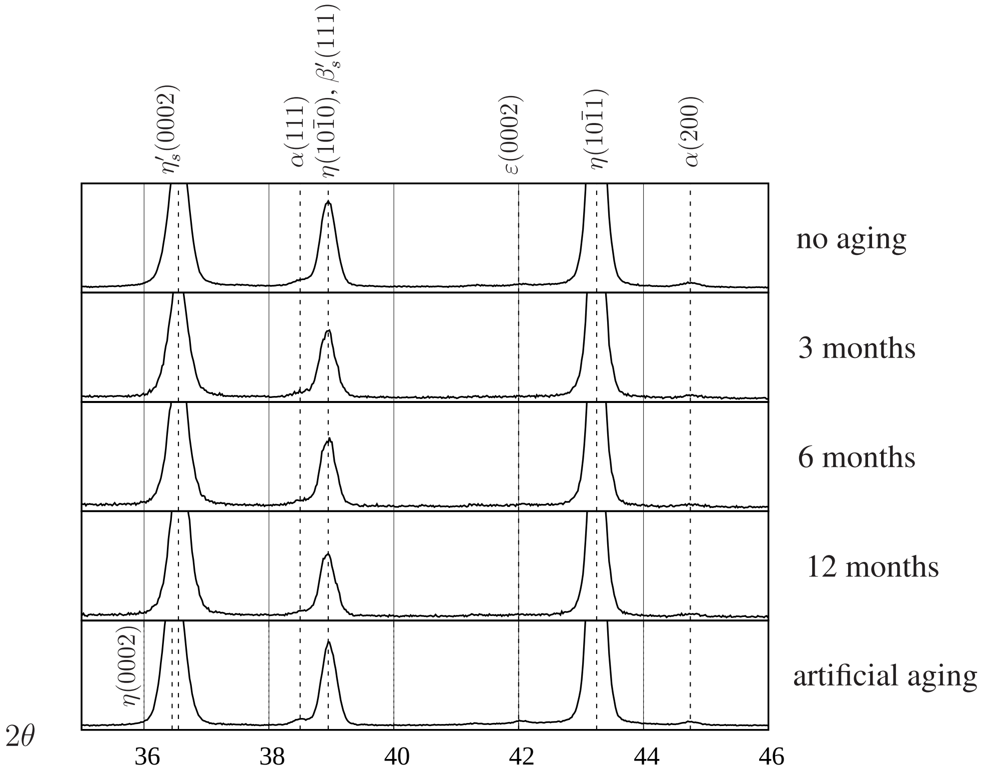

Figure 3.31: X-ray diffractograms for specimens with different aging times. See also (Martinez Page et al., 2019)

Figs. 3.32 and 3.33(a) show the investigations of the microstructure for the specimens with natural aging at $19\,^{\circ}\mathrm{C}$ after 0, 3, 6, and 12 months. Fig. 3.33(b) displays the microstructure for a specimen with artificial aging at $120\,^{\circ}\mathrm{C}$ for 7 days, see measurement in Fig. 3.27(a). In Figs. 3.32 and 3.33, the η-phase is identified with the bright globular-dendritic grains in the micrographs. The α-phase, which has a dark color, can be found in the boundaries of the η-grains. This phase, together with the η-phase in a lamellar structure, builds the eutecticum. The α-phase is also found in the precipitates in the zinc-rich grains. As mentioned in (Zhu et al., 2003b), the phases η and ε are hard to distinguish from one to another in the images because of the high amounts of the relatively heavy elements copper and zinc, resulting in a similar atomic contrast. Looking at the microstructure of the alloy with natural aging, we observe an increase in the precipitates in the zinc-rich grains with the time. The specimens at 3 and 6 months of aging show a similarity, which is reflected in the results of the mechanical experiments in Section 3.5, where the two aging times behave in a similar manner. Again, the specimen with twelve months of aging in Fig. 3.33(a) shows an increase in the precipitates. For the specimen with seven days of artificial aging at $120\,^{\circ}\mathrm{C}$, Fig. 3.33(b) shows a complete decomposition of the lamellar α-phase in the eutecticum into the η-phase with α precipitates. Moreover, a formation of α-grains in the boundaries of the η grains takes place.

The composition of the observed phases was measured at several points by means of energy-dispersive X-ray spectroscopy, see Fig. 3.34 and Tab. 3.6. The phase transformation during aging of Zn-Al-Cu alloys consists of three effects, see Zhu et al. (2003b). First, the zinc-rich meta-stable phase decomposes while building α and ε-phases, which precipitate into the zinc-rich grain. This decomposition is visible in all the aging states in Fig. 3.34 with an increase in the precipitates. Moreover, the Al-concentration increases for the specimens of three and six months of age, see Tab. 3.6. Additionally, the ε-phase decomposes following the rule $\alpha + \varepsilon \rightarrow T' + \eta$. This decomposition corresponds to an increase of zinc in the zinc-rich phase, where the aluminum content diffuses and precipitates in the boundaries and the center of the grain. The last effect is the decomposition of the α-phase. In the precipitations, a small amount of Cu is measured, see Tab. 3.6. Although the EDX spot measurements do not show the fine Cu content in the light and dark phases but only in precipitations, a low copper amount is measurable. An EDX line-scan shows a homogeneously distributed amount of Cu. This indicates homogeneously distributed small Cu precipitations and dissolved Cu in the matrix. With increasing aging, a more homogeneous phase is built up. This leads to an increase in thermal diffusivity. Also, precipitations in this homogeneous phase can produce an overall increase in thermal diffusivity as long as the amount of scattering centers for phonons in the aged and homogenized samples is reduced compared to the inhomogeneous phases with shorter aging times, see (Martinez Page et al., 2019). While the difference in the composition between the specimens with natural aging is very low, the artificially aged specimen shows that the bright phase is composed of almost only zinc. The aluminum and copper have diffused to the borders, and the eutecticum is completely decomposed into pure zinc and an aluminum-rich phase.

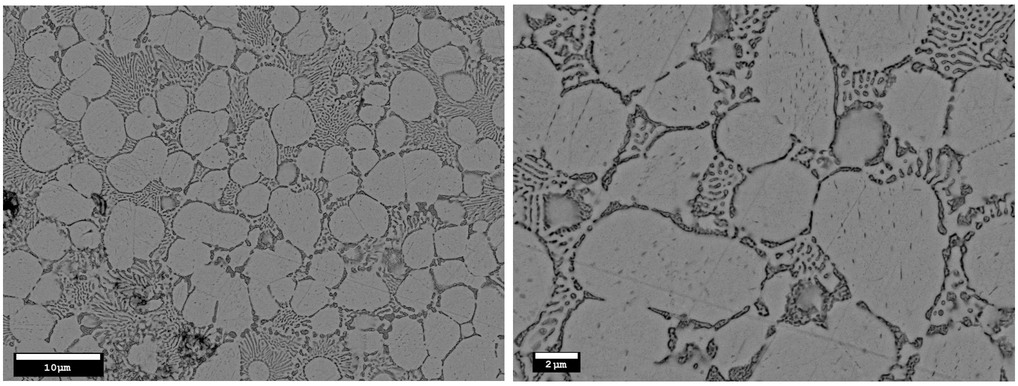

(a) Specimen without aging. It corresponds to the initial state of the alloy after die casting. The alloy is composed of zinc-rich globular-dendritic grains (bright phase) surrounded by a eutectic phase consisting of an aluminum-rich (dark phase) and a zinc-rich phase. There are small precipitations inside the bright grains.

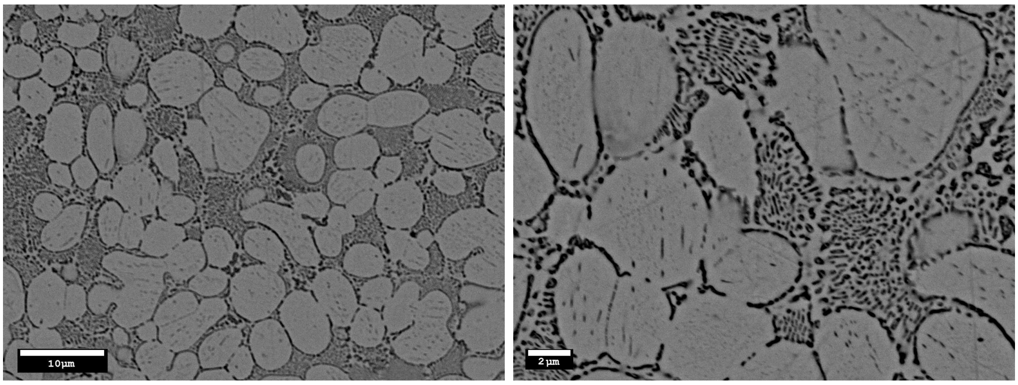

(b) Specimen after three months of natural aging. We observe an increase in the precipitations inside the zinc-rich grains.

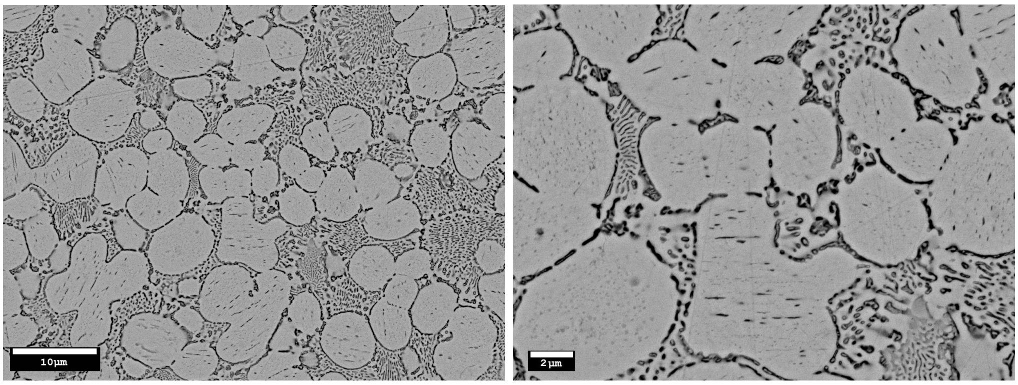

(c) Specimen after six months of natural aging. The microstructure is similar to the state after three months aging.

Figure 3.32: Microstructure of the alloy Zamak 5 after die casting and after 3 and 6 months of natural aging at $19\,^{\circ}\mathrm{C}$, COMPO, $15\,\mathrm{kV}$. See also (Martinez Page et al., 2019)

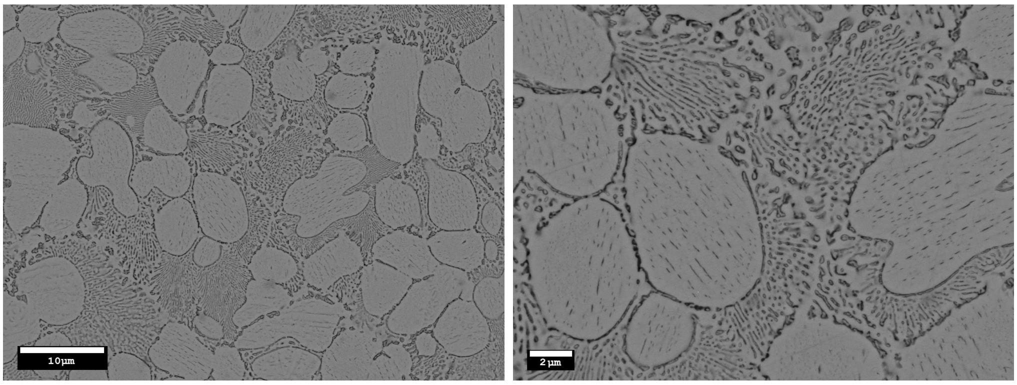

(a) Specimen after twelve months of natural aging. Again, we observe an increase on the precipitates in the zinc-rich grains.

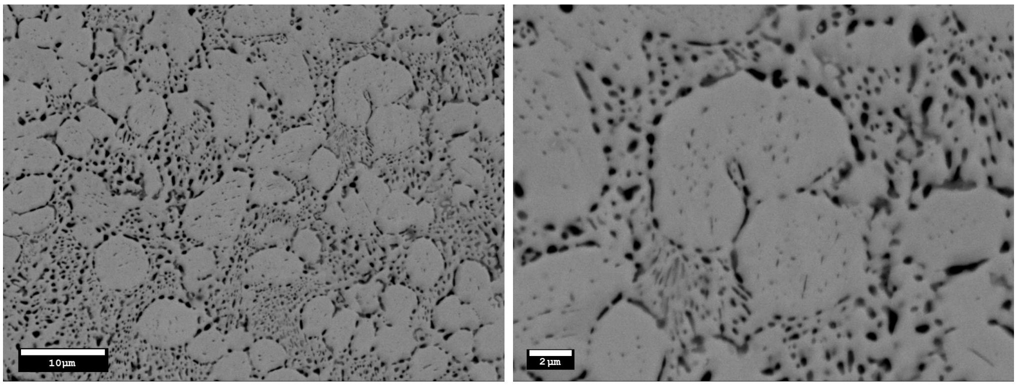

(b) Specimen with seven days of artificial aging. The grain limits are not completely defined anymore. The amount of precipitates inside the zinc-rich grains decrease and the eutecticum decomposes.

Figure 3.33: Microstructure of the alloy Zamak 5 after 12 months of natural aging at 19 °C and 7 days of artificial aging at 120 °C, COMPO, 15 kV. See also (Martinez Page et al., 2019)

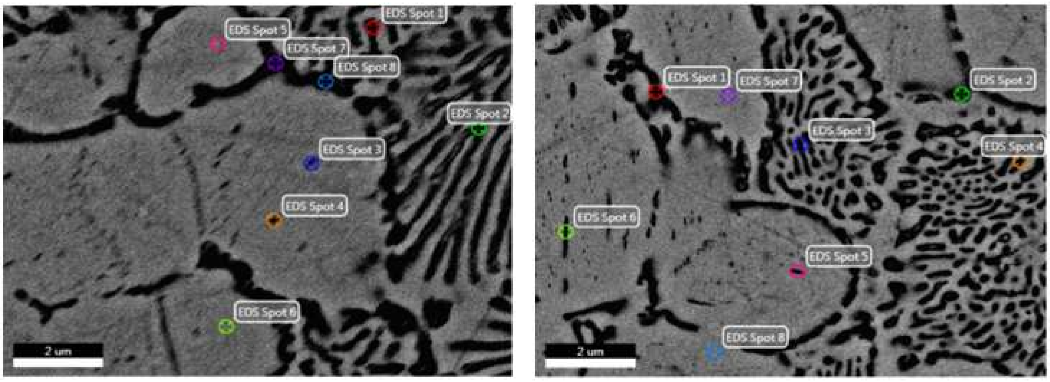

(a) EDX-analysis for the specimen without aging (b) EDX-analysis for three months of natural aging

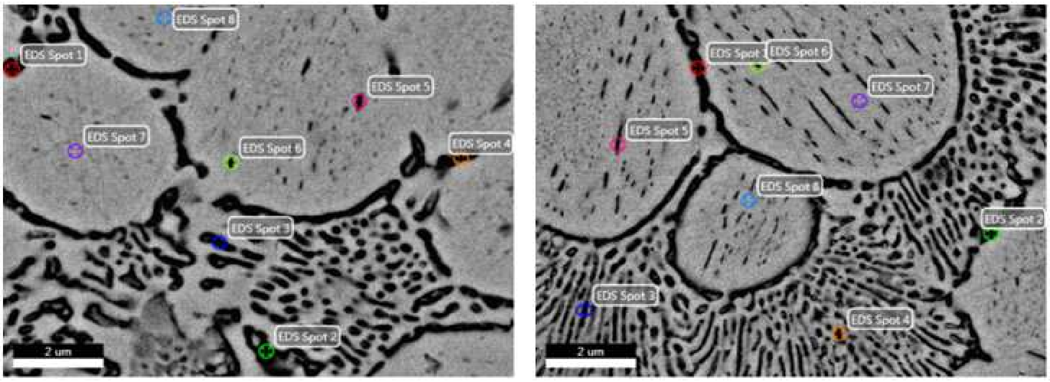

(c) EDX-analysis for six months of natural aging (d) EDX-analysis for twelve months of natural aging

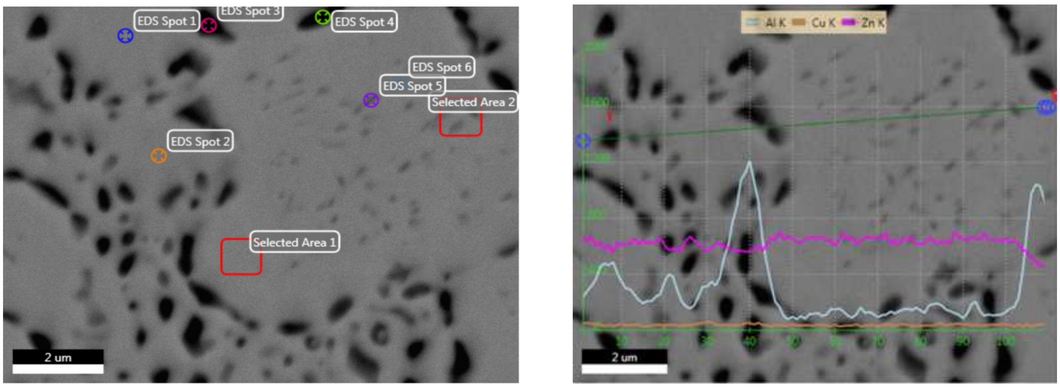

(e) EDX-analysis for the specimen with 7 days of artificial aging at 120 °C

Figure 3.34: EDX analysis of Zamak 5 for the aging times of 0, 3, 6, and 12 months natural aging at 19 °C and 7 days of artificial aging at 120 °C. See also (Martinez Page et al., 2019)

Table 3.6: Results of the EDX-analysis - composition in weight, see Fig.3.34. See also (Martinez Page et al., 2019)

	light phase	dark phase	eutecticum	precipitation
without aging				
Al	1.61%	14.63%	10.49%	2.55%
Cu	1.95%	1.14%	1.05%	1.22%
Zn	97.26%	84.24%	88.46%	96.24%
3 months				
Al	1.34%	14.42%	12.21%	4.83%
Cu	1.18%	1.15%	1.01%	1.21%
Zn	97.49%	84.44%	86.80%	93.98%
6 months				
Al	1.05%	16.79%	13.52%	8.28%
Cu	1.09%	1.09%	1.01%	1.06%
Zn	97.87%	82.12%	85.48%	90.64%
12 months				
Al	1.47%	19.02%	10.75%	2.41%
Cu	1.50%	1.06%	1.26%	1.23%
Zn	97.04%	79.93%	87.99%	96.37%
artificial aging				
Al	$\approx 0\%$	17.90%	-	2.43%
Cu	0%	0%	-	0.24%
Zn	$\approx 100\%$	82.11%	-	97.33%

3.8 Validation Experiments

The last set of experiments corresponds to the validation. These experiments have the goal to offer a non-homogeneous more complex stress and strain state, which can then be compared to simulations in Chapter 7. These results can be used to obtain an indicator of the accuracy of the model. The first group of experiments are performed in order to validate the thermo-mechanical behavior. They are carried out at different strain-rates and temperatures. The second set of experiments serves to validate the aging dependence. They were performed with specimens of different aging times. In these experiments, a displacement or rotation path is given in the testing machine, and the force or the torque are measured. Moreover, with the help of the digital image correlation system (DIC-system) Aramis provided by the company GOM, see (GOM, 2011), the deformations on the surface of the specimens are measured. Some of the experiments at higher temperatures were performed with a thermal chamber. In these cases, the DIC-system monitors the specimen through a glass window of the thermal chamber. These experiments are more complex than the previous ones. Their main difficulty lies in the uncertainties stemming from the DIC-system, such as errors due to the quality of the pattern, positioning and calibration of the system, and the presence of a low quality glass between the specimen and the cameras for the experiments at higher temperatures.

3.8.1 Thermo-Mechanical Experiments

For the thermo-mechanical experiments, the complex geometry shown in Fig. 3.35 is used. It was provided by the Huf group. Unfortunately, the specimens were several years old when the experiments were performed, which implies that the aging dependence cannot be validated for these specimens. Each specimen has a height of approximately $35\,\mathrm{mm}$ and a width of $15\,\mathrm{mm}$. In order to perform the experiments, the com-

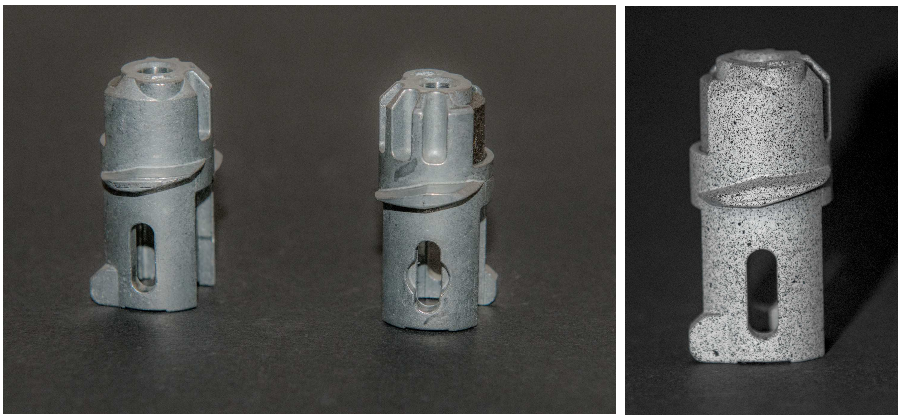

Figure 3.35: Component part for the first set of experiments (left) and part with spray for the measurement (right)

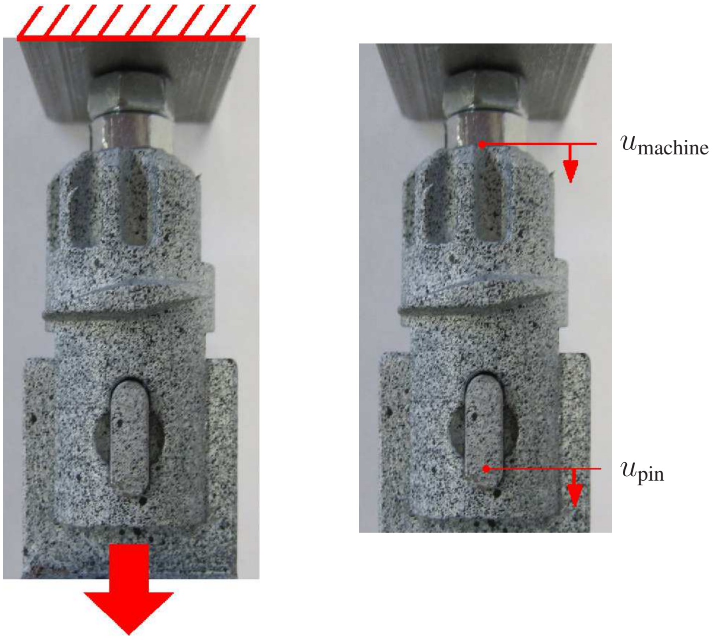

(a) Loading (b) Relative displacement

Figure 3.36: Loading of the component part

ponent part is fixed to the testing machine with the help of a screw (upper side) and a pin (bottom side), see Fig. 3.36(a). The displacement of the traverse of the machine is prescribed. The force is measured with the help of the testing machine, and the deformation on the surface of the geometry is determined using the optical measurement system Aramis. For this measurement, the surface of the component part is painted with a white background color and covered with black dots, see Fig. 3.35, forming a pattern. The 3D digital image correlation system measures the surface displacements and surface strains based on the relative positions of the pattern elements. The testing machine and the construction to load the component part – screw and block – deform during the experiments. Information provided by Aramis is used to obtain the real relative displacement of the component part between the fixed position and the pin. The relative displacement of the pin related to the upper side of the component part is given as the difference $u_{\text{pin}} - u_{\text{machine}}$, see Fig. 3.36(b). This relative displacement will be used for the simulations in Section 7.3 as the loading path.

In total, four experiments were performed. The two first experiments were performed at room temperature, the third one at $50\,^{\circ}\text{C}$, and the last one at $70\,^{\circ}\text{C}$. Moreover, three different orders of magnitude in the displacement rate were investigated. The results of the experiments are shown in Figs. 3.37-3.39. In Figs. 3.37-3.38, the applied displacement in the testing machine u_{T_i} and the measured relative displacement u_{D_i} are displayed over time. Moreover, the measured force is displayed over the relative displacement of the pin. One can notice the large difference between the displacements u_{T_i} and u_{D_i}. The main reason for this difference lies in the translation of the component part caused by the elastic deformation of the testing machine. Moreover, the third specimen breaks during the experiment at the time of $127\,\mathrm{s}$. This can be observed in the reduction in the force for a growing displacement in Fig. 3.38(b). In Fig. 3.39, the measured major strain is shown for the four experiments. The third experiment corresponds to the time $127\,\mathrm{s}$. The remaining experiments correspond to the last point of the experiment. In Fig. 3.40, the break areas of the specimens are shown. They correspond to the areas in which the maximal major strain is measured.

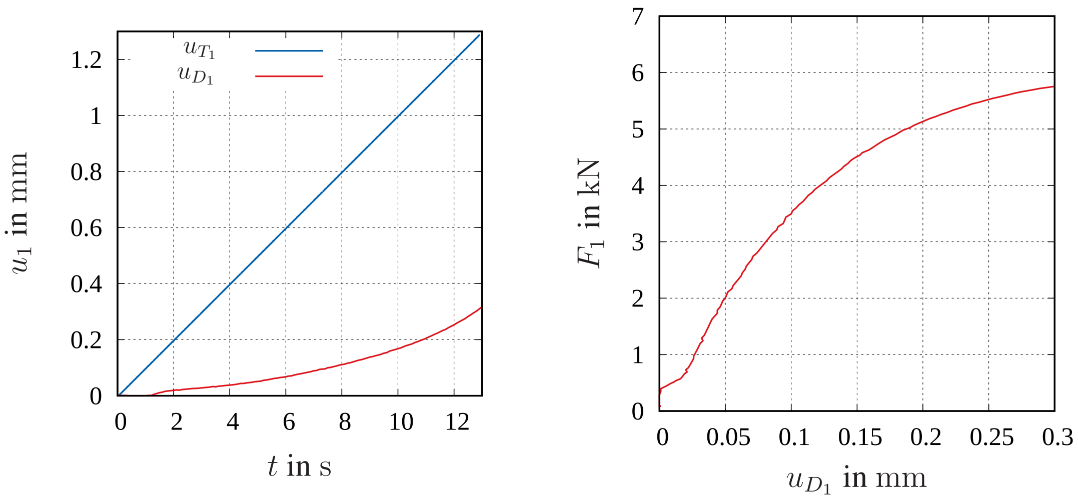

(a) Displacement of the cross-head of the testing machine u_{T_1} and relative displacement of the pin measured with the DIC-system u_{D_1} in the first experiment

(b) Reaction force F_1 over the displacement of the pin u_{D_1} of the first experiment

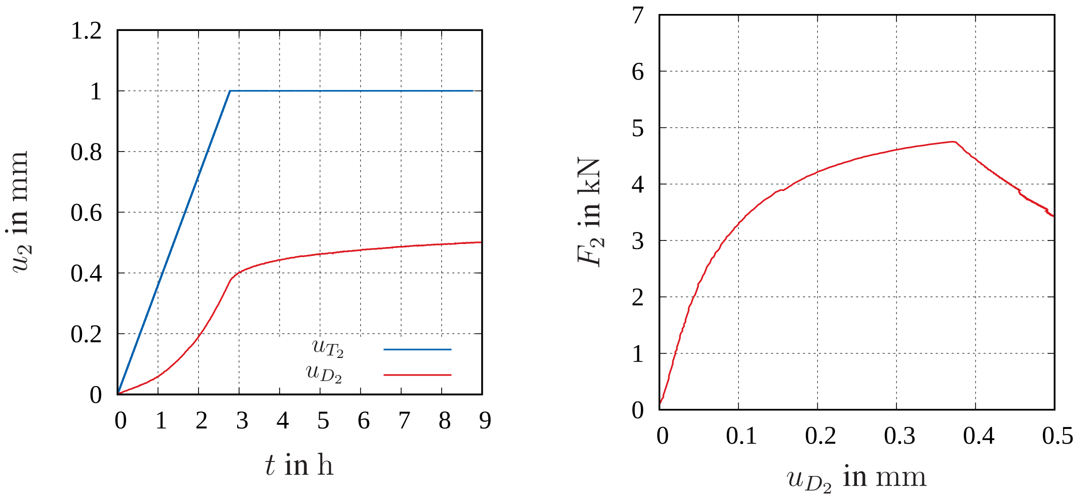

(c) Displacement of the cross-head of the testing machine u_{T_1} and displacement of the DIC-system u_{D_1} in the second experiment

(d) Reaction force F_2 over the displacement of the pin u_{D_2} of the second experiment

Figure 3.37: Measured variables in the experiments at room temperature, see also (Martinez Page and Hartmann, 2018b)

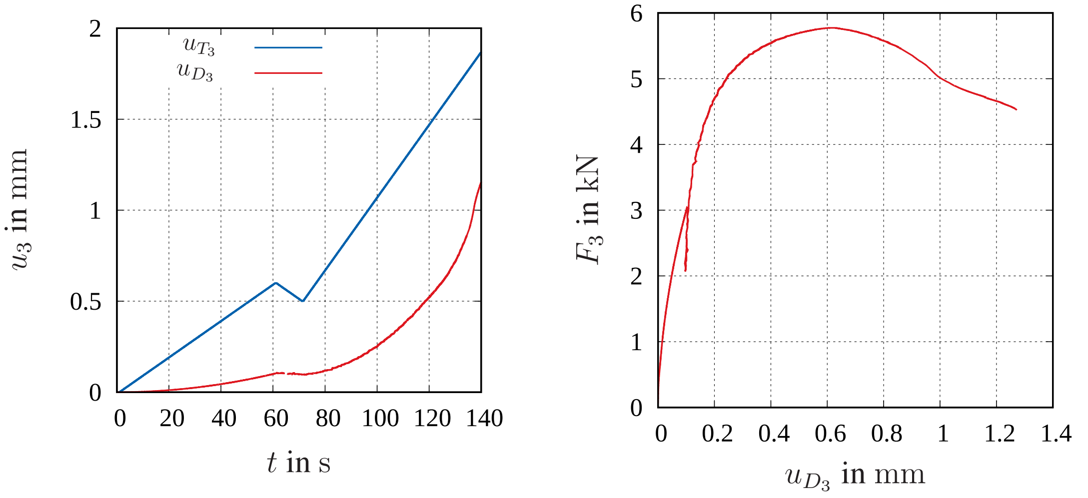

(a) Displacement of the cross-head of the testing machine u_{T_3} and relative displacement of the pin measured with the DIC-system u_{D_3} in the third experiment, $\Theta = 50\,°\mathrm{C}$

(b) Reaction force F_3 over the displacement of the pin u_{D_3} of the third experiment

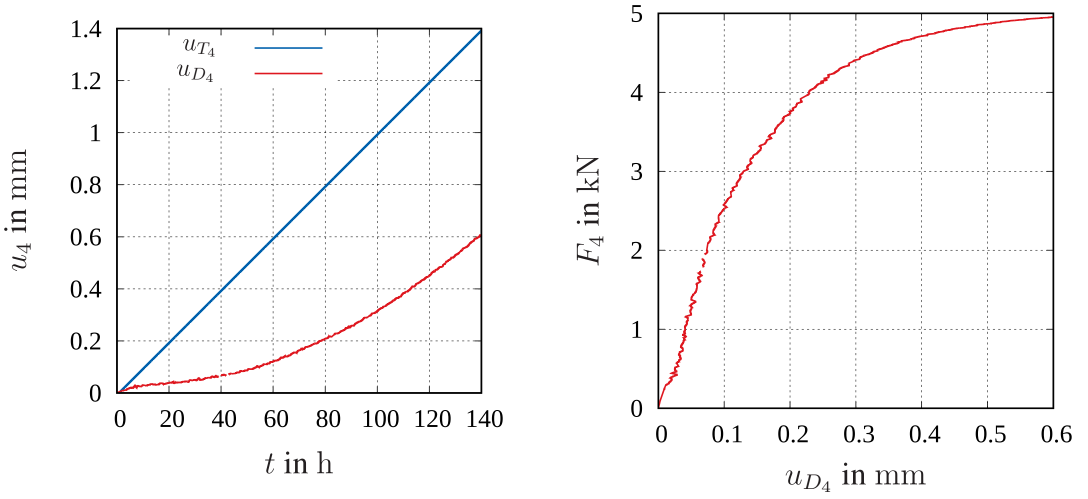

(c) Displacement of the cross-head of the testing machine u_{T_4} and relative displacement of the pin measured with the DIC-system u_{D_4} in the fourth experiment, $\Theta = 70\,°\mathrm{C}$

(d) Reaction force F_4 over the displacement of the pin u_{D_4} in the fourth experiment

Figure 3.38: Measured variables in the experiments at different temperatures

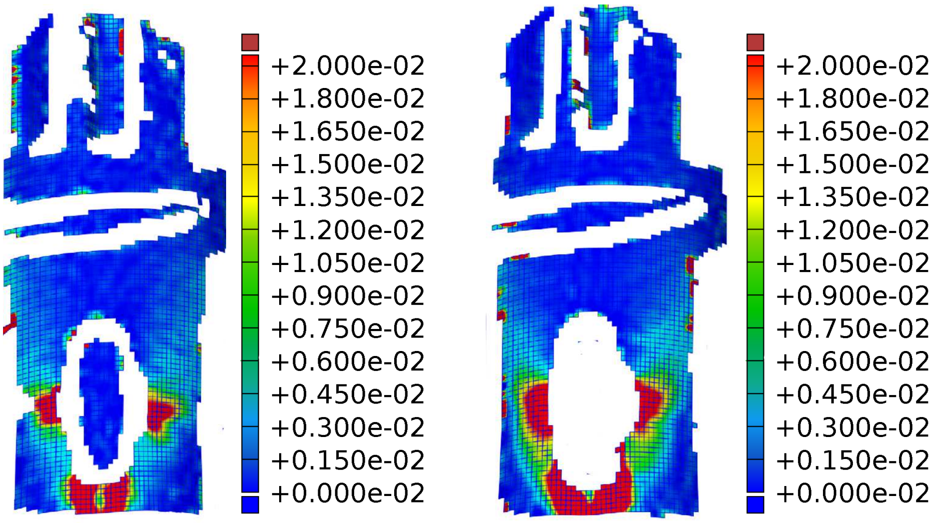

(a) Experiment 1: displacement path u_1 at room temperature and $t = 13.4\,\mathrm{s}$

(b) Experiment 2: displacement path u_2 at room temperature and $t = 9\,\mathrm{h}$

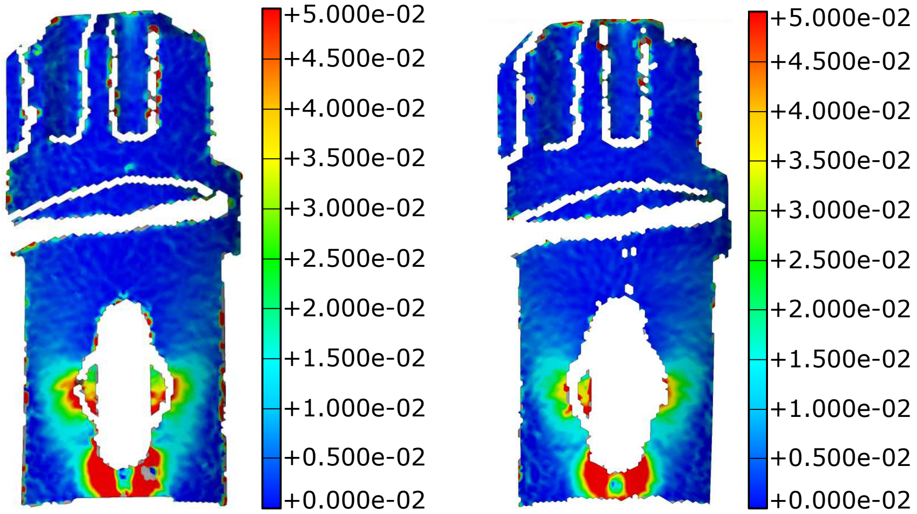

(c) Experiment 3: displacement path u_3 at $\Theta = 50\,^{\circ}\mathrm{C}$ and $t = 127\,\mathrm{s}$

(d) Experiment 4: displacement path u_4 at $\Theta = 70\,^{\circ}\mathrm{C}$ and $t = 140\,\mathrm{s}$

Figure 3.39: Measured major strain with the DIC-system of the thermo-mechanical experiments

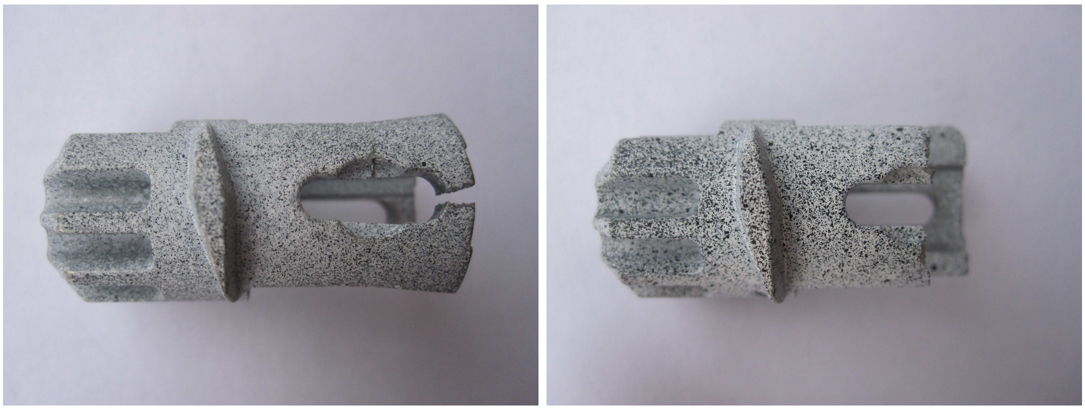

Figure 3.40: Broken component parts at the end of the test. The damaged areas correspond to the maximum strains in the measurements, see red areas in Fig. 3.39

3.8.2 Influence of Aging

For the validation of the aging dependence, the specimens from Section 3.2 are used since its aging state is known. In order to obtain an inhomogeneous strain state, a hole with a radius of $8\,\mathrm{mm}$ is cut out in the middle of the specimen, see Fig. 3.41(a). Specimens with three different aging times are tested: one specimen without aging, one with 12 months of natural aging, and a completely (artificially) aged specimen. The upper area of the specimens is fixed in the testing machine, and a rotational angle is applied to the lower area, following the path in Fig. 3.41(b)[5]. Due to the fact that the effect of aging is more pronounced at room temperature, the temperature was chosen to be close – equal to $27\,^{\circ}\mathrm{C}$. Then, the reaction torque and the deformation on the surface of the specimen are measured. The torque over the applied rotational angle is displayed in Fig. 3.42 for all aging times. Here, one can observe a reduction in the torque with the aging. Moreover, Fig. 3.43 shows the major strain at the last time point of the experiment.

---

[5] This is the path after considering the deformation of the testing machine

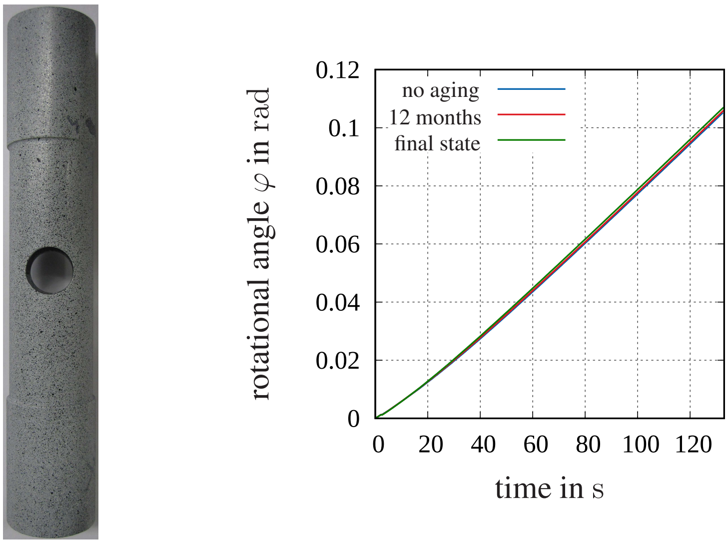

(a) Geometry (b) Applied rotational angle

Figure 3.41: Geometry for the validation experiments with aging and applied rotational angle

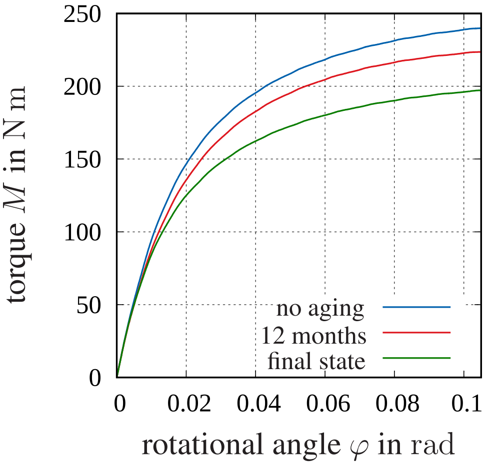

Figure 3.42: Measured torque over the rotational angle

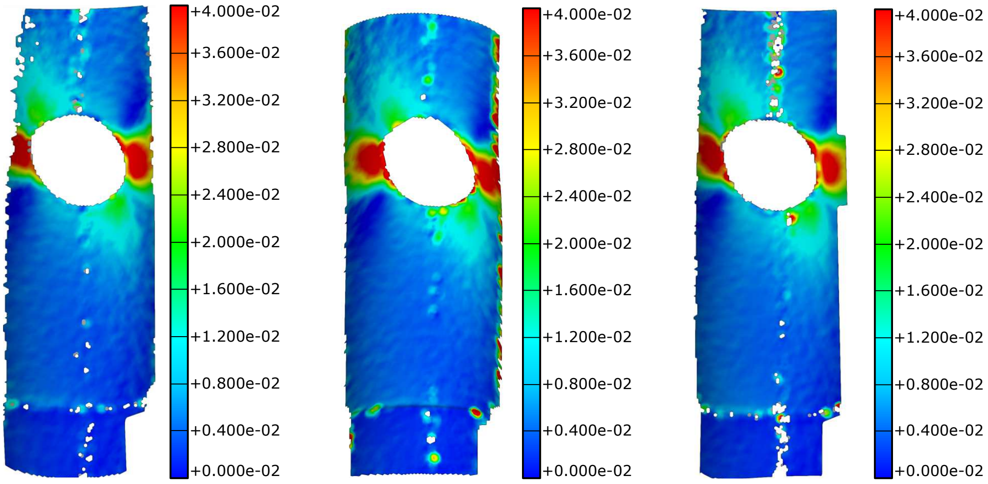

(a) Specimen without aging (b) Specimen with 12 months of natural aging (c) Specimen with artificial aging

Figure 3.43: Major strain at the last point in time of the torsion experiment

4 Constitutive Model

The system of equations composed of balance equations and kinematics for the determination of the motion and deformation of a material body adressed in Chapter 2 is incomplete. In order to obtain a solvable problem, a constitutive model that connects the stresses with the strain history or the temperature with the heat flux is necessary. This constitutive model has to fulfill the requirements discussed in Section 2.4.

Because of its simplicity, the case of small deformations is advantageous to perform the modeling in a first step. As mentioned in Chapter 3, the case of torsion in a thin-walled cylinder represents a one-dimensional purely deviatoric problem, which allows to consider the observations for the modeling in a very simplified manner first. The model can be generalized to the three-dimensional case later on. In a following step, the model can be extended to the large deformations range, in order to also consider problems in which large strains and large rigid body motions are reached.

The modeling is closely tied to the identification process. In this work, modeling and identification are part of an iterative process in which an assumption in modeling is done. This is followed by identifying the parameters, evaluating the suitability of the solution, and modifying the model in order to improve the results. Because of that, several functions are developed within the identification process, and their selection will be justified in Chapter 5.

In this chapter, an overview of the possibilities of modeling the thermo-mechanical behavior of Zamak 5 considering aging is given. After that, a small deformations model is developed based on the observations made in Chapter 3. Afterwards, the model is extended to the finite strains case. Finally, the variables appearing in the heat equation are modeled.

4.1 Overview of the Modeling Possibilities

In the experimental results of Chapter 3, a viscoplastic material response was observed, since the material shows rate dependence and the equilibrium state corresponds to a hysteresis, which is connected to remaining deformations, see (Haupt and Lion, 1995) and (Haupt, 2002). In this work, the material is considered as homogeneous and the modeling proposal is phenomenological. There are three main approaches to model viscoplasticity, see (Haupt, 2002). The first approach consists of the demarcation of an elastic domain by means of a yield surface, also known as Perzyna-type viscoplasticity, see (Perzyna, 1966) and (Chaboche, 1989). The second option is a formulation of evolution equations without a yield surface or case distinction, see, for example, (Valanis, 1971a,b). The third possibility is called overstress-type viscoplasticity. It relies on the decomposition of the total stress into a rate-independent equilibrium stress and a rate-dependent overstress, see (Liu and Krempl, 1979; Haupt and Korzen, 1989; Haupt, 2002; Chaboche, 2008; Haupt and Sedlan, 2001; Hartmann, 2006). This third model class shows advantages in the parameter identification process, since it allows an identification in a partitioned manner. The parameters of the equilibrium stress can be identified independently from the parameters of the overstress.

There are very few proposals for the modeling of the mechanical behavior of zinc die casting alloys in the literature. Mostly of the works focus on the die casting process itself – see, for example, (Führ et al., 2014; Cao et al., 2018) – or on investigations from the point of view of Material Science, see the works of Zhu (Zhu and Orozco, 1995)-(Zhu, 2004) and (Leis and Kallien, 2011). In (Korzeniowski and Weinberg, 2018), a damage model is presented, where weakening effects, such as impurities, pores, and cracks, are considered as distributed defects, and a Markov process is used to model the defect evolution. A model of thermo-viscoplasticity for Zamak 5 is proposed in (Martinez Page and Hartmann, 2018b), and the case of natural aging at room temperature was considered in (Martinez Page and Hartmann, 2018a). These two works serve as the basis for the modeling development in this thesis. Moreover, in (Martinez Page et al., 2018), the thickness dependence was modeled considering the porosity for elastic material behavior. In the area of thermo-viscoplasticity for metals, a wide range of models have been proposed for aluminum alloys and steel, see, for example, recent proposals for aluminum in (Vilamosa et al., 2015, 2016; Brünig and Gerke, 2011; Lin et al., 2012; Schindler et al., 2017; Zhang et al., 2017) and for steel (Egner and Egner, 2014; Hyde et al., 2010; Yu et al., 2012; Zhu et al., 2016). Other alloys are less present, such as titanium, magnesium, nickel or copper alloys, see (Zhang et al., 2011; McDowell, 1992; Rusinek et al., 2010; Li et al., 2014; Lin et al., 2016). For more information, see also the introduction of (Martinez Page and Hartmann, 2018b) and the literature cited therein. Unfortunately, most of these alloys are exposed to some kind of mechanical treatment before they are modeled – or they differ strongly from zinc alloys in their behavior, which make these models inappropriate for a zinc die casting material.

Similarly to the case of polymers – where aging is related to physical and chemical changes, limiting their application period, see (Johlitz and Lion, 2013), for example – aging processes in metals involve metallurgical changes that occur under certain temperature conditions: phase changes, dissolutions, precipitations or coarsening of precipitates have significant influence on the mechanical properties, see (Krempl, 1979; Chaboche, 2008). Regarding the term aging, Chaboche (2008) distinguishes three different types. *Dynamic strain aging* is caused by “dragging” of the dislocations of the atoms in solution and is associated with the “Portevin-Le Chatelier effect”. Moreover, in *static strain aging*, a growth in material strength with time is observed as a reverse effect of static recovery. In the literature, there are several suggestions on how to model these two kinds of aging types in aluminum alloys and steel, but in the present study of Zamak, none of these types of aging was observed. Finally, *aging due to phase changes* is a consequence of dissolutions, precipitations, and phase transformations in alloys, which fits with the observations made in Section 3.7.5. From a macroscopic point of view, the effect of aging can be introduced into the model with an internal variable, see (Marquis and Lemaitre, 1988; Lemaitre and Chaboche, 1990) and in the area of polymers (Lion and Johlitz, 2012; Johlitz, 2012; Johlitz and Lion, 2013; Johlitz and Diercks, 2014; Dippel et al., 2014). There are other proposals in the area of concrete, see (Meschke, 1996; Bazant and Huet, 1999), which are less appropriate for metals. Most of these models do not consider volume changes in consequence of aging.

Taking a look at the previously mentioned modeling possibilities for the different effects under consideration in the material, a Perzyna-type model appears to be unsuitable for the basic mechanical behavior, due to the fact that no conspicuous yield stress could be identified, see Fig. 3.13. Since the overstress-type viscoplasticity shows advantages for the parameter identification process, and information about the equilibrium state is available from the experiments, this modeling concept is followed in this work. For the equilibrium state, an element of endochronic plasticity is used in order to reproduce the equilibrium hysteresis, which is connected in parallel to an elastic element for numerical reasons, in a similar way as in (Hartmann, 2006). For the overstress, a Maxwell-element is chosen. The softening effect observed in the experiments as a change in the initial slope in the loading and unloading, see Section 3.5.2, is modeled with an internal variable with a similar evolution equation as an isotropic hardening, but its effect is included in a material parameter.The temperature dependence is included with the definition of the temperature-dependent material parameter, affecting the equilibrium state and the viscosity. Additionally, the thermal expansion is considered in the model. The effects of aging are modeled with an internal variable that represents the process in which the microstructural changes take place over the course of time. The shrinkage is also considered with a component in the strain in the small strains model and a component in the deformation gradient in the finite strain model.

4.2 A Small Strains Model for Zamak 5

This section focuses on the first considerations for the case of small deformations. This means that the strain is represented by the linearized strain tensor $\mathbf{E}$, see Section 2.4.3, and no distinction between configurations is performed. The constitutive model is motivated by the rheologial model shown in Fig. 4.1, which allows an easily accessible interpretation of the modeling concept, see (Lion, 2000a; Altenbach and Altenbach, 1994). The linearized total strain $\mathbf{E}$ is divided into a mechanical part $\mathbf{E}_{\mathrm{M}}$, a thermal part $\mathbf{E}_{\Theta}$, and a component describing the aging $\mathbf{E}_a$,

$$\mathbf{E} = \mathbf{E}_{\mathrm{M}} + \mathbf{E}_{\Theta} + \mathbf{E}_a. \tag{4.1}$$

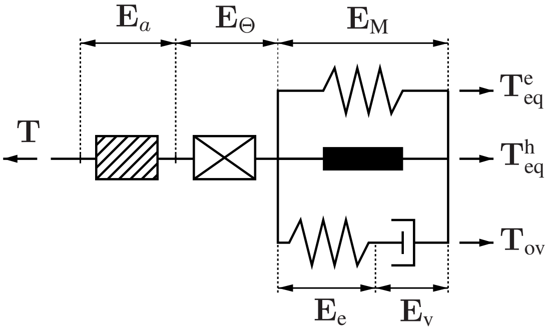

Figure 4.1: Rheological Model

The strain $\mathbf{E}_a$ represents a volume reduction in the material (shrinkage) which takes place during the aging process. It was observed in the experiments of Section 3.6.2. The aging and the thermal parts of the strain are assumed to be purely volumetric

$$\mathbf{E}_\Theta = \alpha_\Theta(\Theta - \Theta_0)\mathbf{I}, \quad \mathbf{E}_a = -\alpha_a a\mathbf{I}. \tag{4.2}$$

Here, the aging variable a is introduced.The aging a is an internal positive growing variable that serves to describe the aging process. Its behavior will be discussed later on. In the Maxwell-element of Fig. 4.1, the mechanical strain is decomposed into an elastic and a viscous part

$$\mathbf{E}_\mathrm{M} = \mathbf{E}_\mathrm{e} + \mathbf{E}_\mathrm{v}. \tag{4.3}$$

Taking a look at the stresses, the total stress $\mathbf{T}$ is decomposed in the mechanical element into an equilibrium part $\mathbf{T}_\mathrm{eq}$ and an overstress part $\mathbf{T}_\mathrm{ov}$. Furthermore, the equilibrium stress consists of an elastic $\mathbf{T}^\mathrm{e}_\mathrm{eq}$ and a plastic (hysteretic) $\mathbf{T}^\mathrm{h}_\mathrm{eq}$ part,

$$\mathbf{T} = \mathbf{T}_\mathrm{eq} + \mathbf{T}_\mathrm{ov} = \mathbf{T}^\mathrm{e}_\mathrm{eq} + \mathbf{T}^\mathrm{h}_\mathrm{eq} + \mathbf{T}_\mathrm{ov}. \tag{4.4}$$

The plastic equilibrium stress $\mathbf{T}^\mathrm{h}_\mathrm{eq}$ represents a rate-independent element of arc-length plasticity, see (Haupt, 2002; Hartmann, 2006). It allows to reproduce the equilibrium hysteresis of the material. A spring element $\mathbf{T}^\mathrm{e}_\mathrm{eq}$ is added to this element in parallel in order to avoid that the stress reaches a saturation value in a loading process, which can cause numerical convergence problems. The overstress part $\mathbf{T}_\mathrm{ov}$ is related to the Maxwell-element and allows to reproduce the rate dependence.

4.2.1 Thermodynamical Consistency

With the previous decomposition of stress and strain, the model has to ensure thermodynamical consistence. To this end, the dissipation inequality has to be evaluated. In the case of small strains, the Clausius-Duhem inequality can be expressed by

$$\frac{1}{\rho}\mathbf{T} \cdot \dot{\mathbf{E}} - \dot{\psi} - \dot{\Theta} s - \frac{1}{\rho\Theta}\vec{q} \cdot \operatorname{grad}\Theta \geq 0. \tag{2.109}$$

The free energy ψ is divided into an elastic equilibrium part $\psi^{\mathrm{e}}_{\mathrm{eq}}$, a plastic equilibrium part $\psi^{\mathrm{h}}_{\mathrm{eq}}$, an overstress part ψ_{ov}, a purely thermal part ψ_{Θ}, and an aging-dependent part ψ_a. The different components depend on the strain variables $\mathbf{E}_{\mathrm{M}}$ and $\mathbf{E}_{\mathrm{e}}$, a further strain-like variable $\mathbf{Y}$ related to the endochronic element in Fig. 4.1, the temperature Θ, and the scalar internal variables softening k, and the aging variable a in the following way

$$\begin{aligned}\psi &= \tilde{\psi}(\mathbf{E}_{\mathrm{M}}, \mathbf{E}_{\mathrm{e}}, \mathbf{Y}, \Theta, k, a) \\ &= \tilde{\psi}^{\mathrm{e}}_{\mathrm{eq}}(\mathbf{E}_{\mathrm{M}}) + \tilde{\psi}^{\mathrm{h}}_{\mathrm{eq}}(\mathbf{Y}, \Theta) + \tilde{\psi}_{\mathrm{ov}}(\mathbf{E}_{\mathrm{e}}, k) + \tilde{\psi}_{\Theta}(\Theta) + \tilde{\psi}_a(a).\end{aligned} \tag{4.5}$$

The process variable k has the goal to model the softening behavior which was observed in the experiments during the unloading process. The time derivative of the free energy can be calculated by applying the chain rule

$$\dot{\psi} = \frac{\partial\psi}{\partial\mathbf{E}_{\mathrm{M}}} \cdot \dot{\mathbf{E}}_{\mathrm{M}} + \frac{\partial\psi}{\partial\mathbf{E}_{\mathrm{e}}} \cdot \dot{\mathbf{E}}_{\mathrm{e}} + \frac{\partial\psi}{\partial\mathbf{Y}} \cdot \dot{\mathbf{Y}} + \frac{\partial\psi}{\partial\Theta}\dot{\Theta} + \frac{\partial\psi}{\partial k}\dot{k} + \frac{\partial\psi}{\partial a}\dot{a}. \tag{4.6}$$

By inserting expression (4.6), the strain (4.1), and the stress decomposition (4.4) into the Clausius-Duhem inequality (2.109) and multiplying by ρ, we obtain

$$\begin{aligned}&(\mathbf{T}^{\mathrm{e}}_{\mathrm{eq}} + \mathbf{T}^{\mathrm{h}}_{\mathrm{eq}} + \mathbf{T}_{\mathrm{ov}}) \cdot \dot{\mathbf{E}}_{\mathrm{M}} + \mathbf{T} \cdot \dot{\mathbf{E}}_{\Theta} + \mathbf{T} \cdot \dot{\mathbf{E}}_a - \rho\frac{\partial\psi}{\partial\mathbf{E}_{\mathrm{M}}} \cdot \dot{\mathbf{E}}_{\mathrm{M}} - \rho\frac{\partial\psi}{\partial\mathbf{E}_{\mathrm{e}}} \cdot \dot{\mathbf{E}}_{\mathrm{e}} - \rho\frac{\partial\psi}{\partial\mathbf{Y}} \cdot \dot{\mathbf{Y}} \\ &- \rho\frac{\partial\psi}{\partial\Theta}\dot{\Theta} - \rho\frac{\partial\psi}{\partial k}\dot{k} - \rho\frac{\partial\psi}{\partial a}\dot{a} - \rho\dot{\Theta}s - \frac{1}{\Theta}\vec{q} \cdot \operatorname{grad}\Theta \geq 0.\end{aligned} \tag{4.7}$$

Rearranging the inequality and introducing definitions (4.2) and (4.3) leads to

$$\begin{aligned}&\left(\mathbf{T}^{\mathrm{e}}_{\mathrm{eq}} - \rho\frac{\partial\psi}{\partial\mathbf{E}_{\mathrm{M}}}\right) \cdot \dot{\mathbf{E}}_{\mathrm{M}} + \mathbf{T}^{\mathrm{h}}_{\mathrm{eq}} \cdot \dot{\mathbf{E}}_{\mathrm{M}} + \mathbf{T}_{\mathrm{ov}} \cdot \dot{\mathbf{E}}_{\mathrm{v}} + \left(\mathbf{T}_{\mathrm{ov}} - \rho\frac{\partial\psi}{\partial\mathbf{E}_{\mathrm{e}}}\right) \cdot \dot{\mathbf{E}}_{\mathrm{e}} - \rho\frac{\partial\psi}{\partial\mathbf{Y}} \cdot \dot{\mathbf{Y}} \\ &- \rho\frac{\partial\psi}{\partial k}\dot{k} + \left(\alpha_a(\operatorname{tr}\mathbf{T}) - \rho\frac{\partial\psi}{\partial a}\right)\dot{a} + \left(\alpha_{\Theta}(\operatorname{tr}\mathbf{T}) - \rho\frac{\partial\psi}{\partial\Theta} - \rho s\right)\dot{\Theta} - \frac{1}{\Theta}\vec{q} \cdot \operatorname{grad}\Theta \geq 0.\end{aligned} \tag{4.8}$$

As a sufficient condition, the following relations are defined

$$\mathbf{T}^{\mathrm{e}}_{\mathrm{eq}} = \rho\frac{\partial\psi}{\partial\mathbf{E}_{\mathrm{M}}}, \tag{4.9}$$

$$\mathbf{T}_{\mathrm{ov}} = \rho\frac{\partial\psi}{\partial\mathbf{E}_{\mathrm{e}}}, \tag{4.10}$$

$$s = \frac{\alpha_{\Theta}}{\rho}(\operatorname{tr}\mathbf{T}) - \frac{\partial\psi}{\partial\Theta}. \tag{4.11}$$

The equilibrium stress part should exhibit a hysteretic behavior in order to reproduce the equilibrium hysteresis. For this case, the following relation is chosen

$$\mathbf{T}^{\mathrm{h}}_{\mathrm{eq}} = \rho\frac{c}{c_\alpha}\frac{\partial\psi}{\partial\mathbf{Y}} = c_\alpha\mathbf{Y}^{\mathrm{D}}, \qquad c, c_\alpha > 0, c_\alpha = \text{const.} \tag{4.12}$$

This expression is similar to the hysteretic stress proposed in Hartmann (2006), with the difference that a dimensionless factor c/c_α is introduced in the relation between the plastic stress $\mathbf{T}_{\text{eq}}^{\text{h}}$ and the partial derivative $\partial\psi/\partial\mathbf{Y}$. This factor plays an important role in the definition of the evolution equation and will be discussed later on. After rearranging terms again and considering the tensor property $\mathbf{A}^{\text{D}}\cdot\mathbf{B} = \mathbf{A}^{\text{D}}\cdot\mathbf{B}^{\text{D}}$, the remaining Clausius-Duhem inequality is equal to

$$\begin{aligned} c_\alpha \mathbf{Y}^{\text{D}} \cdot \left(\dot{\mathbf{E}}_{\text{M}} - \frac{c_\alpha}{c}\dot{\mathbf{Y}}\right)^{\text{D}} + \mathbf{T}_{\text{ov}} \cdot \dot{\mathbf{E}}_{\text{v}} - \rho\frac{\partial\psi}{\partial k}\dot{k} \\ + \left(\alpha_a(\operatorname{tr}\mathbf{T}) - \rho\frac{\partial\psi}{\partial a}\right)\dot{a} - \frac{1}{\Theta}\vec{q}\cdot\operatorname{grad}\Theta \geq 0. \end{aligned} \tag{4.13}$$

In order to fulfill inequality (4.13), the following assumptions are chosen

$$\left(\dot{\mathbf{E}}_{\text{M}} - \frac{c_\alpha}{c}\dot{\mathbf{Y}}\right)^{\text{D}} = \dot{s}_{\text{M}}\beta_{\mathbf{Y}}\mathbf{Y}^{\text{D}}, \quad \beta_{\mathbf{Y}}, \dot{s}_{\text{M}} \geq 0, \tag{4.14}$$

$$\dot{\mathbf{E}}_{\text{v}} = \frac{1}{\eta}\mathbf{T}_{\text{ov}}, \quad \eta \geq 0, \tag{4.15}$$

$$\dot{k} \geq 0, \quad \frac{\partial\psi}{\partial k} \leq 0, \tag{4.16}$$

$$\dot{a} = \beta_a\left(\alpha_a(\operatorname{tr}\mathbf{T}) - \rho\frac{\partial\psi}{\partial a}\right), \quad \beta_a \geq 0, \tag{4.17}$$

$$\vec{q} = -\kappa_\Theta \operatorname{grad}\Theta, \quad \kappa_\Theta \geq 0. \tag{4.18}$$

At this point, several relations ((4.9)-(4.11) and (4.14)-(4.18)) were found, which ensure the thermodynamical consistence of the model. In the next step of modeling, expressions for the components of the free energy have to be chosen. For the elastic component in the rheological model, a linear elastic ansatz is used

$$\rho\psi_{\text{eq}}^{\text{e}} = \frac{K_{\text{eq}}}{2}(\operatorname{tr}\mathbf{E}_{\text{M}})^2 + G_{\text{eq}}\mathbf{E}_{\text{M}}^{\text{D}}\cdot\mathbf{E}_{\text{M}}^{\text{D}}. \tag{4.19}$$

With this selection of the free energy, the elastic equilibrium stress reads

$$\mathbf{T}_{\text{eq}}^{\text{e}} = \rho\frac{\partial\psi}{\partial\mathbf{E}_{\text{M}}} = K_{\text{eq}}(\operatorname{tr}\mathbf{E}_{\text{M}})\mathbf{I} + 2G_{\text{eq}}\mathbf{E}_{\text{M}}^{\text{D}}. \tag{4.20}$$

The parameters K_{eq} and G_{eq} represent the bulk and shear modulus of the elastic part of the equilibrium stress. For the plastic component, expression (4.12) is integrated, obtaining the following for the hysteretic component of the free energy:

$$\rho\psi_{\text{eq}}^{\text{h}} = \frac{c_\alpha^2}{2c(\Theta)}\mathbf{Y}^{\text{D}}\cdot\mathbf{Y}^{\text{D}}. \tag{4.21}$$

The parameter $c(\Theta)$ influences the initial slope of the stress-strain diagram of the equilibrium curve. It is chosen to be dependent on the temperature Θ in order to include the change of the initial slope, which was observed in the experiments, see Figs. 3.15(a) and 3.16-3.17. A further dependence on the temperature is included in the viscosity later on. Moreover, the component of the free energy related to the Maxwell-element is chosen equal to

$$\rho\psi_{\mathrm{ov}} = G_{\mathrm{ov}}(k)\mathbf{E}_{\mathrm{e}}^{\mathrm{D}} \cdot \mathbf{E}_{\mathrm{e}}^{\mathrm{D}}, \tag{4.22}$$

leading to a purely deviatoric overstress

$$\mathbf{T}_{\mathrm{ov}} = \rho\frac{\partial\psi}{\partial\mathbf{E}_{\mathrm{e}}} = 2G_{\mathrm{ov}}(k)\mathbf{E}_{\mathrm{e}}^{\mathrm{D}}. \tag{4.23}$$

Since the shear modulus influences the initial slope in the stress-strain curve as well, it is chosen to be dependent on the softening variable k in order to model the effect observed in Section 3.5.2. Finally, for the purely aging part, a linear ansatz was chosen

$$\rho\psi_a = C_1 - C_2 a, \tag{4.24}$$

where C_1 and C_2 are material parameters. The term of the free energy depending on the temperature ψ_Θ is discussed in Section 4.4.

4.2.2 Evolution Equations

In the following, expressions for the internal variables $\mathbf{Y}$, $\mathbf{E}_{\mathrm{v}}$, k and a have to be found. They have to fulfill conditions (4.14)-(4.18). The motivation of the selection of several temperature- and aging-dependent parameters is done in the frame of the identification process presented in Section 5.4 and also considering previous works, see (Martinez Page and Hartmann, 2018b,a), where several temperature- and aging-dependent functions were found for the small deformation case for Zamak 5.

Softening variable In order to model the change in the initial slope in the loading and unloading observed in Section 3.5, the variable k is introduced. This process variable is a growing function with values between 0 and 1. The value 0 corresponds to the undeformed state, while 1 represents the state in which the maximum softening is reached. Its evolution equation follows the expression

$$\dot{k} = \alpha_k(1-k)\dot{s}_{\mathrm{M}}, \tag{4.25}$$

with α_k a material parameter and $\dot{s}_{\mathrm{M}}$ the rate of the arc-length of the deviatoric mechanical strain

$$\dot{s}_{\mathrm{M}} = \sqrt{\dot{\mathbf{E}}_{\mathrm{M}}^{\mathrm{D}} \cdot \dot{\mathbf{E}}_{\mathrm{M}}^{\mathrm{D}}} \geq 0. \tag{4.26}$$

Since the terms $\mathbf{E}_\Theta$ and $\mathbf{E}_a$ are purely volumetric, this leads to $\mathbf{E}_{\mathrm{M}}^{\mathrm{D}} = \mathbf{E}^{\mathrm{D}}$. With evolution equation (4.25), the first part of condition (4.16) is fulfilled. In order to fulfill the second condition of Eq. (4.16), the partial derivative of the free energy with respect to the softening variable has to be negative

$$\frac{\partial \psi}{\partial k} = \frac{\partial G_{\text{ov}}}{\partial k} \mathbf{E}_{\text{e}}^{\text{D}} \cdot \mathbf{E}_{\text{e}}^{\text{D}} \leq 0. \tag{4.27}$$

Since the term $\mathbf{E}_{\text{e}}^{\text{D}} \cdot \mathbf{E}_{\text{e}}^{\text{D}}$ is non-negative, this condition is fulfilled if

$$\frac{\partial G_{\text{ov}}}{\partial k} \leq 0. \tag{4.28}$$

This means that the function connected to the initial slope of the overstress part $G_{\text{ov}}(k)$ has to be defined to be monotonously decreasing with the softening variable. This behavior corresponds to the effect of the softening. With an increasing loading process, the variable k grows and, thus, the material behaves "weaker".

Plastic strain From condition (4.14), it is clear that the plastic strain $\mathbf{Y}$ is purely deviatoric. Considering that $\mathbf{E}_{\text{M}}^{\text{D}} = \mathbf{E}^{\text{D}}$, Eq. (4.14) can be rewritten as

$$c_\alpha \dot{\mathbf{Y}} = c \dot{\mathbf{E}}^{\text{D}} - c \dot{s}_{\text{M}} \beta_{\mathbf{Y}} \mathbf{Y}. \tag{4.29}$$

By selecting the parameter $\beta_{\mathbf{Y}}$ equal to

$$\beta_{\mathbf{Y}} = \frac{c_\alpha}{c} b, \qquad b > 0, \tag{4.30}$$

and inserting Eqns. (4.12) and (4.30) into Eq. (4.29), one obtains the following equation for the plastic stress

$$\dot{\mathbf{T}}_{\text{eq}}^{\text{h}} = c \dot{\mathbf{E}}^{\text{D}} - b \dot{s}_{\text{M}} \mathbf{T}_{\text{eq}}^{\text{h}}, \tag{4.31}$$

which corresponds to a formulation of an hysteretic stress of rate-independent plasticity, in a similar manner as in (Hartmann, 2006). This evolution equation for the stress is analogous to an Armstrong-Frederic ansatz where the stress is equal to the back-stress $\mathbf{T} = \mathbf{X}$, see (Armstrong and Frederick, 1966). Moreover, it has the property that relation (4.31) is valid for the hysteretic stress also when c is not a constant anymore. The formulation of the hysteretic stress according to Eq. (4.12) allows a proportionality relation between the strain-like variable $\mathbf{Y}$ and the hysteretic stress $\mathbf{T}_{\text{eq}}^{\text{h}}$ and their time derivatives

$$\mathbf{T}_{\text{eq}}^{\text{h}} = c_\alpha \mathbf{Y}, \text{ and } \dot{\mathbf{T}}_{\text{eq}}^{\text{h}} = c_\alpha \dot{\mathbf{Y}}. \tag{4.32}$$

In the experiments, it was observed that the initial slope of the equilibrium hysteresis decreases with growing temperatures. This effect is strongly pronounced for the temperature of 85 °C. Moreover, the viscous effects are reduced for lower temperatures, and, thus, the equilibrium stress is the predominant part of the mechanical response for the experiments at $-40\,^{\circ}\mathrm{C}$. The parameter c is related to the initial slope of the stress-strain diagram. Because of that, the function $c(\Theta)$ was chosen to decrease monotonously with the temperature $c(\Theta)$. It reaches a saturation value for high and low temperatures, as shown in Fig. 4.2.

$$c(\Theta) = c_1(c_2 - \tanh(c_3(\Theta - \Theta_c))). \tag{4.33}$$

In the experiments, a small dependence of the initial slope on the aging time was observed as well, which is most pronounced at room temperature but vanishes for higher temperatures almost completely, see Fig. 3.22. Because of its low influence compared to the effect of the temperature, the aging dependence was not considered in the equilibrium part of the model.

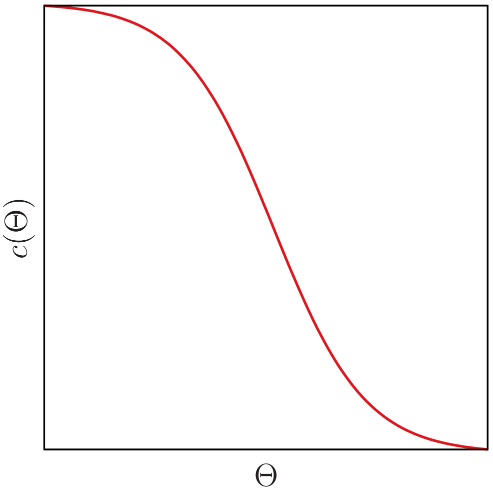

Figure 4.2: Behavior of the function $c(\Theta)$

Viscous strain Inserting Eqns. (4.3) and (4.23) into condition (4.15) and considering that $\mathbf{E}_{\mathrm{M}}^{\mathrm{D}} = \mathbf{E}^{\mathrm{D}}$, the evolution equation for the viscous strain is obtained

$$\dot{\mathbf{E}}_{\mathrm{v}} = \frac{2G_{\mathrm{ov}}(k)}{\eta}(\mathbf{E} - \mathbf{E}_{\mathrm{v}})^{\mathrm{D}}, \tag{4.34}$$

where it is clear that the viscous strain is purely deviatoric. For the shear modulus of the overstress, the following expression is chosen

$$G_{\mathrm{ov}}(k) = G_0((1-k)^{n_{\mathrm{ov}}} + \alpha_{\mathrm{ov}}). \tag{4.35}$$

The values G_0, n_{ov}, and α_{ov} are material parameters. The dependence on the softening is nonlinear, and this non-linearity is characterized with the parameter n_{ov}. Since the softening variable k can only have values between 0 and 1, the limits of the function G_{ov} are

$$G_{\mathrm{ov}}(k=0) = G_0(1+\alpha_{\mathrm{ov}}), \tag{4.36}$$

$$G_{\mathrm{ov}}(k=1) = G_0\alpha_{\mathrm{ov}}. \tag{4.37}$$

From this expression, one can see that G_{ov} decreases with the softening variable for $n_{\mathrm{ov}} > 0$, and, thus, condition (4.28)

$$\frac{\partial G_{\mathrm{ov}}}{\partial k} = -n_{\mathrm{ov}}(1-k)^{n_{\mathrm{ov}}-1} \leq 0 \tag{4.28}$$

is fulfilled. The viscosity is chosen in dependence of the strain-rate through the variable $\dot{s}_{\mathrm{M}}(\dot{\mathbf{E}})$, the temperature Θ, and the aging variable a

$$\eta(\dot{\mathbf{E}},\Theta,a) = \eta_0(\Theta,a)\left(\left(\frac{\dot{s}_{\mathrm{M}}(\dot{\mathbf{E}})}{s_\eta} + \alpha_\eta(\Theta)\right)^{-r_\eta(\Theta)} + 1\right), \tag{4.38}$$

with the following temperature and aging-dependent functions

$$\eta_0(\Theta,a) = (\eta_{01} - \eta_{02}\exp(\eta_{03}a))(1+\tanh(n_\eta(\Theta-\Theta_\eta))), \tag{4.39}$$

$$r_\eta(\Theta) = r_{\eta 1}(1-\tanh(n_\eta(\Theta-\Theta_r))), \tag{4.40}$$

$$\alpha_\eta(\Theta) = \alpha_{\eta 1}\exp(\alpha_{\eta 2}\Theta). \tag{4.41}$$

These dependencies for the different viscosity functions were found during the identification process and will be discussed in Section 5.4.1.

Aging variable Eq. (4.17) represents the evolution equation of the aging variable

$$\dot{a} = \beta_a\left(\alpha_a(\operatorname{tr}\mathbf{T}) - \rho\frac{\partial\psi}{\partial a}\right). \tag{4.17}$$

With the chosen free energy, the partial derivative of ψ with respect to the aging variable is equal to

$$\rho\frac{\partial\psi}{\partial a} = -C_2. \tag{4.42}$$

Inserting this term into Eq. (4.17) leads to

$$\dot{a} = \beta_a\left(C_2 + \alpha_a(\operatorname{tr}\mathbf{T})\right). \tag{4.43}$$

The aging rate $\dot{a}$ is coupled with the hydrostatic stress $\operatorname{tr}\mathbf{T}$. The magnitude of this coupling is characterized by the parameter C_2. In case of a purely deviatoric process, the trace of the stress would be zero $\operatorname{tr}\mathbf{T} = 0$ and only the parameter C_2 would influence the aging rate. Since a negative aging rate is physically unrealistic, the positive parameter C_2 must always be larger in absolute value than the term of $\alpha_a(\operatorname{tr}\mathbf{T})$. To the best knowledge of the author, the literature offers no information that allows to quantify the influence of mechanical deformation or stresses on the aging process of die casting alloys. In (Zhu and Orozco, 1995), the microstructure of a ZnAl20.2Cu1.8 alloy after a tensile test was investigated with X-ray diffraction and SEM, observing that the tensile stress is the cause of microstructure changes and phase transformations. In (Zhu, 2004), it is concluded that stresses accelerate the decomposition of metastable phases in tensile tests. Unfortunately, the studies were made at temperatures over 100 °C and the microstructural changes were not quantified. Moreover, there is no information about the compression or torsion behavior. An increase in the aging rate with the plastic deformation was found experimentally also for aluminum alloys in (Deschamps et al., 1998; Cerri and Leo, 2005). In the application areas of the alloy, aging takes place in a much larger timescale than the mechanical processes – and since there is no information at hand to characterize the influence of the stress on aging, the term C_2 is adopted to be much larger than $\alpha_a(\operatorname{tr}\mathbf{T})$, analogously to the discussion in Lion et al. (2014) for the field of curing or, more recently, in (Martinez Page and Hartmann, 2018a). Thus, the influence of the stresses is neglected

$$C_2 \gg \alpha_a(\operatorname{tr}\mathbf{T}), \tag{4.44}$$

and an approximation of Eq. (4.43) is assumed

$$\dot{a} \approx \beta_a C_2. \tag{4.45}$$

In the experiments, it was found that the isothermal aging process is stronger at the beginning of the process and slows down when approaching saturation, see Figs. 3.25 and 3.27(a). Moreover, it takes place faster at higher temperatures. In order to reproduce this behavior, the aging variable is defined as a process variable with values between 0 an 1. The value 0 corresponds to the initial unaged stage, while 1 represents the completely aged material. In order to fulfill these criteria, the function

$$\beta_a(\Theta, a) = \frac{\beta_{a1}(\Theta)}{C_2}\frac{(1-a)}{(\beta_{a2}+a)}, \tag{4.46}$$

is proposed, see also (Martinez Page and Hartmann, 2018a). The temperature dependence is given by the function $\beta_{a1}(\Theta)$. For this function, an Arrhenius ansatz is chosen, which is a common approach for temperature-driven diffusion processes in metals. In this way, the evolution equation for the aging variable reads

$$\dot{a} = \beta_{a1}(\Theta)\frac{1-a}{\beta_{a2}+a}, \qquad \beta_{a1}(\Theta) = \beta_{a11}\exp(-\beta_{a12}/\Theta), \tag{4.47}$$

with $\beta_{a12} = E_a/R$, E_a is the activation energy and R the universal gas constant. A summary of the constitutive model for small strains is given in Tab. 4.1.

Table 4.1: Summary of the constitutive model for small strains

Decomposition of stress and strain	
$\mathbf{E} = \mathbf{E}_\mathrm{M} + \mathbf{E}_\Theta + \mathbf{E}_a$	(4.1)
$\mathbf{E}_\Theta = \alpha_\Theta(\Theta - \Theta_0)\mathbf{I}, \quad \mathbf{E}_a = -\alpha_a a\mathbf{I}, \quad \mathbf{E}_\mathrm{M} = \mathbf{E}_\mathrm{e} + \mathbf{E}_\mathrm{v}$	(4.2),(4.3)
$\mathbf{T} = \mathbf{T}^\mathrm{e}_\mathrm{eq} + \mathbf{T}^\mathrm{h}_\mathrm{eq} + \mathbf{T}_\mathrm{ov}$	(4.4)
Scalar internal variables	
$\dot{a} = \beta_{a1}(\Theta)\dfrac{1-a}{\beta_{a2}+a}$	(4.47)
$\dot{k} = \alpha_k(1-k)\dot{s}_\mathrm{M}, \quad \dot{s}_\mathrm{M} = \sqrt{\dot{\mathbf{E}}^\mathrm{D} \cdot \dot{\mathbf{E}}^\mathrm{D}}$	(4.25),(4.26)
Equilibrium stress part	
$\mathbf{T}^\mathrm{e}_\mathrm{eq} = K_\mathrm{eq}(\mathrm{tr}\,\mathbf{E})\mathbf{I} + 2G_\mathrm{eq}\mathbf{E}^\mathrm{D} + 3K_\mathrm{eq}(\alpha_a a - \alpha_\Theta(\Theta - \Theta_0))\mathbf{I}$	(4.20)
$\mathbf{T}^\mathrm{h}_\mathrm{eq} = c_\alpha\mathbf{Y}, \quad \dot{\mathbf{Y}} = \dfrac{c(\Theta)}{c_\alpha}\dot{\mathbf{E}}^\mathrm{D} - b\dot{s}_\mathrm{M}\mathbf{Y}$	(4.32),(4.29)
Overstress part	
$\mathbf{T}_\mathrm{ov} = 2G_\mathrm{ov}(k)(\mathbf{E} - \mathbf{E}_\mathrm{v})^\mathrm{D}, \quad \dot{\mathbf{E}}_\mathrm{v} = \dfrac{2G_\mathrm{ov}(k)}{\eta(\dot{\mathbf{E}}, \dot{\Theta}, \Theta, a)}(\mathbf{E} - \mathbf{E}_\mathrm{v})^\mathrm{D}$	(4.23),(4.34)
Temperature, softening and aging-dependent functions	
$\beta_{a1}(\Theta) = \beta_{a11}\exp(-\beta_{a12}/\Theta)$	(4.46)
$c(\Theta) = c_1(c_2 - \tanh(c_3(\Theta - \Theta_c)))$	(4.33)
$G_\mathrm{ov}(k) = G_0((1-k)^{n_\mathrm{ov}} + \alpha_\mathrm{ov})$	(4.35)
$\eta(\dot{\mathbf{E}}, \dot{\Theta}, \Theta, a) = \eta_0(\Theta, a)\left(\left(\dfrac{\dot{s}_\mathrm{M}}{s_\eta} + \alpha_\eta(\Theta)\right)^{-r_\eta(\Theta)} + 1\right)$	(4.38)
$\eta_0(\Theta, a) = (\eta_{01} - \eta_{02}\exp(\eta_{03}a))(1 + \tanh(n_\eta(\Theta - \Theta_\eta)))$	(4.39)
$\alpha_\eta(\Theta) = \alpha_{\eta1}\exp(\alpha_{\eta2}\Theta), \quad r_\eta(\Theta) = r_{\eta1}(1 - \tanh(n_\eta(\Theta - \Theta_r)))$	(4.40),(4.41)
Material parameters	
Thermal expansion: α_Θ, Θ_0 Aging: $\alpha_a, \beta_{a11}, \beta_{a12}, \beta_{a2}$ Equilibrium part: $K_\mathrm{eq}, G_\mathrm{eq}, b, c_1, c_2, c_3, \Theta_c$ Shear modulus overstress: $\alpha_k, G_0, n_\mathrm{ov}, \alpha_\mathrm{ov}$ Viscosity: $\eta_{01}, \eta_{02}, \eta_{03}, \Theta_\eta, \quad \alpha_{\eta1}, \alpha_{\eta2}, r_{\eta1}, n_\eta, \Theta_r$	

4.3 Extension of the Model to Finite Deformations

In order to be able to compute thermo-mechanical processes in which the strain is larger than approximately $5\,\%$, a model of finite deformations is necessary. A finite strain model can be derived with the basis of the model proposed in Tab. 4.1. Here, a multiplicative decomposition of the deformation gradient is considered first, analogous to the additive decomposition of the strain in the small deformations model. With this decomposition, a group of intermediate configurations is defined. The stress power has to be determined for the evaluation of the Clausius-Duhem inequality, from which relations for the stresses and evolution equations are derived. The main difference in the modeling concept between the small and finite strain model lies in the plastic equilibrium stress, where temperature changes take place during the loading process, since in the finite deformations case, the modeling suggesting from Eq. (4.12) could not be followed completely from the point of view of the thermodynamical consistence.

4.3.1 Multiplicative Decomposition of Deformation Gradient

In order to extend the constitutive model from Section 4.2 to finite deformations, the rheological model from Fig. 4.1 is considered again. The model is composed, from the right to the left side, of a mechanical element (spring element, plastic element and Maxwell element), a thermal element, and an aging element. Instead of an additive decomposition of the strains, as in the small deformations case, a multiplicative decomposition of the deformation gradient is commonly performed for finite deformations. The most common decomposition in elasto-plasticity was proposed by Lee and Liu (1967) and Lee (1969), where the deformation gradient consists on an elastic and a plastic component $\mathbf{F} = \mathbf{F}_\mathrm{e}\mathbf{F}_\mathrm{p}$. Other early contributions in this topic are (Fox, 1968; Willis, 1969; Mandel, 1971). A reverse decomposition for elasto-plasticity $\mathbf{F} = \mathbf{F}_\mathrm{p}\mathbf{F}_\mathrm{e}$ is also possible, but it is far less common, see also (Lubarda, 2001) for more information. The decomposition for the case of viscoelasticity is considered in (Lubliner, 1985), and Lu and Pister (1975) treated thermo-elastic problems. The decomposition of the deformation gradient is not unique, and the order of the different effects in the decomposition can influence the final model. The selection of the decomposition can also affect the identification process, see (Rothe, 2015, page 108). There are several proposals for the incorporation of the thermal expansion $\mathbf{F}_\Theta$ in the decomposition, see, for example, Miehe (1988); Lion (2000a); Quint (2012). In (Hartmann, 2012), the equivalence between the decompositions $\mathbf{F} = \mathbf{F}_\Theta\mathbf{F}_\mathrm{M}$ and $\mathbf{F} = \mathbf{F}_\mathrm{M}\mathbf{F}_\Theta$ is demonstrated. In this work, the proposal from Miehe (1988) is chosen. Corresponding to the decomposition in the small deformations case, the deformation gradient is multiplicatively decomposed into an aging $\mathbf{F}_a$, a thermal $\mathbf{F}_\Theta$, and a mechanical part $\mathbf{F}_\mathrm{M}$, see Fig. 4.3,

$$\mathbf{F} = \mathbf{F}_a\mathbf{F}_\Theta\mathbf{F}_\mathrm{M}. \tag{4.48}$$

The thermal and the aging part are defined to be volumetric, i.e.

$$\mathbf{F}_\Theta = \varphi_\Theta(\Theta)\mathbf{I}, \quad \mathbf{F}_a = \varphi_a(a)\mathbf{I}, \tag{4.49}$$

with $\varphi_\Theta(\Theta)$ and $\varphi_a(a)$ as scalar functions of the temperature Θ and of the aging variable a

$$\varphi_\Theta(\Theta) = 1 + \alpha_\Theta(\Theta - \Theta_0), \tag{4.50}$$
$$\varphi_a(a) = 1 - \alpha_a a, \tag{4.51}$$

with $\alpha_\Theta, \alpha_a > 0$. The mechanical part of the deformation gradient $\mathbf{F}_\mathrm{M}$ can be decomposed, as proposed by Flory (1961), into a volumetric part $\hat{\mathbf{F}}_\mathrm{M}$ and an isochoric part $\bar{\mathbf{F}}_\mathrm{M}$

$$\mathbf{F}_\mathrm{M} = \hat{\mathbf{F}}_\mathrm{M}\bar{\mathbf{F}}_\mathrm{M}, \tag{4.52}$$

with the following properties

$$\hat{\mathbf{F}}_\mathrm{M} = (\det \mathbf{F}_\mathrm{M})^{1/3}\mathbf{I}, \quad \det \hat{\mathbf{F}}_\mathrm{M} = \det \mathbf{F}_\mathrm{M}, \tag{4.53}$$
$$\bar{\mathbf{F}}_\mathrm{M} = (\det \mathbf{F}_\mathrm{M})^{-1/3}\mathbf{F}_\mathrm{M}, \quad \det \bar{\mathbf{F}}_\mathrm{M} = 1. \tag{4.54}$$

Moreover, in order to consider the Maxwell element in the rheological model, the mechanical part of the deformation gradient is decomposed into an elastic part $\mathbf{F}_\mathrm{e}$ and an isochoric viscous part $\bar{\mathbf{F}}_\mathrm{v}$,

$$\mathbf{F}_\mathrm{M} = \mathbf{F}_\mathrm{e}\bar{\mathbf{F}}_\mathrm{v} = \hat{\mathbf{F}}_\mathrm{e}\bar{\mathbf{F}}_\mathrm{e}\bar{\mathbf{F}}_\mathrm{v}, \tag{4.55}$$

A further decomposition of the mechanical deformation gradient is necessary in order to include the plastic element. This decomposition is performed, in a similar way as in (Lion, 2000a) and (Tsakmakis and Willuweit, 2004), into an elastic (kinematic-hardening part) $\mathbf{F}_\mathrm{k}$ and a plastic component $\bar{\mathbf{F}}_\mathrm{p}$

$$\mathbf{F}_\mathrm{M} = \mathbf{F}_\mathrm{k}\bar{\mathbf{F}}_\mathrm{p} = \hat{\mathbf{F}}_\mathrm{k}\bar{\mathbf{F}}_\mathrm{k}\bar{\mathbf{F}}_\mathrm{p}. \tag{4.56}$$

As there is no distinction between an elastic and a plastic range, the interpretation of the components differs from (Lion, 2000a; Tsakmakis and Willuweit, 2004). The term $\mathbf{F}_\mathrm{k}$ is related to the strain-like variable $\mathbf{Y}$ in the small deformations case, see Tab. 4.1, which is assigned to the hysteretic response. The components $\bar{\mathbf{F}}_\mathrm{v}$ and $\bar{\mathbf{F}}_\mathrm{p}$ are purely isochoric, in order to consider the condition of inelastic incompressibility. The decomposition of the deformation gradient is illustrated in Fig. 4.3, where $\check{\boldsymbol{\chi}}_t$, $\bar{\boldsymbol{\chi}}_t$, $\hat{\boldsymbol{\chi}}_t$, $\breve{\boldsymbol{\chi}}_t$, $\tilde{\boldsymbol{\chi}}_t$ represent the intermediate configurations caused by the decomposition of $\mathbf{F}$.

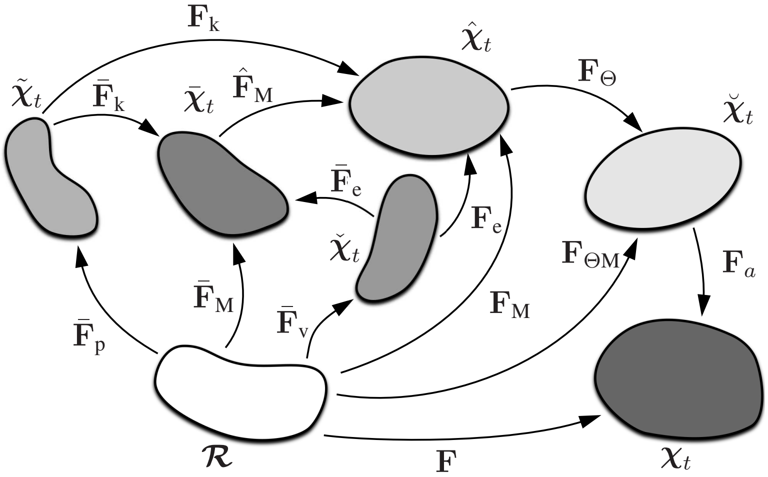

Figure 4.3: Multiplicative split of the deformation gradient

4.3.2 Strains and Strain-Rates

With the previous definitions of the deformation gradient, a series of strains can be defined. With the right Cauchy-Green tensor $\mathbf{C} = \mathbf{F}^{\mathrm{T}}\mathbf{F}$, the Green strain can be written as

$$\mathbf{E} = \frac{1}{2}(\mathbf{C} - \mathbf{I}) = \frac{1}{2}(\mathbf{C} - \mathbf{C}_{\Theta\mathrm{M}}) + \frac{1}{2}(\mathbf{C}_{\Theta\mathrm{M}} - \mathbf{C}_{\mathrm{M}}) + \frac{1}{2}(\mathbf{C}_{\mathrm{M}} - \mathbf{I}). \tag{4.57}$$

With the abbreviations $\mathbf{F}_{\Theta\mathrm{M}} = \mathbf{F}_{\Theta}\mathbf{F}_{\mathrm{M}} = \varphi_{\Theta}\mathbf{F}_{\mathrm{M}}$ and $\mathbf{F} = \varphi_a\varphi_{\Theta}\mathbf{F}_{\mathrm{M}}$, the components $\mathbf{C}_{\mathrm{M}}$, $\mathbf{C}_{\Theta\mathrm{M}}$ and $\mathbf{C}$ are equal to

$$\mathbf{C}_{\mathrm{M}} = \mathbf{F}_{\mathrm{M}}^{\mathrm{T}}\mathbf{F}_{\mathrm{M}}, \tag{4.58}$$

$$\mathbf{C}_{\Theta\mathrm{M}} = \mathbf{F}_{\Theta\mathrm{M}}^{\mathrm{T}}\mathbf{F}_{\Theta\mathrm{M}} = \varphi_{\Theta}^2\mathbf{F}_{\mathrm{M}}^{\mathrm{T}}\mathbf{F}_{\mathrm{M}}, \tag{4.59}$$

$$\mathbf{C} = \mathbf{F}^{\mathrm{T}}\mathbf{F} = \varphi_a^2\varphi_{\Theta}^2\mathbf{F}_{\mathrm{M}}^{\mathrm{T}}\mathbf{F}_{\mathrm{M}}. \tag{4.60}$$

Inserting Eqns. (4.58)-(4.60) into Eq. (4.57) results in

$$\mathbf{E} = \frac{1}{2}(\varphi_a^2 - 1)\varphi_{\Theta}^2\mathbf{C}_{\mathrm{M}} + \frac{1}{2}(\varphi_{\Theta}^2 - 1)\mathbf{C}_{\mathrm{M}} + \frac{1}{2}(\mathbf{C}_{\mathrm{M}} - \mathbf{I}) = \mathbf{E}_a + \mathbf{E}_{\Theta} + \mathbf{E}_{\mathrm{M}}. \tag{4.61}$$

In this way, we obtain a decomposition of the Green strain into three different components: the aging strain $\mathbf{E}_a$, the thermal strain $\mathbf{E}_{\Theta}$, and a mechanical strain $\mathbf{E}_{\mathrm{M}}$,

$$\mathbf{E}_a = \frac{1}{2}(\varphi_a^2 - 1)\varphi_{\Theta}^2\mathbf{C}_{\mathrm{M}}, \quad \mathbf{E}_{\Theta} = \frac{1}{2}(\varphi_{\Theta}^2 - 1)\mathbf{C}_{\mathrm{M}}, \quad \mathbf{E}_{\mathrm{M}} = \frac{1}{2}(\mathbf{C}_{\mathrm{M}} - \mathbf{I}). \tag{4.62}$$

In an analogous way, the mechanical strain $\mathbf{E}_{\mathrm{M}}$ can be decomposed into the Maxwell and endochronic elements

$$\mathbf{E}_{\mathrm{M}} = \frac{1}{2}(\mathbf{C}_{\mathrm{M}} - \mathbf{I}) = \frac{1}{2}(\mathbf{C}_{\mathrm{M}} - \bar{\mathbf{C}}_{\mathrm{v}}) + \frac{1}{2}(\bar{\mathbf{C}}_{\mathrm{v}} - \mathbf{I}) = \mathbf{E}_{\mathrm{e}} + \mathbf{E}_{\mathrm{v}}, \tag{4.63}$$

$$\mathbf{E}_{\mathrm{M}} = \frac{1}{2}(\mathbf{C}_{\mathrm{M}} - \mathbf{I}) = \frac{1}{2}(\mathbf{C}_{\mathrm{M}} - \bar{\mathbf{C}}_{\mathrm{p}}) + \frac{1}{2}(\bar{\mathbf{C}}_{\mathrm{p}} - \mathbf{I}) = \mathbf{E}_{\mathrm{k}} + \mathbf{E}_{\mathrm{p}}, \tag{4.64}$$

with $\bar{\mathbf{C}}_\mathrm{v} = \bar{\mathbf{F}}_\mathrm{v}^\mathrm{T}\bar{\mathbf{F}}_\mathrm{v}$ and $\bar{\mathbf{C}}_\mathrm{p} = \bar{\mathbf{F}}_\mathrm{p}^\mathrm{T}\bar{\mathbf{F}}_\mathrm{p}$. Thus, the mechanical strain is also decomposed into an elastic and a viscous part in the Maxwell-element $\mathbf{E}_\mathrm{M} = \mathbf{E}_\mathrm{e} + \mathbf{E}_\mathrm{v}$ or an elastic and plastic part $\mathbf{E}_\mathrm{M} = \mathbf{E}_\mathrm{k} + \mathbf{E}_\mathrm{p}$ in the plastic element

$$\mathbf{E}_\mathrm{e} = \frac{1}{2}(\mathbf{C}_\mathrm{M} - \bar{\mathbf{C}}_\mathrm{v}), \qquad \mathbf{E}_\mathrm{v} = \frac{1}{2}(\bar{\mathbf{C}}_\mathrm{v} - \mathbf{I}), \tag{4.65}$$

$$\mathbf{E}_\mathrm{k} = \frac{1}{2}(\mathbf{C}_\mathrm{M} - \bar{\mathbf{C}}_\mathrm{p}), \qquad \mathbf{E}_\mathrm{p} = \frac{1}{2}(\bar{\mathbf{C}}_\mathrm{p} - \mathbf{I}). \tag{4.66}$$

As one can see in Eqns. (4.62)-(4.66), the strains $\mathbf{E}_\mathrm{M}$, $\mathbf{E}_\mathrm{v}$, and $\mathbf{E}_\mathrm{p}$ depend exclusively on the part of the deformation gradient, which are described by $\mathbf{F}_\mathrm{M}$, $\bar{\mathbf{F}}_\mathrm{v}$, and $\bar{\mathbf{F}}_\mathrm{p}$ respectively. Within the concept of dual variables, strain measures can be defined relative to different configurations in order to obtain material relations. Analogously to (Hamkar, 2013), the mechanical part of the strain tensor $\varepsilon_\mathrm{M} = \frac{1}{2}(\mathbf{F}_\mathrm{e}^\mathrm{T}\mathbf{F}_\mathrm{e} - \bar{\mathbf{F}}_\mathrm{v}^{-\mathrm{T}}\bar{\mathbf{F}}_\mathrm{v}^{-1})$ relative to the elastic intermediate configuration $\check{\chi}_t$, see Fig. 4.4, can be decomposed in a purely elastic component ε_e and a purely viscous part ε_v

$$\varepsilon_\mathrm{e} = \frac{1}{2}(\mathbf{F}_\mathrm{e}^\mathrm{T}\mathbf{F}_\mathrm{e} - \mathbf{I}), \quad \varepsilon_\mathrm{v} = \frac{1}{2}(\mathbf{I} - \bar{\mathbf{F}}_\mathrm{v}^{-\mathrm{T}}\bar{\mathbf{F}}_\mathrm{v}^{-1}). \tag{4.67}$$

Analogously, one can find quantities relative to the plastic configuration $\tilde{\chi}_t$, namely the mechanical strain $\tilde{\varepsilon}_\mathrm{M} = \frac{1}{2}(\mathbf{F}_\mathrm{k}^\mathrm{T}\mathbf{F}_\mathrm{k} - \bar{\mathbf{F}}_\mathrm{p}^{-\mathrm{T}}\bar{\mathbf{F}}_\mathrm{p}^{-1})$, which can be decomposed into a component exclusively depending on $\mathbf{F}_\mathrm{k}$ and one depending on $\bar{\mathbf{F}}_\mathrm{p}$

$$\tilde{\varepsilon}_\mathrm{k} = \frac{1}{2}(\mathbf{F}_\mathrm{k}^\mathrm{T}\mathbf{F}_\mathrm{k} - \mathbf{I}), \quad \tilde{\varepsilon}_\mathrm{p} = \frac{1}{2}(\mathbf{I} - \bar{\mathbf{F}}_\mathrm{p}^{-\mathrm{T}}\bar{\mathbf{F}}_\mathrm{p}^{-1}). \tag{4.68}$$

A summary of the kinematic relations in the different configurations is given in Fig. 4.4, and the definition and transformation between the different strain-rates are given in Fig. 4.5. The basic concepts of the transformations for the strains and strain-rates between different configurations were already discussed in Section 2.4.2.

4.3.3 Decomposition of Stress and Evaluation of Stress Power

Now that the strain measures are fixed, an analysis of the stress is needed. Analogously to the small deformation case in Section 4.2 and considering the rheological element in Fig. 4.1, the total stress $\tilde{\mathbf{T}}$ is decomposed into an equilibrium stress part $\tilde{\mathbf{T}}_\mathrm{eq}$ and an overstress part $\tilde{\mathbf{T}}_\mathrm{ov}$. The equilibrium stress part possesses an elastic stress related to the spring $\tilde{\mathbf{T}}_\mathrm{eq}^\mathrm{e}$ and a plastic component related to the plastic element $\tilde{\mathbf{T}}_\mathrm{eq}^\mathrm{h}$. The overstress represents the Maxwell-element. Thus, the total stress can be expressed by

$$\tilde{\mathbf{T}} = \tilde{\mathbf{T}}_\mathrm{eq} + \tilde{\mathbf{T}}_\mathrm{ov} = \tilde{\mathbf{T}}_\mathrm{eq}^\mathrm{e} + \tilde{\mathbf{T}}_\mathrm{eq}^\mathrm{h} + \tilde{\mathbf{T}}_\mathrm{ov}. \tag{4.69}$$

$$\begin{tikzcd}[column sep=huge, row sep=large]
\begin{array}{l} \mathcal{R}[\mathcal{B}] \\ \boxed{\begin{array}{l}
\mathbf{E} = \mathbf{E}_a + \mathbf{E}_\Theta + \mathbf{E}_{\mathrm{M}} \\
\mathbf{E}_a = \frac{1}{2}(\mathbf{F}^{\mathrm{T}}\mathbf{F} - \mathbf{F}_{\Theta\mathrm{M}}^{\mathrm{T}}\mathbf{F}_{\Theta\mathrm{M}}) \\
\mathbf{E}_\Theta = \frac{1}{2}(\mathbf{F}_{\Theta\mathrm{M}}^{\mathrm{T}}\mathbf{F}_{\Theta\mathrm{M}} - \mathbf{F}_{\mathrm{M}}^{\mathrm{T}}\mathbf{F}_{\mathrm{M}}) \\
\mathbf{E}_{\mathrm{M}} = \frac{1}{2}(\mathbf{F}_{\mathrm{M}}^{\mathrm{T}}\mathbf{F}_{\mathrm{M}} - \mathbf{I}) \\
\mathbf{E}_{\mathrm{M}} = \mathbf{E}_{\mathrm{e}} + \mathbf{E}_{\mathrm{v}} = \mathbf{E}_{\mathrm{k}} + \mathbf{E}_{\mathrm{p}} \\
\mathbf{E}_{\mathrm{v}} = \frac{1}{2}(\bar{\mathbf{F}}_{\mathrm{v}}^{\mathrm{T}}\bar{\mathbf{F}}_{\mathrm{v}} - \mathbf{I}) \\
\mathbf{E}_{\mathrm{p}} = \frac{1}{2}(\bar{\mathbf{F}}_{\mathrm{p}}^{\mathrm{T}}\bar{\mathbf{F}}_{\mathrm{p}} - \mathbf{I})
\end{array}} \end{array}
\arrow[r, "\bar{\mathbf{F}}_{\mathrm{p}}^{-\mathrm{T}}(\,\cdot\,)\bar{\mathbf{F}}_{\mathrm{p}}^{-1}"]
\arrow[d, "\bar{\mathbf{F}}_{\mathrm{v}}^{-\mathrm{T}}(\,\cdot\,)\bar{\mathbf{F}}_{\mathrm{v}}^{-1}"]
\arrow[dr, "\grave{\mathbf{F}}_{\mathrm{M}}^{-\mathrm{T}}(\,\cdot\,)\mathbf{F}_{\mathrm{M}}^{-1}"]
\arrow[dd, bend right, "\mathbf{F}^{-\mathrm{T}}(\,\cdot\,)\mathbf{F}^{-1}"']
&
\begin{array}{l} \tilde{\chi}_t[\mathcal{B}] \\ \boxed{\begin{array}{l}
\tilde{\varepsilon} = \tilde{\varepsilon}_a + \tilde{\varepsilon}_\Theta + \tilde{\varepsilon}_{\mathrm{M}} \\
\tilde{\varepsilon}_a = \frac{1}{2}(\mathbf{F}_{a\Theta\mathrm{k}}^{\mathrm{T}}\mathbf{F}_{a\Theta\mathrm{k}} - \mathbf{F}_{\Theta\mathrm{k}}^{\mathrm{T}}\mathbf{F}_{\Theta\mathrm{k}}) \\
\tilde{\varepsilon}_\Theta = \frac{1}{2}(\mathbf{F}_{\Theta\mathrm{k}}^{\mathrm{T}}\mathbf{F}_{\Theta\mathrm{k}} - \mathbf{F}_{\mathrm{k}}^{\mathrm{T}}\mathbf{F}_{\mathrm{k}}) \\
\tilde{\varepsilon}_{\mathrm{M}} = \frac{1}{2}(\mathbf{F}_{\mathrm{k}}^{\mathrm{T}}\mathbf{F}_{\mathrm{k}} - \bar{\mathbf{F}}_{\mathrm{p}}^{-\mathrm{T}}\bar{\mathbf{F}}_{\mathrm{p}}^{-1}) \\
\tilde{\varepsilon}_{\mathrm{M}} = \tilde{\varepsilon}_{\mathrm{k}} + \tilde{\varepsilon}_{\mathrm{p}} \\
\tilde{\varepsilon}_{\mathrm{k}} = \frac{1}{2}(\mathbf{F}_{\mathrm{k}}^{\mathrm{T}}\mathbf{F}_{\mathrm{k}} - \mathbf{I}) \\
\tilde{\varepsilon}_{\mathrm{p}} = \frac{1}{2}(\mathbf{I} - \bar{\mathbf{F}}_{\mathrm{p}}^{-\mathrm{T}}\bar{\mathbf{F}}_{\mathrm{p}}^{-1})
\end{array}} \end{array}
\arrow[d, "\mathbf{F}_{\mathrm{k}}^{-\mathrm{T}}(\,\cdot\,)\mathbf{F}_{\mathrm{k}}^{-1}"]
\\
\begin{array}{l} \check{\chi}_t[\mathcal{B}] \\ \boxed{\begin{array}{l}
\varepsilon = \varepsilon_a + \varepsilon_\Theta + \varepsilon_{\mathrm{M}} \\
\varepsilon_a = \frac{1}{2}(\mathbf{F}_{a\Theta\mathrm{e}}^{\mathrm{T}}\mathbf{F}_{a\Theta\mathrm{e}} - \mathbf{F}_{\Theta\mathrm{e}}^{\mathrm{T}}\mathbf{F}_{\Theta\mathrm{e}}) \\
\varepsilon_\Theta = \frac{1}{2}(\mathbf{F}_{\Theta\mathrm{e}}^{\mathrm{T}}\mathbf{F}_{\Theta\mathrm{e}} - \mathbf{F}_{\mathrm{e}}^{\mathrm{T}}\mathbf{F}_{\mathrm{e}}) \\
\varepsilon_{\mathrm{M}} = \frac{1}{2}(\mathbf{F}_{\mathrm{e}}^{\mathrm{T}}\mathbf{F}_{\mathrm{e}} - \bar{\mathbf{F}}_{\mathrm{v}}^{-\mathrm{T}}\bar{\mathbf{F}}_{\mathrm{v}}^{-1}) \\
\varepsilon_{\mathrm{M}} = \varepsilon_{\mathrm{e}} + \varepsilon_{\mathrm{v}} \\
\varepsilon_{\mathrm{e}} = \frac{1}{2}(\mathbf{F}_{\mathrm{e}}^{\mathrm{T}}\mathbf{F}_{\mathrm{e}} - \mathbf{I}) \\
\varepsilon_{\mathrm{v}} = \frac{1}{2}(\mathbf{I} - \bar{\mathbf{F}}_{\mathrm{v}}^{-\mathrm{T}}\bar{\mathbf{F}}_{\mathrm{v}}^{-1})
\end{array}} \end{array}
\arrow[r, "\mathbf{F}_{\mathrm{e}}^{-\mathrm{T}}(\,\cdot\,)\mathbf{F}_{\mathrm{e}}^{-1}"]
&
\begin{array}{l} \hat{\chi}_t[\mathcal{B}] \\ \boxed{\begin{array}{l}
\mathbf{\Gamma} = \mathbf{\Gamma}_a + \mathbf{\Gamma}_\Theta + \mathbf{\Gamma}_{\mathrm{M}} \\
\mathbf{\Gamma}_a = \frac{1}{2}(\mathbf{F}_{a\Theta}^{\mathrm{T}}\mathbf{F}_{a\Theta} - \mathbf{F}_\Theta^{\mathrm{T}}\mathbf{F}_\Theta) \\
\mathbf{\Gamma}_\Theta = \frac{1}{2}(\mathbf{F}_\Theta^{\mathrm{T}}\mathbf{F}_\Theta - \mathbf{I}) \\
\mathbf{\Gamma}_{\mathrm{M}} = \frac{1}{2}(\mathbf{I} - \mathbf{F}_{\mathrm{M}}^{-\mathrm{T}}\mathbf{F}_{\mathrm{M}}^{-1}) \\
\mathbf{\Gamma}_{\mathrm{M}} = \mathbf{\Gamma}_{\mathrm{e}} + \mathbf{\Gamma}_{\mathrm{v}} = \mathbf{\Gamma}_{\mathrm{k}} + \mathbf{\Gamma}_{\mathrm{p}} \\
\mathbf{\Gamma}_{\mathrm{v}} = \frac{1}{2}(\mathbf{F}_{\mathrm{e}}^{-\mathrm{T}}\mathbf{F}_{\mathrm{e}}^{-1} - \mathbf{F}_{\mathrm{M}}^{-\mathrm{T}}\mathbf{F}_{\mathrm{M}}^{-1}) \\
\mathbf{\Gamma}_{\mathrm{p}} = \frac{1}{2}(\mathbf{F}_{\mathrm{k}}^{-\mathrm{T}}\mathbf{F}_{\mathrm{k}}^{-1} - \mathbf{F}_{\mathrm{M}}^{-\mathrm{T}}\mathbf{F}_{\mathrm{M}}^{-1})
\end{array}} \end{array}
\arrow[d, "\mathbf{F}_\Theta^{-\mathrm{T}}(\,\cdot\,)\mathbf{F}_\Theta^{-1}"]
\\
\begin{array}{l} \chi_t[\mathcal{B}] \\ \boxed{\begin{array}{l}
\mathbf{A} = \mathbf{A}_a + \mathbf{A}_\Theta + \mathbf{A}_{\mathrm{M}} \\
\mathbf{A}_a = \frac{1}{2}(\mathbf{I} - \mathbf{F}_a^{-\mathrm{T}}\mathbf{F}_a^{-1}) \\
\mathbf{A}_\Theta = \frac{1}{2}(\mathbf{F}_a^{-\mathrm{T}}\mathbf{F}_a^{-1} - \mathbf{F}_{a\Theta}^{-\mathrm{T}}\mathbf{F}_{a\Theta}^{-1}) \\
\mathbf{A}_{\mathrm{M}} = \frac{1}{2}(\mathbf{F}_{a\Theta}^{-\mathrm{T}}\mathbf{F}_{a\Theta}^{-1} - \mathbf{F}^{-\mathrm{T}}\mathbf{F}^{-1}) \\
\mathbf{A}_{\mathrm{M}} = \mathbf{A}_{\mathrm{e}} + \mathbf{A}_{\mathrm{v}} = \mathbf{A}_{\mathrm{k}} + \mathbf{A}_{\mathrm{p}} \\
\mathbf{A}_{\mathrm{v}} = \frac{1}{2}(\mathbf{F}_{a\Theta\mathrm{e}}^{-\mathrm{T}}\mathbf{F}_{a\Theta\mathrm{e}}^{-1} - \mathbf{F}^{-\mathrm{T}}\mathbf{F}^{-1}) \\
\mathbf{A}_{\mathrm{p}} = \frac{1}{2}(\mathbf{F}_{a\Theta\mathrm{k}}^{-\mathrm{T}}\mathbf{F}_{a\Theta\mathrm{k}}^{-1} - \mathbf{F}^{-\mathrm{T}}\mathbf{F}^{-1})
\end{array}} \end{array}
&
\begin{array}{l} \breve{\chi}_t[\mathcal{B}] \\ \boxed{\begin{array}{l}
\gamma = \gamma_a + \gamma_\Theta + \gamma_{\mathrm{M}} \\
\gamma_a = \frac{1}{2}(\mathbf{F}_a^{\mathrm{T}}\mathbf{F}_a - \mathbf{I}) \\
\gamma_\Theta = \frac{1}{2}(\mathbf{I} - \mathbf{F}_\Theta^{-\mathrm{T}}\mathbf{F}_\Theta^{-1}) \\
\gamma_{\mathrm{M}} = \frac{1}{2}(\mathbf{F}_\Theta^{-\mathrm{T}}\mathbf{F}_\Theta^{-1} - \mathbf{F}_{\Theta\mathrm{M}}^{-\mathrm{T}}\mathbf{F}_{\Theta\mathrm{M}}^{-1}) \\
\gamma_{\mathrm{M}} = \gamma_{\mathrm{e}} + \gamma_{\mathrm{v}} = \gamma_{\mathrm{k}} + \gamma_{\mathrm{p}} \\
\gamma_{\mathrm{v}} = \frac{1}{2}(\mathbf{F}_{\Theta\mathrm{e}}^{-\mathrm{T}}\mathbf{F}_{\Theta\mathrm{e}}^{-1} - \mathbf{F}_{\Theta\mathrm{M}}^{-\mathrm{T}}\mathbf{F}_{\Theta\mathrm{M}}^{-1}) \\
\gamma_{\mathrm{p}} = \frac{1}{2}(\mathbf{F}_{\Theta\mathrm{k}}^{-\mathrm{T}}\mathbf{F}_{\Theta\mathrm{k}}^{-1} - \mathbf{F}_{\Theta\mathrm{M}}^{-\mathrm{T}}\mathbf{F}_{\Theta\mathrm{M}}^{-1})
\end{array}} \end{array}
\arrow[l, "\mathbf{F}_a^{-\mathrm{T}}(\,\cdot\,)\mathbf{F}_a^{-1}"']
\end{tikzcd}$$

Figure 4.4: Transformation of the strains in the different configurations

$$\begin{tikzcd}[column sep=huge, row sep=large]
\begin{array}{l} \mathcal{R}[\mathcal{B}] \\ \boxed{\begin{array}{l}
\dot{\mathbf{E}} = \dot{\mathbf{E}}_a + \dot{\mathbf{E}}_\Theta + \dot{\mathbf{E}}_\mathrm{M} \\
\dot{\mathbf{E}}_a = \frac{1}{2}(\dot{\mathbf{C}} - \dot{\mathbf{C}}_{\Theta\mathrm{M}}) \\
\dot{\mathbf{E}}_\Theta = \frac{1}{2}(\dot{\mathbf{C}}_{\Theta\mathrm{M}} - \dot{\mathbf{C}}_\mathrm{M}) \\
\dot{\mathbf{E}}_\mathrm{M} = \frac{1}{2}\dot{\mathbf{C}}_\mathrm{M} \\
\dot{\mathbf{E}}_\mathrm{M} = \dot{\mathbf{E}}_\mathrm{e} + \dot{\mathbf{E}}_\mathrm{v} = \dot{\mathbf{E}}_\mathrm{k} + \dot{\mathbf{E}}_\mathrm{p} \\
\dot{\mathbf{E}}_\mathrm{v} = \frac{1}{2}\dot{\mathbf{C}}_\mathrm{v} \\
\dot{\mathbf{E}}_\mathrm{p} = \frac{1}{2}\dot{\mathbf{C}}_\mathrm{p}
\end{array}} \end{array}
\arrow[r, "\bar{\mathbf{F}}_\mathrm{p}^{-\mathrm{T}}(\,\cdot\,)\bar{\mathbf{F}}_\mathrm{p}^{-1}"]
\arrow[d, "\bar{\mathbf{F}}_\mathrm{v}^{-\mathrm{T}}(\,\cdot\,)\bar{\mathbf{F}}_\mathrm{v}^{-1}"]
\arrow[dr, "\grave{\mathbf{F}}_\mathrm{M}^{-\mathrm{T}}(\,\cdot\,)\mathbf{F}_\mathrm{M}^{-1}"]
\arrow[dd, bend right=60, swap, "\mathbf{F}^{-\mathrm{T}}(\,\cdot\,)\mathbf{F}^{-1}"]
&
\begin{array}{l} \tilde{\chi}_t[\mathcal{B}] \\ \boxed{\begin{array}{l}
\overset{\triangle}{\tilde{\boldsymbol{\varepsilon}}} = \overset{\triangle}{\tilde{\boldsymbol{\varepsilon}}}_a + \overset{\triangle}{\tilde{\boldsymbol{\varepsilon}}}_\Theta + \overset{\triangle}{\tilde{\boldsymbol{\varepsilon}}}_\mathrm{M} \\
\overset{\triangle}{\tilde{\boldsymbol{\varepsilon}}}_a = \dot{\tilde{\boldsymbol{\varepsilon}}}_a + \mathbf{L}_\mathrm{p}^\mathrm{T}\tilde{\boldsymbol{\varepsilon}}_a + \tilde{\boldsymbol{\varepsilon}}_a\mathbf{L}_\mathrm{p} \\
\overset{\triangle}{\tilde{\boldsymbol{\varepsilon}}}_\Theta = \dot{\tilde{\boldsymbol{\varepsilon}}}_\Theta + \mathbf{L}_\mathrm{p}^\mathrm{T}\tilde{\boldsymbol{\varepsilon}}_\Theta + \tilde{\boldsymbol{\varepsilon}}_\Theta\mathbf{L}_\mathrm{p} \\
\overset{\triangle}{\tilde{\boldsymbol{\varepsilon}}}_\mathrm{M} = \dot{\tilde{\boldsymbol{\varepsilon}}}_\mathrm{M} + \mathbf{L}_\mathrm{p}^\mathrm{T}\tilde{\boldsymbol{\varepsilon}}_\mathrm{M} + \tilde{\boldsymbol{\varepsilon}}_\mathrm{M}\mathbf{L}_\mathrm{p} \\
\overset{\triangle}{\tilde{\boldsymbol{\varepsilon}}}_\mathrm{M} = \overset{\triangle}{\tilde{\boldsymbol{\varepsilon}}}_\mathrm{k} + \overset{\triangle}{\tilde{\boldsymbol{\varepsilon}}}_\mathrm{p} \\
\overset{\triangle}{\tilde{\boldsymbol{\varepsilon}}}_\mathrm{p} = \frac{1}{2}(\mathbf{L}_\mathrm{p}^\mathrm{T} + \mathbf{L}_\mathrm{p}) = \mathbf{D}_\mathrm{p} \\
\overset{\triangle}{\tilde{\boldsymbol{\varepsilon}}}_\mathrm{k} = \dot{\tilde{\boldsymbol{\varepsilon}}}_\mathrm{k} + \mathbf{L}_\mathrm{p}^\mathrm{T}\tilde{\boldsymbol{\varepsilon}}_\mathrm{k} + \tilde{\boldsymbol{\varepsilon}}_\mathrm{k}\mathbf{L}_\mathrm{p}
\end{array}} \end{array}
\arrow[d, "\mathbf{F}_\mathrm{k}^{-\mathrm{T}}(\,\cdot\,)\mathbf{F}_\mathrm{k}^{-1}"]
\\
\begin{array}{l} \check{\chi}_t[\mathcal{B}] \\ \boxed{\begin{array}{l}
\overset{\triangle}{\boldsymbol{\varepsilon}} = \overset{\triangle}{\boldsymbol{\varepsilon}}_a + \overset{\triangle}{\boldsymbol{\varepsilon}}_\Theta + \overset{\triangle}{\boldsymbol{\varepsilon}}_\mathrm{M} \\
\overset{\triangle}{\boldsymbol{\varepsilon}}_a = \dot{\boldsymbol{\varepsilon}}_a + \mathbf{L}_\mathrm{v}^\mathrm{T}\boldsymbol{\varepsilon}_a + \boldsymbol{\varepsilon}_a\mathbf{L}_\mathrm{v} \\
\overset{\triangle}{\boldsymbol{\varepsilon}}_\Theta = \dot{\boldsymbol{\varepsilon}}_\Theta + \mathbf{L}_\mathrm{v}^\mathrm{T}\boldsymbol{\varepsilon}_\Theta + \boldsymbol{\varepsilon}_\Theta\mathbf{L}_\mathrm{v} \\
\overset{\triangle}{\boldsymbol{\varepsilon}}_\mathrm{M} = \dot{\boldsymbol{\varepsilon}}_\mathrm{M} + \mathbf{L}_\mathrm{v}^\mathrm{T}\boldsymbol{\varepsilon}_\mathrm{M} + \boldsymbol{\varepsilon}_\mathrm{M}\mathbf{L}_\mathrm{v} \\
\overset{\triangle}{\boldsymbol{\varepsilon}}_\mathrm{M} = \overset{\triangle}{\boldsymbol{\varepsilon}}_\mathrm{e} + \overset{\triangle}{\boldsymbol{\varepsilon}}_\mathrm{v} \\
\overset{\triangle}{\boldsymbol{\varepsilon}}_\mathrm{e} = \dot{\boldsymbol{\varepsilon}}_\mathrm{e} + \mathbf{L}_\mathrm{v}^\mathrm{T}\boldsymbol{\varepsilon}_\mathrm{e} + \boldsymbol{\varepsilon}_\mathrm{e}\mathbf{L}_\mathrm{v} \\
\overset{\triangle}{\boldsymbol{\varepsilon}}_\mathrm{v} = \frac{1}{2}(\mathbf{L}_\mathrm{v}^\mathrm{T} + \mathbf{L}_\mathrm{v}) = \mathbf{D}_\mathrm{v}
\end{array}} \end{array}
\arrow[r, "\mathbf{F}_\mathrm{e}^{-\mathrm{T}}(\,\cdot\,)\mathbf{F}_\mathrm{e}^{-1}"]
&
\begin{array}{l} \hat{\chi}_t[\mathcal{B}] \\ \boxed{\begin{array}{l}
\overset{\triangle}{\boldsymbol{\Gamma}} = \overset{\triangle}{\boldsymbol{\Gamma}}_a + \dot{\boldsymbol{\Gamma}}_\Theta + \dot{\boldsymbol{\Gamma}}_\mathrm{M} \\
\overset{\triangle}{\boldsymbol{\Gamma}}_a = \dot{\boldsymbol{\Gamma}}_a + \mathbf{L}_\mathrm{M}^\mathrm{T}\boldsymbol{\Gamma}_a + \boldsymbol{\Gamma}_a\mathbf{L}_\mathrm{M} \\
\overset{\triangle}{\boldsymbol{\Gamma}}_\Theta = \dot{\boldsymbol{\Gamma}}_\Theta + \mathbf{L}_\mathrm{M}^\mathrm{T}\boldsymbol{\Gamma}_\Theta + \boldsymbol{\Gamma}_\Theta\mathbf{L}_\mathrm{M} \\
\overset{\triangle}{\boldsymbol{\Gamma}}_\mathrm{M} = \mathbf{D}_\mathrm{M} \\
\overset{\triangle}{\boldsymbol{\Gamma}}_\mathrm{M} = \overset{\triangle}{\boldsymbol{\Gamma}}_\mathrm{e} + \overset{\triangle}{\boldsymbol{\Gamma}}_\mathrm{v} = \overset{\triangle}{\boldsymbol{\Gamma}}_\mathrm{k} + \overset{\triangle}{\boldsymbol{\Gamma}}_\mathrm{p} \\
\overset{\triangle}{\boldsymbol{\Gamma}}_\mathrm{v} = \dot{\boldsymbol{\Gamma}}_\mathrm{v} + \mathbf{L}_\mathrm{M}^\mathrm{T}\boldsymbol{\Gamma}_\mathrm{v} + \boldsymbol{\Gamma}_\mathrm{v}\mathbf{L}_\mathrm{M} \\
\overset{\triangle}{\boldsymbol{\Gamma}}_\mathrm{p} = \dot{\boldsymbol{\Gamma}}_\mathrm{p} + \mathbf{L}_\mathrm{M}^\mathrm{T}\boldsymbol{\Gamma}_\mathrm{p} + \boldsymbol{\Gamma}_\mathrm{p}\mathbf{L}_\mathrm{M}
\end{array}} \end{array}
\arrow[d, "\mathbf{F}_\Theta^{-\mathrm{T}}(\,\cdot\,)\mathbf{F}_\Theta^{-1}"]
\\
\begin{array}{l} \chi_t[\mathcal{B}] \\ \boxed{\begin{array}{l}
\overset{\triangle}{\mathbf{A}} = \overset{\triangle}{\mathbf{A}}_a + \overset{\triangle}{\mathbf{A}}_\Theta + \overset{\triangle}{\mathbf{A}}_\mathrm{M} = \mathbf{D} \\
\overset{\triangle}{\mathbf{A}}_a = \dot{\mathbf{A}}_a + \mathbf{L}^\mathrm{T}\mathbf{A}_a + \mathbf{A}_a\mathbf{L} \\
\overset{\triangle}{\mathbf{A}}_\Theta = \dot{\mathbf{A}}_\Theta + \mathbf{L}^\mathrm{T}\mathbf{A}_\Theta + \mathbf{A}_\Theta\mathbf{L} \\
\overset{\triangle}{\mathbf{A}}_\mathrm{M} = \dot{\mathbf{A}}_\mathrm{M} + \mathbf{L}^\mathrm{T}\mathbf{A}_\mathrm{M} + \mathbf{A}_\mathrm{M}\mathbf{L} \\
\overset{\triangle}{\mathbf{A}}_\mathrm{M} = \overset{\triangle}{\mathbf{A}}_\mathrm{e} + \overset{\triangle}{\mathbf{A}}_\mathrm{v} = \overset{\triangle}{\mathbf{A}}_\mathrm{k} + \overset{\triangle}{\mathbf{A}}_\mathrm{p} \\
\overset{\triangle}{\mathbf{A}}_\mathrm{v} = \dot{\mathbf{A}}_\mathrm{v} + \mathbf{L}^\mathrm{T}\mathbf{A}_\mathrm{v} + \mathbf{A}_\mathrm{v}\mathbf{L} \\
\overset{\triangle}{\mathbf{A}}_\mathrm{k} = \dot{\mathbf{A}}_\mathrm{k} + \mathbf{L}^\mathrm{T}\mathbf{A}_\mathrm{k} + \mathbf{A}_\mathrm{k}\mathbf{L}
\end{array}} \end{array}
&
\begin{array}{l} \breve{\chi}_t[\mathcal{B}] \\ \boxed{\begin{array}{l}
\overset{\triangle}{\boldsymbol{\gamma}} = \overset{\triangle}{\boldsymbol{\gamma}}_a + \overset{\triangle}{\boldsymbol{\gamma}}_\Theta + \overset{\triangle}{\boldsymbol{\gamma}}_\mathrm{M} \\
\overset{\triangle}{\boldsymbol{\gamma}}_a = \dot{\boldsymbol{\gamma}}_a + \mathbf{L}_{\Theta\mathrm{M}}^\mathrm{T}\boldsymbol{\gamma}_a + \boldsymbol{\gamma}_a\mathbf{L}_{\Theta\mathrm{M}} \\
\overset{\triangle}{\boldsymbol{\gamma}}_\Theta = \dot{\boldsymbol{\gamma}}_\Theta + \mathbf{L}_{\Theta\mathrm{M}}^\mathrm{T}\boldsymbol{\gamma}_\Theta + \boldsymbol{\gamma}_\Theta\mathbf{L}_{\Theta\mathrm{M}} \\
\overset{\triangle}{\boldsymbol{\gamma}}_\mathrm{M} = \dot{\boldsymbol{\gamma}}_\mathrm{M} + \mathbf{L}_{\Theta\mathrm{M}}^\mathrm{T}\boldsymbol{\gamma}_\mathrm{M} + \boldsymbol{\gamma}_\mathrm{M}\mathbf{L}_{\Theta\mathrm{M}} \\
\overset{\triangle}{\boldsymbol{\gamma}}_\mathrm{M} = \overset{\triangle}{\boldsymbol{\gamma}}_\mathrm{e} + \overset{\triangle}{\boldsymbol{\gamma}}_\mathrm{v} = \overset{\triangle}{\boldsymbol{\gamma}}_\mathrm{k} + \overset{\triangle}{\boldsymbol{\gamma}}_\mathrm{p} \\
\overset{\triangle}{\boldsymbol{\gamma}}_\mathrm{v} = \dot{\boldsymbol{\gamma}}_\mathrm{v} + \mathbf{L}_{\Theta\mathrm{M}}^\mathrm{T}\boldsymbol{\gamma}_\mathrm{v} + \boldsymbol{\gamma}_\mathrm{v}\mathbf{L}_{\Theta\mathrm{M}} \\
\overset{\triangle}{\boldsymbol{\gamma}}_\mathrm{p} = \dot{\boldsymbol{\gamma}}_\mathrm{p} + \mathbf{L}_{\Theta\mathrm{M}}^\mathrm{T}\boldsymbol{\gamma}_\mathrm{p} + \boldsymbol{\gamma}_\mathrm{p}\mathbf{L}_{\Theta\mathrm{M}}
\end{array}} \end{array}
\arrow[l, "\mathbf{F}_a^{-\mathrm{T}}(\,\cdot\,)\mathbf{F}_a^{-1}"]
\end{tikzcd}$$

Figure 4.5: Transformations of the strain-rates in the different configurations

$$\begin{tikzcd}[column sep=huge, row sep=large]
\overset{\mathcal{R}[\mathcal{B}]}{\boxed{\begin{array}{l}\tilde{\mathbf{T}} = J\mathbf{F}^{-1}\mathbf{T}\mathbf{F}^{-\mathrm{T}} \\ \dot{\tilde{\mathbf{T}}}\end{array}}} \arrow[r, "\bar{\mathbf{F}}_{\mathrm{p}}(\,\cdot\,)\bar{\mathbf{F}}_{\mathrm{p}}^{\mathrm{T}}"] \arrow[d, "\bar{\mathbf{F}}_{\mathrm{v}}(\,\cdot\,)\bar{\mathbf{F}}_{\mathrm{v}}^{\mathrm{T}}"] \arrow[dr, "\mathbf{F}_{\mathrm{M}}(\,\cdot\,)\mathbf{F}_{\mathrm{M}}^{\mathrm{T}}"] \arrow[dd, bend right=60, swap, "\mathbf{F}(\,\cdot\,)\mathbf{F}^{\mathrm{T}}"] & \overset{\tilde{\chi}_t[\mathcal{B}]}{\boxed{\begin{array}{l}\tilde{\mathbf{S}} = \bar{\mathbf{F}}_{\mathrm{p}}\tilde{\mathbf{T}}\bar{\mathbf{F}}_{\mathrm{p}}^{\mathrm{T}} \\ \overset{\triangledown}{\tilde{\mathbf{S}}} = \dot{\tilde{\mathbf{S}}} - \mathbf{L}_{\mathrm{p}}\tilde{\mathbf{S}} - \tilde{\mathbf{S}}\mathbf{L}_{\mathrm{p}}^{\mathrm{T}}\end{array}}} \arrow[d, "\mathbf{F}_{\mathrm{k}}(\,\cdot\,)\mathbf{F}_{\mathrm{k}}^{\mathrm{T}}"] \\
\overset{\check{\chi}_t[\mathcal{B}]}{\boxed{\begin{array}{l}\check{\mathbf{S}} = \bar{\mathbf{F}}_{\mathrm{v}}\tilde{\mathbf{T}}\bar{\mathbf{F}}_{\mathrm{v}}^{\mathrm{T}} \\ \overset{\triangledown}{\check{\mathbf{S}}} = \dot{\check{\mathbf{S}}} - \mathbf{L}_{\mathrm{v}}\check{\mathbf{S}} - \check{\mathbf{S}}\mathbf{L}_{\mathrm{v}}^{\mathrm{T}}\end{array}}} \arrow[r, swap, "\mathbf{F}_{\mathrm{e}}(\,\cdot\,)\mathbf{F}_{\mathrm{e}}^{\mathrm{T}}"] & \overset{\hat{\chi}_t[\mathcal{B}]}{\boxed{\begin{array}{l}\mathbf{S}_{\mathrm{M}} = \mathbf{F}_{\mathrm{M}}\tilde{\mathbf{T}}\mathbf{F}_{\mathrm{M}}^{\mathrm{T}} \\ \overset{\triangledown}{\mathbf{S}}_{\mathrm{M}} = \dot{\mathbf{S}}_{\mathrm{M}} - \mathbf{L}_{\mathrm{M}}\mathbf{S}_{\mathrm{M}} - \mathbf{S}_{\mathrm{M}}\mathbf{L}_{\mathrm{M}}^{\mathrm{T}}\end{array}}} \arrow[d, "\mathbf{F}_{\Theta}(\,\cdot\,)\mathbf{F}_{\Theta}^{\mathrm{T}}"] \\
\overset{\chi_t[\mathcal{B}]}{\boxed{\begin{array}{l}\mathbf{S} = \mathbf{F}\tilde{\mathbf{T}}\mathbf{F}^{\mathrm{T}} = J\mathbf{T} \\ \overset{\triangledown}{\mathbf{S}} = \dot{\mathbf{S}} - \mathbf{L}\mathbf{S} - \mathbf{S}\mathbf{L}^{\mathrm{T}}\end{array}}} & \overset{\breve{\chi}_t[\mathcal{B}]}{\boxed{\begin{array}{l}\breve{\mathbf{S}} = \mathbf{F}_{\Theta\mathrm{M}}\tilde{\mathbf{T}}\mathbf{F}_{\Theta\mathrm{M}}^{\mathrm{T}} \\ \overset{\triangledown}{\breve{\mathbf{S}}} = \dot{\breve{\mathbf{S}}} - \mathbf{L}_{\Theta\mathrm{M}}\breve{\mathbf{S}} - \breve{\mathbf{S}}\mathbf{L}_{\Theta\mathrm{M}}^{\mathrm{T}}\end{array}}} \arrow[l, swap, "\mathbf{F}_{a}(\,\cdot\,)\mathbf{F}_{a}^{\mathrm{T}}"]
\end{tikzcd}$$

Figure 4.6: Transformation of the stress and stress rates in the different configurations

Within the theory of dual variables, the stresses can be expressed into the different configurations. An overview of the transformations of the stresses in the different configurations is given in Fig. 4.6. Here, the definition of the contravariant Oldroyd derivative is given in Eq. (2.83), see Section 2.4.

As discussed in Section 2.3.5, the Clausius-Duhem inequality has to be evaluated in order to ensure the thermodynamical consistence of the model, see also (Haupt, 2002). In this equation, an expression for the stress power in dependence on the model variables is necessary. The stress power formulated with quantities relative to the reference configuration is equal to

$$\tilde{\mathbf{T}} \cdot \dot{\mathbf{E}} = \tilde{\mathbf{T}} \cdot \dot{\mathbf{E}}_{\mathrm{M}} + \tilde{\mathbf{T}} \cdot \dot{\mathbf{E}}_{\Theta} + \tilde{\mathbf{T}} \cdot \dot{\mathbf{E}}_{a}. \tag{4.70}$$

First, considering the invariance of the stress power with the configurational change, we can express the term $\tilde{\mathbf{T}} \cdot \dot{\mathbf{E}}_{\mathrm{M}}$ as

$$\tilde{\mathbf{T}} \cdot \dot{\mathbf{E}}_{\mathrm{M}} = \tilde{\mathbf{T}} \cdot \mathbf{F}_{\mathrm{M}}^{\mathrm{T}}\overset{\vartriangle}{\mathbf{\Gamma}}_{\mathrm{M}}\mathbf{F}_{\mathrm{M}} = \mathbf{F}_{\mathrm{M}}\tilde{\mathbf{T}}\mathbf{F}_{\mathrm{M}}^{\mathrm{T}} \cdot \overset{\vartriangle}{\mathbf{\Gamma}}_{\mathrm{M}} = \mathbf{S}_{\mathrm{M}} \cdot \overset{\vartriangle}{\mathbf{\Gamma}}_{\mathrm{M}}, \tag{4.71}$$

with $\mathbf{S}_{\mathrm{M}} = \mathbf{F}_{\mathrm{M}}\tilde{\mathbf{T}}\mathbf{F}_{\mathrm{M}}^{\mathrm{T}}$ being the stress tensor relative to the mechanical configuration $\hat{\chi}_t$, see Fig. 4.6. Analogously, the term of the thermal part $\tilde{\mathbf{T}} \cdot \dot{\mathbf{E}}_{\Theta}$ is equal to

$$\tilde{\mathbf{T}} \cdot \dot{\mathbf{E}}_{\Theta} = \tilde{\mathbf{T}} \cdot \mathbf{F}_{\mathrm{M}}^{\mathrm{T}}\overset{\vartriangle}{\mathbf{\Gamma}}_{\Theta}\mathbf{F}_{\mathrm{M}} = \mathbf{F}_{\mathrm{M}}\tilde{\mathbf{T}}\mathbf{F}_{\mathrm{M}}^{\mathrm{T}} \cdot \overset{\vartriangle}{\mathbf{\Gamma}}_{\Theta} = \mathbf{S}_{\mathrm{M}} \cdot \overset{\vartriangle}{\mathbf{\Gamma}}_{\Theta}. \tag{4.72}$$

Inserting the covariant Oldroyd rate of the thermal strain $\overset{\triangle}{\boldsymbol{\Gamma}}_\Theta$

$$\overset{\triangle}{\boldsymbol{\Gamma}}_\Theta = \dot{\boldsymbol{\Gamma}}_\Theta + \mathbf{L}_\mathrm{M}^\mathrm{T}\boldsymbol{\Gamma}_\Theta + \boldsymbol{\Gamma}_\Theta\mathbf{L}_\mathrm{M} = \varphi_\Theta \frac{\partial\varphi_\Theta}{\partial\Theta}\dot{\Theta}\mathbf{I} + (\varphi_\Theta^2 - 1)\overset{\triangle}{\boldsymbol{\Gamma}}_\mathrm{M} \tag{4.73}$$

into the thermal stress power, it can be expressed by scalar quantities of the temperature and tensorial quantities relative to the mechanical configuration

$$\tilde{\mathbf{T}}\cdot\dot{\mathbf{E}}_\Theta = \varphi_\Theta\frac{\partial\varphi_\Theta}{\partial\Theta}\dot{\Theta}(\operatorname{tr}\mathbf{S}_\mathrm{M}) + (\varphi_\Theta^2-1)\mathbf{S}_\mathrm{M}\cdot\overset{\triangle}{\boldsymbol{\Gamma}}_\mathrm{M}. \tag{4.74}$$

The last term to be evaluated is the aging contribution $\tilde{\mathbf{T}}\cdot\dot{\mathbf{E}}_a$

$$\tilde{\mathbf{T}}\cdot\dot{\mathbf{E}}_a = \tilde{\mathbf{T}}\cdot\mathbf{F}_{\Theta\mathrm{M}}^\mathrm{T}\overset{\triangle}{\gamma}_a\mathbf{F}_{\Theta\mathrm{M}} = \mathbf{F}_{\Theta\mathrm{M}}\tilde{\mathbf{T}}\mathbf{F}_{\Theta\mathrm{M}}^\mathrm{T}\cdot\overset{\triangle}{\gamma}_a = \breve{\mathbf{S}}\cdot\overset{\triangle}{\gamma}_a, \tag{4.75}$$

with $\breve{\mathbf{S}} = \mathbf{F}_{\Theta\mathrm{M}}\tilde{\mathbf{T}}\mathbf{F}_{\Theta\mathrm{M}}^\mathrm{T}$ being the stress tensor relative to the thermal configuration. The covariant Oldroyd rate $\overset{\triangle}{\gamma}_a$ is equal to

$$\overset{\triangle}{\gamma}_a = \dot{\gamma}_a + \mathbf{L}_{\Theta\mathrm{M}}^\mathrm{T}\gamma_a + \gamma_a\mathbf{L}_{\Theta\mathrm{M}}. \tag{4.76}$$

The spatial velocity gradient $\mathbf{L}_{\Theta\mathrm{M}}$ can be decomposed into the sum of the thermal $\mathbf{L}_\Theta$ and mechanical $\mathbf{L}_\mathrm{M}$ parts[1]

$$\mathbf{L}_{\Theta\mathrm{M}} = \mathbf{L}_\Theta + \mathbf{L}_\mathrm{M}, \quad \mathbf{L}_\Theta = \mathbf{L}_\Theta^\mathrm{T} = \frac{1}{\varphi_\Theta}\frac{\partial\varphi_\Theta}{\partial\Theta}\dot{\Theta}\mathbf{I}. \tag{4.77}$$

Making use of $\overset{\triangle}{\boldsymbol{\Gamma}}_\mathrm{M} = \frac{1}{2}(\mathbf{L}_\mathrm{M}^\mathrm{T} + \mathbf{L}_\mathrm{M})$ and Eq. (4.77), one obtains

$$\overset{\triangle}{\gamma}_a = \varphi_a\frac{\partial\varphi_a}{\partial a}\dot{a}\mathbf{I} + \frac{1}{\varphi_\Theta}\frac{\partial\varphi_\Theta}{\partial\Theta}\dot{\Theta}(\varphi_a^2-1)\mathbf{I} + (\varphi_a^2-1)\overset{\triangle}{\boldsymbol{\Gamma}}_\mathrm{M}. \tag{4.78}$$

Inserting this expression into Eq. (4.75) leads to

$$\tilde{\mathbf{T}}\cdot\dot{\mathbf{E}}_a = \left(\varphi_a\frac{\partial\varphi_a}{\partial a}\dot{a} + \frac{1}{\varphi_\Theta}\frac{\partial\varphi_\Theta}{\partial\Theta}\dot{\Theta}(\varphi_a^2-1)\right)\varphi_\Theta^2\operatorname{tr}\mathbf{S}_\mathrm{M} + (\varphi_a^2-1)\varphi_\Theta^2\mathbf{S}_\mathrm{M}\cdot\overset{\triangle}{\boldsymbol{\Gamma}}_\mathrm{M}, \tag{4.79}$$

where $\breve{\mathbf{S}} = \mathbf{F}_\Theta^\mathrm{T}\mathbf{S}_\mathrm{M}\mathbf{F}_\Theta = \varphi_\Theta^2\mathbf{S}_\mathrm{M}$ is used. Inserting expressions (4.71), (4.74), and (4.79) into Eq. (4.70), yields for the stress power

$$\tilde{\mathbf{T}}\cdot\dot{\mathbf{E}} = \varphi_\Theta^2\varphi_a^2\mathbf{S}_\mathrm{M}\cdot\overset{\triangle}{\boldsymbol{\Gamma}}_\mathrm{M} + \varphi_a^2\varphi_\Theta\frac{\partial\varphi_\Theta}{\partial\Theta}(\operatorname{tr}\mathbf{S}_\mathrm{M})\dot{\Theta} + \varphi_a\varphi_\Theta^2\frac{\partial\varphi_a}{\partial a}(\operatorname{tr}\mathbf{S}_\mathrm{M})\dot{a}. \tag{4.80}$$

Here, all terms are related to the intermediate mechanical configuration.

---

[1] Considering the relation $\mathbf{F}_{\Theta\mathrm{M}} = \varphi_\Theta\mathbf{F}_\mathrm{M}$.

4.3.4 Thermodynamical Consistence

Analogously to Section 4.2.1, the free energy ψ is chosen in dependence of the mechanical strain $\mathbf{E}_{\mathrm{M}}$, the elastic strain $\boldsymbol{\varepsilon}_{\mathrm{e}}$, the strain variable related to the plastic element $\tilde{\boldsymbol{\varepsilon}}_{\mathrm{k}}$, a softening variable k, the temperature Θ, and the aging variable a

$$\psi = \hat{\psi}(\mathbf{E}_{\mathrm{M}}, \boldsymbol{\varepsilon}_{\mathrm{e}}, \tilde{\boldsymbol{\varepsilon}}_{\mathrm{k}}, k, \Theta, a). \tag{4.81}$$

It is divided into an elastic part $\psi^{\mathrm{e}}_{\mathrm{eq}}$, a plastic part $\psi^{\mathrm{h}}_{\mathrm{eq}}$, an overstress part ψ_{ov}, a thermal ψ_{Θ}, and an aging part ψ_a

$$\psi = \psi^{\mathrm{e}}_{\mathrm{eq}}(\mathbf{E}_{\mathrm{M}}) + \psi^{\mathrm{h}}_{\mathrm{eq}}(\tilde{\boldsymbol{\varepsilon}}_{\mathrm{k}}, \Theta) + \psi_{\mathrm{ov}}(\boldsymbol{\varepsilon}_{\mathrm{e}}, k) + \psi_{\Theta}(\Theta) + \psi_a(a). \tag{4.82}$$

The time derivative of the free energy can be computed by

$$\dot{\psi} = \frac{\partial \psi}{\partial \mathbf{E}_{\mathrm{M}}} \cdot \dot{\mathbf{E}}_{\mathrm{M}} + \frac{\partial \psi}{\partial \tilde{\boldsymbol{\varepsilon}}_{\mathrm{k}}} \cdot \dot{\tilde{\boldsymbol{\varepsilon}}}_{\mathrm{k}} + \frac{\partial \psi}{\partial \boldsymbol{\varepsilon}_{\mathrm{e}}} \cdot \dot{\boldsymbol{\varepsilon}}_{\mathrm{e}} + \frac{\partial \psi}{\partial k}\dot{k} + \frac{\partial \psi}{\partial \Theta}\dot{\Theta} + \frac{\partial \psi}{\partial a}\dot{a}. \tag{4.83}$$

According to Eq. (2.80), the Clausius-Duhem inequality is equal to

$$\frac{1}{\rho_{\mathrm{R}}}\tilde{\mathbf{T}} \cdot \dot{\mathbf{E}} - \dot{\psi} - s\dot{\Theta} - \frac{1}{\rho_{\mathrm{R}}\Theta}\vec{q}_R \cdot \vec{g}_R \geq 0, \tag{2.80}$$

By inserting the stress power, Eq. (4.80), and the computed time derivative of the free energy, Eq. (4.83), into the Clausius-Duhem inequality, one obtains

$$\begin{aligned}
&\frac{1}{\rho_{\mathrm{R}}}\left(\varphi_{\Theta}^2\varphi_a^2\mathbf{S}_{\mathrm{M}} \cdot \overset{\triangle}{\mathbf{\Gamma}}_{\mathrm{M}} + \varphi_a^2\varphi_{\Theta}\frac{\partial \varphi_{\Theta}}{\partial \Theta}(\operatorname{tr}\mathbf{S}_{\mathrm{M}})\dot{\Theta} + \varphi_a\varphi_{\Theta}^2\frac{\partial \varphi_a}{\partial a}(\operatorname{tr}\mathbf{S}_{\mathrm{M}})\dot{a}\right) - \frac{\partial \psi}{\partial \mathbf{E}_{\mathrm{M}}} \cdot \dot{\mathbf{E}}_{\mathrm{M}} \\
&- \frac{\partial \psi}{\partial \boldsymbol{\varepsilon}_{\mathrm{e}}} \cdot \dot{\boldsymbol{\varepsilon}}_{\mathrm{e}} - \frac{\partial \psi}{\partial \tilde{\boldsymbol{\varepsilon}}_{\mathrm{k}}} \cdot \dot{\tilde{\boldsymbol{\varepsilon}}}_{\mathrm{k}} - \frac{\partial \psi}{\partial \Theta}\dot{\Theta} - \frac{\partial \psi}{\partial k}\dot{k} - \frac{\partial \psi}{\partial a}\dot{a} - s\dot{\Theta} - \frac{1}{\rho_{\mathrm{R}}\Theta}\vec{q}_R \cdot \vec{g}_R \geq 0.
\end{aligned} \tag{4.84}$$

The term $\partial\psi/\partial\mathbf{E}_{\mathrm{M}} \cdot \dot{\mathbf{E}}_{\mathrm{M}}$ can be rewritten as

$$\frac{\partial \psi}{\partial \mathbf{E}_{\mathrm{M}}} \cdot \dot{\mathbf{E}}_{\mathrm{M}} = \mathbf{F}_{\mathrm{M}}\frac{\partial \psi}{\partial \mathbf{E}_{\mathrm{M}}}\mathbf{F}_{\mathrm{M}}^{\mathrm{T}} \cdot \overset{\triangle}{\mathbf{\Gamma}}_{\mathrm{M}}. \tag{4.85}$$

Moreover, the total stress in the mechanical configuration $\hat{\boldsymbol{\chi}}_t$ is decomposed into the elastic, plastic, and overstress part

$$\mathbf{S}_{\mathrm{M}} = \mathbf{S}_{\mathrm{Meq}} + \mathbf{S}_{\mathrm{Mov}} = \mathbf{S}^{\mathrm{e}}_{\mathrm{Meq}} + \mathbf{S}^{\mathrm{h}}_{\mathrm{Meq}} + \mathbf{S}_{\mathrm{Mov}}. \tag{4.86}$$

With the expressions (4.85) and (4.86), and by rearranging the terms, Eq. (4.84) can be expressed as

$$\begin{aligned}
&\left(\frac{\varphi_{\Theta}^2\varphi_a^2}{\rho_{\mathrm{R}}}\mathbf{S}^{\mathrm{e}}_{\mathrm{Meq}} - \mathbf{F}_{\mathrm{M}}\frac{\partial \psi}{\partial \mathbf{E}_{\mathrm{M}}}\mathbf{F}_{\mathrm{M}}^{\mathrm{T}}\right) \cdot \overset{\triangle}{\mathbf{\Gamma}}_{\mathrm{M}} + \frac{\varphi_{\Theta}^2\varphi_a^2}{\rho_{\mathrm{R}}}\left(\mathbf{S}^{\mathrm{h}}_{\mathrm{Meq}} + \mathbf{S}_{\mathrm{Mov}}\right) \cdot \overset{\triangle}{\mathbf{\Gamma}}_{\mathrm{M}} \\
&- \frac{\partial \psi}{\partial \boldsymbol{\varepsilon}_{\mathrm{e}}} \cdot \dot{\boldsymbol{\varepsilon}}_{\mathrm{e}} - \frac{\partial \psi}{\partial \tilde{\boldsymbol{\varepsilon}}_{\mathrm{k}}} \cdot \dot{\tilde{\boldsymbol{\varepsilon}}}_{\mathrm{k}} - \frac{\partial \psi}{\partial k}\dot{k} + \left(\frac{\varphi_{\Theta}\varphi_a^2}{\rho_{\mathrm{R}}}\frac{\partial \varphi_{\Theta}}{\partial \Theta}(\operatorname{tr}\mathbf{S}_{\mathrm{M}}) - \frac{\partial \psi}{\partial \Theta} - s\right)\dot{\Theta} \\
&+ \left(\frac{\varphi_{\Theta}^2\varphi_a}{\rho_{\mathrm{R}}}\frac{\partial \varphi_a}{\partial a}(\operatorname{tr}\mathbf{S}_{\mathrm{M}}) - \frac{\partial \psi}{\partial a}\right)\dot{a} - \frac{1}{\rho_{\mathrm{R}}\Theta}\vec{q}_R \cdot \vec{g}_R \geq 0.
\end{aligned} \tag{4.87}$$

According to (Coleman and Noll, 1963) and (Truesdell and Noll, 1965), inequality (4.87) has to be fulfilled for any thermodynamical possible process. A sufficient condition can be obtained for the elastic stress $\mathbf{S}^{\mathrm{e}}_{\mathrm{Meq}}$ and the entropy s

$$\mathbf{S}^{\mathrm{e}}_{\mathrm{Meq}} = \frac{\rho_{\mathrm{R}}}{\varphi_\Theta^2 \varphi_a^2} \mathbf{F}_{\mathrm{M}} \frac{\partial \psi}{\partial \mathbf{E}_{\mathrm{M}}} \mathbf{F}_{\mathrm{M}}^{\mathrm{T}}, \tag{4.88}$$

$$s = \frac{\varphi_\Theta \varphi_a^2}{\rho_{\mathrm{R}}} \frac{\partial \varphi_\Theta}{\partial \Theta} (\operatorname{tr} \mathbf{S}_{\mathrm{M}}) - \frac{\partial \psi}{\partial \Theta}. \tag{4.89}$$

Now, the remaining terms of the Clausius-Duhem inequality have to be discussed. To this end, Eq. (4.87) is decomposed for the different considered effects in the following parts

$$\frac{\varphi_\Theta^2 \varphi_a^2}{\rho_{\mathrm{R}}} \mathbf{S}^{\mathrm{h}}_{\mathrm{Meq}} \cdot \overset{\triangle}{\boldsymbol{\Gamma}}_{\mathrm{M}} - \frac{\partial \psi}{\partial \tilde{\boldsymbol{\varepsilon}}_{\mathrm{k}}} \cdot \dot{\tilde{\boldsymbol{\varepsilon}}}_{\mathrm{k}} \geq 0 \qquad \text{plastic element} \tag{4.90}$$

$$\frac{\varphi_\Theta^2 \varphi_a^2}{\rho_{\mathrm{R}}} \mathbf{S}_{\mathrm{Mov}} \cdot \overset{\triangle}{\boldsymbol{\Gamma}}_{\mathrm{M}} - \frac{\partial \psi}{\partial \boldsymbol{\varepsilon}_{\mathrm{e}}} \cdot \dot{\boldsymbol{\varepsilon}}_{\mathrm{e}} \geq 0 \qquad \text{Maxwell-element} \tag{4.91}$$

$$-\frac{\partial \psi}{\partial k} \dot{k} \geq 0 \qquad \text{softening} \tag{4.92}$$

$$\frac{1}{\rho_{\mathrm{R}}} \left(\varphi_\Theta^2 \varphi_a \frac{\partial \varphi_a}{\partial a} (\operatorname{tr} \mathbf{S}_{\mathrm{M}}) - \rho_{\mathrm{R}} \frac{\partial \psi}{\partial a} \right) \dot{a} \geq 0 \qquad \text{aging} \tag{4.93}$$

$$-\frac{1}{\rho_{\mathrm{R}} \Theta} \vec{q}_R \cdot \vec{g}_R \geq 0 \qquad \text{thermal conduction} \tag{4.94}$$

The special cases of the Maxwell element and the plastic element are considered separately.

Maxwell Element The terms of the Clausius-Duhem inequality related to the Maxwell-element are

$$\frac{\varphi_\Theta^2 \varphi_a^2}{\rho_{\mathrm{R}}} \mathbf{S}_{\mathrm{Mov}} \cdot \overset{\triangle}{\boldsymbol{\Gamma}}_{\mathrm{M}} - \frac{\partial \psi}{\partial \boldsymbol{\varepsilon}_{\mathrm{e}}} \cdot \dot{\boldsymbol{\varepsilon}}_{\mathrm{e}} \geq 0. \tag{4.91}$$

The covariant Oldroyd derivative of the mechanical strain can be decomposed into the sum of the elastic part $\overset{\triangle}{\boldsymbol{\Gamma}}_{\mathrm{e}}$ and the viscous part $\overset{\triangle}{\boldsymbol{\Gamma}}_{\mathrm{v}}$. The term $\mathbf{S}_{\mathrm{Mov}} \cdot \overset{\triangle}{\boldsymbol{\Gamma}}_{\mathrm{M}}$ is now expressed in the viscous intermediate configuration $\check{\boldsymbol{\chi}}_t$

$$\mathbf{S}_{\mathrm{Mov}} \cdot \overset{\triangle}{\boldsymbol{\Gamma}}_{\mathrm{M}} = \check{\mathbf{S}}_{\mathrm{ov}} \cdot \overset{\triangle}{\boldsymbol{\varepsilon}}_{\mathrm{M}} = \check{\mathbf{S}}_{\mathrm{ov}} \cdot (\overset{\triangle}{\boldsymbol{\varepsilon}}_{\mathrm{e}} + \overset{\triangle}{\boldsymbol{\varepsilon}}_{\mathrm{v}}). \tag{4.95}$$

Additionally, the Oldroyd derivative $\overset{\triangle}{\boldsymbol{\varepsilon}}_{\mathrm{e}}$ is equal to

$$\overset{\triangle}{\boldsymbol{\varepsilon}}_{\mathrm{e}} = \dot{\boldsymbol{\varepsilon}}_{\mathrm{e}} + \mathbf{L}_{\mathrm{v}}^{\mathrm{T}} \boldsymbol{\varepsilon}_{\mathrm{e}} + \boldsymbol{\varepsilon}_{\mathrm{e}} \mathbf{L}_{\mathrm{v}}, \tag{4.96}$$

see Fig. 4.5. Inserting Eq. (4.95) and (4.96) into Eq. (4.91) leads to

$$\left(\frac{\varphi_\Theta^2\varphi_a^2}{\rho_\mathrm{R}}\check{\mathbf{S}}_\mathrm{ov}-\frac{\partial\psi}{\partial\boldsymbol{\varepsilon}_\mathrm{e}}\right)\cdot\overset{\triangle}{\boldsymbol{\varepsilon}}_\mathrm{e}+\frac{\varphi_\Theta^2\varphi_a^2}{\rho_\mathrm{R}}\check{\mathbf{S}}_\mathrm{ov}\cdot\overset{\triangle}{\boldsymbol{\varepsilon}}_\mathrm{v}+\frac{\partial\psi}{\partial\boldsymbol{\varepsilon}_\mathrm{e}}\cdot(\mathbf{L}_\mathrm{v}^\mathrm{T}\boldsymbol{\varepsilon}_\mathrm{e}+\boldsymbol{\varepsilon}_\mathrm{e}\mathbf{L}_\mathrm{v})\geq 0. \tag{4.97}$$

From this expression, we have a sufficient condition for the term of the overstress with the following definition

$$\check{\mathbf{S}}_\mathrm{ov}=\frac{\rho_\mathrm{R}}{\varphi_\Theta^2\varphi_a^2}\frac{\partial\psi}{\partial\boldsymbol{\varepsilon}_\mathrm{e}}. \tag{4.98}$$

With definition (4.98), the remaining term of Eq. (4.97) can be simplified to

$$\frac{\varphi_\Theta^2\varphi_a^2}{\rho_\mathrm{R}}\check{\mathbf{S}}_\mathrm{ov}\cdot\overset{\triangle}{\boldsymbol{\varepsilon}}_\mathrm{v}+\frac{\partial\psi}{\partial\boldsymbol{\varepsilon}_\mathrm{e}}\cdot(\mathbf{L}_\mathrm{v}^\mathrm{T}\boldsymbol{\varepsilon}_\mathrm{e}+\boldsymbol{\varepsilon}_\mathrm{e}\mathbf{L}_\mathrm{v})=\frac{\varphi_\Theta^2\varphi_a^2}{\rho_\mathrm{R}}\mathbf{C}_\mathrm{e}\check{\mathbf{S}}_\mathrm{ov}\cdot\overset{\triangle}{\boldsymbol{\varepsilon}}_\mathrm{v}, \tag{4.99}$$

with $\mathbf{C}_\mathrm{e}=\mathbf{F}_\mathrm{e}^\mathrm{T}\mathbf{F}_\mathrm{e}$, as well as making use of the symmetry of the tensor $\boldsymbol{\varepsilon}_\mathrm{e}=(\mathbf{C}_\mathrm{e}-\mathbf{I})/2$, the definition of $\overset{\triangle}{\boldsymbol{\varepsilon}}_\mathrm{v}=(\mathbf{L}_\mathrm{v}^\mathrm{T}+\mathbf{L}_\mathrm{v})/2$ and the isotropy of $\partial\psi/\partial\boldsymbol{\varepsilon}_\mathrm{e}$, see also (Hamkar, 2013, page 45). In this way, the following expression is obtained for the Maxwell-element:

$$\frac{\varphi_\Theta^2\varphi_a^2}{\rho_\mathrm{R}}\mathbf{C}_\mathrm{e}\check{\mathbf{S}}_\mathrm{ov}\cdot\overset{\triangle}{\boldsymbol{\varepsilon}}_\mathrm{v}\geq 0. \tag{4.100}$$

Plastic Element The terms of the Clausius-Duhem inequality related to the plastic element are given by

$$\frac{\varphi_\Theta^2\varphi_a^2}{\rho_\mathrm{R}}\mathbf{S}_\mathrm{Meq}^\mathrm{h}\cdot\overset{\triangle}{\boldsymbol{\Gamma}}_\mathrm{M}-\frac{\partial\psi}{\partial\tilde{\boldsymbol{\varepsilon}}_\mathrm{k}}\cdot\dot{\tilde{\boldsymbol{\varepsilon}}}_\mathrm{k}\geq 0. \tag{4.90}$$

The considerations made for this element are analogous to the Maxwell-element. The term $\mathbf{S}_\mathrm{Meq}^\mathrm{h}\cdot\overset{\triangle}{\boldsymbol{\Gamma}}_\mathrm{M}$ is expressed with quantities relative to the plastic intermediate configuration $\tilde{\boldsymbol{\chi}}_t$

$$\mathbf{S}_\mathrm{Meq}^\mathrm{h}\cdot\overset{\triangle}{\boldsymbol{\Gamma}}_\mathrm{M}=\tilde{\mathbf{S}}_\mathrm{eq}^\mathrm{h}\cdot\overset{\triangle}{\tilde{\boldsymbol{\varepsilon}}}_\mathrm{M}=\tilde{\mathbf{S}}_\mathrm{eq}^\mathrm{h}\cdot(\overset{\triangle}{\tilde{\boldsymbol{\varepsilon}}}_\mathrm{k}+\overset{\triangle}{\tilde{\boldsymbol{\varepsilon}}}_\mathrm{p}). \tag{4.101}$$

The Oldroyd derivative $\overset{\triangle}{\tilde{\boldsymbol{\varepsilon}}}_\mathrm{k}$ is equal to

$$\overset{\triangle}{\tilde{\boldsymbol{\varepsilon}}}_\mathrm{k}=\dot{\tilde{\boldsymbol{\varepsilon}}}_\mathrm{k}+\mathbf{L}_\mathrm{p}^\mathrm{T}\tilde{\boldsymbol{\varepsilon}}_\mathrm{k}+\tilde{\boldsymbol{\varepsilon}}_\mathrm{k}\mathbf{L}_\mathrm{p}, \tag{4.102}$$

see Fig. 4.5. Inserting Eq. (4.101) and (4.102) into Eq. (4.90) yields

$$\left(\frac{\varphi_\Theta^2\varphi_a^2}{\rho_\mathrm{R}}\tilde{\mathbf{S}}_\mathrm{eq}^\mathrm{h}-\frac{\partial\psi}{\partial\tilde{\boldsymbol{\varepsilon}}_\mathrm{k}}\right)\cdot\overset{\triangle}{\tilde{\boldsymbol{\varepsilon}}}_\mathrm{k}+\frac{\varphi_\Theta^2\varphi_a^2}{\rho_\mathrm{R}}\tilde{\mathbf{S}}_\mathrm{eq}^\mathrm{h}\cdot\overset{\triangle}{\tilde{\boldsymbol{\varepsilon}}}_\mathrm{p}+\frac{\partial\psi}{\partial\tilde{\boldsymbol{\varepsilon}}_\mathrm{k}}\cdot(\mathbf{L}_\mathrm{p}^\mathrm{T}\tilde{\boldsymbol{\varepsilon}}_\mathrm{k}+\tilde{\boldsymbol{\varepsilon}}_\mathrm{k}\mathbf{L}_\mathrm{p})\geq 0. \tag{4.103}$$

Here, a sufficient condition for the plastic stress part is obtained from

$$\tilde{\mathbf{S}}^{\mathrm{h}}_{\mathrm{eq}} = \frac{\rho_{\mathrm{R}}}{\varphi_{\Theta}^{2}\varphi_{a}^{2}} \frac{\partial \psi}{\partial \tilde{\varepsilon}_{\mathrm{k}}}. \tag{4.104}$$

With the definition (4.104), the term (4.103) can be simplified

$$\frac{\varphi_{\Theta}^{2}\varphi_{a}^{2}}{\rho_{\mathrm{R}}} \tilde{\mathbf{S}}^{\mathrm{h}}_{\mathrm{eq}} \cdot \overset{\triangle}{\tilde{\varepsilon}}_{\mathrm{p}} + \frac{\partial \psi}{\partial \tilde{\varepsilon}_{\mathrm{k}}} \cdot \left(\mathbf{L}_{\mathrm{p}}^{\mathrm{T}} \tilde{\varepsilon}_{\mathrm{k}} + \tilde{\varepsilon}_{\mathrm{k}} \mathbf{L}_{\mathrm{p}}\right) = \frac{\varphi_{\Theta}^{2}\varphi_{a}^{2}}{\rho_{\mathrm{R}}} \mathbf{C}_{\mathrm{k}} \tilde{\mathbf{S}}^{\mathrm{h}}_{\mathrm{eq}} \cdot \overset{\triangle}{\tilde{\varepsilon}}_{\mathrm{p}}, \tag{4.105}$$

with $\mathbf{C}_{\mathrm{k}} = \mathbf{F}_{\mathrm{k}}^{\mathrm{T}} \mathbf{F}_{\mathrm{k}}$, as well as using the symmetry of the tensor $\tilde{\varepsilon}_{\mathrm{k}} = (\mathbf{C}_{\mathrm{k}} - \mathbf{I})/2$, the definition of $\overset{\triangle}{\tilde{\varepsilon}}_{\mathrm{p}} = (\mathbf{L}_{\mathrm{p}}^{\mathrm{T}} + \mathbf{L}_{\mathrm{p}})/2$ and the isotropy of $\partial\psi/\partial\tilde{\varepsilon}_{\mathrm{k}}$. The term of the Clausius-Duhem inequality related to the plastic element is then

$$\frac{\varphi_{\Theta}^{2}\varphi_{a}^{2}}{\rho_{\mathrm{R}}} \mathbf{C}_{\mathrm{k}} \tilde{\mathbf{S}}^{\mathrm{h}}_{\mathrm{eq}} \cdot \overset{\triangle}{\tilde{\varepsilon}}_{\mathrm{p}} \geq 0. \tag{4.106}$$

Evaluation of the Clausius-Duhem Inequality Inserting expressions (4.100) and (4.106) into the Clausius-Duhem inequality (4.87) leads to

$$\begin{aligned} &\frac{\varphi_{\Theta}^{2}\varphi_{a}^{2}}{\rho_{\mathrm{R}}} \mathbf{C}_{\mathrm{k}} \tilde{\mathbf{S}}^{\mathrm{h}}_{\mathrm{eq}} \cdot \overset{\triangle}{\tilde{\varepsilon}}_{\mathrm{p}} + \frac{\varphi_{\Theta}^{2}\varphi_{a}^{2}}{\rho_{\mathrm{R}}} \mathbf{C}_{\mathrm{e}} \check{\mathbf{S}}_{\mathrm{ov}} \cdot \overset{\triangle}{\varepsilon}_{\mathrm{v}} - \frac{\partial \psi}{\partial k} \dot{k} \\ &+ \frac{1}{\rho_{\mathrm{R}}} \left(\varphi_{a} \varphi_{\Theta}^{2} \frac{\partial \varphi_{a}}{\partial a} (\operatorname{tr} \mathbf{S}_{\mathrm{M}}) - \rho_{\mathrm{R}} \frac{\partial \psi}{\partial a} \right) \dot{a} - \frac{1}{\rho_{\mathrm{R}} \Theta} \vec{q}_{R} \cdot \vec{g}_{R} \geq 0. \end{aligned} \tag{4.107}$$

Thus, the Clausius-Duhem inequality is fulfilled with the following relations

$$\overset{\triangle}{\tilde{\varepsilon}}_{\mathrm{p}} = \beta_{\mathbf{Y}} \dot{s}_{\mathrm{M}} \mathbf{C}_{\mathrm{k}} \tilde{\mathbf{S}}^{\mathrm{h}}_{\mathrm{eq}}, \qquad \beta_{\mathbf{Y}}, \dot{s}_{\mathrm{M}} > 0, \tag{4.108}$$

$$\overset{\triangle}{\varepsilon}_{\mathrm{v}} = \frac{1}{\hat{\eta}} \mathbf{C}_{\mathrm{e}} \check{\mathbf{S}}_{\mathrm{ov}}, \qquad \hat{\eta} > 0, \tag{4.109}$$

$$\dot{k} \geq 0, \qquad \frac{\partial \psi}{\partial k} \leq 0, \tag{4.110}$$

$$\dot{a} = \hat{\beta}_{a} \left(\varphi_{a} \varphi_{\Theta}^{2} \frac{\partial \varphi_{a}}{\partial a} (\operatorname{tr} \mathbf{S}_{\mathrm{M}}) - \rho_{\mathrm{R}} \frac{\partial \psi}{\partial a} \right), \qquad \hat{\beta}_{a} > 0, \tag{4.111}$$

$$\vec{q}_{R} = -\boldsymbol{\kappa}_{\Theta}^{\mathrm{R}} \operatorname{Grad} \Theta, \qquad \text{and} \qquad \vec{g}_{R} = \operatorname{Grad} \Theta. \tag{4.112}$$

In Eq. (4.112), the term $\boldsymbol{\kappa}_{\Theta}^{\mathrm{R}}$ represents the thermal conductivity tensor, which will be discussed in Section 4.4. It can be observed that Eqns. (4.108) and (4.109) fulfill the condition of plastic incompressibility (since $\det \bar{\mathbf{F}}_{\mathrm{p}} = 1$ and $\det \bar{\mathbf{F}}_{\mathrm{v}} = 1$), as can be seen considering the time derivatives

$$\frac{\mathrm{d}}{\mathrm{d}t}(\det \bar{\mathbf{F}}_{\mathrm{p}}) = (\det \bar{\mathbf{F}}_{\mathrm{p}})(\operatorname{tr} \mathbf{L}_{\mathrm{p}}) = (\det \bar{\mathbf{F}}_{\mathrm{p}})(\operatorname{tr} \mathbf{D}_{\mathrm{p}}) = 0 \rightarrow \operatorname{tr} \mathbf{D}_{\mathrm{p}} = \operatorname{tr} \overset{\triangle}{\tilde{\varepsilon}}_{\mathrm{p}} = 0, \tag{4.113}$$

$$\frac{\mathrm{d}}{\mathrm{d}t}(\det \bar{\mathbf{F}}_{\mathrm{v}}) = (\det \bar{\mathbf{F}}_{\mathrm{v}})(\operatorname{tr} \mathbf{L}_{\mathrm{v}}) = (\det \bar{\mathbf{F}}_{\mathrm{v}})(\operatorname{tr} \mathbf{D}_{\mathrm{v}}) = 0 \rightarrow \operatorname{tr} \mathbf{D}_{\mathrm{v}} = \operatorname{tr} \overset{\triangle}{\varepsilon}_{\mathrm{v}} = 0. \tag{4.114}$$

Moreover, the plastic element has the goal to represent a rate-independent process. To this end, the term $\overset{\triangle}{\tilde{\varepsilon}}_{\mathrm{p}}$ is defined proportional to the *isochoric*[2] rate of the mechanical arc-length $\dot{s}_{\mathrm{M}}$

$$\dot{s}_{\mathrm{M}} = \sqrt{\overset{\triangle}{\bar{\tilde{\varepsilon}}}_{\mathrm{M}} \cdot \overset{\triangle}{\bar{\tilde{\varepsilon}}}_{\mathrm{M}}}, \tag{4.115}$$

with $\tilde{\varepsilon}_{\mathrm{M}} = \frac{1}{2}(\mathbf{F}_{\mathrm{k}}^{\mathrm{T}}\mathbf{F}_{\mathrm{k}} - \bar{\mathbf{F}}_{\mathrm{p}}^{-\mathrm{T}}\bar{\mathbf{F}}_{\mathrm{p}}^{-1})$ the mechancial strain expressed with quantities of the intermediate configuration $\tilde{\boldsymbol{\chi}}_t$, and $\bar{\tilde{\varepsilon}}_{\mathrm{M}}$ as its isochoric part, see Fig. 4.5. The parameter $\beta_{\mathbf{Y}}$ from Eq. (4.108) is defined by

$$\beta_{\mathbf{Y}} = \frac{\hat{b}}{\mu_{\mathrm{eq}}(\Theta)}, \tag{4.116}$$

where $\hat{b}$ is a material parameter and $\mu_{\mathrm{eq}}(\Theta)$ a function of the temperature. In order to provide an overview of the obtained relations, a summary of the constitutive equations up to this point is given in Tab. 4.2. In the next sections, specific expressions for the free energy, the stresses, and the evolution equations are proposed. These expressions are based on the experimental observations and the previously presented model of small strains.

4.3.5 Free Energy and Stresses

At this point, expressions for the free energy are necessary. The functions are chosen trying to obtain an analogous behavior of the small strains model. The different components of the free energy from Eq. (4.82) are treated separately.

Spring Element An expression of near incompressibility is chosen for the elastic component $\psi_{\mathrm{eq}}^{\mathrm{e}}(\mathbf{E}_{\mathrm{M}})$, where the free energy is decomposed into a volumetric and an isochoric component

$$\rho_{\mathrm{R}}\psi_{\mathrm{eq}}^{\mathrm{e}}(\mathbf{E}_{\mathrm{M}}) = U(J_{\mathrm{M}}) + \bar{\omega}(\bar{\mathbf{C}}_{\mathrm{M}}). \tag{4.117}$$

The volume changing part of the energy function $U(J_{\mathrm{M}})$ depends on the determinant of the mechanical deformation gradient $J_{\mathrm{M}} = \det \mathbf{F}_{\mathrm{M}}$, and it is chosen according to (Hartmann and Neff, 2003) and (Hartmann, 2003) as

$$U(J_{\mathrm{M}}) = \frac{K}{50}(J_{\mathrm{M}}^{5} + J_{\mathrm{M}}^{-5} - 2). \tag{4.118}$$

---

[2] Only the isochoric component of the mechanical strain-rate $\overset{\triangle}{\tilde{\varepsilon}}_{\mathrm{M}}$ is considered for the function $\dot{s}_{\mathrm{M}}$ in order to avoid that purely volumetric processes influence the inelastic deformation.

Table 4.2: General constitutive model related to variables in intermediate configurations

Kinematic	
$\mathbf{F} = \mathbf{F}_a\mathbf{F}_\Theta\mathbf{F}_\mathrm{M} = \mathbf{F}_a\mathbf{F}_\Theta\mathbf{F}_\mathrm{k}\bar{\mathbf{F}}_\mathrm{p} = \mathbf{F}_a\mathbf{F}_\Theta\mathbf{F}_\mathrm{e}\bar{\mathbf{F}}_\mathrm{v}$	(4.48),(4.55),(4.56)
$\mathbf{F}_\Theta = \varphi_\Theta(\Theta)\mathbf{I}, \quad \mathbf{F}_a = \varphi_a(a)\mathbf{I}$	(4.49)
$\mathbf{E} = \mathbf{E}_a + \mathbf{E}_\Theta + \mathbf{E}_\mathrm{M}, \quad \mathbf{E}_\mathrm{M} = \mathbf{E}_\mathrm{k} + \mathbf{E}_\mathrm{p} = \mathbf{E}_\mathrm{e} + \mathbf{E}_\mathrm{v}$	(4.61),(4.63),(4.64)
Free energy	
$\psi = \psi^\mathrm{e}_\mathrm{eq}(\mathbf{E}_\mathrm{M}) + \psi^\mathrm{h}_\mathrm{eq}(\tilde{\boldsymbol{\varepsilon}}_\mathrm{k}, \Theta) + \psi_\mathrm{ov}(\boldsymbol{\varepsilon}_\mathrm{e}, k, \Theta) + \psi_\Theta(\Theta) + \psi_a(a)$	(4.82)
Entropy and heat flux	
$s = \dfrac{\varphi_\Theta\varphi_a^2}{\rho_\mathrm{R}}\dfrac{\partial\varphi_\Theta}{\partial\Theta}(\mathrm{tr}\,\mathbf{S}_\mathrm{M}) - \dfrac{\partial\psi}{\partial\Theta}$	(4.89)
$\vec{q}_R = -\boldsymbol{\kappa}^\mathrm{R}_\Theta \mathrm{Grad}\,\Theta$	(4.112)
Stress	
$\tilde{\mathbf{T}} = \tilde{\mathbf{T}}_\mathrm{eq} + \tilde{\mathbf{T}}_\mathrm{ov} = \tilde{\mathbf{T}}^\mathrm{e}_\mathrm{eq} + \tilde{\mathbf{T}}^\mathrm{h}_\mathrm{eq} + \tilde{\mathbf{T}}_\mathrm{ov}$	(4.69)
$\mathbf{S}^\mathrm{e}_\mathrm{Meq} = \dfrac{\rho_\mathrm{R}}{\varphi_\Theta^2\varphi_a^2}\mathbf{F}_\mathrm{M}\dfrac{\partial\psi}{\partial\mathbf{E}_\mathrm{M}}\mathbf{F}_\mathrm{M}^\mathrm{T}, \quad \tilde{\mathbf{T}}^\mathrm{e}_\mathrm{eq} = \mathbf{F}_\mathrm{M}^{-1}\mathbf{S}^\mathrm{e}_\mathrm{Meq}\mathbf{F}_\mathrm{M}^{-\mathrm{T}}$	(4.88)
$\tilde{\mathbf{S}}^\mathrm{h}_\mathrm{eq} = \dfrac{\rho_\mathrm{R}}{\varphi_\Theta^2\varphi_a^2}\dfrac{\partial\psi}{\partial\tilde{\boldsymbol{\varepsilon}}_\mathrm{k}}, \quad \tilde{\mathbf{T}}^\mathrm{h}_\mathrm{eq} = \bar{\mathbf{F}}_\mathrm{p}^{-1}\mathbf{S}^\mathrm{h}_\mathrm{Meq}\bar{\mathbf{F}}_\mathrm{p}^{-\mathrm{T}}$	(4.104)
$\check{\mathbf{S}}_\mathrm{ov} = \dfrac{\rho_\mathrm{R}}{\varphi_\Theta^2\varphi_a^2}\dfrac{\partial\psi}{\partial\boldsymbol{\varepsilon}_\mathrm{e}}, \quad \tilde{\mathbf{T}}_\mathrm{ov} = \bar{\mathbf{F}}_\mathrm{v}^{-1}\check{\mathbf{S}}_\mathrm{ov}\bar{\mathbf{F}}_\mathrm{v}^{-\mathrm{T}}$	(4.98)
Evolution equations	
$\overset{\triangle}{\tilde{\boldsymbol{\varepsilon}}}_\mathrm{p} = \beta_\mathbf{Y}\dot{s}_\mathrm{M}\mathbf{C}_\mathrm{k}\tilde{\mathbf{S}}^\mathrm{h}_\mathrm{eq}, \quad \dot{s}_\mathrm{M} = \sqrt{\overset{\triangle}{\bar{\tilde{\boldsymbol{\varepsilon}}}}_\mathrm{M} \cdot \overset{\triangle}{\bar{\tilde{\boldsymbol{\varepsilon}}}}_\mathrm{M}}$	(4.108),(4.115)
$\overset{\triangle}{\boldsymbol{\varepsilon}}_\mathrm{v} = \dfrac{1}{\hat{\eta}}\mathbf{C}_\mathrm{e}\check{\mathbf{S}}_\mathrm{ov}$	(4.109)
$\dot{k} > 0, \quad \partial\psi/\partial k < 0$	(4.110)
$\dot{a} = \hat{\beta}_a(\Theta, a)\left(\varphi_a\varphi_\Theta^2\dfrac{\partial\varphi_a}{\partial a}(\mathrm{tr}\,\mathbf{S}_\mathrm{M}) - \rho_\mathrm{R}\dfrac{\partial\psi}{\partial a}\right)$	(4.111)

This function fulfills the condition of convexity and provides a physical[3] material response. The isochoric component depends on the unimodular mechanical right Cauchy-Green tensor $\bar{\mathbf{C}}_\mathrm{M}$, which is equal to the total unimodular Cauchy-Green tensor $\bar{\mathbf{C}}_\mathrm{M} = \bar{\mathbf{C}}$, considering that the aging and the thermal part are purely volumetric. For this term, a Neo-Hooke ansatz is chosen

$$\bar{\omega}(\bar{\mathbf{C}}_\mathrm{M}) = c_{10}(I_{\bar{\mathbf{C}}_\mathrm{M}} - 3), \qquad \bar{\mathbf{C}}_\mathrm{M} = (\det \mathbf{C}_\mathrm{M})^{-1/3}\mathbf{C}_\mathrm{M}. \tag{4.119}$$

With this selection of the free energy $\psi^\mathrm{e}_\mathrm{eq}$, an expression for the elastic equilibrium stress part can be determined from Eq. (4.88)

$$\begin{aligned}\mathbf{S}^\mathrm{e}_\mathrm{Meq} &= \frac{\rho_\mathrm{R}}{\varphi_\Theta^2\varphi_a^2}\mathbf{F}_\mathrm{M}\frac{\partial\psi}{\partial\mathbf{E}_\mathrm{M}}\mathbf{F}_\mathrm{M}^\mathrm{T} = \frac{2\rho_\mathrm{R}}{\varphi_\Theta^2\varphi_a^2}\mathbf{F}_\mathrm{M}\frac{\partial\psi}{\partial\mathbf{C}_\mathrm{M}}\mathbf{F}_\mathrm{M}^\mathrm{T}\\ &= 2(\varphi_\Theta\varphi_a)^{-2}\mathbf{F}_\mathrm{M}\left(\frac{\mathrm{d}U}{\mathrm{d}\mathbf{C}_\mathrm{M}} + \frac{\mathrm{d}\omega(\bar{\mathbf{C}}_\mathrm{M})}{\mathrm{d}\mathbf{C}_\mathrm{M}}\right)\mathbf{F}_\mathrm{M}^\mathrm{T}. \end{aligned} \tag{4.120}$$

The partial derivatives of the free energy (4.117) are equal to

$$\frac{\mathrm{d}U(J_\mathrm{M})}{\mathrm{d}\mathbf{C}_\mathrm{M}} = \frac{K}{20}(J_\mathrm{M}^5 - J_\mathrm{M}^{-5})\mathbf{C}_\mathrm{M}^{-1}, \tag{4.121}$$

$$\frac{\mathrm{d}\omega(\bar{\mathbf{C}}_\mathrm{M})}{\mathrm{d}\mathbf{C}_\mathrm{M}} = c_{10}J_\mathrm{M}^{-2/3}\mathbf{C}_\mathrm{M}^{-1}\mathbf{C}_\mathrm{M}^\mathrm{D}, \tag{4.122}$$

see the appendix for a detailed derivation. Inserting Eqns. (4.121) and (4.122) into Eq. (4.120), one obtains

$$\mathbf{S}^\mathrm{e}_\mathrm{Meq} = 2(\varphi_\Theta\varphi_a)^{-2}\mathbf{F}_\mathrm{M}\left(\frac{K}{20}(J_\mathrm{M}^5 - J_\mathrm{M}^{-5})\mathbf{C}_\mathrm{M}^{-1} + c_{10}J_\mathrm{M}^{-2/3}\mathbf{C}_\mathrm{M}^{-1}\mathbf{C}_\mathrm{M}^\mathrm{D}\right)\mathbf{F}_\mathrm{M}^\mathrm{T} \tag{4.123}$$

$$= (\varphi_\Theta\varphi_a)^{-2}\frac{K}{10}(J_\mathrm{M}^5 - J_\mathrm{M}^{-5})\mathbf{I} + (\varphi_\Theta\varphi_a)^{-2}2c_{10}\bar{\mathbf{B}}_\mathrm{M}^\mathrm{D}. \tag{4.124}$$

The stress is pulled back into the reference configuration

$$\tilde{\mathbf{T}}^\mathrm{e}_\mathrm{eq} = \mathbf{F}_\mathrm{M}^{-1}\mathbf{S}^\mathrm{e}_\mathrm{Meq}\mathbf{F}_\mathrm{M}^{-\mathrm{T}} = (\varphi_\Theta\varphi_a)^{-2}\left(\frac{K}{10}(J_\mathrm{M}^5 - J_\mathrm{M}^{-5})\mathbf{C}_\mathrm{M}^{-1} + 2c_{10}J_\mathrm{M}^{-2/3}\mathbf{C}_\mathrm{M}^{-1}\mathbf{C}_\mathrm{M}^\mathrm{D}\right), \tag{4.125}$$

Making use of the relations

$$\mathbf{F}_\mathrm{M} = (\varphi_a\varphi_\Theta)^{-1}\mathbf{F}, \qquad J_\mathrm{M} = (\varphi_a\varphi_\Theta)^{-3}J, \qquad J = \det\mathbf{F} \tag{4.126}$$

$$\mathbf{C}_\mathrm{M} = \mathbf{F}_\mathrm{M}^\mathrm{T}\mathbf{F}_\mathrm{M} = (\varphi_a\varphi_\Theta)^{-2}\mathbf{C}, \qquad \mathbf{C}_\mathrm{M}^{-1} = \mathbf{F}_\mathrm{M}^{-1}\mathbf{F}_\mathrm{M}^{-\mathrm{T}} = (\varphi_a\varphi_\Theta)^{2}\mathbf{C}^{-1}, \tag{4.127}$$

---

[3] Physical in the sense of plausibility. The volumetric part of the free energy U has to fulfill several plausibility conditions, see (Hartmann, 2003, page 76), which is the case for the chosen function.

the elastic equilibrium stress part can be decomposed into two components

$$\tilde{\mathbf{T}}^{\mathrm{e}}_{\mathrm{vol}} = \frac{K}{10}\left(J_{\mathrm{M}}^{5} - J_{\mathrm{M}}^{-5}\right)\mathbf{C}^{-1}, \qquad J_{\mathrm{M}} = \frac{J}{(\varphi_a\varphi_\Theta)^3}, \tag{4.128}$$

$$\tilde{\mathbf{T}}^{\mathrm{e}}_{\mathrm{iso}} = 2c_{10}J^{-2/3}\mathbf{C}^{-1}\mathbf{C}^{\mathrm{D}}. \tag{4.129}$$

Both stress tensors are symmetric[4]. After a push-forward operation into the current configuration, $\mathbf{S}^{\mathrm{e}}_{\mathrm{vol}} = \mathbf{F}\tilde{\mathbf{T}}^{\mathrm{e}}_{\mathrm{vol}}\mathbf{F}^{\mathrm{T}}$ and $\mathbf{S}^{\mathrm{e}}_{\mathrm{iso}} = \mathbf{F}\tilde{\mathbf{T}}^{\mathrm{e}}_{\mathrm{iso}}\mathbf{F}^{\mathrm{T}}$, these two stress tensors correspond to a purely hydrostatic stress $\mathbf{S}^{\mathrm{e}}_{\mathrm{vol}}$ related to the volume-changing energy function $U(J_{\mathrm{M}})$, and a deviatoric stress $\mathbf{S}^{\mathrm{e}}_{\mathrm{iso}}$ related to the Neo-Hooke ansatz $\omega(\bar{\mathbf{C}}_{\mathrm{M}})$

$$\mathbf{S}^{\mathrm{e}}_{\mathrm{vol}} = \frac{K}{10}\left(J_{\mathrm{M}}^{5} - J_{\mathrm{M}}^{-5}\right)\mathbf{I}, \tag{4.130}$$

$$\mathbf{S}^{\mathrm{e}}_{\mathrm{iso}} = 2c_{10}\bar{\mathbf{B}}^{\mathrm{D}}_{\mathrm{M}}. \tag{4.131}$$

Plastic Element and Maxwell-Element The plastic element and the Maxwell element show similarities in their definition, see Eqns. (4.108) and (4.109). Both are able to reproduce a hysteretic behavior, with the difference that the Maxwell-element is rate-dependent. The rate-independence is included in the plastic element with definition (4.108) due to the proportionality of the strain-rate $\overset{\triangle}{\tilde{\boldsymbol{\varepsilon}}}_{\mathrm{p}}$ to the rate of the arc-length $\dot{s}_{\mathrm{M}}$. According to (Lion, 2000b) for the case of elastomers, the Maxwell element can be modeled with a Neo-Hooke ansatz

$$\bar{\psi}_{\mathrm{ov}}(\boldsymbol{\varepsilon}_{\mathrm{e}}) = \bar{\omega}_{\mathrm{ov}}(\bar{\mathbf{C}}_{\mathrm{e}}(\mathbf{C}_{\mathrm{e}})). \tag{4.132}$$

This ansatz is chosen with a small modification to include the softening in the case of the overstress and the temperature for the plastic element

$$\rho_{\mathrm{R}}\psi^{\mathrm{h}}_{\mathrm{eq}}(\tilde{\boldsymbol{\varepsilon}}_{\mathrm{k}},\Theta) = \mu_{\mathrm{eq}}(\Theta)(I_{\bar{\mathbf{C}}_{\mathrm{k}}} - 3), \qquad \bar{\mathbf{C}}_{\mathrm{k}} = (\det\mathbf{C}_{\mathrm{k}})^{-1/3}\mathbf{C}_{\mathrm{k}}, \tag{4.133}$$

$$\rho_{\mathrm{R}}\psi_{\mathrm{ov}}(\boldsymbol{\varepsilon}_{\mathrm{e}},k) = \mu_{\mathrm{ov}}(k)(I_{\bar{\mathbf{C}}_{\mathrm{e}}} - 3), \qquad \bar{\mathbf{C}}_{\mathrm{e}} = (\det\mathbf{C}_{\mathrm{e}})^{-1/3}\mathbf{C}_{\mathrm{e}}. \tag{4.134}$$

Expressions for the stresses $\tilde{\mathbf{S}}^{\mathrm{h}}_{\mathrm{eq}}$ and $\check{\mathbf{S}}_{\mathrm{ov}}$ can be computed considering Eqns. (4.98), (4.104), (4.133), and (4.134) in an analogous way to Eq. (4.122), obtaining

$$\tilde{\mathbf{S}}^{\mathrm{h}}_{\mathrm{eq}} = \frac{\rho_{\mathrm{R}}}{\varphi_\Theta^2\varphi_a^2}\frac{\partial\psi^{\mathrm{h}}_{\mathrm{eq}}}{\partial\tilde{\boldsymbol{\varepsilon}}_{\mathrm{k}}} = 2\mu_{\mathrm{eq}}(\varphi_\Theta\varphi_a)^{-2}\mathbf{C}_{\mathrm{k}}^{-1}\bar{\mathbf{C}}_{\mathrm{k}}^{\mathrm{D}}, \tag{4.135}$$

$$\check{\mathbf{S}}_{\mathrm{ov}} = \frac{\rho_{\mathrm{R}}}{\varphi_\Theta^2\varphi_a^2}\frac{\partial\psi_{\mathrm{ov}}}{\partial\boldsymbol{\varepsilon}_{\mathrm{e}}} = 2\mu_{\mathrm{ov}}(\varphi_\Theta\varphi_a)^{-2}\mathbf{C}_{\mathrm{e}}^{-1}\bar{\mathbf{C}}_{\mathrm{e}}^{\mathrm{D}}. \tag{4.136}$$

---

[4] Since the product $\mathbf{C}^{-1}\mathbf{C}^{\mathrm{D}}$ results in the sum of two symmetric tensors $\mathbf{C}^{-1}\mathbf{C}^{\mathrm{D}} = \mathbf{I} - (1/3)\mathrm{tr}\,(\mathbf{C})\mathbf{C}^{-1}$.

The plastic stress and the overstress can be expressed with the second Piola-Kirchhoff-type stress relative to the reference configuration with the help of a pull-back operation $\tilde{\mathbf{T}}^{\mathrm{h}}_{\mathrm{eq}} = \bar{\mathbf{F}}_{\mathrm{p}}^{-1}\mathbf{S}^{\mathrm{h}}_{\mathrm{Meq}}\bar{\mathbf{F}}_{\mathrm{p}}^{-\mathrm{T}}$ and $\tilde{\mathbf{T}}_{\mathrm{ov}} = \bar{\mathbf{F}}_{\mathrm{v}}^{-1}\check{\mathbf{S}}_{\mathrm{ov}}\bar{\mathbf{F}}_{\mathrm{v}}^{-\mathrm{T}}$, which leads to

$$\tilde{\mathbf{T}}^{\mathrm{h}}_{\mathrm{eq}} = 2\mu_{\mathrm{eq}}(\varphi_\Theta\varphi_a)^{-2}\bar{\mathbf{F}}_{\mathrm{p}}^{-1}\mathbf{C}_{\mathrm{k}}^{-1}\bar{\mathbf{C}}_{\mathrm{k}}^{\mathrm{D}}\bar{\mathbf{F}}_{\mathrm{p}}^{-\mathrm{T}} = 2\mu_{\mathrm{eq}}J^{-2/3}\mathbf{C}^{-1}(\mathbf{C}\bar{\mathbf{C}}_{\mathrm{p}}^{-1})^{\mathrm{D}}, \tag{4.137}$$

$$\tilde{\mathbf{T}}_{\mathrm{ov}} = 2\mu_{\mathrm{ov}}(\varphi_\Theta\varphi_a)^{-2}\bar{\mathbf{F}}_{\mathrm{v}}^{-1}\mathbf{C}_{\mathrm{e}}^{-1}\bar{\mathbf{C}}_{\mathrm{e}}^{\mathrm{D}}\bar{\mathbf{F}}_{\mathrm{v}}^{-\mathrm{T}} = 2\mu_{\mathrm{ov}}J^{-2/3}\mathbf{C}^{-1}(\mathbf{C}\bar{\mathbf{C}}_{\mathrm{v}}^{-1})^{\mathrm{D}}. \tag{4.138}$$

After a push-forward operation of Eq. (4.137) and Eq. (4.138) into the current configuration, $\mathbf{S}^{\mathrm{h}}_{\mathrm{eq}} = \mathbf{F}\tilde{\mathbf{T}}^{\mathrm{h}}_{\mathrm{eq}}\mathbf{F}^{\mathrm{T}}$ and $\mathbf{S}_{\mathrm{ov}} = \mathbf{F}\tilde{\mathbf{T}}_{\mathrm{ov}}\mathbf{F}^{\mathrm{T}}$, one can see that the plastic stress part $\mathbf{S}^{\mathrm{h}}_{\mathrm{eq}}$ and the overstress $\mathbf{S}_{\mathrm{ov}}$ in the current configuration are purely deviatoric

$$\mathbf{S}^{\mathrm{h}}_{\mathrm{eq}} = 2\mu_{\mathrm{eq}}\bar{\mathbf{B}}_{\mathrm{k}}^{\mathrm{D}}, \tag{4.139}$$

$$\mathbf{S}_{\mathrm{ov}} = 2\mu_{\mathrm{ov}}\bar{\mathbf{B}}_{\mathrm{e}}^{\mathrm{D}}, \tag{4.140}$$

which shows that $\mathbf{S}^{\mathrm{e}}_{\mathrm{vol}}$ is the only volumetric component of the stress in the current configuration. Moreover, $\mathbf{S}^{\mathrm{e}}_{\mathrm{vol}}$ is also the only component connected to elastic volumetric processes, see Eq. (4.130).

Aging Analogously to the small strains case, the aging component of the free energy ψ_a is defined with a linear relation by

$$\rho_{\mathrm{R}}\psi_a(a) = C_1 - C_2 a. \tag{4.141}$$

Here, C_1 and C_2 are material parameters. The last component of the free energy, which depends only on the temperature ψ_Θ, is discussed in Section 4.4.

4.3.6 Evolution Equations

In order to obtain evolution equations for the plastic $\tilde{\boldsymbol{\varepsilon}}_{\mathrm{p}}$ and the viscous strain $\boldsymbol{\varepsilon}_{\mathrm{v}}$, conditions (4.108) and (4.109) from the thermodynamical consistence are considered. The derived stresses from Eq. (4.135) and Eq. (4.136) are inserted into Eqns. (4.108) and (4.109), which leads to

$$\overset{\triangle}{\tilde{\boldsymbol{\varepsilon}}}_{\mathrm{p}} = 2\mu_{\mathrm{eq}}\beta_{\mathbf{Y}}(\varphi_\Theta\varphi_a)^{-2}\dot{s}_{\mathrm{M}}\bar{\mathbf{C}}_{\mathrm{k}}^{\mathrm{D}}, \tag{4.142}$$

$$\overset{\triangle}{\boldsymbol{\varepsilon}}_{\mathrm{v}} = \frac{2\mu_{\mathrm{ov}}}{\hat{\eta}}(\varphi_\Theta\varphi_a)^{-2}\bar{\mathbf{C}}_{\mathrm{e}}^{\mathrm{D}}. \tag{4.143}$$

In order to obtain equivalent evolution equations expressed with quantities relative to the reference configuration, a pull-back operation is performed considering the relations $\mathbf{F}_{\mathrm{M}} = \mathbf{F}_{\mathrm{e}}\bar{\mathbf{F}}_{\mathrm{v}} = \mathbf{F}_{\mathrm{k}}\bar{\mathbf{F}}_{\mathrm{p}}$ and $\bar{\mathbf{C}}_{\mathrm{M}} = \bar{\mathbf{C}} = J^{-2/3}\mathbf{C}$. This leads to

$$\dot{\mathbf{C}}_{\mathrm{p}} = 4(\varphi_a\varphi_\Theta)^{-2}J^{-2/3}\beta_{\mathbf{Y}}\mu_{\mathrm{eq}}\dot{s}_{\mathrm{M}}\bar{\mathbf{C}}_{\mathrm{p}}(\bar{\mathbf{C}}_{\mathrm{p}}^{-1}\mathbf{C})^{\mathrm{D}}, \tag{4.144}$$

$$\dot{\mathbf{C}}_{\mathrm{v}} = \frac{4\mu_{\mathrm{ov}}}{\hat{\eta}}(\varphi_a\varphi_\Theta)^{-2}J^{-2/3}\bar{\mathbf{C}}_{\mathrm{v}}(\bar{\mathbf{C}}_{\mathrm{v}}^{-1}\mathbf{C})^{\mathrm{D}}. \tag{4.145}$$

A more detailed calculation is offered in the appendix. Here, the tensors $\bar{\mathbf{C}}_{\mathrm{p}}(\bar{\mathbf{C}}_{\mathrm{p}}^{-1}\mathbf{C})^{\mathrm{D}}$ and $\bar{\mathbf{C}}_{\mathrm{v}}(\bar{\mathbf{C}}_{\mathrm{v}}^{-1}\mathbf{C})^{\mathrm{D}}$ are symmetric tensors, considering that they can be expressed as the sum of two symmetric tensors

$$\bar{\mathbf{C}}_{\mathrm{p}}(\bar{\mathbf{C}}_{\mathrm{p}}^{-1}\mathbf{C})^{\mathrm{D}} = \bar{\mathbf{C}}_{\mathrm{p}}(\bar{\mathbf{C}}_{\mathrm{p}}^{-1}\mathbf{C} - \frac{1}{3}\mathrm{tr}\,(\bar{\mathbf{C}}_{\mathrm{p}}^{-1}\mathbf{C})\mathbf{I}) = \mathbf{C} - \frac{1}{3}\mathrm{tr}\,(\bar{\mathbf{C}}_{\mathrm{p}}^{-1}\mathbf{C})\bar{\mathbf{C}}_{\mathrm{p}}, \tag{4.146}$$

$$\bar{\mathbf{C}}_{\mathrm{v}}(\bar{\mathbf{C}}_{\mathrm{v}}^{-1}\mathbf{C})^{\mathrm{D}} = \bar{\mathbf{C}}_{\mathrm{v}}(\bar{\mathbf{C}}_{\mathrm{v}}^{-1}\mathbf{C} - \frac{1}{3}\mathrm{tr}\,(\bar{\mathbf{C}}_{\mathrm{v}}^{-1}\mathbf{C})\mathbf{I}) = \mathbf{C} - \frac{1}{3}\mathrm{tr}\,(\bar{\mathbf{C}}_{\mathrm{v}}^{-1}\mathbf{C})\bar{\mathbf{C}}_{\mathrm{v}}. \tag{4.147}$$

The rate of the arc-length $\dot{s}_{\mathrm{M}}$ has to be determined in dependence of the variables of the reference configuration. It is a function of the isochoric mechanical strain-rate $\overset{\triangle}{\bar{\tilde{\boldsymbol{\varepsilon}}}}_{\mathrm{M}}$, which is equal to

$$\overset{\triangle}{\bar{\tilde{\boldsymbol{\varepsilon}}}}_{\mathrm{M}} = \bar{\mathbf{F}}_{\mathrm{p}}^{-\mathrm{T}}\dot{\bar{\mathbf{E}}}_{\mathrm{M}}\bar{\mathbf{F}}_{\mathrm{p}}^{-1}, \tag{4.148}$$

with the isochoric strain-rate depending on the right Cauchy-Green tensor

$$\dot{\bar{\mathbf{E}}}_{\mathrm{M}} = \frac{J^{-2/3}}{2}\mathbf{C}(\mathbf{C}^{-1}\dot{\mathbf{C}})^{\mathrm{D}}, \tag{4.149}$$

see also the appendix for a detailed derivation. With Eq. (4.149), the rate of the arc-length $\dot{s}_{\mathrm{M}}$ can be expressed by

$$\dot{s}_{\mathrm{M}} = \sqrt{\overset{\triangle}{\bar{\tilde{\boldsymbol{\varepsilon}}}}_{\mathrm{M}} \cdot \overset{\triangle}{\bar{\tilde{\boldsymbol{\varepsilon}}}}_{\mathrm{M}}} = \frac{J^{-2/3}}{2}\sqrt{\bar{\mathbf{C}}_{\mathrm{p}}^{-1}\mathbf{C}(\mathbf{C}^{-1}\dot{\mathbf{C}})^{\mathrm{D}}\bar{\mathbf{C}}_{\mathrm{p}}^{-1} \cdot \mathbf{C}(\mathbf{C}^{-1}\dot{\mathbf{C}})^{\mathrm{D}}}. \tag{4.150}$$

For the softening variable k, analogously to the small deformations case in Eq. (4.25), the following evolution equation is chosen

$$\dot{k} = \alpha_k(1-k)\dot{s}_{\mathrm{M}}. \tag{4.151}$$

The softening is a growing rate-independent variable with values between 0 and 1. Finally, an evolution equation for the aging variable a has to be found. From Eqns. (4.111) and (4.141), one obtains

$$\dot{a} = \hat{\beta}_a\left(C_2 + \varphi_a\varphi_\Theta^2\frac{\partial\varphi_a}{\partial a}(\mathrm{tr}\,\mathbf{S}_{\mathrm{M}})\right). \tag{4.152}$$

The discussion of this equation is done in an analogous way as Eq. (4.43). The aging rate is proportional to a parameter C_2 and a term depending on the trace of the stress $\mathbf{S}_{\mathrm{M}}$. The sign of $\mathrm{tr}\,\mathbf{S}_{\mathrm{M}}$ determines whether the aging process is accelerated or decelerated. A negative aging rate would correspond to a reversible aging process, which is physically unrealistic. Because of that, the term C_2 has to be larger than $\varphi_a\varphi_\Theta^2(\partial\varphi_a/\partial a)(\mathrm{tr}\,\mathbf{S}_{\mathrm{M}})$. Since it was not possible to characterize the influence of the stress experimentally, and since we are considering processes where the aging variable evolves in longer time scales than the mechanical processes, the parameter C_2 was chosen much larger than $\varphi_a \varphi_\Theta^2 (\partial \varphi_a / \partial a)(\operatorname{tr} \mathbf{S}_\mathrm{M})$, in an analogous way as in (Lion et al., 2014), which leads to

$$\dot{a} \approx C_2 \hat{\beta}_a. \tag{4.153}$$

The function $\hat{\beta}_a(\Theta, a)$ is chosen equal to

$$\hat{\beta}_a(\Theta, a) = \frac{\beta_{a1}(\Theta)}{C_2} \frac{1-a}{\beta_{a2}+a}, \qquad \beta_{a1}(\Theta) = \beta_{a11} \exp(-\beta_{a12}/\Theta). \tag{4.154}$$

leading to the following evolution equation for the aging variable

$$\dot{a} = \beta_{a1}(\Theta) \frac{1-a}{\beta_{a2}+a}. \tag{4.155}$$

4.3.7 Functions for the Material Parameters

The functions $\mu_\mathrm{eq}(\Theta)$, $\eta(\dot{\mathbf{C}}, \mathbf{C}, \Theta, \bar{\mathbf{C}}_\mathrm{p}, a)$, and $\mu_\mathrm{ov}(k)$ are defined similar to the small deformations case in Section 4.2.2. The parameter $\mu_\mathrm{eq}(\Theta)$ is connected to the initial slope of the plastic equilibrium stress. Linearizing Eq. (4.139) yields[5]

$$\mathbf{S}^\mathrm{h}_\mathrm{eq} \approx \mathbf{T}^\mathrm{h}_{\mathrm{eq}_\mathrm{L}} = 4\mu_\mathrm{eq} \mathbf{E}^\mathrm{D}_{\mathrm{k}_\mathrm{L}}, \tag{4.156}$$

where $\mathbf{T}^\mathrm{h}_{\mathrm{eq}_\mathrm{L}}$ is the linearized stress and $\mathbf{E}^\mathrm{D}_{\mathrm{k}_\mathrm{L}}$ the linearized strain. Comparing this expression to Eq. (4.32), it is clear that the strain variable $\mathbf{Y}$ is analogous to $\mathbf{E}^\mathrm{D}_{\mathrm{k}_\mathrm{L}}$. A more detailed analysis of the linearization of the finite strain model is provided in the appendix. The function $\mu_\mathrm{eq}(\Theta)$ is chosen analogously to the parameter $c(\Theta)$ in the small deformation model

$$\mu_\mathrm{eq}(\Theta) = \hat{c}_1(\hat{c}_2 - \tanh(\hat{c}_3(\Theta - \hat{\Theta}_c))). \tag{4.157}$$

The shear modulus of the overstress μ_ov is dependent on the softening variable k, and it resembles $G_\mathrm{ov}(k)$

$$\mu_\mathrm{ov}(k) = \hat{G}_0((1-k)^{\hat{n}_\mathrm{ov}} + \hat{\alpha}_\mathrm{ov}). \tag{4.158}$$

The parameter μ_ov represents the initial slope of the overstress. The viscosity is chosen in dependence of the right Cauchy-Green tensor $\mathbf{C}$, the plastic right Cauchy-Green tensor $\bar{\mathbf{C}}_\mathrm{p}$, the aging a, and the temperature Θ considering the dependencies of the variable $\dot{s}_\mathrm{M}(\dot{\mathbf{C}}, \mathbf{C}, \Theta, \bar{\mathbf{C}}_\mathrm{p}, a)$

$$\hat{\eta}(\dot{\mathbf{C}}, \mathbf{C}, \Theta, \bar{\mathbf{C}}_\mathrm{p}, a) = \hat{\eta}_0(\Theta, a) \left(\left(\frac{1}{s_\eta} \dot{s}_\mathrm{M}(\dot{\mathbf{C}}, \mathbf{C}, \Theta, \bar{\mathbf{C}}_\mathrm{p}, a) + \hat{\alpha}_\eta(\Theta) \right)^{-\hat{r}_\eta(\Theta)} + 1 \right), \tag{4.159}$$

---

[5] Considering that $\mathbf{C}^\mathrm{D} = 2\mathbf{E}^\mathrm{D}$ and that for small deformations $\varphi_a \approx \varphi_\Theta \approx 1$, $\mathbf{E} \approx \mathbf{E}_\mathrm{L}$ and $\mathbf{B} \approx \mathbf{C}$.

with the following temperature and aging-dependent functions

$$\hat{\eta}_0(\Theta, a) = (\hat{\eta}_{01} - \hat{\eta}_{02} \exp(\hat{\eta}_{03} a))(1 + \tanh(\hat{n}_\eta(\Theta - \hat{\Theta}_\eta))), \tag{4.160}$$

$$\hat{r}_\eta(\Theta) = \hat{r}_{\eta 1}(1 - \tanh(\hat{n}_\eta(\Theta - \hat{\Theta}_r))), \tag{4.161}$$

$$\hat{\alpha}_\eta(\Theta) = \hat{\alpha}_{\eta 1} \exp(\hat{\alpha}_{\eta 2}\Theta). \tag{4.162}$$

A summary of the finite deformations model is given in Tab. 4.3.

4.4 Heat Conduction Equation and Thermal Properties

This section starts off by deriving the heat conduction equation for the case of finite strains – followed by the small strains case. The heat conduction equation describes the temperature development of a material body during a thermal or thermo-mechanical loading process. It is derived from the local form of the balance of energy (2.69), in which the internal energy is expressed in dependence of the Helmholz free energy and specific entropy $e = \psi + s\Theta$

$$\dot{\psi} + s\dot{\Theta} + \Theta\dot{s} = -\frac{1}{\rho_\mathrm{R}} \operatorname{Div} \vec{q}_R + \frac{1}{\rho_\mathrm{R}} \tilde{\mathbf{T}} \cdot \dot{\mathbf{E}} + r. \tag{4.163}$$

The term $\delta = \tilde{\mathbf{T}} \cdot \dot{\mathbf{E}}/\rho_\mathrm{R} - \dot{\psi} - s\dot{\Theta}$ represents the internal inelastic dissipation, see Eq. (2.80), which can be abbreviated, leading to

$$\Theta\dot{s} = -\frac{1}{\rho_\mathrm{R}} \operatorname{Div} \vec{q}_R + \delta + r. \tag{4.164}$$

The time derivative of the entropy $\dot{s}$ is computed considering Eq. (4.89). Here, s shows a dependence on the variables $s = \hat{s}(\mathbf{E}_\mathrm{M}, \Theta, \tilde{\boldsymbol{\varepsilon}}_\mathrm{k}, a)$. Applying the chain rule, one obtains

$$\dot{s} = \frac{\partial s}{\partial \mathbf{E}_\mathrm{M}} \cdot \dot{\mathbf{E}}_\mathrm{M} + \frac{\partial s}{\partial \Theta}\dot{\Theta} + \frac{\partial s}{\partial \tilde{\boldsymbol{\varepsilon}}_\mathrm{k}} \cdot \dot{\tilde{\boldsymbol{\varepsilon}}}_\mathrm{k} + \frac{\partial s}{\partial a}\dot{a}. \tag{4.165}$$

Inserting Eq. (4.165) into Eq. (4.164) leads to

$$\Theta\frac{\partial s}{\partial \Theta}\dot{\Theta} = -\frac{1}{\rho_\mathrm{R}} \operatorname{Div} \vec{q}_R + \delta + r - \Theta\left(\frac{\partial s}{\partial \mathbf{E}_\mathrm{M}} \cdot \dot{\mathbf{E}}_\mathrm{M} + \frac{\partial s}{\partial \tilde{\boldsymbol{\varepsilon}}_\mathrm{k}} \cdot \dot{\tilde{\boldsymbol{\varepsilon}}}_\mathrm{k} + \frac{\partial s}{\partial a}\dot{a}\right). \tag{4.166}$$

The heat production due to internal dissipation ω is obtained by summarizing the terms $\delta - \Theta\dot{s}$, and it is equal to

$$\omega = \delta - \Theta\left(\frac{\partial s}{\partial \mathbf{E}_\mathrm{M}} \cdot \dot{\mathbf{E}}_\mathrm{M} + \frac{\partial s}{\partial \tilde{\boldsymbol{\varepsilon}}_\mathrm{k}} \cdot \dot{\tilde{\boldsymbol{\varepsilon}}}_\mathrm{k} + \frac{\partial s}{\partial a}\dot{a}\right). \tag{4.167}$$

Table 4.3: Summary of the constitutive model

Stress in the reference configuration	
$\tilde{\mathbf{T}} = \tilde{\mathbf{T}}_{\text{eq}} + \tilde{\mathbf{T}}_{\text{ov}} = \tilde{\mathbf{T}}^{\text{e}}_{\text{eq}} + \tilde{\mathbf{T}}^{\text{h}}_{\text{eq}} + \tilde{\mathbf{T}}_{\text{ov}}$	(4.69)
$\tilde{\mathbf{T}}^{\text{e}}_{\text{eq}} = \frac{K}{10}\left(J_{\text{M}}^{5} - J_{\text{M}}^{-5}\right)\mathbf{C}^{-1} + 2c_{10}J^{-2/3}\mathbf{C}^{-1}\mathbf{C}^{\text{D}}$, $J_{\text{M}} = (\varphi_a\varphi_\Theta)^{-3}J$	(4.128),(4.129)
$\tilde{\mathbf{T}}^{\text{h}}_{\text{eq}} = 2\mu_{\text{eq}}J^{-2/3}\mathbf{C}^{-1}(\mathbf{C}\bar{\mathbf{C}}_{\text{p}}^{-1})^{\text{D}}$	(4.137)
$\tilde{\mathbf{T}}_{\text{ov}} = 2\mu_{\text{ov}}J^{-2/3}\mathbf{C}^{-1}(\mathbf{C}\bar{\mathbf{C}}_{\text{v}}^{-1})^{\text{D}}$	(4.138)
Stress in the current configuration	
$\mathbf{S} = \mathbf{S}^{\text{e}}_{\text{vol}} + \mathbf{S}^{\text{e}}_{\text{iso}} + \mathbf{S}^{\text{h}}_{\text{eq}} + \mathbf{S}_{\text{ov}}$	
$\mathbf{S}^{\text{e}}_{\text{vol}} = \frac{K}{10}\left(J_{\text{M}}^{5} - J_{\text{M}}^{-5}\right)\mathbf{I}$, $\mathbf{S}^{\text{e}}_{\text{iso}} = 2c_{10}\bar{\mathbf{B}}^{\text{D}}_{\text{M}}$	(4.130),(4.131)
$\mathbf{S}^{\text{h}}_{\text{eq}} = 2\mu_{\text{eq}}\bar{\mathbf{B}}^{\text{D}}_{\text{k}}$	(4.139)
$\mathbf{S}_{\text{ov}} = 2\mu_{\text{ov}}\bar{\mathbf{B}}^{\text{D}}_{\text{e}}$	(4.140)
Evolution equations in the reference configuration	
$\dot{s}_{\text{M}} = J^{-2/3}/2\sqrt{\bar{\mathbf{C}}_{\text{p}}^{-1}\mathbf{C}(\mathbf{C}^{-1}\dot{\mathbf{C}})^{\text{D}}\bar{\mathbf{C}}_{\text{p}}^{-1} \cdot \mathbf{C}(\mathbf{C}^{-1}\dot{\mathbf{C}})^{\text{D}}}$	(4.150)
$\dot{a} = \beta_{a1}(\Theta)\frac{1-a}{\beta_{a2}+a}$	(4.155)
$\dot{k} = \alpha_k(1-k)\dot{s}_{\text{M}}$	(4.151)
$\dot{\mathbf{C}}_{\text{p}} = 4(\varphi_a\varphi_\Theta)^{-2}J^{-2/3}\,\hat{b}\,\dot{s}_{\text{M}}\bar{\mathbf{C}}_{\text{p}}(\bar{\mathbf{C}}_{\text{p}}^{-1}\mathbf{C})^{\text{D}}$	(4.146)
$\dot{\mathbf{C}}_{\text{v}} = \frac{4\mu_{\text{ov}}}{\hat{\eta}}(\varphi_a\varphi_\Theta)^{-2}J^{-2/3}\bar{\mathbf{C}}_{\text{v}}(\bar{\mathbf{C}}_{\text{v}}^{-1}\mathbf{C})^{\text{D}}$	(4.147)
Temperature, softening and aging-dependent functions	
$\beta_{a1}(\Theta) = \beta_{a11}\exp(-\beta_{a12}/\Theta)$	(4.154)
$\mu_{\text{eq}}(\Theta) = \hat{c}_1(\hat{c}_2 - \tanh(\hat{c}_3(\Theta - \hat{\Theta}_c)))$	(4.157)
$\mu_{\text{ov}}(k) = \hat{G}_0((1-k)^{\hat{n}_{\text{ov}}} + \hat{\alpha}_{\text{ov}})$	(4.158)
$\hat{\eta}(\dot{\mathbf{C}}, \mathbf{C}, \Theta, \bar{\mathbf{C}}_{\text{p}}, a) = \hat{\eta}_0(\Theta, a)\left(\left(\frac{\dot{s}_{\text{M}}}{s_\eta} + \hat{\alpha}_\eta(\Theta)\right)^{-\hat{r}_\eta(\Theta)} + 1\right)$	(4.159)
$\hat{\eta}_0(\Theta, a) = (\hat{\eta}_{01} - \hat{\eta}_{02}\exp(\hat{\eta}_{03}a))(1 + \tanh(\hat{n}_\eta(\Theta - \hat{\Theta}_\eta)))$	(4.160)
$\hat{\alpha}_\eta(\Theta) = \hat{\alpha}_{\eta1}\exp(\hat{\alpha}_{\eta2}\Theta)$, $\hat{r}_\eta(\Theta) = \hat{r}_{\eta1}(1 - \tanh(\hat{n}_\eta(\Theta - \hat{\Theta}_r)))$	(4.161),(4.162)

With the definition of the heat capacity at a constant deformation from (Haupt, 2002)

$$c_{\mathrm{p}} = \Theta \frac{\partial s}{\partial \Theta}, \tag{4.168}$$

the heat conduction equation can be written as

$$c_{\mathrm{p}} \dot{\Theta} = -\frac{1}{\rho_{\mathrm{R}}} \mathrm{Div}\, \vec{q}_R + \omega + r. \tag{4.169}$$

The variable r represents a volumetric heat source, which does not appear in the present application. Thus, it will be neglected. A common approach for the specific heat capacity, see Jansohn (1997); Quint (2012); Hamkar (2013); Rothe (2015), is

$$c_{\mathrm{p}} \approx \Theta \frac{\partial^2 \psi_\Theta}{\partial \Theta^2}. \tag{4.170}$$

Since the experimental results in Section 3.7.3 show a linear behavior of the specific heat capacity in the application range of the alloy, the following expression proposed by (Heimes, 2005) is chosen for the thermal part of the free energy ψ_Θ

$$\rho_{\mathrm{R}} \psi_\Theta(\Theta) = c_{\mathrm{p1}} \left((\Theta - \Theta_0) - \Theta \ln \frac{\Theta}{\Theta_0} (1 - c_{\mathrm{p2}} \Theta) - \frac{1}{2} (\Theta^2 - \Theta_0^2) \right). \tag{4.171}$$

Moreover, a constitutive equation for the heat flux has to be found. Fourier's law provides an expression for the heat flux in the current configuration

$$\vec{q} = -\kappa_\Theta \mathrm{grad}\, \Theta. \tag{4.172}$$

Using the relation between the heat flux in the reference $\vec{q}_R$ and the current configuration $\vec{q}$ from Eq. (2.43), as well as the property $\mathrm{grad}\, \Theta = \mathbf{F}^{-\mathrm{T}} \mathrm{Grad}\, \Theta$, leads to

$$\vec{q}_R = -\boldsymbol{\kappa}_\Theta^{\mathrm{R}} \mathrm{Grad}\, \Theta = -\kappa_\Theta (\det \mathbf{F}) \mathbf{C}^{-1} \mathrm{Grad}\, \Theta. \tag{4.173}$$

The second order tensor $\boldsymbol{\kappa}_\Theta^{\mathrm{R}}$ represents the thermal conductivity of the material. From Eq. (4.173), a relation can be obtained for the thermal conductivity in the current configuration κ_Θ and the thermal conductivity tensor

$$\boldsymbol{\kappa}_\Theta^{\mathrm{R}} = \kappa_\Theta (\det \mathbf{F}) \mathbf{C}^{-1}. \tag{4.174}$$

For positive values of κ_Θ, the tensor $\boldsymbol{\kappa}_\Theta^{\mathrm{R}}$ is positive definite.

The heat conduction equation for the small deformations case can be obtained by linearizing Eq. (4.169)

$$c_{\mathrm{p}} \dot{\Theta} = -\frac{1}{\rho} \mathrm{div}\, \vec{q} + \omega_{\mathrm{L}} + r. \tag{4.175}$$

Here, the approximation for specific heat capacity in Eq. (4.170) is assumed, and the component ψ_Θ for the small strains model is chosen equal to Eq. (4.171). For the small strains model, the production term due to internal dissipation is

$$\omega_{\mathrm{L}} = \frac{1}{\rho} \mathbf{T} \cdot \dot{\mathbf{E}} - \dot{\psi}_{\mathrm{L}} - \dot{\Theta} s_{\mathrm{L}} - \Theta \left(\frac{\partial s_{\mathrm{L}}}{\partial \mathbf{E}_{\mathrm{M}}} \cdot \dot{\mathbf{E}}_{\mathrm{M}} + \frac{\partial s_{\mathrm{L}}}{\partial \mathbf{Y}} \cdot \dot{\mathbf{Y}} + \frac{\partial s_{\mathrm{L}}}{\partial a} \dot{a} \right), \tag{4.176}$$

with ψ_{L} being the free energy defined in Section 4.2.1 and s_{L} the entropy from Eq. (4.11).

Modeling of the Thermo-Physical Properties

In the last step of modeling, it is necessary to find expressions for the thermo-physical properties – the specific heat capacity c_p and thermal conductivity κ_Θ. To this end, the experimental information of Section 3.7 is taken into account. The linear thermal expansion α_Θ was already defined in Eqns. (4.2) and (4.50), with the selection of the thermal deformation $\mathbf{E}_\Theta$ in the small strains model and the thermal part of the deformation gradient $\mathbf{F}_\Theta$ in the finite deformations model.

Specific Heat Capacity

Due to the thermodynamical consistence (4.170), there is a relationship between the specific heat capacity and the free energy. With Eq. (4.171), a linear behavior over the temperature for the specific heat c_p is obtained

$$c_\mathrm{p}(\Theta) = c_\mathrm{p1}(1 + c_\mathrm{p2}(\Theta - \Theta_0)). \tag{4.177}$$

The terms c_p1 and c_p2 are material parameters, and Θ_0 is the reference temperature.

Thermal Diffusivity

Having a look at the experimental results from Section 3.7.2, it can be seen that the thermal diffusivity depends on the temperature and the aging variable. In order to model this behavior, a weighting between the initial unaged stage $\hat{\lambda}_0(\Theta)$ and the final stage $\hat{\lambda}_\infty(\Theta)$ is carried out with the help of $f_{\hat{\lambda}}(\Theta, a)$

$$\hat{\lambda}(\Theta, a) = \hat{\lambda}_\infty(\Theta) f_{\hat{\lambda}}(\Theta, a) + \hat{\lambda}_0(\Theta)(1 - f_{\hat{\lambda}}(\Theta, a)). \tag{4.178}$$

From Fig. 3.27(b), a linear behavior over the temperature is observed for the completely aged stage

$$\hat{\lambda}_\infty(\Theta) = \hat{\lambda}_{\infty 1} - \hat{\lambda}_{\infty 2}\Theta. \tag{4.179}$$

The initial stage shows a constant behavior up to the temperature of $\Theta_0 = 293.15\,\mathrm{K}$. After that, an approximately linear reduction is observed. In order to model this behavior, the following function is chosen

$$\hat{\lambda}_0(\Theta) = \hat{\lambda}_{01} - \hat{\lambda}_{02}(1 + \tanh(\Theta - \Theta_0))(\Theta - \Theta_0). \tag{4.180}$$

The weighting factor $f_{\hat{\lambda}}$ from Eq. (4.178) is a function of the aging and temperature, which have a growing behavior with the aging. It only can obtain values between 0 and 1, where 0 corresponds to the unaged state and and 1 to the completely aged state

$$f_{\hat{\lambda}}(\Theta, a) = a - \alpha_{\hat{\lambda}}(\Theta)(1 - a)a^2, \quad \alpha_{\hat{\lambda}}(\Theta) = \alpha_{\hat{\lambda}1} \exp(-\alpha_{\hat{\lambda}2}\Theta). \tag{4.181}$$

The selection of this expression is justified in the identification step, see Section 5.7.

Thermal Conductivity

The thermal conductivity can be obtained from the relation

$$\kappa_\Theta(\Theta, a) = \rho\hat{\lambda}(\Theta, a)c_\mathrm{p}(\Theta). \tag{4.182}$$

With the proposed expressions for the thermal diffusivity and the specific heat capacity, the thermal conductivity is equal to

$$\kappa_\Theta(\Theta, a) = \rho c_\mathrm{p1}(1 + c_\mathrm{p2}(\Theta - \Theta_0))(\hat{\lambda}_\infty(\Theta)f_{\hat{\lambda}}(\Theta, a) + \hat{\lambda}_0(\Theta)(1 - f_{\hat{\lambda}}(\Theta, a))), \tag{4.183}$$

with the functions $\hat{\lambda}_\infty$, $\hat{\lambda}_0$ and $f_{\hat{\lambda}}$ from Eqns. (4.179)-(4.181).

5 Parameter Identification

The parameter identification problem, also known as inverse problem, is one of the core tasks of material modeling in Continuum Mechanics. In contrast to the direct problem – where, given a specific material model and the corresponding parameters, the response of the model is of interest – the goal of parameter identification is to find suitable material parameters to calibrate the model to the experiments with a minimum error. To this end, the problem is derived into an optimization problem, in which a quadratic error function between model and experiment is minimized. With regard to the theoretical concepts addressed in this chapter, it is necessary to mention the works of Beck and Arnold (1977), Draper and Smith (1998), Mahnken (1998) and Tarantola (2005) and the literature cited therein. As explained in (Mahnken, 1998; Tarantola, 2005), there are several optimization methods that are commonly used in the scope of parameter identification. On one side, there are the gradient-based algorithms such as the Levenberg-Marquardt, Gauss-Newton, or Quasi-Newton method, see, for example (Coleman and Li, 1996; Levenberg, 1944; Marquardt, 1963) – and on the other side, there are the stochastic none gradient-based methods such as Monte Carlo or genetic algorithms. The aforementioned stochastic methods are robust methods which have a low dependence on the initial values, but are very time-consuming. On the other hand, gradient-based algorithms have the advantage of being able to converge quickly in the vicinity of the solution, but they are influenced strongly by the initial values, see (Chaparro et al., 2008).

In the identification task, there are several difficulties which have to be considered, see (Gilbert et al., 2016; Hartmann and Gilbert, 2018). First, from the experimental side, it is necessary to count with the right amount of experimental data with the necessary quality (for example, with moderate noise or dispersion). Moreover, inaccurate computations can cause numerical problems, and, finally, it is often not possible to determine the material parameters in a unique manner based on measurements. In addition to these remarks, the assumptions made during the treatment of the experimental data have to be considered as well. If it is possible to generate a homogeneous stress state experimentally, and if the model can be reduced to the one-dimensional case, the identification can be performed for a scalar equation, see for example (Beck and Arnold, 1977; Krämer et al., 2015). If this is not possible, the whole boundary-value problem has to be solved in order to consider the inhomogeneity in the identification procedure – as discussed in (Mahnken and Stein, 1996, 1997; Mahnken, 2000; Hartmann et al., 2001, 2003, 2018; Johlitz and Diebels, 2011a), for example, and in (Hartmann et al., 2006; Chen and Diebels, 2012b,a, 2014, 2015) for the identification using indentation tests.

In this chapter, the constitutive model developed in Chapter 4 is calibrated to the experimental results of Chapter 3. At first, a short review of the general concepts of parameter identification is offered, and the procedure applied in this work is described. After that, the parameter identification for the small deformation case is adressed. At this point, some of the temperature- and aging-dependent relations are developed and justified. Moreover, based on the solution of the small deformation case, a re-identification with the finite strain model is carried out. After that, both cases are compared and discussed. In the last step, the identification of the thermo-physical properties is carried out.

5.1 Basic Concepts of Parameter Identification

As mentioned before, the goal of parameter identification is to find the material parameters that fit the experimental data with the minimum error. This error is defined with the help of the residuum function $\mathbf{r}(\boldsymbol{\kappa}) = \mathbf{s}(\boldsymbol{\kappa}) - \mathbf{d}$ as the difference between the model (simulation) data $\mathbf{s} \in \mathbb{R}^{n_d}$ and the experimental data $\mathbf{d} \in \mathbb{R}^{n_d}$, which can be expressed by

$$\mathbf{s} = \left\{ \begin{matrix} \mathbf{s}^1 \\ \vdots \\ \mathbf{s}^{n_{\text{exp}}} \end{matrix} \right\}, \qquad \mathbf{d} = \left\{ \begin{matrix} \mathbf{d}^1 \\ \vdots \\ \mathbf{d}^{n_{\text{exp}}} \end{matrix} \right\}, \tag{5.1}$$

where $\mathbf{s}^k$ and $\mathbf{d}^k$ correspond to the k-th simulation and experiment, with n_{exp} being the number of experiments and n_d the total number of points used in the identification, taking all experimental points over time into account. The residuum $\mathbf{r}$ is represented for one experiment in Fig. 5.1. The material parameters are assembled in a vector $\boldsymbol{\kappa} \in \mathbb{R}^{n_\kappa}$ with n_κ material parameters. The parameter identification procedure entails to find the

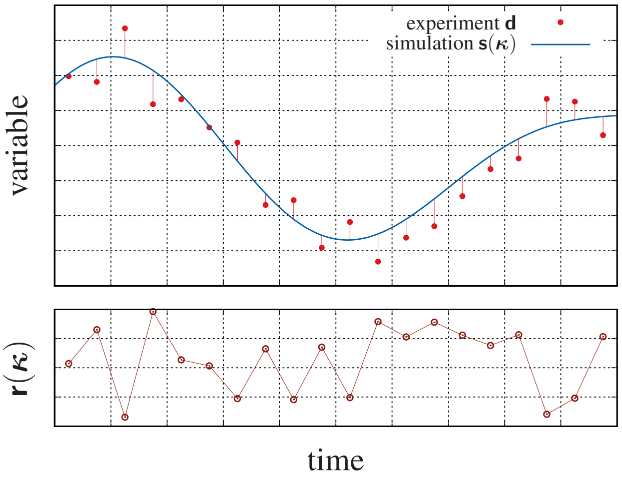

Figure 5.1: Identification problem: fit and experimental data

minimum of the objective function $f(\boldsymbol{\kappa})$

$$\min_{\boldsymbol{\kappa}} f(\boldsymbol{\kappa}) = \min_{\boldsymbol{\kappa}} \frac{1}{2}||\mathbf{r}(\boldsymbol{\kappa})||_2^2 = \min_{\boldsymbol{\kappa}} \frac{1}{2}\mathbf{r}^{\mathrm{T}}(\boldsymbol{\kappa})\mathbf{r}(\boldsymbol{\kappa}). \tag{5.2}$$

In order to obtain a minimum, the following condition has to be fulfilled

$$\mathrm{grad}_{\boldsymbol{\kappa}} f(\boldsymbol{\kappa}) = \mathbf{J}^{\mathrm{T}}(\boldsymbol{\kappa}^*)\mathbf{r}(\boldsymbol{\kappa}^*) \overset{!}{=} \mathbf{0}, \tag{5.3}$$

see Dennis and Schnabel (1996). The variable $\mathbf{J}(\boldsymbol{\kappa}) = \mathrm{d}\mathbf{s}(\boldsymbol{\kappa})/\mathrm{d}\boldsymbol{\kappa}$ represents the Jacobian. Additionally, there might be n_c inequality constraints $g_i(\boldsymbol{\kappa}) \leq 0$, which have to be fulfilled for theoretical reasons, physical reasons (positiveness of parameters), or to restrict their co-domain in a certain range. In the following sections, $\mathbf{s}$ can be an analytical model or the result of the numerical (or analytical) solution of an ordinary differential equation or of an entire boundary-value problem using finite elements.

The optimization method follows the procedure shown in Fig. 5.2. When using gradient based algorithms, it is necessary to choose a vector $\boldsymbol{\kappa}_0$ as an initial guess. Then, the answer of the model with this initial guess is computed and compared with the experimental data building the residuum $\mathbf{r}(\boldsymbol{\kappa}_0)$. After applying an optimization step – providing that the objective function $f(\boldsymbol{\kappa})$ and the increment in the parameters $\Delta\boldsymbol{\kappa}$ fulfill the given termination criteria – the current solution is accepted as the final solution $\boldsymbol{\kappa}^*$. If this is not the case, the iterative process is repeated with a new set of parameters $\boldsymbol{\kappa}_{k+1} = \boldsymbol{\kappa}_k + \Delta\boldsymbol{\kappa}_k$ until the convergence criteria are fulfilled or the maximal number of iterations n_{max} is carried out. This last option leads to an unsatisfactory result.

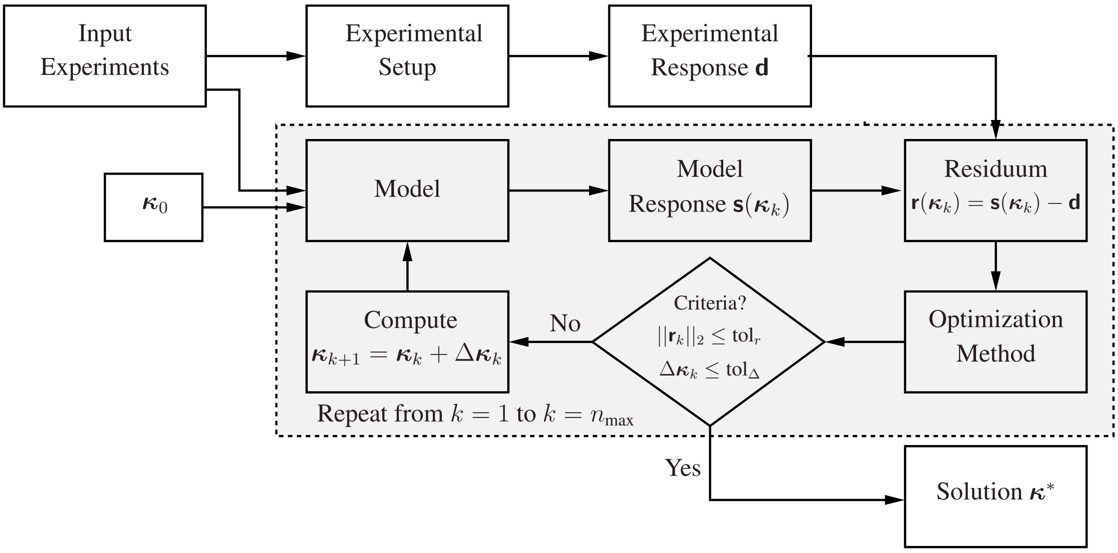

Figure 5.2: Representation of the identification procedure

Parameters of the optimization quality

It is of interest to have a measure of the quality of the identification results. Also, it is known that, given a set of experimental data, the identified parameters are dependent on each other in a specific manner, depending on the selected material model. In order to evaluate the goodness of a fit, the commonly applied quantities are the confidence interval $\boldsymbol{\kappa}^{\text{conf}}$, the correlation matrix $\mathbf{R}$, and the coefficient of determination R^2. Here, the works of Draper and Smith (1998), Kreißig et al. (2001), and Sachs and Hedderich (2012) are considered. In order to motivate these quantities, the residuum is first linearized at the point of the identified parameters $\boldsymbol{\kappa}^*$

$$\mathbf{r}(\boldsymbol{\kappa}) = \mathbf{r}(\boldsymbol{\kappa}^*) + \mathbf{J}(\boldsymbol{\kappa}^*)(\boldsymbol{\kappa} - \boldsymbol{\kappa}^*), \tag{5.4}$$

with $\mathbf{J} = \partial \mathbf{r}(\boldsymbol{\kappa})/\partial \boldsymbol{\kappa} \in \mathbb{R}^{n_d \times n_\kappa}$ the Jacobian. With the help of the Jacobian and the variance σ^2, the covariance matrix can be approximated by

$$\mathbf{P} \approx \sigma^2 [\mathbf{J}^{\mathrm{T}}(\boldsymbol{\kappa}^*)\mathbf{J}(\boldsymbol{\kappa}^*)]^{-1}, \quad \sigma^2 = \frac{\mathbf{r}^{\mathrm{T}}(\boldsymbol{\kappa})\mathbf{r}(\boldsymbol{\kappa})}{n_d - 1}. \tag{5.5}$$

Correlation matrix With the components of the covariance matrix P_{ij}, the correlation matrix can be determined through

$$\mathbf{R} = [r_{ij}] = \left[\frac{P_{ij}}{\sqrt{P_{ii} P_{jj}}} \right]. \tag{5.6}$$

The components of its diagonal r_{ii} are all equal to one. The off-diagonal elements r_{ij}, also known as correlation coefficients, represent the dependence between the two parameters κ_i and κ_j. They can have values between -1 and 1, where 1 represents a total correlation, -1 an inverse total correlation, and 0 no correlation at all. The correlation coefficient provides a measure of how sensitive the change in one parameter affects the other one. Nevertheless, a value close to 1 or -1 for the correlation coefficients can have different origins apart from the modeling choice, for example the lack of experimental information for a unique identification – or that the parameters are expressed as a linear combination and a unique identification is not possible, see Beck and Arnold (1977).

Confidence interval From the diagonal components of the covariance matrix, the confidence interval can be calculated by

$$\boldsymbol{\kappa}^{\text{conf}} = \boldsymbol{\kappa}^* \pm \Delta\boldsymbol{\kappa}^*, \quad \Delta\kappa_i^* = \sqrt{P_{ii}}, \quad i = 1, ..., n_\kappa. \tag{5.7}$$

This measure gives an interval of values, in which the real identified parameter is localized with a certain probability.

Coefficient of determination Commonly, the coefficient of determination is used to describe how well a model fits the experimental data. It is defined by

$$R^2 = 1 - \frac{\displaystyle\sum_{i=1}^{n_d}(d_i - s_i)^2}{\displaystyle\sum_{i=1}^{n_d}(d_i - \bar{d})^2}, \qquad \bar{d} = \frac{1}{n_d}\sum_{i=1}^{n_d} d_i. \tag{5.8}$$

If it reaches the value 1, the model fits the experimental data perfectly. The coefficient of determination compares the fit of the model with the one made by a horizontal straight line with the value $\bar{d}$, meaning the average of all experimental values. However, this parameter presents some disadvantages[1] in the case of the identification of parameters using several sets of experiments. This is why the confidence interval and the correlation matrix are preferred in this thesis, to provide an indicator of the quality of the identification.

5.2 Identification Procedure

The constitutive models summarized in Tab. 4.1 for the small deformations case, and in Tab. 4.3 for the large deformations case, contains 24 material parameter that have to be determined. Moreover, for the thermo-physical properties, 11 parameters have to be found. Since the identification problem is an ill-posed problem, a simultaneous identification of all material parameters would lead to a strong correlation between the parameters and eventually to a local minimum, since no initial values are known. In order to solve this problem, particular phenomena have to be isolated, such as deviatoric behavior, rate or aging dependence, choosing experiments where the influence of other effects can be neglected. In this way, the identification can be carried out step-wise. The identification procedure of the thermo-mechanical behavior with the small strain model is explained in Tab. 5.1, where the parameters marked with a gray background represent the identified parameters in the current identification step. First, the parameters characterizing the aging development are identified with the help of the isothermal dilatometric measurement over time, see Section 3.6.2.

After that, considering the model for small strains, the deviatoric isothermal behavior is identified with the help of the torsion experiments, starting by determining the parameters of the equilibrium state with the help of the equilibrium hysteresis, followed by

---

[1] In the case that the simulation values are close to $\bar{d}$, the second term of the expression is almost 1. It can even reach values larger than 1, resulting in a negative value of R^2. Moreover, in the identification of different effects such as rate or temperature dependence, the constant average value $\bar{d}$ can be so different from the experimental data, that the difference $\sum_{i=1}^{n_d}(d_i - s_i)^2$ becomes much smaller than $\sum_{i=1}^{n_d}(d_i - \bar{d})^2$, leading to a R^2 that is always very close to 1, even for bad identification results.

Table 5.1: Parameter identification procedure with the small deformations model

Experiments	Basic Parameters	Temperature Dependence	Aging Dependence
Isothermal dilatometric	α_a,β_{a2}	β_{a11},β_{a12}	–
Equilibrium Torsion	α_a,β_{a2}, b	β_{a11},β_{a12}, c_1,c_2,c_3,Θ_c	–
Overstress Torsion	α_a,β_{a2},b G_0,α_{ov},α_k,n_{ov}	β_{a11},β_{a12},c_1,c_2,c_3,Θ_c Θ_η,$r_{\eta 1}$,n_η,Θ_r,$\alpha_{\eta 1}$,$\alpha_{\eta 2}$	η_{01},η_{02},η_{03}
Equilibrium Tension/Comp.	α_a,β_{a2},b G_0,α_{ov},α_k,n_{ov}, K_{eq}	β_{a11},β_{a12},c_1,c_2,c_3,Θ_c Θ_η,$r_{\eta 1}$,n_η,Θ_r,$\alpha_{\eta 1}$,$\alpha_{\eta 2}$	η_{01},η_{02},η_{03}

the overstress. In the next step, temperature- and aging-dependent functions are developed for the shear behavior. When the parameters of the deviatoric part of the model are known, the bulk modulus is identified with the help of the equilibrium hysteresis in tension and compression.

The identification procedure for the finite deformations case is shown in Tab. 5.2. For the identification of this case, the tension and compression tests are used, since the case of torsion cannot be considered a one-dimensional problem anymore. Here, the bulk modulus is taken from the identification of small deformations, since it is not possible to identify it at the same time as the shear modulus only with the axial stress/strain curves in tension and compression, see (Gilbert et al., 2016). Then, the parameters of the equilibrium are identified with the equilibrium hysteresis for different temperatures – followed by the parameters of the overstress with the experiments at different strain-rates and the multi-step relaxation tests. In this case, the temperature-dependent functions are already developed.

Finally, the thermo-physical properties are fitted. Here, only the thermal diffusivity represents a considerable difficulty because of its dependence on aging and temperature. A list with the description of all material parameters is given in Tab. 5.3. All identifications are performed with Matlab routines, which can either draw on solutions provided by Matlab itself, or they call up external programs for the computation of the material behavior, see (Krämer et al., 2015). The optimization tool is the nonlinear least-squares solver *lsqnonlin*, see, for example, (Coleman and Li, 1996), (Levenberg, 1944), or (Marquardt, 1963), and the curve fitting tool from Matlab.

Table 5.2: Parameter identification procedure with the finite deformations model

Experiments	Basic Parameters	Temperature Dependence	Aging Dependence
Equilibrium Tension/Comp.	α_a,β_{a2}, $\hat{b}$	β_{a11},β_{a12}, $\hat{c}_1$,$\hat{c}_2$,$\hat{c}_3$,$\hat{\Theta}_c$	–
Overstress Tension/Comp.	α_a,β_{a2},$\hat{b}$ $\hat{G}_0$,$\hat{\alpha}_{\mathrm{ov}}$,$\hat{\alpha}_k$,$\hat{n}_{\mathrm{ov}}$,K	β_{a11},β_{a12},$\hat{c}_1$,$\hat{c}_2$,$\hat{c}_3$,$\hat{\Theta}_c$ $\hat{\Theta}_\eta$,$\hat{r}_{\eta 1}$,$\hat{n}_\eta$,$\hat{\Theta}_r$,$\hat{\alpha}_{\eta 1}$,$\hat{\alpha}_{\eta 2}$	$\hat{\eta}_{01}$,$\hat{\eta}_{02}$,$\hat{\eta}_{03}$

5.3 Calibration of the Aging Variable

In order to identify the aging variable, the measurement of the shrinkage over time for different temperatures shown in Section 3.6.2 is used. We consider the sample geometry from Fig. 5.3 with the initial length L_0 and the cross section $A_0 = B_0 H_0$. During the experiment, there is a heating process up to the time t_1 from room temperature Θ_0 up to the measurement temperature Θ_1, where thermal expansion takes place. After that, the temperature is kept constant over time and the shrinkage takes place. In order to connect the experimental data with the model, the case of small and large deformations are analyzed separately.

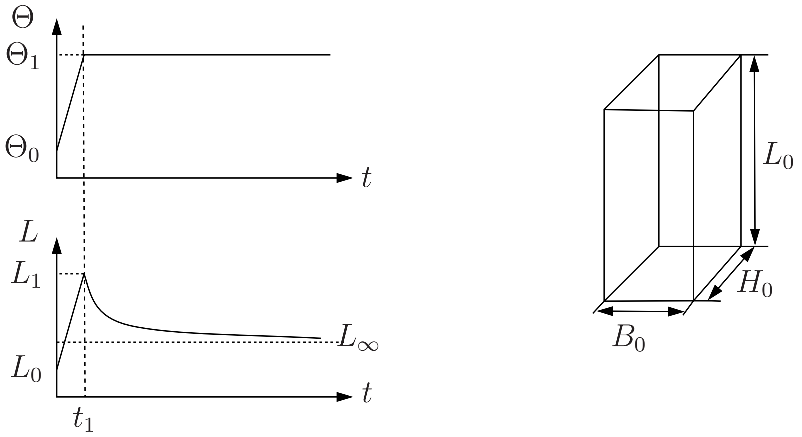

Figure 5.3: Dilatometer experiment

Table 5.3: Description of the material parameters of the mechanical part

Parameter Small strains/Finite strains	Phenomenon	Description
α_a	Aging	Shrinkage, see Eqns. (4.2)/(4.50)
β_{a2},β_{a11},β_{a12}	Aging	Evolution equation of aging, see Eq. (4.46)/(4.154).
α_Θ,Θ_0	Thermal expansion	Linear, thermal expansion α_Θ with the reference temperature Θ_0, see Eqns. (4.2)/(4.51).
K_{eq},G_{eq} / K, c_{10}	Elastic, equilibrium stress	Bulk and shear modulus of the elastic, equilibrium stress, see Eqns. (4.20)/(4.128).
b,c_1,c_2,c_3,Θ_c / $\hat{b}$,$\hat{c}_1$,$\hat{c}_2$,$\hat{c}_3$,$\hat{\Theta}_c$	Plastic, equilibrium stress	b/$\hat{b}$ and $c_1/\hat{c}_1$ are basic parameters of evolution equation of plastic strain in Eqns. (4.29)/(4.146). Temperature dependence included by c_2/c_2, $c_3/\hat{c}_3$ and $\Theta_c/\hat{\Theta}_c$, see Eqns. (4.33)/(4.157).
$\alpha_k/\hat{\alpha}_k$	Softening	Parameter of evolution equation of softening variable, see Eqns. (4.25)/(4.151).
G_0,α_{ov},n_{ov}/$\hat{G}_0$,$\hat{\alpha}_{\mathrm{ov}}$,$\hat{n}_{\mathrm{ov}}$	Overstress	Include softening-dependence. Parameters $G_0/\hat{G}_0$ and $\alpha_{\mathrm{ov}}/\hat{\alpha}_{\mathrm{ov}}$ determine initial slope in loading and unloading. $n_{\mathrm{ov}}/\hat{n}_{\mathrm{ov}}$ drives the change process in the slope, see Eqns. (4.35)/(4.158).
η_{01},η_{02},η_{03},Θ_η/$\hat{\eta}_{01}$,$\hat{\eta}_{02}$,$\hat{\eta}_{03}$,$\hat{\Theta}_\eta$	Viscosity	Parameters of temperature and aging dependent viscosity function $\eta_0(\Theta, a)$. It includes aging effects in the mechanical response, see Eqns. (4.39)/(4.160).
$r_{\eta1}$,Θ_r,n_η / $\hat{r}_{\eta1}$,$\hat{\Theta}_r$,$\hat{n}_\eta$	Viscosity	Parameters of temperature-dependent viscosity function $r_\eta(\Theta)$, see Eqns. (4.40)/(4.161).
$\alpha_{\eta1}$,$\alpha_{\eta2}$ / $\hat{\alpha}_{\eta1}$,$\hat{\alpha}_{\eta2}$	Viscosity	Parameters of temperature-dependent viscosity function $\alpha_\eta(\Theta)$, see Eqns. (4.41)/(4.162).

Small Strains

The total increment in length ΔL has three components. One mechanical ΔL_{M}, one thermal ΔL_{Θ}, and one caused by aging ΔL_a

$$\Delta L = \Delta L_{\mathrm{M}} + \Delta L_{\Theta} + \Delta L_a, \tag{5.9}$$

where the thermal and the aging components can be expressed in dependence of the strain components defined in Eq. (4.2)

$$\Delta L_{\Theta} = \varepsilon_{\Theta} L_0 = \alpha_{\Theta} \vartheta L_0 = \alpha_{\Theta} L_0 (\Theta - \Theta_0), \quad \Delta L_a = \varepsilon_a L_0 = -\alpha_a a L_0. \tag{5.10}$$

Inserting expression (5.10) into Eq. (5.9), one obtains

$$\Delta L = \Delta L_{\mathrm{M}} + \alpha_{\Theta} \vartheta L_0 - \alpha_a a L_0. \tag{5.11}$$

We assume that the dilatometer experiments are carried out with mechanical load $\Delta L_{\mathrm{M}} = 0$, that the heating process until time $t = t_1$ occurs fast enough so that the aging can be neglected, and that the temperature from the time $t = t_1$ onwards is constant throughout the experiment $\Theta = \Theta_0$, see the representation in Fig. 5.3. In this way, the thermal expansion at the time $t = t_1$ is equal to

$$\varepsilon_{\Theta}(t_1) = \alpha_{\Theta} \vartheta(t_1) = \alpha_{\Theta}(\Theta_1 - \Theta_0) = \frac{L_1 - L_0}{L_0} \quad \rightarrow \quad L_0 = \frac{L_1}{1 + \varepsilon_{\Theta}(t_1)}, \tag{5.12}$$

which is constant for $t > t_1$ since the temperature is kept constant. For $t > t_1$, this leads in Eq. (5.9) to

$$\frac{L(t) - L_0}{L_0} = \frac{L_1 - L_0}{L_0} - \alpha_a a. \tag{5.13}$$

Substituting L_0 from Eq. (5.12) leads to

$$\varepsilon_a = -\alpha_a a = (1 + \varepsilon_{\Theta}) \frac{L - L_1}{L_1} \approx \frac{L - L_1}{L_1}, \tag{5.14}$$

since in the case of small deformations $\varepsilon_{\Theta} \ll 1$. The parameter α_a represents the saturation value $\alpha_a = (L_{\infty} - L_1)/L_1$ (when $a = 1$). In this way, the aging variable a, with the evolution equation Eq. (4.47), can be determined with the experimental results from Section 3.6.2 for the case of small deformations.

Large Strains

For the analysis in the case of large deformations, we consider the deformation gradient $\mathbf{F} = \mathbf{F}_a \mathbf{F}_{\Theta} \mathbf{F}_{\mathrm{M}}$. Here, we once again assume that there is no mechanical loading $\mathbf{F}_{\mathrm{M}} = \mathbf{I}$ during the dilatometer experiments, no effect of aging in the thermal loading process until $t = t_1$ (which means that $\varphi_a = 1$ for $t < t_1$), and that the temperature from $t = t_1$ onwards is constant, so that $\mathbf{F}_\Theta = \varphi_\Theta(t_1)\mathbf{I}$ is constant too. Since $\mathbf{F}_\Theta = \varphi_\Theta \mathbf{I}$ and $\mathbf{F}_a = \varphi_a \mathbf{I}$ are purely volumetric, the determinant of $\mathbf{F}$ is equal to $\det \mathbf{F} = \varphi_\Theta^3 \varphi_a^3$. From Eq. (2.48) and for the time $t = t_1$ we obtain

$$\det \mathbf{F}(t_1) = \varphi_\Theta^3(t_1) = \lambda_\Theta^3(t_1) = \frac{L_1}{L_0}\frac{B_1}{B_0}\frac{H_1}{H_0} = \left(\frac{L_1}{L_0}\right)^3, \tag{5.15}$$

since the stretch $\lambda_\Theta = L_1/L_0 = B_1/B_0 = H_1/H_0$ is identical for the diagonal components of $\mathbf{F}$. This leads to

$$L_0 = \varphi_\Theta^{-1}(t_1) L_1. \tag{5.16}$$

Since the temperature is kept constant for $t > t_0$, the determinant of the deformation gradient can here be expressed as

$$\det \mathbf{F} = \varphi_\Theta^3(t_1)\varphi_a^3 = \left(\frac{L}{L_0}\right)^3 = \left(\varphi_\Theta(t_1)\frac{L}{L_1}\right)^3, \tag{5.17}$$

which leads to

$$\varphi_a = \frac{L}{L_1}. \tag{5.18}$$

Inserting the definition $\varphi_a = 1 - \alpha_a a$ in Eq. (5.18), we obtain

$$-\alpha_a a = \frac{L - L_1}{L_1}. \tag{5.19}$$

From Eqns. (5.14) and (5.19), it is clear that the aging variable has the same relation to the experimental data both for the case of the small and for the large deformations. As a consequence, the identification performed in this section is valid for both cases.

Identification

It is necessary to identify the parameters α_a, β_{a2}, and β_{a11}, as well as β_{a12} from Eqns. (4.2) and (4.47). In a first identification step, the parameters α_a, β_{a2} and β_{a1}^i, are identified, with β_{a1}^i, $i = 1, 2, 3$, changing for every temperature $\Theta_1 = 85\,°\mathrm{C}$, $\Theta_2 = 105\,°\mathrm{C}$, $\Theta_3 = 125\,°\mathrm{C}$, see Fig. 5.4(a) and Tab. 5.4.

In the second identification step, the parameters of the Arrhenius equation, β_{a11} and β_{a12}, are identified. To this end, we consider the natural logarithms of Eq. (4.46)

$$\ln \beta_{a1}(\Theta) = \ln(\beta_{a11}) - \beta_{a12}\frac{1}{\Theta}. \tag{5.20}$$

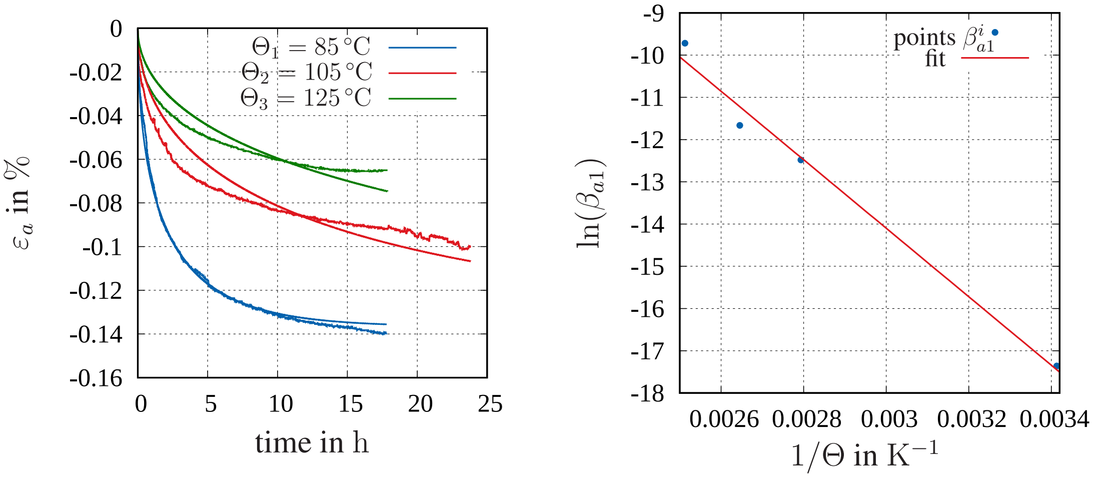

(a) Identification of the isothermal shrinkage measurements.

(b) Identification of the parameter $\beta_{a1}(\Theta)$

Figure 5.4: Results of the first identification step of the aging variable

Table 5.4: Results of the parameter identification for the aging variable

parameter	β_{a2} -	β_{a1}^1 s^{-1}	β_{a1}^2 s^{-1}	β_{a1}^3 s^{-1}	α_a -
initial value	0.2	10^{-4}	10^{-4}	10^{-4}	10^{-3}
final value	10^{-5}	3.8×10^{-6}	8.6×10^{-6}	6.02×10^{-5}	1.37×10^{-3}
conf. interval	9.0×10^{-5}	2.0×10^{-8}	3.5×10^{-8}	3.22×10^{-7}	10^{-7}

Eq. (5.20) corresponds to a linear equation $y(x) = y_0 - mx$, with $y(x) = \ln \beta_{a1}$ in dependence of $x = 1/\Theta$. The parameters $y_0 = \ln(\beta_{a11})$ and $m = \beta_{a12}$ can be identified with the help of the points β^i_{a1} obtained in the previous identification step. The results are shown in Fig. 5.4(b).

The results of the second identification are shown in Fig. 5.5 and Tab. 5.5. Fig. 5.5(b) also shows the prediction of the model at the temperature of 20 °C compared to the measurement from (Johnen, 1981). The brown line represents the prediction of the model with the identified parameters. The black line represents the simulation at 20 °C with the identified parameters but with a change in the saturation value α_a, where the value identified in (Martinez Page and Hartmann, 2018a) is used, since it is clear that the saturation value in the measurement shown in (Johnen, 1981) is different. Here, one can see that the value α_a is different for the tested alloy and the material from (Johnen, 1981), while the process for the developing of the aging variable represented by the parameters β_{a2}, β_{a11}, and β_{a12} is the same.

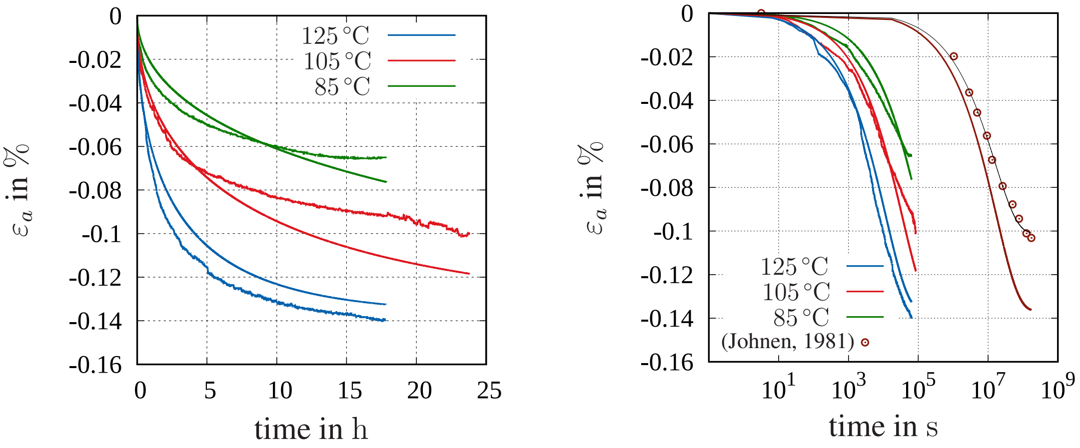

(a) Results of the identification of the shrinkage measurements.

(b) Prediction of the model at room temperature and comparison with the measurement from (Johnen, 1981). The time in seconds is in logarithmic scale.

Figure 5.5: Behavior of the aging variable with the identified function $\beta_{a1}(\Theta)$

From Fig. 5.5, we observe that the model can reproduce the main behavior of the experiments. The small values of the function β_{a1} for temperatures under 80 °C indicates that the aging process happens quite slowly.

Table 5.5: Results of the parameter identification of the Arrhenius equation

parameter	$\ln(\beta_{a11})$ $\ln(\mathrm{s}^{-1})$	β_{a12} K
initial value	1	1
final value	10.24	8113
conf. interval	0.787	2748

5.4 Calibration of Small Strains Model

The identification of the mechanical behavior can be performed in a step-wise manner if several properties of the problem under consideration are exploited. First, we consider the geometrical assumption of a thin-walled cylindrical tube, which holds that the case of torsion can be interpreted as a one-dimensional purely deviatoric problem. Thus, the shear behavior can be isolated from the volumetric behavior as seen in Chapter 3. In this way, the parameters of the deviatoric part of the stress state are identified first. The second advantage lies in the partitioned structure of the constitutive model, which allows to separate the equilibrium state from the remaining part of the model. In this case, the equilibrium hysteresis is used first to obtain the parameters of the deviatoric part of the equilibrium stress. Then, the parameters of the overstress part are identified with the experiments at different strain-rates under torsion. Finally, the remaining parameters are determined using the data from the tension and compression experiments. Moreover, in order to develop temperature and aging-dependent functions, the identification is carried out in every step first at every temperature and aging rate. After that, a temperature- or aging-dependent function is found for the identified values.

5.4.1 Identification of the Shear Behavior

As considered in the experiments, see Section 3.5.3, the thermal part of the strain is given by $\mathbf{E}_\Theta = \mathbf{0}$ in the isothermal process representing the experiment, since the measurement starts after the thermal expansion. Moreover, we assume that the aging variable develops much slower than the mechanical processes that take place during the experiments. In this way, the shrinkage can be assumed equal to zero, $\mathbf{E}_a = \mathbf{0}$. Accordingly, the stress and strain tensors can be expressed by

$$\mathbf{T} = \begin{bmatrix} 0 & 0 & 0 \\ 0 & 0 & \tau \\ 0 & \tau & 0 \end{bmatrix}, \qquad \mathbf{E} = \mathbf{E}_\mathrm{M} = \begin{bmatrix} 0 & 0 & 0 \\ 0 & 0 & \gamma/2 \\ 0 & \gamma/2 & 0 \end{bmatrix}. \tag{5.21}$$

Due to definitions (4.31) and (4.23), the hysteretic stress $\mathbf{T}_\mathrm{eq}^\mathrm{h}$ and the overstress $\mathbf{T}_\mathrm{ov}$ are purely deviatoric. The main advantage of the case of torsion for small deformations with a thin-walled cylinder becomes evident, since this problem can be simplified to the one-dimensional case

$$\tau(\gamma) = \tau^{\mathrm{e}}_{\mathrm{eq}}(\gamma) + \tau^{\mathrm{h}}_{\mathrm{eq}}(\gamma) + \tau_{\mathrm{ov}}(\gamma). \tag{5.22}$$

Equilibrium Stress Part

The equilibrium stress state would be achieved by an infinitely slow loading process, which means $\dot{\gamma} \ll 1$. In this case, the overstress is close to zero, leaving only the equilibrium stress. For a constant shear strain-rate $\dot{\gamma} = K$, $\gamma(t) = Kt$, the equilibrium shear stress from Eqns. (4.20) and (4.31) is equal to an elastic and an hysteretic part

$$\tau_{\mathrm{eq}} = \tau^{\mathrm{e}}_{\mathrm{eq}} + \tau^{\mathrm{h}}_{\mathrm{eq}} = G_{\mathrm{eq}} K t + \tau^{\mathrm{h}}_{\mathrm{eq}}. \tag{5.23}$$

In this case, the rate of the arc-length is equal to $\dot{s}_{\mathrm{M}} = |K|/\sqrt{2}$, and the hysteretic stress is given by

$$\dot{\tau}^{\mathrm{h}}_{\mathrm{eq}} = c(\Theta)\frac{K}{2} - b\frac{|K|}{\sqrt{2}}\tau^{\mathrm{h}}_{\mathrm{eq}}. \tag{5.24}$$

The shear modulus of the equilibrium stress part G_{eq} in Eq. (5.23) allows a continuous growth of the stress function. Using only the hysteretic part, the equilibrium stress state would reach a saturation for large γ, which sometimes causes numerical problems. This can be resolved with a small superimposed part $\tau^{\mathrm{e}}_{\mathrm{eq}}$ in the equilibrium stress. In this way, the parameter G_{eq} is set equal to $G_{\mathrm{eq}} = 100\,\mathrm{MPa}$ for numerical purposes. This parameter has a minor influence on the entire model's response.

In the following, the identification procedure for the equilibrium is carried out in three steps. First, the parameters b and c are identified independently for the equilibrium stress state at each temperature and aging time with the help of the equilibrium hysteresis, which is represented by dots in Fig. 3.22. After analyzing the results of this first step, the temperature dependence is introduced into the parameter c, since it was observed that the initial slope of the equilibrium hysteresis was clearly influenced by the temperature. In the second step, the parameter b is kept constant and equal for all temperatures and aging times, and the parameter c is re-identified. The identified values for c are represented by the blue dots in Fig. 5.6(a). Here, we observe that the aging has only a minor influence on the initial slope of the stress-strain curve compared to the influence of the temperature. For this reason, in the third step, a temperature-dependent function is found for the identified points of c

$$c(\Theta) = c_1(c_2 - \tanh(c_3(\Theta - \Theta_c))). \tag{4.33}$$

This function is fitted to the points identified in the previous step. Here, all identifications are performed in Matlab with the help of the nonlinear least-squares solver *lsqnonlin*. The results of the identification of the function $c(\Theta)$ are shown in Fig. 5.6(b),

Table 5.6: Identified parameters of the equilibrium part in torsion

parameter	b –	c_1 MPa	c_2 MPa	c_3 –	Θ_c K
initial value	164	3.0×10^4	1.2	0.033	290
final value	219.079	2.317×10^4	1.10	0.024	283.44
conf. interval	8.1526	1.1932×10^3	0.365	0.002	1.84

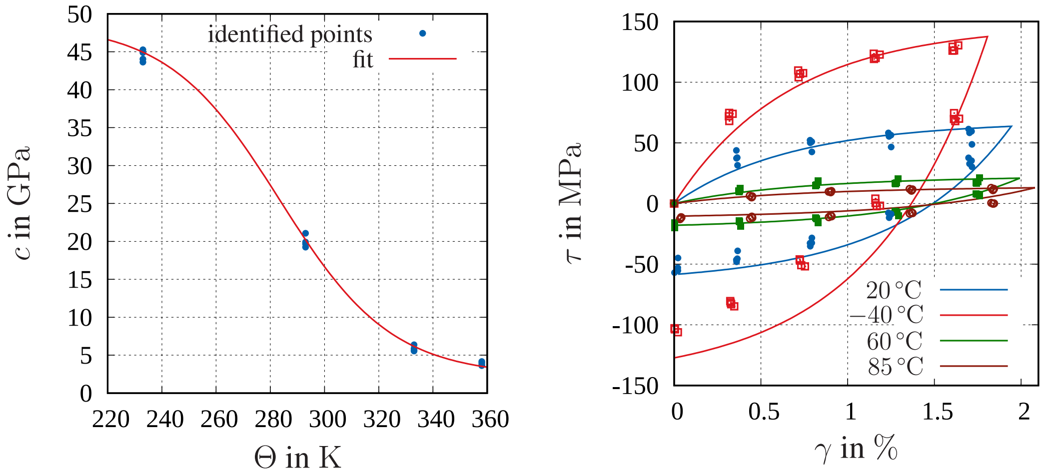

(a) Fit of the identified values for c with Eq. (4.33) over the temperature for all aging times

(b) Results of the identification of the equilibrium hysteresis for the different temperatures (different colors) and all aging times

Figure 5.6: Results of the identification in torsion for the equilibrium stress state for the different aging times and temperatures. The experiments are represented by points and the model with lines.

and Tab. 5.6 displays the identified parameters with their confidence interval. There is a good agreement between the experiments and the fit.
The correlation matrix of the identification is equal to

$$\mathbf{R} = \left[\begin{array}{cccccc} & b & c_1 & c_2 & c_3 & \Theta_c \\ b & 1 & 0.389 & 0.009 & 0.004 & 0.018 \\ c_1 & & 1 & -0.868 & -0.8962 & -0.783 \\ c_2 & & & 1 & 0.931 & 0.688 \\ c_3 & & & & 1 & 0.856 \\ \Theta_c & & & & & 1 \end{array}\right] . \tag{5.25}$$

Here, a correlation between the parameters which describe the temperature dependence can be observed.

Overstress

The total shear stress in the model is decomposed into the equilibrium stress part and the overstress $\tau = \tau_{\text{eq}} + \tau_{\text{ov}}$, where the parameters of the equilibrium are known and the parameters of the deviatoric overstress part have to be identified. The remaining information for the identification of the overstress can be obtained from the experiments at different strain-rates and the multi-step relaxation tests from Section 3.5. Considering Eqns. (4.23), the overstress τ_{ov} is equal to

$$\tau_{\text{ov}} = G_{\text{ov}}(k)\,(\gamma - \gamma_{\text{v}})\,. \tag{5.26}$$

The viscous shear strain γ_{v} is defined in Eq. (4.34), obtaining for the torsion case

$$\dot{\gamma}_{\text{v}} = \frac{2G_{\text{ov}}(k)}{\eta(\dot{\gamma}, \Theta, a)}\,(\gamma - \gamma_{\text{v}})\,. \tag{5.27}$$

Here, there are two main phenomena to describe: the initial slope of the overstress in the stress-strain curve, which is represented by the shear modulus of the overstress G_{ov}, and the viscosity η, which influences the maximum value of the stress in the stress-strain curve, the separation between the different curves at different strain-rates and the relaxation. In the identification process, the relaxation steps of the multi-step relaxation tests are considered first. The relaxation provides us with information regarding the viscosity for a strain-rate equal to zero. After that, the initial slope during the loading is determined with the experiments at different strain-rates and the multi-step relaxation test for the unloading process. Finally, the experiments at different strain-rates are evaluated in order to determine the viscosity and the parameter of the softening variable.

Isothermal Relaxation In an isothermal relaxation process at the constant temperatures of $\Theta = \hat{\Theta}_i$, $i = 1, ..., 4$, the strain is kept constant, $\gamma = \hat{\gamma} = \text{const.}$, and, thus, the strain-rate is equal to zero, $\dot{\gamma} = 0$. This leads to the value zero of other variables which depend on the strain-rate, such as the rate of the arc-length, $\dot{s}_{\mathrm{M}} = 0$, and the rate of the softening variable $\dot{k} = 0$, see Eq. (4.25). Therefore, the softening variable for every relaxation step l is constant $k = \hat{k}_l$. Since the aging dependence is not considered in this first step , the shear modulus G_{ov} and the viscosity η are constant during relaxation in a first estimation of the identification, see Eq. (4.35) and (4.38),

$$\eta(\hat{\Theta}_i) = \hat{\eta}_i = \text{const.}, \quad \text{and} \quad G_{\mathrm{ov}}(\hat{k}_l) = \hat{G}_{\mathrm{ov}l} = \text{const.} \tag{5.28}$$

Inserting equations (5.28) into (5.27) leads to

$$\dot{\gamma}_{\mathrm{v}} + \frac{2\hat{G}_{\mathrm{ov}l}}{\hat{\eta}_i}\gamma_{\mathrm{v}} = \frac{2\hat{G}_{\mathrm{ov}l}}{\hat{\eta}_i}\hat{\gamma}. \tag{5.29}$$

This differential equation can be solved analytically, and its result can be written as

$$\gamma_{\mathrm{v}}(t) = (\gamma_{\mathrm{v}}(0) - \hat{\gamma}) \exp\left(\frac{-2G_{\mathrm{ov}l}}{\hat{\eta}_{ij}}t\right) + \hat{\gamma}. \tag{5.30}$$

Here, for every relaxation step $\hat{k}_l$ and every temperature $\hat{\Theta}_i$, the value $G_{\mathrm{ov}l}/\hat{\eta}_i$ is found. This information is used in the next identification steps. After identifying the shear modulus $G_{\mathrm{ov}}(k)$ in the next section, the value for the viscosity during the relaxation $\hat{\eta}_i$ can be found for every temperature, obtaining an additional point in the identification of the viscosity including information regarding the relaxation.

Monotonic loading The experiments at different strain-rates represent a monotonic isothermal loading process in which the strain-rate is kept constant, $\dot{\gamma} = K$, and the shear strain is equal to $\gamma(t) = Kt$. In this case, Eq. (5.27) cannot be solved analytically, which is why it is solved numerically in Matlab.

In this section, the first parameter to identify is the shear modulus of the overstress G_{ov}. According to Eq. (4.35), there are two different aspects that have to be considered. First, the initial slope in the loading and unloading, which is determined by the parameters G_0 and α_{ov}, and second, the change in the initial slope during the loading process, which is driven by the parameters n_{ov} and α_k.

For the identification of the parameter α_{ov}, the initial slope of the overstress during the loading is determined with the experiments at different strain-rates, and the initial slope of the unloading with the multi-step relaxation tests. For the initial slope of the loading, the softening parameter has the value zero $k = 0$, and it is set equal to the value 1 for the unloading. With these conditions, the shear modulus is equal to

$$G_{\mathrm{ov}}(k = 0) = G_0(1 + \alpha_{\mathrm{ov}}) \quad \text{for the initial loading} \tag{5.31}$$

$$G_{\mathrm{ov}}(k = 1) = G_0\alpha_{\mathrm{ov}} \quad \text{for the unloading.} \tag{5.32}$$

The parameter α_{ov} can be obtained from the relation between the initial slope for loading and unloading

$$\frac{G_{\mathrm{ov}}(k=0)}{G_{\mathrm{ov}}(k=1)} = \frac{1+\alpha_{\mathrm{ov}}}{\alpha_{\mathrm{ov}}} \rightarrow \alpha_{\mathrm{ov}} = \left(\frac{G_{\mathrm{ov}}(k=0)}{G_{\mathrm{ov}}(k=1)} - 1\right)^{-1}. \tag{5.33}$$

The parameters G_0 and α_{ov} are determined with the experiment at different temperatures and aging times. The obtained values are $G_0 = 32.08\,\mathrm{GPa}$ and $\alpha_{\mathrm{ov}} = 0.2$. Moreover, the parameter n_{ov} and the softening parameter α_k have to be found. To this end, the full set of stress-strain curves at different rates, temperatures, and aging times are considered. There is a restriction in the identification for α_k, so that its value is equal to 1 at the end of the loading, in order to fulfill Eq. (5.32). These parameters are identified together with a value of the viscosity η_{ijk}, which is different for every strain-rate, temperature, and aging time. We obtain a value of $\alpha_k = 350$ with a confidence interval of 73.4 and $n_{\mathrm{ov}} = 0.35$ with a confidence interval of 0.11. The correlation between the parameters is -0.7682. Fig. 5.7 shows the identified function $G_{\mathrm{ov}}(k)$. Here, one can observe a decrease in the initial slope with the softening. When the softening reaches its maximal value, the shear modulus of the overstress is approximately 16% of the initial value at the beginning of the loading. The set of parameters of the shear modulus G_{ov} are compiled in Tab. 5.7.

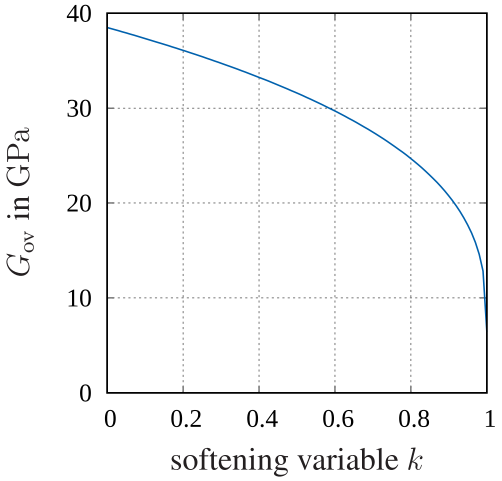

Figure 5.7: Shear modulus of the overstress over the softening variable

Next, the viscosity has to be modeled and identified. This process is done in a stepwise manner as well. Since the amount of results of the intermediate identification steps is very large, only the final results of the identification are shown.

A first identification is carried out for the viscosity as a constant value. Thus, a constant value η_{ijm} is identified for each temperature Θ_i, $i = 1, ..., 4$, each aging time a_j,

Table 5.7: Results of the parameter identification for G_{ov}, see Eq. (4.35)

parameter	G_0 GPa	α_{ov} $-$	n_{ov} $-$	α_k $-$
value	32.08	0.2	0.35	350

$j = 1, ..., 4$, and each strain-rate $\dot{\gamma}_m$, $m = 1, ..., 4$. This results in a total number of 64 values for the viscosity.

In the next step, a first modeling assumption is made for the rate dependence of the viscosity

$$\eta(\dot{\gamma}) = \eta_{0ij} \left(\left(\frac{|\dot{\gamma}|}{\sqrt{2} s_\eta} + \alpha_{\eta_i} \right)^{-r_{\eta_i}} + 1 \right). \tag{5.34}$$

The parameters[2] η_{0ij}, α_{η_i}, and r_{η_i} from Eq. (5.34) are now identified for each temperature and aging time separately[3] with the previously identified points η_{ijm} and the additional values identified for the relaxation in the previous section. To this end, the logarithm of function Eq. (5.34) is considered in order to simplify the identification process. The parameter s_η has the goal to obtain a dimensionless expression, and it is set equal to $1\,\text{s}^{-1}$.

In the last identification step, the identified points η_{0ij}, α_{η_i} and r_{η_i} are used to fit the chosen temperature and aging dependent functions

$$\eta_0(\Theta, a) = (\eta_{01} - \eta_{02} \exp(\eta_{03} a))(1 + \tanh(n_\eta(\Theta - \Theta_\eta))), \tag{4.39}$$

$$r_\eta(\Theta) = r_{\eta 1}(1 - \tanh(n_\eta(\Theta - \Theta_r)), \tag{4.40}$$

$$\alpha_\eta(\Theta) = \alpha_{\eta 1} \exp(\alpha_{\eta 2} \Theta). \tag{4.41}$$

The results of the identification are shown in Tabs. 5.8 and 5.9 as well as in Figs. 5.9-5.12. The correlation matrices are equal to

$$\mathbf{R} = \left[\begin{array}{lcccc} & \eta_{01} & \eta_{02} & \eta_{03} & \Theta_\eta \\ \eta_{01} & 1 & 0.761 & 0.772 & 0.845 \\ \eta_{02} & & 1 & -0.946 & -0.884 \\ \eta_{03} & & & 1 & -0.779 \\ \Theta_\eta & & & & 1 \end{array} \right], \tag{5.35}$$

---

[2] The index i represents the temperature dependence and j aging dependence of the parameters.

[3] The identification of the values η_{0ij}, α_{η_i}, and r_{η_i} is performed using all experiments at different strain-rates for each temperature and each aging time separately. Thus, four different values are obtained for α_η and r_η due to the temperature dependence – and 16 different values are obtained for η_0 due to its temperature and aging dependence.

Table 5.8: Results of the parameter identification for the viscosity function η_0 of Eq. (4.39)

parameter	η_{01} $\mathrm{MPa\,s}$	η_{02} $\mathrm{MPa\,s}$	η_{03} $-$	Θ_η K
initial value	0.144	0.868	0.180	300
final value	1550	6.357	4.518	373.6
conf. interval	24	3.751	1.246	0.638

Table 5.9: Results of the parameter identification for the viscosity functions r_η and α_η from Eqns. (4.40) and (4.41)

parameter	$r_{\eta 1}$ $-$	n_η K^{-1}	Θ_r K	$\alpha_{\eta 1}$ $-$	$\alpha_{\eta 2}$ K^{-1}
initial value	0.1419	0.01	300	1.0×10^{-9}	0.01
final value	0.495	$0.011\,54$	426.3	1.26×10^{-9}	0.0136
conf. interval	0.0635	0.0101	98	2.15×10^{-10}	0.01

and

$$\mathbf{R} = \left[\begin{array}{cccc} & r_{\eta 1} & n_\eta & \Theta_r \\ r_{\eta 1} & 1 & -0.498 & -0.854 \\ n_\eta & & 1 & 0.302 \\ \Theta_r & & & 1 \end{array}\right], \quad \mathbf{R} = \left[\begin{array}{ccc} & \alpha_{\eta 1} & \alpha_{\eta 2} \\ \alpha_{\eta 1} & 1 & -0.898 \\ \alpha_{\eta 2} & & 1 \end{array}\right]. \tag{5.36}$$

In order to expose the behavior of the developed viscosity function with the identified parameters, the function $\eta(\Theta, a, \dot{\gamma})$ is displayed over the temperature and the aging for each displacement rate in Fig. 5.8. This function has a maximum for the temperature, whose position changes with the strain-rate. It decreases with the aging time.

Moreover, Figs. 5.9-5.12 show the complete results of the identification for the different strain-rates in torsion. Here, we observe a good agreement between experiments and model if we take into account that a total number of 96 experiments were fitted, with 13 parameters that model the rate, relaxation, temperature, and aging dependence. The results of the identification of the relaxation steps are shown in Fig. 5.13. Here, one can see that the model can reproduce the relaxation more accurately for higher temperatures. The results for lower temperatures are only moderately represented. It might be possible to achieve an improvement by adding more temperature-dependent Maxwell-elements in the model, but this approach is not pursued since it would lead to a larger amount of material parameters, which would strongly correlate in the identification process. Furthermore, the number of internal variables would drastically increase (six more per Maxwell-element). The model is also able to reproduce the multi-step relaxation process as can be seen in Fig. 5.14, where the results for the experiments without aging are shown. Additional results of the prediction of the model are shown in the appendix. During the unloading process, lower temperatures are overestimated.

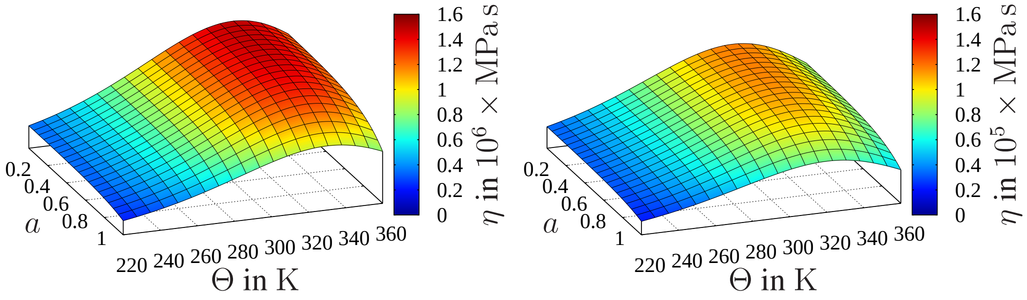

(a) Strain-rate $\dot{\gamma}_1 = 3.2 \times 10^{-4}\,\mathrm{s}^{-1}$ (b) Strain-rate $\dot{\gamma}_2 = 3.2 \times 10^{-5}\,\mathrm{s}^{-1}$

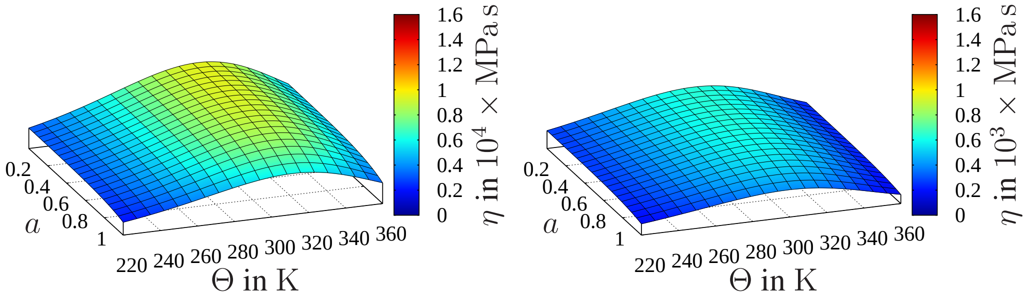

(c) Strain-rate $\dot{\gamma}_3 = 3.2 \times 10^{-6}\,\mathrm{s}^{-1}$ (d) Strain-rate $\dot{\gamma}_4 = 3.2 \times 10^{-7}\,\mathrm{s}^{-1}$

Figure 5.8: Representation of the function $\eta(\Theta, a, \dot{\gamma})$ for the identified parameters. Please note the change in the order of magnitude of η for the different strain-rates

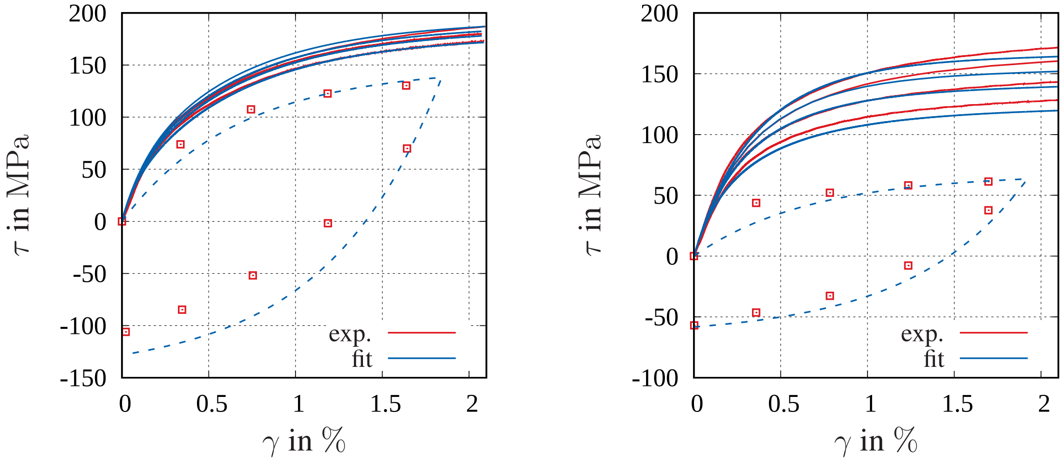

(a) $\Theta = -40\,^\circ\mathrm{C}$

(b) $\Theta = 20\,^\circ\mathrm{C}$

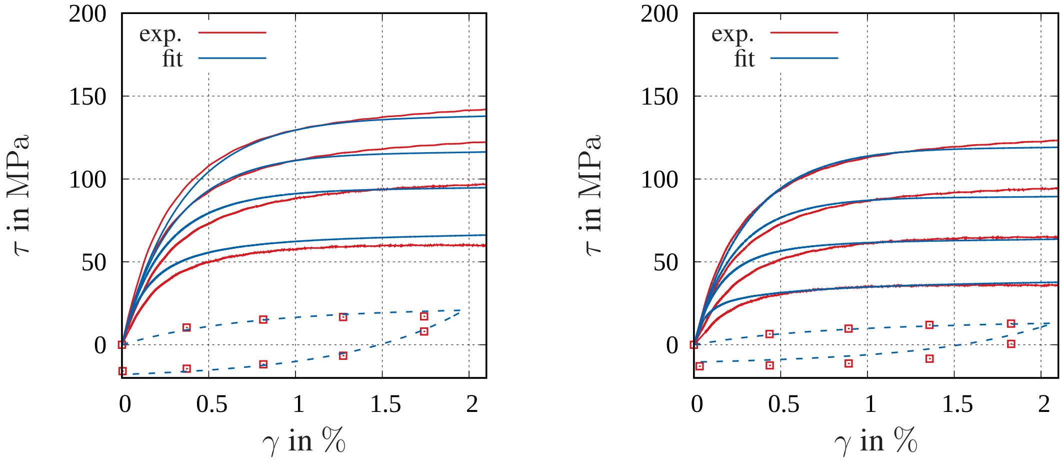

(c) $\Theta = 60\,^\circ\mathrm{C}$

(d) $\Theta = 85\,^\circ\mathrm{C}$

Figure 5.9: Results of the parameter identification in torsion (without aging)

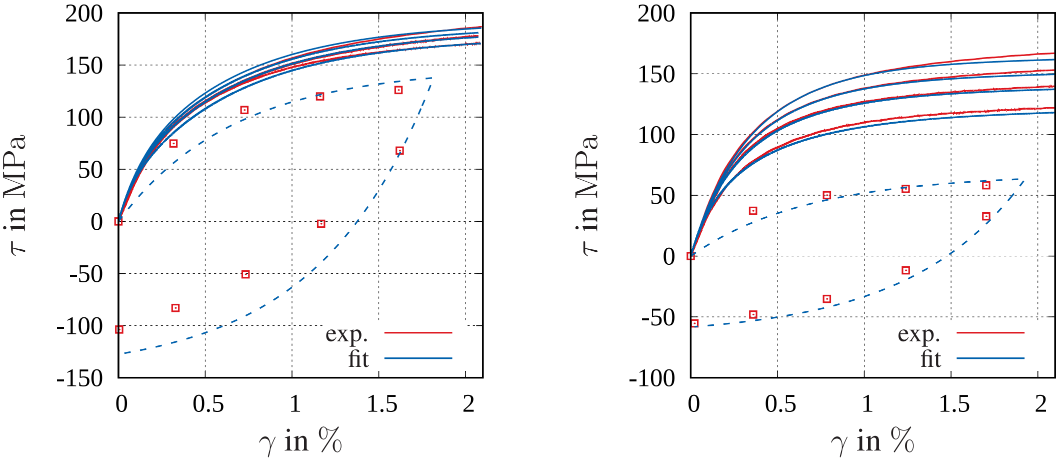

(a) $\Theta = -40\,°\mathrm{C}$ (b) $\Theta = 20\,°\mathrm{C}$

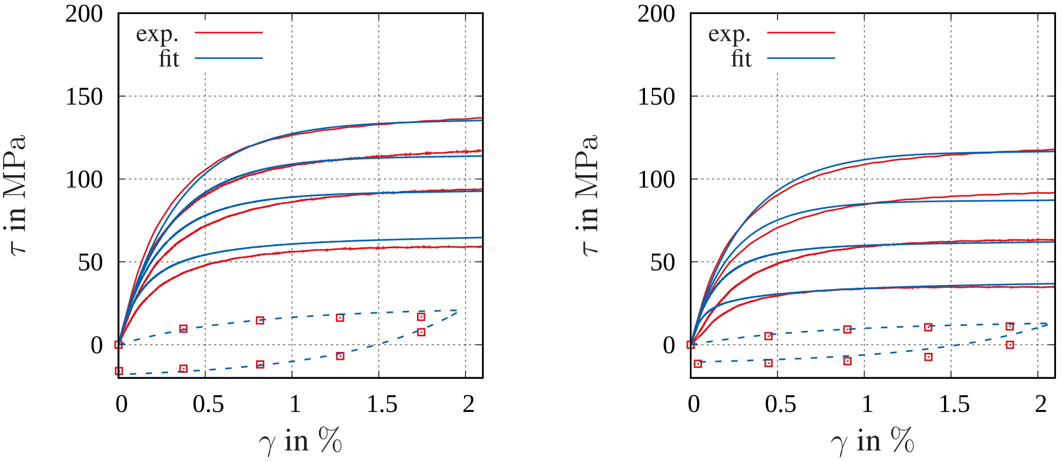

(c) $\Theta = 60\,°\mathrm{C}$ (d) $\Theta = 85\,°\mathrm{C}$

Figure 5.10: Results of the parameter identification in torsion (3 months of aging)

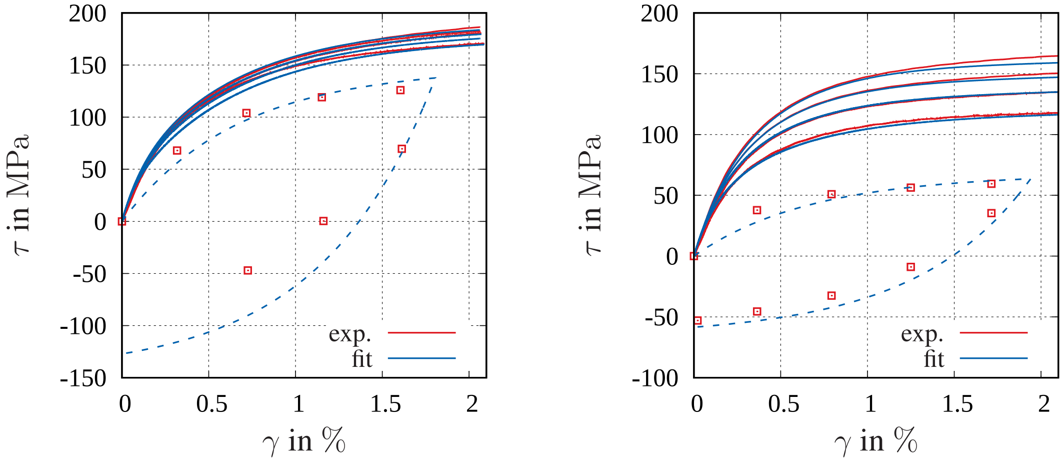

(a) $\Theta = -40\,^{\circ}\mathrm{C}$ (b) $\Theta = 20\,^{\circ}\mathrm{C}$

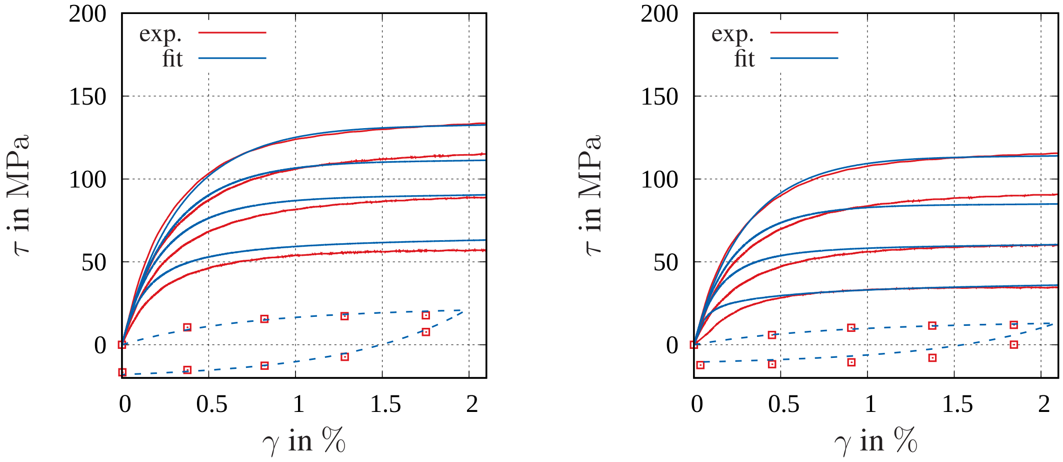

(c) $\Theta = 60\,^{\circ}\mathrm{C}$ (d) $\Theta = 85\,^{\circ}\mathrm{C}$

Figure 5.11: Results of the parameter identification in torsion (6 months of aging)

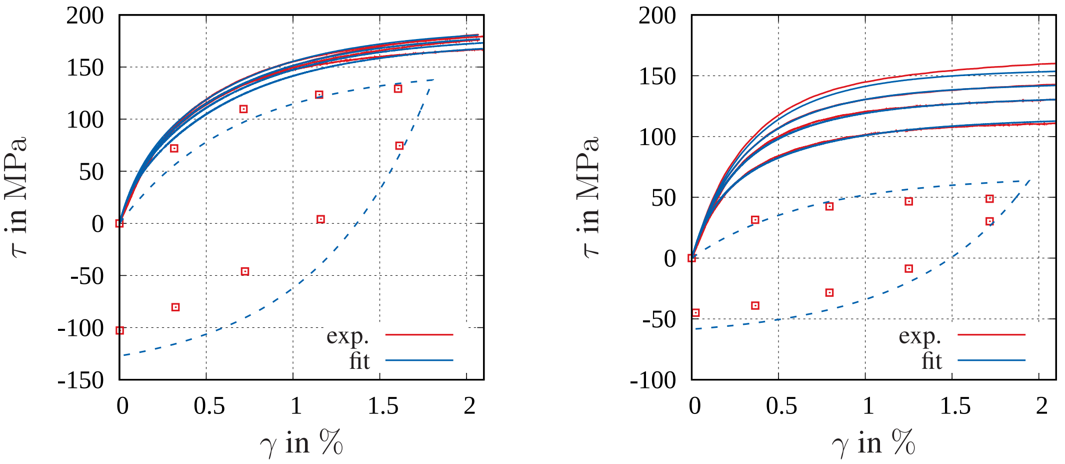

(a) $\Theta = -40\,^{\circ}\mathrm{C}$ (b) $\Theta = 20\,^{\circ}\mathrm{C}$

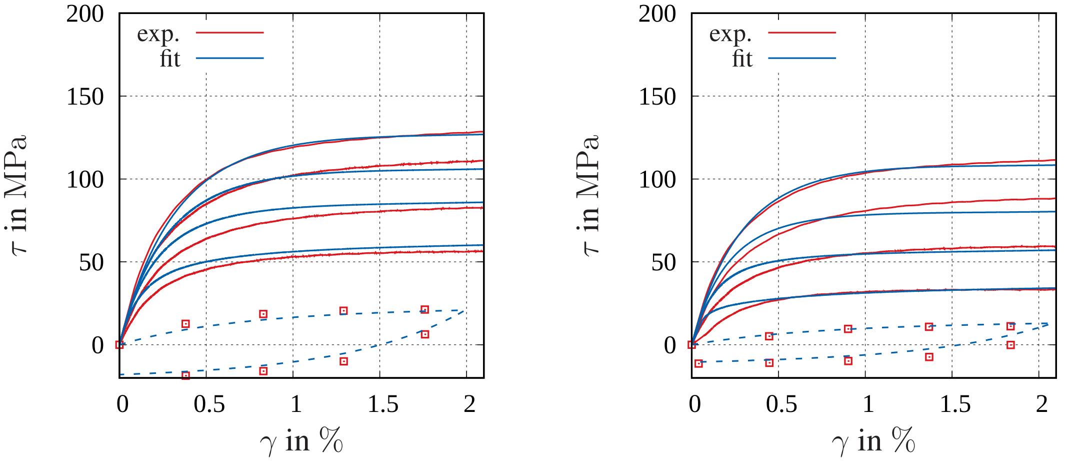

(c) $\Theta = 60\,^{\circ}\mathrm{C}$ (d) $\Theta = 85\,^{\circ}\mathrm{C}$

Figure 5.12: Results of the parameter identification in torsion (12 months of aging)

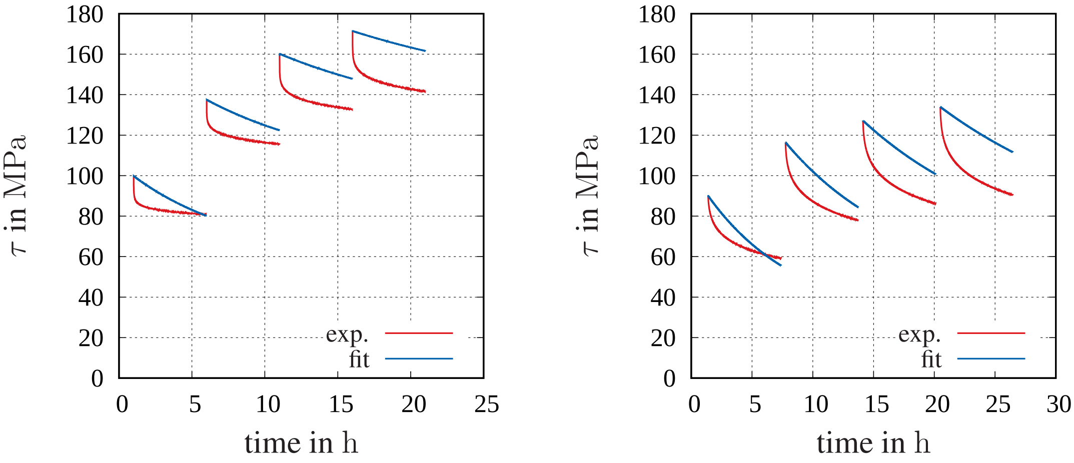

(a) $\Theta = -40\,°\mathrm{C}$ (b) $\Theta = 20\,°\mathrm{C}$

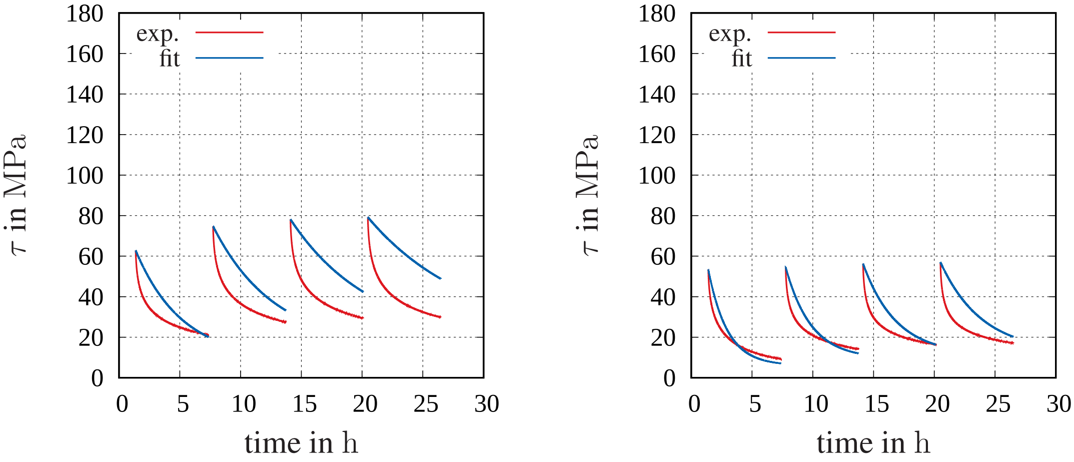

(c) $\Theta = 60\,°\mathrm{C}$ (d) $\Theta = 85\,°\mathrm{C}$

Figure 5.13: Results of the identification for the different relaxation steps (specimens without aging)

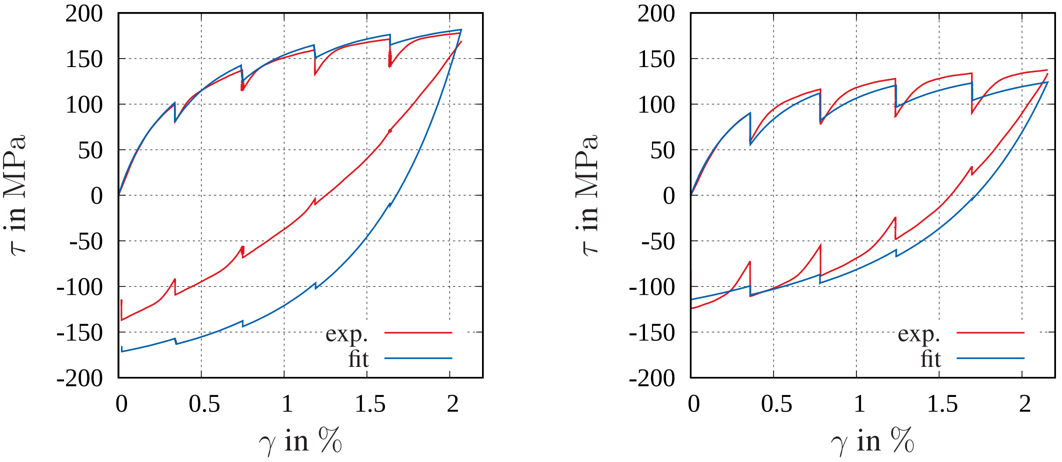

(a) $\Theta = -40\,^{\circ}\mathrm{C}$ (b) $\Theta = 20\,^{\circ}\mathrm{C}$

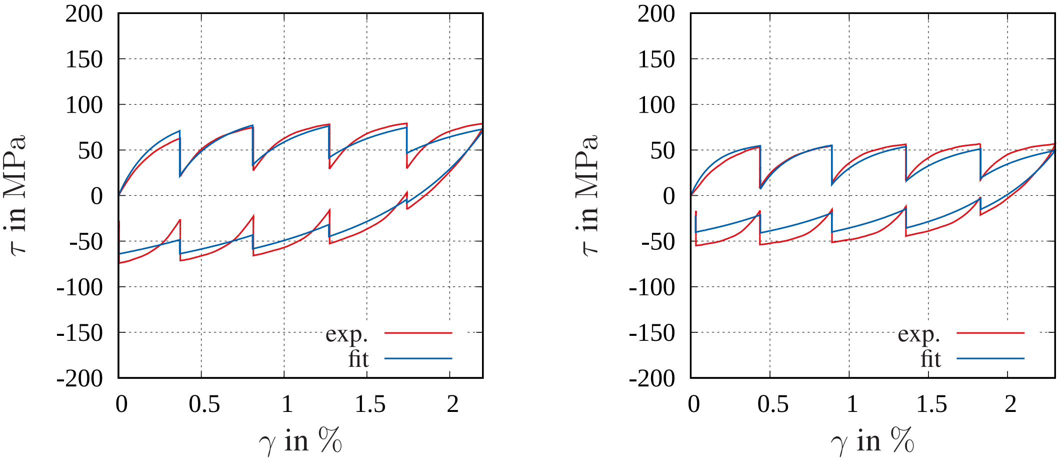

(c) $\Theta = 60\,^{\circ}\mathrm{C}$ (d) $\Theta = 85\,^{\circ}\mathrm{C}$

Figure 5.14: Prediction of the multi-step relaxation test in torsion

5.4.2 Identification in Tension-Compression

With the results of the identification with the torsion experiments, the last unknown parameter is the bulk modulus K_{eq}. In the case of tension and compression, it is necessary to consider the complete three-dimensional model of Tab. 4.1. In order to determine the response of the model, the procedure proposed in (Krämer et al., 2015) is considered, where the three-dimensional behavior of a tension or compression test is simulated for a single Gauss-point and compared with the experimental results. The parameter K_{eq} is identified with the help of the equilibrium hysteresis in tension and compression for the different temperatures and aging times. The identified value for the bulk modulus is $K_{\text{eq}} = 49.5\,\text{GPa}$. The results of the identification for the equilibrium hysteresis in tension and compression are shown in Fig. 5.15. One can observe a good agreement between experiment and identification. The remaining experiments at different strain-rates for the different temperatures and aging times and the multi-step relaxation tests are not used for the identification of the model, since all the parameters are known at this point.

The predictions of the model for the different strain-rates and temperatures are shown in Figs. 5.16-5.18 and Fig. 5.16 shows the temperature dependence in tension-compression. Fig. 5.17 displays the multi-step relaxation test for the material without aging at different temperatures. In Fig. 5.18, the aging dependence is displayed for two different temperatures and all strain-rates. Here, one can observe that even if almost all the parameters are identified with the torsion tests, the prediction of the model in tension and compression is accurate. Because of the tension-compression asymmetry, the model is better at reproducing the behavior in tension than in compression. The model is able to reproduce the aging dependence as well. Additional results of the identification are shown in the appendix.

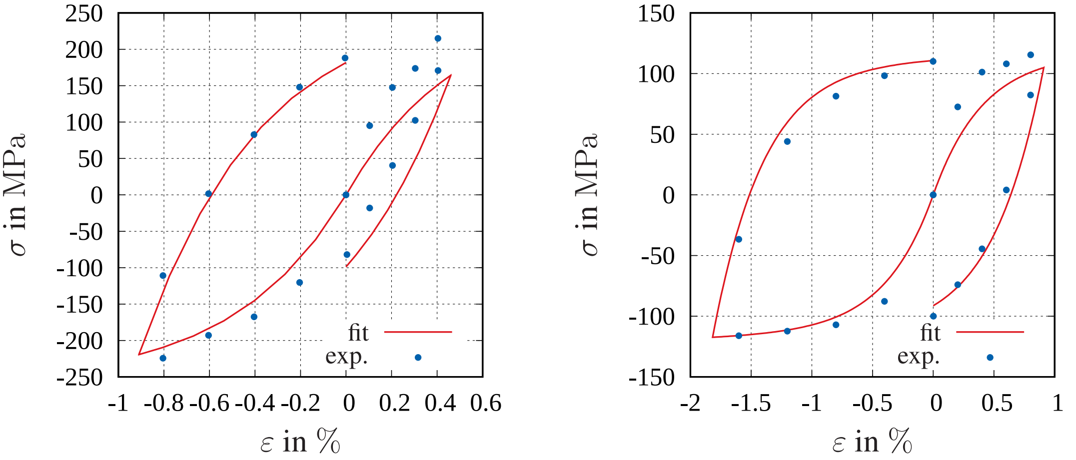

(a) $\Theta = -40\,^\circ\mathrm{C}$ (b) $\Theta = 20\,^\circ\mathrm{C}$

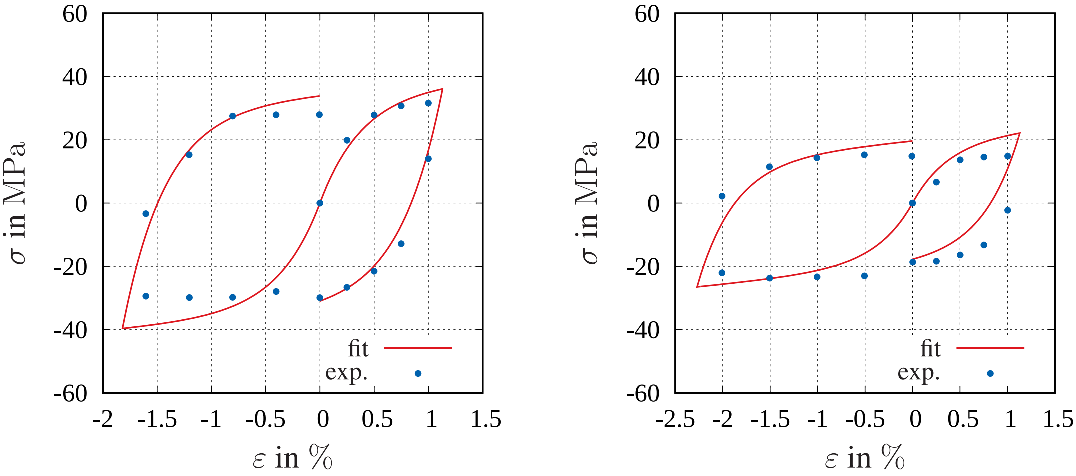

(c) $\Theta = 60\,^\circ\mathrm{C}$ (d) $\Theta = 85\,^\circ\mathrm{C}$

Figure 5.15: Results of the parameter identification for tension and compression

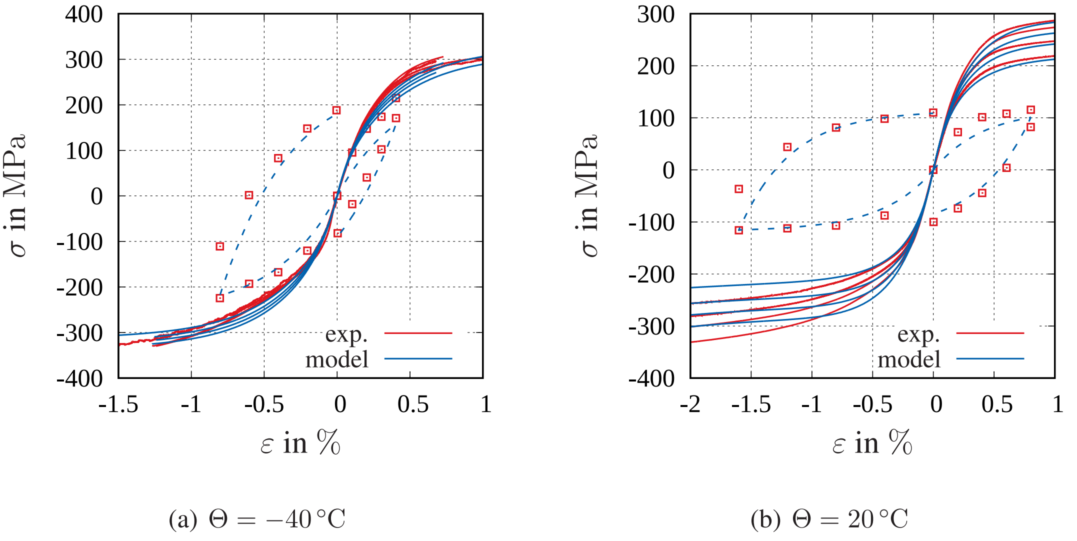

(a) $\Theta = -40\,°\mathrm{C}$ (b) $\Theta = 20\,°\mathrm{C}$

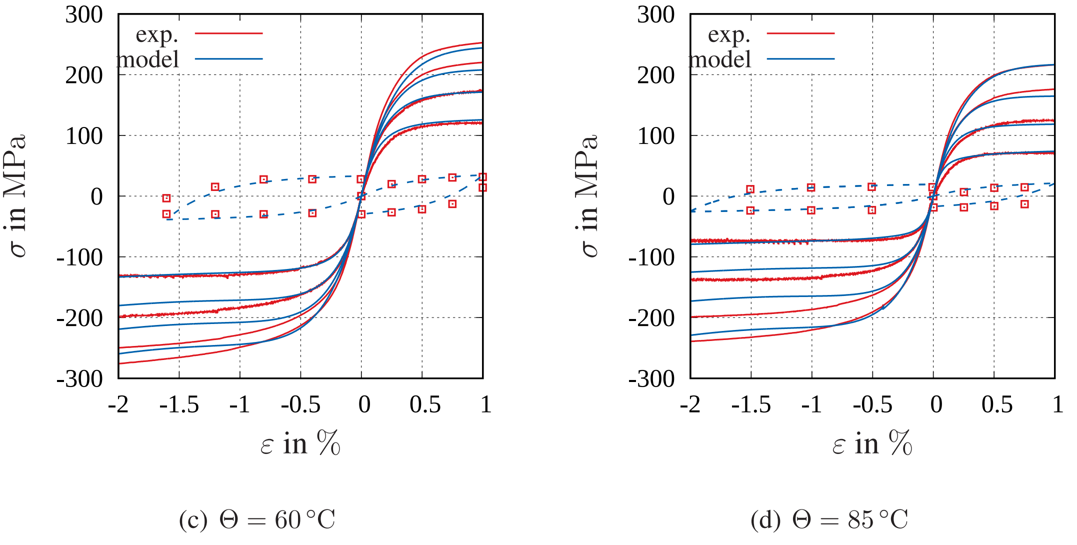

(c) $\Theta = 60\,°\mathrm{C}$ (d) $\Theta = 85\,°\mathrm{C}$

Figure 5.16: Prediction in tension and compression with the identified parameters, without aging

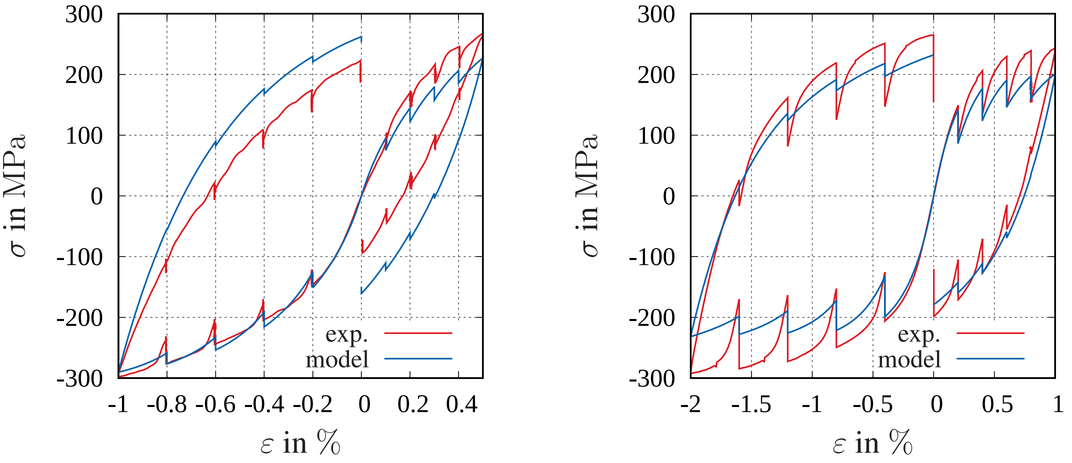

(a) $\Theta = -40\,°\text{C}$ (b) $\Theta = 20\,°\text{C}$

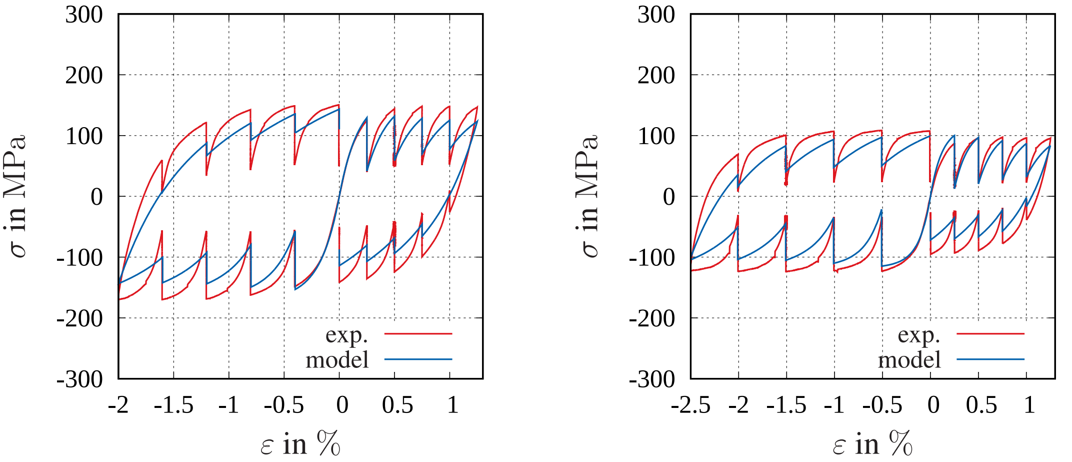

(c) $\Theta = 60\,°\text{C}$ (d) $\Theta = 85\,°\text{C}$

Figure 5.17: Prediction of the multi-step relaxation test in tension and compression, without aging

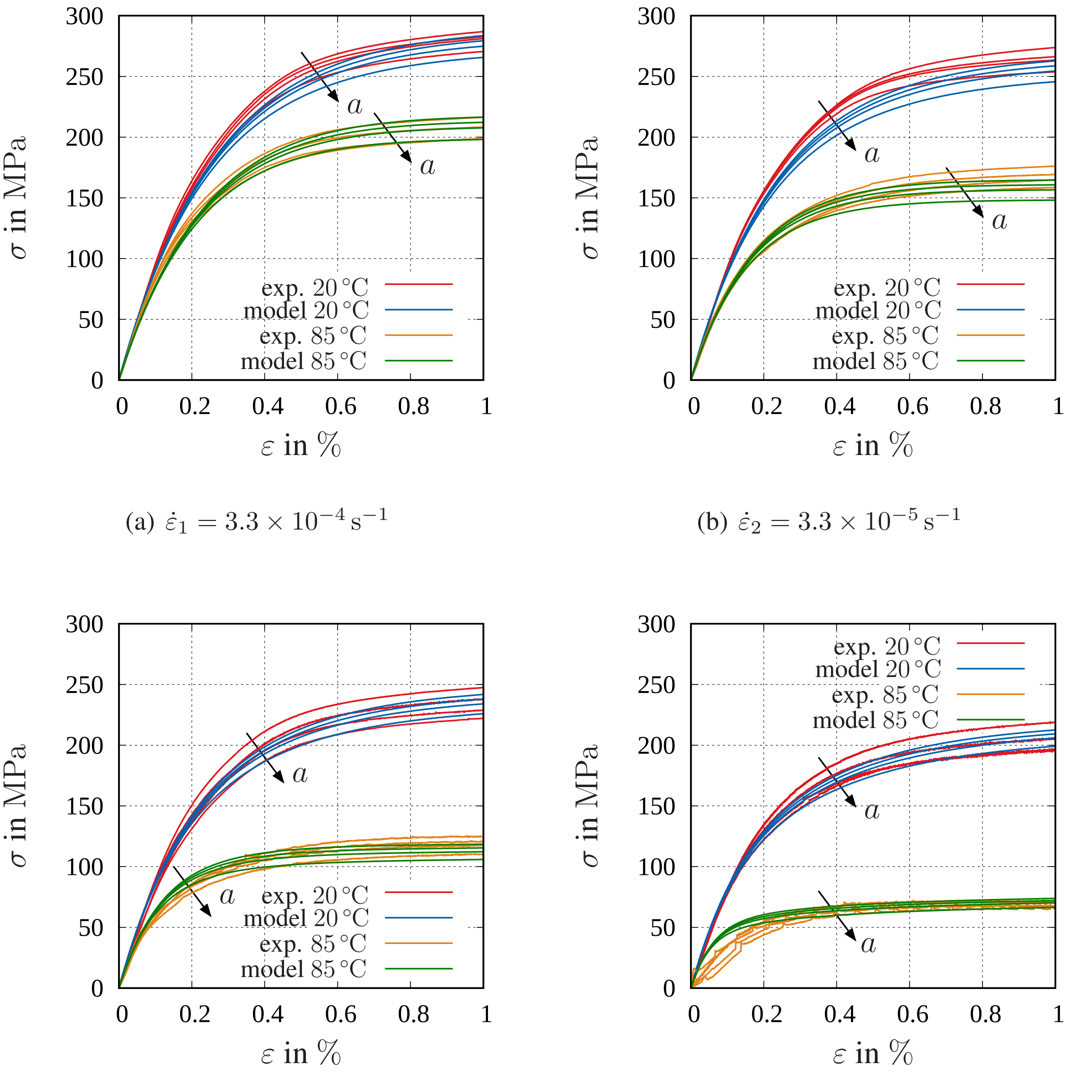

(a) $\dot{\varepsilon}_1 = 3.3 \times 10^{-4}\,\mathrm{s}^{-1}$

(b) $\dot{\varepsilon}_2 = 3.3 \times 10^{-5}\,\mathrm{s}^{-1}$

(c) $\dot{\varepsilon}_3 = 3.3 \times 10^{-5}\,\mathrm{s}^{-1}$

(d) $\dot{\varepsilon}_4 = 3.3 \times 10^{-7}\,\mathrm{s}^{-1}$

Figure 5.18: Predictions of the model for the aging behavior for two different temperatures and four strain-rates. The arrow points in the direction of growing aging times

5.5 Identification for Finite Deformations

Using the modeled temperature and aging-dependent functions in the case of small deformations, a re-identification can be performed with the model of finite deformations. For the finite deformations model, the case of torsion is not purely deviatoric anymore, since a reaction force in longitudinal direction appears. Thus, the uniaxial tension/compression experiments are used in the identification with the help of the procedure exposed in Krämer et al. (2015). The modular structure of the model is used for the identification again. The parameters of the equilibrium stress state are identified first with the equilibrium hysteresis and the overstress with the experiments at different strain-rates and multi-step relaxation tests.

Since the torsion tests are not used in the identification of this model – and because there is no information about the lateral contraction of the material at hand – it is not possible to identify the bulk modulus properly, based only on the axial information of the tensile tests. This parameter is then taken from the identification of the results of the small strains case. The relation between the bulk modulus in the small K_{eq} and large deformation case K is after geometric linearization

$$K = K_{\text{eq}} = 49.5\,\text{GPa}, \tag{5.37}$$

see also the appendix. Moreover, the parameter c_{10} corresponds to the shear modulus of the elastic equilibrium stress G_{eq}. This parameter has a minor influence on the model and is set to the value $100\,\text{MPa}$ as in the model for small deformations, see Section 5.4.1. The relation between the parameters of both models is

$$c_{10} = \frac{G_{\text{eq}}}{2} = 0.05\,\text{GPa}. \tag{5.38}$$

These two parameters K and c_{10} are taken form the small deformations case in order to prevent correlation between the parameters. The identification is performed with the help of the in-house code “mat1D”, which simulates the material behavior under the assumption of homogeneity, and the optimization scheme proposed in Krämer et al. (2015) for uniaxial tension/compression for large deformation. The initial values of the identification steps correspond to the identified values for the model of small deformations, since it is reasonable to assume that the parameters are in a similar range.

Equilibrium state

The set of parameters of the equilibrium stress state $\boldsymbol{\kappa} = \{\hat{b}, \hat{c}_1, \hat{c}_2, \hat{c}_3, \hat{\Theta}_c\}$ in Eq. (4.157) is identified with the equilibrium hysteresis in tension and compression at different temperatures. The results of the identification of the equilibrium state are shown in Tab. 5.10 and Fig. 5.19. Here, σ_R represents the axial component of 1st Piola-Kirchhof tensor and λ the stretch.

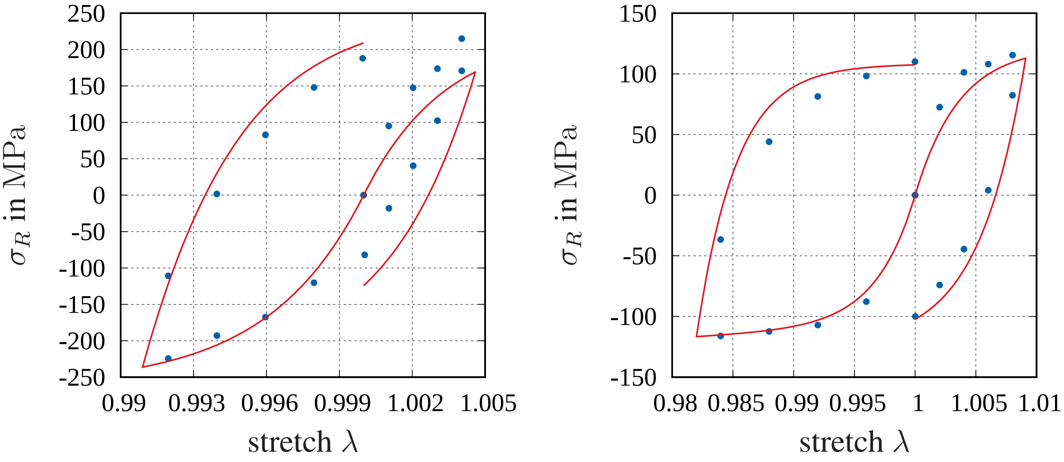

(a) $\Theta = -40\,°\mathrm{C}$ (b) $\Theta = 20\,°\mathrm{C}$

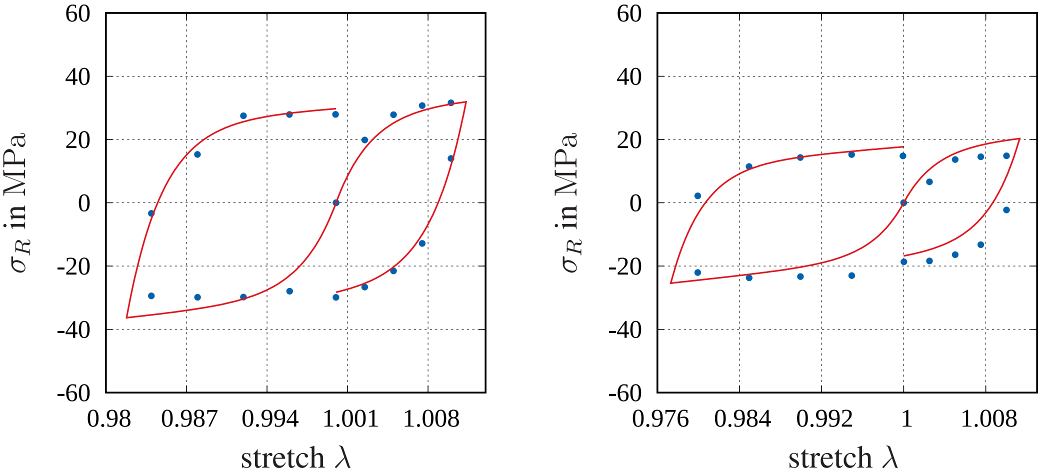

(c) $\Theta = 60\,°\mathrm{C}$ (d) $\Theta = 85\,°\mathrm{C}$

Figure 5.19: Results of the identification in tension/compression for the equilibrium stress state for the different temperatures. The experiments are represented by points and the model with lines.

Table 5.10: Identified parameters of the equilibrium stress part in tension/compression

parameter	$\hat{b}$	$\hat{c}_1$	$\hat{c}_2$	$\hat{c}_3$	$\hat{\Theta}_c$
	–	MPa	MPa	–	K
initial value	54.77	5793.5	1.1	0.24	283.44
final value	58.94	5924.8	1.12	0.0279	288.03
conf. interval	4.14	541.5	0.02	0.0019	3.77

The correlation matrix is equal to

$$\mathsf{R} = \left[\begin{array}{cccccc} & \hat{b} & \hat{c}_1 & \hat{c}_2 & \hat{c}_3 & \hat{\Theta}_c \\ \hat{b} & 1 & 0.342 & 0.114 & 0.033 & 0.146 \\ \hat{c}_1 & & 1 & -0.617 & -0.516 & -0.729 \\ \hat{c}_2 & & & 1 & 0.865 & 0.602 \\ \hat{c}_3 & & & & 1 & 0.689 \\ \hat{\Theta}_c & & & & & 1 \end{array}\right] . \tag{5.39}$$

Overstress

In the identification process of the overstress, the parameters of the shear modulus μ_{ov} are identified first. After that, the parameters of the viscosity η are found. Here, the temperature dependence is the first feature to be considered. These two identifications are performed with the experiments without aging, which are 40 experimental curves in total: four different strain-rates plus the multi-step relaxation test at four different temperatures and for tension and compression. In the last step, the aging dependence is identified. Here, the experiments with different aging times are used.

Shear Modulus For the identification of the shear modulus, there are three parameters that have to be identified: $\boldsymbol{\kappa} = \{\hat{G}_0, \hat{\alpha}_{\text{ov}}, \hat{n}_{\text{ov}}\}$. The parameter of the softening is set to the value $\alpha_k = 350$, analogously to the small deformations case, so that it reaches the value 1 at the end of the loading. During this identification, the value of the viscosity is identified independently for every strain-rate and temperature for the material without aging η_{im}, similar to the identification of the small strains case, but these values η_{im} are not used. The results of the identification are shown in Tab. 5.11. The correlation matrix is equal to

$$\mathsf{R} = \left[\begin{array}{cccc} & \hat{G}_0 & \hat{\alpha}_{\text{ov}} & \hat{n}_{\text{ov}} \\ \hat{G}_0 & 1 & -0.324 & 0.496 \\ \hat{\alpha}_{\text{ov}} & & 1 & 0.608 \\ \hat{n}_{\text{ov}} & & & 1 \end{array}\right] . \tag{5.40}$$

Table 5.11: Results of the parameter identification for μ_{ov}, see Eq. (4.158)

parameter	$\hat{G}_0$ MPa	$\hat{\alpha}_{\mathrm{ov}}$ –	$\hat{n}_{\mathrm{ov}}$ –
initial value	1.604×10^4	2.0×10^{-1}	3.5×10^{-1}
final value	1.424×10^4	2.531×10^{-1}	3.349×10^{-1}
conf. interval	15.3	5.71×10^{-4}	6.8×10^{-4}

Viscosity With the known parameters of the shear modulus of Tab. 5.11, the first identification of the viscosity parameters is performed. Here, we identify the parameters $\boldsymbol{\kappa} = \{\hat{\Theta}_\eta, \hat{r}_{\eta 1}, \hat{\Theta}_r, \hat{n}_\eta, \hat{\alpha}_{\eta 1}, \hat{\alpha}_{\eta 2}\}$, which are related to the temperature and rate-dependence. A value for the function $\hat{\eta}_0(a = 0) = \hat{\eta}_{01} - \hat{\eta}_{02}$, see Eq. (4.160), is identified, but it is not used.Tab. 5.12 shows the results of the identification. Here, we observe that the values change very little from the identified values for the small deformations model, but the confidence intervals are generally very small. The correlation matrix is equal to

Table 5.12: Results of the parameter identification for the temperature-dependence of the viscosity

parameter	$\hat{\Theta}_\eta$ K	$\hat{r}_{\eta 1}$ –	$\hat{\Theta}_r$ K	$\hat{n}_\eta$ K^{-1}	$\hat{\alpha}_{\eta 1}$ –	$\hat{\alpha}_{\eta 2}$ K^{-1}
initial value	373.6	0.480	426.3	0.0115	1.26×10^{-9}	0.0135
final value	375.2	0.479	428.2	0.0117	3.47×10^{-10}	0.0173
conf. interval	0.837	2.8×10^{-4}	0.192	9.7×10^{-6}	4.80×10^{-11}	4.1×10^{-4}

$$\mathbf{R} = \left[\begin{array}{ccccccc} & \hat{\Theta}_\eta & \hat{r}_{\eta 1} & \hat{\Theta}_r & \hat{n}_\eta & \hat{\alpha}_{\eta 1} & \hat{\alpha}_{\eta 2} \\ \hat{\Theta}_\eta & 1 & 0.916 & -0.876 & -0.645 & 0.394 & -0.391 \\ \hat{r}_{\eta 1} & & 1 & -0.826 & -0.539 & 0.405 & -0.386 \\ \hat{\Theta}_r & & & 1 & 0.222 & -0.452 & 0.452 \\ \hat{n}_\eta & & & & 1 & -0.136 & 0.134 \\ \hat{\alpha}_{\eta 1} & & & & & 1 & -0.997 \\ \hat{\alpha}_{\eta 2} & & & & & & 1 \end{array}\right] . \tag{5.41}$$

Here, we can observe a strong correlation between the parameters $\hat{\Theta}_\eta$, $\hat{r}_{\eta 1}$, and $\hat{\Theta}_r$, which consider the temperature dependence of the functions $\hat{\eta}_0$ and $\hat{r}_\eta$, and also between the parameters $\hat{\alpha}_{\eta 1}$ and $\hat{\alpha}_{\eta 2}$ from the function $\hat{\alpha}_\eta(\Theta)$.

Finally, the parameters of the aging dependence are identified. To this end, the identification for the value $\hat{\eta}_0(a)$ is performed separately for each aging time. After that, the function with the aging dependence $\hat{\eta}_0(a) = \hat{\eta}_{01} - \hat{\eta}_{02}\exp(\hat{\eta}_{03}a)$ is fitted with the identified points using the Matlab fitting tool. The results are shown in Tab. 5.13 and Fig. 5.20. The results of the identification of the temperature dependence are shown in Fig. 5.21 and the aging dependence in Fig. 5.22. Additional results are shown in the appendix. One can observe a very good agreement between the experiments and the fit for the tensile tests, and a good agreement for compression. The difference originates in the tension/compression asymmetry, which is not considered in the model.

Table 5.13: Results of the parameter identification for the viscosity function $\hat{\eta}_0(a)$ of Eq. (4.160)

parameter	$\hat{\eta}_{01}$ $\mathrm{MPa\,s}$	$\hat{\eta}_{02}$ $\mathrm{MPa\,s}$	$\hat{\eta}_{03}$ $-$
initial value	0.265	0.068	0.305
final value	1612	81.93	1.862
conf. interval	285.75	9.6	0.78

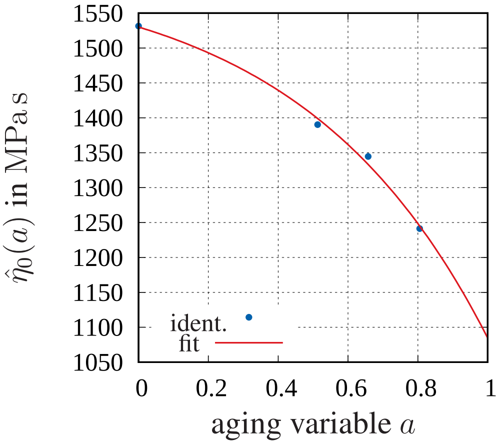

Figure 5.20: Identification of the aging-dependence of the viscosity function $\hat{\eta}_0(a)$

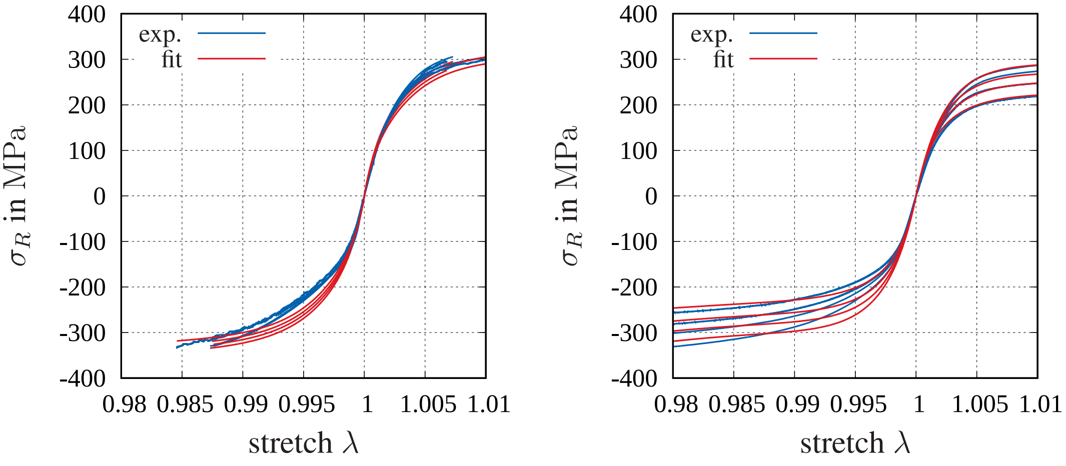

(a) $\Theta = -40\,^\circ\mathrm{C}$ (b) $\Theta = 20\,^\circ\mathrm{C}$

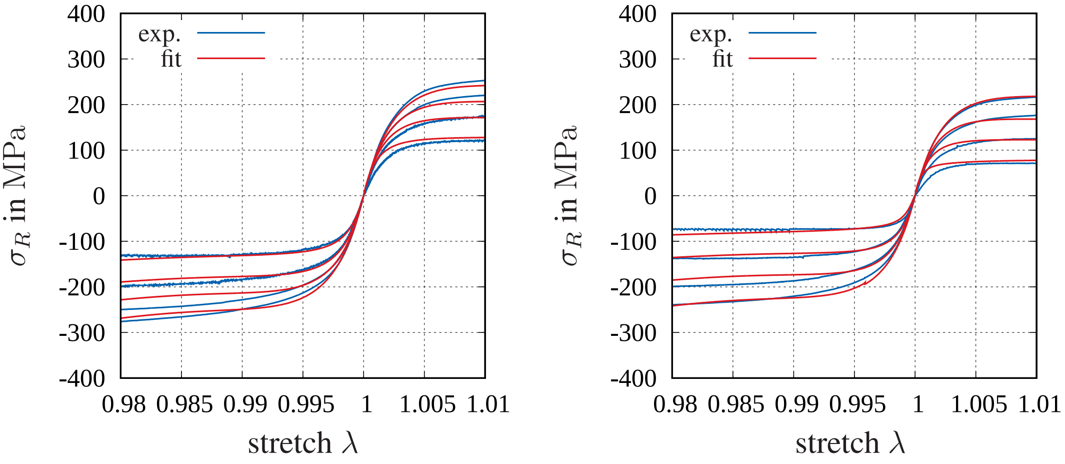

(c) $\Theta = 60\,^\circ\mathrm{C}$ (d) $\Theta = 85\,^\circ\mathrm{C}$

Figure 5.21: Results of the identification in tension/compression for the overstress for the different temperatures (experiments and fit without aging)

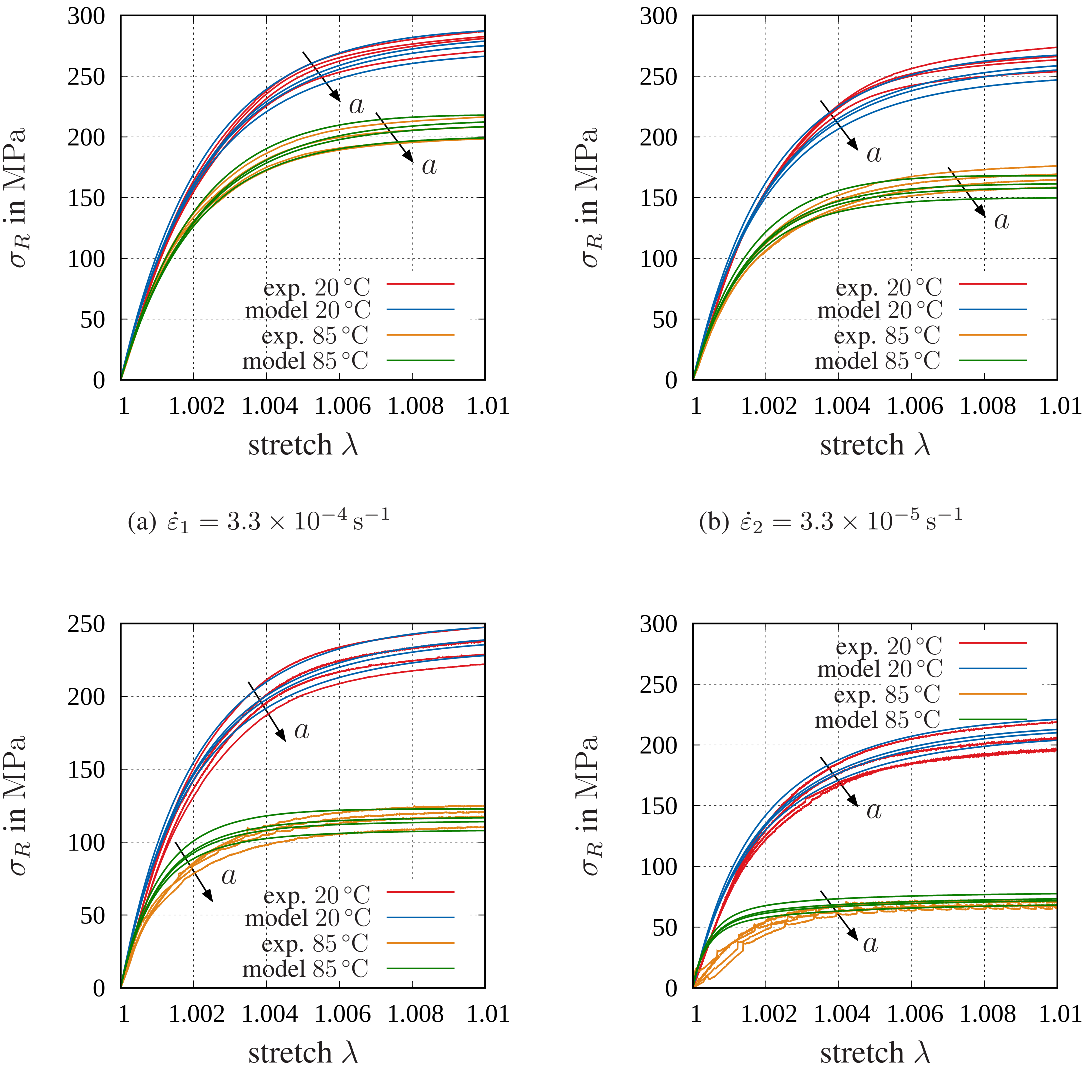

(a) $\dot{\varepsilon}_1 = 3.3 \times 10^{-4}\,\mathrm{s}^{-1}$

(b) $\dot{\varepsilon}_2 = 3.3 \times 10^{-5}\,\mathrm{s}^{-1}$

(c) $\dot{\varepsilon}_3 = 3.3 \times 10^{-5}\,\mathrm{s}^{-1}$

(d) $\dot{\varepsilon}_4 = 3.3 \times 10^{-7}\,\mathrm{s}^{-1}$

Figure 5.22: Results of the identification for the aging dependence. Experiments and fit at two different temperatures for all strain-rates and aging times. The arrow points in the direction of growing aging times

5.6 Summary of Identification of the Mechanical Part

Tab. 5.14 represents a summary of the identified parameters for the small deformations model and the finite deformations model. The parameters of the large deformations model, which were taken from the small deformations case, are marked in gray. Comparing Fig. 5.16 and Fig. 5.21, one can observe that the fit of the tensile and compression experiments is better in the case of finite deformations than for small deformations. The reason for this is that the tensile tests in the case of small deformations were used to identify only one parameter, while the experiments served as a basis to perform the entire identification in the case of large deformations. Both models can reproduce the experimental observations for the monotonic loading paths and the equilibrium hysteresis in a good manner. The unloading is reproduced adequately as well, as can be seen in the simulation of the multi-step relaxation tests. Moreover, the model can describe the relaxation behavior only moderately. As mentioned in Section 5.4.1, in order to model this behavior, it would be necessary to include three Maxwell-elements, which would increase the number of material parameters and internal variables by a huge amount. Additionally, Tab. 5.14 shows that although the case of small deformations was mostly identified with the torsion tests and the finite deformations case was identified with tensile and compression tests, the identified parameters for both cases are very similar if the following relations are taken into account after linearizing the finite strains model, see the appendix,

$$K = K_{\text{eq}}, \;\; c_{10} = \frac{G_{\text{eq}}}{2}, \;\; \hat{b} = \frac{b}{4}, \;\; \mu_{\text{eq}} = \frac{c}{4}, \;\; \mu_{\text{ov}} = \frac{G_{\text{ov}}}{2}, \;\; \eta = \hat{\eta}.$$

Table 5.14: Summary of the identification

parameter small strains	value	parameter finite strains	value	dimension
K_{eq}	4.95×10^4	K	4.95×10^4	MPa
G_{eq}	100	c_{10}	50	MPa
b	219.079	$\hat{b}$	58.94	–
c_1	2.317×10^4	$\hat{c}_1$	5.925×10^3	MPa
c_2	1.10	$\hat{c}_2$	1.12	MPa
c_3	0.024	$\hat{c}_3$	0.028	K^{-1}
Θ_c	283.44	$\hat{\Theta}_c$	288.03	K
α_k	350	$\hat{\alpha}_k$	350	–
G_0	3.208×10^4	$\hat{G}_0$	1.424×10^4	MPa
α_{ov}	0.2	$\hat{\alpha}_{\text{ov}}$	0.253	–
n_{ov}	0.35	$\hat{n}_{\text{ov}}$	0.335	–
η_{01}	1550	$\hat{\eta}_{01}$	1612	MPa s
η_{02}	6.357	$\hat{\eta}_{02}$	81.93	MPa s
η_{03}	4.518	$\hat{\eta}_{03}$	1.862	–
Θ_η	373.6	$\hat{\Theta}_\eta$	375.2	K
$r_{\eta 1}$	0.495	$\hat{r}_{\eta 1}$	0.479	–
Θ_r	426.3	$\hat{\Theta}_r$	428.2	K
n_η	0.012	$\hat{n}_\eta$	0.012	K^{-1}
$\alpha_{\eta 1}$	1.26×10^{-9}	$\hat{\alpha}_{\eta 1}$	3.47×10^{-10}	–
$\alpha_{\eta 2}$	0.0136	$\hat{\alpha}_{\eta 2}$	0.0173	K^{-1}

5.7 Identification of Thermo-Physical Properties

The last parameters that have to be calibrated are the thermal expansion coefficient α_Θ, the specific heat capacity c_p, and the thermal diffusivity $\hat{\lambda}$. The two first variables can be calibrated easily, since they depend only linearly on the temperature. The identification process for the thermal diffusivity is related to the modeling process and is more complicated because of its dependence on the aging variable. Once all these parameters are known, the thermal conductivity can be determined.

Thermal Expansion

The dilatometric measurements versus temperature of Section 3.6.1 show a clear linear thermal expansion in the investigated temperature range. The thermal expansion coefficient is then identified equal to $\alpha_\Theta = 2.8109 \times 10^{-5}\,\text{K}^{-1}$, with the reference temperature $\Theta_0 = 20\,°\text{C}/293.15\,\text{K}$, see Fig. 5.23(a).

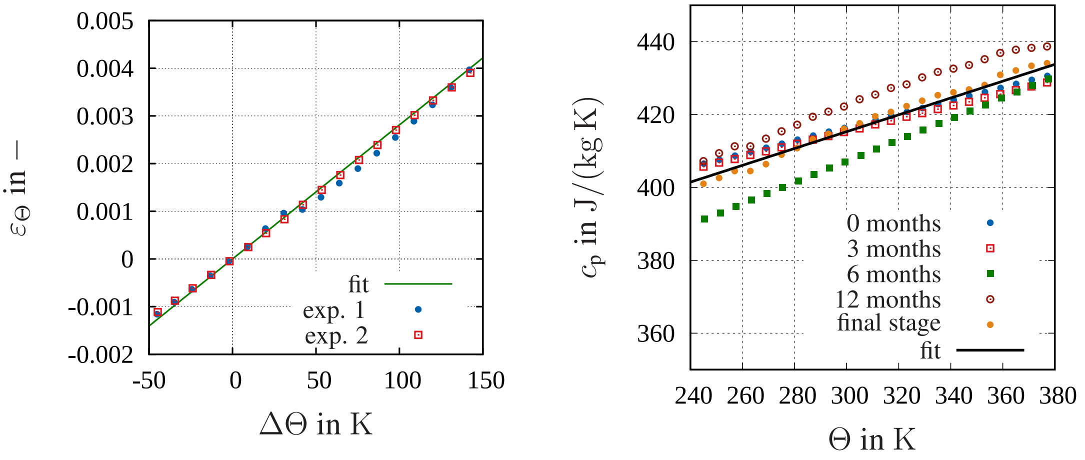

(a) Thermal expansion, $\Theta_0 = 20\,°\text{C}/293.15\,\text{K}$

(b) Specific heat capacity over the temperature for different aging times

Figure 5.23: Results of the identification for the thermal expansion and the specific hear capacity

Specific Heat Capacity

The parameters of the linear function of the specific heat capacity, see Eq. (4.177), are identified with the measurements of Section 3.7.3. The identified parameters are $c_\text{p1} = 413.724\,\text{J}\,\text{kg}^{-1}\text{K}^{-1}$ and $c_\text{p2} = 5.581 \times 10^{-4}\,\text{K}^{-1}$, see Fig. 5.23(b).

Thermal Diffusivity

The identification of the thermal diffusivity is carried out in two steps. In Eq. (4.178), the thermal diffusivity is expressed as a weighting between the initial unaged stage $\hat{\lambda}_0(\Theta)$ and the final stage $\hat{\lambda}_\infty(\Theta)$ by means of a weighting factor $f_{\hat{\lambda}}(\Theta, a)$

$$\hat{\lambda}(\Theta, a) = \hat{\lambda}_\infty(\Theta) f_{\hat{\lambda}}(\Theta, a) + \hat{\lambda}_0(\Theta)(1 - f_{\hat{\lambda}}(\Theta, a)). \tag{4.178}$$

In the first step, the initial and final stage are identified and, afterwards, the weighting factor is determined. In the first step of identification, the functions $\hat{\lambda}_0(\Theta)$ and $\hat{\lambda}_\infty(\Theta)$ have a total number of four parameters to be identified $\boldsymbol{\kappa} = \{\hat{\lambda}_{\infty 1}, \hat{\lambda}_{\infty 2}, \hat{\lambda}_{01}, \hat{\lambda}_{02}\}$. The parameter Θ_0 corresponds to the reference temperature and is set to $\Theta_0 = 293.15\,\mathrm{K}$,

$$\hat{\lambda}_\infty(\Theta) = \hat{\lambda}_{\infty 1} - \hat{\lambda}_{\infty 2}\Theta, \tag{4.179}$$

$$\hat{\lambda}_0(\Theta) = \hat{\lambda}_{01} - \hat{\lambda}_{02}(1 + \tanh(\Theta - \Theta_0))(\Theta - \Theta_0). \tag{4.180}$$

The identification of these parameter is carried out with the measurements over the temperature for the unaged specimen ($a = 0$ and $f_{\hat{\lambda}}(\Theta, 0) = 0$) and the completely aged specimen ($a = 1$ and $f_{\hat{\lambda}}(\Theta, 1) = 1$). The results of this identification are summarized in Tab. 5.15 and in Fig. 5.25, represented by black and blue lines. Additionally, a function for the weighting factor has to be found. To this end, an experimental value for $f_{\hat{\lambda}\text{exp}}$ is calculated with the help of Eq. (4.178) using the experimental points by

Table 5.15: Results of the parameter identification of the functions $\hat{\lambda}_0(\Theta)$ and $\hat{\lambda}_\infty(\Theta)$

parameter	$\hat{\lambda}_{\infty 1}$ $\mathrm{mm^2s^{-1}}$	$\hat{\lambda}_{\infty 2}$ $\mathrm{mm^2s^{-1}K^{-1}}$	$\hat{\lambda}_{01}$ $\mathrm{mm^2s^{-1}}$	$\hat{\lambda}_{02}$ $\mathrm{mm^2s^{-1}K^{-1}}$
initial value	1	1	42	5.0×10^{-3}
final value	55.07	2.92×10^{-2}	41.74	4.63×10^{-3}
conf. interval	0.345	0.12×10^{-2}	0.074	1.2×10^{-3}

$$f_{\hat{\lambda}\text{exp}}(\Theta_i, a_j) = \frac{\hat{\lambda}_{\text{exp}}(\Theta_i, a_j) - \hat{\lambda}_{\text{exp}}(\Theta_i, 0)}{\hat{\lambda}_{\text{exp}}(\Theta_i, 1) - \hat{\lambda}_{\text{exp}}(\Theta_i, 0)}, \tag{5.42}$$

where $\hat{\lambda}_{\text{exp}}(\Theta_i, a_j)$ represents the measured point at the temperature Θ_i and the aging time a_j, $\hat{\lambda}_{\text{exp}}(\Theta_i, 0)$ denotes the initial stage ($a = 0$), and $\hat{\lambda}_{\text{exp}}(\Theta_i, 1)$ is the final stage ($a = 1$). The function $f_{\hat{\lambda}\text{exp}}$ is determined for the temperatures from $-60\,°\mathrm{C}$ to $20\,°\mathrm{C}$, since one can assume that the aging does not evolve during the time of the experiments for these temperatures. These experimental points are used to develop a function for the weighting factor

$$f_{\hat{\lambda}}(\Theta, a) = a - \alpha_{\hat{\lambda}}(\Theta)(1 - a)a^2, \quad \alpha_{\hat{\lambda}}(\Theta) = \alpha_{\hat{\lambda}1}\exp(-\alpha_{\hat{\lambda}2}\Theta). \tag{4.181}$$

The parameters of this function are identified in the following. At first, the factor $f_{\hat{\lambda}}(\hat{\Theta} = \text{const.}, a)$ is determined independently for each temperature. Afterwards, the function $\alpha_{\hat{\lambda}}(\Theta)$ is fitted to the results of this pre-identification. The results are shown in Fig. 5.24 and Tab. 5.16.

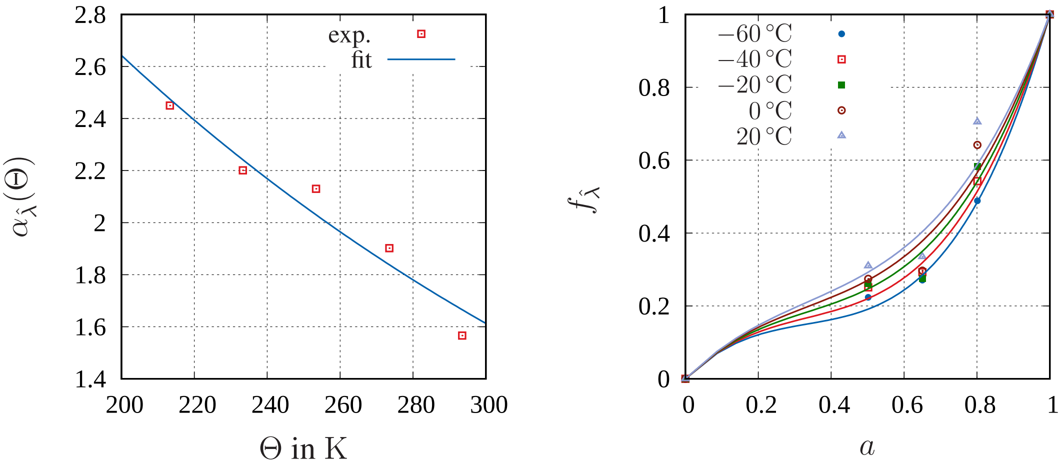

(a) Results of the identification of $\alpha_{\hat{\lambda}}(\Theta)$

(b) Experimentally determined weighting factor $f_{\hat{\lambda}\text{exp}}(\Theta_i, a_j)$ (points) and model (lines) over the aging variable for constant values of the temperature

Figure 5.24: Determination of the weighting factor $f_{\hat{\lambda}}(\Theta, a)$

Table 5.16: Results of the parameter identification of the weighting factor $f_{\hat{\lambda}}(\Theta, a)$

parameter	$\alpha_{\hat{\lambda}1}$ $-$	$\alpha_{\hat{\lambda}2}$ K^{-1}
initial value	1	10^{-2}
final value	7.093	4.937×10^{-3}
conf. interval	1.0	2.301×10^{-4}

The results of the entire identification of the thermal diffusivity are shown in Fig. 5.25. There, one can also see the small deviation between the simulation and the experiment for the 3 and 6 months old samples. However, the modeled function can reproduce properly the complex experimental behavior.

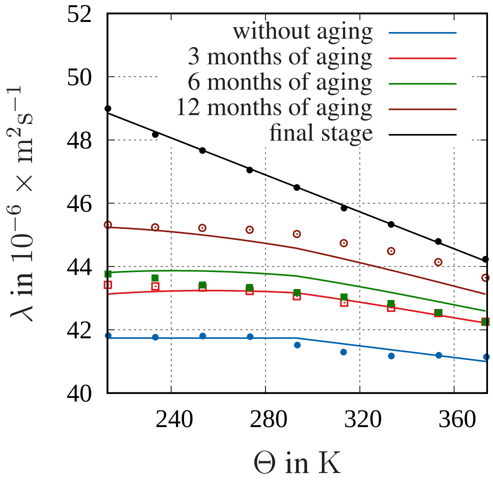

Figure 5.25: Results of the identification of the thermal diffusivity. Experimental values represented with points and model with lines

Thermal Conductivity

The identified values of the thermal diffusivity, the specific heat capacity, and the measured density are used to calculate the parameter of the thermal conductivity according to Eq. (4.182). The determined thermal conductivity is shown in Fig. 5.26 in dependence of the temperature for different aging times. A summary of the identified parameters for the thermal properties is given in Tab. 5.17.

Table 5.17: Summary of the parameter identification for the thermal properties

ρ	α_Θ	Θ_0	c_{p1}	c_{p2}	
$\mathrm{kg\,m^{-3}}$	$\mathrm{K^{-1}}$	K	$\mathrm{J\,kg^{-1}K^{-1}}$	$\mathrm{K^{-1}}$	
6.15×10^3	2.81×10^{-5}	293.15	413.72	5.58×10^{-4}	
$\hat{\lambda}_{\infty 1}$	$\hat{\lambda}_{\infty 2}$	$\hat{\lambda}_{01}$	$\hat{\lambda}_{02}$	$\alpha_{\hat{\lambda}1}$	$\alpha_{\hat{\lambda}2}$
$\mathrm{m^2s^{-1}}$	$\mathrm{m^2s^{-1}K^{-1}}$	$\mathrm{m^2s^{-1}}$	$\mathrm{m^2s^{-1}K^{-1}}$	–	$\mathrm{K^{-1}}$
5.51×10^{-5}	2.92×10^{-8}	4.17×10^{-5}	4.63×10^{-9}	7.09	4.94×10^{-3}

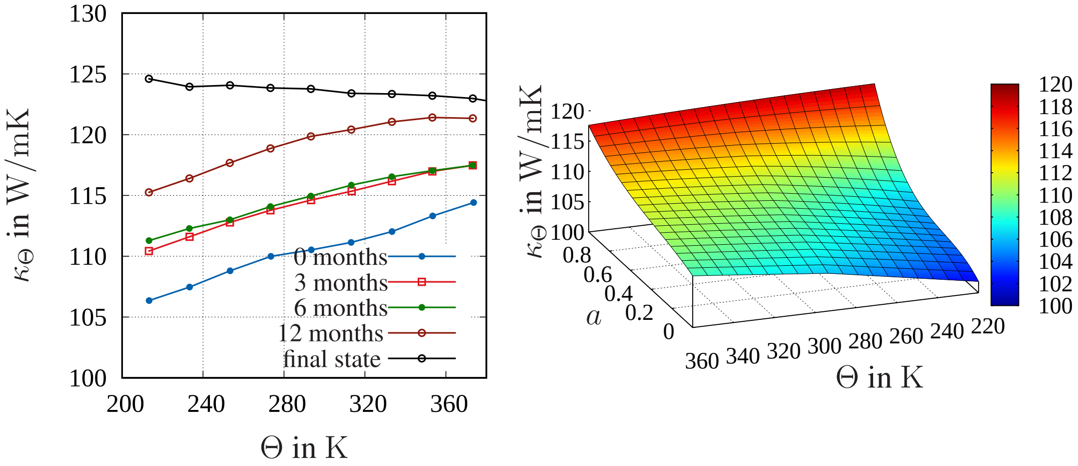

(a) Thermal conductivity for different aging times over the temperature

(b) 3D-representation of the function $\kappa_\Theta(\Theta, a)$

Figure 5.26: Determined thermal conductivity with the identified parameters

6 Initial Boundary Value Problem and Solution Procedure

The system of equations composed of the balance of linear momentum (2.54) and the heat equation (4.169), along with the constitutive relations to describe the material behavior developed in Chapter 4, provides a framework to determine the thermo-mechan ical response of a material body subjected to a series of mechanical and thermal loads. This system of equations – together with initial and boundary conditions – forms an initial boundary value problem (IBVP), which can generally not be solved analytically. Therefore, it is common to reformulate it into its variational form, to which the method of vertical lines (MOL) can be applied. The method of vertical lines, see (Schiesser, 1991), leads, after performing a spatial discretization of the local form of IBVP and a further time discretization, to a system of nonlinear equations. This system of equations can be solved with numerical methods.

In this chapter, the IBVP is presented first in its local form. Afterwards, its variational form is derived. Then, the spatial discretization with the Finite Element Method (FEM) is discussed, leading to a system of differential-algebraic equations (DAE-system). In the next step, the time discretization is performed using the Backward Euler method. The Multilevel Newton Algorithm (MLNA) is presented to solve the resulting nonlinear system of equations. The last part of the chapter addresses the stress algorithm for the models from Chapter 4 and serves to describe the consistent tangent computation.

6.1 Initial Boundary Value Problem

In this section, the local form of the initial boundary value problem (IBVP) is presented and its variational form is derived. In the present case, it is considered that the treated problems are quasi-static, so that inertia effects can be neglected. The remaining balance equations are also considered in the formulation of the problem. The balance of mass is fulfilled in solid mechanics, since the control volume coincides with the material body and no transfer of mass takes place through the outer surface. The balance of rotational momentum is fulfilled with the chosen definition of the material representation. Finally, by considering the thermodynamical consistence in Chapter 4, the energy and entropy balance equations are fulfilled.

6.1.1 Local Form of Initial Boundary Value Problem

The local form of the balance of linear momentum (2.54), and the heat equation (4.169), can be written as

$$\vec{0} = \operatorname{Div} \mathbf{T}_{\mathrm{R}} + \rho_{\mathrm{R}} \vec{k}, \tag{2.54}$$

$$c_{\mathrm{p}} \dot{\Theta} = -\frac{1}{\rho_{\mathrm{R}}} \operatorname{Div} \vec{q}_R + \omega. \tag{4.169}$$

Since, in the quasi-static case, one can assume that $\mathrm{d}\vec{v}/\mathrm{d}t \approx \vec{0}$ holds and that no volumetric heat source is considered $(r = 0)$. Here, the stress relation for a material point $\vec{X}$ over time can be expressed as a function of the deformation depending on the right Cauchy-Green tensor $\mathbf{C}$, the temperature Θ, and the vector of internal variables q

$$\tilde{\mathbf{T}}(\vec{X}, t) = \mathbf{h}(\mathbf{C}(\vec{X}, t), \Theta(\vec{X}, t), \mathsf{q}(\vec{X}, t)), \tag{6.1}$$

with the dependence between the first and second Piola-Kirchhoff tensor $\tilde{\mathbf{T}} = \mathbf{F}^{-1}\mathbf{T}_{\mathrm{R}}$. The internal variables follow evolution equations described by ordinary differential equations of first order

$$\dot{\mathsf{q}} = \mathsf{r}(\mathbf{C}(\vec{X}, t), \Theta(\vec{X}, t), \mathsf{q}(\vec{X}, t)). \tag{6.2}$$

In the presented constitutive model, the vector q is composed of the plastic strains, the viscous strains, the softening, and the aging variable $\mathsf{q}^{\mathrm{T}} = \{\bar{\mathbf{C}}_{\mathrm{p}}^{\mathrm{T}}, \bar{\mathbf{C}}_{\mathrm{v}}^{\mathrm{T}}, k, a\}$.

The IBVP requires initial conditions to be solved. Since inertia effects are neglected, it is not necessary to prescribe initial values for the velocity, see (Fritzen, 1997b). Nevertheless, the time-dependence of the solution is given by transient boundary conditions and time-dependent internal processes. Thus, initial conditions for the displacement, temperature, and the internal variables are necessary. These are given in the material representation by

$$\vec{u}(\vec{X}, t_0) = \vec{u}_0(\vec{X}), \qquad \forall \vec{X} \in \mathcal{R}[\mathcal{B}], \tag{6.3}$$

$$\Theta(\vec{X}, t_0) = \Theta_0(\vec{X}), \qquad \forall \vec{X} \in \mathcal{R}[\mathcal{B}], \tag{6.4}$$

$$\mathsf{q}(\vec{X}, t_0) = \mathsf{q}_0(\vec{X}), \qquad \forall \vec{X} \in \mathcal{R}[\mathcal{B}]. \tag{6.5}$$

The problem additionally requires boundary conditions to be completely defined. There are two kinds of boundary conditions: Dirichlet and Neumann boundary conditions. The Dirichlet boundary conditions are known as geometric boundary conditions. They specify the value of the displacement and temperature in certain border regions of the material body, respectively $\partial_{\mathrm{u}}\boldsymbol{\mathcal{R}}\,[\mathcal{B}]$ and $\partial_{\Theta}\boldsymbol{\mathcal{R}}\,[\mathcal{B}]$

$$\vec{u}(\vec{X}, t) = \bar{\vec{u}}(\vec{X}, t), \qquad \forall \vec{X} \in \partial_{\mathrm{u}}\boldsymbol{\mathcal{R}}\,[\mathcal{B}]\,, \tag{6.6}$$

$$\Theta(\vec{X}, t) = \bar{\Theta}(\vec{X}, t), \qquad \forall \vec{X} \in \partial_{\Theta}\boldsymbol{\mathcal{R}}\,[\mathcal{B}]\,. \tag{6.7}$$

Moreover, Neumann boundary conditions are also known as natural or dynamic boundary conditions. In the present case, they are defined for the stress vector $\partial_{\mathrm{s}}\boldsymbol{\mathcal{R}}\left[\mathcal{B}\right]$ and the heat flux $\partial_{\mathrm{q}}\boldsymbol{\mathcal{R}}\left[\mathcal{B}\right]$

$$\vec{t}_{\mathrm{R}} = \mathbf{T}_{\mathrm{R}}\vec{n}_{\mathrm{R}} = \vec{s}(\vec{X},t), \qquad \forall\vec{X} \in \partial_{\mathrm{s}}\boldsymbol{\mathcal{R}}\left[\mathcal{B}\right], \tag{6.8}$$

$$q_{\mathrm{R}} = -\vec{q}_R \cdot \vec{n}_{\mathrm{R}} = \hat{f}_q(\vec{X},t), \qquad \forall\vec{X} \in \partial_{\mathrm{q}}\boldsymbol{\mathcal{R}}\left[\mathcal{B}\right]. \tag{6.9}$$

In order to define the boundary conditions, the material surface $\partial\boldsymbol{\mathcal{R}}\left[\mathcal{B}\right]$ is divided, for simplicity, into subsets

$$\partial\boldsymbol{\mathcal{R}}\left[\mathcal{B}\right] = \partial_{\mathrm{u}}\boldsymbol{\mathcal{R}}\left[\mathcal{B}\right] \cup \partial_{\mathrm{s}}\boldsymbol{\mathcal{R}}\left[\mathcal{B}\right] = \partial_{\Theta}\boldsymbol{\mathcal{R}}\left[\mathcal{B}\right] \cup \partial_{\mathrm{q}}\boldsymbol{\mathcal{R}}\left[\mathcal{B}\right], \tag{6.10}$$

with

$$\partial_{\mathrm{u}}\boldsymbol{\mathcal{R}}\left[\mathcal{B}\right] \cap \partial_{\mathrm{s}}\boldsymbol{\mathcal{R}}\left[\mathcal{B}\right] = \varnothing, \quad \partial_{\Theta}\boldsymbol{\mathcal{R}}\left[\mathcal{B}\right] \cap \partial_{\mathrm{q}}\boldsymbol{\mathcal{R}}\left[\mathcal{B}\right] = \varnothing. \tag{6.11}$$

Eq. (6.11) implies that it is not possible to apply Dirichlet and Neumann boundary conditions at the same position. There is a third kind of boundary condition that is not treated in this work. It consists of a combination of Dirichlet and Neumann boundary conditions.

For heat transfer due to convection q_{cond} and radiation q_{rad}, the following expressions can be included in the problem, see, for example, (Rothe, 2015)

$$q_{\mathrm{cond}} = h_c(\Theta - \Theta_f), \qquad \text{for } \vec{x} \in \partial_{\Theta\,\mathrm{q}}\boldsymbol{\chi}_t\left[\mathcal{B}\right] \text{ and } t \in \left]t_i, t_e\right[, \tag{6.12}$$

$$q_{\mathrm{rad}} = \epsilon\sigma(\Theta^4 - \Theta_\infty^4), \qquad \text{for } \vec{x} \in \partial_{\Theta\,\mathrm{q}}\boldsymbol{\chi}_t\left[\mathcal{B}\right] \text{ and } t \in \left]t_i, t_e\right[. \tag{6.13}$$

Here, h_c is the heat transfer coefficient, Θ_f the fluid temperature, ϵ the emissivity of the material, σ the Stefan-Bolzmann constant, and Θ_∞ the temperature of the surroundings.

The entire thermo-mechanical problem is summarized in Tab. 6.1. Since this problem can generally not be solved analytically, a further treatment is required to make a numerical solution possible.

6.1.2 Variational Form of Initial Boundary Value Problem

The variational formulation of the IVBP, also known as *weak form*, is necessary to apply the Finite Element Method. In order to obtain this formulation, the local form is scalar multiplied with test functions and integrated over the volume of the material body. This implies a reduction of the order of the derivatives of the system by one, which increases the amount of admissible functions. Nevertheless, it can be shown that the weak and the strong form are equivalent in the analytical case, see (Hughes, 2000). For the case of finite deformations, it is more convenient to perform the derivations in the reference configuration, see (Zwienkiewicz et al., 2005). Moreover, mathematical tools such as the Gauss integral theorem and the Cauchy's divergence theorem are necessary for the

Table 6.1: Local form of initial boundary value problem

Find the displacement field $\vec{u}(\vec{X},t)$ and the temperature field $\Theta(\vec{X},t)$ in the region $\boldsymbol{\mathcal{R}}\,[\mathcal{B}] \times\,]t_0, t_e[$ solving the system of equations	
$\vec{0} = \mathrm{Div}\,\mathbf{T}_\mathrm{R} + \rho_\mathrm{R}\vec{k}$	(2.54)
$c_\mathrm{p}\dot{\Theta} = -1/\rho_\mathrm{R}\mathrm{Div}\,\vec{q}_R + \omega$	(4.169)
$\dot{\mathbf{q}} = \mathbf{r}(\mathbf{C}, \Theta, \mathbf{q})$	(6.2)
with the constitutive relations	
$\tilde{\mathbf{T}} = \mathbf{h}(\mathbf{C}, \Theta, \mathbf{q}), \qquad \tilde{\mathbf{T}} = \mathbf{F}^{-1}\mathbf{T}_\mathrm{R}$	(6.1)
$\vec{q}_R = -\boldsymbol{\kappa}^\mathrm{R}_\Theta \mathrm{Grad}\,\Theta, \qquad \boldsymbol{\kappa}^\mathrm{R}_\Theta = \kappa_\Theta(\det\mathbf{F})\mathbf{C}^{-1}$	(4.173)
for the initial values and boundary conditions	
$\vec{u}(\vec{X},t_0) = \vec{u}_0(\vec{X}), \quad \Theta(\vec{X},t_0) = \Theta_0(\vec{X}) \quad \mathbf{q}(\vec{X},t_0) = \mathbf{q}_0(\vec{X})$	
$\vec{u}(\vec{X},t) = \bar{\vec{u}}(\vec{X},t), \qquad \mathbf{T}_\mathrm{R}\vec{n}_\mathrm{R} = \vec{s}(\vec{X},t)$	
$\Theta(\vec{X},t) = \bar{\Theta}(\vec{X},t), \quad -\vec{q}_R\cdot\vec{n}_\mathrm{R} = \hat{f}_q(\vec{X},t)$	

derivations. The Cauchy's divergence theorem provides a product rule for the divergence of an scalar Ψ multiplying a vector variable $\vec{v}$ or a tensor variable $\mathbf{T}$

$$\mathrm{Div}\,(\Psi\vec{v}) = \mathrm{Grad}\,\Psi\cdot\vec{v} + \Psi\cdot\mathrm{Grad}\,\vec{v}, \tag{6.14}$$

$$\mathrm{Div}\,(\Psi\mathbf{T}) = \mathbf{T}\mathrm{Grad}\,\Psi + \Psi\mathrm{Div}\,\mathbf{T}. \tag{6.15}$$

The Gauss' integral theorem stipulates that an integral expression of the divergence of a vector $\vec{v}$ or a tensor variable $\mathbf{T}$ over the volume of a region V is equivalent to the integral over its outer surface A. This is expressed respectively by

$$\int_V (\mathrm{Div}\,\vec{v})\,\mathrm{d}V = \int_A \vec{v}\cdot\vec{n}\,\mathrm{d}A, \tag{6.16}$$

$$\int_V (\mathrm{Div}\,\mathbf{T})\,\mathrm{d}V = \int_A \mathbf{T}\vec{n}\,\mathrm{d}A, \tag{6.17}$$

where $\vec{n}$ denotes the normal vector to the outer surface A.

Weak Form of Balance of Momentum

In order to obtain the weak form of the balance of momentum, a set $\mathcal{F}_u$ of test functions $\delta\vec{u} \in \mathcal{F}_u$ is defined

$$\mathcal{F}_u := \left\{ \delta\vec{u} : \boldsymbol{\mathcal{R}}\left[\mathcal{B}\right] \rightarrow \mathbb{R}^3 | \delta\vec{u}(\vec{X}) = \vec{0} \text{ for } \vec{X} \in \partial_u \boldsymbol{\mathcal{R}}\left[\mathcal{B}\right] \right\}. \tag{6.18}$$

The test functions $\delta\vec{u}$ represent virtual displacements, which vanish at the positions where Dirichlet boundary conditions are applied. For the variational form, the Neumann boundary conditions are automatically satisfied in an integral manner, which simplifies the formulation of approximate solutions, see (Jeltsch-Fricker, 2007) and the literature cited therein. The local form of the balance of momentum (2.54) is multiplied by the test functions $\delta\vec{u}$ and is integrated over the volume

$$\int\limits_{\boldsymbol{\mathcal{R}}[\mathcal{B}]} \operatorname{Div} \mathbf{T}_{\mathrm{R}}(\vec{X},t) \cdot \delta\vec{u}(\vec{X}) \, \mathrm{d}V + \int\limits_{\boldsymbol{\mathcal{R}}[\mathcal{B}]} \rho_{\mathrm{R}}(\vec{X}) \vec{k}(\vec{X},t) \cdot \delta\vec{u}(\vec{X}) \, \mathrm{d}V = 0. \tag{6.19}$$

Considering the product rule

$$\operatorname{Div} \mathbf{T}_{\mathrm{R}} \cdot \delta\vec{u} = \operatorname{Div} (\mathbf{T}_{\mathrm{R}}^T \delta\vec{u}) - \mathbf{T}_{\mathrm{R}} \cdot \operatorname{Grad} \delta\vec{u}, \tag{6.20}$$

relation (6.17) and Eq. (2.36) are chosen to reformulate expression (6.19)

$$\int\limits_{\boldsymbol{\mathcal{R}}[\mathcal{B}]} \mathbf{T}_{\mathrm{R}} \cdot \operatorname{Grad} \delta\vec{u} \, \mathrm{d}V = \int\limits_{\boldsymbol{\mathcal{R}}[\mathcal{B}]} \rho_{\mathrm{R}} \vec{k} \cdot \delta\vec{u} \, \mathrm{d}V + \int\limits_{\partial_s \boldsymbol{\mathcal{R}}[\mathcal{B}]} \vec{t}_{\mathrm{R}} \cdot \delta\vec{u} \, \mathrm{d}A. \tag{6.21}$$

The second Piola-Kirchhoff stress tensor $\tilde{\mathbf{T}}$ is introduced instead of the first Piola-Kirchhoff stress tensor $\mathbf{T}_{\mathrm{R}}$ through the relation $\mathbf{T}_{\mathrm{R}} = \mathbf{F}\tilde{\mathbf{T}}$. Moreover, the scalar product $\tilde{\mathbf{T}} \cdot (\mathbf{F}^{\mathrm{T}} \operatorname{Grad} \delta\vec{u})$ can be formulated as

$$\tilde{\mathbf{T}} \cdot \left(\mathbf{F}^{\mathrm{T}} \operatorname{Grad} \delta\vec{u}\right) = \tilde{\mathbf{T}} \cdot \frac{1}{2} \left[\mathbf{F}^{\mathrm{T}} \operatorname{Grad} \delta\vec{u} + (\operatorname{Grad} \delta\vec{u})^T \mathbf{F}\right]. \tag{6.22}$$

Building the Gateaux derivative of the Green strain with respect to the virtual displacement $\mathrm{D}_{\vec{u}}\mathbf{E}\,(\vec{u})\,[\delta\vec{u}]$, one obtains the definition of the virtual Green strain tensor

$$\delta\mathbf{E} := \mathrm{D}_{\vec{u}}\mathbf{E}\,(\vec{u})\,[\delta\vec{u}] = \frac{1}{2}\left(\mathbf{F}^{\mathrm{T}} \operatorname{Grad} \delta\vec{u} + (\operatorname{Grad} \delta\vec{u})^T \, \mathbf{F}\right). \tag{6.23}$$

Inserting Eqns. (6.22) and (6.23) into Eq. (6.21), the balance of linear momentum in the weak form results in

$$\int\limits_{\boldsymbol{\mathcal{R}}[\mathcal{B}]} \tilde{\mathbf{T}} \cdot \delta\mathbf{E} \mathrm{d}V = \int\limits_{\boldsymbol{\mathcal{R}}[\mathcal{B}]} \rho_{\mathrm{R}} \vec{k} \cdot \delta\vec{u} \mathrm{d}V + \int\limits_{\partial_s \boldsymbol{\mathcal{R}}[\mathcal{B}]} \vec{t}_{\mathrm{R}} \cdot \delta\vec{u} \mathrm{d}A. \tag{6.24}$$

The weak form can also be expressed in the current configuration

$$\int\limits_{\boldsymbol{\chi}_t[\mathcal{B}]} \mathbf{T}(\vec{x},t)\cdot \operatorname{grad}\delta\vec{u}\,\mathrm{d}v = \int\limits_{\boldsymbol{\chi}_t[\mathcal{B}]} \rho(\vec{x},t)\vec{k}(\vec{x},t)\cdot\delta\vec{u}\,\mathrm{d}v + \int\limits_{\partial_{\mathrm{s}}\boldsymbol{\chi}_t[\mathcal{B}]} \vec{t}(\vec{x},t)\cdot\delta\vec{u}\,\mathrm{d}a. \tag{6.25}$$

Here, $\mathbf{T}$ denotes the Cauchy stress tensor from Eq. (2.38), and the relation between the material and spatial gradient $\operatorname{Grad}\delta\vec{u} = (\operatorname{grad}\delta\vec{u})\mathbf{F}$ has been considered.

Weak Form of Heat Conduction Equation

In order to obtain the weak form of the heat equation, test functions representing virtual temperatures $\delta\Theta \in \mathcal{F}_\Theta$ are introduced analogously

$$\mathcal{F}_\Theta := \left\{\delta\Theta : \boldsymbol{\mathcal{R}}\,[\mathcal{B}] \to \mathbb{R} \,|\, \delta\Theta(\vec{X}) = 0 \ \text{ for } \ \vec{X}\in\partial_\Theta\boldsymbol{\mathcal{R}}\,[\mathcal{B}]\right\}. \tag{6.26}$$

The local form of the heat equation (4.169) is multiplied with the test functions $\delta\Theta$ and subsequently integrated over the volume

$$\int\limits_{\boldsymbol{\mathcal{R}}[\mathcal{B}]} \rho_{\mathrm{R}}c_{\mathrm{p}}\dot{\Theta}\delta\Theta\mathrm{d}V = -\int\limits_{\boldsymbol{\mathcal{R}}[\mathcal{B}]} \operatorname{Div}\vec{q}_{\mathrm{R}}\delta\Theta\,\mathrm{d}V + \int\limits_{\boldsymbol{\mathcal{R}}[\mathcal{B}]} \rho_{\mathrm{R}}\omega\delta\Theta\mathrm{d}V. \tag{6.27}$$

Applying the divergence theorem to Eq. (6.27) and drawing on the product rule (6.16)

$$\operatorname{Div}\vec{q}_{\mathrm{R}}\cdot\delta\Theta = \operatorname{Div}(\vec{q}_{\mathrm{R}}\delta\Theta) - \vec{q}_{\mathrm{R}}\cdot\operatorname{Grad}\delta\Theta, \tag{6.28}$$

one obtains

$$\int\limits_{\boldsymbol{\mathcal{R}}[\mathcal{B}]} \rho_{\mathrm{R}}c_{\mathrm{p}}\dot{\Theta}\delta\Theta\,\mathrm{d}V = \int\limits_{\boldsymbol{\mathcal{R}}[\mathcal{B}]} \vec{q}_{\mathrm{R}}\cdot\operatorname{Grad}\delta\Theta\,\mathrm{d}V - \int\limits_{\partial_{\mathrm{q}}\boldsymbol{\mathcal{R}}[\mathcal{B}]} \vec{q}_{\mathrm{R}}\cdot\vec{n}_{\mathrm{R}}\delta\Theta\,\mathrm{d}A + \int\limits_{\boldsymbol{\mathcal{R}}[\mathcal{B}]} \rho_{\mathrm{R}}\omega\delta\Theta\mathrm{d}V. \tag{6.29}$$

With the constitutive relation (4.112), the variational form of the heat equation in the reference configuration is given by

$$\begin{aligned}\int\limits_{\boldsymbol{\mathcal{R}}[\mathcal{B}]} \rho_{\mathrm{R}}c_{\mathrm{p}}\dot{\Theta}\delta\Theta\,\mathrm{d}V + \int\limits_{\boldsymbol{\mathcal{R}}[\mathcal{B}]} \boldsymbol{\kappa}^{\mathrm{R}}_{\Theta}\operatorname{Grad}\Theta\cdot\operatorname{Grad}\delta\Theta\,\mathrm{d}V &= \\ -\int\limits_{\partial_{\mathrm{q}}\boldsymbol{\mathcal{R}}[\mathcal{B}]} \vec{q}_{\mathrm{R}}\cdot\vec{n}_{\mathrm{R}}\delta\Theta\,\mathrm{d}A + \int\limits_{\boldsymbol{\mathcal{R}}[\mathcal{B}]} \rho_{\mathrm{R}}\omega\delta\Theta\mathrm{d}V.\end{aligned} \tag{6.30}$$

The weak form in the current configuration is expressed by

$$\begin{aligned}\int\limits_{\boldsymbol{\chi}_t[\mathcal{B}]} \rho c_{\mathrm{p}}\dot{\Theta}\delta\Theta\,\mathrm{d}v + \int\limits_{\boldsymbol{\chi}_t[\mathcal{B}]} \kappa_\Theta\operatorname{grad}\Theta\cdot\operatorname{grad}\delta\Theta\,\mathrm{d}v &= \\ -\int\limits_{\partial_{\mathrm{q}}\boldsymbol{\chi}_t[\mathcal{B}]} \vec{q}\cdot\vec{n}\delta\Theta\,\mathrm{d}a + \int\limits_{\boldsymbol{\chi}_t[\mathcal{B}]} \rho\omega\delta\Theta\,\mathrm{d}v.\end{aligned} \tag{6.31}$$

A summary of the weak form of the IBVP is given in Tab. 6.2.

Table 6.2: Variational form of the coupled thermo-mechanical problem

Find the displacement field $\vec{u}(\vec{X}, t)$ and the temperature field $\Theta(\vec{X}, t)$ on the region $\boldsymbol{\mathcal{R}}\,[\mathcal{B}] \times\,]t_0, t_e[$ solving the equations system

$$\begin{aligned}\pi_u(\vec{u}, \Theta, \mathbf{q}, \delta\vec{u}) = & \int\limits_{\boldsymbol{\mathcal{R}}[\mathcal{B}]} \tilde{\mathbf{T}} \cdot \delta\mathbf{E}\,\mathrm{d}V - \int\limits_{\boldsymbol{\mathcal{R}}[\mathcal{B}]} \rho_{\mathrm{R}}\vec{k} \cdot \delta\vec{u}\,\mathrm{d}V \\ & - \int\limits_{\partial_{\mathrm{s}}\boldsymbol{\mathcal{R}}[\mathcal{B}]} \vec{t}_{\mathrm{R}} \cdot \delta\vec{u}\,\mathrm{d}A = 0, \quad \text{for all } \delta\vec{u} \in \mathcal{F}_u \end{aligned} \qquad (6.24)$$

$$\begin{aligned}\pi_\Theta(\vec{u}, \Theta, \mathbf{q}, \delta\vec{u}) = & \int\limits_{\boldsymbol{\mathcal{R}}[\mathcal{B}]} \rho_{\mathrm{R}}(c_{\mathrm{p}}\dot{\Theta} - \omega)\delta\Theta\,\mathrm{d}V - \int\limits_{\boldsymbol{\mathcal{R}}[\mathcal{B}]} \vec{q}_R \cdot \operatorname{Grad}\delta\Theta\,\mathrm{d}V \\ & + \int\limits_{\partial_{\mathrm{q}}\boldsymbol{\mathcal{R}}[\mathcal{B}]} \vec{q}_{\mathrm{R}} \cdot \vec{n}_{\mathrm{R}}\delta\Theta\,\mathrm{d}A = 0, \quad \text{for all } \delta\Theta \in \mathcal{F}_\Theta \end{aligned} \qquad (6.30)$$

with the constitutive relations

$$\tilde{\mathbf{T}} = \mathbf{h}(\mathbf{C}, \Theta, \mathbf{q}), \qquad \dot{\mathbf{q}} = \mathbf{r}(\mathbf{C}, \Theta, \mathbf{q}) \qquad (6.1), (6.2)$$

$$\vec{q}_R = -\boldsymbol{\kappa}^{\mathrm{R}}_\Theta \operatorname{Grad}\Theta, \qquad \boldsymbol{\kappa}^{\mathrm{R}}_\Theta = \kappa_\Theta(\det\mathbf{F})\mathbf{C}^{-1} \qquad (4.173)$$

for the initial values and boundary conditions

$$\vec{u}(\vec{X}, t_0) = \vec{u}_0(\vec{X}), \quad \Theta(\vec{X}, t_0) = \Theta_0(\vec{X}), \quad \mathbf{q}(\vec{X}, t_0) = \mathbf{q}_0(\vec{X})$$

$$\vec{u}(\vec{X}, t) = \bar{\vec{u}}(\vec{X}, t), \qquad \mathbf{T}_{\mathrm{R}}\vec{n}_{\mathrm{R}} = \vec{s}(\vec{X}, t)$$

$$\Theta(\vec{X}, t) = \bar{\Theta}(\vec{X}, t), \quad -\vec{q}_R \cdot \vec{n}_{\mathrm{R}} = \hat{f}_q(\vec{X}, t)$$

6.2 Numerical Solution

This section addresses the solution procedure of the IBVP in its weak form with the method of lines (MOL). The method of lines is a two-step procedure to solve partial differential equation, see (Schiesser, 1991; Großmann and Roos, 2005). Usually, the time and spatial variables are treated differently, see (Schiesser and Griffiths, 2009). The spatial discretization is performed first with the Finite Element Method (FEM), leaving the time variables continuous, see (Becker et al., 1981; Hughes, 2000). The method of vertical lines results from the following time discretization[1]. Basic descriptions of the FEM can be found in (Hughes, 2000; Simo and Hughes, 1998; Bathe, 1996; Zwienkiewicz and Taylor, 2005). For nonlinear processes, the works of Belytschko et al. (2000); Wriggers (2009) are mentioned. A comprehensive literature review of the topic is given in (Grafenhorst, 2018).

For the spatial discretization, different element formulations are possible. Within the h-version, which is the classical formulation, an increase in accuracy in the solution is reached with the refinement of the mesh. The ansatz functions for the approximation of the geometry and the primary variables of the model are composed of Lagrange-polynomials. The h-type elements are commonly based on linear or quadratic ansatz functions. In the p-version, the ansatz functions are formulated with higher order – and an increase in the accuracy can be obtained without a refinement of the mesh, merely with an increase in the polynomial order, see (Szabó and Babuška, 1991; Szabó et al., 2004; Szabo et al., 2004; Netz and Hartmann, 2015).

The spatial discretization leads to a system of differential-algebraic equations (DAE-system), which is discretized in time. The interpretation of the nonlinear finite element system as a DAE-system was proposed by Wittekindt (1991), Fritzen (1997a) and Ellsiepen and Hartmann (2001). By applying the method of vertical lines, it is possible to combine time-integration methods of higher order with the FEM – such as, for example, diagonal implicit Runge-Kutta (DIRK) methods, see (Hartmann, 2002), (Bier and Hartmann, 2006), (Hartmann et al., 2008a). An efficient time-step control is applied in (Hartmann et al., 2008b; Rothe et al., 2012; Hartmann and Bier, 2008). In (Diebels et al., 1999), an embedded error-controlled Runge-Kutta time integration procedure is applied in order to obtain an accurate solution in the presence of localization phenomena. Thermal problems are treated in (Quint et al., 2011), and thermo-mechanical problems are considered in e.g. (Birken et al., 2010; Hartmann et al., 2009; Quint, 2012; Hartmann and Rothe, 2013). An iteration-free procedure is applied with Rosenbrock methods in (Hamkar, 2013; Hartmann and Hamkar, 2010; Hamkar et al., 2012; Netz et al., 2013b). Moreover, for high order space and time discretization, the works (Netz et al., 2013a,b) have to be mentioned. A comparison between different time

---

[1] When the time discretization is performed first, followed by the spatial discretization, the method is known as method of horizontal lines, see (Lang, 2001; Deulhard and Bornemann, 2008). Alternatively, time and space can be discretized simultaneously, which is known as space-time Finite Element Method, see (Hughes and Hulbert, 1988; Hulbert and Hughes, 1990).

integration methods is given in (Rothe et al., 2012).

Finally, the resulting nonlinear system of equations is solved numerically. This can be done using the Newton-Raphson method (NRM), provided that no iterations are necessary to compute the internal variables on a local level, or otherwise with the Multilevel Newton Algorithm (MLNA), see (Rabbat et al., 1979; Hoyer and Schmidt, 1984; Hartmann, 2005). For a coupled problem, the solution procedure can be performed monolithically or partitioned, see (Rothe et al., 2015) for the case of thermoviscoplasticity. As mentioned in (Hartmann, 2005; Rothe, 2015), the solution of the discretized system from Tab. 6.2 with Abaqus can be interpreted as a solution with the MLNA.

6.2.1 Spatial Discretization with the Finite Element Method

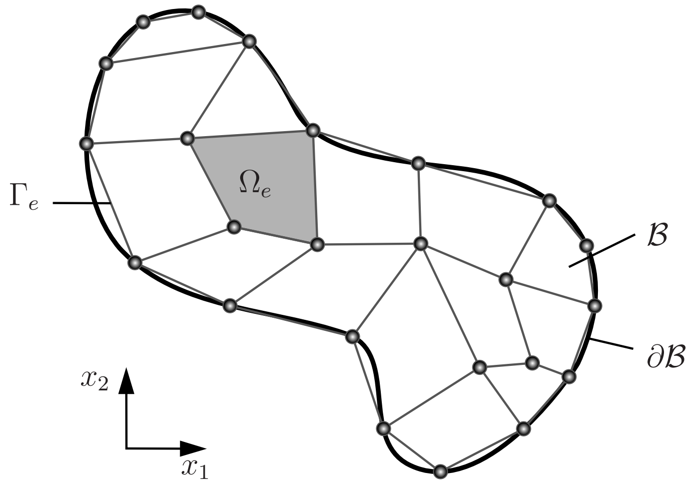

Figure 6.1: Representation of the spatial discretization with finite elements for a two-dimensional body

In the Finite Element Method, the material body $\mathcal{B}$ is approximated with a discrete body $\mathcal{B}^{\mathrm{h}}$, which consists of a set of non-overlapping n_e finite elements $\Omega_e \subset \mathcal{B}^{\mathrm{h}}$ in the reference configuration, see Fig. 6.1, or $\omega_e \subset \mathcal{B}^{\mathrm{h}}$ in the current configuration

$$\mathcal{B} \approx \mathcal{B}^{\mathrm{h}} = \bigcup_{e=1}^{n_e} \Omega_e, \qquad \text{or} \qquad \mathcal{B} \approx \mathcal{B}^{\mathrm{h}} = \bigcup_{e=1}^{n_e} \omega_e. \tag{6.32}$$

The n_n discretized points of the geometry, which join the different elements, are called nodes. The field variables displacement $\vec{u}$ and temperature Θ as well as the virtual field variables $\delta\vec{u}$ and $\delta\Theta$ are approximated by discrete functions $\boldsymbol{u}^{\mathrm{h}}$, $\delta\boldsymbol{u}^{\mathrm{h}}$, Θ^{h}, and $\delta\Theta^{\mathrm{h}}$

on the nodes of the elements with a linear combination of ansatz functions[2] N_a, with $a = 1, ..., n_n$

$$\boldsymbol{u}(\boldsymbol{x}, t) \approx \boldsymbol{u}^{\mathrm{h}}(\boldsymbol{x}^{\mathrm{h}}, t) = \sum_{a=1}^{n_n} N_a(\boldsymbol{x}^{\mathrm{h}}) \mathbf{u}_a^{\mathrm{h}}(t), \tag{6.33}$$

$$\delta\boldsymbol{u}(\boldsymbol{x}) \approx \delta\boldsymbol{u}^{\mathrm{h}}(\boldsymbol{x}^{\mathrm{h}}) = \sum_{a=1}^{n_n} N_a(\boldsymbol{x}^{\mathrm{h}}) \delta\boldsymbol{u}_a^{\mathrm{h}}, \tag{6.34}$$

$$\Theta(\boldsymbol{x}, t) \approx \Theta^{\mathrm{h}}(\boldsymbol{x}^{\mathrm{h}}, t) = \sum_{a=1}^{n_n} N_a(\boldsymbol{x}^{\mathrm{h}}) \Theta_a^{\mathrm{h}}(t), \tag{6.35}$$

$$\delta\Theta(\boldsymbol{x}) \approx \delta\Theta^{\mathrm{h}}(\boldsymbol{x}^{\mathrm{h}}) = \sum_{a=1}^{n_n} N_a(\boldsymbol{x}^{\mathrm{h}}) \delta\Theta_a^{\mathrm{h}}. \tag{6.36}$$

In the isoparametric formulation, the geometry and the field variables are interpolated with the same shape functions. In the 3D-case, finite elements frequently take a tetrahedral or hexahedral shape. The polynomial order of the shape functions determines the order of the element. The most common shape functions are linear or quadratic. In the isoparametric formulation, the elements of the reference configuration Ω_e or current configuration ω_e are transformed into a normed reference space $\Omega_\square$ with the local coordinates $\boldsymbol{\xi} = \{\xi, \eta, \zeta\}$, see Fig. 6.2

$$\mathbf{x} = \chi_t^e(\boldsymbol{\xi}) \Leftrightarrow \boldsymbol{\xi} = \varphi_t^e(\mathbf{x}), \qquad \mathbf{X} = \chi_{\mathrm{R}}^e(\boldsymbol{\xi}) \Leftrightarrow \boldsymbol{\xi} = \varphi_{\mathrm{R}}^e(\mathbf{X}). \tag{6.37}$$

Here, the functions χ_t^e, φ_t^e for the current configuration and χ_{R}^e, φ_{R}^e for the reference configuration represent the transformation between the global and local coordinates in an element. The local coordinates have values between -1 and 1. The transformation between the normed element configuration and the current configuration is defined by the Jacobian $\mathbf{j}^e$, with $\det \mathbf{j}^e > 0$, and with respect to the reference configuration by $\mathbf{J}^e$, with $\det \mathbf{J}^e > 0$, so that the line elements can be expressed by

$$\mathrm{d}\mathbf{x} = \mathbf{j}^e \mathrm{d}\boldsymbol{\xi}, \qquad \mathrm{d}\mathbf{X} = \mathbf{J}^e \mathrm{d}\boldsymbol{\xi}, \qquad \mathrm{d}\mathbf{x} = \mathbf{F}^e \mathrm{d}\mathbf{X}, \tag{6.38}$$

with $\mathbf{F}^e = \mathbf{j}^e \mathbf{J}^{e-1}$. The Jacobians are given by

$$\mathbf{j}^e = \left[\frac{\partial \chi_t^e}{\partial \boldsymbol{\xi}}\right] = \mathrm{Grad}_\xi\, \chi_t^e, \qquad \mathbf{J}^e = \left[\frac{\mathrm{d}\chi_{\mathrm{R}}^e}{\mathrm{d}\boldsymbol{\xi}}\right] = \mathrm{Grad}_\xi\, \chi_{\mathrm{R}}^e. \tag{6.39}$$

With the isoparametric transformation, it is possible to express the global field variables

---

[2] The discretized quantities can be expressed in dependence of spatial coordinates related to the current configuration $\boldsymbol{x}^{\mathrm{h}} \in \mathbb{R}^3$, as well as to coordinates of the reference configuration $\boldsymbol{X}^{\mathrm{h}} \in \mathbb{R}^3$. The displacement in material representation corresponds to $\hat{\boldsymbol{u}}^{\mathrm{h}}(\boldsymbol{X}^{\mathrm{h}}, t) = \boldsymbol{u}^{\mathrm{h}}(\chi_{\mathrm{R}}^{\mathrm{h}}(\boldsymbol{X}^{\mathrm{h}}, t), t)$, with $\boldsymbol{x}^{\mathrm{h}} = \chi_{\mathrm{R}}^{\mathrm{h}}(\boldsymbol{X}^{\mathrm{h}}, t)$.

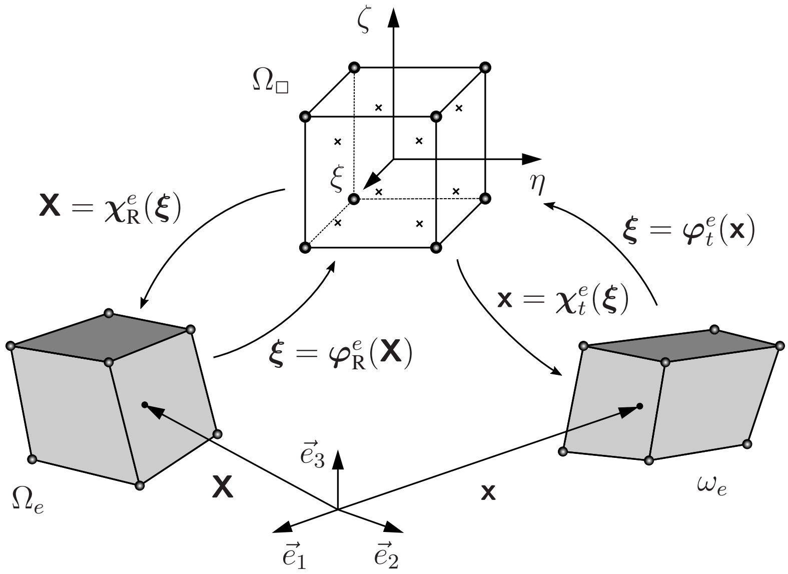

Figure 6.2: Isoparametric transformation of a linear hexahedral element into the reference volume $\Omega_\square$

from Eqns. (6.33)-(6.36) in each element $\mathbf{x} \in \omega_e$, where the index e refers to a variable related to the element ω_e

$$\mathbf{u}^{\mathrm{h}}(\mathbf{x}, t) = \mathbf{N}^e_u(\boldsymbol{\varphi}^e(\mathbf{x}))\mathbf{u}^e(t), \qquad \delta\mathbf{u}^{\mathrm{h}}(\mathbf{x}) = \mathbf{N}^e_u(\boldsymbol{\varphi}^e(\mathbf{x}))\delta\mathbf{u}^e, \tag{6.40}$$

$$\Theta^{\mathrm{h}}(\mathbf{x}, t) = \mathbf{N}^{eT}_\Theta(\boldsymbol{\varphi}^e(\mathbf{x}))\boldsymbol{\Theta}^e(t), \qquad \delta\Theta^{\mathrm{h}}(\mathbf{x}) = \mathbf{N}^{eT}_\Theta(\boldsymbol{\varphi}^e(\mathbf{x}))\delta\boldsymbol{\Theta}^e, \tag{6.41}$$

$$\dot{\Theta}^{\mathrm{h}}(\mathbf{x}, t) = \mathbf{N}^{eT}_\Theta(\boldsymbol{\varphi}^e(\mathbf{x}))\dot{\boldsymbol{\Theta}}^e(t). \tag{6.42}$$

Here, $\mathbf{u}^{\mathrm{h}} \in \mathbb{R}^3$ and $\delta\mathbf{u}^{\mathrm{h}} \in \mathbb{R}^3$ are three-dimensional field variables, $\mathbf{u}^e \in \mathbb{R}^{n^e_{\mathrm{u}}}$ and $\boldsymbol{\Theta}^e \in \mathbb{R}^{n^e_\Theta}$ are DOF related to the element, and the matrix and vector of the shape functions are $\mathbf{N}^e_u \in \mathbb{R}^{3\times n^e_{\mathrm{u}}}$ and $\mathbf{N}^{\mathrm{e}}_\Theta \in \mathbb{R}^{n^e_\Theta}$. The values n^e_{u} and n^e_Θ represent the number of displacement and temperature degrees of freedom per element. The shape functions $N_a(\boldsymbol{\xi})$ are commonly Lagrange polynomial functions, which are equal to 1 in one node of the element and equal to 0 in the remaining nodes. The sum of all shape functions within an element is equal to one, see (Schwarz and Köckler, 2004) for more detailed information.

Moreover, the global node displacements and temperatures are expressed as a column vector $\boldsymbol{u}_a \in \mathbb{R}^{n_{\mathrm{ua}}}$ and $\boldsymbol{\Theta}_a \in \mathbb{R}^{n_{\Theta\mathrm{a}}}$, which can be divided into known (prescribed) variables $\overline{\boldsymbol{u}} \in \mathbb{R}^{n_{\mathrm{up}}}$, $\overline{\boldsymbol{\Theta}} \in \mathbb{R}^{n_{\Theta\mathrm{p}}}$, and unknown variables $\boldsymbol{u} \in \mathbb{R}^{n_{\mathrm{uu}}}$, $\boldsymbol{\Theta} \in \mathbb{R}^{n_{\Theta\mathrm{u}}}$

$$\boldsymbol{u}^{\mathrm{T}}_{\mathrm{a}} = \{\boldsymbol{u}^{\mathrm{T}}\overline{\boldsymbol{u}}^{\mathrm{T}}\} \qquad \text{and} \qquad \boldsymbol{\Theta}^{\mathrm{T}}_{\mathrm{a}} = \{\boldsymbol{\Theta}^{\mathrm{T}}\,\overline{\boldsymbol{\Theta}}^{\mathrm{T}}\}. \tag{6.43}$$

At this point, the incidence matrices $\boldsymbol{Z}^{\mathrm{e}}$ are introduced, see (Hartmann, 2003). They allow to assemble field variables connecting the local variables of the element with the global ones

$$\mathbf{u}^{\mathrm{h}}(\mathbf{x},t) = \mathbf{N}_u^e(\boldsymbol{\varphi}_t^e(\mathbf{x}))\boldsymbol{Z}_{\mathrm{ua}}^{\ e}\boldsymbol{u}_{\mathrm{a}} = \mathbf{N}_u^e(\boldsymbol{\varphi}_t^e(\mathbf{x}))\left\{\boldsymbol{Z}_u^{\mathrm{e}}\boldsymbol{u}(t) + \overline{\boldsymbol{Z}}{}_u^{\mathrm{e}}\overline{\boldsymbol{u}}(t)\right\}, \tag{6.44}$$

$$\Theta^{\mathrm{h}}(\mathbf{x},t) = \mathbf{N}_\Theta^{eT}(\boldsymbol{\varphi}_t^e(\mathbf{x}))\boldsymbol{Z}_{\Theta\mathrm{a}}^{\ e}\boldsymbol{\Theta}_{\mathrm{a}} = \mathbf{N}_\Theta^{eT}(\boldsymbol{\varphi}_t^e(\mathbf{x}))\left\{\boldsymbol{Z}_\Theta^{\mathrm{e}}\boldsymbol{\Theta}(t) + \overline{\boldsymbol{Z}}{}_\Theta^{\mathrm{e}}\overline{\boldsymbol{\Theta}}(t)\right\}, \tag{6.45}$$

$$\dot{\Theta}^h(\mathbf{x},t) = \mathbf{N}_\Theta^{eT}(\boldsymbol{\varphi}_t^e(\mathbf{x}))\boldsymbol{Z}_{\Theta\mathrm{a}}^{\ e}\dot{\boldsymbol{\Theta}}_{\mathrm{a}} = \mathbf{N}_\Theta^{eT}(\boldsymbol{\varphi}_t^e(\mathbf{x}))\left\{\boldsymbol{Z}_\Theta^{\mathrm{e}}\dot{\boldsymbol{\Theta}}(t) + \overline{\boldsymbol{Z}}{}_\Theta^{\mathrm{e}}\dot{\overline{\boldsymbol{\Theta}}}(t)\right\}, \tag{6.46}$$

with $\boldsymbol{Z}_u^{\mathrm{e}} \in \mathbb{R}^{n_{\mathrm{u}}^e \times n_{\mathrm{uu}}}$, $\overline{\boldsymbol{Z}}{}_u^{\mathrm{e}} \in \mathbb{R}^{n_{\mathrm{u}}^e \times n_{\mathrm{up}}}$, $\boldsymbol{Z}_\Theta^{\mathrm{e}} \in \mathbb{R}^{n_\Theta^e \times n_{\Theta\mathrm{u}}}$ and $\overline{\boldsymbol{Z}}{}_\Theta^{\mathrm{e}} \in \mathbb{R}^{n_\Theta^e \times n_{\Theta\mathrm{p}}}$. The incidence matrices are composed by zeros and ones in order to allow a formal representation of the connection between global and local variables. They are not computed in the actual computation as this would pose an unnecessary effort, see (Hartmann, 2003). Since the virtual displacements and temperatures are equal to zero on the surface, where Dirichlet boundary conditions are applied, the terms $\delta\overline{\boldsymbol{u}} = \mathbf{0}$ and $\delta\overline{\boldsymbol{\Theta}} = \mathbf{0}$ are equal to zero. This results in

$$\delta\mathbf{u}^{\mathrm{h}}(\mathbf{x}) = \mathbf{N}_u^e(\boldsymbol{\varphi}_t^e(\mathbf{x}))\boldsymbol{Z}_{\mathrm{ua}}^{\mathrm{e}}\delta\boldsymbol{u}_{\mathrm{a}} = \mathbf{N}_u^e(\boldsymbol{\varphi}_t^e(\mathbf{x}))\boldsymbol{Z}_u^{\mathrm{e}}\delta\boldsymbol{u}, \tag{6.47}$$

$$\delta\Theta^{\mathrm{h}}(\mathbf{x}) = \mathbf{N}_\Theta^{eT}(\boldsymbol{\varphi}_t^e(\mathbf{x}))\boldsymbol{Z}_{\Theta\mathrm{a}}^{\ e}\delta\Theta_{\mathrm{a}} = \mathbf{N}_\Theta^{eT}(\boldsymbol{\varphi}_t^e(\mathbf{x}))\boldsymbol{Z}_\Theta^{\mathrm{e}}\delta\boldsymbol{\Theta}. \tag{6.48}$$

Discretization of the Balance of Linear Momentum

With the previously defined ansatz (6.44)-(6.48), the weak form of the balance of linear momentum (6.24) can be discretized

$$\tilde{\pi}_{\mathrm{M}}(\vec{u},\Theta,\mathbf{q},\delta\vec{u},t) \rightarrow \tilde{\pi}_{\mathrm{M}}^h(\boldsymbol{u}^{\mathrm{h}},\boldsymbol{\Theta}^{\mathrm{h}},\boldsymbol{q},\delta\boldsymbol{u}^{\mathrm{h}},t). \tag{6.49}$$

Making use of the symmetry of the tensorial variables, the expression can be written in matrix form, see (Hartmann, 2003),

$$\tilde{\pi}_{\mathrm{M}}^h(\boldsymbol{u},\boldsymbol{\Theta},\boldsymbol{q},\delta\boldsymbol{u},t) =$$
$$\delta\boldsymbol{u}^{\mathrm{T}}\left\{\sum_{e=1}^{n_e}\boldsymbol{Z}_u^{\mathrm{eT}}\int_{\Omega_e}\tilde{\mathbf{B}}_u^{\mathrm{eT}}(\mathbf{u}^e(t),\mathbf{X})\,\tilde{\mathbf{h}}^{\mathrm{e}}(\mathbf{C}^{\mathrm{e}}(\mathbf{X},t),\boldsymbol{\Theta}^{\mathrm{e}}(\mathbf{X},t),\mathbf{q}^{\mathrm{e}}(\mathbf{X},t))\mathrm{d}\Omega_e - \overline{\boldsymbol{p}}(\mathbf{X},t)\right\} = 0. \tag{6.50}$$

Here, the strain-displacement matrix $\tilde{\mathbf{B}}^{\mathrm{e}} = [\tilde{\mathbf{B}}_{\mathrm{u}1}^{\mathrm{e}}...\tilde{\mathbf{B}}_{\mathrm{u}n_{\mathrm{en}}}^{\mathrm{e}}]$ is introduced, with n_{en} being the number of nodes per element, see Eq. (37) in the appendix. This matrix contains the derivative of the shape functions with respect to the material coordinates, and it is related to the virtual strains by

$$\delta\mathbf{E} = \sum_{j=1}^{n_{\mathrm{en}}}\tilde{\mathbf{B}}_{\mathrm{u}\,j}^{\mathrm{e}}\delta\mathbf{u}_j^{\mathrm{e}}. \tag{6.51}$$

The stress relation in the discretized form is equal to

$$\tilde{\mathbf{T}}^{\mathrm{e}} = \tilde{\mathbf{h}}^{\mathrm{e}}(\mathbf{C}^{\mathrm{e}}(\mathbf{X},t), \boldsymbol{\Theta}^{\mathrm{e}}(\mathbf{X},t), \mathbf{q}^{\mathrm{e}}(\mathbf{X},t)). \tag{6.52}$$

The vectors[3] $\delta\mathbf{E}$ and $\tilde{\mathbf{T}}$

$$\delta\mathbf{E} = \left\{\delta E_{11} \quad \delta E_{22} \quad \delta E_{33} \quad 2\delta E_{12} \quad 2\delta E_{23} \quad 2\delta E_{31}\right\}^{\mathrm{T}}, \tag{6.53}$$

$$\tilde{\mathbf{T}} = \left\{\tilde{T}_{11} \quad \tilde{T}_{22} \quad \tilde{T}_{33} \quad \tilde{T}_{12} \quad \tilde{T}_{23} \quad \tilde{T}_{31}\right\}^{\mathrm{T}}, \tag{6.54}$$

allow to compute the scalar product of the tensors $\tilde{\mathrm{T}} \cdot \delta\mathrm{E}$ in the form $\tilde{\mathrm{T}} \cdot \delta\mathrm{E} = \delta\mathbf{E}^{\mathrm{T}}\tilde{\mathbf{T}}$, including the factor two into $\delta\mathbf{E}$ in order to consider the components outside the diagonal from the tensorial form. The vector $\overline{\boldsymbol{p}}(\mathbf{X},t)$ contains the volume-distributed loads and the traction acting on the surface

$$\overline{\boldsymbol{p}}(\mathbf{X},t) := \sum_{e=1}^{n_e} \boldsymbol{Z}_u^{\mathrm{e}^{\mathrm{T}}} \int_{\Omega_e} \mathbf{N}^{\mathrm{e}^{\mathrm{T}}}(\mathbf{X})\rho_{\mathrm{R}}(\mathbf{X})\mathbf{k}^{\mathrm{e}}\,\mathrm{d}\Omega_e + \int_{\gamma_e} \mathbf{N}^{\mathrm{e}^{\mathrm{T}}}(\mathbf{x})\,\mathbf{t}^{\mathrm{e}}(\mathbf{x},t)\,\mathrm{d}\gamma_e, \tag{6.55}$$

see (Rothe, 2015; Grafenhorst, 2018) for more details. Since the virtual displacements are arbitrary, Eq. (6.50) results in the system of nonlinear equations

$$\tilde{\boldsymbol{g}}_u(\boldsymbol{u},\Theta,\boldsymbol{q},t) = \sum_{e=1}^{n_{\mathrm{e}}} \boldsymbol{Z}_u^{\mathrm{e}^{\mathrm{T}}} \int_{\Omega_e} \tilde{\mathbf{B}}_u^{\mathrm{e}^{\mathrm{T}}}(\mathbf{u}^e(t),\mathbf{X})\tilde{\mathbf{T}}^{\mathrm{e}}(\mathbf{X},t)\,\mathrm{d}\Omega_e - \overline{\boldsymbol{p}}(\mathbf{X},t) = \boldsymbol{0}. \tag{6.56}$$

The equivalent formulation of Eq. (6.56) expressed with quantities relative to the current configuration is obtained with the help of the push-forward operator in matrix notation $\mathbf{F}_{23}^{\mathrm{e}}$, see Eq. (38) in the appendix and (Hartmann, 2003; Hamkar, 2013), and is equal to

$$\boldsymbol{g}_u(\boldsymbol{u},\Theta,\boldsymbol{q},t) = \sum_{e=1}^{n_{\mathrm{e}}} \boldsymbol{Z}_u^{\mathrm{e}^{\mathrm{T}}} \int_{\Omega_e} \mathbf{B}_u^{\mathrm{e}^{\mathrm{T}}}(\mathbf{x})\mathbf{S}^{\mathrm{e}}(\mathbf{x},t)\mathrm{d}\Omega_e - \overline{\boldsymbol{p}}(\mathbf{x},t) = \boldsymbol{0}. \tag{6.57}$$

The strain displacement matrix $\mathbf{B}_u^{\mathrm{e}}$ represents the derivative of the ansatz functions $\mathbf{N}^{\mathrm{e}}$ with respect to the coordinates in the current configuration

$$\mathbf{B}_u^{\mathrm{e}}(\boldsymbol{\varphi}_t^e(\mathbf{x})) = \left[\mathbf{B}_{u1}^{\mathrm{e}} \dots \mathbf{B}_{un_u^e}^{\mathrm{e}}\right] \in \mathbb{R}^{6\times n_u^e}, \tag{6.58}$$

where, for the three dimensional case, they are given by

$$\mathbf{B}_{\mathrm{ua}}^{\mathrm{e}}(\boldsymbol{\varphi}_t^e(\mathbf{x})) = \begin{bmatrix} N_{\mathrm{ua},x}^e & 0 & 0 \\ 0 & N_{\mathrm{ua},y}^e & 0 \\ 0 & 0 & N_{\mathrm{ua},z}^e \\ N_{\mathrm{ua},y}^e & N_{\mathrm{ua},x}^e & 0 \\ 0 & N_{\mathrm{ua},z}^e & N_{\mathrm{ua},y}^e \\ N_{\mathrm{ua},z}^e & 0 & N_{\mathrm{ua},x}^e \end{bmatrix}, \qquad a = 1,\dots,n_{en}. \tag{6.59}$$

---

[3] In the notation of Abaqus, the shear components have a different order:

$$\delta\mathbf{E} = \left\{\delta E_{11} \quad \delta E_{22} \quad \delta E_{33} \quad 2\delta E_{12} \quad 2\delta E_{13} \quad 2\delta E_{23}\right\}^{\mathrm{T}}, \; \tilde{\mathbf{T}} \; = \left\{\tilde{T}_{11} \quad \tilde{T}_{22} \quad \tilde{T}_{33} \quad \tilde{T}_{12} \quad \tilde{T}_{13} \quad \tilde{T}_{23}\right\}^{\mathrm{T}}.$$

Here, the shape function $N_a^e(\boldsymbol{\xi})$ is defined at the node a within the domain $\Omega_\square$. The tensor $\mathbf{S}^\mathrm{e}$ is the weighted Cauchy stress, related to the second Piola-Kirchhoff tensor by $\mathbf{S}^\mathrm{e} = \mathbf{F}^\mathrm{e}_{23}\tilde{\mathbf{T}}^\mathrm{e}$. The equivalent expression in the reference configuration can be written as

$$\boldsymbol{g}_u(\boldsymbol{u}, \boldsymbol{\Theta}, \boldsymbol{q}, t) = \sum_{e=1}^{n_\mathrm{e}} \boldsymbol{Z}_u^{\mathrm{e}^\mathrm{T}} \int_{\Omega_e} \mathbf{B}_u^{\mathrm{e}^\mathrm{T}}(\mathbf{X})\mathbf{F}^\mathrm{e}_{23}\tilde{\mathbf{T}}^\mathrm{e}(\mathbf{X}, t)\,\mathrm{d}\Omega_e - \overline{\boldsymbol{p}}(\mathbf{X}, t) = \boldsymbol{0}, \tag{6.60}$$

which is equivalent to Eq. (6.56) with the relation $\tilde{\mathbf{B}}_u^{\mathrm{e}^\mathrm{T}} = \mathbf{B}_u^{\mathrm{e}^\mathrm{T}}\mathbf{F}^\mathrm{e}_{23}$. The integration is performed numerically in the reference domain $\Omega_\square$ of each element Ω_e with a Gauss quadrature, see (Dhatt and Touzot, 1985; Schwarz and Köckler, 2004). This method shows advantages regarding its accuracy, since a polynomial of the order $2n_\mathrm{GP} - 1$ can be integrated exactly

$$\begin{aligned}
\int_{\Omega_e} \mathbf{B}_u^{\mathrm{e}^\mathrm{T}}(\mathbf{x})\mathbf{S}^\mathrm{e}(\mathbf{x}, t)\,\mathrm{d}\Omega_e &= \int_{\Omega_\square} \mathbf{B}_u^{\mathrm{e}^\mathrm{T}}(\boldsymbol{\xi})\mathbf{S}^\mathrm{e}(\boldsymbol{\xi}, t)\det \mathbf{j}^e\,\mathrm{d}\Omega_\square \\
&= \int_{-1}^{+1}\int_{-1}^{+1}\int_{-1}^{+1} \mathbf{B}_u^{\mathrm{e}^\mathrm{T}}(\boldsymbol{\xi})\mathbf{S}^\mathrm{e}(\boldsymbol{\xi}, t)\det \mathbf{j}^e(\boldsymbol{\xi})\,\mathrm{d}\xi\,\mathrm{d}\eta\,\mathrm{d}\zeta \qquad (6.61)\\
&\approx \sum_{l=1}^{n_\mathrm{GP}} w_l \mathbf{B}_u^{\mathrm{e}^\mathrm{T}}(\boldsymbol{\xi}_l)\mathbf{S}^\mathrm{e}(\boldsymbol{\xi}_l, t)\det \mathbf{j}^e(\boldsymbol{\xi}_l). \qquad (6.62)
\end{aligned}$$

Here, the local coordinate space is $\boldsymbol{\xi} = \{\xi, \eta, \zeta\}^T$, where $\xi \in [-1, 1]$, $\eta \in [-1, 1]$ and $\zeta \in [-1, 1]$. In the Gauss quadrature, $\boldsymbol{\xi}_l = \{\xi, \eta, \zeta\}_l^T$ represent the Gauss coordinates and w_l the weighting factors of each Gauss point. The assembly procedure of the internal variables is shown in Fig. 6.3. The internal variables are necessary to compute the stress relation. They are computed at the spatial integration points $\boldsymbol{\xi}_l$ from the evolution

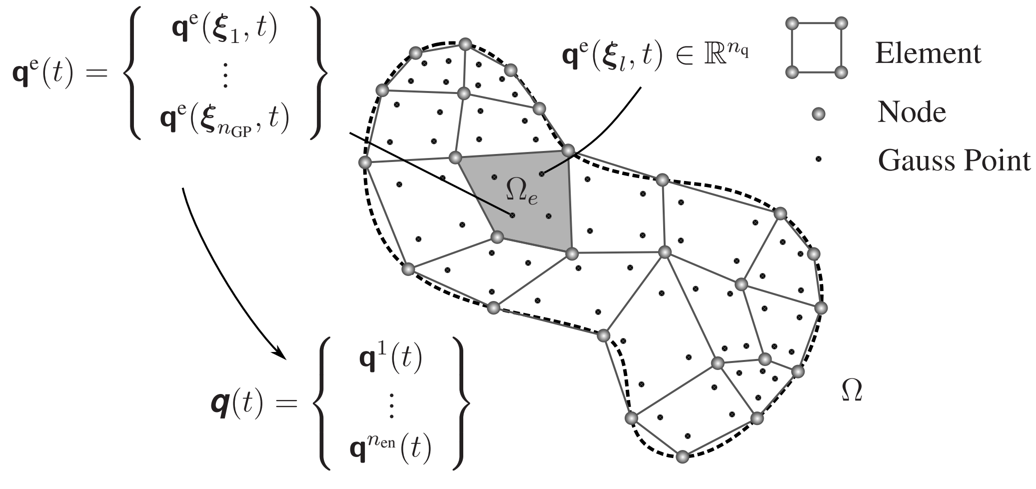

Figure 6.3: Representation of assembly of internal variables

equations

$$\dot{\mathbf{q}}^{\mathrm{e}}(\boldsymbol{\xi}_l,t)=\tilde{\mathbf{r}}^{\mathrm{e}}\left(\mathbf{C}^{\mathrm{e}}(\boldsymbol{\xi}_l,t),\boldsymbol{\Theta}^{\mathrm{e}}(\boldsymbol{\xi}_l,t),\mathbf{q}^{\mathrm{e}}(\boldsymbol{\xi}_l,t),t\right),\qquad \mathbf{q}^{\mathrm{e}}\in\mathbb{R}^{n_{\mathrm{q}}}. \tag{6.63}$$

They are assembled into a global vector $\boldsymbol{q}(t)\in\mathbb{R}^{n_Q}$ with the length $n_Q=n_{\mathrm{q}}n_{\mathrm{e}}n_{\mathrm{GP}}$, equal to the number of internal variables per material point n_{q} multiplied with the number of elements n_{e} and number of Gauss points per element n_{GP}. Analogously to the displacement of the element nodes, a coincidence matrix for the internal variables $\boldsymbol{Z}^{\mathrm{e}}_{\mathrm{q}l}\in\mathbb{R}^{n_{\mathrm{q}}\times n_Q}$ can be defined. This matrix selects the internal variables $\mathbf{q}^{\mathrm{e}}$ at the Gauss point $\boldsymbol{\xi}_l$ for the element e from the global vector $\boldsymbol{q}$, see (Hartmann, 2005; Hamkar, 2013)

$$\mathbf{q}^{\mathrm{e}}(\boldsymbol{\xi}_l,t)=\boldsymbol{Z}^{\mathrm{e}}_{\mathrm{q}l}\,\boldsymbol{q}(t),\qquad \mathbf{q}^{\mathrm{e}}(\boldsymbol{\xi}_l,t)\in\mathbb{R}^{n_{\mathrm{q}}}. \tag{6.64}$$

Since the internal variables and their evolution equations are decoupled on the Gauss points, the inverse relation

$$\boldsymbol{q}(t)=\sum_{e=1}^{n_e}\sum_{l=1}^{n_{\mathrm{GP}}}\boldsymbol{Z}^{\mathrm{e}^{\mathrm{T}}}_{\mathrm{q}l}\,\mathbf{q}^{\mathrm{e}}(\boldsymbol{\xi}_l,t), \tag{6.65}$$

is valid. In this way, the evolution equations of the internal variables can be summarized as a system of ordinary differential equations of first order, which depend on the displacement $\boldsymbol{u}(t)$ and the temperature $\Theta(t)$ field

$$\dot{\boldsymbol{q}}(t)-\boldsymbol{r}_{\mathrm{q}}(t,\boldsymbol{u}(t),\Theta(t),\boldsymbol{q}(t))=\boldsymbol{0},\qquad \boldsymbol{q}(t)\in\mathbb{R}^{n_Q}. \tag{6.66}$$

Here, the temperature field is determined from the solution of the weak form of the heat equation (6.30).

Discretization of the Heat Equation

The discretization of the heat equation is performed analogously to the balance of momentum. The weak form of the heat conduction equation is approximated with the help of ansatz functions

$$\pi_\Theta(\vec{u},\Theta,\dot{\Theta},\mathbf{q},\delta\Theta,t)\rightarrow\pi^h_\Theta(\boldsymbol{u}^{\mathrm{h}},\boldsymbol{\Theta}^{\mathrm{h}},\dot{\boldsymbol{\Theta}}^{\mathrm{h}},\boldsymbol{q},\delta\boldsymbol{\Theta}^{\mathrm{h}},t), \tag{6.67}$$

leading to the expression

$$\pi^h_\Theta(\boldsymbol{u}^{\mathrm{h}},\boldsymbol{\Theta}^{\mathrm{h}},\dot{\boldsymbol{\Theta}}^{\mathrm{h}},\boldsymbol{q},\delta\Theta^{\mathrm{h}},t)= \tag{6.68}$$

$$\delta\boldsymbol{\Theta}^{\mathrm{T}}\left\{\sum_{e=1}^{n_e}\boldsymbol{Z}^{\mathrm{e}^{\mathrm{T}}}_{\Theta}\left\{\int_{\omega_e}\rho(\mathbf{x})c^{\mathrm{h}}_{\mathrm{p}}\mathbf{N}^{\mathrm{e}}_{\Theta}(\mathbf{x})\mathbf{N}^{\mathrm{e}^{\mathrm{T}}}_{\Theta}(\mathbf{x})\mathrm{d}\omega_e\,\dot{\boldsymbol{\Theta}}^{\mathrm{e}}+\int_{\omega_e}\mathbf{B}^{\mathrm{e}^{\mathrm{T}}}_{\Theta}(\mathbf{x})\kappa^{\mathrm{h}}_{\Theta}\mathbf{B}^{\mathrm{e}}_{\Theta}(\mathbf{x})\mathrm{d}\omega_e\,\boldsymbol{\Theta}^{\mathrm{e}}\right.\right.$$

$$\left.\left.-\int_{\omega_e}\rho(\mathbf{x})\omega^{\mathrm{h}}\mathbf{N}^{\mathrm{e}}_{\Theta}\mathrm{d}\omega_e-\int_{\gamma_e}f_q\mathbf{N}^{\mathrm{e}}_{\Theta}\mathrm{d}\gamma_e\right\}\right\}=0. \tag{6.69}$$

with $f_q = -\mathbf{q} \cdot \mathbf{n}$ being the scalar product between the heat flux $\mathbf{q}$ and the normal vector $\mathbf{n}$. The gradient of the temperature $\operatorname{grad}\Theta$ and of the virtual temperature $\operatorname{grad}\delta\Theta$ can be approximated by the expressions

$$\operatorname{grad}\Theta \approx \operatorname{grad}\Theta^h = \mathbf{B}^{\mathrm{e}}_{\Theta}(\boldsymbol{\varphi}^e_t(\mathbf{x}))\boldsymbol{\Theta}^{\mathrm{e}} = \mathbf{B}^{\mathrm{e}}_{\Theta}(\boldsymbol{\varphi}^e_t(\mathbf{x}))\left\{\boldsymbol{Z}^{\mathrm{e}}_{\Theta}\boldsymbol{\Theta}(t) + \overline{\boldsymbol{Z}}^{\mathrm{e}}_{\Theta}\overline{\boldsymbol{\Theta}}(t)\right\}, \quad (6.70)$$

$$\operatorname{grad}\delta\Theta \approx \operatorname{grad}\delta\Theta^h = \mathbf{B}^{\mathrm{e}}_{\Theta}(\boldsymbol{\varphi}^e_t(\mathbf{x}))\delta\boldsymbol{\Theta}^{\mathrm{e}} = \mathbf{B}^{\mathrm{e}}_{\Theta}(\boldsymbol{\varphi}^e_t(\mathbf{x}))\boldsymbol{Z}^{\mathrm{e}}_{\Theta}\delta\boldsymbol{\Theta}. \quad (6.71)$$

The temperature-gradient matrix is defined in an analogous way to the strain-displacement matrix

$$\mathbf{B}^{\mathrm{e}}_{\Theta}(\boldsymbol{\varphi}^e_t(\mathbf{x})) = \left[\mathbf{B}^{\mathrm{e}}_{\Theta 1} \dots \mathbf{B}^{\mathrm{e}}_{\Theta n^{\mathrm{e}}_{\Theta}}\right] \in \mathbb{R}^{3\times n^{\mathrm{e}}_{\Theta}}, \quad (6.72)$$

which represent the derivative of the shape functions with respect to the spatial coordinates at the node a

$$\mathbf{B}^{\mathrm{e}}_{\Theta a}(\boldsymbol{\varphi}^e_t(\mathbf{x})) = \begin{Bmatrix} N^e_{\Theta a,x} \\ N^e_{\Theta a,y} \\ N^e_{\Theta a,z} \end{Bmatrix}, \qquad a = 1, \dots, n^{\mathrm{e}}_{\Theta}. \quad (6.73)$$

Since the virtual temperatures $\delta\Theta$ are arbitrary, expression

$$\sum_{e=1}^{n_e} \boldsymbol{Z}^{\mathrm{e}^{\mathrm{T}}}_{\Theta} \left\{ \int_{\omega_e} \rho(\mathbf{x}) c^{\mathrm{h}}_{\mathrm{p}} \mathbf{N}^{\mathrm{e}}_{\Theta}(\mathbf{x}) \mathbf{N}^{\mathrm{e}^{\mathrm{T}}}_{\Theta}(\mathbf{x}) \mathrm{d}\omega_e\, \dot{\boldsymbol{\Theta}}^{\mathrm{e}} + \int_{\omega_e} \mathbf{B}^{\mathrm{e}^{\mathrm{T}}}_{\Theta}(\mathbf{x}) \kappa^{\mathrm{h}}_{\Theta} \mathbf{B}^{\mathrm{e}}_{\Theta}(\mathbf{x}) \mathrm{d}\omega_e\, \boldsymbol{\Theta}^{\mathrm{e}} \right.$$
$$\left. - \int_{\omega_e} \rho(\mathbf{x}) \omega^{\mathrm{h}} \mathbf{N}^{\mathrm{e}}_{\Theta} \mathrm{d}\omega_e - \int_{\gamma_e} f_q \mathbf{N}^{\mathrm{e}}_{\Theta} \mathrm{d}\gamma_e \right\} = \mathbf{0} \quad (6.74)$$

has to be equal to zero. In order to compute this term, several variables are rearranged. The heat capacity matrix is defined by

$$\boldsymbol{C}_{\mathrm{p}}(t, \boldsymbol{u}(t), \Theta(t)) := \sum_{e=1}^{n_e} \boldsymbol{Z}^{\mathrm{e}^{\mathrm{T}}}_{\Theta} \left[\int_{\omega_e} \rho\, c^{\mathrm{h}}_{\mathrm{p}}\, \mathbf{N}^{\mathrm{e}}_{\Theta} \mathbf{N}^{\mathrm{e}^{\mathrm{T}}}_{\Theta}\, \mathrm{d}\omega_e \right] \boldsymbol{Z}^{\mathrm{e}}_{\Theta} \quad \in \mathbb{R}^{n_{\Theta\mathrm{u}} \times n_{\Theta\mathrm{u}}}. \quad (6.75)$$

The thermal conductivity matrix $\boldsymbol{C}_{\kappa}$ depends on the discretized temperatures and internal variables, since the thermal conductivity is aging-dependent. It can be expressed by

$$\boldsymbol{C}_{\kappa}(t, \boldsymbol{u}(t), \Theta(t), \boldsymbol{q}(t)) := \sum_{e=1}^{n_e} \boldsymbol{Z}^{\mathrm{e}^{\mathrm{T}}}_{\Theta} \left[\int_{\omega_e} \kappa^{\mathrm{e}}_{\Theta} \mathbf{B}^{\mathrm{e}^{\mathrm{T}}}_{\Theta} \mathbf{B}^{\mathrm{e}}_{\Theta} \mathrm{d}\omega_e \right] \boldsymbol{Z}^{\mathrm{e}}_{\Theta} \quad \in \mathbb{R}^{n_{\Theta\mathrm{u}} \times n_{\Theta\mathrm{u}}}. \quad (6.76)$$

Moreover, two additional components are introduced

$$\boldsymbol{p}^{\mathrm{V}}_{\Theta}(t, \boldsymbol{u}(t), \Theta(t), \boldsymbol{q}(t)) := \sum_{e=1}^{n_e} \boldsymbol{Z}^{\mathrm{e}^{\mathrm{T}}}_{\Theta} \int_{\omega_e} \rho \omega^{\mathrm{h}} \mathbf{N}^{\mathrm{e}}_{\Theta} \mathrm{d}\omega_e, \quad (6.77)$$

$$\boldsymbol{p}^{\mathrm{S}}_{\Theta}(t, \boldsymbol{u}(t), \Theta(t)) := \sum_{e=1}^{n_e} \boldsymbol{Z}^{\mathrm{e}^{\mathrm{T}}}_{\Theta} \int_{\gamma_e} f_q \mathbf{N}^{\mathrm{e}}_{\Theta} \mathrm{d}\gamma_e. \quad (6.78)$$

The term $\boldsymbol{p}_\Theta^{\mathrm{V}}$ is the volumetric heat source caused by the dissipation ω. The term $\boldsymbol{p}_\Theta^{\mathrm{S}}$ denotes the heat flux over the surface. If the surface changes significantly, the heat flux per unit surface is influenced. For a detailed consideration of these terms, see (Grafenhorst, 2018). The prescribed temperatures are summarized in the term

$$\overline{\boldsymbol{p}}_\Theta(t, \boldsymbol{u}(t), \Theta(t)) = \bar{\boldsymbol{C}}_{\mathrm{p}}(t, \boldsymbol{u}(t), \Theta(t))\dot{\overline{\Theta}}(t) + \bar{\boldsymbol{C}}_\kappa \overline{\Theta}(t), \tag{6.79}$$

where $\bar{\boldsymbol{C}}_{\mathrm{p}}$ and $\bar{\boldsymbol{C}}_\kappa$ denote the heat capacity matrix and thermal conductivity matrix for the nodes with prescribed temperatures

$$\bar{\boldsymbol{C}}_{\mathrm{p}}(t, \boldsymbol{u}(t), \Theta(t)) := \sum_{e=1}^{n_e} \boldsymbol{Z}_\Theta^{\mathrm{e}^{\mathrm{T}}} \left[\int_{\omega_e} \rho \, c_{\mathrm{p}}^{\mathrm{h}} \, \mathbf{N}_\Theta^{\mathrm{e}} \mathbf{N}_\Theta^{\mathrm{e}^{\mathrm{T}}} \mathrm{d}\omega_e \right] \overline{\boldsymbol{Z}}_\Theta^{\mathrm{e}} \quad \in \mathbb{R}^{n_{\Theta\mathrm{u}} \times n_{\Theta\mathrm{p}}}, \tag{6.80}$$

$$\bar{\boldsymbol{C}}_\kappa(t, \boldsymbol{u}(t), \Theta(t), \boldsymbol{q}(t)) := \sum_{e=1}^{n_e} \boldsymbol{Z}_\Theta^{\mathrm{e}^{\mathrm{T}}} \left[\int_{\omega_e} \kappa_\Theta^{\mathrm{h}} \mathbf{B}_\Theta^{\mathrm{e}^{\mathrm{T}}} \mathbf{B}_\Theta^{\mathrm{e}} \mathrm{d}\omega_e \right] \overline{\boldsymbol{Z}}_\Theta^{\mathrm{e}} \quad \in \mathbb{R}^{n_{\Theta\mathrm{u}} \times n_{\Theta\mathrm{p}}}. \tag{6.81}$$

The terms (6.76)-(6.79) are summarized in the function

$$\boldsymbol{r}_\Theta(t, \boldsymbol{u}(t), \Theta(t), \boldsymbol{q}) := -\boldsymbol{C}_\kappa \Theta + \boldsymbol{p}_\Theta^{\mathrm{V}} + \boldsymbol{p}_\Theta^{\mathrm{S}} - \overline{\boldsymbol{p}}_\Theta. \tag{6.82}$$

By inserting Eqns. (6.75) and (6.82) into Eq. (6.74) and bringing the function $\boldsymbol{r}_\Theta$ to the right-hand side of the equation, one obtains a system of ordinary differential equations which approximates the heat conduction equation

$$\boldsymbol{C}_{\mathrm{p}}(t, \boldsymbol{u}(t), \Theta(t)) \, \dot{\Theta}(t) = \boldsymbol{r}_\Theta(t, \boldsymbol{u}(t), \Theta(t), \boldsymbol{q}(t)). \tag{6.83}$$

Tab. 6.3 summarizes the semi-discretized thermo-mechanical problem, which results from the spatial discretization of the balance of momentum, the evolution equations, and the heat equation. This system of equations has to be discretized in time to be solved.

Table 6.3: Semi-discretized coupled thermo-mechanical problem

The displacements $\boldsymbol{u}(t)$, temperatures $\Theta(t)$, and internal variables $\boldsymbol{q}(t)$ on the time interval $t \in [t_0, t_e]$ have to be found solving the DAE-system		
$\boldsymbol{0} = \boldsymbol{g}_u(t, \boldsymbol{u}(t), \Theta(t), \boldsymbol{q}(t)),$	$\boldsymbol{u}(t_0) = \boldsymbol{u}_0$	(6.57)
$\boldsymbol{C}_{\mathrm{p}} \, \dot{\Theta}(t) = \boldsymbol{r}_\Theta(t, \boldsymbol{u}(t), \Theta(t), \boldsymbol{q}(t)),$	$\Theta(t_0) = \Theta_0$	(6.83)
$\dot{\boldsymbol{q}}(t) = \boldsymbol{r}_{\mathrm{q}}(t, \boldsymbol{u}(t), \Theta(t), \boldsymbol{q}(t)),$	$\boldsymbol{q}(t_0) = \boldsymbol{q}_0$	(6.66)

Case of small deformations In this case, there is no distinction between the reference and current configuration. Since $\mathbf{x}^{\mathrm{h}} \approx \mathbf{X}^{\mathrm{h}}$, the deformation gradient is approximately one, $\mathbf{F}^{\mathrm{e}} \approx \mathbf{I}$, and the density is approximately equal in both configurations

$\rho^{\mathrm{e}}_{\mathrm{R}}(\mathbf{X}^{\mathrm{h}}) \approx \rho^{\mathrm{e}}(\mathbf{x}^{\mathrm{h}})$. The Jacobians from the isoparametric transformation are approximately equal, $\mathbf{j}^{e}(\boldsymbol{\xi}) \approx \mathbf{J}^{e}(\boldsymbol{\xi})$, as well as the strain-displacement matrix in the different configurations $\tilde{\mathbf{B}}^{\mathrm{e}}_{u}(\boldsymbol{\xi}) \approx \mathbf{B}^{\mathrm{e}}_{u}(\boldsymbol{\xi})$. The strain tensor corresponds to the linearized strain tensor $\mathbf{E}_{\mathrm{L}} \approx \mathbf{E} \approx \mathbf{B}^{\mathrm{e}}_{u}\mathbf{u}^{\mathrm{e}}$. Moreover, the second Piola-Kirchhoff tensor and the Cauchy stress are approximately equal $\mathbf{T}^{\mathrm{e}} \approx \tilde{\mathbf{T}}^{\mathrm{e}}$. The procedure of the spatial discretization is analogous to the method discussed before.

6.2.2 Time Discretization

The Backward Euler method is used for the time discretization of the DAE-system of Tab. 6.3, since the time discretization in Abaqus Standard is performed with this method, see (ABAQUS, 2019). Further possibilities for the time-discretization for DAE-systems in quasi-static problems are mentioned in (Grafenhorst, 2018). Especially, for diagonal-implicit Runge-Kutta methods, the topic has been widely treated, see (Hartmann et al., 2009), (Ellsiepen and Hartmann, 2001), (Hartmann, 2005), (Hartmann and Bier, 2008) and (Hartmann, 1999).

For the time discretization, the ε-embedded method is applied to DAE-systems, see Hairer et al. (2002). In order to convert the DAE-system from Tab. 6.3 into a system of differential equations, a small parameter $0 < \varepsilon \ll 1$ is introduced

$$\varepsilon \dot{\boldsymbol{u}} = \boldsymbol{g}_{u}(t, \boldsymbol{u}(t), \Theta(t), \boldsymbol{q}(t)), \tag{6.84}$$

$$\boldsymbol{C}_{\mathrm{p}}\, \dot{\Theta}(t) = \boldsymbol{r}_{\Theta}(t, \boldsymbol{u}(t), \Theta(t), \boldsymbol{q}(t)), \tag{6.85}$$

$$\dot{\boldsymbol{q}}(t) = \boldsymbol{r}_{\mathrm{q}}(t, \boldsymbol{u}(t), \Theta(t), \boldsymbol{q}(t)). \tag{6.86}$$

The Backward Euler method is applied to the system (6.84)-(6.86), which leads to

$$\varepsilon \mathbf{u}_{n+1} = \varepsilon \mathbf{u}_{n} + \Delta t \boldsymbol{g}_{u}(t_{n+1}, \boldsymbol{u}_{n+1}, \Theta_{n+1}, \boldsymbol{q}_{n+1}), \tag{6.87}$$

$$\boldsymbol{C}_{\mathrm{p}}\, \Theta_{n+1} = \boldsymbol{C}_{\mathrm{p}}\, \Theta_{n} + \Delta t \boldsymbol{r}_{\Theta}(t_{n+1}, \boldsymbol{u}_{n+1}, \Theta_{n+1}, \boldsymbol{q}_{n+1}), \tag{6.88}$$

$$\boldsymbol{q}_{n+1} = \boldsymbol{q}_{n} + \Delta t \boldsymbol{r}_{\mathrm{q}}(t_{n+1}, \boldsymbol{u}_{n+1}, \Theta_{n+1}, \boldsymbol{q}_{n+1}). \tag{6.89}$$

Here, the discretized variables at the time steps t_n and t_{n+1} are represented by the indices n and $n+1$, respectively. Considering the case that $\varepsilon \to 0$, one obtains

$$\boldsymbol{0} = \boldsymbol{g}_{u}(t_{n+1}, \boldsymbol{u}_{n+1}, \Theta_{n+1}, \boldsymbol{q}_{n+1}), \tag{6.90}$$

$$\boldsymbol{0} = \boldsymbol{C}_{\mathrm{p}} \frac{\boldsymbol{\Theta}_{n+1} - \boldsymbol{\Theta}_{n}}{\Delta t} - \boldsymbol{r}_{\Theta}(t_{n+1}, \boldsymbol{u}_{n+1}, \boldsymbol{\Theta}_{n+1}, \boldsymbol{q}_{n+1}), \tag{6.91}$$

$$\boldsymbol{0} = \frac{\boldsymbol{q}_{n+1} - \boldsymbol{q}_{n+1}}{\Delta t} - \boldsymbol{r}_{\mathrm{q}}(t_{n+1}, \boldsymbol{u}_{n+1}, \boldsymbol{\Theta}_{n+1}, \boldsymbol{q}_{n+1}). \tag{6.92}$$

In this way, a system of nonlinear equations is obtained, which has to be solved for each time point t_{n+1} for the unknown nodal displacements $\boldsymbol{u}_{n+1}$, nodal temperatures Θ_{n+1}, and internal variables $\boldsymbol{q}_{n+1}$

$$\boldsymbol{G}_u(\boldsymbol{u},\Theta,\boldsymbol{q}) := \boldsymbol{g}_u(t_{n+1},\boldsymbol{u}_{n+1},\Theta_{n+1},\boldsymbol{q}_{n+1}) = \boldsymbol{0}, \tag{6.93}$$

$$\boldsymbol{G}_\Theta(\boldsymbol{u},\Theta,\boldsymbol{q}) := \boldsymbol{C}_\mathrm{p}\frac{\Theta_{n+1}-\Theta_n}{\Delta t} - \boldsymbol{r}_\Theta(t_{n+1},\boldsymbol{u}_{n+1},\Theta_{n+1},\boldsymbol{q}_{n+1}) = \boldsymbol{0}, \tag{6.94}$$

$$\boldsymbol{L}_\mathrm{q}(\boldsymbol{u},\Theta,\boldsymbol{q}) := \frac{\boldsymbol{q}_{n+1}-\boldsymbol{q}_n}{\Delta t} - \boldsymbol{r}_\mathrm{q}(t_{n+1},\boldsymbol{u}_{n+1},\Theta_{n+1},\boldsymbol{q}_{n+1}) = \boldsymbol{0}. \tag{6.95}$$

6.2.3 Solution of the System of Nonlinear Equations

The Multilevel Newton Algorithm is based on the decomposition of the system of equations (6.93)-(6.95) into a global level $\boldsymbol{G}(\boldsymbol{v},\boldsymbol{q})$, in which the equilibrium condition and the heat equation are solved, and a local level $\boldsymbol{L}(\boldsymbol{v},\boldsymbol{q})$ in which the internal variables are computed. This local level corresponds to the Gauss-point level. Here, the displacements and temperatures are consolidated into the vector $\boldsymbol{v}^\mathrm{T} = \{\boldsymbol{u}^\mathrm{T}\ \Theta^T\}$ and the internal variables are represented by $\boldsymbol{q}$. The system of equations (6.93)-(6.95) can be expressed by

$$\boldsymbol{G}(\boldsymbol{v},\boldsymbol{q}) = \left\{\begin{matrix}\boldsymbol{G}_u(\boldsymbol{u},\Theta,\boldsymbol{q})\\ \boldsymbol{G}_\Theta(\boldsymbol{u},\Theta,\boldsymbol{q})\end{matrix}\right\} = \boldsymbol{0}, \tag{6.96}$$

$$\boldsymbol{L}(\boldsymbol{v},\boldsymbol{q}) = \boldsymbol{L}_\mathrm{q}(\boldsymbol{u},\Theta,\boldsymbol{q}) = \boldsymbol{0}. \tag{6.97}$$

Now, the implicit function theorem is applied to Eqns. (6.96)-(6.97). To this end, it is considered that there exists a solution $\boldsymbol{q} = \hat{\boldsymbol{q}}(\boldsymbol{v})$, which is inserted into Eq. (6.96)

$$\boldsymbol{G}(\boldsymbol{v},\hat{\boldsymbol{q}}(\boldsymbol{v})) = \boldsymbol{0}, \tag{6.98}$$

which leads to an equation only depending on the global variables $\boldsymbol{v}$. The classical Newton-Raphson method can be applied, leading to

$$\left[\frac{\partial \boldsymbol{G}}{\partial \boldsymbol{v}} + \frac{\partial \boldsymbol{G}}{\partial \boldsymbol{q}}\frac{\mathrm{d}\hat{\boldsymbol{q}}}{\mathrm{d}\boldsymbol{v}}\right]_{\boldsymbol{v}^{(m)}} \Delta\boldsymbol{v}^{(m)} = -\boldsymbol{G}(\boldsymbol{v}^{(m)},\boldsymbol{q}^{(m+1)}), \tag{6.99}$$

with m as the iteration number. The right-hand side is equal to $\boldsymbol{G}^T = \{\boldsymbol{G}_u^\mathrm{T}\ \boldsymbol{G}_\Theta^\mathrm{T}\}$ and the increment $\Delta\boldsymbol{v}^\mathrm{T} = \{\Delta\boldsymbol{u}^\mathrm{T}\ \Delta\Theta^T\}$. The matrix on the left-hand side of Eq. (6.99) is known as the consistent tangent operator, see (Simo and Taylor, 1985). The components of this matrix for the thermo-mechanical coupled problem are given by

$$\left[\frac{\partial \boldsymbol{G}}{\partial \boldsymbol{v}} + \frac{\partial \boldsymbol{G}}{\partial \boldsymbol{q}}\frac{\mathrm{d}\hat{\boldsymbol{q}}}{\mathrm{d}\boldsymbol{v}}\right] = \begin{bmatrix}\dfrac{\partial \boldsymbol{G}_u}{\partial \boldsymbol{u}} + \dfrac{\partial \boldsymbol{G}_u}{\partial \boldsymbol{q}}\dfrac{\partial \hat{\boldsymbol{q}}}{\partial \boldsymbol{u}} & \dfrac{\partial \boldsymbol{G}_u}{\partial \Theta} + \dfrac{\partial \boldsymbol{G}_u}{\partial \boldsymbol{q}}\dfrac{\partial \hat{\boldsymbol{q}}}{\partial \Theta}\\ \dfrac{\partial \boldsymbol{G}_\Theta}{\partial \boldsymbol{u}} + \dfrac{\partial \boldsymbol{G}_\Theta}{\partial \boldsymbol{q}}\dfrac{\partial \hat{\boldsymbol{q}}}{\partial \boldsymbol{u}} & \dfrac{\partial \boldsymbol{G}_\Theta}{\partial \Theta} + \dfrac{\partial \boldsymbol{G}_\Theta}{\partial \boldsymbol{q}}\dfrac{\partial \hat{\boldsymbol{q}}}{\partial \Theta}\end{bmatrix}. \tag{6.100}$$

The quantities $\hat{\boldsymbol{q}}(\boldsymbol{v})$ and $\mathrm{d}\hat{\boldsymbol{q}}/\mathrm{d}\boldsymbol{v}$ are, in general, unknown. They can be provided from Eq. (6.97) on the element level, see (Hartmann, 2005). First, $\hat{\boldsymbol{q}}(\boldsymbol{v})$ is determined from Eq. (6.97) for the given displacements and temperatures $\boldsymbol{v}^{(m)}$

$$\boldsymbol{L}(\boldsymbol{v}^{(m)}, \boldsymbol{q}^{(m+1)}) = \boldsymbol{0} \qquad \rightsquigarrow \qquad \boldsymbol{q}^{(m+1)}. \tag{6.101}$$

Second, the chain rule is applied to Eq. (6.97) with the unknown function $\hat{\boldsymbol{q}}(\boldsymbol{v})$, leading to

$$\boldsymbol{L}(\boldsymbol{v}, \hat{\boldsymbol{q}}(\boldsymbol{v})) = \boldsymbol{0} \quad \longrightarrow \quad \frac{\partial \boldsymbol{L}}{\partial \boldsymbol{v}} + \frac{\partial \boldsymbol{L}}{\partial \boldsymbol{q}} \frac{\mathrm{d}\hat{\boldsymbol{q}}}{\mathrm{d}\boldsymbol{v}} = \boldsymbol{0}. \tag{6.102}$$

In other words, the derivative $\mathrm{d}\hat{\boldsymbol{q}}/\mathrm{d}\boldsymbol{v}$ can be obtained solving the linear system of equations with several right-hand sides

$$\left[\frac{\partial \boldsymbol{L}}{\partial \boldsymbol{q}}\right] \left[\frac{\mathrm{d}\hat{\boldsymbol{q}}}{\mathrm{d}\boldsymbol{v}}\right] = -\left[\frac{\partial \boldsymbol{L}}{\partial \boldsymbol{v}}\right], \tag{6.103}$$

where the matrices $\partial \boldsymbol{L}/\partial \boldsymbol{v}$ and $\partial \boldsymbol{L}/\boldsymbol{q}$ are known from the stress algorithm. The computation of the stress algorithm for the developed material models is shown in Section 6.3. For the thermo-mechanical coupled problem, Eq. (6.103) can be split up for the two components $\boldsymbol{u}$ and Θ,

$$\left[\frac{\partial \boldsymbol{L}}{\partial \boldsymbol{q}}\right] \left[\frac{\partial \hat{\boldsymbol{q}}}{\partial \boldsymbol{u}} \quad \frac{\partial \hat{\boldsymbol{q}}}{\partial \Theta}\right] = -\left[\frac{\partial \boldsymbol{L}}{\partial \boldsymbol{u}} \quad \frac{\partial \boldsymbol{L}}{\partial \Theta}\right]. \tag{6.104}$$

The solution procedure is represented in Tab. 6.4. The computation of the new time step Δt begins with the starting vectors $\boldsymbol{v}^{(0)}$ and $\boldsymbol{q}^{(0)}$. For the given values $(\boldsymbol{u}^{(m)}, \Theta^{(m)}, \boldsymbol{q}^{(m)})$, the iteration is first performed on Gauss-point level, and the new internal variables $\boldsymbol{q}^{(m+1)}$ and the derivative $\mathrm{d}\boldsymbol{q}/\mathrm{d}\boldsymbol{v}|_{\boldsymbol{y}}$ are computed. These values are provided for the global level, where the system of linear equations (6.99) is solved for $\Delta \boldsymbol{v}$. Afterwards, the new value of $\boldsymbol{v}^{(m+1)}$ can be determined and a convergence criterion has to be checked.

6.3 Stress Algorithm

The computation of the Cauchy stresses $\mathbf{T}$, the internal variables $\mathbf{q}$, the derivative $\mathrm{d}\mathbf{q}/\mathrm{d}\mathbf{v}$, and the consistent tangent $\mathbf{C}_t$ is performed on the local level within the stress algorithm. Later, these variables are assembled in global vectors and matrices for the computations on the global level. A detailed description of the relation between the variables on the global and local level is offered in (Grafenhorst, 2018). On the local level, the local time integration step is performed. In some special cases, the evolution equations can be solved either analytically or, after the time discretization, the current value of the internal variables $\mathbf{q}$ can be computed without any further iteration procedure. Nevertheless, for models with a complex structure, an iterative solution procedure has to be used.

Table 6.4: Multilevel Newton Algorithm

```
Given: starting estimation $\boldsymbol{v}^{(0)}$, $\boldsymbol{q}^{(0)}$ and $\Delta t$, $t_{n+1}$
Repeat    $m = 0, \dots$
    local (Gauss-point) level
    given: $\boldsymbol{v}^{(m)} = (\boldsymbol{u}^{(m)}, \boldsymbol{\Theta}^{(m)})$, $\boldsymbol{q}^{(m)}$
    local integration step
        $\boldsymbol{L}(\boldsymbol{v}^{(m)}, \boldsymbol{q}^{(m+1)}) = \boldsymbol{0}$        $\rightsquigarrow \boldsymbol{q}^{(m+1)}$
    consistent linearization, with $\boldsymbol{y} = \left(\boldsymbol{u}^{(m)}, \boldsymbol{\Theta}^{(m)}, \boldsymbol{q}^{(m+1)}\right)$
        $\left.\frac{\partial \boldsymbol{L}}{\partial \boldsymbol{q}}\right|_{\boldsymbol{y}} \left.\frac{\mathrm{d}\hat{\boldsymbol{q}}}{\mathrm{d}\boldsymbol{v}}\right|_{\boldsymbol{y}} = - \left.\frac{\partial \boldsymbol{L}}{\partial \boldsymbol{v}}\right|_{\boldsymbol{y}}$        $\rightsquigarrow \left.\frac{\mathrm{d}\boldsymbol{q}}{\mathrm{d}\boldsymbol{v}}\right|_{\boldsymbol{y}}$
    global level
    solve linear system of equations
        $\left[\left.\frac{\partial \boldsymbol{G}}{\partial \boldsymbol{v}}\right|_{\boldsymbol{y}} + \left.\frac{\partial \boldsymbol{G}}{\partial \boldsymbol{q}}\right|_{\boldsymbol{y}} \left.\frac{\mathrm{d}\hat{\boldsymbol{q}}}{\mathrm{d}\boldsymbol{v}}\right|_{\boldsymbol{y}}\right] \Delta \boldsymbol{v} = -\boldsymbol{G}(\boldsymbol{v}^{(m)}, \boldsymbol{q}^{(m+1)})$    $\rightsquigarrow \Delta \boldsymbol{v}$
    update of global variables
        $\boldsymbol{v}^{(m+1)} \leftarrow \boldsymbol{v}^{(m)} + \Delta \boldsymbol{v}$        $\rightsquigarrow \boldsymbol{v}^{(m+1)}$
until    the convergence criterion is fulfilled
```

Analogously to Eq. (6.65), the relation between the local and global level for discretized system of equation of the internal variables is given by

$$\boldsymbol{L}(\boldsymbol{v},\boldsymbol{q}) = \sum_{e=1}^{n_e}\sum_{l=1}^{n_{\text{GP}}} \boldsymbol{Z}_{\text{q}l}^{\text{e}^{\text{T}}}\, \mathbf{L}(\mathbf{C}_l^{\text{e}},\Theta_l^{\text{e}},\mathbf{q}_l^{\text{e}}), \qquad \mathbf{L}(\mathbf{C}_l^{\text{e}},\Theta_l^{\text{e}},\mathbf{q}_l^{\text{e}}) \in \mathbb{R}^{n_{\text{q}}}. \tag{6.105}$$

Thus, the time-discretized evolution equations can be expressed as a system of equations on the local level

$$\mathbf{L}(\mathbf{C},\Theta,\mathbf{q}) = \mathbf{0}. \tag{6.106}$$

The Newton-Raphson method can be applied to this system of equations, leading to

$$\left[\frac{\mathrm{d}\mathbf{L}}{\mathrm{d}\mathbf{q}}\right]\Bigg|_{\mathbf{q}=\mathbf{q}^{(k)}} \Delta\mathbf{q}^{(k)} = -\mathbf{L}(\mathbf{C},\Theta,\mathbf{q}^{(k)}), \tag{6.107}$$

with the iteration index k for the local level. With the solution $\Delta\mathbf{q}^{(k)}$ of this linear system, the internal variables for the next iteration can be computed by

$$\mathbf{q}^{(k+1)} = \mathbf{q}^{(k)} + \Delta\mathbf{q}^{(k)}. \tag{6.108}$$

This iterative procedure is continued until a chosen convergence criterion is fulfilled, for example

$$\|\mathbf{L}(\mathbf{C},\Theta,\mathbf{q}^{(k)})\| < \text{tol}_{\mathbf{L}} \quad \text{and/or} \quad \|\Delta\mathbf{q}^{(k)}\| < \text{tol}_{\mathbf{q}} \tag{6.109}$$

with the tolerance $\text{tol}_{\mathbf{L}}$ and $\text{tol}_{\mathbf{q}}$. With the known internal variables, the Cauchy stress $\mathbf{T}$ can be computed. In the following, the special cases of the stress algorithm for the developed models from Chapter 4 are shown.

Model of Small Deformations

In the model of small deformations from Tab. 4.1, the vector of internal variables consists of the following components: $\mathbf{q}^{\text{T}} = \{\mathbf{Y}^{\text{T}}, \mathbf{E}_{\text{v}}^{\text{T}}, k, a\}$, where the tensors are written in vector form using their symmetry properties. Since this model features linear evolution equations of the internal variables $\mathbf{Y}$, $\mathbf{E}_{\text{v}}$ and k – and since a quadratic equation is obtained for a – it is possible to compute the value of the internal variables at the current time step without a local Newton-Raphson method. In this case, a pure Newton-Raphson method is applied to solve the global system of equations. After applying a Backward

Euler step to the evolution equations from Tab. 4.1, one obtains

$$a_{n+1} = a_n + \Delta t_n \beta_{a1}(\Theta_{n+1}) \frac{1 - a_{n+1}}{\beta_{a2} + a_{n+1}}, \tag{6.110}$$

$$k_{n+1} = k_n + \Delta t_n \left(\alpha_k (1 - k_{n+1}) \frac{\Delta s_{\mathrm{M}n}}{\Delta t_n} \right), \tag{6.111}$$

$$\mathbf{Y}_{n+1} = \mathbf{Y}_n + \Delta t_n \left(\frac{c(\Theta_{n+1})}{c_\alpha} \mathbf{D} \left(\frac{\Delta \mathbf{E}_n}{\Delta t_n} \right) - b \frac{\Delta s_{\mathrm{M}n}}{\Delta t_n} \mathbf{Y}_{n+1} \right), \tag{6.112}$$

$$\mathbf{E}_{\mathrm{v}n+1} = \mathbf{E}_{\mathrm{v}n} + \frac{2 \Delta t_n G_{\mathrm{ov}}(\Theta_{n+1}, k_{n+1})}{\eta(\Delta s_{\mathrm{M}n}, \Theta_{n+1}, a_{n+1})} \mathbf{D} \left(\mathbf{E}_{n+1} - \mathbf{E}_{\mathrm{v}n+1} \right), \tag{6.113}$$

where $\Delta s_{\mathrm{M}n}$ is the increment in arc-length. It can be obtained by applying a Backward Euler step to the arc-length

$$s_{\mathrm{M}n+1} = s_{\mathrm{M}n} + \dot{s}_{\mathrm{M}} \Delta t_n = s_{\mathrm{M}n} + \Delta s_{\mathrm{M}n}, \tag{6.114}$$

and with definition Eq. (4.26), one obtains

$$\begin{aligned} \Delta s_{\mathrm{M}n} = \dot{s}_{\mathrm{M}} \Delta t_n &= \sqrt{(\mathbf{D}(\mathbf{E}_{n+1} - \mathbf{E}_n))^{\mathrm{T}} \mathbf{M} (\mathbf{D}(\mathbf{E}_{n+1} - \mathbf{E}_n))} \\ &= \sqrt{(\mathbf{D} \Delta \mathbf{E}_n)^{\mathrm{T}} \mathbf{M} (\mathbf{D} \Delta \mathbf{E}_n)}, \end{aligned} \tag{6.115}$$

where the strain vector $\mathbf{E}$ represents the total strains. Here, the scalar product is expressed in matrix notation with

$$\mathrm{A} \cdot \mathrm{A} = \mathbf{A}^{\mathrm{T}} \mathbf{M}^{-1} \mathbf{A} \quad \text{with} \quad \mathbf{M} = \mathrm{diag}(1, 1, 1, 2, 2, 2). \tag{6.116}$$

The deviator operator of a tensor A is given in matrix formulation by

$$\mathbf{A}^{\mathrm{D}} = \mathbf{D}\mathbf{A} \quad \text{with} \quad \mathbf{D} = \frac{1}{3} \begin{bmatrix} 2 & -1 & -1 & & & \\ -1 & 2 & -1 & & & \\ -1 & -1 & 2 & & & \\ & & & 3 & & \\ & & & & 3 & \\ & & & & & 3 \end{bmatrix}. \tag{6.117}$$

Each equation can be solved for the internal variables at the current time step, leading to

$$a_{n+1}(\Theta_{n+1}, a_n) = \frac{1}{2}(a_n - \beta_{a2} - \Delta t_n \beta_{a1}(\Theta_{n+1})) + \sqrt{\frac{1}{4}(\beta_{a2} + \Delta t_n \beta_{a1}(\Theta_{n+1}) - a_n)^2 + \beta_{a2} a_n + \Delta t_n \beta_{a1}(\Theta_{n+1})}, \tag{6.118}$$

$$k_{n+1}(\mathbf{E}_{n+1}, k_n) = \frac{k_n + \alpha_k \Delta s_{\mathrm{M}n}(\mathbf{E}_{n+1})}{1 + \alpha_k \Delta s_{\mathrm{M}n}(\mathbf{E}_{n+1})}, \tag{6.119}$$

$$\mathbf{Y}_{n+1}(\mathbf{E}_{n+1}, \Theta_{n+1}, \mathbf{Y}_n) = \frac{\mathbf{Y}_n + c(\Theta_{n+1})/c_\alpha \mathbf{D}\Delta\mathbf{E}_n}{1 + b\Delta s_{\mathrm{M}n}(\mathbf{E}_{n+1})}, \tag{6.120}$$

$$\mathbf{E}_{\mathrm{v}n+1}(\mathbf{E}_{n+1}, \Theta_{n+1}, a_{n+1}, k_{n+1}) = \frac{\mathbf{E}_{\mathrm{v}n}\eta(\mathbf{E}_{n+1}, \Theta_{n+1}, a_{n+1}) + 2\Delta t_n G_{\mathrm{ov}}(k_{n+1})\mathbf{D}\mathbf{E}_{n+1}}{\eta(\mathbf{E}_{n+1}, \Theta_{n+1}, a_{n+1}) + 2\Delta t_n G_{\mathrm{ov}}(k_{n+1})}. \tag{6.121}$$

The total stress at the current time step $\mathbf{T}_{n+1}$ can be computed by

$$\begin{aligned}\mathbf{T}_{n+1} &= \mathbf{h}(\mathbf{E}_{n+1}, \Theta_{n+1}, a_{n+1}, k_{n+1}, \mathbf{Y}_{n+1}, \mathbf{E}_{\mathrm{v}n+1}) \\ &= \mathbf{T}^{\mathrm{e}}_{\mathrm{eq}n+1}(\mathbf{E}_{n+1}, \Theta_{n+1}, a_{n+1}) + \mathbf{T}^{\mathrm{h}}_{\mathrm{eq}n+1}(\mathbf{Y}_{n+1}) + \mathbf{T}_{\mathrm{ov}n+1}(k_{n+1}, \mathbf{E}_{\mathrm{v}n+1}),\end{aligned} \tag{6.122}$$

with the elastic equilibrium stress

$$\mathbf{T}^{\mathrm{e}}_{\mathrm{eq}n+1} = K_{\mathrm{eq}}(\mathrm{tr}\,\mathbf{E}_{n+1})\mathbf{I} + 2G_{\mathrm{eq}}\mathbf{D}\mathbf{E}_{n+1} + 3K_{\mathrm{eq}}(\beta_{a11}a_{n+1} - \alpha_\Theta(\Theta_{n+1} - \Theta_0))\mathbf{I}, \tag{6.123}$$

the plastic equilibrium stress

$$\mathbf{T}^{\mathrm{h}}_{\mathrm{eq}n+1} = c_\alpha \mathbf{Y}_{n+1}, \tag{6.124}$$

and the overstress

$$\mathbf{T}_{\mathrm{ov}n+1} = 2G_{\mathrm{ov}}(k_{n+1})\mathbf{D}(\mathbf{E}_{n+1} - \mathbf{E}_{\mathrm{v}n+1}). \tag{6.125}$$

The functions of the material parameters can be obtained from Tab. 4.1. The determination of the consistent tangent is discussed at the end of the section.

Model of Finite Deformations

In the case of large deformations, the MLNA has to be applied and a consistent linearization is necessary. In this model, the vector of internal variables $\mathbf{q}^{\mathrm{T}} = \{\mathbf{C}_{\mathrm{p}}^{\mathrm{T}}, \mathbf{C}_{\mathrm{v}}^{\mathrm{T}}, k, a\}$ has two vectorial components, $\mathbf{C}_{\mathrm{p}}$ and $\mathbf{C}_{\mathrm{v}}$, which are expressed in Voigt notation, and two scalar components, k and a. By applying a Backward Euler step to the evolution equations of the internal variables, see Tab. 4.3, one obtains

$$\mathbf{0} = \mathbf{C}_{\mathrm{p}_{n+1}} - \mathbf{C}_{\mathrm{p}_n} - \Delta t_n \left(4(\varphi_a \varphi_\Theta)^{-2} J^{-2/3} b \frac{\Delta s_{\mathrm{M}n}}{\Delta t_n} \mathbf{C}_{\mathrm{p}_{n+1}} \mathbf{D}(\mathbf{C}_{\mathrm{p}_{n+1}}^{-1} \mathbf{C}) \right), \tag{6.126}$$

$$\mathbf{0} = \mathbf{C}_{\mathrm{v}n+1} - \mathbf{C}_{\mathrm{v}n} - \Delta t_n \left(\frac{4\mu_{\mathrm{ov}}}{\eta} (\varphi_a \varphi_\Theta)^{-2} J^{-2/3} \mathbf{C}_{\mathrm{v}n+1} \mathbf{D}(\mathbf{C}_{\mathrm{v}n+1}^{-1} \mathbf{C}) \right), \tag{6.127}$$

$$0 = k_{n+1} - k_n - \Delta t_n \left(\alpha_k (1 - k_{n+1}) \frac{\Delta s_{\mathrm{M}n}}{\Delta t_n} \right), \tag{6.128}$$

$$0 = a_{n+1} - a_n - \Delta t_n \beta_{a1}(\Theta_{n+1}) \frac{1 - a_{n+1}}{\beta_{a2} + a_{n+1}}, \tag{6.129}$$

with the increment of the mechanical arc-length

$$\Delta s_{\mathrm{M}n} = \frac{J^{-2/3}}{2} \sqrt{\left(\mathbf{C}_{\mathrm{p}_{n+1}}^{-1} \mathbf{C} \mathbf{D}(\mathbf{C}^{-1} \Delta \mathbf{C}) \mathbf{C}_{\mathrm{p}_{n+1}}^{-1} \right)^{\mathrm{T}} \mathbf{M}^{-1} \left(\mathbf{C} \mathbf{D}(\mathbf{C}^{-1} \Delta \mathbf{C}) \right)}. \tag{6.130}$$

The discretized form of Eqns. (6.126)-(6.129) leads to a system of nonlinear equations with the form of Eq. (6.106)

$$\mathbf{L}_{\mathrm{p}}(\mathbf{C}, \Theta, \mathbf{C}_{\mathrm{p}}, a) = \mathbf{0}, \tag{6.131}$$

$$\mathbf{L}_{\mathrm{v}}(\mathbf{C}, \Theta, \mathbf{C}_{\mathrm{p}}, \mathbf{C}_{\mathrm{v}}, k, a) = \mathbf{0}, \tag{6.132}$$

$$\mathsf{L}_k(\mathbf{C}, \Theta, \mathbf{C}_{\mathrm{p}}, k) = 0, \tag{6.133}$$

$$\mathsf{L}_a(\Theta, a) = 0. \tag{6.134}$$

After solving this system with the Newton-Raphson method for the internal variables $\mathbf{q}^{\mathrm{T}} = \{\mathbf{C}_{\mathrm{p}_{n+1}}^{\mathrm{T}}, \mathbf{C}_{\mathrm{v}n+1}^{\mathrm{T}}, k_{n+1}, a_{n+1}\}$, the second Piola-Kirchhoff stress can be computed by

$$\begin{aligned} \tilde{\mathbf{T}}_{n+1} &= \tilde{\mathbf{h}}(\mathbf{C}_{n+1}, \Theta_{n+1}, \mathbf{C}_{\mathrm{p}_{n+1}}, \mathbf{C}_{\mathrm{v}n+1}, k_{n+1}, a_{n+1}) \\ &= \tilde{\mathbf{T}}^{\mathrm{e}}_{\mathrm{eq}_{n+1}}(\mathbf{C}_{n+1}, \Theta_{n+1}, a_{n+1}) + \tilde{\mathbf{T}}^{\mathrm{h}}_{\mathrm{eq}_{n+1}}(\mathbf{C}_{n+1}, \Theta_{n+1}, \mathbf{C}_{\mathrm{p}_{n+1}}) \\ &\qquad + \tilde{\mathbf{T}}_{\mathrm{ov}n+1}(\mathbf{C}_{n+1}, \Theta_{n+1}, \mathbf{C}_{\mathrm{v}n+1}). \end{aligned} \tag{6.135}$$

Here, the elastic equilibrium stress is given by

$$\tilde{\mathbf{T}}^{\mathrm{e}}_{\mathrm{eq}_{n+1}} = \frac{K}{10} \left(J_{\mathrm{M}}^{5} - J_{\mathrm{M}}^{-5} \right) \mathbf{C}^{-1} + 2 c_{10} J^{-2/3} \mathbf{C}^{-1} \mathbf{D} \mathbf{C}, \tag{6.136}$$

with $J_{\mathrm{M}} = ((1 - \alpha_a a)(1 + \alpha_\Theta(\Theta - \Theta_0)))^{-3} J$. The plastic equilibrium stress is equal to

$$\tilde{\mathbf{T}}^{\mathrm{h}}_{\mathrm{eq}_{n+1}} = 2\mu_{\mathrm{eq}}(\Theta_{n+1}) J^{-2/3} \mathbf{C}^{-1} \mathbf{D}(\mathbf{C} \mathbf{C}_{\mathrm{p}_{n+1}}^{-1}), \tag{6.137}$$

and the overstress reads

$$\tilde{\mathbf{T}}_{\mathrm{ov}n+1} = 2\mu_{\mathrm{ov}}(k_{n+1}) J^{-2/3} \mathbf{C}^{-1} \mathbf{D}(\mathbf{C} \mathbf{C}_{\mathrm{v}n+1}^{-1}). \tag{6.138}$$

Consistent Tangent Matrix

The consistent tangent matrix $\mathbf{C}_t$, which contains the derivatives of the elasticity relation with respect to the total strains $\mathbf{E}$ and temperature Θ in the case of small deformations

$$\mathbf{C}_t = \left\{ \frac{\mathrm{d}\mathbf{h}}{\mathrm{d}\mathbf{E}} \quad \frac{\mathrm{d}\mathbf{h}}{\mathrm{d}\Theta} \right\}, \tag{6.139}$$

or the derivatives with respect to the right Cauchy-Green tensor $\mathbf{C}$ and the temperature Θ for the case of large deformations

$$\mathbf{C}_t = \left\{ \frac{\mathrm{d}\tilde{\mathbf{h}}}{\mathrm{d}\mathbf{C}} \quad \frac{\mathrm{d}\tilde{\mathbf{h}}}{\mathrm{d}\Theta} \right\}, \tag{6.140}$$

has to be computed on the local level for the consistent linearization. There are several possibilities to compute this variable. A first option is to compute $\mathbf{C}_t$ analytically by applying the chain rule to Eq. (6.139) for the small deformations case

$$\frac{\mathrm{d}\mathbf{h}}{\mathrm{d}\mathbf{E}} = \frac{\partial\mathbf{h}}{\partial\mathbf{E}} + \frac{\partial\mathbf{h}}{\partial\mathbf{q}}\frac{\mathrm{d}\mathbf{q}}{\mathrm{d}\mathbf{E}}, \tag{6.141}$$

$$\frac{\mathrm{d}\mathbf{h}}{\mathrm{d}\Theta} = \frac{\partial\mathbf{h}}{\partial\Theta} + \frac{\partial\mathbf{h}}{\partial\mathbf{q}}\frac{\mathrm{d}\mathbf{q}}{\mathrm{d}\Theta}, \tag{6.142}$$

or Eq. (6.140) for the finite deformations case

$$\frac{\mathrm{d}\tilde{\mathbf{h}}}{\mathrm{d}\mathbf{C}} = \frac{\partial\tilde{\mathbf{h}}}{\partial\mathbf{C}} + \frac{\partial\tilde{\mathbf{h}}}{\partial\mathbf{q}}\frac{\mathrm{d}\mathbf{q}}{\mathrm{d}\mathbf{C}}, \tag{6.143}$$

$$\frac{\mathrm{d}\tilde{\mathbf{h}}}{\mathrm{d}\Theta} = \frac{\partial\tilde{\mathbf{h}}}{\partial\Theta} + \frac{\partial\tilde{\mathbf{h}}}{\partial\mathbf{q}}\frac{\mathrm{d}\mathbf{q}}{\mathrm{d}\Theta}. \tag{6.144}$$

The derivatives of $\mathbf{h}$ and $\tilde{\mathbf{h}}$ with respect to the strains, the internal variables, and the temperature can be computed directly from the elasticity relation. The derivatives of the internal variables $\mathbf{q}$ with respect to $\mathbf{E}$ or $\mathbf{C}$ and the temperature Θ can be obtained solving the nonlinear system of equations Eq. (6.104) on the local level for $\mathrm{d}\mathbf{q}/\mathrm{d}\mathbf{v}$. The computation of the analytical tangent offers the implementation with the fastest and most robust computations – with the main disadvantage that it is very time consuming in its derivation and implementation. The second option is the numerical computation of the derivatives with finite differences, which can lead to slower computations or even prevent the convergence because of the inaccuracy of the numerical computation, see (Rothe, 2015). The third possibility is the use of Automatic Differentiation (AD), see (Griewank and Walther, 2008; Naumann, 2012). With this method, derivatives can be computed efficiently and accurately. A further possibility is to rely on other tools such as the software Acegen. Acegen allows to compute the tangent using Mathematica –

combining symbolic and algebraic operations, automatic code generation, automatic differentiation, and simultaneous optimization of expressions, see (Korelc, 2002, 2009) for more information. In this work, the consistent tangent is computed with this last option. Further possibilities for the computation are mentioned in (Rothe, 2015). A comparison between analytical, numerical, and automatic differentiation is offered in (Rothe and Hartmann, 2015).

7 Numerical Examples

In this chapter, the behavior of the developed material model is investigated with three numerical examples. In the first example, the stiffness of the system of differential equations is analyzed for the one-dimensional case with the help of Matlab. In the second example, a process with a mechanical loading coupled with a temperature driven process, in which the aging variable develops, is investigated in a 3D-component part. The last example focuses on experiments performed on real component parts made of Zamak 5, which are compared to simulations in order to analyze the quality of the prediction of the model. For the second and third example, the commercial finite element code Abaqus is used, see ABAQUS (2019). In all FE-simulations in this chapter, the mesh is chosen to be sufficiently fine so that the spatial error can be assumed to be small.

7.1 Investigation of the Stiffness of the System of Differential Equations

The material model proposed in Chapter 4 is composed of a system of equations with a combination of algebraic and differential equations, containing four internal variables. The evolution equations of the aging a and the softening k are scalar equations, and those of the plastic strain $\mathbf{Y}$ and the viscous strain $\mathbf{E}_{\mathrm{v}}$ are tensorial equations with 6 different components each – due to the symmetry of the tensors. A common problem of systems of differential equations describing physical processes lies in the rate at which every equation evolves. If one equation develops much faster or slower than the others, the system is called *stiff*. This phenomenon has to be considered in order to choose the right time discretization method to avoid stability and robustness problems, see Schwarz and Köckler (2006). The non-linear system of n differential equations for $y_1(x), ..., y_n(x) \in \mathbb{R}$ is considered

$$\dot{y}_1 = f_1(x, y_1(x), y_2(x), ..., y_n(x)), \tag{7.1}$$

$$\dot{y}_2 = f_2(x, y_1(x), y_2(x), ..., y_n(x)), \tag{7.2}$$

$$... \tag{7.3}$$

$$\dot{y}_n = f_n(x, y_1(x), y_2(x), ..., y_n(x)), \tag{7.4}$$

with the Jacobian

$$\mathbf{J} = \left[\frac{\partial f_i}{\partial y_j}\right]. \tag{7.5}$$

One attribute to describe the stiffness of a system of differential equations is proposed in Schwarz and Köckler (2006) as the ratio between the maximal and the minimal eigenvalue of the Jacobi matrix

$$S = \frac{\max\limits_{j} |Re(\lambda_j)|}{\min\limits_{j} |Re(\lambda_j)|} \qquad \text{for all } \lambda_i \text{ with} Re(\lambda_j) < 0. \tag{7.6}$$

A system of differential equations is considered stiff if all eigenvalues have a negative real part and the stiffness S is larger than 10. This means that the difference in the order of magnitude between the eigenvalues is large.

The stiffness of the system of differential equation from Chapter 4 is investigated for the one-dimensional case for the small deformations problem. The case of large deformations is analogous.[1] Here, the driving variables for the system are the strain ε and strain-rate $\dot{\varepsilon}$, as well as the temperature Θ and the temperature rate $\dot{\Theta}$. The variables to be determined are the aging a, the softening k, the plastic strain y, and the viscous strain ε_v. The system of Tab. 4.1 can be formulated for the one-dimensional case as

$$\dot{a} = f_a(\Theta, a) = \beta_{a1}(\Theta)\frac{1-a}{\beta_{a2}+a}, \tag{7.7}$$

$$\dot{k} = f_k(\dot{\varepsilon}, \dot{\Theta}, \Theta, a, k) = \alpha_k \left| \dot{\varepsilon} - \alpha_\Theta \dot{\Theta} + \alpha_a \beta_{a1}(\Theta)\frac{1-a}{\beta_{a2}+a} \right| (1-k), \tag{7.8}$$

$$\begin{aligned} \dot{y} &= f_y(\dot{\varepsilon}, \dot{\Theta}, \Theta, a, y) \qquad (7.9)\\ &= \frac{c(\Theta)}{c_\alpha}\left(\dot{\varepsilon} - \alpha_\Theta\dot{\Theta} + \frac{\alpha_a\beta_{a1}(\Theta)(1-a)}{\beta_{a2}+a}\right) - b\left|\dot{\varepsilon} - \alpha_\Theta\dot{\Theta} + \frac{\alpha_a\beta_{a1}(\Theta)(1-a)}{\beta_{a2}+a}\right| y, \end{aligned}$$

$$\dot{\varepsilon}_\mathrm{v} = f_\mathrm{v}(\dot{\varepsilon}, \varepsilon, \dot{\Theta}, \Theta, a, k, \varepsilon_\mathrm{v}) = \frac{2G_\mathrm{ov}(k)}{\eta(\dot{\varepsilon}, \dot{\Theta}, \Theta, a)}(\varepsilon - \alpha_\Theta(\Theta - \Theta_0) + \alpha_a a - \varepsilon_\mathrm{v}). \tag{7.10}$$

In order to investigate the stiffness of the system of differential equations, the Jacobian $\mathbf{J}$ is determined

$$\mathbf{J} = \begin{pmatrix} \partial f_a/\partial a & 0 & 0 & 0 \\ \partial f_k/\partial a & \partial f_k/\partial k & 0 & 0 \\ \partial f_y/\partial a & 0 & \partial f_y/\partial y & 0 \\ \partial f_\mathrm{v}/\partial a & \partial f_\mathrm{v}/\partial k & 0 & \partial f_\mathrm{v}/\partial \varepsilon_\mathrm{v} \end{pmatrix}. \tag{7.11}$$

The eigenvalues λ are obtained from the equation

$$\det(\mathbf{J} - \lambda\mathbf{I}) = 0, \tag{7.12}$$

---

[1] Both cases are analogous, since the linearization of the large deformations model leads to the small deformations model. Moreover, the rate at which each differential equation develops is given by the material parameters, which are similar in both cases.

with $\mathbf{I} \in \mathbb{R}^{4\times 4}$ being the identity matrix. For the case of the present triangular matrix, the determinant can be computed as the product of its diagonal values

$$\det(\mathbf{J} - \lambda \mathbf{I}) = \left(\frac{\partial f_a}{\partial a} - \lambda\right)\left(\frac{\partial f_k}{\partial k} - \lambda\right)\left(\frac{\partial f_y}{\partial y} - \lambda\right)\left(\frac{\partial f_\mathrm{v}}{\partial \varepsilon_\mathrm{v}} - \lambda\right) = 0, \tag{7.13}$$

Four eigenvalues can be obtained from Eq. (7.13), directly connected to each of the effects described by the model. The eigenvalue λ_a is connected to the aging, λ_k to the softening, λ_y to the equilibrium state, and λ_v to the viscous effects

$$\lambda_a(\Theta, a) = \frac{\partial f_a}{\partial a} = -\frac{\beta_{a1}(\Theta)}{\beta_{a2} + a}\left(1 + \frac{1-a}{\beta_{a2} + a}\right), \tag{7.14}$$

$$\lambda_k(\dot{\varepsilon}, \dot{\Theta}, \Theta, a) = \frac{\partial f_k}{\partial k} = -\alpha_k \left|\dot{\varepsilon} - \alpha_\Theta \dot{\Theta} + \frac{\alpha_a \beta_{a1}(\Theta)(1-a)}{\beta_{a2} + a}\right|, \tag{7.15}$$

$$\lambda_y(\dot{\varepsilon}, \dot{\Theta}, \Theta, a) = \frac{\partial f_y}{\partial y} = -b \left|\dot{\varepsilon} - \alpha_\Theta \dot{\Theta} + \frac{\alpha_a \beta_{a1}(\Theta)(1-a)}{\beta_{a2} + a}\right|, \tag{7.16}$$

$$\lambda_\mathrm{v}(\dot{\varepsilon}, \dot{\Theta}, \Theta, a, k) = \frac{\partial f_\mathrm{v}}{\partial \varepsilon_\mathrm{v}} = -\frac{2G_\mathrm{ov}(k)}{\eta(\dot{\varepsilon}, \dot{\Theta}, \Theta, a)}. \tag{7.17}$$

Since all material parameters are positive, these values are always negative – and thus, the stability of the system of differential equations is ensured, see (Schwarz and Köckler, 2006). For the identified material parameters, the eigenvalues are

$$\lambda_a(\Theta, a) = -\frac{2.8 \times 10^4 \exp(-8113/\Theta)}{10^{-5} + a}\left(1 + \frac{1-a}{10^{-5} + a}\right), \tag{7.18}$$

$$\lambda_k(\dot{\varepsilon}, \dot{\Theta}, \dot{a}) = -350|\dot{\varepsilon} - \alpha_\Theta \dot{\Theta} + \alpha_a \dot{a}|, \tag{7.19}$$

$$\lambda_y(\dot{\varepsilon}, \dot{\Theta}, \dot{a}) = -219|\dot{\varepsilon} - \alpha_\Theta \dot{\Theta} + \alpha_a \dot{a}|, \tag{7.20}$$

$$\lambda_\mathrm{v}(\dot{\varepsilon}, \dot{\Theta}, \Theta, a, k) = -\frac{6.416 \times 10^4}{\eta(\dot{\varepsilon}, \dot{\Theta}, \dot{a}, \Theta, a)}((1-k)^{0.35} + 0.2). \tag{7.21}$$

Several eigenvalues of the aging variable $\lambda_a(\Theta, a)$ are shown in Tab. 7.1. Here, one can observe that this parameter has a broad interval of values. The maximum value is reached for all temperatures for the initial state $a = 0$. The value decreases rapidly for a constant temperature with increasing aging time. Moreover, higher temperatures accelerate the aging process, which is reflected in the increase of $\lambda_a(\Theta, a)$ together with the temperature. This can be seen if one compares, for example, the case of $\Theta = 200\,°\mathrm{C}$ with $\Theta = 20\,°\mathrm{C}$, where there is a difference of 4 orders of magnitude. The eigenvalues λ_k and λ_y are both of the same order of magnitude, as one can see in Eqns. (7.19) and (7.20). Their order of magnitude depends on the mechanical strain-rate. The mechanical strain-rate has values between 0 and 10^{-3}, so the values for λ_k and λ_y are of an order of magnitude between 0 and -10^{-2}. Finally, the eigenvalue $\lambda_\mathrm{v}(\dot{\varepsilon}, \dot{\Theta}, \Theta, a, k)$ depends on several variables, and has to be analyzed in more detail under different loading conditions. In the following, two different loading cases are considered.

Table 7.1: Eigenvalues of the aging variable in dependence of temperature and aging time

Θ	$\lambda_a(\Theta,0)$	$\lambda_a(\Theta,0.1)$	$\lambda_a(\Theta,0.5)$	$\lambda_a(\Theta,1)$
$-40\,°\mathrm{C}$	-0.21	-2.11×10^{-9}	-10^{-10}	-10^{-11}
$20\,°\mathrm{C}$	-2.64×10^{2}	-2.64×10^{-6}	-2.93×10^{-7}	-10^{-8}
$60\,°\mathrm{C}$	-7.35×10^{3}	-7.35×10^{-5}	-8.17×10^{-6}	-10^{-7}
$100\,°\mathrm{C}$	-10^{5}	-10^{-3}	-1.11×10^{-4}	-10^{-5}
$200\,°\mathrm{C}$	-10^{7}	-10^{-1}	-4×10^{-3}	-10^{-3}

First Loading Path

The first loading path is displayed in Fig. 7.1. A first loading-unloading process up to a deformation $\varepsilon_1 = 1.5\,\%$ takes place during $t_1 = 60\,\mathrm{s}$, followed by 5 days without a load. After that, the loading-unloading process is repeated. The temperature is constant. The two different temperatures $\Theta_1 = 20\,°\mathrm{C}$ and $\Theta_2 = 100\,°\mathrm{C}$ are investigated. Fig. 7.2 shows the four eigenvalues determined with Eqns. (7.18)-(7.21) for the first loading path and the two different temperatures. The scale of both axes is logarithmic. Here, one can see a continuous reduction in the eigenvalue related to the aging variable λ_a. It exhibits its maximum at the time $t = 0$, see Tab. 7.1, which means that the aging rate is very high. With increasing values of aging, the aging becomes a very slow process. The other eigenvalues are connected to the loading process. When the load disappears, they turn out roughly four orders of magnitude smaller. The eigenvalues λ_k and λ_y are both connected to rate-independent equations, which explains why they behave similarly. λ_v is related to viscous effects, which are present in the relaxation process during the five days after the first loading.

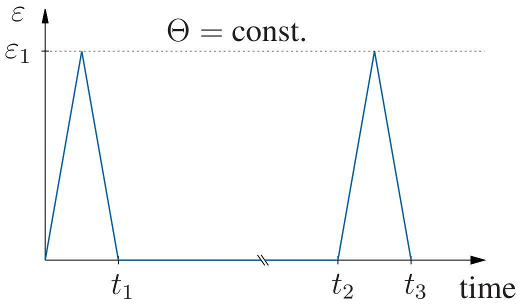

Figure 7.1: First loading path: loading-unloading until ε_1 with $\dot{\varepsilon}_1 = 5.0\times10^{-4}\,\mathrm{s}^{-1}$, followed by five days without a load and further loading-unloading

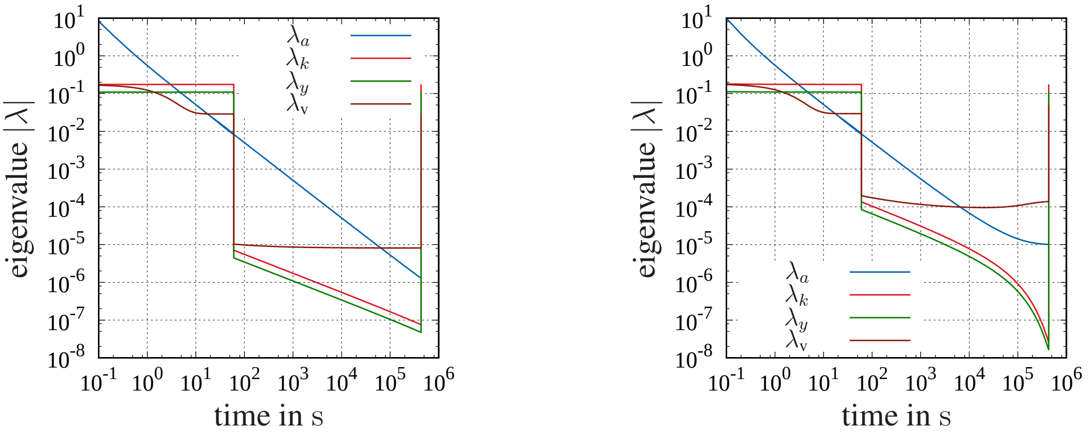

(a) $\Theta = 20\,^\circ\mathrm{C}$

(b) $\Theta = 100\,^\circ\mathrm{C}$

Figure 7.2: Eigenvalues for the first loading case at two different temperatures

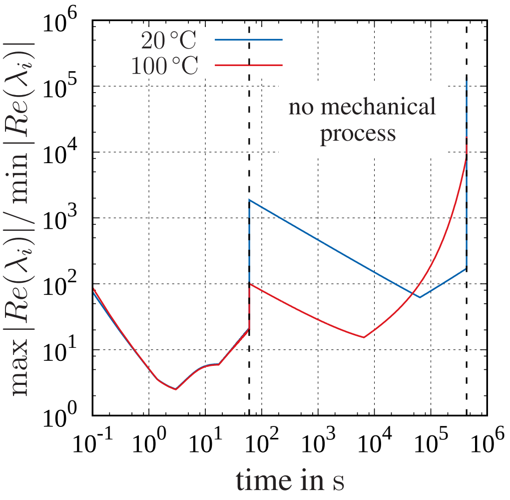

Figure 7.3: Stiffness measure S of the first loading case

In Fig. 7.3, the stiffness S determined from Eq. (7.6) is represented for both temperatures over time. Both axis scales are logarithmic. Although this is not shown in the diagram, the stiffness is very high at the time $t = 0$ – of the order of 10^3 for $\Theta = 20\,°\mathrm{C}$ and 10^5 for $\Theta = 100\,°\mathrm{C}$ – and it reduces strongly in less than a second. In the diagram 7.3, it can be seen that the value of S is lower than 100 during the first 60 seconds of the loading process. Then, it decreases monotonously until roughly 10 seconds. After that, the system becomes stiff for the case of room temperature. For the process at $\Theta = 100\,°\mathrm{C}$, the system becomes stiff after one day – approximately $8.5 \times 10^4\,\mathrm{s}$. During the second loading process, the stiffness of the system increases strongly in both cases with values over 10^4.

Second Loading Path

For the second loading case, a relaxation process with two different temperature paths is investigated, see Fig. 7.4. The constant strain-rate to reach the strain $\varepsilon_1 = 1.5\,\%$ is one order of magnitude lower than in the previous example $\dot{\varepsilon}_2 = 5.0 \times 10^{-5}\,\mathrm{s}^{-1}$. A constant temperature path equal to $\Theta_1 = 20\,°\mathrm{C}$ is chosen first. Moreover, the path shown in Fig. 7.4(b) is chosen. This is a sinusoidal temperature path with an average temperature of $\Theta_0 = 25\,°\mathrm{C}$, an amplitude of $\pm 5\,°\mathrm{C}$, and a wave length of one day – exhibiting periodical temperature changes during the five days.

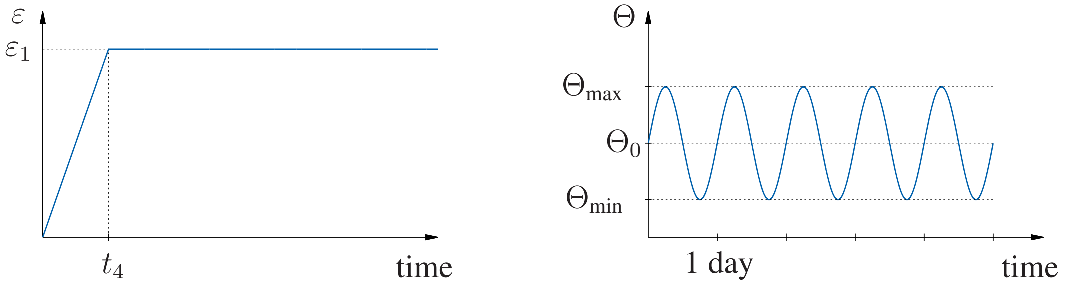

(a) Loading until $\varepsilon_1 = 1.5\,\%$ with $\dot{\varepsilon}_2 = 5.0 \times 10^{-5}\,\mathrm{s}^{-1}$ and furhter relaxation. Simulations at the constant temperature $\Theta_1 = 20\,°\mathrm{C}$ and temperature path from Fig. 7.4(b)

(b) Temperatute path $\Theta_2(t) = A \sin(\omega t) + B$, $A = 5\,\mathrm{K}$, $\omega = 2\pi/(8.64 \times 10^4 \mathrm{s}^{-1})$, $B = 25\,°\mathrm{C}$

Figure 7.4: Second loading path

The eigenvalues for both cases are shown in Fig. 7.5. The results for the constant temperature are similar to Fig. 7.2(a). In Fig. 7.5(b), one can see that the relaxation is affected by the periodic temperature changes. The values of λ_y and λ_k oscillate. With this second loading path, the eigenvalue related to the viscosity λ_{v} is frequently the highest eigenvalue of the system.

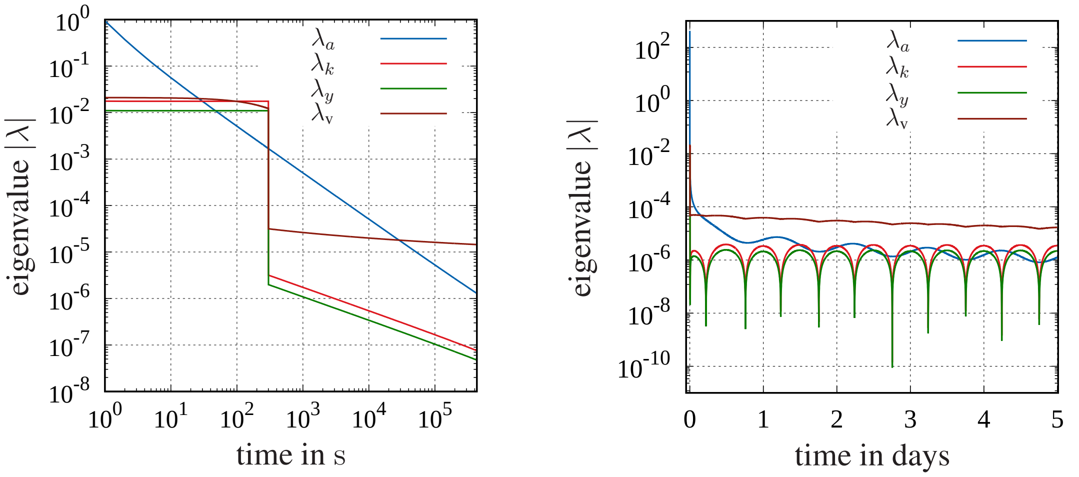

(a) Constant temperature $\Theta = 20\,^{\circ}\mathrm{C}$. Both axes scales are logarithmic

(b) Temperature path shown in Fig. 7.4(b). Time in days

Figure 7.5: Eigenvalues for the second loading case. Two different temperature paths are represented

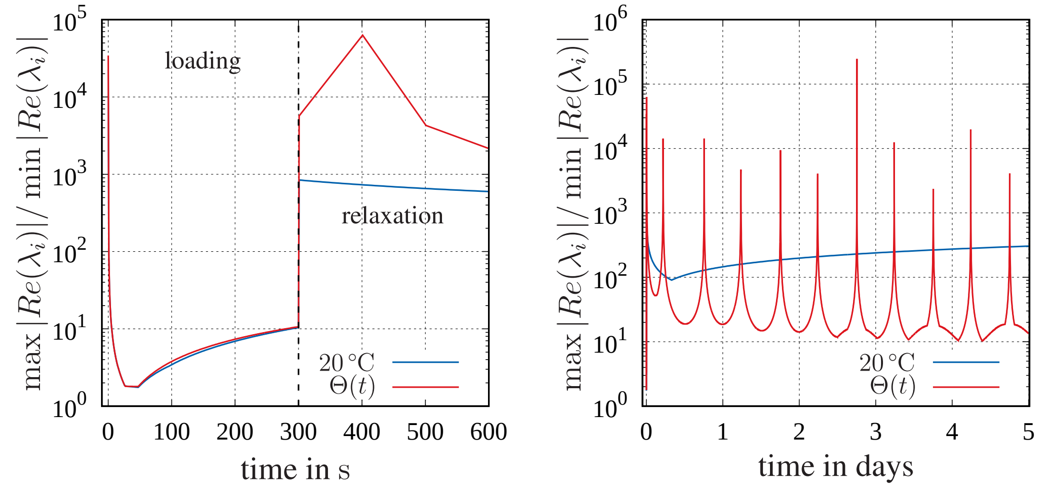

(a) Stiffness measure S at the first $600\,\mathrm{s}$

(b) Stiffness measure S

Figure 7.6: Stiffness measure S of the second loading case

In Fig. 7.6(a), the stiffness S is displayed for the first $600\,\mathrm{s}$. During the loading process, the system is strongly stiff during the first second – but the stiffness reduces below the value 100 after that. During the relaxation, see also Fig. 7.6(b), the simulation at a constant temperature shows stiffness values higher than 10^2. The sinusoidal temperature path exhibits an oscillating stiffness with punctually very high values. This originates in the very small values of the eigenvalue λ_y in Fig. 7.5(b), which are related to a rate $\dot{y}$ close to zero.

Selection of the Time Increment

Summarizing the observations of the previous results, the system of differential equations is frequently very stiff for several combinations of temperature and mechanical loading paths. In order to ensure the stability of the numerical solution on the local level, implicit methods are used for the time integration. The Backward Euler method fulfills the stability conditions for all time increments Δt, since it is L-stable with the entire left half of the complex plane as a stability region, see (Schwarz and Köckler, 2006) and (Hairer and Wanner, 1996). Moreover, the time increment has to be chosen in such a way that all effects are computed accurately – which means that the time increment is conditioned by the fastest effect of the differential equation system, which is given by the largest eigenvalue in absolute value. During the loading-unloading processes, the mechanical variables y, k, and ε_v are predominant for the determination of the time increment, see Fig. 7.2. Fig. 7.7 shows the absolute time discretization error of the aging variable with the Backward Euler method for different temperatures. In Fig. 7.7(a), one can see that the temperature has a strong effect on the error of the aging variable in dependence of the time increment. Processes at higher temperatures develop faster, and, thus, a smaller time increment is needed. Since the aging is an effect that evolves over a long period of time compared to the typical mechanical loading, the necessary time step to obtain an acceptable error in the aging variable is large. On the other hand Fig. 7.7(b) shows that the maximum error occurs for low values of the aging variable. Since the aging tends to the saturation value 1 with increasing time, the error tends to zero for values near to 1.

The maximum relative error $\mathrm{err}_\mathrm{max} = |f_{i\mathrm{num}} - f_{i\mathrm{analyt}}| / \max_i |f_{i\mathrm{analyt}}|$ is displayed in Fig. 7.8 for the mechanical variables y, p and ε_v over the time increment for two different temperatures and different constant strain-rates. At low temperatures, all the variables show a similar behavior over the time increment. Moreover, processes at lower strain-rates can be computed accurately with higher time increments. For the case of higher temperature, the rate-independent variables p and y exhibit a higher error.

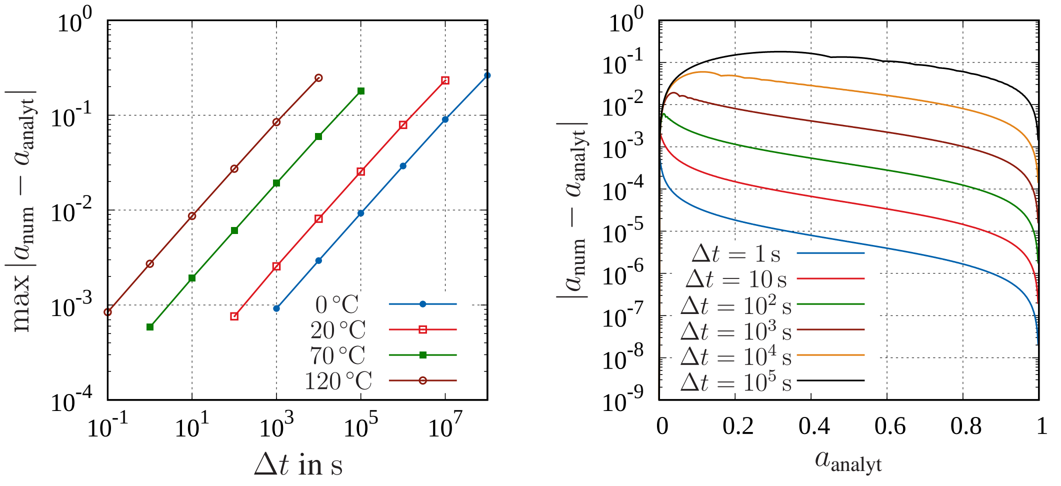

(a) Maximum absolute error in the numerically computed aging variable over the time increment for different temperatures

(b) Absolute error in the numerically computed aging variable over the analytical value for different time increments and 70 °C

Figure 7.7: Integration error in the aging variable with the Backward Euler method

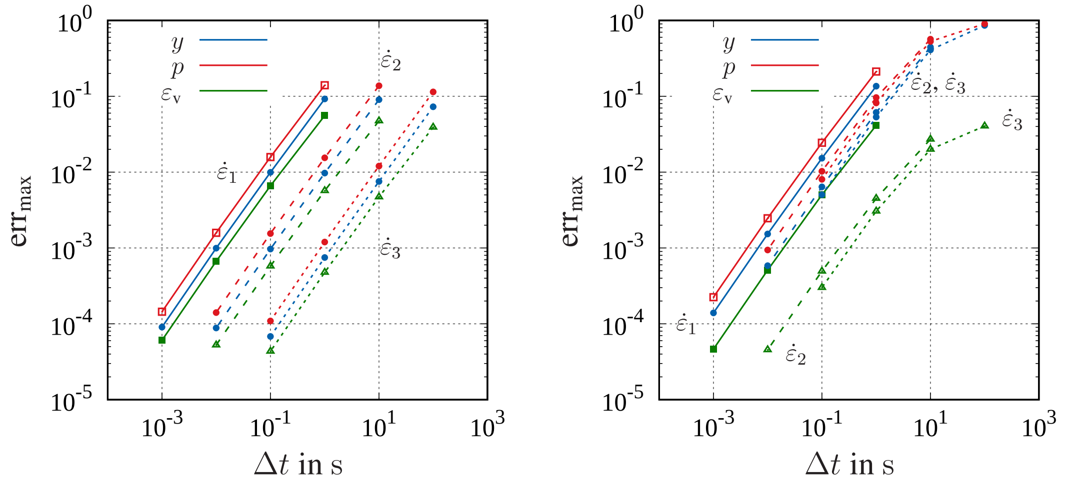

(a) Maximum relative error at 20 °C

(b) Maximum relative error at 100 °C

Figure 7.8: Maximal integration error in the mechanical internal variables with the Backward Euler method for different processes at the strain-rates $\dot{\varepsilon}_1 = 2.5 \times 10^{-3}\,\text{s}^{-1}$, $\dot{\varepsilon}_2 = 2.5 \times 10^{-4}\,\text{s}^{-1}$, $\dot{\varepsilon}_3 = 2.5 \times 10^{-5}\,\text{s}^{-1}$ and two different temperatures

7.2 Simulation of the Effect of Aging

The goal of this example is to describe the behavior of the aging variable and its influence in the model. To this end, a thermo-mechanical loading process at different time scales is chosen, in which a mechanical load acts in a short period of time, combined with a long thermal process. During the long thermal process, the aging variable develops. In this example, the geometry shown in Fig. 7.9(a) is considered. The geometry is modeled and meshed in Abaqus Standard. It consists of $13\,388$ twenty-noded hexahedral elements, with a total number of $68\,791$ nodes.

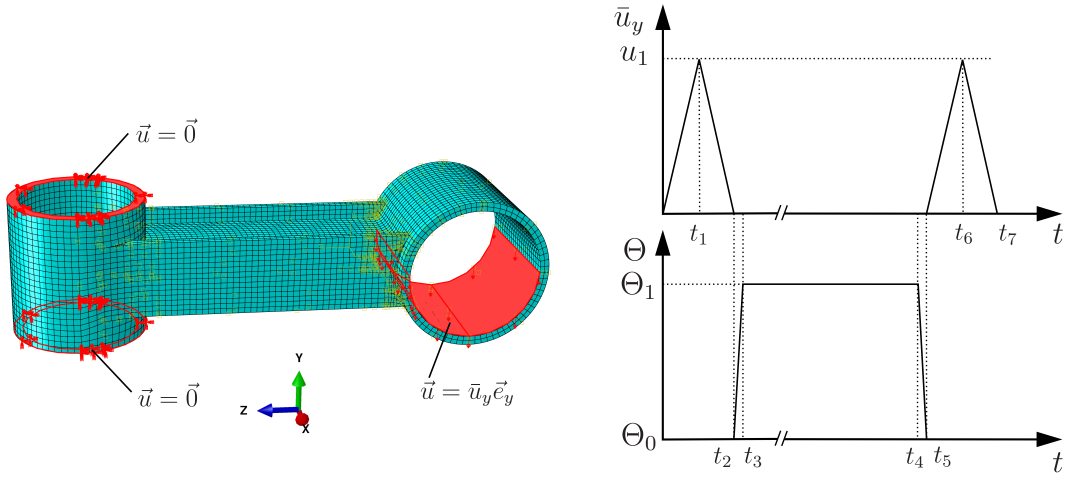

(a) Geometry, mesh and boundary conditions

(b) Loading path: $t_1 = 30\,\mathrm{s}$, $t_2 = 60\,\mathrm{s}$, $t_3 = 70\,\mathrm{s}$, $t_4 = 4.3199 \times 10^5\,\mathrm{s}$, $t_5 = 4.32 \times 10^5\,\mathrm{s}$, $\Theta_0 = 20\,^\circ\mathrm{C}$, $\Theta_1 = 70\,^\circ\mathrm{C}$, $u_1 = 5\,\mathrm{mm}$

Figure 7.9: Problem definition for the second example

The marked upper and lower surfaces on the left side of the geometry are fixed. A displacement in y-direction is prescribed on the right marked surface, following the mechanical loading path shown in Fig. 7.9(b). The mechanical load is defined in three steps: a first loading-unloading, a relaxation process, and a second loading-unloading similar to the example addressed in the previous section, see Fig. 7.9(b). In the first step, the component is loaded up to $\bar{u}_y = u_1 = 5\,\mathrm{mm}$ in $t_1 = 30\,\mathrm{s}$ and unloaded in $30\,\mathrm{s}$ until the initial position $\bar{u}_y = 0\,\mathrm{mm}$ is reached. After that, there is an increase of the temperature from $\Theta_0 = 20\,^\circ\mathrm{C}/293.15\,\mathrm{K}$ up to $\Theta_1 = 70\,^\circ\mathrm{C}/343.15\,\mathrm{K}$ in $t_3 - t_2 = 10\,\mathrm{s}$. This temperature is kept constant for 5 days. After that, the temperature is again reduced to $\Theta_0 = 20\,^\circ\mathrm{C}/293.15\,\mathrm{K}$ in a time of $t_5 - t_4 = 10\,\mathrm{s}$, and the loading-unloading path is applied again. This temperature path is prescribed for all the nodes of the model. The simulation is divided into three steps. The first one is defined from $t_0 = 0\,\mathrm{s}$ to $t_2 = 60\,\mathrm{s}$ and corresponds to the first loading-unloading process. The time step is constant and equal to $\Delta t = 0.5\,\mathrm{s}$. The second step takes place from the end of the first time step until $t_4 = 4.3199 \times 10^5\,\mathrm{s}$. Here, since the process develops very slowly, the automatic step-size control of Abaqus[2] is used to obtain larger time increments. The minimum increment is chosen equal to $\Delta t_{\text{min}} = 0.5\,\mathrm{s}$, the maximum is $\Delta t_{\text{max}} = 10^4\,\mathrm{s}$, and the maximum temperature increment per time-step is chosen equal to $\Delta\Theta = 10\,\mathrm{K}$. The third step takes place in the last 70 seconds of the simulation – $10\,\mathrm{s}$ for the cooling phase and $60\,\mathrm{s}$ for the second loading- unloading – and the time step is once again defined as constant, equal to $\Delta t = 0.5\,\mathrm{s}$. The applied material model is the model developed for finite deformations. The initial values of the internal variables are $\bar{\mathbf{C}}_{\text{v}} = \mathbf{I}$, $\bar{\mathbf{C}}_{\text{p}} = \mathbf{I}$, $k = 0$, and $a = 0$.

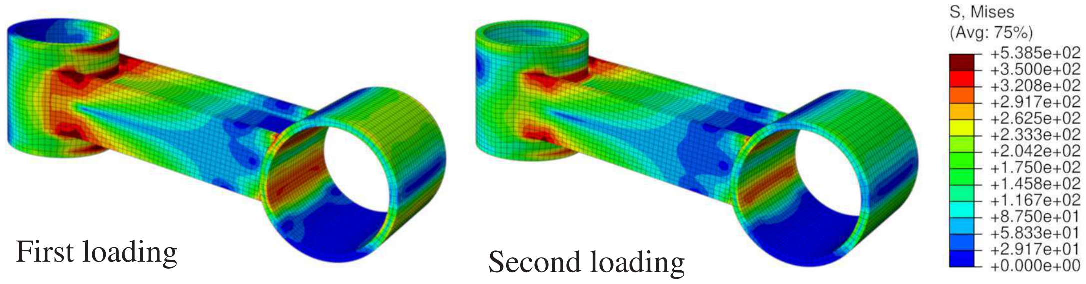

Figure 7.10: Comparison between the von Mises stress of the first loading path at t_1 (with $a \approx 0$) and the second loading path at t_6 after the unloading and 5 days relaxation at $\Theta = 70\,^\circ\mathrm{C}$ (with $a = 0.746$)

The results of the simulation are shown in Figs. 7.10 and 7.11. In Fig. 7.11(a), the development of the aging variable is displayed over time.[3] The aging variable is approximately constant during the short time of the loading-unloading phases at $20\,^\circ\mathrm{C}$ and develops continuously during the heating phase until the value of $a = 0.746$. During the heating phase, there is an initial thermal expansion of $\varepsilon_\Theta = 0.14\,\%$, which overlaps with the shrinkage caused by the aging described by $\varepsilon_a = -\alpha_a a$, with a final value equal to $\varepsilon_a = -0.1\,\%$ after 5 days. After the cooling phase to the initial temperature of $20\,^\circ\mathrm{C}$, there is only the effect of the shrinkage. Fig. 7.11(b) displays the reaction force over time. After the first loading-unloading process, there is a remaining force which relaxes to the equilibrium stress during the first day. The reaction force is displayed over the prescribed displacement for the first and the second loading-unloading processes in Fig. 7.11(c). The initial force for the second loading is not equal to zero, since the remaining reaction force after the relaxation acts together with the effect of the shrinkage. Here, one can observe the effect of the softening and aging in the complex geometry.

---

[2] The automatic time step control of Abaqus/Standard considers the maximum force residuals in every iteration and the amount of iterations until convergence as a criterion to choose the size of the new time increment. See (ABAQUS, 2019) for more information.

[3] Since there are no temperature differences over the geometry, the aging variable is constant in the space. The value is the same for all Gauss-points.

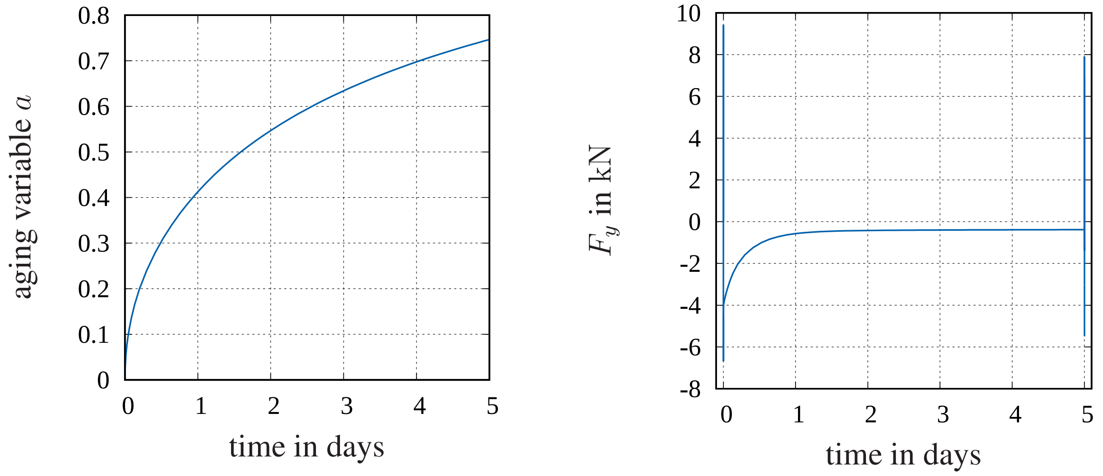

(a) Development of the aging variable over time

(b) Relaxation behavior of the reaction force over time. The loading processes, which are not visible here, are displayed in Fig. 7.11(c)

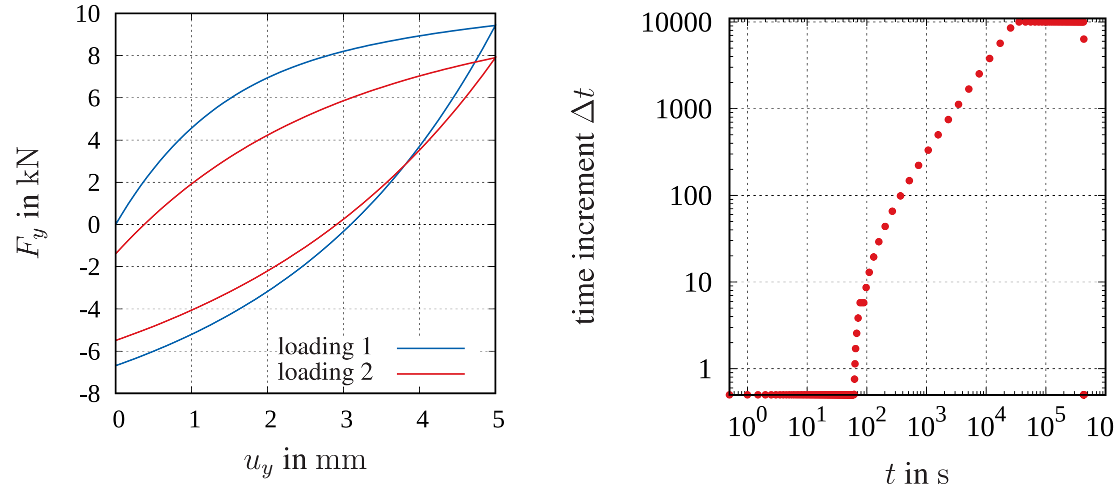

(c) Comparison between the first and second loading-unloading paths. The reaction force is displayed over the prescribed displacement

(d) Time increment over time. The fast mechanical processes require a smaller time increment. The long period of time at 70 °C can be computed with a large time increment

Figure 7.11: Results of the simulation of the second example

The initial slope and hysteresis in the force-displacement diagram is smaller for the second loading path. There is a reduction in the maximum force of $16\,\%$ for a loading at the same displacement rate and temperature. In Fig. 7.10, the Von Mises stresses for both loading processes are compared at the times t_1 and t_6, see also Fig. 7.9(b). For the same prescribed displacement, the stresses are higher in the first loading process than in the second one. Moreover, the time increment over time is shown in Fig. 7.11(d) in logarithmic scale. The mechanical processes generally occur in a much shorter period of time than the aging development. In this example, the temperature loading occurs during $4.32 \times 10^5\,\mathrm{s}$ while the mechanical loading-unloading takes $60\,\mathrm{s}$. Because of the strong increase in the time increment for the time in which only the temperature loading is applied, it is possible to reduce the total computation time, since the total amount of time steps is reduced drastically.

7.3 Simulation of a Real Component Part

In this section, the thermo-mechanical response with the influence of aging of the constitutive model is validated with simulations of complex geometries. Their real behavior was determined by the measurements addressed in Section 3.8. The thermo-mechanical behavior with a completely aged material is simulated first with the complex geometry from Section 3.8.1. Here, the behavior in tension/compression is predominant. Moreover, the effect of aging is investigated with simulations in torsion with specimens at $27\,^\circ\mathrm{C}$. As shown in Section 3.8.2, at temperatures close to room temperature, the effect of aging in the mechanical behavior is more pronounced.

7.3.1 Goals of the Validation

The goal of this section is to determine the predictive capability of the computational model. To this end, the concepts of verification and validation have to be introduced. As defined in (AIAA, 1998), *verification* is the process of determining that a model implementation is able to accurately represent the developer's conceptual description of the model and the solution to the model. *Validation* is the process of determining the degree to which a model is an accurate representation of the real world from the perspective of the application of the model. Validation involves the comparison of observed physical events with those predicted by the mathematical model in question, which has to be validated. As mentioned in (Babuska and Oden, 2004), validation processes involve the use of measures of accuracy – by determining measures of error and specifying tolerances to judge whether the accuracy is acceptable. Moreover, as specified in (Schwer, 2007), validation is specific to a particular computational model for a particular intended use. Verification must precede validation.

The need for validation experiments and the associated accuracy requirements for computational model predictions are based on the intended use of the model. According to (Oberkampf and Trucano, 2002), a validation quantity would require additional information from quantities which are unknown in the present work. These are a measure of the uncertainty of the experimental results, a measure of the error of the modeling assumptions, an error considering the postprocessing of the experimental results, and a measure of the performed numerical error. It is not always possible to acquire all this information, just as it is not always possible to verify and validate all possible application cases of the model. In this work, validation values are thus determined based on the available information.

Since, based on the experiments, a value of the quantity of interest is measured over time for different processes (instead of having one unique value for one experiment that is repeated several times) the metric proposed in (Oberkampf and Trucano, 2002) is adapted to this case. There are n_{exp} different experiments with n_p^i points per experiment for the i-experiment. For a certain quantity of interest, the experimental value is represented as y_e and the response of the model (simulation) as y_m. As an error measure, the maximal relative error E is used. It is defined as the maximal relative error of all the experiments

$$E = \max|\epsilon_i|, \qquad \epsilon_i = \frac{y^i_{mj} - y^i_{ej}}{y^i_{e\text{max}}}. \tag{7.22}$$

Here, i represents an experiment and j a point of the experiment. $y^i_{e\text{max}}$ is the maximal value of the experiment i. The experiment with the maximal relative error is denoted with the index E. In a similar way as proposed in (Oberkampf and Trucano, 2002), the confidence interval for this error is a normalized measure by the maximal experimental value evaluated at the point where the maximum relative error metric occurs

$$\left|\frac{\text{CI}}{y^E_{e\ \max}}\right| = \frac{t_{0.05,\nu}}{\sqrt{n^E_p}}\left|\frac{s_{\text{E}}}{y^E_{e\ \max}}\right|, \qquad \text{with} \qquad s_E = \left(\frac{1}{n^E_p - 1}\sum_{j=1}^{n^E_p}(y^E_{mj} - \bar{y}^E_e)^2\right). \tag{7.23}$$

Here, $t_{0.05,\nu}$ is the t-distribution for 90% confidence, with $\nu = n_p - 1$, and the mean value of the experimental points of an experiment i is written as $\bar{y}^i_e$. The value $y^E_{e\ \max}$ has the goal to norm the confidence interval in the same way as the error E, in order to make them comparable. The application of the model corresponds to non-cyclic quasi-static processes up to a maximum strain of approximately $10\,\%$ with Zamak 5. Processes at different strain-rates, temperatures, and aging times are included in the validation with influence of torsion and tension/compression. To this end, we can draw on the experiments shown in Figs. 3.35-3.43 of Section 3.8 with two different geometries. The first geometry in Figs. 3.35 provides two experiments at the same temperature and different strain-rates, where the rate-dependence is included. Moreover, with tests at two additional temperatures, the temperature dependence is considered. Finally, the second geometry in Fig. 3.41 is used to validate the aging dependence. Since the displacement and rotational angle are prescribed in simulation and experiment, the quantity of interest to determine the quality of the model is defined by the reaction force or the torque.

7.3.2 Component Part at Different Temperatures

In this example, the ability of the model to reproduce the thermo-mechanical behavior is investigated. To this end, the complex geometry from Fig. 3.35 is modeled in Abaqus Standard. The experiments involve simulations at three different temperatures and with different loading paths. The main difficulty in this section lies in the definition of the boundary conditions, which have to give an exact reproduction of the experimental behavior. Measurement errors and uncertainties in the boundary conditions can lead to differences between simulation and experiment, which do not lie in the validity of the model or applied numerical methods. The main error in the present case lies in the calibration error due to the digital image correlation (DIC) system using the thermal chamber. Moreover, the major strain exhibits a strong noise over time, which is reflected in the measured strains over time, see Fig. 7.17(b), for example.

Mesh and Boundary Conditions

Fig. 7.12(b) shows the geometry, mesh, and boundary conditions, with the goal of reproducing the experimental conditions from Fig. 7.12(a). Using Abaqus Standard, the pin is modeled as linear elastic with the standard properties for steel ($E = 210\,\mathrm{GPa}$, $\nu = 0.3$). For the component part made of Zamak, the proposed constitutive model of finite deformations is chosen. The pin is meshed with linear hexahedral elements, and quadratic tetrahedral elements are used for the component part. The number of elements of the simulation is equal to $54\,078$, and the number of nodes is $85\,569$. As boundary conditions, the region fixed by the screw in Fig. 7.12(a) has a displacement equal to zero. A displacement in negative z-direction is applied on the upper surface of the pin, in order to reproduce the effect of the traverse of the testing machine pulling the pin. Due to the elastic deformation of the testing machine during the experiments, and the additional deformation of the screw, the relative displacement between the upper part of the complex geometry and the pin is given in the simulations for the prescribed displacement path, see Fig. 7.13 and Section 3.8.1. The temperature is kept constant in each simulation. The initial value of the aging variable is set equal to one $a(t = 0) = 1$ in all simulations, corresponding to the completely aged material. The contact formulation "node-to-surface" is chosen for the contact between the pin and the component part. For the tangential behavior, a friction coefficient of 0.5 is assumed, see (Rabinowicz, 1951). For the normal and tangential behavior, the standard options of Abaqus for the penalty method are chosen. The simulations are carried out with automatic controlled time-step incrementation. The values of the initial minimal and maximal time step for the four simulations are shown in Tab. 7.2. During the loading, the displacement rate in the second simulation is three orders of magnitude slower than the first one, which is why a larger time step is chosen, see also the investigations on the time step of Fig. 7.8.

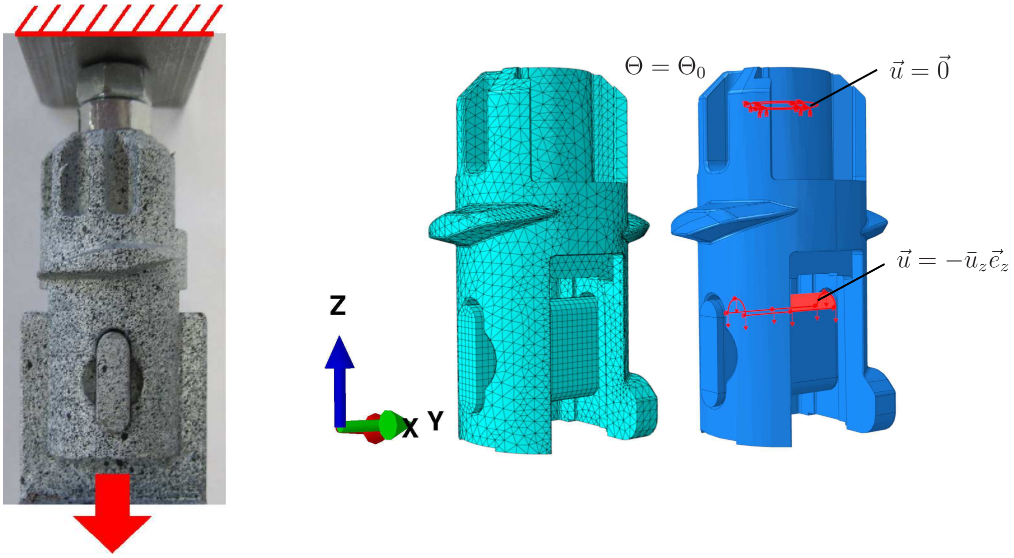

(a) Loading conditions in the experiments

(b) Geometry and boundary conditions in Abaqus

Figure 7.12: Complex geometry in the experiment and modeling for the simulation

Table 7.2: Definition of time step in the simulations

	simulation 1	simulation 2	simulation 3	simulation 4
Δt_0	0.1	100	1	1
Δt_{min}	10^{-3}	10^{-2}	10^{-3}	10^{-3}
Δt_{max}	0.1	210	1	1

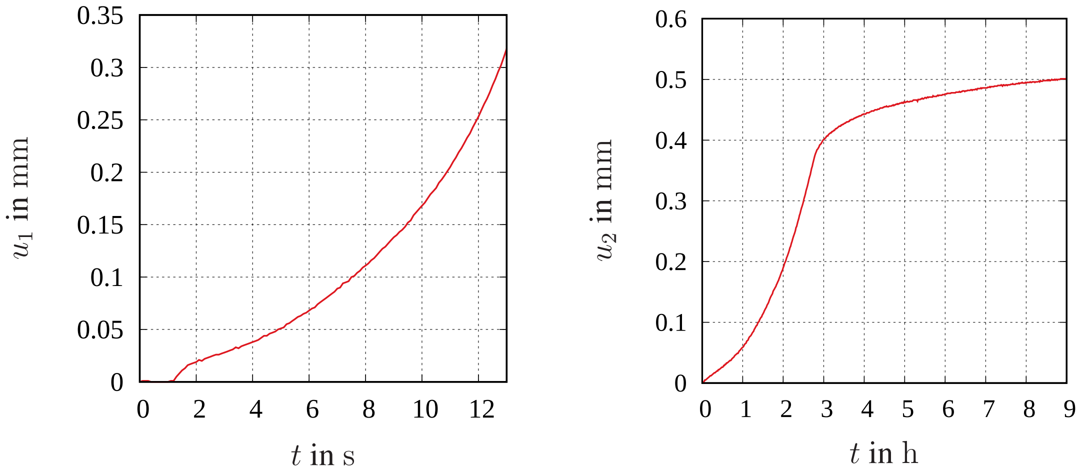

(a) First experiment: fast loading path u_1 at 20 °C

(b) Second experiment: slow loading path u_2 at 20 °C

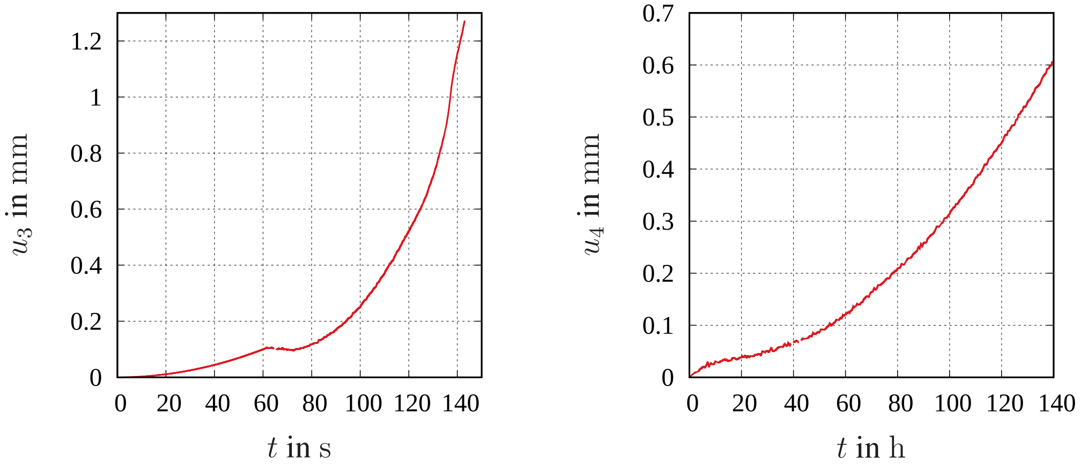

(c) Third experiment: fast loading path u_3 at 50 °C

(d) Fourth experiment: fast loading path u_4 at 70 °C

Figure 7.13: Prescribed displacement for the simulation. The temperature is constant in all simulations. Data obtained from the experiments in Section 3.8

Results of the simulation of the thermo-mechanical behavior

The results of the simulations are displayed in Figs. 7.14-7.17, showing the reaction force over the prescribed displacement of the pin for each simulation. Moreover, the true major strain, see Eq. (2.25), for the measured surface of the component part is shown at the last time step of the simulation for both the experimental and simulation results. The major strain at a chosen point of the surface is displayed over the time in each case.

Generally, there are difficulties when trying to reproduce the starting phase of the experiments when the displacements are still very small, see Figs. 7.14(a), 7.16(a) and 7.17(a). The reason is that the boundary conditions *at the beginning of the loading* do not correspond exactly to the real conditions of the experiments, due to components that are not completely in contact. In the three first experiments, there is a good agreement between experiment and simulation regarding the reaction force. Having a look at the first and second experiments at room temperature in Figs. 7.14(a) and 7.15(a), one can see that the rate-dependence is predicted approximately. Although the displacement in the cross-head is kept constant in the second experiment, the measurements with the DIC-system show a small increase in the displacement. This can be observed in Fig. 7.15(a) in the range of the displacement between $0.38\,\mathrm{mm}$ and $0.5\,\mathrm{mm}$, where the force relaxes but the displacement is not constant. Comparing all the measurements, one can see that the model is also able to provide a good representation of the temperature dependence. In Fig. 7.16(a), one can observe that the material is unable to provide an exact reproduction of the small unloading at the time $t = 60\,\mathrm{s}$. Moreover, during this experiment, the component part begins to break at the time $t = 127\,\mathrm{s}$. This can be observed in the reduction of the force at this time. Since the presented model is not a designated damage model, the results near to this point differ from the experiment. The force in the last experiment is overestimated from the point $u_z = 0.3\,\mathrm{mm}$ onwards.

Regarding the deformation, a generally good agreement between experiment and simulation is observed as well. Nevertheless, the experiments at room temperature are slightly overestimated – one can see that the red area in Figs. 7.14(d) and 7.15(d) are larger than in the experiments. In the experiments at $50\,^{\circ}\mathrm{C}$ and $70\,^{\circ}\mathrm{C}$, the green lateral bands, which can be observed in the simulation, are not present. They are visible in the experiments at room temperature. Moreover, the strain in the lower area is underestimated, and it is overestimated in the lateral areas around the hole. The reason lies not only in the model, but also in the lower accuracy of these measurements. They were performed using a thermal chamber, which implies that a glass is placed between the measurement system and the specimen, see Section 3.8.1. The glass reduces the accuracy of the measurement due to distortions of the optical measurement system. In Fig. 7.17(b), one can see a strong noise and a jump in the strain at the time $t = 95\,\mathrm{s}$ and $t = 125\,\mathrm{s}$, which is connected to the previously mentioned measurement inaccuracy. This makes it difficult to use the information of the DIC-system in this case to obtain a statement about the prediction ability of the model.

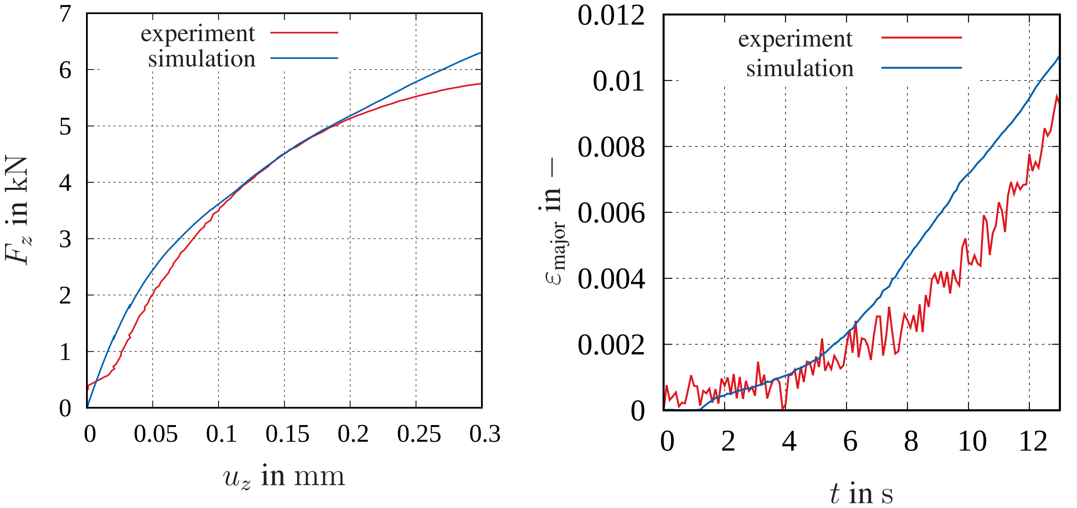

(a) Reaction force over the pin-displacement

(b) Major strain over the time at the position $\mathcal{P}_1$, see Fig. 7.14

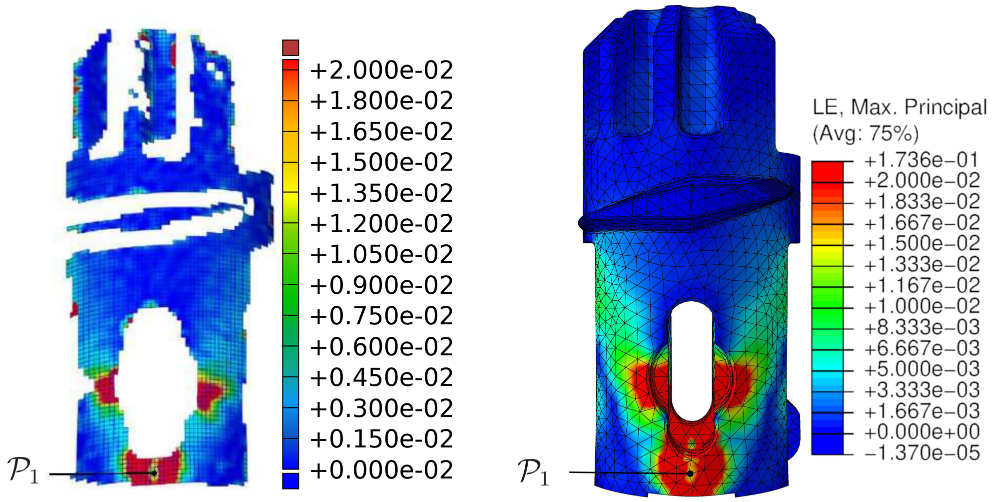

(c) Major strain in the range from 0% to 2% (experiment)

(d) Major strain in the range from 0% to 2% (simulation)

Figure 7.14: Results of experiment and simulation for the displacement $\bar{u}_z(t) = u_1(t)$ at room temperature. Higher values than 2% are marked in red, also in Fig. 7.14(c) and 7.14(d)

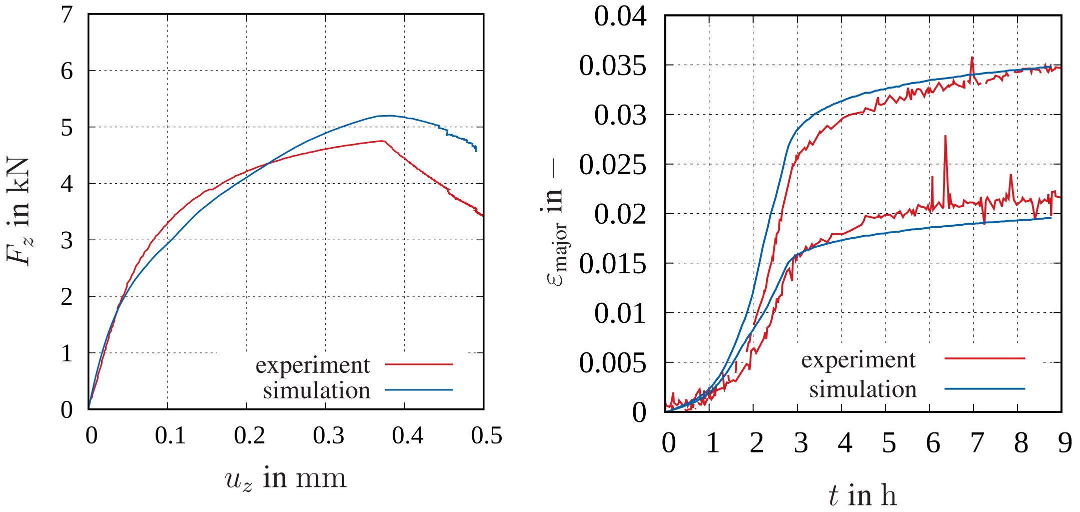

(a) Reaction force versus the pin-displacement

(b) Major strain over the time at the positions $\mathcal{P}_2$ and $\mathcal{P}_3$, see Fig. 7.14

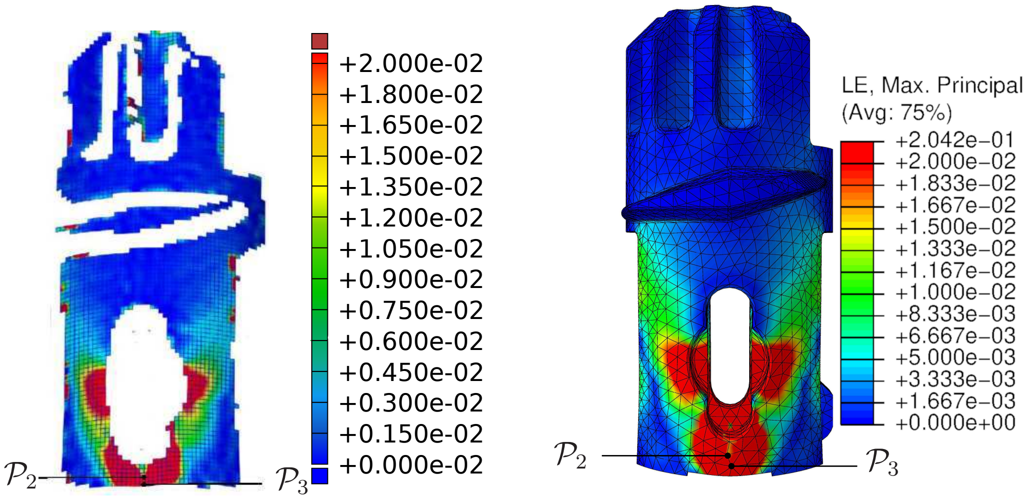

(c) Major strain in the experiment after loading and 6 h relaxation

(d) Major strain in the simulation after loading and 6 h relaxation

Figure 7.15: Results of experiment and simulation for the displacement $\bar{u}_z(t) = u_2(t)$ at room temperature. Higher values than 2% are marked in red, also in Fig. 7.15(c) and 7.15(d)

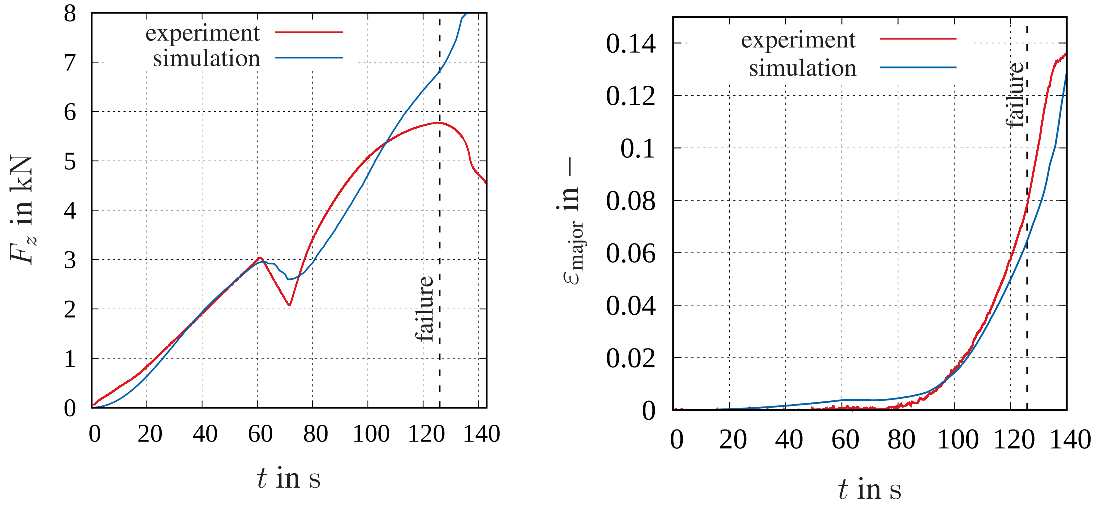

(a) Reaction force over the time

(b) Major strain over the time at the position $\mathcal{P}_4$, see Fig. 7.16(d)

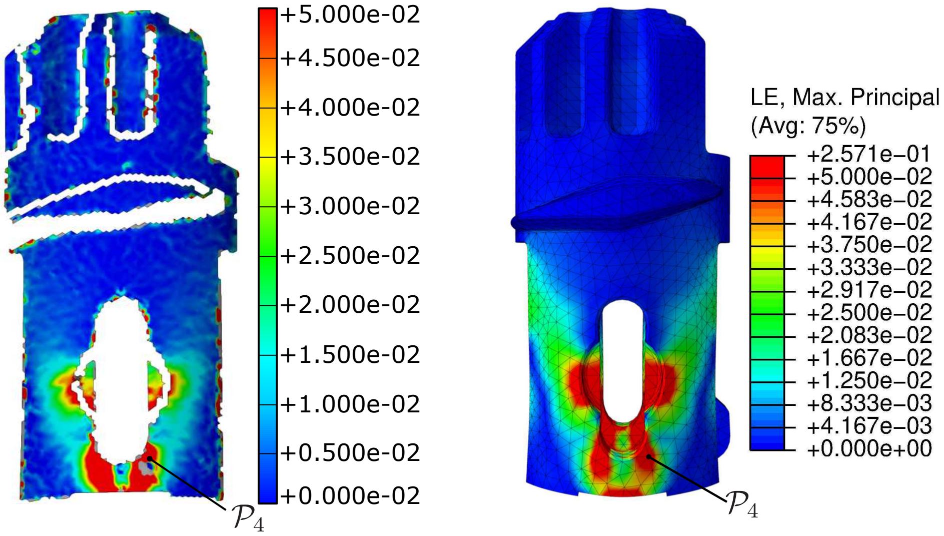

(c) Major strain in the experiment at $t = 127\,\text{s}$

(d) Major strain in the simulation for the last time step $t = 127\,\text{s}$

Figure 7.16: Results of experiment and simulation for the third loading case $\bar{u}_z(t) = u_3(t)$, $\Theta = 50\,°\text{C}$. Higher values than 5% are marked in red, also in Fig. 7.16(c) and 7.16(d)

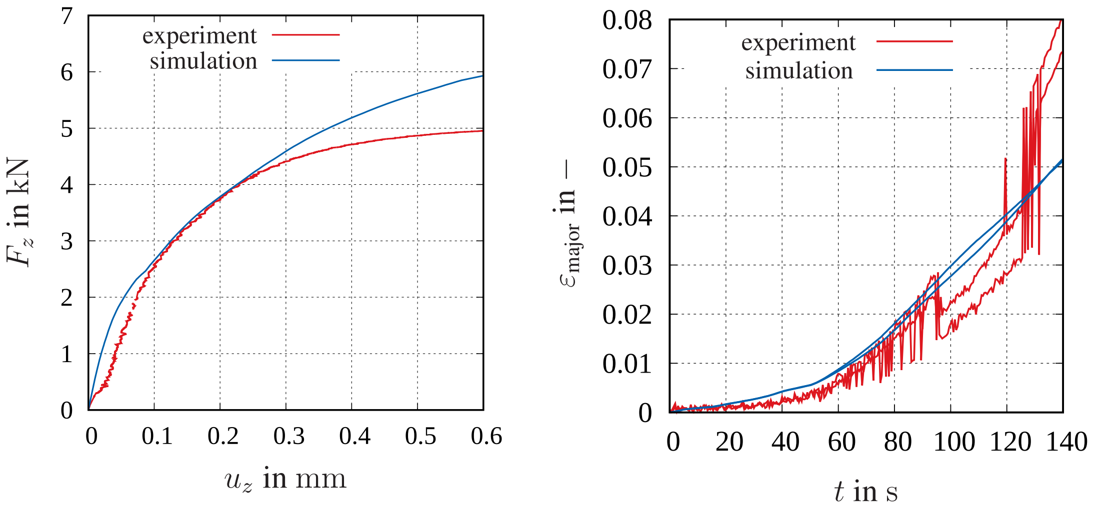

(a) Reaction force versus the pin-displacement

(b) Major strain over the time at the position $\mathcal{P}_5$ and $\mathcal{P}_6$, see Fig. 7.17(d)

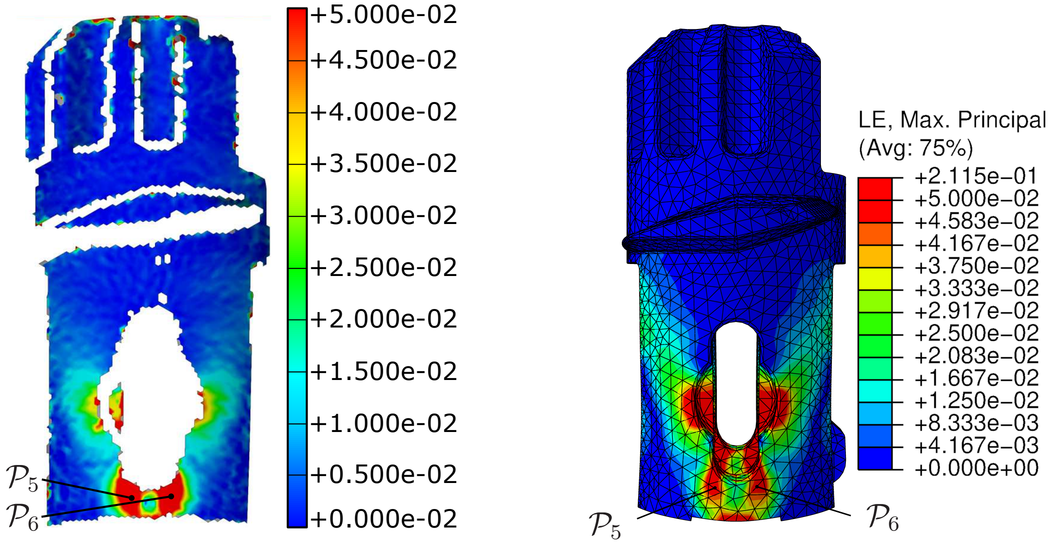

(c) Experiment

(d) Simulation

Figure 7.17: Results of experiment and simulation for the fourth loading case $\bar{u}_z(t) = u_4(t)$, $\Theta = 70\,^\circ\mathrm{C}$. Higher values than 5% are marked in red, also in Fig. 7.14(c) and 7.14(d)

7.3.3 Tube at Different Aging Times

The effect of aging is validated with torsion tests in tubes with a hole in the middle area, see Fig. 7.18. The specimens from Section 3.8.2 with the three different aging times – initial state, 12 months of natural aging, and final state reached through artificial aging – are used to this end. Since the aging effect is more pronounced at temperatures close to room temperature, the temperature of the experiments is chosen equal to $27\,^\circ\mathrm{C}$.

Mesh and Boundary Conditions

The geometry used in the experiments of Section 3.8.2 is generated with the same dimensions in Abaqus Standard. The geometry is meshed with $18\,608$ quadratic hexahedral elements, see Fig. 7.18. It has $97\,759$ nodes in total. In order to reproduce the conditions of the experiment described in Section 3.8.2, the upper outer surface of the geometry (upper red area in Fig. 7.18(a)) is fixed $\vec{u} = \vec{0}$. Moreover, the lower outer surface (lower red area in Fig. 7.18(a)) is coupled with a reference point RP-2 to which the rotation $\vec{\varphi} = \varphi_y \vec{e}_y$ is applied, and the displacement is equal to zero $\vec{u}_{\text{RP-2}} = \vec{0}$. The prescribed rotational angle φ_y is taken from the measurements in Section 3.8.2 and is shown for the three simulations in Fig. 7.18(b). The temperature is constant during the simulation, equal to $\Theta = 27\,^\circ\mathrm{C}$. The model of finite deformations is used for all simulations. The initial conditions for the internal variables correspond to a state without previous deformation ($\bar{\mathbf{C}}_\text{v} = \mathbf{I}$, $\bar{\mathbf{C}}_\text{p} = \mathbf{I}$, and $k = 0$) and with the following values of the aging variable

$$a_{\text{sim1}} = 0, \qquad a_{\text{sim2}} = 0.802, \qquad a_{\text{sim3}} = 1, \tag{7.24}$$

which correspond to the material without aging in simulation 1, with 12 months natural aging in simulation 2, and the final state in simulation 3. The initial values for the aging variable are obtained from the solution of Eq. (4.155) at $19\,^\circ\mathrm{C}$ for the corresponding aging times in seconds.[4] The constant time step is set equal to $\Delta t = 1\,\mathrm{s}$.

Results

The results of the simulation are shown in Figs. 7.19-7.23. For each simulation, a comparison between the major strain at the last time step of the simulation and the experiment is provided in Figs. 7.19 and 7.20. Moreover, Figs. 7.21-7.23 represent the reaction torque, reaction force, and major strain over time in several points. The results of the major strain at the last time step indicate a very good agreement between experiment and simulation in the three different cases. The red areas on the sides of the hole, where the maximal major strain is reached, match the simulation – as well as the second green areas that appear near the red ones. Having a look at the reaction torque in Figs. 7.21(a),

---

[4] $\Theta = 19\,^\circ\mathrm{C}$ is the temperature at which the specimens were stored during natural aging.

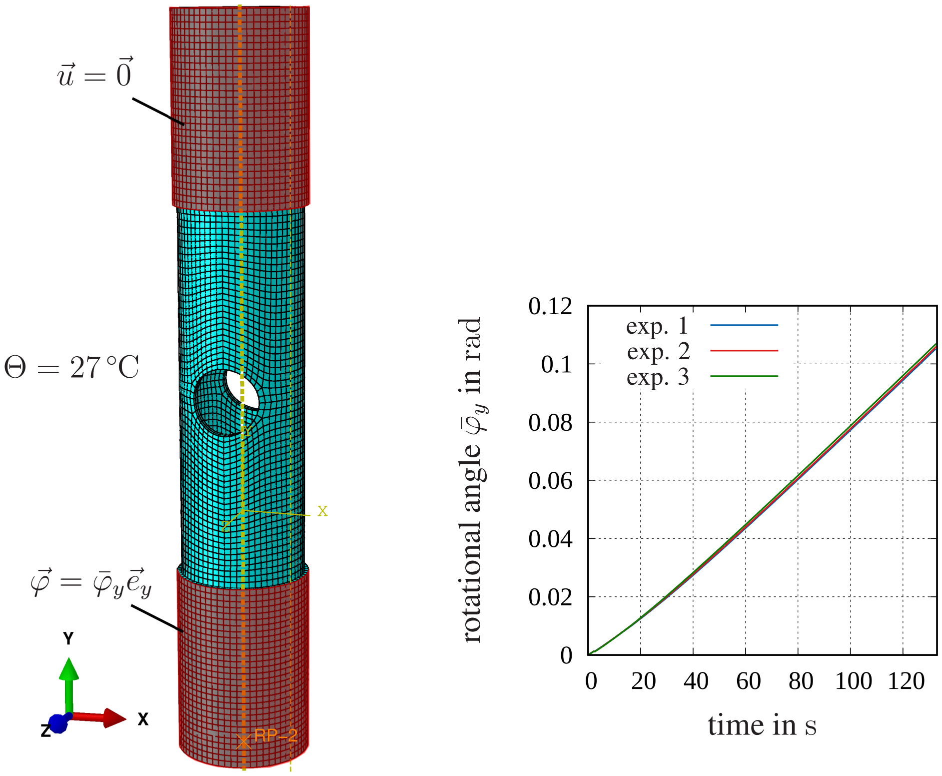

(a) Mesh and boundary conditions

(b) Input simulation

Figure 7.18: Mesh and boundary conditions for the torsion experiments at different aging times

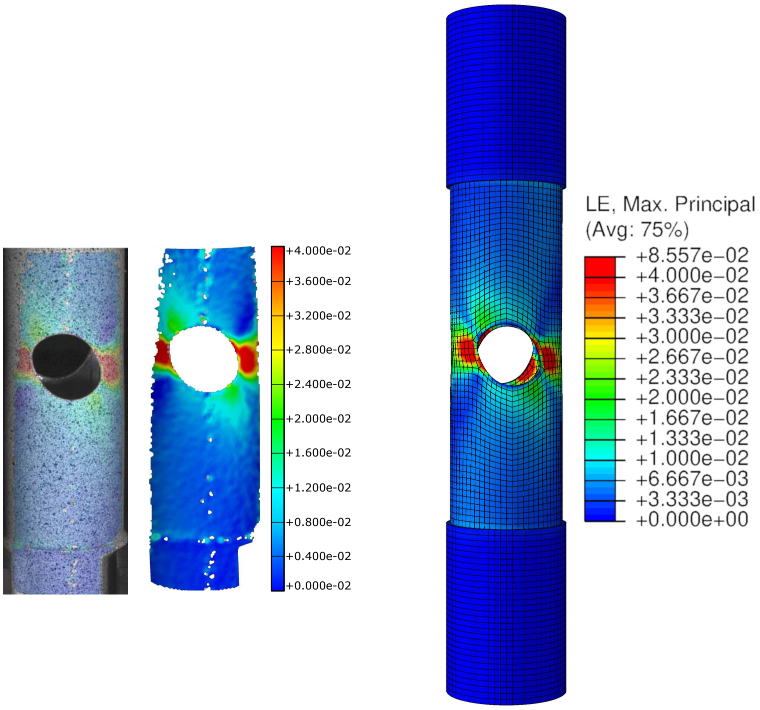

(a) Specimen without aging. Left experiment and right simulation

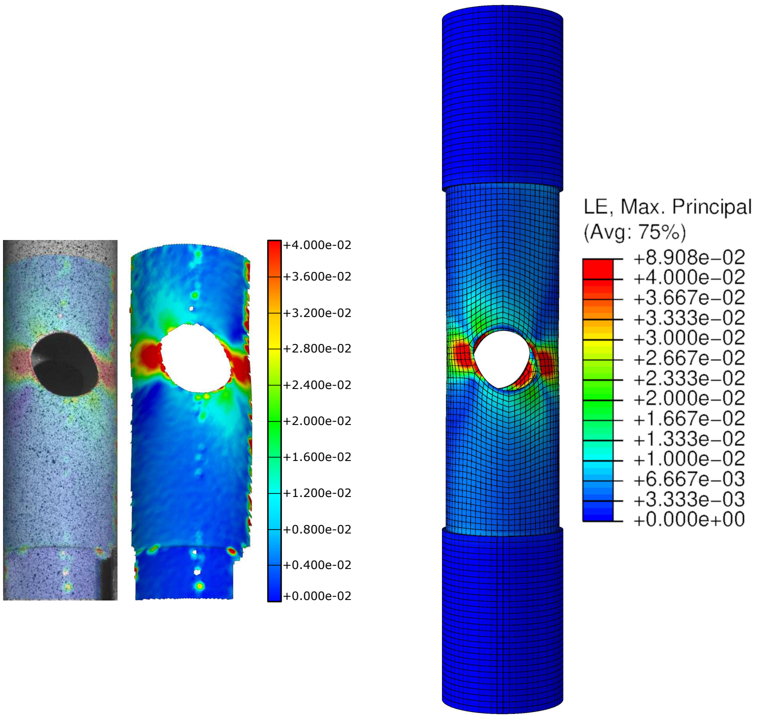

(b) Specimen with 12 months of natural aging. Left experiment and right simulation

Figure 7.19: True major strain in the range from 0% to 4% at the last time step $t = 133\,\mathrm{s}$ for experiment and simulation

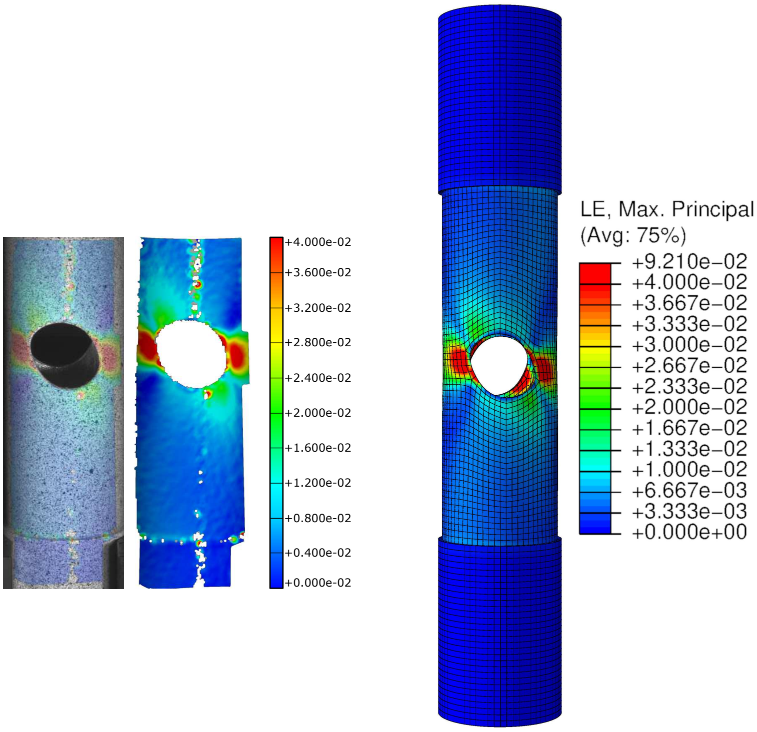

Figure 7.20: True major strain in the range from 0% to 4% at the last time step $t = 133\,\mathrm{s}$ for the completely aged specimen. Left experiment and right simulation

7.22(a), and 7.23(a), one can observe a good agreement between experiment and simulation for the specimens without aging and 12 months of natural aging. For the case of the specimen with artificial aging, the torque is overestimated, which is due to the fact that only data for natural aging was used in the identification process. Taking into account the size of the geometry, the obtained reaction force is small.[5] The reaction force during the simulation is underestimated, and its curvature over time is more pronounced for the simulation(for the experiment it is almost linear). The origin of this difference might be in the model but could also be due to differences in the boundary conditions. Moreover, since the displacement is prescribed, it is to be expected that the major strain between experiment and simulation is in a good agreement. In Figs. 7.21(c)-7.21(d), 7.22(c)-7.22(d), and 7.23(c)-7.23(d), one can observe a very good agreement between experiment and simulation. This will be discussed and specified in the following section.

---

[5] In comparison, for example, with the experiments for material characterization in Section 3.5. There, the measured force is approximately $40\,\mathrm{kN}$ in the tension tests at room temperature with a similar geometry.

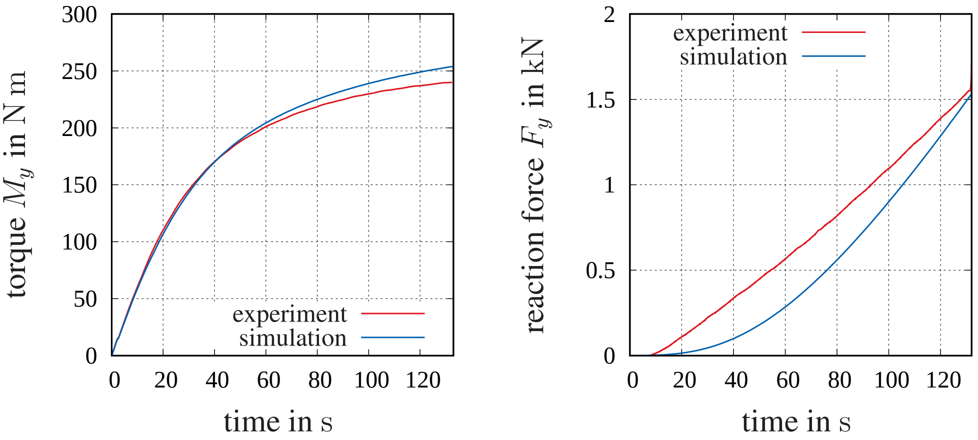

(a) Reaction torque over the time

(b) Reaction force over time

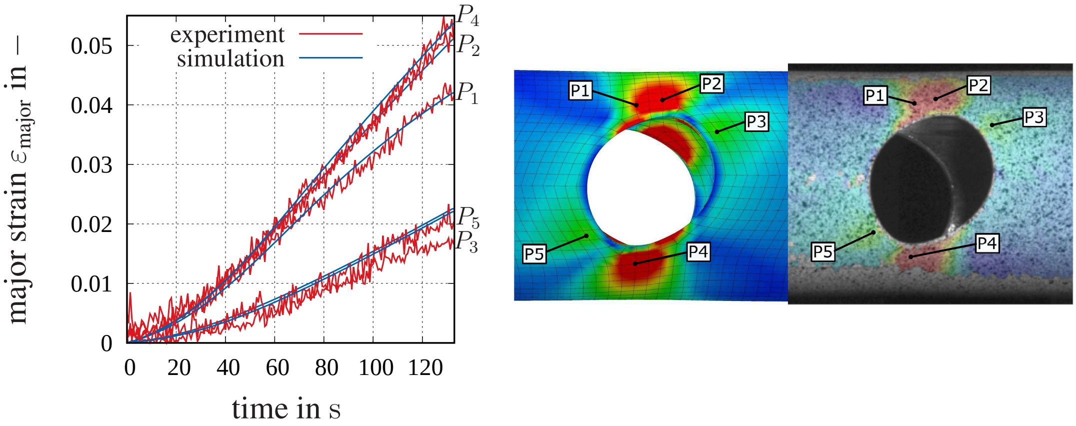

(c) Major strain over time for different points

(d) Point position from measurement and simulation in Fig. 7.21(c)

Figure 7.21: Comparison between experiment and simulation for the material without aging

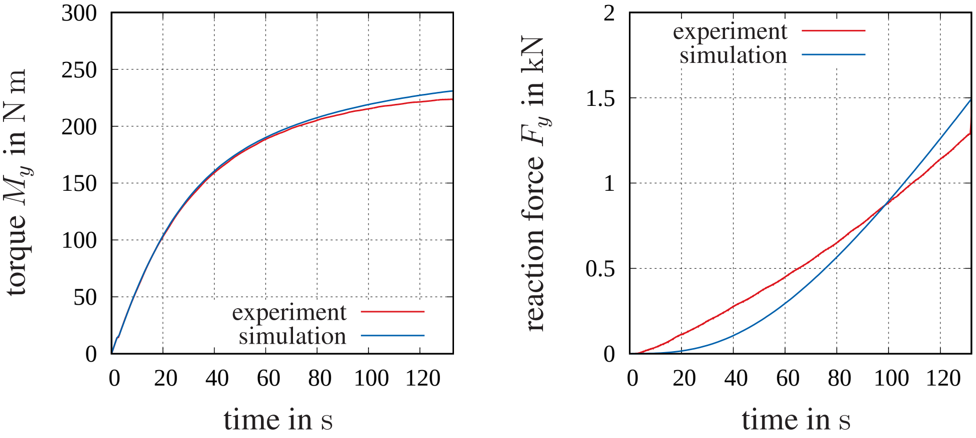

(a) Reaction torque over time

(b) Reaction force over time

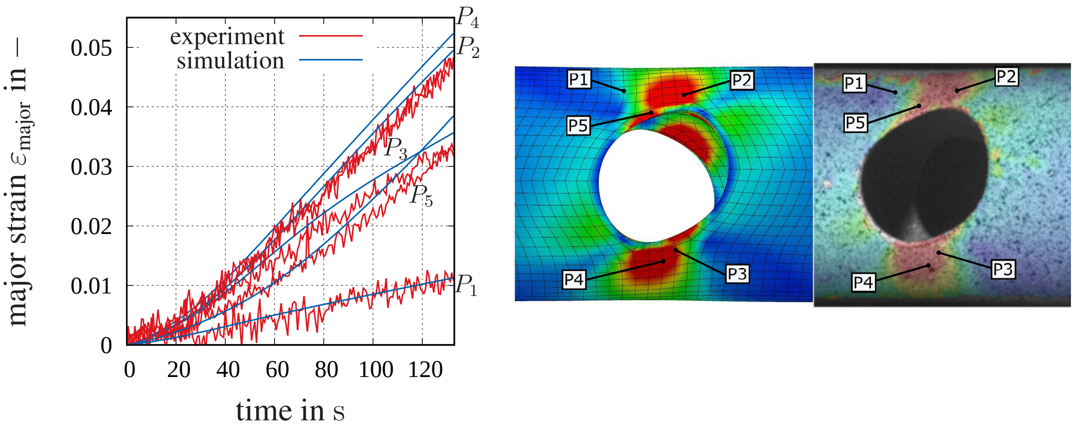

(c) Major strain over time for different points

(d) Point position from measurement and simulation in Fig. 7.22(c)

Figure 7.22: Comparison between experiment and simulation for the material with 12 months of natural aging

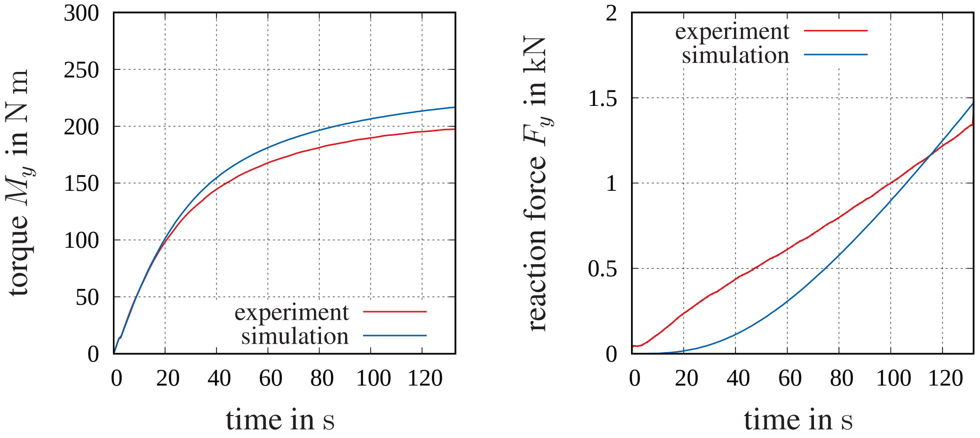

(a) Reaction torque over the time

(b) Reaction force over time

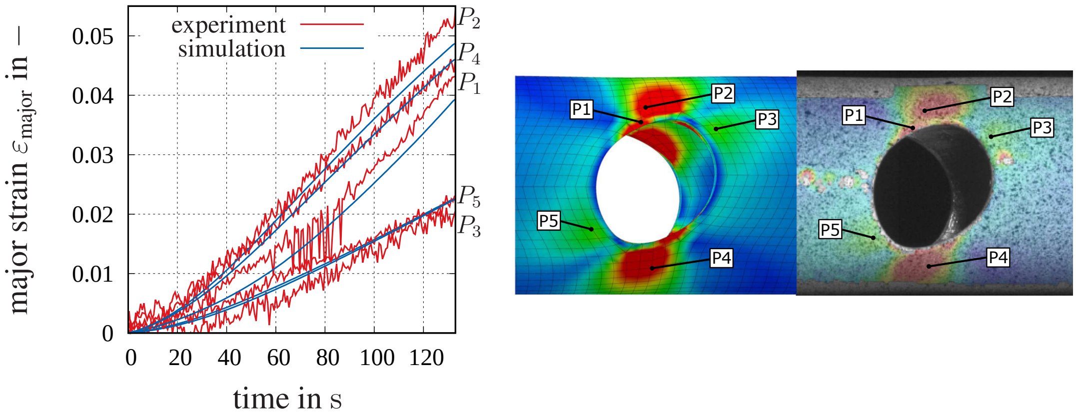

(c) Major strain over time for different points

(d) Point position from measurement and simulation in Fig. 7.23(c)

Figure 7.23: Comparison between experiment and simulation for the completely aged material

7.3.4 Evaluation of the Results

In order to analyze the results of the simulation and to compare them with the experiment, we start off by determining the absolute error $\mathrm{err}_{F\mathrm{abs}}$ and relative error $\mathrm{err}_{F\mathrm{rel}}$ in the force of the evaluations in the complex geometry in Section 7.3.2, see Figs. 7.14-7.17,

$$\mathrm{err}_{F\mathrm{abs}} = |F_{\mathrm{exp}} - F_{\mathrm{sim}}|, \tag{7.25}$$

$$\mathrm{err}_{F\mathrm{rel}} = 100 \times \frac{\mathrm{err}_{F\mathrm{abs}}}{|F_{\mathrm{exp}}|}, \tag{7.26}$$

and in the torque in the evaluations for the cylindrical tube with the hole of Section 7.3.3, see Figs. 7.21-7.23,

$$\mathrm{err}_{M\mathrm{abs}} = |M_{\mathrm{exp}} - M_{\mathrm{sim}}|, \tag{7.27}$$

$$\mathrm{err}_{M\mathrm{rel}} = 100 \times \frac{\mathrm{err}_{M\mathrm{abs}}}{|M_{\mathrm{exp}}|}. \tag{7.28}$$

They are displayed in Figs. 7.24 and 7.25. Here, one can observe that the relative error is, in general, very high at the beginning, where the displacement or rotational angle are very small. There are two main reasons for that. The slope in the force-displacement diagram is larger for small displacements, and because of that, proportionally, small absolute errors are relatively large. Moreover, the measured force is near to zero in certain time intervals at the beginning of the experiments – but not in the simulation, which causes high relative errors. Additionally, one can see that the relative error is smaller for the torsion experiments at different aging times than for the complex geometry. This was to be expected, since the specimens used for the torsion experiments were produced in the same batch as the specimens used for the experimental material characterization – and they have the same thickness and approximately the same porosity, which is not the case for the component part of Section 7.24. It is also observed that the errors are larger for the artificially aged specimen, see Fig. 7.25. The model tends to overestimate the torque and force for a completely aged material, since these values were not used in the identification. The component part used in Section 7.24 is also completely aged, which implies an additional error in the simulation.

By applying the validation metric from Eqns. (7.22) and (7.23) to the measurements, the values of Tab. 7.3 are obtained. The maximal error corresponds to the fourth experiment and simulation at the temperature of 70 °C. This error is equal to $E = 31.33\%$

Table 7.3: Relative error and confidence interval for every experiment

	Exp. 1	Exp.2	Exp. 3	Exp. 4	Exp. 5	Exp. 6	Exp. 7
E in –	0.2067	0.2626	0.1816	0.3133	0.0574	0.0364	0.1007
CI in –	0.0473	0.0224	0.0053	0.0053	0.0119	0.0113	0.0122

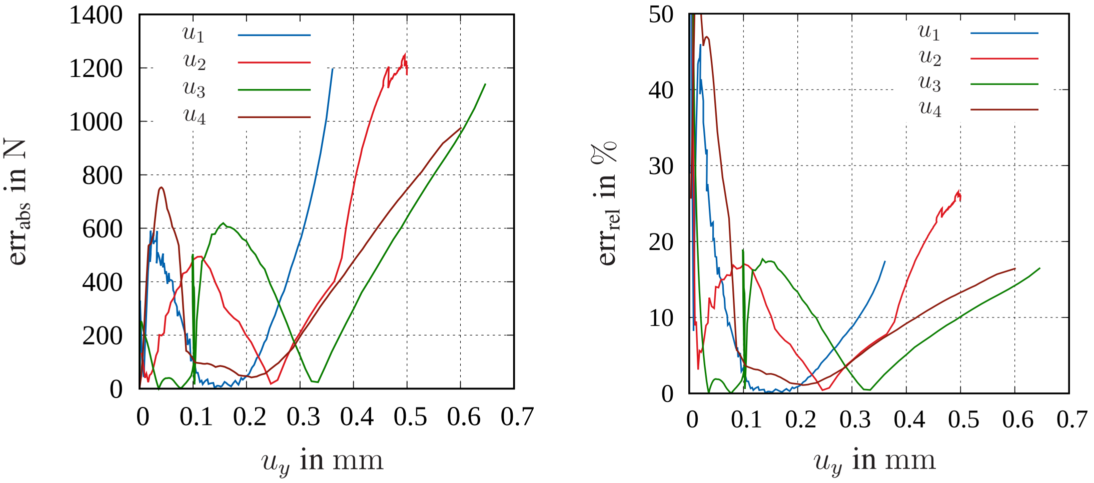

(a) Absolute error in the reaction force

(b) Relative error of the reaction force

Figure 7.24: Absolute and relative error in the reaction force over time between experiment and simulation for the experiments at different temperatures and displacement paths

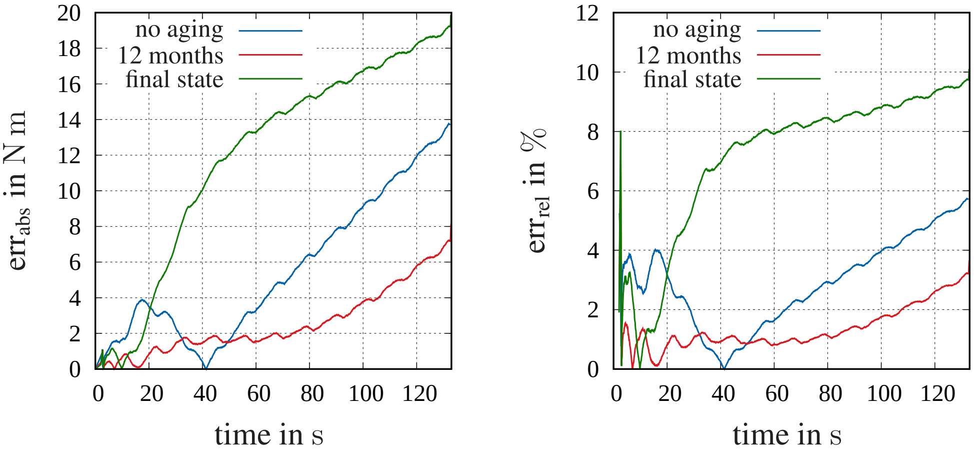

(a) Absolute error in the torque

(b) Relative error in the torque

Figure 7.25: Absolute and relative error of the torque over time between experiment and simulation for the experiments at different aging times

with a confidence interval of 0.53%. From the previous results, one can conclude that the simulation is able to predict the experiments with a maximal relative error of $31.33\,\%$ for deformations of at least $5\,\%$.[6] This relative error is, in general, smaller for lower deformations – and it is also connected to other factors such as the thickness of the specimen and other microstructural imperfections.

---

[6] Since this value was reached in all experiments.

8 Conclusions

In this thesis, a constitutive model of thermo-viscoplasticity for finite deformations for the zinc die casting alloy Zamak 5 with the influence of aging was developed on the basis of an extensive experimental campaign. The alloy Zamak 5 is commonly used in the industry for component of cars and machines, and it exhibits a complex thermo-mechanical behavior that is not reproduced by the currently available material models.

The experimental results show that the material is strongly rate-dependent even at room temperature. The relaxation takes several days to reach the equilibrium state, which makes it difficult to reach the termination points of the relaxation during a multi-step relaxation test. Thus, they have to be estimated with an assumption. The temperature influences the viscous effects and the equilibrium state. For higher temperatures ($85\,^{\circ}\mathrm{C}$ or higher), the equilibrium stress state tends to disappear and the viscous effects become predominant. For very low temperatures, the material behavior tends to purely rate-independent plasticity, meaning that the rate-dependent effects disappear and the material response can be identified with a rate-independent hysteresis. Natural aging influences the viscous behavior in a more pronounced way than the equilibrium stress behavior. At room temperature, the effect of natural aging is also stronger than at higher or lower temperatures. As it was not possible to obtain specimens in the final state of aging, the investigations were carried out with 3, 6, and 12 months of natural aging. Another aspect to be considered is a reduction in the dimensions of the material caused by the microstructural changes related to aging, which is comparable in its order of magnitude to the thermal expansion for a temperature increment of $50\,^{\circ}\mathrm{C}$. Moreover, the thermal conductivity depends on the aging and the temperature. This dependence originates in the thermal diffusivity, which increases with the aging time and decreases with the temperature. The origin of this dependence could lie in the formation of a more homogeneous phase and the presence of precipitations in the zinc-rich grains. The specific heat capacity depends linearly on the temperature in the investigated temperature range, but not on the aging.

Considering the experimental results, a material model was proposed. The model was first developed for the small deformation case and afterwards extended to finite deformations. Both models are based on the decomposition of the stress tensor into an equilibrium and an overstress part. This modeling concept shows advantages in the parameter identification process. In the small deformations case, the strain is additively decomposed into three components, which correspond to each effect that has to be modeled: a mechanical, a thermal, and an aging part. The equilibrium state is modeled with an element of endochronic plasticity, without distinguishing between an elastic or plastic domain. A Maxwell-element is used for the viscous effects. Moreover, two additional internal variables to include a softening effect and the effect of aging are defined. In the case of finite deformations, the deformation gradient is multiplicatively decomposed into three components – namely for the aging, the temperature, and the mechanical parts. This decomposition generates a series of intermediate configurations. In both models, the temperature and aging dependence is included by defining temperature and aging dependent material functions. Both models are thermodynamically consistent.

The complex identification process is explained in the parameter identification of Chapter 5. The identification is performed first with the small deformation model. Since modeling and identification are connected, some of the material functions depending on the temperature and aging are developed during this process. The parameters of the evolution equation for the aging variable are identified with the measurements of the temporal shrinkage behavior. Moreover, for the mechanical behavior, the deviatoric stress component is identified first with the results of the torsion experiments, which for a thin-walled cylinder corresponds to the identification of a one-dimensional problem. Here, the modular structure of the model is exploited with the identification of the parameters of the equilibrium state using the measured equilibrium hysteresis. Afterwards, the parameters of the overstress part with the experiments at different strain-rates are chosen. When the parameters of the deviatoric part of the model are known, there is only the compression modulus left to be identified. This is done based on the tensile equilibrium stress. The tensile experiments at different strain-rates are not used for the identification and show the predictability of the model. For the case of large deformations, the torsion tests cannot be reduced to a one-dimensional problem anymore, and can be only used for identification considering the entire 3D-problem. Since there is no information about the transverse contraction of the tensile tests available, and since the shear and volumetric behavior cannot be identified separately, the compression modulus is taken from the results of the identification with the small strains model. The remaining parameters are identified with the tensile and compression tests. Here, the equilibrium state is identified first with the equilibrium hysteresis, and the parameters of the overstress are identified with the experiments at different strain-rates. Finally, the parameters of the thermal properties are identified. The case of the thermal diffusivity is complex due to its dependence on the temperature and aging. Here, a weighting between the unaged state and the completely aged state is performed. Generally, the results of the identification show a sufficient agreement between the experimental behavior and the model.

In Chapter 6, the numerical solution with the Finite Element Method of the coupled thermo-mechanical problem is addressed. The time integration is presented for the Backward Euler method, since this is the method used in Abaqus. For the small deformations case, the local level can be solved without a local Newton iteration, so the system of nonlinear equations is solved with the Newton-Rahpson method. This is not the case for the finite strain model, which is thus solved with the Multilevel Newton Algorithm. The stress algorithm for both cases is provided, as well as the necessary information to compute the consistent tangent.

The behavior of the model is demonstrated drawing on three different examples. In the first one, it is shown that the system of differential equations composed by the internal variables is stiff. This information is important for the selection of the time discretization method and the time increment. With the application of implicit time integration methods, the stability problems are excluded. In general, the mechanical processes are the ones which determine the time increment, since the aging develops on larger time scales. In the second example, the behavior of the model is shown for a process with a short mechanical load and a long temperature change. The evolution of the aging and its effect in the model is demonstrated. In the last example, the behavior of the model is validated with a comparison between simulations and experiments in more complex geometries, in which the stress and strain states are not homogeneous anymore.

In conclusion, this thesis serves to provide more detailed knowledge about the thermo-mechanical behavior of the zinc die casting alloy Zamak 5, also with regard to natural aging. It provides a large amount of experimental results to characterize the volumetric and deviatoric behavior with regard to rate, temperature, and aging dependence. Moreover, the shrinkage at different temperatures and the thermo-physical properties are provided. A new model with the corresponding material parameters is proposed, together with the stress algorithm. This model can be used to simulate the rate, temperature, and aging-dependent mechanical behavior of component parts made of this material, with a maximum error of $31\,\%$ in the presented validation examples. As the error made in simulations with a model is generally not known, it is of advantage to have this information available in this concrete case for different validation experiments.

There are still several aspects that will have to be investigated in the future. The material exhibits porosity, which originates in the die casting process. This porosity influences the mechanical behavior and fracture behavior, and generally exhibits an inhomogeneous distribution. Moreover, the influence of the die casting process on the microstructure and material properties could be interesting for future investigations, since the process parameters influence the final microstructural state and the porosity. The size-dependence is another effect observed for this material – with two possible causes: one is the porosity distribution, and the other is the outer layer with a finer microstructure, originating from the die casting process itself. Other aspects such as the fracture behavior or the cyclic behavior should be of interest for the industry as well. It is always possible to go into more detail within a specific investigation area – and new problems arise with every solution to a problem, which is why the expertise of an engineer will always be necessary.

Appendix

1 Additional Evaluations for the Finite Strain Model

In this section, additional intermediate calculations for the derivation of the finite strain model are presented.

Derivatives of the Free Energy

In order to calculate the elastic component of the stress tensor $\mathbf{S}^{\mathrm{e}}_{\mathrm{Meq}}$, the derivatives

$$\frac{\mathrm{d}U(J_{\mathrm{M}})}{\mathrm{d}\mathbf{C}_{\mathrm{M}}} = \frac{\partial U(J_{\mathrm{M}})}{\partial J_{\mathrm{M}}}\frac{\mathrm{d}J_{\mathrm{M}}}{\mathrm{d}\mathbf{C}_{\mathrm{M}}}, \qquad \frac{\mathrm{d}\omega(\bar{\mathbf{C}}_{\mathrm{M}})}{\mathrm{d}\mathbf{C}_{\mathrm{M}}} = c_{10}\frac{\mathrm{d}I_{\bar{\mathbf{C}}_{\mathrm{M}}}}{\mathrm{d}\mathbf{C}_{\mathrm{M}}}, \tag{1}$$

have to be determined, see also (Hartmann, 2003). Considering the chosen volumetric part of the free energy $U(J_{\mathrm{M}}) = \dfrac{K}{50}(J_{\mathrm{M}}^5 + J_{\mathrm{M}}^{-5} - 2)$, with $J_{\mathrm{M}} = \det \mathbf{F}_{\mathrm{M}}$, the terms of $\mathrm{d}U(J_{\mathrm{M}})/\mathrm{d}\mathbf{C}_{\mathrm{M}}$ in Eq. (1) are given by

$$\frac{\partial U(J_{\mathrm{M}})}{\partial J_{\mathrm{M}}} = \frac{K}{50}(5J_{\mathrm{M}}^4 - 5J_{\mathrm{M}}^{-6}) = \frac{K}{10}(J_{\mathrm{M}}^4 - J_{\mathrm{M}}^{-6}), \tag{2}$$

$$\frac{\mathrm{d}J_{\mathrm{M}}}{\mathrm{d}\mathbf{C}_{\mathrm{M}}} = \frac{1}{2}(\det \mathbf{C}_{\mathrm{M}})^{-1/2}(\det \mathbf{C}_{\mathrm{M}})\mathbf{C}_{\mathrm{M}}^{-1} = \frac{1}{2}(\det \mathbf{C}_{\mathrm{M}})^{1/2}\mathbf{C}_{\mathrm{M}}^{-1} = \frac{1}{2}J_{\mathrm{M}}\mathbf{C}_{\mathrm{M}}^{-1}. \tag{3}$$

In this way, one obtains

$$\frac{\mathrm{d}U(J_{\mathrm{M}})}{\mathrm{d}\mathbf{C}_{\mathrm{M}}} = \frac{\partial U(J_{\mathrm{M}})}{\partial J_{\mathrm{M}}}\frac{\mathrm{d}J_{\mathrm{M}}}{\mathrm{d}\mathbf{C}_{\mathrm{M}}} = \frac{K}{20}(J_{\mathrm{M}}^5 - J_{\mathrm{M}}^{-5})\mathbf{C}_{\mathrm{M}}^{-1}. \tag{4}$$

With the chosen isochoric part of the free energy $\bar{\omega}(\bar{\mathbf{C}}_{\mathrm{M}}) = c_{10}(I_{\bar{\mathbf{C}}_{\mathrm{M}}} - 3)$, with $\bar{\mathbf{C}}_{\mathrm{M}} = (\det \mathbf{C}_{\mathrm{M}})^{-1/3}\mathbf{C}_{\mathrm{M}}$ and considering $I_{\bar{\mathbf{C}}_{\mathrm{M}}} = \operatorname{tr}((\det \mathbf{C}_{\mathrm{M}})^{-1/3}\mathbf{C}_{\mathrm{M}}) = (\det \mathbf{C}_{\mathrm{M}})^{-1/3}(\operatorname{tr} \mathbf{C}_{\mathrm{M}})$, the chain rule can be applied to Eq. (1)

$$\begin{aligned}
\frac{\mathrm{d}I_{\bar{\mathbf{C}}_{\mathrm{M}}}}{\mathrm{d}\mathbf{C}_{\mathrm{M}}} &= \frac{\mathrm{d}[(\det \mathbf{C}_{\mathrm{M}})^{-1/3}]}{\mathrm{d}\mathbf{C}_{\mathrm{M}}}(\operatorname{tr} \mathbf{C}_{\mathrm{M}}) + (\det \mathbf{C}_{\mathrm{M}})^{-1/3}\frac{\mathrm{d}[(\operatorname{tr} \mathbf{C}_{\mathrm{M}})]}{\mathrm{d}\mathbf{C}_{\mathrm{M}}} \\
&= (\det \mathbf{C}_{\mathrm{M}})^{-1/3}[\mathbf{I} - \frac{1}{3}(\operatorname{tr} \mathbf{C}_{\mathrm{M}})\mathbf{C}_{\mathrm{M}}^{-1}] \\
&= (\det \mathbf{C}_{\mathrm{M}})^{-1/3}\mathbf{C}_{\mathrm{M}}^{-1}[\mathbf{C}_{\mathrm{M}} - \frac{1}{3}(\operatorname{tr} \mathbf{C}_{\mathrm{M}})\mathbf{I}] = \mathbf{C}_{\mathrm{M}}^{-1}\bar{\mathbf{C}}_{\mathrm{M}}^{\mathrm{D}}.
\end{aligned} \tag{5}$$

In this way, one obtains

$$\frac{\mathrm{d}\omega(\bar{\mathbf{C}}_{\mathrm{M}})}{\mathrm{d}\mathbf{C}_{\mathrm{M}}} = c_{10} J_{\mathrm{M}}^{-2/3} \mathbf{C}_{\mathrm{M}}^{-1} \mathbf{C}_{\mathrm{M}}^{\mathrm{D}}. \tag{6}$$

The determination of the derivatives $\mathrm{d}\psi_{\mathrm{eq}}^{\mathrm{h}}/\mathrm{d}\mathbf{C}_{\mathrm{k}}$ and $\mathrm{d}\psi_{\mathrm{ov}}/\mathrm{d}\mathbf{C}_{\mathrm{e}}$ is analogous to this term.

Isochoric Strain-Rate

From the relation $\mathbf{F} = \varphi_a \varphi_\Theta \mathbf{F}_{\mathrm{M}}$ it is clear that the isochoric part depends only on the mechanical part of the deformation gradient $\bar{\mathbf{F}} = \bar{\mathbf{F}}_{\mathrm{M}}$. The isochoric mechanical part of the Green strain tensor is defined by

$$\bar{\mathbf{E}}_{\mathrm{M}} = \frac{1}{2}(\bar{\mathbf{C}}_{\mathrm{M}} - 1) = \frac{1}{2}(J^{-2/3}\mathbf{C} - \mathbf{I}), \tag{7}$$

with $\bar{\mathbf{C}}_{\mathrm{M}} = \bar{\mathbf{F}}_{\mathrm{M}}^{\mathrm{T}} \bar{\mathbf{F}}_{\mathrm{M}}$. The time derivative of this term can be determined using the chain rule

$$\dot{\bar{\mathbf{E}}}_{\mathrm{M}} = \frac{1}{2} \frac{\mathrm{d}[(J^{-2/3}\mathbf{C} - \mathbf{I})]}{\mathrm{d}t} = \frac{1}{2}\left(-\frac{2}{3} J^{-5/3} \dot{J} \mathbf{C} + J^{-2/3} \dot{\mathbf{C}}\right). \tag{8}$$

The rate of the Jacobian $J = \det \mathbf{F}$ is equal to

$$\dot{J} = (\det \mathbf{F})\mathbf{F}^{-\mathrm{T}} \cdot \dot{\mathbf{F}} = J(\dot{\mathbf{F}}^{\mathrm{T}} \mathbf{F}^{-\mathrm{T}}) \cdot \mathbf{I} = J(\mathbf{F}^{-\mathrm{T}} \dot{\mathbf{F}}^{\mathrm{T}}) \cdot \mathbf{I} = J(\operatorname{tr} \mathbf{L}). \tag{9}$$

Inserting Eq. (9) into Eq. (8) leads

$$\dot{\bar{\mathbf{E}}}_{\mathrm{M}} = \frac{J^{-2/3}}{2}\left(\dot{\mathbf{C}} - \frac{2}{3}(\operatorname{tr} \mathbf{L})\mathbf{C}\right). \tag{10}$$

Considering $\dot{\mathbf{C}} = \dot{\mathbf{F}}^{\mathrm{T}}\mathbf{F} + \mathbf{F}^{\mathrm{T}}\dot{\mathbf{F}}$, one can obtain the relation

$$\mathbf{F}^{-\mathrm{T}} \dot{\mathbf{C}} \mathbf{F}^{-1} = \mathbf{L}^{\mathrm{T}} + \mathbf{L} \rightarrow \operatorname{tr}(\mathbf{C}^{-1}\dot{\mathbf{C}}) = 2(\operatorname{tr} \mathbf{L}). \tag{11}$$

Inserting relation (11) into Eq. (10), an expression for the mechanical isochoric strain-rate is obtained

$$\dot{\bar{\mathbf{E}}}_{\mathrm{M}} = \frac{J^{-2/3}}{2}\left(\dot{\mathbf{C}} - \frac{1}{3}(\operatorname{tr}(\mathbf{C}^{-1}\dot{\mathbf{C}}))\mathbf{C}\right) = \frac{J^{-2/3}}{2}\mathbf{C}(\mathbf{C}^{-1}\dot{\mathbf{C}})^{\mathrm{D}}. \tag{12}$$

Pull-Back Operation for the Evolution Equations

The evolution equation

$$\overset{\triangle}{\tilde{\boldsymbol{\varepsilon}}}_{\mathrm{p}} = 2\mu_{\mathrm{eq}} \beta_{\mathbf{Y}} (\varphi_\Theta \varphi_a)^{-2} \dot{s}_{\mathrm{M}} \bar{\mathbf{C}}_{\mathrm{k}}^{\mathrm{D}} \tag{13}$$

has to be pulled back into the reference configuration. Considering

$$\overset{\triangle}{\tilde{\boldsymbol{\varepsilon}}}_{\rm p} = \bar{\mathbf{F}}_{\rm p}^{-\rm T}\dot{\mathbf{E}}_{\rm p}\bar{\mathbf{F}}_{\rm p}^{-1} = 1/2\bar{\mathbf{F}}_{\rm p}^{-\rm T}\dot{\mathbf{C}}_{\rm p}\bar{\mathbf{F}}_{\rm p}^{-1}, \text{ and } \bar{\mathbf{C}}_{\rm k} = \bar{\mathbf{F}}_{\rm k}^{\rm T}\bar{\mathbf{F}}_{\rm k} = \bar{\mathbf{F}}_{\rm p}^{-\rm T}\bar{\mathbf{F}}_{\rm M}^{\rm T}\bar{\mathbf{F}}_{\rm M}\bar{\mathbf{F}}_{\rm p}^{-1} \tag{14}$$

see also Tab. 4.5, Eq. (13) can be rewritten as

$$1/2\bar{\mathbf{F}}_{\rm p}^{-\rm T}\dot{\mathbf{C}}_{\rm p}\bar{\mathbf{F}}_{\rm p}^{-1} = 2\mu_{\rm eq}\beta_{\mathbf{Y}}(\varphi_\Theta\varphi_a)^{-2}\dot{s}_{\rm M}(\bar{\mathbf{F}}_{\rm p}^{-\rm T}\bar{\mathbf{F}}_{\rm M}^{\rm T}\bar{\mathbf{F}}_{\rm M}\bar{\mathbf{F}}_{\rm p}^{-1} - \frac{1}{3}\mathrm{tr}\,(\bar{\mathbf{F}}_{\rm p}^{-\rm T}\bar{\mathbf{F}}_{\rm M}^{\rm T}\bar{\mathbf{F}}_{\rm M}\bar{\mathbf{F}}_{\rm p}^{-1})\mathbf{I}), \tag{15}$$

Moreover, with the property of the trace

$$\mathrm{tr}\,(\bar{\mathbf{F}}_{\rm p}^{-\rm T}\bar{\mathbf{F}}_{\rm M}^{\rm T}\bar{\mathbf{F}}_{\rm M}\bar{\mathbf{F}}_{\rm p}^{-1}) = \mathrm{tr}\,(\bar{\mathbf{F}}_{\rm p}^{-1}\bar{\mathbf{F}}_{\rm p}^{-\rm T}\bar{\mathbf{F}}_{\rm M}^{\rm T}\bar{\mathbf{F}}_{\rm M}) = \mathrm{tr}\,(\bar{\mathbf{C}}_{\rm p}^{-1}\bar{\mathbf{C}}_{\rm M}), \tag{16}$$

one obtains

$$\dot{\mathbf{C}}_{\rm p} = 4\mu_{\rm eq}\beta_{\mathbf{Y}}(\varphi_\Theta\varphi_a)^{-2}\dot{s}_{\rm M}(\bar{\mathbf{C}}_{\rm M} - \frac{1}{3}\mathrm{tr}\,(\bar{\mathbf{C}}_{\rm p}^{-1}\bar{\mathbf{C}}_{\rm M})\bar{\mathbf{C}}_{\rm p}) \tag{17}$$

$$= 4\mu_{\rm eq}\beta_{\mathbf{Y}}(\varphi_\Theta\varphi_a)^{-2}\dot{s}_{\rm M}\bar{\mathbf{C}}_{\rm p}(\bar{\mathbf{C}}_{\rm p}^{-1}\bar{\mathbf{C}}_{\rm M} - \frac{1}{3}\mathrm{tr}\,(\bar{\mathbf{C}}_{\rm p}^{-1}\bar{\mathbf{C}}_{\rm M})\mathbf{I}). \tag{18}$$

Since $\bar{\mathbf{C}}_{\rm M} = \bar{\mathbf{C}} = J^{-2/3}\mathbf{C}$, Eq. (18) can be written by

$$\dot{\mathbf{C}}_{\rm p} = 4(\varphi_a\varphi_\Theta)^{-2}J^{-2/3}\beta_{\mathbf{Y}}\mu_{\rm eq}\dot{s}_{\rm M}\bar{\mathbf{C}}_{\rm p}(\bar{\mathbf{C}}_{\rm p}^{-1}\mathbf{C})^{\rm D}. \tag{19}$$

Analogously to this procedure, one can obtain the pull-back operation for the evolution equation

$$\overset{\triangle}{\boldsymbol{\varepsilon}}_{\rm v} = 2\frac{\mu_{\rm ov}}{\eta}(\varphi_\Theta\varphi_a)^{-2}\bar{\mathbf{C}}_{\rm e}^{\rm D} \tag{20}$$

into

$$\dot{\mathbf{C}}_{\rm v} = 4\frac{\mu_{\rm ov}}{\eta}(\varphi_a\varphi_\Theta)^{-2}J^{-2/3}\bar{\mathbf{C}}_{\rm v}(\bar{\mathbf{C}}_{\rm v}^{-1}\mathbf{C})^{\rm D}. \tag{21}$$

2 Linearization of the Finite Strain Model

Considering the assumptions made in Section 2.4.3, the finite strain model of Section 4.3 can be linearized. Since there is no distinction between configurations $\tilde{\mathbf{T}} \approx \mathbf{T}_{\rm R} \approx \mathbf{S} \approx \mathbf{T}$, the total stress can be expressed in this case approximately equal to the linearized total stress $\mathbf{T}_{\rm L}$, which can be decomposed in the different components of the stress from Tab. 4.3

$$\tilde{\mathbf{T}} \approx \mathbf{S} \approx \mathbf{T}_{\rm L} = \mathbf{T}^{\rm e}_{\rm volL} + \mathbf{T}^{\rm e}_{\rm isoL} + \mathbf{T}^{\rm h}_{\rm eq_L} + \mathbf{T}_{\rm ovL} \tag{22}$$

Volumetric Stress

For the considerations of the volumetric stress, only isothermal processes without the influence of aging ($\varphi_a = \varphi_\Theta = 1$) are considered. The volumetric part of the stress in the current configuration is expressed by

$$\mathbf{S}^{\mathrm{e}}_{\mathrm{vol}} = \frac{K}{10}\left(J^5 - J^{-5}\right)\mathbf{I}. \tag{23}$$

Since for the geometric linarization $\mathbf{E} \approx \mathbf{A} \approx \frac{1}{2}(\mathbf{H}+\mathbf{H}^{\mathrm{T}})$, the trace of the strain is equal to $\operatorname{tr}\mathbf{E} \approx \operatorname{tr}\mathbf{A} \approx \operatorname{tr}\mathbf{H}$, and thus holds $J = \det\mathbf{F} \approx 1+\operatorname{tr}\mathbf{H} \approx 1+\operatorname{tr}\mathbf{E}$. It follows that

$$J^5 \approx (1+\operatorname{tr}\mathbf{E})^5 = 1 + 5(\operatorname{tr}\mathbf{E}) + 10(\operatorname{tr}\mathbf{E})^2 + O(\delta^3), \tag{24}$$

with $O(\delta^3)$ the error of order 3 or higher. The term $(J^5 - J^{-5})$ can be expressed by

$$\begin{aligned} J^5 - J^{-5} &= 1 + 5(\operatorname{tr}\mathbf{E}) + 10(\operatorname{tr}\mathbf{E})^2 + O(\delta^3) - \frac{1}{1 + 5(\operatorname{tr}\mathbf{E}) + 10(\operatorname{tr}\mathbf{E})^2 + O(\delta^3)} \\ &= \frac{(1 + 5(\operatorname{tr}\mathbf{E}) + 10(\operatorname{tr}\mathbf{E})^2 + O(\delta^3))^2 - 1}{1 + 5(\operatorname{tr}\mathbf{E}) + 10(\operatorname{tr}\mathbf{E})^2 + O(\delta^3)} \\ &= \frac{10(\operatorname{tr}\mathbf{E}) + 45(\operatorname{tr}\mathbf{E})^2 + O(\delta^3)}{1 + 5(\operatorname{tr}\mathbf{E}) + 10(\operatorname{tr}\mathbf{E})^2 + O(\delta^3)}. \end{aligned} \tag{25}$$

Neglecting the terms of 2nd order or higher and considering for the denominator that $(\operatorname{tr}\mathbf{E}) \ll 1$, leads to

$$J^5 - J^{-5} \approx 10(\operatorname{tr}\mathbf{E}). \tag{26}$$

In this way, one obtains the linearized hydrostatic stress

$$\mathbf{T}^{\mathrm{e}}_{\mathrm{volL}} = K(\operatorname{tr}\mathbf{E}_{\mathrm{L}})\mathbf{I}. \tag{27}$$

Isochoric Stress

The elastic component of the isochoric stress in the current configuration is equal to

$$\mathbf{S}^{\mathrm{e}}_{\mathrm{iso}} = 2c_{10}\bar{\mathbf{B}}^{\mathrm{D}}_{\mathrm{M}}. \tag{28}$$

Since $\bar{\mathbf{B}}^{\mathrm{D}}_{\mathrm{M}} = \bar{\mathbf{B}}^{\mathrm{D}}$ and considering the linearization property $\bar{\mathbf{B}}^{\mathrm{D}} \approx \mathbf{B}^{\mathrm{D}} \approx \mathbf{C}^{\mathrm{D}} = 2\mathbf{E}^{\mathrm{D}}_{\mathrm{L}}$, the linearized stress can be expressed by

$$\mathbf{T}^{\mathrm{e}}_{\mathrm{isoL}} = 4c_{10}\mathbf{E}^{\mathrm{D}}_{\mathrm{L}}. \tag{29}$$

Analogously, for the equilibrium stress part, it holds $\bar{\mathbf{B}}_{\mathrm{k}} \approx \mathbf{B}_{\mathrm{k}} \approx \mathbf{C}_{\mathrm{k}} = 2\tilde{\boldsymbol{\varepsilon}}_{\mathrm{k}} + \mathbf{I}$. In the linearized case, there is no distinction between the configurations $\mathbf{E}_{\mathrm{kL}} \approx \mathbf{E}_{\mathrm{k}} \approx \tilde{\boldsymbol{\varepsilon}}_{\mathrm{k}} \approx \mathbf{A}_{\mathrm{k}}$, and thus the linearized hysteretic stress is equal to

$$\mathbf{T}^{\mathrm{h}}_{\mathrm{eq_L}} = 4\mu_{\mathrm{eq}}\mathbf{E}^{\mathrm{D}}_{\mathrm{k_L}} \tag{30}$$

In the same way, $\bar{\mathbf{B}}_\mathrm{e} \approx \mathbf{B}_\mathrm{e} \approx \mathbf{C}_\mathrm{e} = 2\boldsymbol{\varepsilon}_\mathrm{e} + \mathbf{I}$ and $\mathbf{E}_\mathrm{eL} \approx \mathbf{E}_\mathrm{e} \approx \boldsymbol{\varepsilon}_\mathrm{e} \approx \mathbf{A}_\mathrm{e}$ hold for the Maxwell-Element, which leads to the linearized overstress

$$\mathbf{T}_\mathrm{ovL} = 4\mu_\mathrm{ov}\mathbf{E}^\mathrm{D}_{\mathrm{e_L}}. \tag{31}$$

Evolution Equations

The evolutions equations of the tensor variables

$$\overset{\triangle}{\tilde{\boldsymbol{\varepsilon}}}_\mathrm{p} = 2\mu_\mathrm{eq}\beta_\mathbf{Y}(\varphi_\Theta\varphi_a)^{-2}\dot{s}_\mathrm{M}\bar{\mathbf{C}}^\mathrm{D}_\mathrm{k}, \quad \text{with} \quad \beta_\mathbf{Y} = \hat{b}/\mu_\mathrm{eq} \tag{32}$$

$$\overset{\triangle}{\boldsymbol{\varepsilon}}_\mathrm{v} = \frac{2\mu_\mathrm{ov}}{\hat{\eta}}(\varphi_\Theta\varphi_a)^{-2}\bar{\mathbf{C}}^\mathrm{D}_\mathrm{e}, \tag{33}$$

can be linearized considering the evaluations for the stresses. For small deformations, it holds $(\varphi_\Theta\varphi_a)^{-2} \approx 1$. Since there is no distinction between configurations $\overset{\triangle}{\boldsymbol{\varepsilon}} \approx \overset{\triangle}{\tilde{\boldsymbol{\varepsilon}}} \approx \dot{\mathbf{E}}$, and no distinction between isochoric and volumetric parts. For Eqns. (32)-(33) this leads to

$$\dot{\mathbf{E}}_{\mathrm{p_L}} = \dot{\mathbf{E}}^\mathrm{D}_{\mathrm{p_L}} = \dot{\mathbf{E}}^\mathrm{D}_{\mathrm{M_L}} - \dot{\mathbf{E}}^\mathrm{D}_{\mathrm{k_L}} = 4\hat{b}\dot{s}_\mathrm{M}\mathbf{E}^\mathrm{D}_{\mathrm{k_L}}, \tag{34}$$

$$\dot{\mathbf{E}}_\mathrm{vL} = \frac{4\mu_\mathrm{ov}}{\hat{\eta}}\mathbf{E}^\mathrm{D}_{\mathrm{e_L}} = \frac{\mathbf{T}_\mathrm{ovL}}{\hat{\eta}}. \tag{35}$$

In this case, the linearized rate of the arc-length is equal to

$$\dot{s}_\mathrm{M} = \sqrt{\overset{\triangle}{\bar{\tilde{\boldsymbol{\varepsilon}}}}_\mathrm{M} \cdot \overset{\triangle}{\bar{\tilde{\boldsymbol{\varepsilon}}}}_\mathrm{M}} \approx \sqrt{\dot{\mathbf{E}}_\mathrm{ML} \cdot \dot{\mathbf{E}}_\mathrm{ML}}. \tag{36}$$

Comparing Eq. (34) with Eq. (4.29), the analogy between the strain-like variable $\mathbf{Y}$ from the small strain model and $\mathbf{E}^\mathrm{D}_{\mathrm{k_L}}$ becomes evident. However, one can see that the factor $c(\Theta)/c_\alpha$ does not appear in the finite strain case. Both models are only equivalent for isothermal processes. The scalar evolution equations for the aging variable (4.155) and the softening (4.151) are analogous in the small and finite strain models. Compared to the small strain model of Tab. 4.1, one obtains the relations in Tab. 1.

3 Results of the Identification of the Mechanical Behavior

In this section, additional results of the parameter identification, which were not shown in Chapter 5, are provided.

Table 1: Relation between the parameters of the small strain model and the linearized finite strain model

parameter	small strain model	finite strain model
Bulk Modulus	K_{eq}	K
Elastic Parameter Equilibrium	G_{eq}	$2c_{10}$
Plastic Parameter Equilibrium	b	$4\hat{b}$
Plastic Parameter Equilibrium	c	$4\mu_{\mathrm{eq}}$
Shear Modulus Maxwell Element	G_{ov}	$2\mu_{\mathrm{ov}}$
Viscosity Maxwell Element	η	$\hat{\eta}$

3.1 Small Deformations Torsion

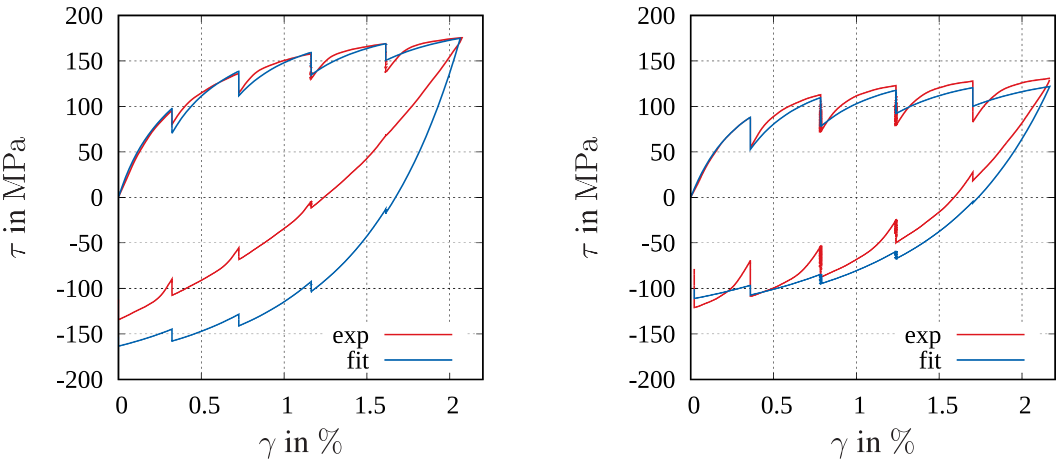

(a) $\Theta = -40\,^\circ\mathrm{C}$

(b) $\Theta = 20\,^\circ\mathrm{C}$

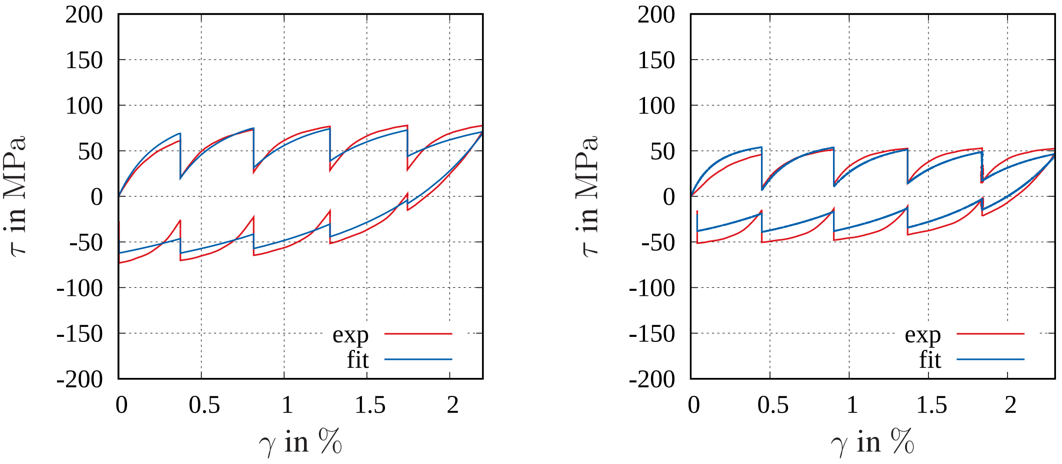

(c) $\Theta = 60\,^\circ\mathrm{C}$

(d) $\Theta = 85\,^\circ\mathrm{C}$

Figure 1: Prediction of the multi-step relaxation test in torsion (3 months of natural aging)

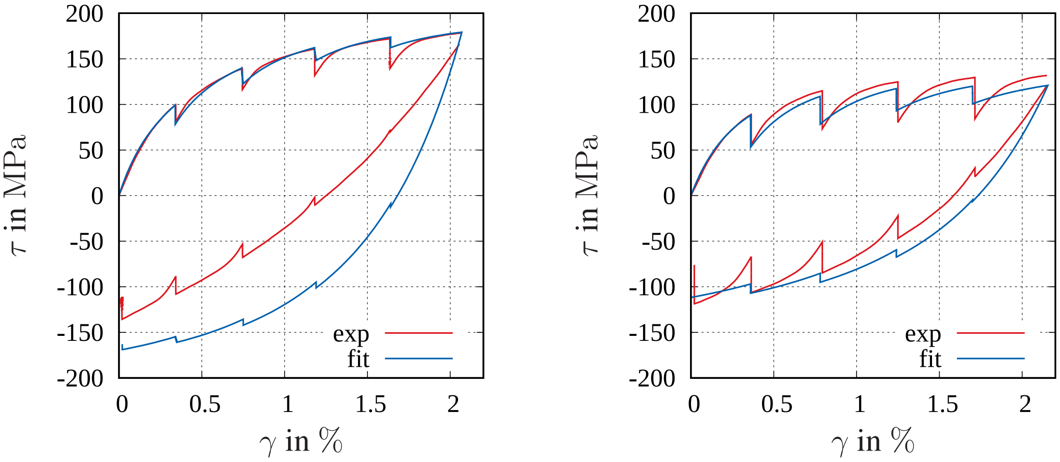

(a) $\Theta = -40\,^{\circ}\mathrm{C}$ (b) $\Theta = 20\,^{\circ}\mathrm{C}$

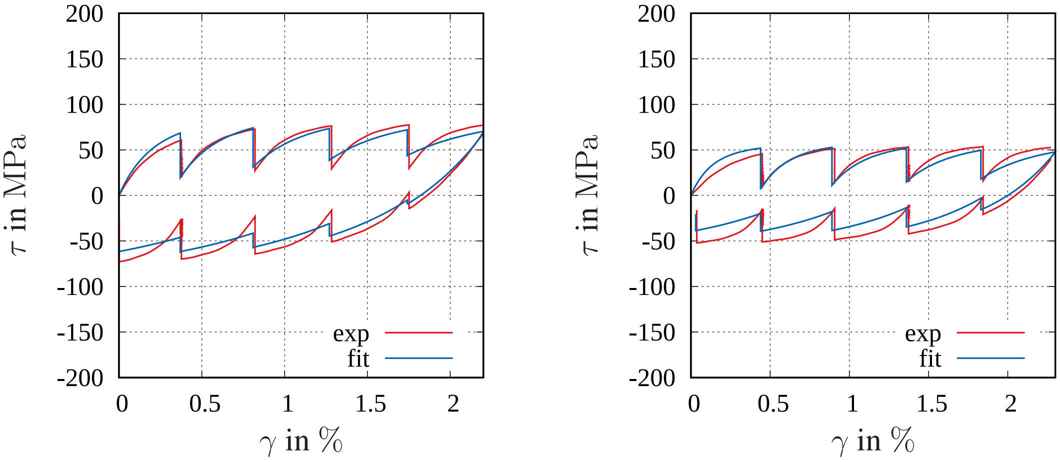

(c) $\Theta = 60\,^{\circ}\mathrm{C}$ (d) $\Theta = 85\,^{\circ}\mathrm{C}$

Figure 2: Prediction of the multi-step relaxation test in torsion (6 months of natural aging)

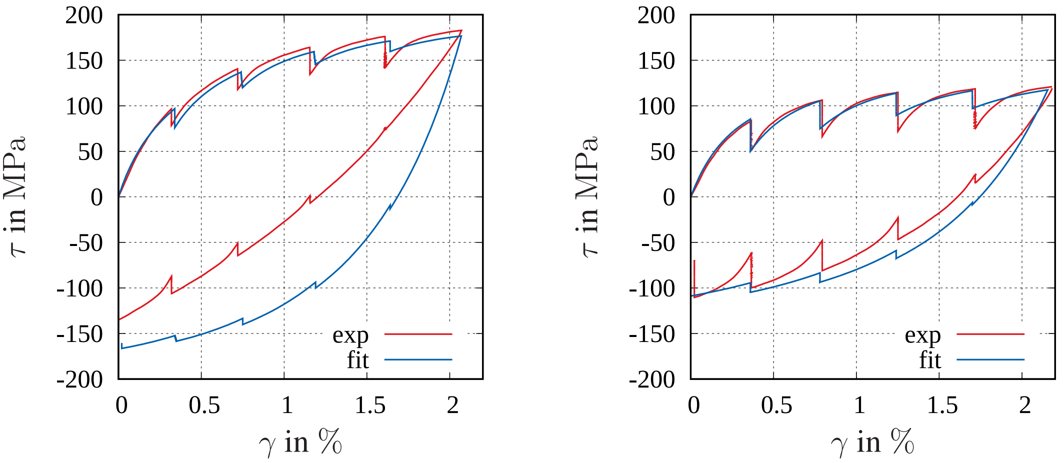

(a) $\Theta = -40\,°\mathrm{C}$ (b) $\Theta = 20\,°\mathrm{C}$

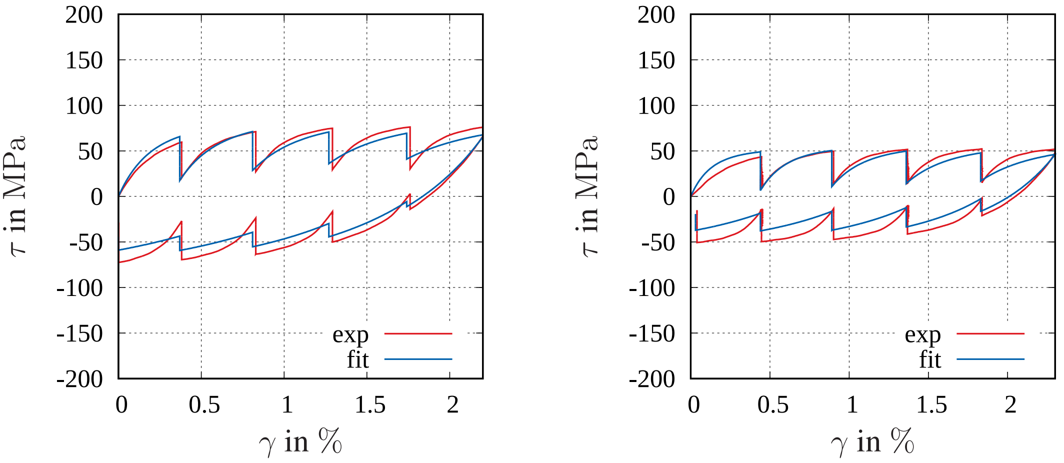

(c) $\Theta = 60\,°\mathrm{C}$ (d) $\Theta = 85\,°\mathrm{C}$

Figure 3: Prediction of the multi-step relaxation test in torsion (12 months of natural aging)

3.2 Small Deformations Tension and Compression

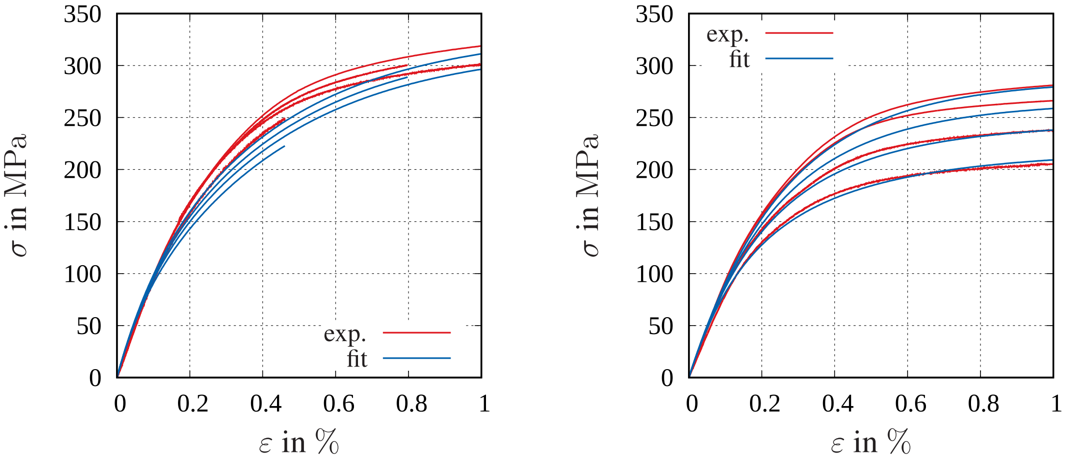

(a) $\Theta = -40\,^\circ\mathrm{C}$ (b) $\Theta = 20\,^\circ\mathrm{C}$

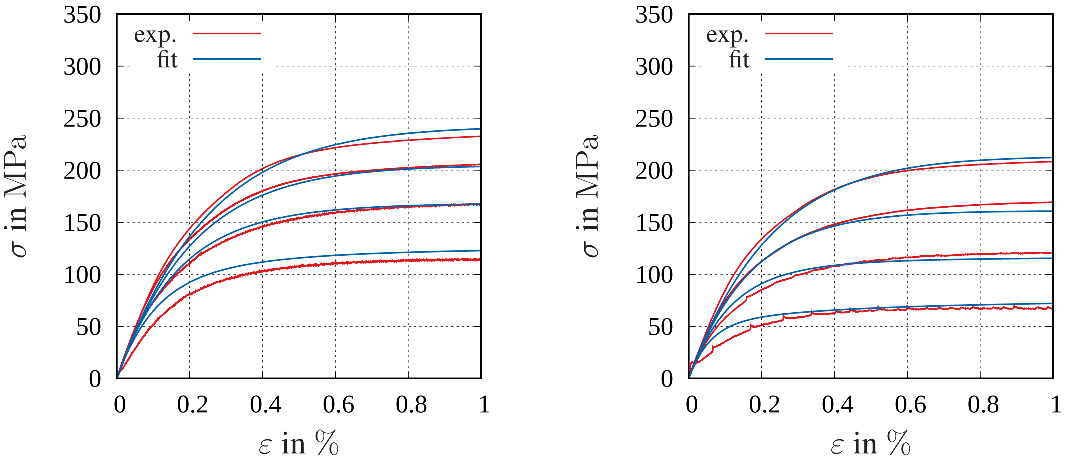

(c) $\Theta = 60\,^\circ\mathrm{C}$ (d) $\Theta = 85\,^\circ\mathrm{C}$

Figure 4: Results of the identification in tension with the small strain model (3 months of natural aging)

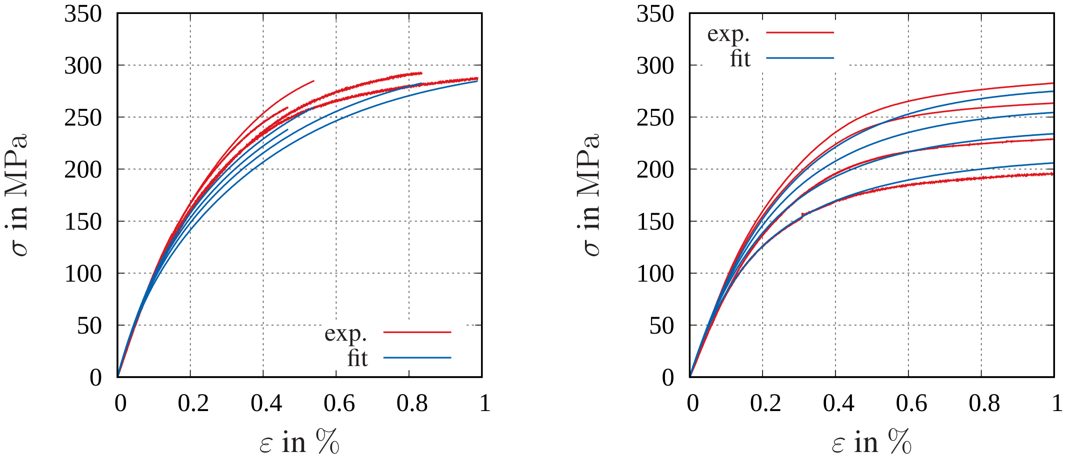

(a) $\Theta = -40\,^\circ\mathrm{C}$

(b) $\Theta = 20\,^\circ\mathrm{C}$

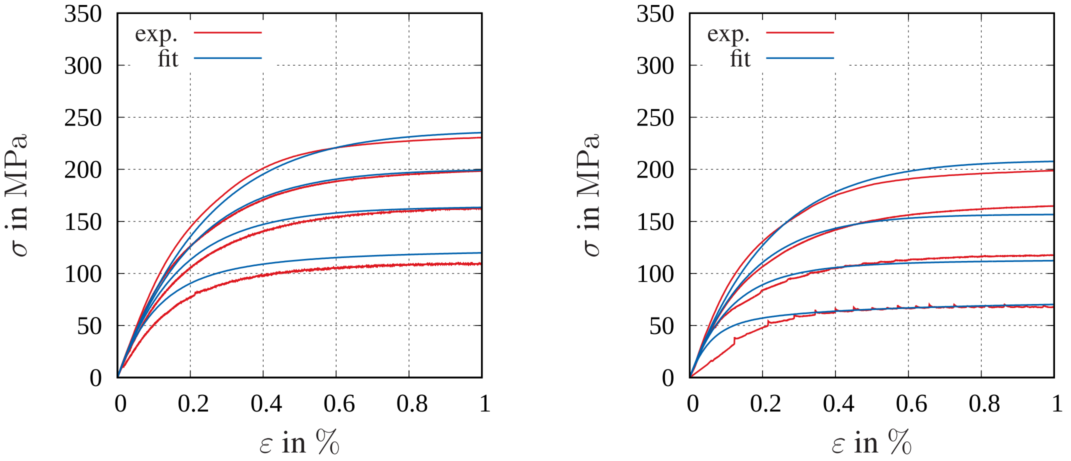

(c) $\Theta = 60\,^\circ\mathrm{C}$

(d) $\Theta = 85\,^\circ\mathrm{C}$

Figure 5: Results of the identification in tension with the small strain model (6 months of natural aging)

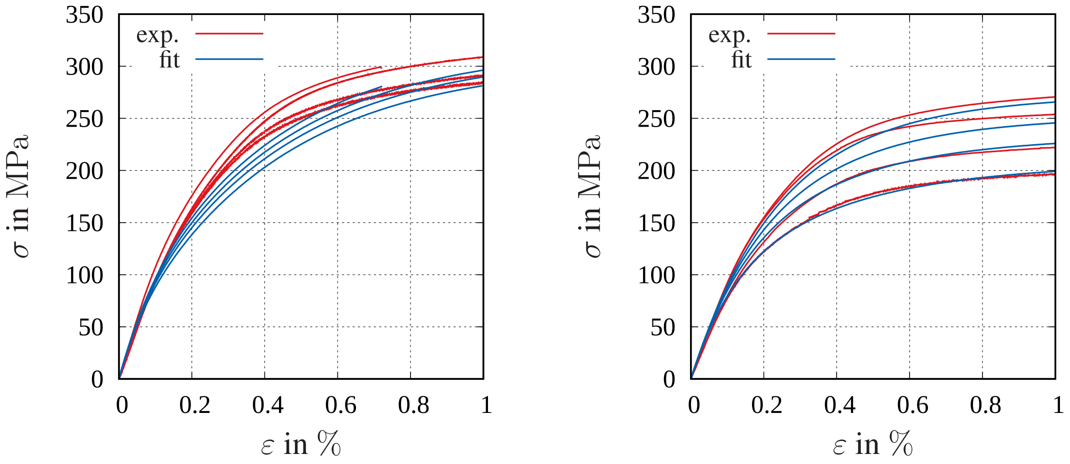

(a) $\Theta = -40\,^\circ\mathrm{C}$

(b) $\Theta = 20\,^\circ\mathrm{C}$

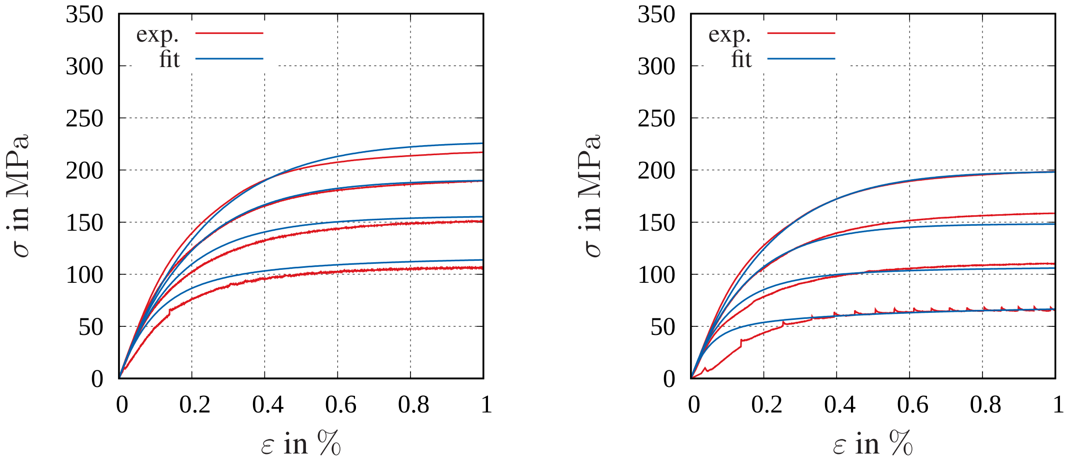

(c) $\Theta = 60\,^\circ\mathrm{C}$

(d) $\Theta = 85\,^\circ\mathrm{C}$

Figure 6: Results of the identification in tension with the small strain model (12 months of natural aging)

3.3 Large Deformations

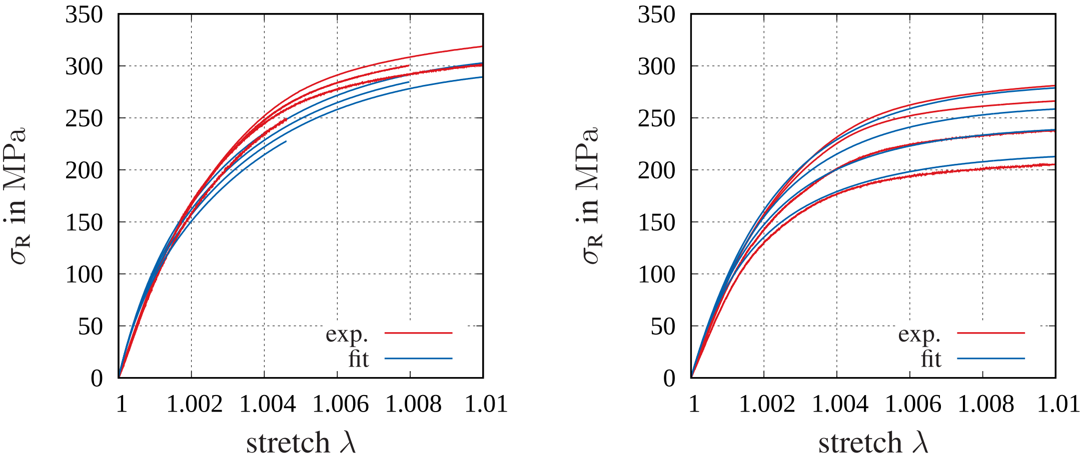

(a) $\Theta = -40\,°C$

(b) $\Theta = 20\,°C$

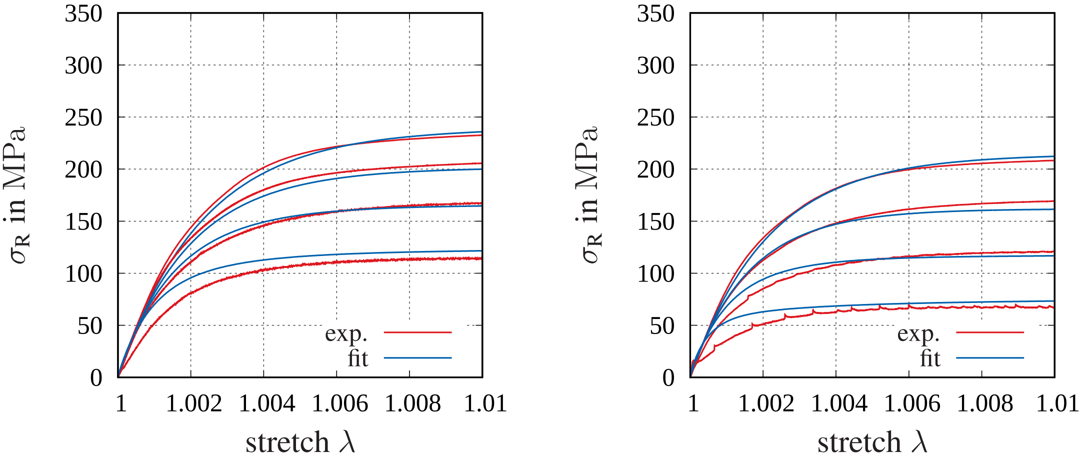

(c) $\Theta = 60\,°C$

(d) $\Theta = 85\,°C$

Figure 7: Results of the identification in tension with the finite strain model (3 months of natural aging)

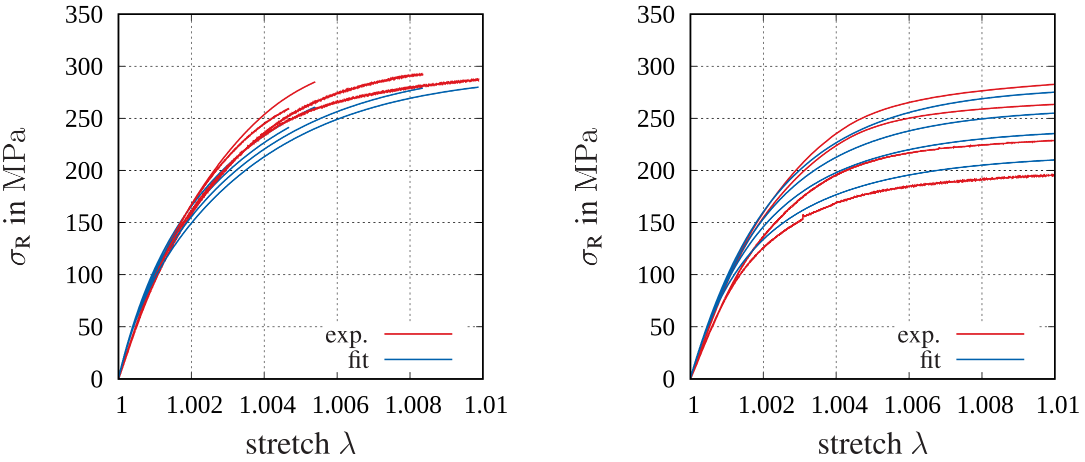

(a) $\Theta = -40\,^\circ\mathrm{C}$ (b) $\Theta = 20\,^\circ\mathrm{C}$

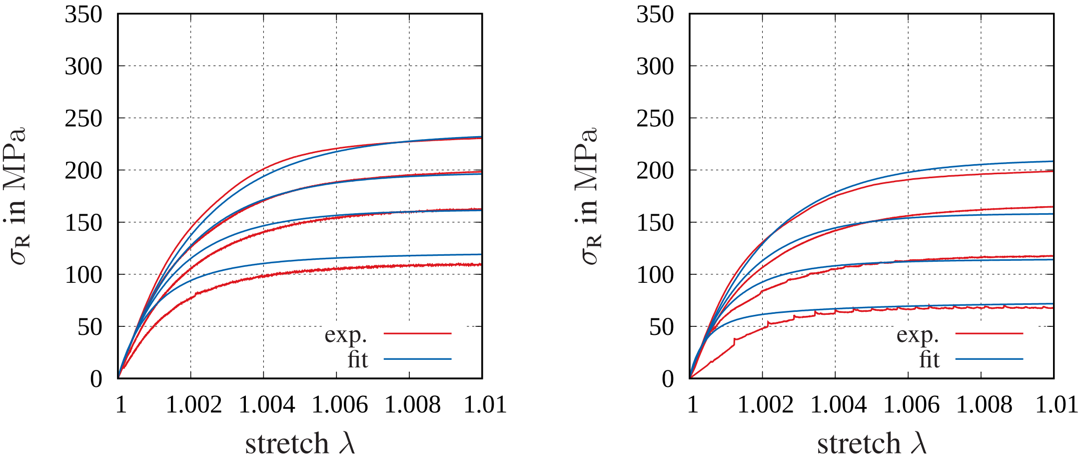

(c) $\Theta = 60\,^\circ\mathrm{C}$ (d) $\Theta = 85\,^\circ\mathrm{C}$

Figure 8: Results of the identification in tension with the finite strain model (6 months of natural aging)

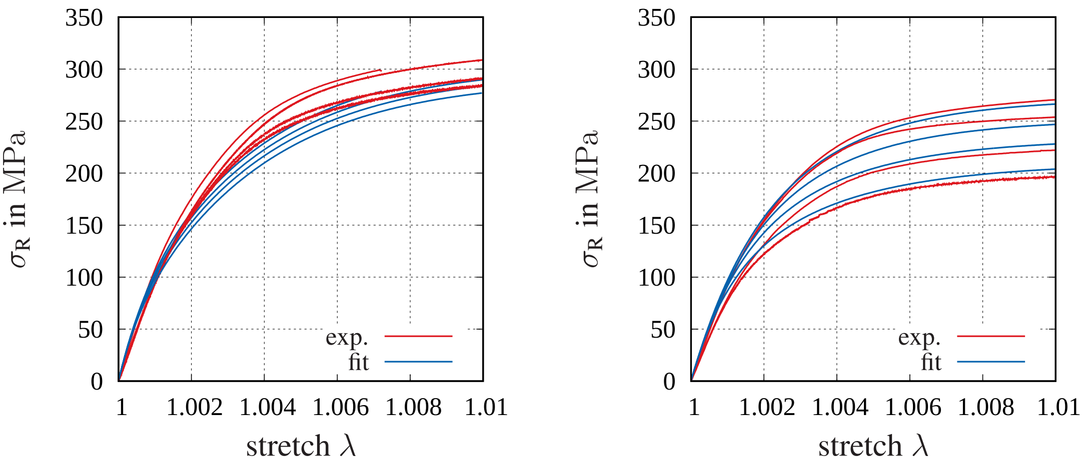

(a) $\Theta = -40\,°\mathrm{C}$

(b) $\Theta = 20\,°\mathrm{C}$

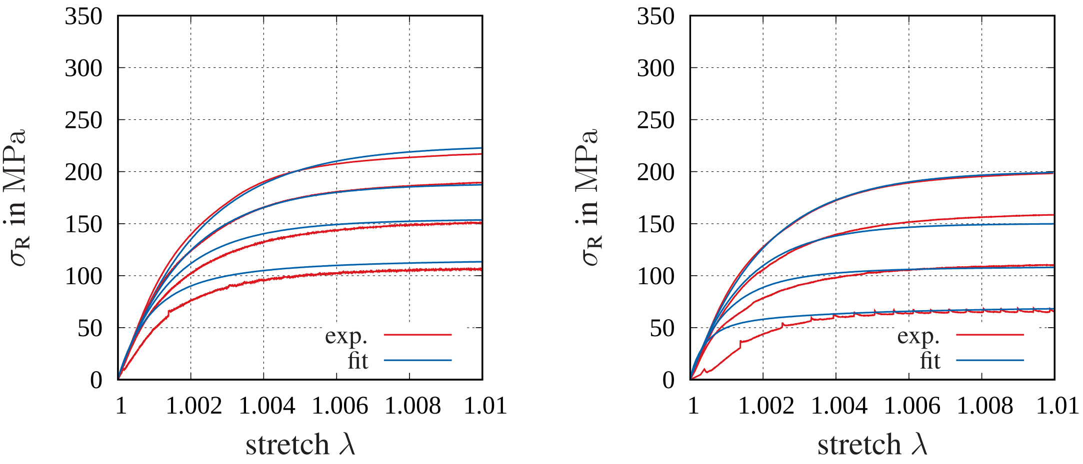

(c) $\Theta = 60\,°\mathrm{C}$

(d) $\Theta = 85\,°\mathrm{C}$

Figure 9: Results of the identification in tension with the finite strain model (12 months of natural aging)

4 Matrix Representation

This work draws on the notation exposed in (Hartmann, 2003) for the representation of the discretized system of equations in Chapter 6. The strain displacement matrix can be written as

$$\tilde{\mathsf{B}}_a = \begin{bmatrix} F_{11}N_{a,X} & F_{21}N_{a,X} & F_{31}N_{a,X} \\ F_{12}N_{a,Y} & F_{22}N_{a,Y} & F_{32}N_{a,Y} \\ F_{13}N_{a,Z} & F_{23}N_{a,Z} & F_{33}N_{a,Z} \\ F_{11}N_{a,Y} + F_{12}N_{a,X} & F_{21}N_{a,Y} + F_{22}N_{a,X} & F_{31}N_{a,Y} + F_{32}N_{a,X} \\ F_{12}N_{a,Z} + F_{13}N_{a,Y} & F_{22}N_{a,Z} + F_{23}N_{a,Y} & F_{32}N_{a,Z} + F_{33}N_{a,Y} \\ F_{13}N_{a,X} + F_{11}N_{a,Z} & F_{23}N_{a,X} + F_{21}N_{a,Z} & F_{33}N_{a,X} + F_{31}N_{a,Z} \end{bmatrix} . \tag{37}$$

Here, the index $a = 1, \ldots, n_{\text{en}}$ changes from one up to the number of nodes per element. Moreover, the matrix representation of the tensor $[\mathbf{F} \otimes \mathbf{F}]^{\mathrm{T}_{23}}$ is required in order to perform the transformation of the second Piola Kirchhoff tensor $\tilde{\mathsf{T}}^{\mathrm{e}}$ into the weighted Cauchy stress $\mathsf{S}^{\mathrm{e}} = \mathsf{F}^{\mathrm{e}}_{23}\tilde{\mathsf{T}}^{\mathrm{e}}$

$$\mathsf{F}^{\mathrm{e}}_{23} = \begin{bmatrix} \mathrm{F}_{11}\mathrm{F}_{11} & \mathrm{F}_{12}\mathrm{F}_{12} & \mathrm{F}_{13}\mathrm{F}_{13} & 2\mathrm{F}_{11}\mathrm{F}_{12} & 2\mathrm{F}_{12}\mathrm{F}_{13} & 2\mathrm{F}_{13}\mathrm{F}_{11} \\ \mathrm{F}_{21}\mathrm{F}_{21} & \mathrm{F}_{22}\mathrm{F}_{22} & \mathrm{F}_{23}\mathrm{F}_{23} & 2\mathrm{F}_{21}\mathrm{F}_{22} & 2\mathrm{F}_{22}\mathrm{F}_{23} & 2\mathrm{F}_{23}\mathrm{F}_{21} \\ \mathrm{F}_{31}\mathrm{F}_{31} & \mathrm{F}_{32}\mathrm{F}_{32} & \mathrm{F}_{33}\mathrm{F}_{33} & 2\mathrm{F}_{31}\mathrm{F}_{32} & 2\mathrm{F}_{32}\mathrm{F}_{33} & 2\mathrm{F}_{33}\mathrm{F}_{31} \\ \mathrm{F}_{11}\mathrm{F}_{21} & \mathrm{F}_{12}\mathrm{F}_{22} & \mathrm{F}_{13}\mathrm{F}_{23} & \mathrm{F}_{11}\mathrm{F}_{22} + \mathrm{F}_{12}\mathrm{F}_{21} & \mathrm{F}_{12}\mathrm{F}_{23} + \mathrm{F}_{13}\mathrm{F}_{22} & \mathrm{F}_{13}\mathrm{F}_{21} + \mathrm{F}_{11}\mathrm{F}_{23} \\ \mathrm{F}_{21}\mathrm{F}_{31} & \mathrm{F}_{22}\mathrm{F}_{32} & \mathrm{F}_{23}\mathrm{F}_{33} & \mathrm{F}_{21}\mathrm{F}_{32} + \mathrm{F}_{22}\mathrm{F}_{31} & \mathrm{F}_{22}\mathrm{F}_{33} + \mathrm{F}_{23}\mathrm{F}_{32} & \mathrm{F}_{23}\mathrm{F}_{31} + \mathrm{F}_{21}\mathrm{F}_{33} \\ \mathrm{F}_{31}\mathrm{F}_{11} & \mathrm{F}_{32}\mathrm{F}_{12} & \mathrm{F}_{33}\mathrm{F}_{13} & \mathrm{F}_{31}\mathrm{F}_{12} + \mathrm{F}_{32}\mathrm{F}_{11} & \mathrm{F}_{32}\mathrm{F}_{13} + \mathrm{F}_{33}\mathrm{F}_{12} & \mathrm{F}_{33}\mathrm{F}_{11} + \mathrm{F}_{31}\mathrm{F}_{13} \end{bmatrix} . \tag{38}$$

For more detail see (Hartmann, 2003).

5 System of Units

Since no unit system is predefined in Abaqus, the user has to choose the appropriate units for the quantities in the computations and ensure them to be consistent. Tab. 2 shows the used system of units of this work and its equivalence in the international system of units SI.

Table 2: System of units used in the computations with Abaqus

Quantity	Dimension	Used Unit	SI	Conversion Factor
Length	$[\mathrm{L}]$	mm	m	10^3
Mass	$[\mathrm{M}]$	t	kg	10^{-3}
Time	$[\mathrm{T}]$	s	s	1
Temperature	$[\Theta]$	K	K	1
Density	$[\mathrm{M}][\mathrm{L}]^{-3}$	$\mathrm{t\,mm^{-3}}$	$\mathrm{kg\,m^{-3}}$	10^{-12}
Force	$[\mathrm{M}][\mathrm{L}][\mathrm{T}]^{-2}$	N	N	1
Stress	$[\mathrm{M}][\mathrm{L}]^{-1}[\mathrm{T}]^{-2}$	MPa	Pa	10^{-6}
Energy	$[\mathrm{M}][\mathrm{L}]^2[\mathrm{T}]^{-2}$	$\mathrm{t\,mm^2\,s^{-2}}$	J	10^3
Power	$[\mathrm{M}][\mathrm{L}]^2[\mathrm{T}]^{-3}$	$\mathrm{t\,mm^2\,s^{-3}}$	W	10^3
Heat Capacity	$[\mathrm{L}]^2[\mathrm{T}]^{-2}[\Theta]^{-1}$	$\mathrm{mm^2\,s^{-2}\,K^{-1}}$	$\mathrm{J\,kg^{-1}\,K^{-1}}$	10^6
Thermal Conductivity	$[\mathrm{M}][\mathrm{L}][\mathrm{T}]^{-3}[\Theta]^{-1}$	$\mathrm{t\,mm\,s^{-3}\,K^{-1}}$	$\mathrm{W\,m^{-2}\,K^{-1}}$	1

Glossary

DAE	Differential-algebraic equations system.
DIC	Digital image correlation.
DIRK	Diagonal implizit Runge-Kutta methods.
DSC	Differential scanning calorimetry.
EDX	Energy-dispersive X-ray spectroscopy.
FEM	Finite Element Method.
IBVP	Initial boundary value problem.
MLNA	Multilevel Newton Algorithm.
MOL	Method of vertical lines.
NRM	Newton-Raphson method.
SEM	Scanning electron microscope.
XRD	X-ray diffraction.

Scalars

$\mu_{\mathbf{ov}}$	Shear modulus of the overstress, finite strain model.
N_a	Shapefunctions of the node a.
n_e	Number of finite elements.
n_n	Number of Nodes.
A	Area.
a	Aging time.
α_a	Aging shrinkage coefficient.
α_k	Softening coefficient.
α_Θ	Thermal expansion coefficient.
β_a	Parameter of the aging development.
$\beta_{\mathbf{Y}}$	Function of the small strain model.
b	Parameter of the plastic equilibrium stress, small strain model.
c	Plastic equilibrium parameter of the small strain model.
c_α	Parameter of the plastic equilibrium part of the small strain model.
$c_{\mathbf{p}}$	Specific heat capacity.

d	Thickness.
e	Energy density.
E	Inertial energy.
s	Entropy.
ε	Strain.
$\dot{\varepsilon}$	Strain rate.
F	Force.
$f_{\mathbf{err}}$	Error estimation for linear elasticity.
G	Shear modulus.
γ	Shear strain.
$G_{\mathbf{eq}}$	Shear modulus of the elastic part of the equilibrium stress, finite strain model.
G_{ov}	Shear modulos of the overstress part of the small strain model.
H	Entropy supply of a system.
I_T	Area moment of inertia.
J	Determinant of the deformation gradient.
$J_{\mathbf{M}}$	Determinant of the mechanical deformation gradient.
k	Softening variable.
K	Kinetic energy.
κ_Θ	Thermal conductivity.
$K_{\mathbf{eq}}$	Bulk modulus of the elastic part of the equilibrium stress, finite strain model.
L	Length.
L_e	Mechanical power of external forces.
λ	Axial strech.
$\hat{\lambda}$	Thermal diffusivity.
m	Mass of a body.
M_T	Torque.
$\mu_{\mathbf{eq}}$	Elasticity parameter of the finite strain model.
n_d	Number of identification points.
$n_{\mathbf{exp}}$	Number of experiments.
n_κ	Number of material parameters.
ω	Production term.
ϕ	Rotation angle.
φ_a	Function of the shrinkage, finite strain model.
φ_Θ	Function of the thermal expansion, finite strain model.
ψ	Helmholu free energy.
ψ_a	Aging part of the free energy.
$\psi^{\mathbf{e}}_{\mathbf{eq}}$	Equilibrium part of the free energy.
$\psi_{\mathbf{ov}}$	Overstress part of the free energy.
$\psi^{\mathbf{h}}_{\mathbf{eq}}$	Plastic part of the free energy.
ψ_Θ	Thermal part of the free energy.
q	Scalar heat flux in the current configuration.

Q	Thermal energy.
R	Universal gas constant.
R^2	Coefficient of determination.
ρ	Density in the current configuration.
$\rho_{\mathbf{R}}$	Density in the reference configuration.
s_d	Standard deviation.
S	Entropy of a body.
σ	Axial stress.
$s_{\mathbf{M}}$	Arc-length of the deviatoric mechanical strain.
t	Time.
τ	Shear stress.
$\tau_{\mathbf{eq}}$	Shear equilibrium stress.
$\tau_{\mathbf{ov}}$	Shear overstress.
Θ	Temperature of a body.
U	Energy function.
V	Volume.
$\mathrm{d}v$	Volume element in the current configuration.
$\mathrm{d}V$	Volume element in the reference configuration.
(x_1, x_2, x_3)	Current coordinate triplet.
(X_1, X_2, X_3)	Reference coordinate triplet.

Tensors

$\mathbf{A}$	Almansi strain tensor.
$\mathbf{B}$	Left Cauchy-Green tensors.
$\mathbf{B_e}$	Kinematik left Cauchy-Green tensor.
$\mathbf{B_k}$	Elastic left Cauchy-Green tensor.
$\mathbf{C}$	Right Cauchy-Green tensors.
$\bar{\mathbf{C}}$	Unimodular Cauchy-Green tensor.
$\mathbf{C_e}$	Elastic right Cauchy-Green tensor.
$\bar{\mathbf{C}}_{\mathbf{p}}$	Plastic right Cauchy-Green tensor.
$\mathbf{C_k}$	Kinematik right Cauchy-Green tensor.
$\bar{\mathbf{C}}_{\mathbf{v}}$	Viscous right Cauchy-Green tensor.
$\mathbf{C}_{\mathrm{M}}$	Mechanical right Cauchy-Green tensor.
$\mathbf{D}$	Strain rate tensor.
$\mathbf{D_p}$	Plastic strain-rate tensor.
$\mathbf{D_v}$	Viscous strain-rate tensor.
$\mathbf{E}$	Green strain tensor.
$\mathbf{E}_a$	Aging component of the total strain $\mathbf{E}$.
$\mathbf{E_e}$	Elastic part of the mechanical strain $\mathbf{E}_{\mathrm{M}}$.

$\mathbf{E}_{\ln}$	True strain tensor.
$\mathbf{E}_{\mathbf{M}}$	Mechanical part of the total strain $\mathbf{E}$.
$\mathbf{E}_{\mathbf{k}}$	Kinematik part of the mechanical strain.
$\mathbf{E}_{\mathbf{p}}$	Plastic part of the mechanical strain.
$\mathbf{E}_{\Theta}$	Thermal part of the total strain $\mathbf{E}$.
$\mathbf{E}_{\mathbf{v}}$	Viscous part of the mechanical strain $\mathbf{E}_{\mathrm{M}}$.
$\boldsymbol{\varepsilon}_{\mathbf{M}}$	Mechanical part of the strain tensor relative to the elastic intermediate configuration $\check{\boldsymbol{\chi}}_t$.
$\boldsymbol{\varepsilon}_{\mathbf{e}}$	Elastic part of the mechanical strain tensor in the thermal intermediate configuration $\check{\boldsymbol{\chi}}_t$.
$\boldsymbol{\varepsilon}_{\mathbf{v}}$	Viscous part of the mechanical strain tensor in the elastic intermediate configuration $\check{\boldsymbol{\chi}}_t$.
$\tilde{\boldsymbol{\varepsilon}}_{\mathbf{M}}$	Mechanical part of the strain tensor in the plastic intermediate configuration $\tilde{\boldsymbol{\chi}}_t$.
$\tilde{\boldsymbol{\varepsilon}}_{\mathbf{k}}$	Kinematic hardening part of the mechanical strain tensor in the plastic intermediate configuration $\tilde{\boldsymbol{\chi}}_t$.
$\tilde{\boldsymbol{\varepsilon}}_{\mathbf{p}}$	Plastic part of the mechanical strain tensor in the plastic intermediate configuration $\tilde{\boldsymbol{\chi}}_t$.
$\mathbf{F}_a$	Aging component of the deformation gradient.
$\mathbf{F}_{\mathbf{e}}$	Elastic component of the deformation gradient.
$\mathbf{F}_{\mathbf{M}}$	Mechanical component of the deformation gradient.
$\bar{\mathbf{F}}_{\mathbf{M}}$	Isochoric part of the mechanical deformation gradient.
$\mathbf{F}_{\mathbf{k}}$	Kinematic hardening part of the mechanical deformation gradient.
$\bar{\mathbf{F}}_{\mathbf{p}}$	Plastic part of the mechanical deformation gradient.
$\bar{\mathbf{F}}_{\mathbf{v}}$	Viscous part of the mechanical deformation gradient.
$\hat{\mathbf{F}}_{\mathbf{M}}$	Volumetric part of the mechanical deformation gradient.
$\mathbf{F}_{\Theta}$	Thermal component of the deformation gradient.
$\boldsymbol{\Gamma}_{\mathbf{M}}$	Mechanical strain tensor in the mechanical intermediate configuration $\hat{\boldsymbol{\chi}}_t$.
$\boldsymbol{\Gamma}_{\Theta}$	Thermal strain tensor in the mechanical intermediate configuration $\hat{\boldsymbol{\chi}}_t$.
$\boldsymbol{\gamma}_a$	Aging component in the thermal intermediate configuration $\check{\boldsymbol{\chi}}_t$.
$\mathbf{H}$	Displacement gradient.
$\mathbf{I}$	Unit tensor.
$\boldsymbol{\kappa}_{\Theta}^{\mathbf{R}}$	Thermal conductivity tensor.
$\mathbf{L}$	Spatial velocity gradient.
$\mathbf{L}_{\mathbf{M}}$	Mechanical part of the spatial velocity gradient.
$\mathbf{L}_{\mathbf{p}}$	Plastic spacial velocity gradient.
$\mathbf{L}_{\Theta}$	Thermal part of the spatial velocity gradient.
$\mathbf{L}_{\mathbf{v}}$	Viscous spacial velocity gradient.
$\mathbf{R}$	Rotation tensor.
$\mathbf{S}$	Kirchhoff stress tensor.
$\check{\mathbf{S}}$	Stress tensor relative to the viscous configuration $\check{\boldsymbol{\chi}}_t$.
$\check{\mathbf{S}}_{\mathbf{ov}}$	Overstress part of the stress tensor relative to the viscous configuration $\check{\boldsymbol{\chi}}_t$.

$\mathbf{S}^{\mathbf{e}}_{\mathbf{iso}}$	Isochoric part of the elastic equilibrium stress.
$\mathbf{S}^{\mathbf{e}}_{\mathbf{vol}}$	Volumetric part of the elastic equilibrium stress.
$\breve{\mathbf{S}}$	Stress tensor in the thermal intermediate configuration $\breve{\chi}_t$.
$\mathbf{S}_{\mathbf{M}}$	Stress tensor relative to the mechanical configuration $\hat{\chi}_t$.
$\mathbf{S}^{\mathbf{e}}_{\mathbf{Meq}}$	Elastic part of the stress tensor relative to the mechanical configuration $\hat{\chi}_t$.
$\mathbf{S}^{\mathbf{h}}_{\mathbf{Meq}}$	Plastic part of the stress tensor relative to the mechanical configuration $\hat{\chi}_t$.
$\mathbf{S}_{\mathbf{Mov}}$	Overstress part of the stress tensor relative to the mechanical configuration $\hat{\chi}_t$.
$\tilde{\mathbf{S}}$	Stress tensor relative to the plastic configuration $\tilde{\chi}_t$.
$\tilde{\mathbf{S}}^{\mathbf{h}}_{\mathbf{eq}}$	Plastic part of the stress tensor relative to the plastic configuration $\tilde{\chi}_t$.
$\mathbf{T}$	Cauchy (true) stress tensor.
$\mathbf{T}_{\mathbf{eq}}$	Equilibrium part of the total stress $\mathbf{T}$.
$\mathbf{T}^{\mathbf{e}}_{\mathbf{eq}}$	Elastic part of the equilibrium stress $\mathbf{T}_{\text{eq}}$.
$\tilde{\mathbf{T}}^{\mathbf{e}}_{\mathbf{iso}}$	Isochoric part of the elastic equilibrium stress.
$\tilde{\mathbf{T}}^{\mathbf{e}}_{\mathbf{vol}}$	Volumetric part of the elastic equilibrium stress.
$\mathbf{T}^{\mathbf{h}}_{\mathbf{eq}}$	Plastic (hysteretic) part of the equilibrium stress $\mathbf{T}_{\text{eq}}$.
$\mathbf{T}_{\mathbf{ov}}$	Overstress part of the total stress $\mathbf{T}$.
$\mathbf{T}_{\mathbf{R}}$	First Piola-Kirchhoff stress tensor.
$\tilde{\mathbf{T}}$	Second Piola-Kirchhoff stress tensor.
$\tilde{\mathbf{T}}_{\mathbf{eq}}$	Equilibrium stress part of $\tilde{\mathbf{T}}$.
$\tilde{\mathbf{T}}^{\mathbf{e}}_{\mathbf{eq}}$	Elastic stress part of the equilibrium stress $\tilde{\mathbf{T}}_{\text{eq}}$.
$\tilde{\mathbf{T}}^{\mathbf{h}}_{\mathbf{eq}}$	Plastic stress part of the equilibrium stress $\tilde{\mathbf{T}}_{\text{eq}}$.
$\tilde{\mathbf{T}}_{\mathbf{ov}}$	Overstress part of $\tilde{\mathbf{T}}$.
$\mathbf{U}$	Right stretch tensor.
$\mathbf{V}$	Left stretch tensor.
$\mathbf{W}$	Spin or vorticity tensor.
$\mathbf{X}$	Back stress tensor.
$\mathbf{Y}$	Strain like variable.

Vectors

$\vec{c}$	Material line in the current configuration.
$\vec{C}$	Material line in the reference configuration.
$\mathrm{d}\vec{a}$	Surface element in the current configuration.
$\mathrm{d}\vec{A}$	Surface element in the reference configuration.
$\vec{D}_{\vec{c}}$	Angular momentum of a body with respect to the point $\vec{c}$.
$\mathrm{d}\vec{f}$	Infinitesimal force vector.
$\mathrm{d}\vec{x}$	Material line element in the current configuration.
$\mathrm{d}\vec{X}$	Material line element in the reference configuration.

$\vec{e}_i$	Unit vector in the current configuration.
$\vec{E}_i$	Unit vector in the reference configuration.
$\vec{I}$	Linear Momentum of a body.
$\vec{n}$	Normal vector of the surface $\mathrm{d}a$ in the current configuration.
$\vec{n}_i$	Eigenvectors.
$\vec{n}_{\mathbf{R}}$	Normal vector of the surface $\mathrm{d}A$ in the reference configuration.
$\vec{q}$	Cauchy (true) heat flux.
$\vec{q}_{\mathbf{R}}$	Piola-Kirchhoff heat flux.
$\vec{t}$	Stress vector.
$\vec{t}_{\mathbf{R}}$	Piola-Kirchhoff stress vector.
$\vec{u}$	Displacement vector of a material point.
$\vec{x}$	Position vector in the current configuration.
$\vec{X}$	Position vector in the reference configuration.

Matrices

$\mathbf{B}^{\mathbf{e}}_{u}$	Strain-displacement matrix on element level with respect to the current configuration.
$\mathbf{B}^{\mathbf{e}}_{\mathbf{u}a}$	Strain-displacement matrix on element level for the node a with respect to the current configuration.
$\mathbf{B}^{\mathbf{e}}_{\Theta a}$	Temperature gradient matrix on element level for the node a with respect to the current configuration.
$\mathbf{B}^{\mathbf{e}}_{\Theta}$	Temperature gradient matrix on element level with respect to the current configuration.
$\tilde{\mathbf{B}}^{\mathbf{e}}_{u}$	Strain-displacement matrix on element level with respect to the reference configuration.
$\tilde{\mathbf{B}}^{\mathbf{e}}_{\Theta}$	Temperature gradient matrix on element level with respect to the reference configuration.
$\boldsymbol{C}_{\kappa}$	Thermal conductivity matrix.
$\bar{\boldsymbol{C}}_{\kappa}$	Thermal conductivity matrix.
$\boldsymbol{C}_{\mathbf{p}}$	Heat capacity matrix.
$\bar{\boldsymbol{C}}_{\mathbf{p}}$	Heat capacity matrix.
$\delta\mathbf{E}$	Virtual strain tensor in matrix notation.
$\mathbf{d}$	Simulation data.
$\mathbf{F}^{\mathbf{e}}_{\mathbf{23}}$	Push-forward operator in matrix notation.
$\boldsymbol{g}_{u}$	Discretized principle of virtual displacements with respect to the current configuration.
$\tilde{\boldsymbol{g}}_{u}$	Discretized principle of virtual displacements with respect to the reference configuration.
$\mathbf{J}$	Jacobian.

$\boldsymbol{\kappa}$	Vector of material parametes.
$\boldsymbol{\kappa}^{\mathbf{conf}}$	Confidence interval.
$\boldsymbol{\kappa}^{*}$	Vector of identified material parametes.
$\boldsymbol{L}_{\mathbf{q}}$	Nonlinear equation system (differential part of DAE-system).
$\mathbf{P}$	Covariance matrix.
$\boldsymbol{G}_{\Theta}$	Nonlinear equation system (thermal part of DAE-system).
$\boldsymbol{G}_{u}$	Nonlinear equation system (mechanical part of DAE-system).
$\boldsymbol{p}_{\Theta}^{\mathrm{S}}$	Heat flux over the surface.
$\overline{\boldsymbol{p}}_{\Theta}$	Prescribed temperatures.
$\boldsymbol{p}_{\Theta}^{\mathrm{V}}$	Volumetric heat source.
$\mathbf{q}$	Internal variables at the gauss point.
$\boldsymbol{q}$	Internal variables of the whole mesh.
$\boldsymbol{r}_{\mathbf{q}}$	Right side of the semi-discretized system for the internal variables.
$\boldsymbol{r}_{\Theta}$	Right side of the semi-discretized heat equation.
$\mathbf{R}$	Correlation matrix.
$\mathbf{r}$	Residual function.
$\mathbf{s}$	Simulation data.
$\boldsymbol{\Theta}$	Unknown nodal displacements.
$\boldsymbol{\Theta}_{\mathbf{a}}$	Nodal displacements of the complete mesh.
$\overline{\boldsymbol{\Theta}}$	Prescribed nodal displacements.
$\tilde{\mathbf{T}}$	Second Piola-Kirchhoff tensor in matrix notation.
$\boldsymbol{u}$	Unknown nodal displacements.
$\boldsymbol{u}_{\mathbf{a}}^{\mathrm{T}}$	Nodal displacements of the complete mesh.
$\mathbf{u}^{e}$	Displacements of an element.
$\boldsymbol{u}^{\mathbf{h}}$	Displacements of a discretized body.
$\overline{\boldsymbol{u}}$	Prescribed nodal displacements.
$\boldsymbol{\xi}$	Local coordinates.
$\boldsymbol{\xi}_{l}$	Spatial integration points.
$\boldsymbol{Z}_{\Theta}^{\mathbf{e}}$	Incidence matrix for the unknown nodal temperatures.
$\overline{\boldsymbol{Z}}_{\Theta}^{\mathbf{e}}$	Incidence matrix for the prescribed nodal displacements.
$\boldsymbol{Z}_{u}^{\mathbf{e}}$	Incidence matrix for the unknown nodal displacements.
$\overline{\boldsymbol{Z}}_{u}^{\mathbf{e}}$	Incidence matrix for the prescribed nodal displacements.

Miscellaneous

$\mathcal{B}$	Material body.
$\mathcal{B}^{\mathbf{h}}$	Discretized material body.
χ_t	Current configuration.
$\check{\chi}_t$	Viscous intermediate configuration.
$\bar{\chi}_t$	Isochore intermediate configuration.

$\hat{\boldsymbol{\chi}}_t$	Mechanical intermediate configuration.
$\check{\boldsymbol{\chi}}_t$	Thermal intermediate configuration.
$\tilde{\boldsymbol{\chi}}_t$	Plastic intermediate configuration.
π_Θ	Weak form of the heat conduction.
π_u	Weak form of the balance of linear momentum.
$\mathbb{E}^3$	Three-dimensional euclidean point space.
o	Origin of a coordinate system in the current configuration.
O	Origin of a coordinate system in the reference configuration.
$\mathcal{P}$	Set of material points.
$\mathcal{R}$	Reference configuration.
$\mathbb{R}^3$	Three-dimensional euclidean space.
$\mathbb{V}^3$	Three-dimensional euclidean vector space.

Mathematical operators

$\mathbf{A}^{\mathbf{D}}$	Deviator of a tensor.
$\mathbf{A}^{\mathbf{T}}$	Transpose of a tensor.
div	Divergence operator with respect to the spatial coordinates.
Div	Divergence operator with respect to the material coordinates.
$\dot{\mathbf{A}}$	Material time derivative.
$\otimes$	Dyadic product.
$\dfrac{\partial y}{\partial x}$	Partial derivative of y with respect to x.
$\dfrac{\mathrm{d}y}{\mathrm{d}x}$	Total derivative of y with respect to x.
$f'(x)$	Derivative of f with respect to x.
grad	Gradient operator with respect to the spatial coordinates.
Grad	Gradient operator with respect to the material coordinates.
$\overset{\triangle}{\mathbf{A}}$	Oldroyd derivative.
$\cdot$	Scalar product.
tr	Trace operator.

Bibliography

ABAQUS (2019). *ABAQUS Theory Guide*, v.6.14 edition.

AIAA (1998). Guide for the verification and validation of computational fluid dynamics simulations (aiaa g-077-1998(2002)). Technical report, American Institute of Aeronautics and Astronautics.

Altenbach, H. (2015). *Kontinuumsmechanik – Einführung in die materialunabhängigen und materialabhängigen Gleichungen*. Springer-Verlag, Berlin Heidelberg, 3st edition.

Altenbach, J. and Altenbach, H. (1994). *Einführung in die Kontinuumsmechanik*. Teubner Verlag, Stuttgart, 1st edition.

Armstrong, P. J. and Frederick, C. O. (1966). A mathematical representation of the multiaxial Bauschinger effect. Technical Report General Electricity Generating Board, Report No.: RD/B/N731, Berceley Nuclear Laboratories.

Babuska, I. and Oden, J. T. (2004). Verification and validation in computational engineering and science: basic concepts. *Computer Methods in Applied Mechanics and Engineering*, 193:4057–4066.

Bathe, K.-J. (1996). *Finite Element Procedures*. Prentice Hall, New Jersey.

Bazant, Z. P. and Huet, C. (1999). Thermodynamic functions for ageing viscoelasicity: integral form wihout internal variables. *International Journal of Solids and Structures*, 36:3993–4016.

Beck, J. V. and Arnold, K. J. (1977). *Parameter estimation in engineering and science*. John Wiley & Sons, New York.

Becker, E. B., Carey, G. F., and Oden, J. T. (1981). *Finite Elements: An Introduction, Volume 1*. Prentice Hall, New Jersey.

Becker, W. and Bürger, W. (1975). *Kontinuumsmechanik*. Teubner Verlag, Stuttgart.

Belytschko, T., Liu, W. K., and Moran, B. (2000). *Nonlinear Finite Elements for Continua and Structures*. John Wiley and Sons, Chichester.

Bertram, A. (2003). Finite thermoplasticity based on isomorphisms. *International Journal of Plasticity*, 19(11):2027 – 2050.

Bier, W. and Hartmann, S. (2006). A finite strain constitutive model for metal powder compaction using a unique and convex single surface yield function. *European Journal of Mechanics, Series A/Solids*, 25:1009–1030.

Birken, P., Quint, K. J., Hartmann, S., and Meister, A. (2010). A time-adaptive fluid-structure interaction method for thermal coupling. *Computing and Visualization in Science*, 13:331–340.

Brünig, M. and Gerke, S. (2011). Simulation of damage evolution in ductile metals undergoing dynamic loading conditions. *International Journal of Plasticity*, 27:1598–1617.

Buffiere, J.-Y., Savelli, S., Jouneau, P., Maire, E., and Fougeres, R. (2001). Experimental study of porosity and its relation to fatigue mechanisms of model Al-Si7-Mg0.3 cast Al alloys. *Material Science and Engineering*, 316:115–126.

Callister, W. D. and Rethwisch, D. (2016). *Fundamentals of materials science and engineering*. Wiley.

Cao, L., Liao, D., Sun, F., Chen, T., Teng, Z., and Tang, Y. (2018). Prediction of gas entrapment defects during zinc alloy high-pressure die casting based on gas-liquid multiphase flow model. *The International Journal of Advanced Manufacturing Technology*, 94(1):807–815.

Carol, I. and Bazant, Z. (1993). Viscoplasticity with aging caused by solidification of nonaging constituent. *Journal of Engineering Mechanics*, 119:2252–2269.

Cerri, E. and Leo, P. (2005). Influence of severe plastic deformation on aging of Al–Mg–Si alloys. *Materials Science and Engineering: A*, 410-411:226 – 229. The Langdon Symposium: Flow and forming of Crystalline Materials.

Chaboche, J. (2008). A review of some plasticity and viscoplasticity constitutive theories. *International Journal of Plasticity*, 24(10):1642 – 1693. Special Issue in Honor of Jean-Louis Chaboche.

Chaboche, J. L. (1989). Constitutive equations for cyclic plasticity and cyclic viscoplasticity. *International Journal of Plasticity*, 5:247–302.

Chaparro, B., Thuillier, S., Menezes, L., Manach, P., and Fernandes, J. (2008). Material parameters identification: Gradient-based, genetic and hybrid optimization algorithms. *Computational Materials Science*, 44:339–346.

Chen, Z. and Diebels, S. (2012a). Modelling and parameter re-identification of nanoindentation of soft polymers taking into account effects of surface roughness. *Computers and Mathematics with Applications*, 64(9):2775 – 2786.

Chen, Z. and Diebels, S. (2012b). Nanoindentation of hyperelastic polymer layers at finite deformation and parameter re-identification. *Archive of Applied Mechanics*, 82(8):1041–1056.

Chen, Z. and Diebels, S. (2014). Nanoindentation of soft polymers: modeling, experiments and parameter identification. *Technische Mechanik*, 34(3-4):166–189.

Chen, Z. and Diebels, S. (2015). Indentation of PU at different scales and computational modeling: identification of viscoelasticity and quantification of adhesion effects. *Archive of Applied Mechanics*, 85(9):1225–1243.

Coleman, B. and Noll, W. (1963). The thermodynamics of elastic materials with heat conduction and viscosity. *Archive for Rational Mechanics and Analysis*, 13:167 –178.

Coleman, T. and Li, Y. (1996). An interior trust region approach for nonlinear minimization subject to bounds. *SIAM Journal on Optimization*, 6:418–445.

Cowan, R. D. (1963). Pulse method of measuring thermal diffusivity at high temperatures. *Journal of Applied Physics*, 34:926.

Dennis, J. E. and Schnabel, R. B. (1996). *Numerical methods for unconstrained optimization and nonlinear equations*. SIAM, Philadelphia.

Deschamps, A., Livet, F., and Bréchet, Y. (1998). Influence of predeformation on ageing in an Al–Zn–Mg alloy—I. microstructure evolution and mechanical properties. *Acta Materialia*, 47(1):281 – 292.

Deulhard, P. and Bornemann, F. A. (2008). *Numerische Mathematik II: Gewönliche Differentialgleichungen*. de Gruyter, Berlin.

Dhatt, G. and Touzot, G. (1985). *The finite element method displayed*. Wiley and Sons, Chichester.

Diebels, S., Ellsiepen, P., and Ehlers, W. (1999). Error-controlled Runge-Kutta time integration of a viscoplastic hybrid two-phase model. *Technische Mechanik*, 19:19–27.

Diebels, S. and Geringer, A. (2012). Modelling inhomogeneous mechanical properties in adhesive bonds. *The Journal of Adhesion*, 88(11-12):924–940.

Diebels, S., Johlitz, M., Steeb, H., Chatzouridou, A., Batal, J., and Possart, W. (2007). A continuum-based model capturing size effects in polymer bonds. *Journal of Physics: Conference Series*, 62:34–42.

Diebels, S. and Steeb, H. (2002). The size effect in foams and its theoretical and numerical investigation. *Proceedings of the Royal Society of London. Series A: Mathematical, Physical and Engineering Sciences*, 458.

Diebels, S., Steeb, H., and Possart, W. (2005). Effects of the interphase on the mechanical behaviour of thin adhesive films-a modeling approach. in adhesion-current research and applications. *Adhesion-Current Research and Applications*, pages 319–335.

DIN EN 1774 (1997). Zink und zinklegierungen – gußlegierungen – in blockform und in flüssiger form. Norm.

Dippel, B., Johlitz, M., and Lion, A. (2014). Ageing of polymer bonds: a coupled chemomechanical modelling approach. *Continuum Mechanics and Thermodynamics*, 26:247–257.

Draper, N. R. and Smith, H. (1998). *Applied regression analysis*. John Wiley & Sons, New-York, 3. edition.

Egner, H. and Egner, W. (2014). Modeling of a tempered martensitic hot work tool steel behavior in the presence of thermo-viscoplastic coupling. *International Journal of Plasticity*, 57:77–91.

Ellsiepen, P. and Hartmann, S. (2001). Remarks on the interpretation of current non-linear finite-element-analyses as differential-algebraic equations. *International Journal for Numerical Methods in Engineering*, 51:679–707.

Flory, P. J. (1961). Thermodynamic relations for high elastic materials. *Transaction of the Faraday Society*, 57:829–838.

Fox, N. (1968). On the continuum theories of dislocations and plasticity. *The Quarterly Journal of Mechanics and Applied Mathematics*, 21(1):67–75.

Fritzen, P. (1997a). *Numerische Behandlung nichtlinearer Probleme der Elastizitäts- und Plastizitätstheorie*. Doctoral thesis, Department of Mathematics, University of Darmstadt.

Fritzen, P. (1997b). *Numerische Behandlung nichtlinearer Probleme der Elastizitäts- und Plastizitätstheorie*. PhD thesis, Technische Universität Darmstadt.

Führ, L., Ludwig, G. A., Martins, M., Vecchia, F., Rieder, E., Malfatti, C., and Oliveira, C. (2014). Effects of mould temperature in squeeze casting of zamak 5. In *20th Brazilian Conference on Materials Science and Engineering*, volume 775 of *Materials Science Forum*, pages 729–732. Trans Tech Publications.

Gebhard, E. (1940). Die Zinkecke des Dreistoffsystems Zink-Aluminium-Kupfer. *Zeitschrift für Metallkunde*, 32(4):78–85.

Gebhard, E. (1941). Über den β-Zerfall in aluminiumhaltigen Zinklegierungen und den Einfluss kleiner Beimengungen auf die Zerfallsgeschwindigkeit. *Zeitschrift für Metallkunde*, 33(8/9):328–332.

Gebhard, E. (1942). Über den Aufbau und die Volumenänderung der Zink-Kupfer-Aluminium-Legierungen. *Zeitschrift für Metallkunde*, 34(9):208–215.

Gelfi, M., Bontempi, E., Pola, A., Roberti, R., Rollez, D., and Depero, L. E. (2004). Microstructural and mechanical properties of zinc die casting. *Advanced Engineering Materials*, 6:818–822.

Gilbert, R., Hartmann, S., Kudela, L., Rank, E., Sahar, G., Yosibash, Z., and Yossef, O. (2016). Parameter identification of the passive response in arteries. *Technical Report Series Fac3-16-01, Faculty of Mathematics/Computer Science and Mechanical Engineering, Clausthal University of Technology (Germany).*

GOM (2011). *Aramis – User Manual: The basics of strain*. GOM – Gesellschaft für optische Messtechnik, Braunschweig, Germany.

Grafenhorst, M. (2018). *Zeitadaptive Finite-Elemente-Berechnungen thermomechanisch gekoppelter Problemstellungen sowie Mortarkontakt*. Phd-thesis, report no. 2/2018, Institute of Applied Mechanics, Clausthal University of Technology, Clausthal-Zellerfeld.

Griewank, A. and Walther, A. (2008). *Evaluating Derivatives: Principles and Techniques of Algorithmic Differentiation*. SIAM Society for Industrial and Applied Mathematics, Philadelphia.

Großmann, C. and Roos, H. (2005). *Numerische Behandlung partieller Differentialgleichungen*. Teubner Verlag, Stuttgart.

Gutman, E., Unigovski, Y., Levkovitch, M., and Koren, Z. (1998). Influence of porosity and casting conditions on creep of die-cast Mg alloy. *Journal of Materials Science Letters*, 17:1787–1789.

Hairer, E. and Wanner, G. (1996). *Solving ordinary differential equations II: Stiff and differential-algebraic problems*. Springer Verlag, Berlin, 2. edition.

Hairer, E., Wanner, G., and Lubich, C. (2002). *Geometric Numerical Integration: Structure-Preserving Algorithms for Ordinary Differential Equations*. Springer, Berlin.

Hamkar, A.-W. (2013). *Eine iterationsfreie Finite-Elemente Methode im Rahmen der finiten Thermoviskoelastizität*. Phd-thesis, report no. 1/2013, Institute of Applied Mechanics, Clausthal University of Technology, Clausthal-Zellerfeld.

Hamkar, A.-W., Hartmann, S., and Rang, J. (2012). A stiffly accurate Rosenbrock-type method of order 2 applied to FE-analyses in finite strain viscoelasticity. *Applied Numerical Mathematics*, 62(12):1837 – 1848.

Hänsel, G. (1988). Zinklegierungen; Zusammensetzung und Eigenschaften. *Metall*, 42(9):871–874.

Hartmann, S. (1999). A time-adaptive FE-analysis of inelastic structures. In Wunderlich, W., editor, *ECCM '99 European Conference on Computational Mechanics*, pages on CD–ROM, Munich. ECCM.

Hartmann, S. (2002). Computation in finite strain viscoelasticity: finite elements based on the interpretation as differential-algebraic equations. *Computer Methods in Applied Mechanics and Engineering*, 191(13-14):1439–1470.

Hartmann, S. (2003). *Finite-Elemente Berechnung inelastischer Kontinua. Interpretation als Algebro-Differentialgleichungssysteme*. Habilitation, University of Kassel, Institute of Mechanics. Report No. 1/2003.

Hartmann, S. (2005). A remark on the application of the Newton-Raphson method in non-linear finite element analysis. *Computational Mechanics*, 36(2):100–116.

Hartmann, S. (2006). A thermomechanically consistent constitutive model for polyoxymethylene: experiments, material modeling and computation. *Archive of Applied Mechanics*, 76:349–366.

Hartmann, S. (2012). Comparison of the multiplicative decompositions $\mathbf{F} = \mathbf{F}_\Theta \mathbf{F}_m$ and $\mathbf{F} = \mathbf{F}_m \mathbf{F}_\Theta$ in finite strain thermo-elasticity. Technical Report Series Fac3-12-01, Faculty of Mathematics/Computer Sciences and Mechanical Engineering, Clausthal University of Technology (Germany).

Hartmann, S. (2015). *Technische Mechanik*. Wiley-VCH Verlag.

Hartmann, S. and Bier, W. (2008). High-order time integration applied to metal powder plasticity. *International Journal of Plasticity*, 24(1):17–54.

Hartmann, S., Gibmeier, J., and Scholtes, B. (2006). Experiments and material parameter identification using finite elements. uniaxial tests and validation using instrumented indentation tests. *Experimental Mechanics*, 46(1):5–18.

Hartmann, S. and Gilbert, R. (2018). Identifiability of material parameters in solid mechanics. *Archive of Applied Mechanics*, 88:3–26.

Hartmann, S., Gilbert, R. R., and Sguazzo, C. (2018). Basic studies in biaxial tensile tests. *GAMM-Mitteilungen*, 41(1):e201800004.

Hartmann, S. and Hamkar, A.-W. (2010). Rosenbrock-type methods applied to finite element computations within finite strain viscoelasticity. *Computer Methods in Applied Mechanics and Engineering*, 199(23-24):1455–1470.

Hartmann, S., Haupt, P., and Tschöpe, T. (2001). Parameter identification with a direct search method using finite elements. In Besdo, D., Schuster, R., and Ihlemann, J., editors, *Constitutive Models of Rubber II*, pages 249–256, Lisse. Balkema.

Hartmann, S., Kuhl, D., and Quint, K. J. (2009). Time-adaptive computation of thermoviscoplastic structures. In Steinhoff, K., Maier, H. J., and Biermann, D., editors, *Functionally graded materials in industrial mass production*, chapter 3.1, pages 269 – 282. Verlag Wissenschaftliche Scripten, Auerbach (Germany).

Hartmann, S. and Neff, P. (2003). Polyconvexity of generalized polynomial-type hyperelastic strain energy functions for near-incompressibility. *International Journal of Solids and Structures*, 40(11):2767–2791.

Hartmann, S., Quint, K. J., and Arnold, M. (2008a). On plastic incompressibility within time-adaptive finite elements combined with projection techniques. *Computer Methods in Applied Mechanics and Engineering*, 198:178–193.

Hartmann, S., Quint, K. J., and Hamkar, A.-W. (2008b). Displacement control in time-adaptive non-linear finite-element analysis. *ZAMM Journal of Applied Mathematics and Mechanics*, 88(5):342–364.

Hartmann, S. and Rothe, S. (2013). A rigorous application of the method of vertical lines to coupled systems in finite element analysis. In Ansorge, R., Bijl, H., Meister, A., and Sonar, T., editors, *Recent Developments in the Numerics of Nonlinear Hyperbolic Conservation Laws*, volume 120 of *Notes on Numerical Fluid Mechanics and Multidisciplinary Design*, pages 161–175. Springer Berlin / Heidelberg.

Hartmann, S., Tschöpe, T., Schreiber, L., and Haupt, P. (2003). Large deformations of a carbon black-filled rubber. Experiment, optical measurement and parameter identification using finite elements. *European Journal of Mechanics, Series A/Solids*, 22:309–324.

Haupt, P. (2002). *Continuum Mechanics and Theory of Materials*. Springer Verlag, Berlin, 2nd edition.

Haupt, P. and Korzen, M. (1989). On the mathematical modelling of material behavior in continuum mechanics. In Jinghong, F. and Murakami, S., editors, *Advances in Constitutive Laws for Engineering Materials*, pages 456–459.

Haupt, P. and Lion, A. (1995). Experimental identification and mathematical modelling of viscoplastic material behavior. *Journal of Continuum Mechanics and Thermodynamics*, 7:73–96.

Haupt, P. and Sedlan, K. (2001). Viscoplasticity of elastomeric materials: experimental facts and constitutive modelling. *Archive of Applied Mechanics*, 71:89–109.

Haupt, P. and Tsakmakis, C. (1989). On the application of dual variables in continuum mechanics. *Journal of Continuum Mechanics and Thermodynamics*, 1:165–196.

Haupt, P. and Tsakmakis, C. (1996). Stress tensors associated with deformation tensors via duality. *Archive of Mechanics*, 48:347–384.

Heimes, T. (2005). *Finite Thermoinelastizität*. Number 709 in Fortschrittsberichte, Reihe 5, Grund- und Werkstoffe/Kunststoffe. VDI-Verlag, Düsseldorf.

Holzapfel, G. A. (2000). *Nonlinear Solid Mechanics*. Wiley & Sons, Chichester.

Hoyer, W. and Schmidt, J. W. (1984). Newton-type decomposition methods for equations arising in network analysis. *ZAMM Zeitschrift für Angewandte Mathematik und Mechanik*, 64:397–405.

Hughes, T. J. and Hulbert, G. M. (1988). Space-time finite element methods for elastodynamics: Formulations and error estimates. *Computer Methods in Applied Mechanics and Engineering*, 66(3):339 – 363.

Hughes, T. J. R. (2000). *The Finite Element Method: Linear Static and Dynamic Finite Element Analysis*. Dover Publications, Mineola.

Hulbert, G. M. and Hughes, T. J. (1990). Space-time finite element methods for second-order hyperbolic equations. *Computer Methods in Applied Mechanics and Engineering*, 84(3):327 – 348.

Hyde, C. J., Sun, W., and Leen, S, B. (2010). Cyclic thermo-mechanical material modelling and testing of 316 stainless steel. *International Journal of Pressure Vessels and Piping*, 87:365–372.

ILZG (2019). International Lead and Zinc Study Group `www.ilzsg.org`.

IZ (2019). Initiative Zink `www.initiative-zink.de`.

IZA (2018). Zinc die casting alloys – mechanical properties. The International Zinc Association `www.zinc.org`.

Jansohn, W. (1997). Formulierung und Integration von Stoffgesetzen zur Berechnung großer Deformationen in der Thermoplastizität und -viskoplastizität. Technical Report FZKA 6002, Forschungszentrum Karlsruhe, Karlsruhe (Germany).

Jareño, E. D., Castro, M. J., Maldonado, S. I., and Hernández, F. A. (2010). The effects of Cu and cooling rate on the fraction and distribution of epsilon phase in Zn-4Al-(3-5.6)Cu alloys. *Journal of Alloys and Compounds*, 490(1-2):524–530.

Jeltsch-Fricker, R. (2007). Variationsrechnung. Skript zur Vorlesung in den Technikstudiengängen der Universität Kassel.

Johlitz, M. (2012). On the representation of ageing phenomena. *The Journal of Adhesion*, 88:620–648.

Johlitz, M. and Diebels, S. (2011a). Characterisation of a polymer using biaxial tension tests. part i: Hyperelasticity. *Archive of Applied Mechanics*, 81(10):1333–1349.

Johlitz, M. and Diebels, S. (2011b). Effective mechanical behavior of filled polymers. *Mechanics of Advanced Materials and Structures*, 18(2):106–114.

Johlitz, M., Diebels, S., Batal, J., Steeb, H., and Possart, W. (2008a). Size effects in polyurethane bonds: experiments, modelling and parameter identification. *Journal of Materials Science*, 43(14):4768–4779.

Johlitz, M. and Diercks, Nico ans Lion, A. (2014). Thermo-oxidative ageing of elastomers: A modelling approach based on a finite strain theory. *International Journal of Plasticity*, 63:138–151.

Johlitz, M. and Lion, A. (2013). Chemo-thermomechanical ageing of elastomers based on multiphase continuum mechanics. *Continuum Mechanics and Thermodynamics*, 25:605–624.

Johlitz, M., Steeb, H., Jänicke, R., and Diebels, S. (2008b). Effective properties and size effects in filled polymers. *GAMM-Mitteilungen*, 31(2):210–224.

Johnen, H. (1981). *Zink-Taschenbuch*. Metall-Verlag, Berlin-Heidelberg, 3rd edition.

Kallien, L. H. and Busse, M. (2009). Ursachen und Möglichkeiten zur Minimierung der Alterungsvorgänge bei Zinkdruckgusslegierungen. Technical report, Hochschule Aalen and IFAM Bremen.

Korelc, J. (2002). Multi-language and multi-environment generation of nonlinear finite element codes. *Engineering with Computers*, 18(4):312–327.

Korelc, J. (2009). Automation of primal and sensitivity analysis of transient coupled problems. *Computational Mechanics*, 44(5):631–649.

Korzeniowski, T. and Weinberg, K. (2018). A markov chain approach to damage evolution in die-cast ZAMAK. *Technische Mechanik*, 38:135–147.

Krämer, S., Rothe, S., and Hartmann, S. (2015). Homogeneous stress-strain states computed by 3D-stress algorithms of FE-codes: application to material parameter identification. *Engineering with Computers*, 31:141–159.

Kreißig, R., Benedix, U., and Görke, U. J. (2001). Statistical aspects of the identification of material parameters for elasto-plastic models. *Archive of Applied Mechanics*, 71:123–134.

Krempl, E. (1979). Viscoplasticity based on total strain. the modelling of creep with special considerations on initial strain and aging. *Journal of Engineering Materials and Technology*, 101:380–386.

Lang, J. (2001). Adaptive multilevel solution of nonlinear parabolic pde systems - theory, algorithm, and applications. In *Lecture Notes in Computational Science and Engineering*.

Lee, E. (1969). Elastic-plastic deformation at finite strains. *Journal of Applied Mechanics*, 36:1–6.

Lee, E. H. and Liu, D. T. (1967). Finite-strain elastic-plastic theory of application to plane wave analysis. *Journal of Applied Physics*, 38:19–27.

Leis, W. and Kallien, L. H. (2011). Ageing of zink alloys. *International Foundry Research*, 64(1):2–23.

Lemaitre, J. and Chaboche, J.-L. (1990). *Mechanics of solid materials*. Cambridge University Press, Cambridge.

Levenberg, K. (1944). A method for the solution of certain problems in least squares. *Quarterly of Applied Mathematics*, 2:164–168.

Li, X., Guo, G., Xiao, J., Song, N., and Li, D. (2014). Constitutive modeling and the effects of strain-rate and temperature on the formability of Ti-6Al-4V alloy sheet. *Materials and Design*, 55:325–334.

Lin, Y. C., Chen, X. M., Wen, D. X., and Chen, M. S. (2016). A novel unified dislocation density-based model for hot deformation behavior of a nickel-based superalloy under dynamic recrystallization conditions. *Applied Physics A*, 122(9):1–16.

Lin, Y. C., Li, L., and Jiang, Y. (2012). A phenomenological constitutive model for describing thermo-viscoplastic behavior of Al-Zn-Mg-Cu alloy under hot working condition. *Experimental Mechanics*, 52(8):993–1002.

Lion, A. (1994). *Materialeigenschaften der Viskoplastizität*. PhD thesis, Universität Gesamthochschule Kassel.

Lion, A. (2000a). Constitutive modelling in finite thermoviscoplasticity: a physical approach based on nonlinear rheological models. *International Journal of Plasticity*, 16:469–494.

Lion, A. (2000b). *Thermomechanik von Elastomeren. Experimente und Materialtheorie*. Habilitation, Institute of Mechanics, University of Kassel. Report No. 1/2000.

Lion, A., Dippel, B., and Liebl, C. (2014). Thermomechanical material modelling based on a hybrid free energy density depending on pressure, isochoric deformation and temperature. *International Journal of Solids and Structures*, 51:729–739.

Lion, A. and Johlitz, M. (2012). On the representation of chemical ageing of rubber in continuum mechanics. *International Journal of Solids and Structures*, 49:1227–1240.

Liu, M. C. M. and Krempl, E. (1979). A uniaxial viscoplastic model based on total strain and overstress. *Journal of the Mechanics and Physics of Solids*, 27:377–391.

Liu, Y., Li, H.-y., Jiang, H.-f., and Lu, X.-c. (2013). Effects of heat treatment on microstructure and mechanical properties of ZA27 alloy. *Transactions of Nonferrous Metals Society of China*, 23(3):642–649.

Lu, S. and Pister, K. (1975). Decomposition of deformation and representation of the free energy function for isotropic thermoelastic solids. *International Journal of Solids and Structures*, 11(7):927 – 934.

Lubarda, V. A. (2001). *Elastoplasticity Theory*. CRC Press, Boca Raton.

Lubliner, J. (1985). A model of rubber viscoelasticity. *Mechanics Research Communications*, 12:93–99.

Lubliner, J. (1990). *Plasticity Theory*. Macmillan Publishing Company, New York.

Maghous, S. and Creus, G. (2003). Periodic homogenization in thermoviscoelasticity: case of multilayered media with ageing. *International Journal of Solids and Structures*, 40:851–870.

Mahnken, R. (1998). Theoretische und numerische Aspekte zur Parameteridentifikation und Modellierung bei metallischen Werkstoffen. Technical report, Institut für Baumechanik und Numerische Mechanik, Universität Hannover.

Mahnken, R. (2000). An inverse finite-element algorithm for parameter identification of thermoelastic damage models. *International Journal for Numerical Methods in Engineering*, 48(7):1015–1036.

Mahnken, R. and Stein, E. (1996). A unified approach for parameter identification of inelastic material models in the frame of the finite element method. *Computer Methods in Applied Mechanics and Engineering*, 136:225–258.

Mahnken, R. and Stein, E. (1997). Parameter identification for finite deformation elastoplasticity in principal directions. *Computer Methods in Applied Mechanics and Engineering*, 147:17–39.

Malvern, L. E. (1969). *Introduction to the mechanics of a continuous medium*. Prentice-Hall, Englewood Cliffs, NJ.

Mandel, J. (1971). *Plasticité classique et viscoplasticité, Courses and Lectures, No. 97*. International Center for Mechanical Sciences, Udine, Springer, New York.

Marquardt, D. W. (1963). An algorithm for least-squares estimation of nonlinear parameters. *Journal of the Society for Industrial and Applied Mathematics*, 11(2):431–441.

Marquis, D. and Costa Mattos, H. (1991). Modeling of plasticity and aging as coupled phenomena. *International Journal of Plasticity*, 7:865–877.

Marquis, D. and Lemaitre, J. (1988). Constitutive equations for the coupling between elasto-plasticity damage and aging. *Revue de Physique Appliquée*, 23:615–624.

Martinez Page, M. and Hartmann, S. (2018a). Modeling of aging effects in a zinc die casting alloy. *Technische Mechanik*, 38:55–72.

Martinez Page, M. A. and Hartmann, S. (2018b). Experimental characterization, material modeling, identification and finite element simulation of the thermo-mechanical behavior of a zinc die-casting alloy. *International Journal of Plasticity*, 101:74–105.

Martinez Page, M. A., Ruf, M., and Hartmann, S. (2018). Numerical modeling of the thickness dependence of zinc die-cast materials. *Computational Mechanics*, 62(4):655–667.

Martinez Page, M. A., Weidenfeller, B., and Hartmann, S. (2019). Influence of temperature and aging on the thermal diffusivity, thermal conductivity and heat capacity of a zinc die casting alloy. *Journal of Alloys and Compounds*, 786:1060 – 1067.

McDowell, D. L. (1992). A nonlinear kinematic hardening theory for cyclic thermoplasticity and thermoviscoplasticity. *International Journal of Plasticity*, 8(6):695–728.

Meschke, G. (1996). Consideration of aging of shotcrete in the context of a 3D viscoplastic material model. *International Journal for Numerical Methods in Engineering*, 39:3123–3143.

Miehe, C. (1988). *Zur numerischen Behandlung thermomechanischer Prozesse*. Report No. F88/6, University of Hannover, Institut für Baumechanik und Numerische Mechanik.

Murray, J. (1983). The Al-Zn (aluminium-zinc) system. *B. Alloy Phase Diagrams*, 4:55–73.

Naumann, U. (2012). *The art of differentiating computer programs: an introduction to algorithmic differentiation*. SIAM Society for Industrial and Applied Mathematics.

Netz, T., Düster, A., and Hartmann, S. (2013a). High-order finite elements compared to low-order mixed element formulations. *ZAMM Journal of Applied Mathematics and Mechanics*, 93:163 – 176.

Netz, T., Hamkar, A.-W., and Hartmann, S. (2013b). High-order quasi-static finite element computations in space and time with application to finite strain viscoelasticity. *Computers and Mathematics with Applications*, 66:441 – 459.

Netz, T. and Hartmann, S. (2015). A monolithic finite element approach using high-order schemes in time and space applied to finite strain thermo-viscoelasticity. *Computers and Mathematics with Applications*, 70:1457–1480.

Nogowizin, B. (2011). *Theorie und Praxis des Druckgusses*. Schiele & Schön, Berlin, 1st edition.

Oberkampf, W. L. and Trucano, T. G. (2002). Verification and validation in computational fluid dynamics. *Progress in Aerospace Sciences*, 38:209–272.

Perzyna, P. (1966). Fundamental problems in viscoplasticity. *Advances in Applied Mechanics*, 9:243–377.

Pola, A., Gelfi, M., M., L. V. G., and Montesano, L. (2015). On the aging of a hyper-eutectic Zn-Al alloy. *La Metallurgia Italiana*, 4(4):37–41.

Quint, K. J. (2012). *Thermomechanically coupled processes for functionally graded materials: experiments, modelling, and finite element analysis using high-order DIRK-methods*. Phd-thesis, report no. 2/2012, Institute of Applied Mechanics, Clausthal University of Technology, Clausthal-Zellerfeld.

Quint, K. J., Hartmann, S., Rothe, S., Saba, N., and Steinhoff, K. (2011). Experimental validation of high-order time-integration for non-linear heat transfer problems. *Computational Mechanics*, 48:81–96.

Rabbat, N. B. G., Sangiovanni-Vincentelli, A. L., and Hsieh, H. Y. (1979). A multilevel Newton algorithm with macromodeling and latency for the analysis of large-scale nonlinear circuits in the time domain. *IEEE Transactions on Circuits and Systems*, 26:733–740.

Rabinowicz, E. (1951). The nature of the static and kinetic coefficients of friction. *Journal of Applied Phisics*, 22:1373–1379.

Reese, S. (2001). *Thermomechanische Modellierung gummiartiger Polymer-Strukturen*. Habilitation, Institut für Baumechanik und Numerische Mechanik, Universität Hannover. Report No. F01/4.

Rothe, S. (2015). *Electro-Thermo-Mechanical Modeling of Field Assisted Sintering Technology: Experiments, Constitutive Modeling and Finite Element Analysis*. Phd-thesis, report no. 1/2015, Institute of Applied Mechanics, Clausthal University of Technology, Clausthal-Zellerfeld.

Rothe, S., Erbts, P., Düster, A., and Hartmann, S. (2015). Monolithic and partitioned coupling schemes for thermo-viscoplasticity. *Computer Methods in Applied Mechanics and Engineering*, 293:375 – 410.

Rothe, S., Hamkar, A.-W., Quint, K. J., and Hartmann, S. (2012). Comparison of diagonal-implicit, linear-implicit and half-explicit Runge-Kutta methods in non-linear finite element analyses. *Archive of Applied Mechanics*, 82(8):1057 – 1074.

Rothe, S. and Hartmann, S. (2015). Automatic differentiation for stress and consistent tangent computation. *Archive of Applied Mechanics*, 85:1103–1125.

Rusinek, A., Rodriguez-Martinez, J. A., and Arias, A. (2010). A thermo-viscoplastic constitutive model for FCC metals with application to OFHC copper. *International Journal of Mechanical Science*, 52(2):120–135.

Sachs, L. and Hedderich, J. (2012). *Angewandte Statistik*. Springer-Verlag Berlin Heidelberg, Berlin/Heidelberg.

Savaskan, T. and Pasa Hekimoglu, A. (2014). Microstructure and mechanical properties of Zn-15Al-based ternary and quaternary alloys. *Materials Science and Engineering A*, 603:52–57.

Schiesser, W. E. (1991). *The Numerical Method of Lines: Integration of Partial Differential Equations*. Academic Press.

Schiesser, W. E. and Griffiths, G. W. (2009). *A compendium of partial differential equation models: Method of lines analysis with Matlab*. Cambridge University Press, New York.

Schindler, S., Steinmann, P., Aurich, J. C., and Zimmermann, M. (2017). A thermo-viscoplastic constitutive law for isotropic hardening of metals. *Archive of Applied Mechanics*, 87(1):129–157.

Schwarz, H. R. and Köckler, N. (2004). *Numerische Mathematik*. Teubner, Stuttgart.

Schwarz, H. R. and Köckler, N. (2006). *Numerische Mathematik*. Teubner Verlag, Wiesbaden, 6. edition.

Schwer, L. E. (2007). An overview of the ptc 60/v&v 10: guide for verification and validation in computational solid mechanics. *Engineering with Computers*, 23(4):245–252.

Simo, J. C. and Hughes, T. J. R. (1998). *Computational Inelasticity*. Springer Verlag, New York.

Simo, J. C. and Taylor, R. L. (1985). Consistent tangent operators for rate-independent elastoplasticity. *Computer Methods in Applied Mechanics and Engineering*, 48:101–118.

Steeb, H. and Diebels, S. (2004). Modeling thin films applying an extended continuum theory based on a scalar-valued order parameter.: Part i: isothermal case. *International Journal of Solids and Structures*, 41(18):5071 – 5085.

Szabó, B., Düster, A., and Rank, E. (2004). *The p-Version of the Finite Element Method*. Hrsg. von E. Stein, R. de Borst and T.J.R. Hughes. John Wiley and Sons, 2 edition.

Szabó, B. and Babuška, I. (1991). *Finite Element Analysis*. John Wiley & Sons, New York.

Szabo, B., Düster, A., and Rank, E. (2004). The p-version of the finite element method. In *Encyclopedia of Computational Mechanics*, chapter 5, pages 119–139. John Wiley & Sons.

Tarantola, A. (2005). *Inverse Problem Theory and Methods for Model Parameter Estimation*. SIAM, Philadelphia.

Truesdell, C. and Noll, W. (1965). *The Non-Linear Field Theories of Mechanics*, volume III/3 of *Encyclopedia of Physics*. Springer Verlag, Berlin.

Truesdell, C. and Noll, W. (2004). *The Non-Linear Field Theories of Mechanics*. Springer Verlag, Berlin, 3st edition.

Tsakmakis, C. and Willuweit, A. (2004). A comparative study of kinematic hardening rules at finite deformations. *International Journal of Non-Linear Mechanics*, 39(4):539 – 554.

Valanis, K. C. (1971a). A theory of viscoplasticity without a yield surface, Part I generaltheory. *Archives of Mechanics*, 23:517–533.

Valanis, K. C. (1971b). A theory of viscoplasticity without a yield surface, Part II. application to mechanical behavior of metals. *Archives of Mechanics*, 23:535–551.

Vilamosa, V., Clausen, H., Børvik, T., Holmedal, B., and Hopperstand, O. (2016). A physically-based constitutive model applied to AA6082 aluminium alloy at large strains, high strain rates and elevated temperatures. *Materials and Design*, 103:391–405.

Vilamosa, V., Clausen, H., Børvik, T., and Skjervold, S. (2015). Behaviour of Al-Mg-Si alloys at a wide range of temperatures and strain rates. *International Journal of Impact Engineering*, 86:223–239.

Willis, J. (1969). Some constitutive equations applicable to problems of large dynamic plastic deformation. *Journal of the Mechanics and Physics of Solids*, 17(5):359 – 369.

Wittekindt, J. (1991). *Die numerische Lösung von Anfangs-Randwertproblemen zur Beschreibung inelastischen Werkstoffverhaltens*. Doctoral thesis, Department of Mathematics, University of Darmstadt.

Wriggers, P. (2009). *Nonlinear Finite Element Methods*. Springer Verlag, Berlin.

Wu, Z., Sandlöbes, S., Wu, L., Hu, W., and Korte-Kerzel, S. (2016). Mechanical behaviour of Zn–Al–Cu–Mg alloys: Deformation mechanisms of as-cast microstructures. *Material Science and Engineering*, 651:675–687.

Yu, D., Chen, X., Yu, W., and Chen, G. (2012). Thermo-viscoplastic modeling incorporating dynamic strain aging effect on the uniaxial behavior of Z2CND18. 12N stainless steel. *International Journal of Plasticity*, 37:119–139.

ZD (2019). Zinc-diecasting `www.zinc-diecasting.info`.

Zhang, J., Yu, Q., Jiang, Y., and Li, Q. (2011). An experimental study of cyclic deformation of extruded AZ61A magnesium alloy. *International Journal of Plasticity*, 27(5):768–787.

Zhang, P., Li, Z., Liu, B., and Ding, W. (2017). Tensile properties and deformation behaviors of a new aluminum alloy for high pressure die casting. *Journal of Materials Science & Technology*, 33:367–378.

Zhu, Y. (2001). Phase transformations of eutectoid Zn-Al alloys. *Journal of Materials Science*, 36:3973–3980.

Zhu, Y. (2004). General rule of phase decomposition in Zn-Al based alloys (II) – on effects of external stresses on phase transformations –. *Material Transactions*, 45(11):3083–3097.

Zhu, Y., Hinojosa, J., Yue, T., and Lee, W. (2002). Structural evolution in a continuously cast eutectoid Zn–Al-based alloy. *Materials Characterization*, 48:315–322.

Zhu, Y., Kang, G., Kan, Q., Bruhns, O. T., and Liu, Y. (2016). Thermo-mechanically coupled cyclic elasto-viscoplastic constitutive model of metals: Theory and application. *International Journal of Plasticity*, 79:111–152.

Zhu, Y., Lee, W., and To, S. (2003a). Ageing characteristics of Zn-Al based alloy (ZnAl7Cu3). *Journal of Materials Science*, 38:1945–1952.

Zhu, Y., Man, H., Dorantes-Rosales, H., and Lee, W. (2003b). Ageing characteristics of furnace cooled eutectoid Zn-Al based alloys. *Journal of Materials Science*, 38:2925–2934.

Zhu, Y., Man, H., and Lee, W. (1999). Exothermic reaction in eutectoid Zn–Al based alloys. *Materials Science and Engineering: A*, 268(1):147 – 153.

Zhu, Y. H. and Orozco, E. (1995). Effects of tensile stress on microstructural change of eutectoid Zn-Al alloy. *Metallurgical and Materials Transactions A*, 26(10):2611–2615.

Zwienkiewicz, O. C. and Taylor (2005). *The finite element method: Its basis and fundamentals*. Butterworth-Heinemann, Burlington, 6th edition.

Zwienkiewicz, O. C., Taylor, R. L., and Zhu, J. Z. (2005). *The finite element method for solid and structural mechanics*. Butterworth-Heinemann, Burlington, 6th edition.

List of publications

1. Martinez Page, M. A., Weidenfeller, B., Hartmann, S.: Influence of temperature and aging on the thermal diffusivity, thermal conductivity and heat capacity of a zinc die casting alloy, *Journal of Alloys and Compounds* 786, 1060–1067, 2019

2. Martinez Page, M. A., Hartmann, S.: Experimental characterization, material modeling, identification and finite element simulation of the thermo-mechanical behavior of a zinc die-casting alloy, *International Journal of Plasticity* 101, 74–105, 2018

3. Martinez Page, M. A., Hartmann, S.: Modeling of aging effects in a zinc die casting alloy, *Technische Mechanik* 38, 55–72, 2018

4. Martinez Page, M. A., Ruf, M., Hartmann, S.: Numerical modeling of the thickness dependence of zinc die-cast materials, *Computational Mechanics* 62, 655–667, 2018

5. Martinez Page, M. A., Hartmann, S.: Effects of aging in the thermo-mechanical response of a die casting alloy, *PAMM Proceedings in Applied Mathematics and Mechanics* 18, 2018, e201800043, pp. 1–2

6. Martinez Page, M. A., Hartmann, S.: Experimental characterization and modeling of the thermo-mechanical behavior of a zinc die-casting material, in: (Ed.) Clausthaler Zentrum für Materialtechnik, Tagungsband 2. Niedersächsisches Symposium Materialtechnik, 23. bis 24. Februar 2017, *Fortschrittsberichte der Materialforschung und Werkstofftechnik/Bulletin of Materials Research and Engineering*, Shaker Verlag, Aachen, 41–52, 2017

7. Martinez Page, M. A., Ruf, M., Hartmann, S.: Modeling and Simulation of the Thickness Dependence in Die Casting Structures. *PAMM Proceedings in Applied Mathematics and Mechanics* 17, 449–450, 2017

8. Martinez Page, M. A., Hartmann, S.: Experimental investigation, material modeling and parameter identification of a zinc die-casting alloy, *PAMM Proceedings in Applied Mathematics and Mechanics* 16, 371–372, 2016

Curriculum Vitae

Personal Data

Name	Maria de los Angeles Martinez Page
Date of birth	24 December 1988
Place of birth	Murcia (Spain)
Nationality	Spanish

Professional Experience

10/2013 – 04/2019	Research Assistant, Clausthal University of Technology, Clausthal-Zellerfeld (Germany)
02/2013 – 04/2013	Internship, Huf Hülsbeck & Fürst GmbH & Co. KG, Günding (Germany)

Education

10/2013 – 04/2019	PhD student, Clausthal University of Technology, Clausthal-Zellerfeld (Germany)
Research Topic	“Thermo-mechanical behavior of a zinc die casting alloy considering natural aging”
03/2011 – 09/2013	Diploma student of Mechanical Engineering, Double degree program: Cooperation between Clausthal University of Technology (Germany) and Universidad Politécnica de Valencia (Spain)
Main topics	Finite Element Method, Computational Inelasticity, Tribology
student research project	“Parameter estimation of a machine’s model”
student research project	“Construction and testing of an analog strain gauge transducer for industrial application with automatic adjustment of the offset voltage”
Diploma Thesis	“Investigation of a material model of compressible plasticity and its implementation in Abaqus”
09/2006 – 09/2013	Student of mechanical Engineering, Universidad Politécnica de Valencia, Valencia (Spain)
09/2002 – 06/2006	High school student, Instituto Alfonso X el Sabio, Murcia (Spain)